Journal of Nanomaterials

Hierarchical Nanostructures: Novel Synthetic Strategies and Advanced Applications

Lead Guest Editor: Nguyen Duc Cuong
Guest Editors: Duong Tuan Quang, Tran Xuan Mau, and Mai Duy Hien

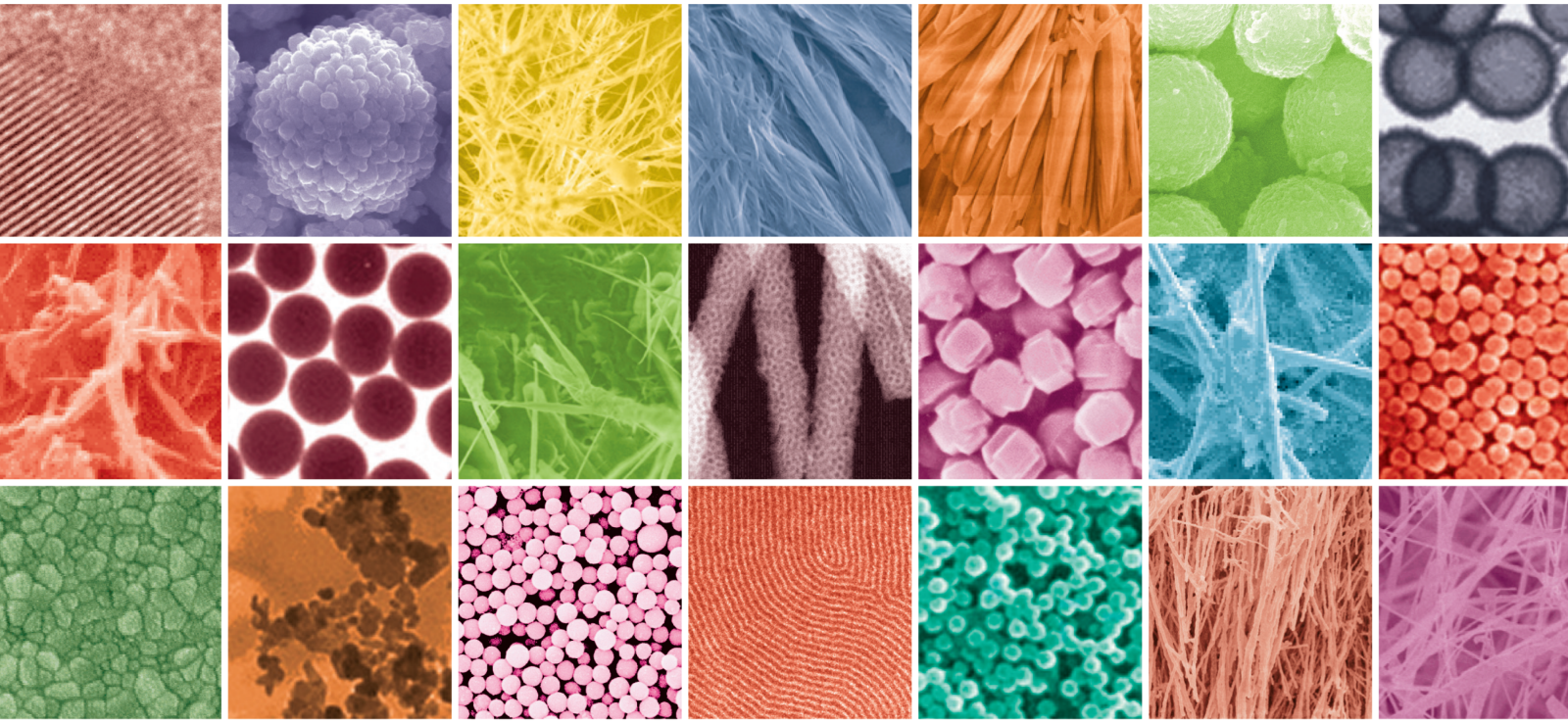

Hierarchical Nanostructures: Novel Synthetic Strategies and Advanced Applications

Journal of Nanomaterials

Hierarchical Nanostructures: Novel Synthetic Strategies and Advanced Applications

Lead Guest Editor: Nguyen Duc Cuong
Guest Editors: Duong Tuan Quang, Tran Xuan Mau, and Mai Duy Hien

Contents

Hindawi
Journal of Nanomaterials
Volume 2021, Article ID 6135920, 11 pages
https://doi.org/10.1155/2021/6135920

Research Article

Synthesis of Biogenic Silver Nanoparticles with Eco-Friendly Processes Using *Ganoderma lucidum* Extract and Evaluation of Their Theranostic Applications

Vinh Phu Nguyen,[1,2] Hieu Le Trung,[1] Thu Huong Nguyen,[1] DongQuy Hoang,[3,4] and Thai Hoa Tran[1]

[1]*Department of Chemistry, University of Sciences, Hue University, 77 Nguyen Hue Street, Hue City 530000, Vietnam*
[2]*Faculty of Basic Sciences, University of Medicine and Pharmacy, Hue University, 06 Ngo Quyen Street, Hue City 530000, Vietnam*
[3]*Faculty of Materials Science and Technology, University of Science, Vietnam National University Ho Chi Minh City, 700000, Vietnam*
[4]*Vietnam National University Ho Chi Minh City, 700000, Vietnam*

Correspondence should be addressed to DongQuy Hoang; htdquy@hcmus.edu.vn and Thai Hoa Tran; tthaihoa@hueuni.edu.vn

Received 16 April 2021; Accepted 16 July 2021; Published 4 August 2021

Academic Editor: Dong kee Yi

The green synthesis of silver nanoparticles (AgNPs) using plant extract, the cost-effective solution, and the abundance and environmental issue have been gaining much attention to scientists. *Ganoderma lucidum* (GL) commonly known as Lingzhi in Chinese and Reishi in Japanese, with a proven anticancer benefit, is discovered in the buffer zone of Bach Ma National Park, Nam Dong district, Thua Thien Hue province. In this work, the AgNPs were synthesized in a simple and effective biochemical reduction process using GL which is one of the biological organisms, as a reducing and stable agent. The optimum conditions of various experimental parameters such as pH, reaction time, concentration, and temperature were investigated. Obtained AgNPs were characterized by UV-Vis, FTIR, SEM, energy-dispersive X-ray spectroscopy (EDX), X-ray diffraction (XRD), and transmission electron microscopy (TEM). The effects of AgNP/GL materials and GL aqueous extraction on the antiproliferative activities of HepG2 and MCF-7 cells were studied. The novel AgNP/GL-based multicomponent suspension is a key compound that could find a good application in the medical and pharmaceutical sciences.

1. Introduction

Cancer is a disease caused when the normal cell proliferation control is lost. Human hepatocellular carcinoma (HepG2) is one of the types of cancer which causes a number of deaths with cirrhosis in each year [1]. Besides, breast cancer (MCF-7) is the cancer that forms in the cells of the breast and immense among women in the world, recording the second public inception of death in women with 16% of all female cancers [2]. In recent years, although there are a number of methods for treating cancer disease, they spend a lot of money cost and have more weak points such as the limitation on distinguishing between normal and diseased cells and elimination from the human body [3]. To solve this phenomenon, developing a new material with the ability to hold and release drugs in environments with suitable pH and temperature is essential [4]. Metal nanomaterials have received a great deal of scientist's concern [5].

Noble metal nanomaterials such as Au, Ag, and Pt with size particles between 1 and 100 nanometers have distinguished properties such as the chemical and optical properties due to a surface plasmon resonance (SPR) [6–9]. Silver metal has attracted substantial attention because of a potential application in different areas such as antibacterial agents, catalysis, biological and chemical sensors, water treatment, and biomedicine [10–14]. Besides, the nanosized silver particles (AgNPs) have the ability to inhibit a variety of cancer cells especially HepG2 and MCF-7 [15, 16] and the

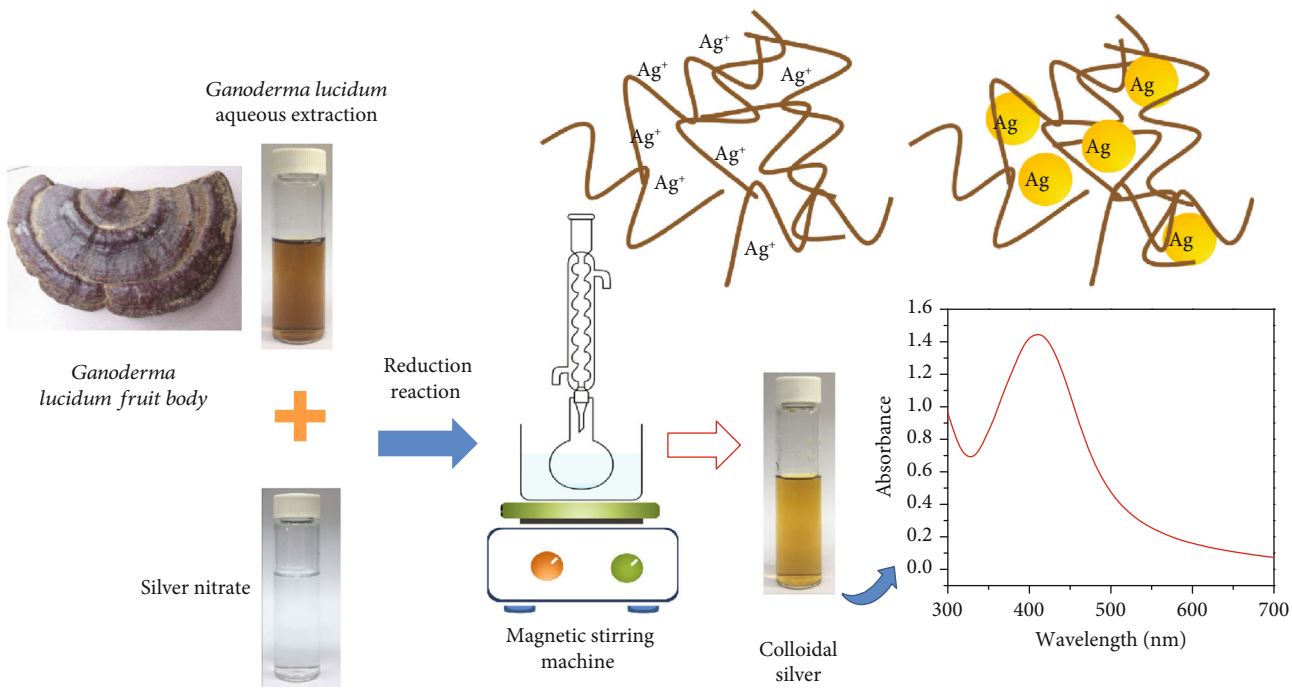

Figure 1: Schematic diagram of the biosynthesis of AgNPs using aqueous extract of GL.

anticancer activity of AgNPs was dependent on the size, shape, and surface charge of these particles [17].

In general, the AgNPs are synthesized by two main methods: the physical and chemical methods [18]. Although the particles synthesized by these two methods have defined shape and size, the procedures require a lot of expensive equipment and often use toxic and hazardous chemicals, which are considered highly harmful to human health [19, 20]. Hence, a novel green strategy for producing AgNPs has been developed by using extracted solutions from natural resources such as bacteria [21], fungi [22, 23], marine algae [24], lichens [25], and plants [26]. These extracted solutions not only are biocompatible and nontoxic to the human body but also play an important factor in reducing and protecting agents in the process of synthesis of AgNPs [27, 28]. Moreover, this method also provides an advance over other methods because it could be cataloged, eco-friendly, and low cost [29].

Ganoderma lucidum (GL) has been known as a medical mushroom and applied to traditional medicine for past centuries [30] and is one of the biological resources for the synthesis AgNPs. Although GL contains different natural compounds, polysaccharide and triterpenoids are the most important components [31] and these compounds cause biological activities such as antiallergic [32], anti-inflammatory [33], antiviral [34], anticancer [35], and antidiabetes [36], which contributes to health benefits.

In this research, the AgNPs were synthesized by the "green method" and the process was carried out by a reduction reaction of silver nitrate using the aqueous extraction of *G. lucidum* as a reducing and protecting agent. This research focused on the impact of the reaction parameters such as temperature, time, concentration of silver nitrate, and pH value. The AgNPs were characterized in the aspects of the morphological properties, structure, and size distribution. The preliminary in vitro cytotoxicity was investigated on both human hepatocellular carcinoma (HepG2) and human breast cancer cell (MCF-7) via the MTT method.

2. Experimental Methods

2.1. Materials. The fruit bodies of GL collected from the buffer zone of Bach Ma National Park from Nam Dong district, Thua Thien Hue province, were dried and ground into powder.

Silver nitrate ($AgNO_3{\cdot}5H_2O$, 98%), ammonium hydroxide (NH_4OH, 25%), nitric acid (HNO_3, 90%), and ethanol (C_2H_5OH, 98%) were purchased from Xilong Chemical Co., Ltd. Human hepatocellular carcinoma (HepG2) and human breast carcinoma (MCF-7), Dulbecco's modified Eagle's medium (DMEM), fetal bovine serum (FBS), penicillin, streptomycin, 3-(4,5-dimethylthiazol-2-yl)-2,5-diphenyltetrazolium bromide (MTT), and dimethyl sulfoxide (DMSO) were purchased from Sigma-Aldrich Chemical Company, USA. All chemicals were used without further purification.

2.2. Preparation of Aqueous Extraction of Ganoderma lucidum. Aqueous extraction of GL was prepared by using the reflux method [37]. A 2.0 g of mushroom powder was added to 200 mL of distilled water. The mixture was heated to 85°C for 4 h under stirring condition. A yellowish solution was then centrifuged with 4300 rpm for 20 min. The solution was concentrated to 50 mL. In addition, four times the volume of 96% ethanol was added to the concentrated solution. The mixture was placed in a refrigerator for 24 h,

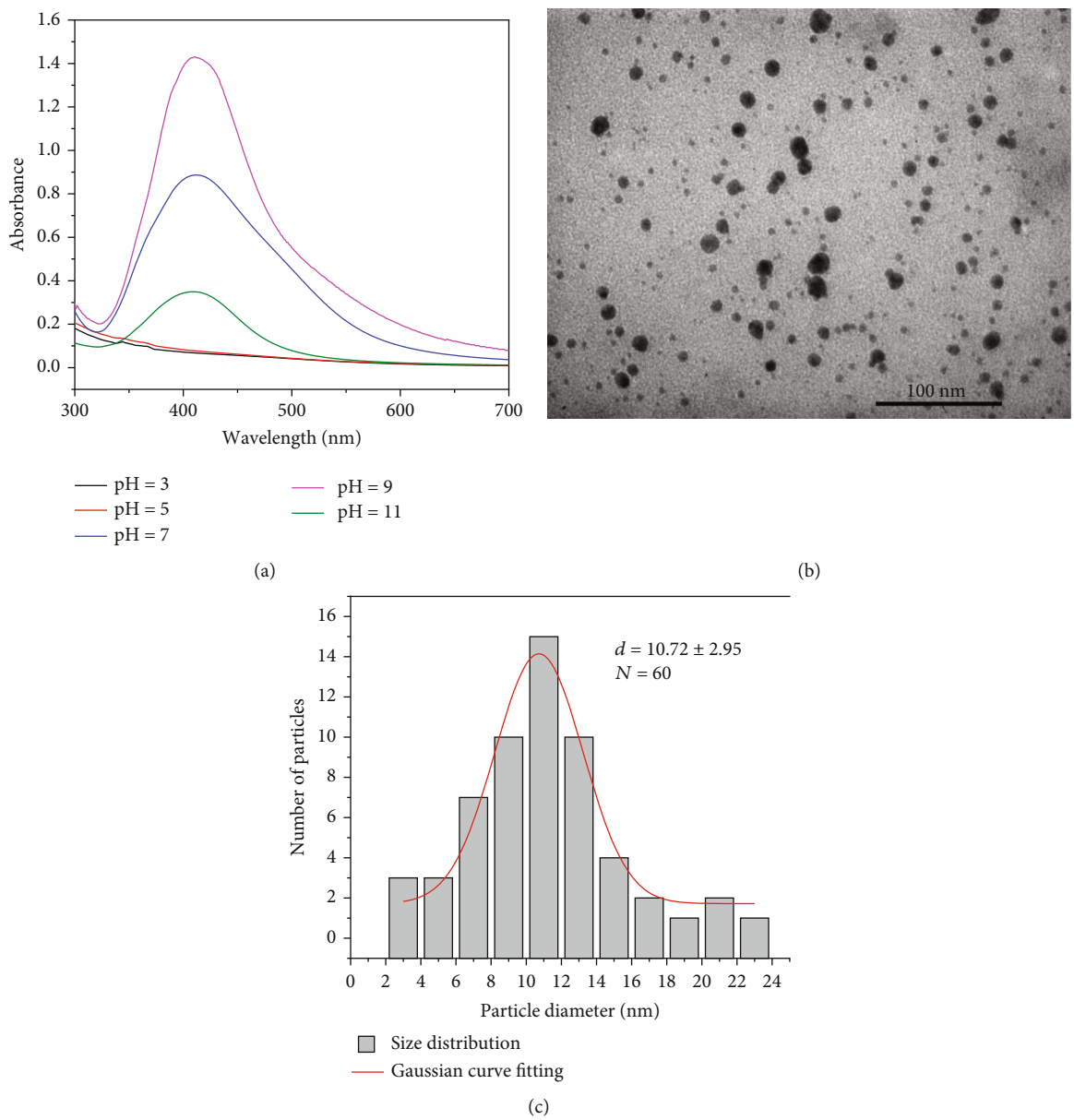

Figure 2: (a) UV-Vis spectra of AgNPs/GL obtained with different pH values; (b) TEM image of AgNPs/GL with pH 9; (c) histogram size distribution curve of AgNPs/GL (pH 9).

subsequently centrifuging (4300 rpm, 20 min). The precipitate was washed with acetone and dried at 75°C for 6 h. The dried aqueous extraction was stored for further experiments.

2.3. Biosynthesis of Silver Nanoparticles. In a typical process, the dry aqueous extract of *G. lucidum* was redissolved in distilled water to obtain an aqueous extraction solution of GL (A-GL) with a concentration of 1 g·mL^{-1}. 90 mL of this solution was mixed with 10 mL aqueous solution of silver nitrate with different concentrations. The reaction mixture was conducted under the stirring condition at 120 rpm. The pH of the mixture was adjusted by adding dropwise ammonia solution (25%, *v*/*v*) or nitric acid solution 0.01 M. The optimum condition for the synthesis process of AgNPs was studied by varying some reaction factors such as pH (3, 5, 7, 9, and 11), time (0.5 to 7 h), concentration of silver nitrate (0.5, 1, and 1.5 mM), and reaction temperature (65, 75, 85, and 95°C). To obtain AgNPs, the suspension was precipitated overnight by ethanol 95% (*v*/*v*), followed by centrifugation (4000 rpm, 20 min). The precipitate was dried at 75°C under vacuum for 24 h. The obtained pellets were symbolized as AgNPs/GL and stored for further studies.

2.4. Characterization of Silver Nanoparticles. The optical properties of AgNPs/GL were investigated by measuring optical absorption spectra in the UV-Vis region with a V-630 spectrometer. The crystal phase of products was characterized by X-ray diffraction (XRD, D8-BRUKER, Germany) equipped with Cu Kα radiation ($\lambda = 1.5406$ Å). The morphology and particle size distribution of the synthesis products were observed by transmission electron microscopy (TEM, JEOL-1010, Japan); also, the surface characteristics

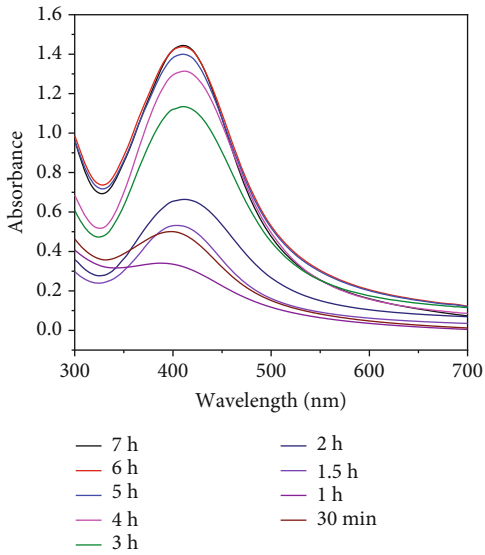

Figure 3: UV-Vis spectra of AgNPs/GL obtained at different time intervals (30 min–7 h).

were assessed using a scanning electron microscope (SEM) (JEOL JSM-6510, Japan). The presence of silver elements was confirmed by energy-dispersive X-ray spectroscopy (EDX). To investigate the functional groups of both A-GL and AgNPs/GL, a Fourier-transform infrared (FTIR) study was carried out with the R-Prestige-21 Shimadzu FTIR spectrophotometer, using KBr pellet method.

2.5. Cell Culture and Cytotoxicity Studies

2.5.1. Culture of Cells. HepG2 and MCF-7 cells were cultivated in DMEM medium, complemented with 10% FBS, penicillin (100 U/mL), and streptomycin (100 μg/mL) in the standard condition (37°C, 98% humidity, 5% CO_2, and absolutely sterile). After 24 h incubation, the cells were trypsinized, centrifuged, and washed with sterile PBS buffer solution. The viable cell count and viability were estimated using Trypan blue exclusion method. These cells having the viabilities above 95% were used to study the cytotoxicity assessment [38].

2.5.2. Cytotoxicity Assessment by MTT Assay. Firstly, the cytotoxic activities of *G. lucidum* aqueous extract and AgNPs/GL on HepG2 and MCF-7 were determined using MTT assay [39, 40]; the tumor cells were seeded with density 3×10^4 cells/mL in 96-well plates and each well was filled with 200 μL of cell suspension (HepG2 and MCF-7). This was followed by incubation of plates at 37°C with 5% CO_2 overnight to allow cell attachment. After that, the *G. lucidum* aqueous extract and AgNP/GL suspension with the concentrations of 2, 8, 32, and 128 μg·mL^{-1} were added into appropriate wells. These wells were incubated at 37°C, 5% CO_2 in 72 h. The control sample and blank sample were the well with culture medium and the well containing cells without samples, respectively. The experiments were repeated three times for validity. After the incubation period, 200 μL of MTT (5 mg·L^{-1}) was added to each well and it was continuously incubated for 4 h. The culture medium was removed, and

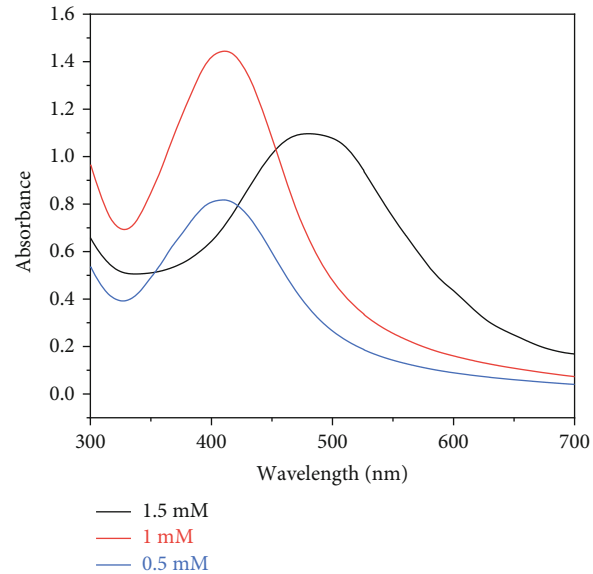

(a)

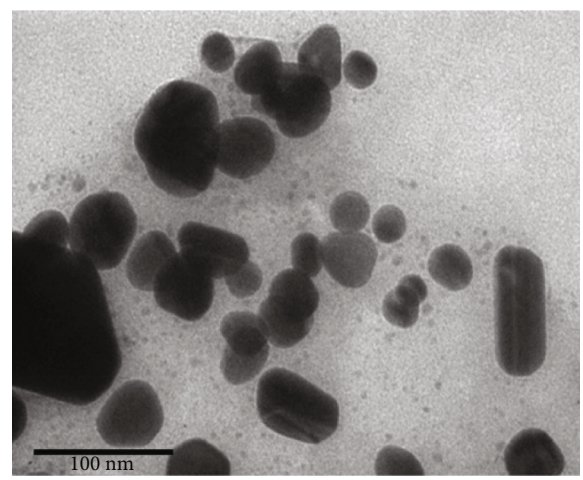

(b)

Figure 4: (a) UV-Vis spectra of AgNPs/GL obtained by varying the concentration of silver nitrate (0.5–1.5 mM). (b) TEM image of AgNPs/GL with C_{AgNO_3} = 1.5 mM.

100 μL of DMSO was added to each well. The TECAN microplate reader was used to measure the absorbance of each well at the wavelength 540 nm. The proliferation of each cell line was expressed by the percentage of cell viability.

Each concentration of treated cells, control sample, and blank sample was repeated three times for validity. After 72 h, 200 μL of MTT (5 mg·L^{-1}) was added to each well and it was incubated for 4 h. The medium was removed, and 100 μL of DMSO was added to each well. The absorbance of the 96-well plates was measured at 540 nm using a TECAN microplate reader. The effect of the sample on the proliferation of HepG2 and MCF-7 was expressed as the percentage of growth inhibition cell, using the following formula:

$$\%\text{Inhibition} = \frac{A_{\text{treated cell}} - A_{\text{blank}}}{A_{\text{control}} - A_{\text{blank}}} \cdot 100\%, \quad (1)$$

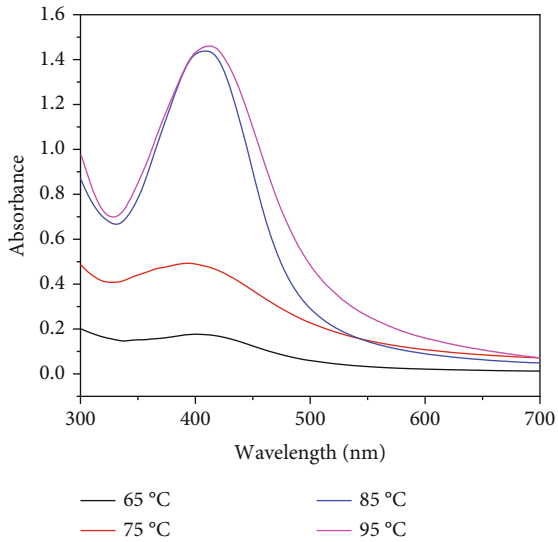

Figure 5: UV-Vis spectra of AgNPs/GL obtained by varying the temperature reaction from 65 to 95°C.

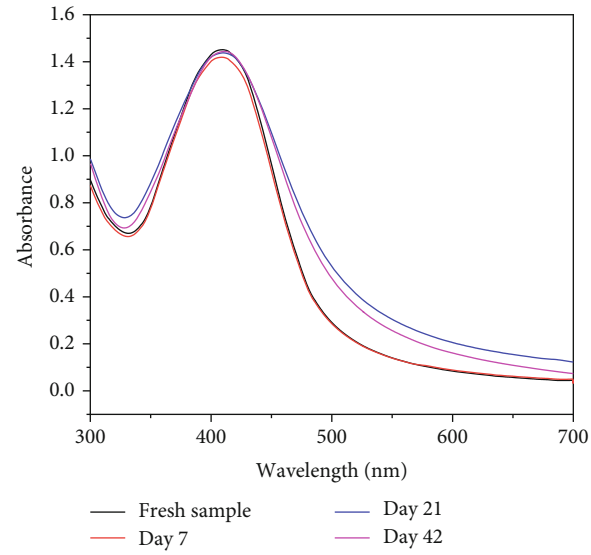

Figure 6: UV-Vis spectra of AgNP/GL colloidal solution at different storage times.

Table 1: The maximum absorbance of sample at different temperatures and storage times.

Temperature (°C)	Initially	2 weeks	4 weeks	6 weeks
65	0.1764	0.1464	0.1032	Agglomeration
75	0.4924	0.4124	Agglomeration	Agglomeration
85	1.4374	1.4314	1.4234	1.4144
95	1.4597	1.4317	1.4226	1.3882

where $A_{\text{treated cell}}$, A_{control}, and A_{blank} were absorbance peaks of treated cell sample, control sample, and blank sample, respectively. IC_{50} values were defined as sample concentration inhibiting 50% of cell growth, and they were obtained from the linear regression of calibration curve by using Microsoft Excel software.

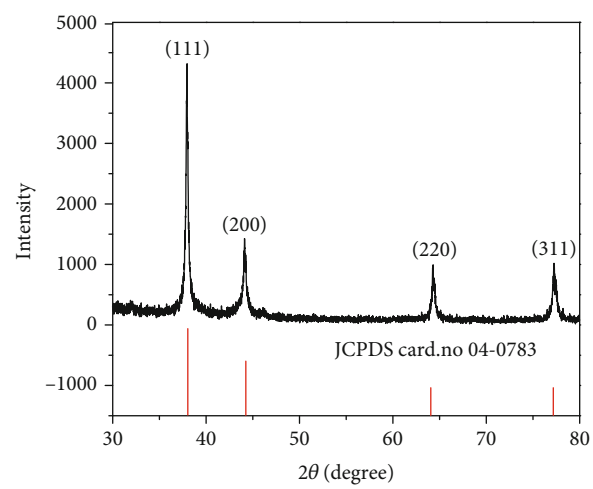

Figure 7: XRD pattern of AgNPs/GL.

3. Results and Discussion

3.1. Visual Observation. The process of biosynthesis of AgNPs/GL is shown in Figure 1. The color of the GL aqueous extract was yellow before its treatment with silver nitrate solution. After reaction, the color of the mixture became dark brown. This observation is contributed to confirm the formation of AgNPs due to the surface plasmon resonance. Moreover, the UV-Vis spectra of samples had the surface plasmon resonance peak of mixture reaction at a wavelength around 407 nm, which indicates the formation of AgNPs.

3.2. Reaction Condition Optimization. The pH was investigated in order to find the suitable pH for the formation of AgNPs. The pH of the solution was adjusted from its original value of pH 7 to the desired pH (3, 5, 9, and 11) by a dropwise addition of nitric acid (HNO_3) or ammonium hydroxide (NH_4OH) dilute solutions. The other chemical parameters were constant: C_{AgNO_3} = 1 mM, reaction time: 4 h, and reaction temperature: 75°C. The UV-Vis spectra of samples in different pH are shown in Figure 2(a). At the pH values of 3 and 5, the SPR peaks were not detected, indicating that the acidic condition was not suitable for generating the AgNPs. This phenomenon could be explained that the reducing power of these functional groups such as hydroxyl and carbonyl in the acidic environment is declined and so that it cannot be able to reduce silver ions [41]. Besides, in the pH range from 7 to 11, the color of AgNPs was turned to deep brown and the UV-Vis spectra presented SPR peaks from 405 to 415 nm, demonstrating that the AgNPs were formed. In neutral and alkaline conditions, both reducing and protecting abilities become more efficient. Therefore, more silver nanoparticles were generated and the agglomeration between these particles was prevented [41, 42]. By comparing the shape and peak intensities between UV-Vis spectra, the sample synthesized at pH 9 was narrow and had the highest intensity. Thus, the synthesis process of AgNPs achieved a high performance and these particles were

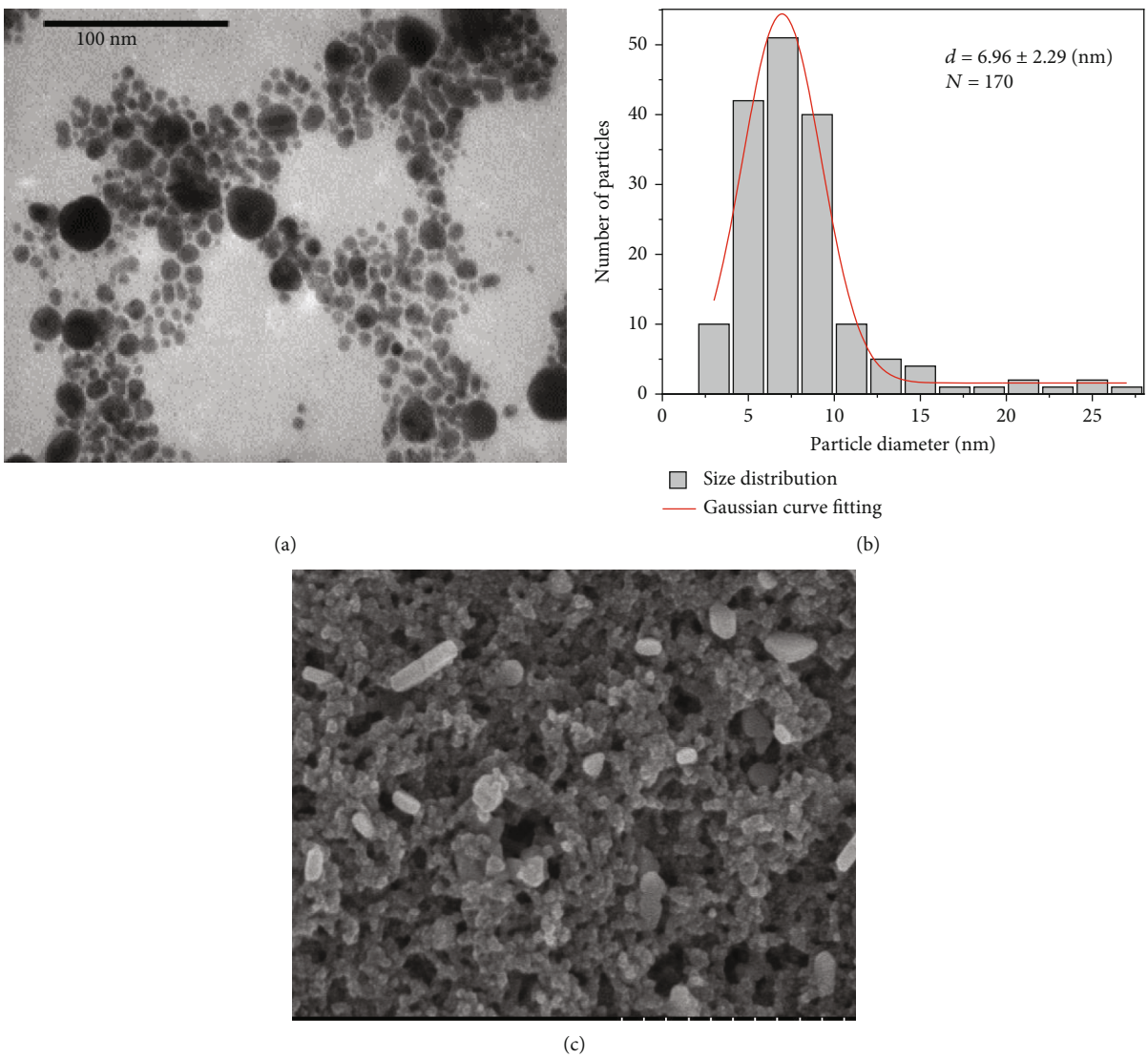

Figure 8: (a) TEM image of AgNPs/GL. (b) Particle diameter of AgNPs/GL. (c) SEM image of AgNPs/GL.

obtained with uniform size distribution. Hence, the alkaline condition was suitable for synthesizing AgNPs and pH 9 was selected as the optimum pH value. The morphology and particle size of AgNPs/GL synthesized with pH 9 were confirmed by TEM image and shown in Figure 2(b). It can be seen that the AgNPs/GL obtained was spherical and uniform. The histogram size distribution curve of AgNPs/GL (pH 9) is shown in Figure 2(c) with the particle size around 10.72 nm.

In the process synthesis of AgNPs/GL, reaction time was also an important parameter. Therefore, reaction time was studied with the other factors keeping intact: $C_{AgNO_3} = 1$ mM, reaction temperature: 75°C, and pH 9 (optimum pH). Figure 3 shows the absorption spectra of AgNPs at different reaction times from 30 min to 7 h. It is clear that in the first 30 min, the UV-Vis spectrum shows a broader peak with a lower intensity. By increasing the reaction time, the solution changed from pale-yellow to brown and dark brown and the intensity of peaks was also increased, which indicates that the AgNPs were generated continuously. From 5 to 7 h, the intensity peak at λ_{max} value (407 nm) slightly increased and remained unchanged at 6 h so that this leads to the completion of AgNP formation in this solution. Therefore, the optimum reaction time was 6 h and chosen for further studies.

The concentration of silver nitrate is one of the important parameters affecting the size and productivity of AgNPs. In terms of studying the effect of ion silver, the concentration of ion silver is varied from 0.5 to 1.5 mM and the other experimental conditions were kept steady (pH 9, 75°C, and 6 h). The UV-Vis spectra in Figure 4(a) show the samples of AgNPs in different concentrations. By changing the concentration of silver ion from 0.5 to 1 mM, the intensity of SPR peak would be increased significantly, which leads to more silver atoms being generated with high levels of productivity. However, at high concentrations (1.5 mM), the maximum wavelength shifted to the red shift and the peak became broader. This observation could be explained by the assumption that at this concentration, although the rate of reduction was increased, the size of silver particles was increased due to the agglomeration of these clusters. Figure 4(b) shows the TEM image of AgNPs with the concentration of silver nitrate

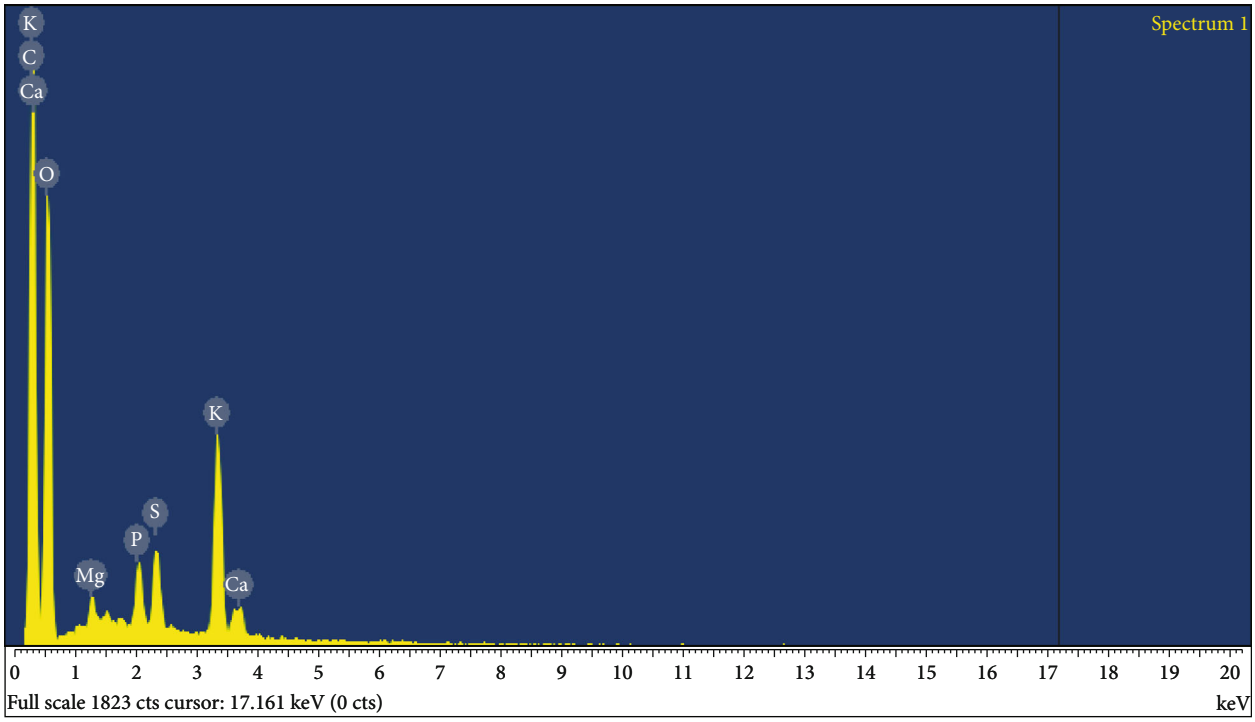

(a)

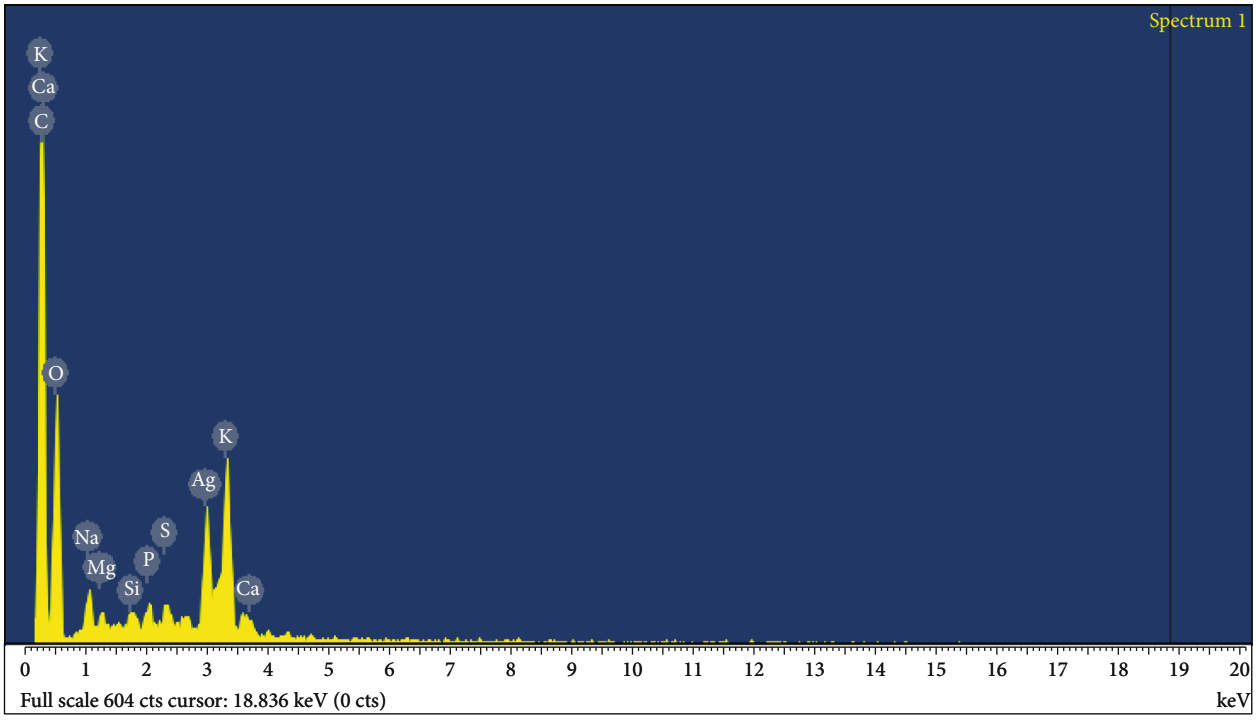

(b)

Figure 9: The EDX spectrum of (a) GL and (b) AgNPs/GL.

1.5 mM, and it was compared with the sample synthesized at 1 mM (Figure 2(b)). It can be seen that the AgNPs obtained at 1.5 mM were larger and nonuniform, which reasserts that the quantity of ion silver in the reaction solution influenced the agglomeration and the size of AgNPs. Therefore, the optimum concentration of silver nitrate was 1 mM.

Reaction temperature is also an important parameter impacting on the synthesis of AgNPs. Hence, four different temperatures from 65 to 95°C were investigated and the other parameters were chosen as the optimal values in previous studies. The UV-Vis spectra of silver colloidal solutions at four different temperatures are shown in Figure 5. The result

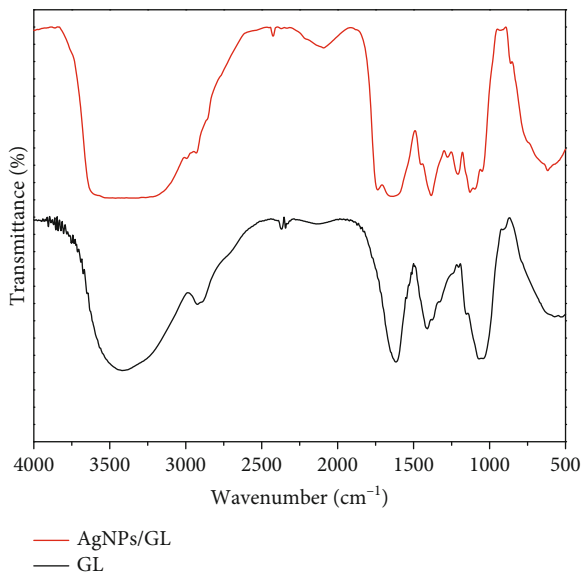

Figure 10: FTIR spectra of AgNPs/GL and GL.

showed that by increasing the synthesis temperature, the SPR peaks of AgNPs shifted to lower wavelengths and had higher intensities. The reason may be that at higher temperatures, not only the reaction rate and the movement of atoms on the solution were increased but also many initial nuclei were created at the same time, which led to a generation of more small particle size [43]. Besides, the UV-Vis spectra of samples synthesized at 85°C and above were sharper and this proved that the particles were relatively more uniform [41].

In order to investigate the effect of temperature on the stability of AgNPs, the silver colloidal solutions were retained and determined the maximum absorbance after different storage times. The result showed in Table 1 that, at 85°C and higher, the AgNPs obtained were more stable, whereas the AgNPs synthesized at a lower temperature (65 and 75°C) were not stable and agglomerated after 6 weeks. Although the AgNPs synthesized at 95°C were not coagulated after 6 weeks, the maximum absorbance was decreased significantly and thus it was less durable than the sample at 85°C. This reason might be that, at 95°C and in alkaline environment, the polysaccharides in fungal aqueous extraction were degraded to smaller weight molecules [44], thereby providing less protection ability and more particles agglomerated. Therefore, in the range of investigated temperature, AgNPs were the most durable at reaction temperature 85°C and this temperature was selected as the optimum temperature value. Consequently, the AgNPs/GL were synthesized with optimal condition as follows: pH 9, silver concentration: 1 mM, reaction temperature: 85°C, and reaction time: 6 h.

3.3. The Stability of the Suspension. In order to evaluate the stability of AgNP/GL colloidal solution, the UV-Vis spectra of the colloidal solution containing the AgNPs synthesized at the optimal conditions were studied at different times at room temperature (Figure 6). The initial sample showed an absorption peak at 409 nm because of the visual surface plasmon resonance band of the metallic silver nanomaterial. The intensity of absorption peak slightly decreased after 6 weeks (42 days), which demonstrates that the AgNP/GL colloidal solution is more stable. This phenomenon could be proven that there are some organic compounds in A-GL containing functional groups such as hydroxyl and carbonyl decorating onto the surface of AgNPs; hence, this prevents agglomeration between these particles.

3.4. Characteristics of the Obtained Materials. In optimized synthetic condition, the AgNPs/GL were obtained and characterized with some techniques such as XRD, TEM, EDX, and FTIR.

The X-ray diffraction (XRD) pattern was used to analyze the crystalline nature and identify the phases presented in the prepared sample. The XRD pattern of the AgNPs/GL in Figure 7 presented the typical diffraction peaks at 37.96°, 44.12°, 64.26°, and 77.25° which corresponded to (111), (200), (220), and (311) planes of faced-centered cubic silver (JCPDS card no. 04-0783).

The morphology and particle size of AgNPs/GL were investigated by SEM and TEM techniques. The SEM image showed in Figure 8 that there were AgNPs attaching to the surface of the macromolecule of GL aqueous extract and distributing uniformly. Besides, Figure 8 shows the TEM image of AgNPs/GL revealing the shape and the size distribution of as-prepared nanoparticles and these particles were spherical and quite uniform. These results demonstrated a good agreement with the results of UV-Vis spectra. Moreover, in order to analyze the size distribution of AgNPs, the diameter of approximately 170 particles was determined, and then, the data was demonstrated by a histogram. The diameter of the particle of the AgNPs was around 6.96 ± 2.29 nm.

The elemental composition was determined by using EDX as presented in Figure 9. The EDX spectrum reveals the purity and the complete chemical composition of silver nanoparticles synthesized. The EDX analysis illustrates the percentage of relative composition of elements found in AgNPs/GL (Figure 9(b)) such as C, O, Mg, P, S, K, Ca, and Ag. In fact, in the composition of AgNPs/GL, there were not only silver metal but also other chemical elements serving as capping organic agent bond to the surface of silver nanoparticles. This phenomenon was verified by the analysis of the composition of aqueous extraction of GL, and the result is shown in Figure 9(a). The composition of GL aqueous extract is similar to the other chemical elements found in the composition of AgNPs/GL.

Figure 10 shows the FTIR spectrum of AgNPs/GL and GL aqueous extract. In the spectra of GL aqueous extraction, the absorption peak observed at 3408 cm^{-1} was assigned to the stretching vibration of the hydroxyl group. The peak at 2914 cm^{-1} was attributed to the methylene group, and the peak at 1614 cm^{-1} could be ascribed to the carbonyl group (-C=O) stretching vibration considering the presence of hydroxyl hemiacetal groups. In addition, the peak that appeared near 2918 cm^{-1} confirmed the C-N stretching vibrations of aliphatic amines of protein and the peak at 1415 cm^{-1} related to the C-H bending vibration peak [45, 46]. For the spectra of AgNPs/GL, it was exhibited similarity

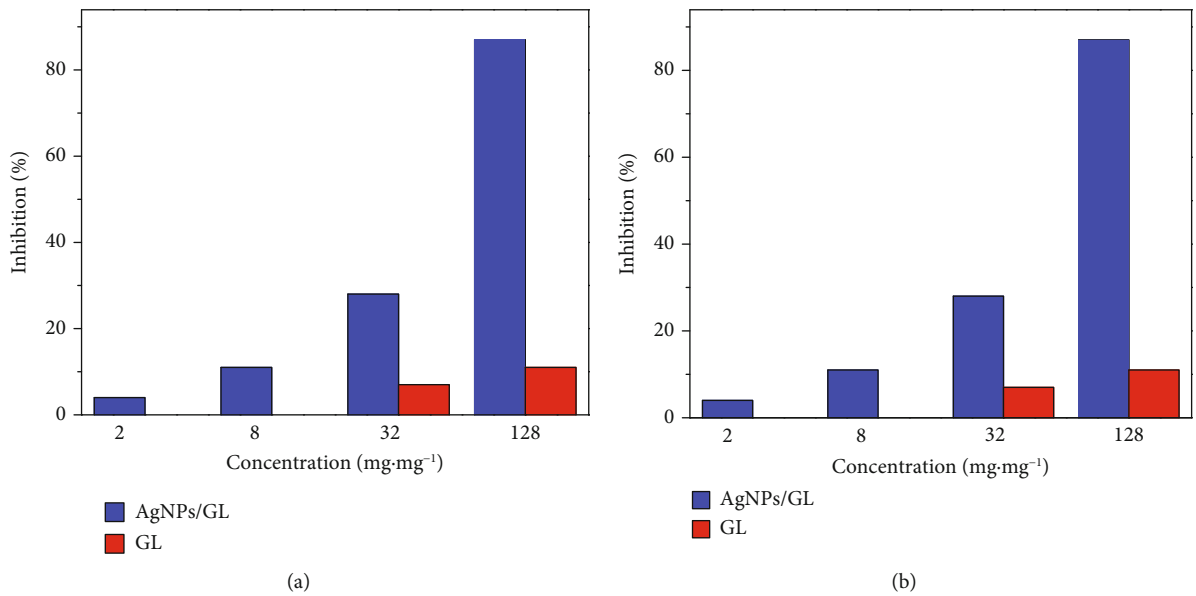

Figure 11: MTT assay results confirming the in vitro cytotoxicity effect of AgNPs/GL and GL aqueous extract with different concentrations against (a) HepG2 cells and (b) MCF-7 cells.

with the FTIR result of GL aqueous extraction and there was a new peak around 1743 cm^{-1} relating to the carboxylic ester groups. Moreover, the intensity peak of the carbonyl group (≈1614 cm^{-1}) was decreased strongly and become wider in comparison with the spectrum of GL aqueous extraction. This observation could be justified by the assumption that some carbonyl groups were oxidized to carboxylic ester groups, which involved reducing ion Ag(I) to Ag(0). The FTIR spectroscopic studies illustrated that the presence of functional groups has the ability to form the layer covering the silver nanoparticles to prevent the agglomeration and stabilizing the silver nanoparticles.

3.5. Determination of Cell Viability. The antiproliferative effect of AgNPs/GL and GL aqueous extract was studied by MTT assay in both cell lines (HepG2 and MCF-7), and the results are shown in Figure 11.

Overall, it is clear that AgNPs/GL inhibited effectively the proliferation of HepG2 cells and MCF-7 cells, compared to the inhibitory ability of GL aqueous extract. In terms of HepG2 cells, GL aqueous extract could not inhibit HepG2 cells with concentrations below 32 $\mu g \cdot mL^{-1}$ and exhibited negligible cytotoxic effect with only 19% inhibition with 128 $\mu g \cdot mL^{-1}$. However, in terms of AgNPs/GL, by increasing the concentration from 2 to 128 $\mu g \cdot mL^{-1}$, the percentage of the inhibition growth rose significantly and reached a peak at 128 $\mu g \cdot mL^{-1}$ concentration with 97% inhibition. The same pattern could be seen for the results of MCF-7 cells with a lower percentage of inhibition. Moreover, the IC_{50} value of AgNPs/GL for HepG2 cells was lower than once for MCF-7 cells with $21.85 \pm 0.2\,\mu g \cdot mL^{-1}$ and $67.77 \pm 1.44\,\mu g \cdot mL^{-1}$, respectively. In summary, by utilizing MTT assay for studying the in vitro cytotoxicity, AgNPs/GL seems to reduce the proliferation of HepG2 cells and MCF-7 cells, thereby having potential application on cancer treatment.

4. Conclusions

In this study, we demonstrated a novel and easy process for the synthesis of AgNPs using aqueous extraction of *G. lucidum*. The reaction parameters affecting the particle size and productive reaction such as pH, reaction time, concentration, and temperature were investigated. The results revealed that pH 9, silver concentration of 1 mM, reaction temperature at 85°C, and reaction time of 6 h were the optimal conditions for the synthesis of AgNPs. The obtained particles were stable and characterized by UV-Vis, SEM, TEM, XRD, EDX, and FTIR. Furthermore, the antiproliferative effect of AgNPs/GL on two cell lines HepG2 and MCF-7 was studied and the results showed that cancer cells were more susceptible to AgNPs/GL with IC_{50} value of $21.85\,\mu g \cdot mL^{-1}$ for HepG2 and $67.77\,\mu g \cdot mL^{-1}$ for MCF-7. The results proposed a potential of utilizing AgNPs/GL in the medical fields, especially cancer treatment in two cell lines HepG2 and MCF-7.

Data Availability

Data is available upon reasonable request.

Conflicts of Interest

There are no conflicts of interest to declare.

Acknowledgments

Vinh Phu Nguyen was funded by Vingroup Joint Stock Company and supported by the Domestic Master/PhD Scholarship Programme of Vingroup Innovation Foundation (VINIF), Vingroup Big Data Institute (VINBIGDATA), code VINIF.2020.ThS.38.

References

[1] J. M. Llovet, C. E. A. Peña, C. D. Lathia et al., "Plasma biomarkers as predictors of outcome in patients with advanced hepatocellular carcinoma," *Clinical Cancer Research*, vol. 18, no. 8, pp. 2290–2300, 2012.

[2] N. Harbeck, F. Penault-Llorca, J. Cortes et al., "Breast cancer," *Nature Reviews Disease Primers*, vol. 5, no. 1, p. 66, 2019.

[3] Z. Li, S. Tan, S. Li, Q. Shen, and K. Wang, "Cancer drug delivery in the nano era: an overview and perspectives," *Oncology Reports*, vol. 38, no. 2, pp. 611–624, 2017.

[4] K. Cho, X. U. Wang, S. Nie, Z. G. Chen, and D. M. Shin, "Therapeutic nanoparticles for drug delivery in cancer," *Clinical Cancer Research*, vol. 14, no. 5, pp. 1310–1316, 2008.

[5] F.-Y. Kong, J.-W. Zhang, R.-F. Li, Z.-X. Wang, W.-J. Wang, and W. Wang, "Unique roles of gold nanoparticles in drug delivery, targeting and imaging applications," *Molecules*, vol. 22, no. 9, p. 1445, 2017.

[6] J. E. Millstone, S. J. Hurst, G. S. Métraux, J. I. Cutler, and C. A. Mirkin, "Colloidal gold and silver triangular nanoprisms," *Small*, vol. 5, no. 6, pp. 646–664, 2009.

[7] S. H. Lee, W.-Y. Rho, S. J. Park, J. Kim, O. S. Kwon, and B.-H. Jun, "Multifunctional self-assembled monolayers via microcontact printing and degas-driven flow guided patterning," *Scientific Reports*, vol. 8, p. 1, 2018.

[8] S. H. Lee, J. H. Sung, and T. H. Park, "Nanomaterial-based biosensor as an emerging tool for biomedical applications," *Annals of Biomedical Engineering*, vol. 40, no. 6, pp. 1384–1397, 2012.

[9] G. Vinci and M. Rapa, "Noble metal nanoparticles applications: recent trends in food control," *Bioengineering*, vol. 6, no. 1, p. 10, 2019.

[10] M. Vaseem, K. M. Lee, A.-R. Hong, and Y.-B. Hahn, "Inkjet printed fractal-connected electrodes with silver nanoparticle ink," *ACS Applied Materials & Interfaces*, vol. 4, no. 6, pp. 3300–3307, 2012.

[11] J. García-Barrasa, J. López-de-Luzuriaga, and M. Monge, "Silver nanoparticles: synthesis through chemical methods in solution and biomedical applications," *Open Chemistry*, vol. 9, no. 1, pp. 7–19, 2011.

[12] W. Xu, W. Jin, L. Lin et al., "Green synthesis of xanthan conformation-based silver nanoparticles: antibacterial and catalytic application," *Carbohydrate Polymers*, vol. 101, pp. 961–967, 2014.

[13] V. Pifferi, V. Marona, M. Longhi, and L. Falciola, "Characterization of polymer stabilized silver nanoparticles modified glassy carbon electrodes for electroanalytical applications," *Electrochimica Acta*, vol. 109, pp. 447–453, 2013.

[14] V. K. Sharma, R. A. Yngard, and Y. Lin, "Silver nanoparticles: green synthesis and their antimicrobial activities," *Advances in Colloid and Interface Science*, vol. 145, no. 1–2, pp. 83–96, 2009.

[15] Y. Xue, T. Zhang, B. Zhang, F. Gong, Y. Huang, and M. Tang, "Cytotoxicity and apoptosis induced by silver nanoparticles in human liver HepG2 cells in different dispersion media," *Journal of Applied Toxicology*, vol. 36, no. 3, pp. 352–360, 2016.

[16] S. Khorrami, A. Zarrabi, M. Khaleghi, M. Danaei, and M. R. Mozafari, "Selective cytotoxicity of green synthesized silver nanoparticles against the MCF-7 tumor cell line and their enhanced antioxidant and antimicrobial properties," *International Journal of Nanomedicine*, vol. 13, pp. 8013–8024, 2018.

[17] Y. Jeong, D. W. Lim, and J. Choi, "Assessment of size-dependent antimicrobial and cytotoxic properties of silver nanoparticles," *Advances in Materials Science and Engineering*, vol. 2014, Article ID 763807, 6 pages, 2014.

[18] S. H. Lee and B.-H. Jun, "Silver nanoparticles: synthesis and application for nanomedicine," *International Journal of Molecular Sciences*, vol. 20, no. 4, p. 865, 2019.

[19] F. Mafuné, J. Kohno, Y. Takeda, T. Kondow, and H. Sawabe, "Formation and size control of silver nanoparticles by laser ablation in aqueous solution," *The Journal of Physical Chemistry. B*, vol. 104, no. 39, pp. 9111–9117, 2000.

[20] P. Slepička, R. Elashnikov, P. Ulbrich, M. Staszek, Z. Kolská, and V. Švorčík, "Stabilization of sputtered gold and silver nanoparticles in PEG colloid solutions," *Journal of Nanoparticle Research*, vol. 17, no. 1, p. 11, 2015.

[21] B. Nair and T. Pradeep, "Coalescence of Nanoclusters and Formation of Submicron Crystallites Assisted byLactobacillus-Strains," *Crystal Growth & Design*, vol. 2, no. 4, pp. 293–298, 2002.

[22] V. V. Makarov, A. J. Love, O. V. Sinitsyna et al., ""Green" nanotechnologies: synthesis of metal nanoparticles using plants," *Acta Naturae*, vol. 6, no. 1, pp. 35–44, 2014.

[23] A. Mohammed Fayaz, K. Balaji, P. T. Kalaichelvan, and R. Venkatesan, "Fungal based synthesis of silver nanoparticles–An effect of temperature on the size of particles," *Colloids Surfaces B Biointerfaces*, vol. 74, no. 1, pp. 123–126, 2009.

[24] J. Venkatesan, S.-K. Kim, and M. S. Shim, "Antimicrobial, antioxidant, and anticancer activities of biosynthesized silver nanoparticles using marine algae Ecklonia cava," *Nanomaterials*, vol. 6, no. 12, p. 235, 2016.

[25] R. Mie, M. W. Samsudin, L. B. Din, A. Ahmad, N. Ibrahim, and S. N. A. Adnan, "Synthesis of silver nanoparticles with antibacterial activity using the lichen Parmotrema praesorediosum," *International Journal of Nanomedicine*, vol. 9, p. 121, 2014.

[26] K. Paulkumar, G. Gnanajobitha, M. Vanaja et al., "Piper nigrum leaf and stem assisted green synthesis of silver nanoparticles and evaluation of its antibacterial activity against agricultural plant pathogens," *The Scientific World Journal*, vol. 2014, Article ID 829894, 9 pages, 2014.

[27] A. Roy, O. Bulut, S. Some, A. K. Mandal, and M. D. Yilmaz, "Green synthesis of silver nanoparticles: biomolecule-nanoparticle organizations targeting antimicrobial activity," *RSC Advances*, vol. 9, no. 5, pp. 2673–2702, 2019.

[28] M. Ghaffari-Moghaddam, R. Hadi-Dabanlou, M. Khajeh, M. Rakhshanipour, and K. Shameli, "Green synthesis of silver nanoparticles using plant extracts," *Korean Journal of Chemical Engineering*, vol. 31, no. 4, pp. 548–557, 2014.

[29] M. Rafique, I. Sadaf, M. S. Rafique, and M. B. Tahir, "A review on green synthesis of silver nanoparticles and their applications," *Artificial Cells, Nanomedicine, and Biotechnology*, vol. 45, no. 7, pp. 1272–1291, 2017.

[30] K. S. Bishop, C. H. J. Kao, Y. Xu, M. P. Glucina, R. R. M. Paterson, and L. R. Ferguson, "From 2000 years of *Ganoderma lucidum* to recent developments in nutraceuticals," *Phytochemistry*, vol. 114, pp. 56–65, 2015.

[31] B. Boh, M. Berovic, J. Zhang, and L. Zhi-Bin, "*Ganoderma lucidum* and its pharmaceutically active compounds," *Biotechnology Annual Review*, vol. 13, pp. 265–301, 2007.

[32] K. Tasaka, M. Akagi, K. Miyoshi, M. Mio, and T. Makino, "Anti-allergic constituents in the culture medium of Ganoderma lucidum.(I) Inhibitory effect of oleic acid on histamine

release," *Agents and Actions*, vol. 23, no. 3–4, pp. 153–156, 1988.

[33] S. Joseph, B. Sabulal, V. George, K. Antony, and K. Janardhanan, "Antitumor and anti-inflammatory activities of polysaccharides isolated from Ganoderma lucidum," *Acta Pharmaceutica*, vol. 61, no. 3, pp. 335–342, 2011.

[34] S.-K. K. Eo, Y.-S. S. Kim, C.-K. K. Lee, and S.-S. S. Han, "Antiviral activities of various water and methanol soluble substances isolated from *Ganoderma lucidum*," *Journal of Ethnopharmacology*, vol. 68, no. 1–3, pp. 129–136, 1999.

[35] C. Kao, A. C. Jesuthasan, K. S. Bishop, M. P. Glucina, and L. R. Ferguson, "Anti-cancer activities of Ganoderma lucidum: active ingredients and pathways," *Functional Foods in Health and Disease*, vol. 3, no. 2, pp. 48–65, 2013.

[36] H.-T. Ma, J.-F. Hsieh, and S.-T. Chen, "Anti-diabetic effects of *Ganoderma lucidum*," *Phytochemistry*, vol. 114, pp. 109–113, 2015.

[37] S. Manickam, K. Muthoosamy, R. G. Bai et al., "Exceedingly biocompatible and thin-layered reduced graphene oxide nanosheets using an eco-friendly mushroom extract strategy," *International Journal of Nanomedicine*, vol. 10, p. 1505, 2015.

[38] F. Faedmaleki, F. H Shirazi, A.-A. Salarian, H. Ahmadi Ashtiani, and H. Rastegar, "Toxicity effect of silver nanoparticles on mice liver primary cell culture and HepG2 cell line," *Iranian Journal of Pharmaceutical Research*, vol. 13, no. 1, pp. 235–242, 2014.

[39] D. A. Scudiero, R. H. Shoemaker, K. D. Paull et al., "Evaluation of a soluble tetrazolium/formazan assay for cell growth and drug sensitivity in culture using human and other tumor cell lines," *Cancer Research*, vol. 48, no. 17, pp. 4827–4833, 1988.

[40] R. I. Freshney and M. G. Freshney, *Culture of Epithelial Cells*, John Wiley & Sons, 2004.

[41] R. Seifipour, M. Nozari, and L. Pishkar, "Green synthesis of silver nanoparticles using Tragopogon collinus leaf extract and study of their antibacterial effects," *Journal of Inorganic and Organometallic Polymers and Materials*, vol. 30, no. 8, pp. 2926–2936, 2020.

[42] M. Sathishkumar, K. Sneha, S. W. Won, C.-W. Cho, S. Kim, and Y.-S. Yun, "*Cinnamon zeylanicum* bark extract and powder mediated green synthesis of nano-crystalline silver particles and its bactericidal activity," *Colloids Surfaces B Biointerfaces*, vol. 73, no. 2, pp. 332–338, 2009.

[43] B. Sumi Maria, A. Devadiga, V. Shetty Kodialbail, and M. B. Saidutta, "Synthesis of silver nanoparticles using medicinal Zizyphus xylopyrus bark extract," *Applied Nanoscience*, vol. 5, no. 6, pp. 755–762, 2015.

[44] B. Wu, Q. H. Feng, L. L. Geng, K. W. Shu, and D. Zhang, "Study on the optimal hydrolysis conditions of *Ganoderma lucidum* spore powder under microwave irradiation," *Advanced Materials Research*, vol. 900, pp. 293–296, 2014.

[45] M. Ibrahim, M. Alaam, H. el-Haes, A. F. Jalbout, and A. De Leon, "Analysis of the structure and vibrational spectra of glucose and fructose," *Eclética Química*, vol. 31, no. 3, pp. 15–21, 2006.

[46] J. Wang and L. Zhang, "Structure and chain conformation of five water-soluble derivatives of a β-d- glucan isolated from *Ganoderma lucidum*," *Carbohydrate Research*, vol. 344, no. 1, pp. 105–112, 2009.

Hindawi
Journal of Nanomaterials
Volume 2021, Article ID 9941202, 11 pages
https://doi.org/10.1155/2021/9941202

Research Article

Hydrothermal Synthesis of MoS_2/rGO Heterostructures for Photocatalytic Degradation of Rhodamine B under Visible Light

Thi Thuy Trang Phan,[1] Thi Thanh Huong Nguyen,[1] Ha Tran Huu,[2] Thanh Tam Truong,[1] Le Tuan Nguyen,[1] Van Thang Nguyen,[1,2] Vy Anh Tran,[3,4] Thi Lan Nguyen,[1] Hong Lien Nguyen,[5] and Vien Vo[1,2]

[1]*Faculty of Natural Sciences, Quy Nhon University, Quy Nhon 55000, Vietnam*
[2]*Applied Research Institute for Science and Technology, Quy Nhon University, Quy Nhon 55000, Vietnam*
[3]*Institute of Research and Development, Duy Tan University, Da Nang 50000, Vietnam*
[4]*Faculty of Environmental and Chemical Engineering, Duy Tan University, Da Nang 50000, Vietnam*
[5]*School of Chemical Engineering, Hanoi University of Science and Technology, Hanoi 100000, Vietnam*

Correspondence should be addressed to Vien Vo; vovien@qnu.edu.vn

Received 30 March 2021; Accepted 26 June 2021; Published 29 July 2021

Academic Editor: Donglu Shi

MoS_2/rGO composites were synthesized by hydrothermal method from the precursors of MoS_2 and reduced graphene oxide (rGO) prepared in the former steps. The influence of the synthesis conditions including hydrothermal temperature and mass ratio of MoS_2 to rGO on the structure, morphology, and optical absorption capacity of the MoS_2/rGO composites was systematically investigated using physicochemical characterizations. The photocatalytic performance of as-prepared samples was investigated on the degradation of Rhodamine B under visible light, in which, the composites obtained at hydrothermal temperature of 180°C and MoS_2/rGO mass ratio of 4/1 exhibited the highest photodegradation efficiency of approx. 80% after 4 hours of reaction. This enhancement in photocatalytic behaviour of composites could be assigned to the positive effect of rGO in life time expansion of photoinduced electrons—holes.

1. Introduction

The limited source of fresh water in earth crust, which is suffering from pollution caused by the persistent organic pollutants such as dyes, pesticides, and antibiotics, raises a huge challenge for human being to find more sustainable way in use and recycling wastewater [1, 2]. A variety of strategies have been investigated in effort to remove those contaminants in wastewater for recycle or discard into environment within harmless effect [3, 4]. However, the traditional methods are tough to achieve high efficiency, owing to the sophisticated organic pollutants. The most prominent among applications is photocatalytic technology due to its advantageous features such as high light-harvesting efficiency, environmental safety, low cost, and thorough degradation using naturally available solar energy sources [5–7]. In recent years, the transition metal oxide-based semiconductors, including TiO_2 and ZnO, have attracted much attention of scientific community by their promising photocatalytic performances [3, 8–10]. However, the nature as large band gap semiconductors limits their practical application due to the fact that they are only active under the UV light. Therefore, MoS_2 with narrow band gap and fully activated under visible light could overcome this limitation. Nevertheless, the high rate of recombination of photoinduced charge carriers in single-phase MoS_2 normally prohibits its photocatalytic performance. Therefore, the integration of two or more photocatalysts to form a composite has been favorably considered [11–18]. One of the most successful strategies in coupling materials toward a better photocatalytic performance is grafting with a highly electronic conductive counterpart such as carbon-based materials. Among this family of materials, graphene, a

two-dimensional (2D) material constructed from the sp^2-hybridized carbon elements, has attracted interest owing to its unique properties such as large specific surface area, good electrical conductivity, and high optical transmittance [19, 20]. These properties allow graphene to be utilized in the broad scope of application, including adsorption, photocatalyst, supercapacitors, and batteries. It is considered as a potential support when combining with a semiconductor material, leading to reduction in the recombination rate of charge carriers [3]. Accordingly, semiconductor/graphene photocatalysts have been widely used in many areas, such as water splitting for H_2 evolution, CO_2 reduction, organic synthesis, disinfection, and advanced oxidation processes in wastewater treatment [21]. The chemical-exfoliated graphene oxide (GO) is reported as low electrical conductivity [22]. By the reduction of oxygen-based functional group on the surface, the reduced graphene oxide (rGO) with recover sp^2-hybridized framework performs better electronic conduction [23]. Therefore, as an analogue of graphene, rGO is a promising candidate for coupling and improving the conductivity of final composite.

In this current work, we designed and highlighted the interfacial interaction of MoS_2 with rGO using a two-step hydrothermal process, in which rGO nanosheets functioned as a framework for scaffolding MoS_2, leading to enhanced properties of MoS_2/rGO hybrid nanostructures. Specifically, the impact of hydrothermal temperature and ratio of precursors has been systematically investigated. It was indicated by RhB degradation activities that the photocatalytic performance of the optimized MoS_2/rGO conventional hybrid structure was substantially improved.

2. Materials and Methods

2.1. Chemicals. Chemicals used for this study include graphite powder (≥99%), L-ascorbic acid (≥99%), $KMnO_4$ (≥99%), $NaNO_3$ (≥99%) H_2SO_4 (98%), HCl (37%), H_2O_2 (30%), C_2H_5OH (98%), $(NH_4)_6Mo_7O_{24}.4H_2O$ (≥99%), thiourea (≥99%), and Rhodamin B (≥99%), which were purchased from Merck and used as received without further purification.

2.2. Synthesis of Materials

2.2.1. Synthesis of Graphene Oxide. Graphene oxide (GO) was fabricated from graphite powder by the modified Hummer's method [24, 25]. Firstly, 15 mL of H_2SO_4 solution was slowly added to a 500 mL flask containing 0.6 g of graphite powder and 0.3 g of $NaNO_3$. The suspension was stirred for 24 hours at room temperature. Next, the mixture was cooled down to 3-5°C and kept at this temperature for 2 hours. Then, 1.8 g of $KMnO_4$ was added to the mixture and stirred for 5 hours at room temperature, which was then heated to 98°C, and kept at this temperature for 30 min. After that, the mixture was cooled down to 40°C in air. Thereafter, 90 mL distilled water and 7.5 mL H_2O_2 30% were added. Finally, the suspension was centrifuged, washed 3 times in diluted HCl (5%), 3 times in distilled water, 3 times in ethanol, and dried in air at 80°C for 12 hours. After that, ascorbic acid was employed as a reducing agent to achieve rGO.

2.2.2. Synthesis of MoS_2/rGO Composites. Firstly, MoS_2 was synthesized via a facile method of annealing the mixture of $(NH_4)_6Mo_7O_{24}.4H_2O$ and $(NH_2)_2CS$ under Ar gas at 650°C as described in the previous publication [24]. The MoS_2/rGO composites were fabricated from the two separate components (rGO and MoS_2) by the hydrothermal method. To investigate the influence of the hydrothermal temperature on the composite properties, a fixed weight ratio of MoS_2 to rGO (=4/1) was added to the ethanol-water solution before applying the ultrasonication for 1 h and continuously stirring for 5 h to form a homogeneous mixture. After that, the obtained mixture was transferred to a 100 mL Teflon-lined autoclave and heated at different temperatures (140, 160, 180, and 200°C) for 10 h. Finally, the obtained mixture was filtered, washed with water, and centrifuged before being dried at 80°C for 12 h to obtain the samples, which are denoted as MoS_2/rGO (4/1-T) composites with $T = 140$, 160, 180, and 200°C, respectively. In order to investigate the effect of the ratio of MoS_2 to rGO, a series of samples with different weight MoS_2/rGO ratios was prepared following the same procedure for MoS_2/rGO (4/1-180°C) and denoted as MoS_2/rGO (x-180°C) with $x = 2/1$, 4/1, and 6/1, respectively.

2.3. Characterization of Materials. The crystal phase of the synthesized samples was characterized by the X-ray powder diffraction (Brucker D8 Advance with Ni-filtered Cu Kα radiation ($\lambda = 1.5418$ Å). The Fourier-transform infrared spectroscopy of the samples was recorded on FT-IR-GX-PerkinElmerLabRAM HR Evolution (Horiba) with a 647.1 nm laser as an excitation source. The surface morphology and elemental composition were analyzed by scanning electron microscope (SEM-SEM-JEOL-JSM 5410 LV) and energy scattering spectroscope (EDX-JEOL 5410), respectively. The specific surface area obtained by Brunauer–Emmett–Teller (BET) analysis and pore size distribution from Barrett-Joyner-Halenda (BJH) technique were measured on a Tristar II 3202 instrument using N_2 adsorption-desorption at 77 K. The UV–Vis diffuse reflectance spectroscopy (UV-Vis-DRS) of the samples was analysed using UV-Vis-Cary 5000 spectrophotometer (Varian). The X-ray photoelectron spectroscopy (XPS) was recorded on Theta Probe AR-XPS System (Thermo Fisher Scientific). The Raman spectroscopy was carried out T64000 Raman with a 647.1 nm laser as an excitation source, and detector CCD was cooled by liquid nitrogen.

2.4. Evaluation of Photocatalytic Activity. The photocatalytic activities of the obtained materials were evaluated *via* the photodegradation of RhB in an aqueous solution under visible light irradiation. For a typical experiment, 100 mg of the catalyst was added into 400 mL of 20 mg/L RhB solution. Before illumination, the reaction mixture was stirred continuously for 2 h in the dark to reach adsorption-desorption equilibrium. Next, the mixture was illuminated by compact lamp (60 W–220 V). After every interval of 30 min, 4 mL of the reaction solution was collected and removed from the photocatalyst by centrifugation for further measurement. The residual concentration of RhB was recorded using a UV-Vis spectrometer.

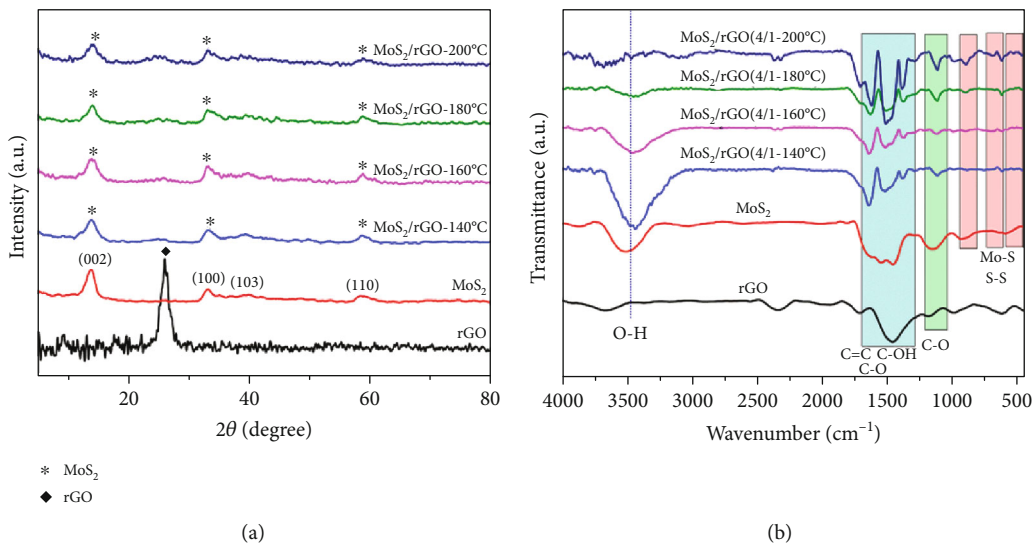

Figure 1: XRD patterns (a) and IR spectra (b) of rGO, MoS_2, and MoS_2/rGO (4/1-T) composites (T = 140, 160, 180, and 200°C).

3. Results and Discussion

3.1. Effect of the Hydrothermal Temperature. The effect of the hydrothermal temperature on the MoS_2/rGO composites was first investigated in a series of samples with a fixed weight ratio of MoS_2 to rGO (=4/1). The presence of MoS_2 in MoS_2/rGO (4/1-T) composites (T = 140, 160, 180, and 200°C) is confirmed by XRD and FT-IR showed in Figures 1(a) and 1(b), respectively.

According to Figure 1(a), the XRD patterns of MoS_2/rGO composites exhibit characteristic peaks at $2\theta = 14.1$; 33.6; 39.84; and 58.1°, which correspond to predominate (002), (100), (103), and (110) planes, respectively, and are consistent with the 2H hexagonal phase of MoS_2 [26]. These featured peaks in composites were obtuse and lower (peak at 002) than those of pristine MoS_2 due to the overlap of the rGO layers between MoS_2 crystals because of composite formation (as shown in Figure 1(a)). Notably, the intensity of the peaks corresponding to MoS_2 gradually decreases with the increase of temperature, indicating formation of a more solid and stable composite structure. A similar phenomenon was also observed in the previous report of Guo et al. [27].

To further evaluate the impact of MoS_2 supported on rGO nanosheet, chemical bonding characteristics of the as-prepared materials were revealed by the FTIR spectra (as shown in Figure 1(b)). While the peaks in the wavenumber of about 530, 630, and 920 cm^{-1} can be assigned to Mo-S bonds [28–30], a peak at about 550 cm^{-1} can be attributed S-S vibration modes [31]. The peaks in the range of 1550-1650 cm^{-1} represent the bonds in sp^2 hybridization such as C=C and C-O-C [32]. Furthermore, a broad band from 1112 to 1393 cm^{-1} is associated with the existence of C-O and C-OH bonds [33]. Vibration bands in the region of 3200-3700 cm^{-1} can be ascribed to the –OH bonds from adsorbed H_2O molecules of the rGO in the composites. As the hydrothermal temperature increases, the intensity of most characteristic peaks decreases, especially at T = 180°C. At high temperature (T = 200°C), a reduction of functional groups may come from change of rGO structure to almost-like grapheme [27].

UV-Vis-DRS curves of MoS_2 and MoS_2/rGO-T composites are presented in Figure 2(a). Accordingly, the absorption edges of both the MoS_2 and MoS_2/rGO composites extend to the wavelength range from 400 to 700 nm. Based on the absorption edge, the bandgap energy of as-synthesized composites obviously shift towards the visible light region, which proves that the combination of MoS_2 and rGO could enhance the light-harvesting ability and expand the optical absorption range to the region of solar energy [12]. As shown in Figure 2(b), the Tauc plots of MoS_2 and MoS_2/rGO-T composites were present using Kulbeka–Munk equation:

$$(\alpha h\nu)^{1/n} = C(h\nu - Eg), \quad (1)$$

in which, $h\nu$ is incident photoenergy, C is constanst, E_g is band gap value, and n is exponent. For direct band gap, $n = 1/2$ was applied, and the E_g value was determined as the intercept of tangent of Tauc plot on x-axis.

The SEM images for the MoS_2/rGO (4/1-T) composites are shown in Figure 3. It is obvious that the hydrothermal temperature exhibits a significant effect on the surface morphology of the MoS_2/rGO-T composites. For MoS_2/rGO (4/1-140°C) (Figure 3(a)), its morphology is in nanosheets, similar to rGO (Figure 3(e)), without the clear presence of the structure of MoS_2. When the hydrothermal temperature increases to 160°C, MoS_2 nanosheets in the form of flakes clearly appear on the material surface but nonuniformly distribute (Figure 3(b)). While at 180°C (Figure 3(c)), the composite displays uniform formation between MoS_2 layers and rGO nanosheets. However, as the hydrothermal temperature increases to 200°C (Figure 3(d)), the MoS_2 layers densely appeared, stacked, and covered the rGO nanosheets. This phenomenon is consistent with the results observed from the XRD patterns.

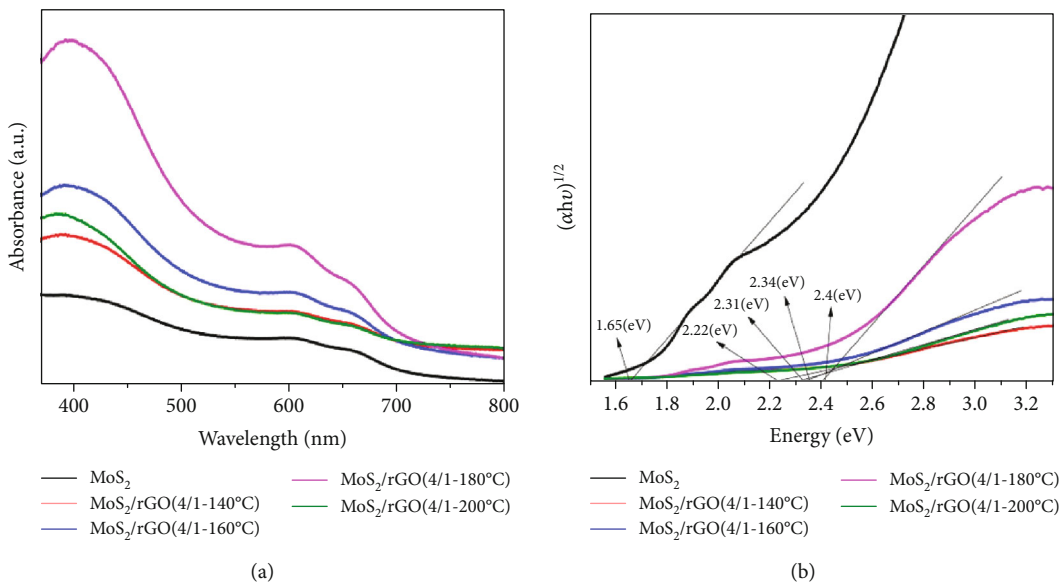

Figure 2: UV-Vis diffuse reflectance spectra of MoS_2 and MoS_2/rGO (4/1-T) composites (T = 140, 160, 180, and 200°C).

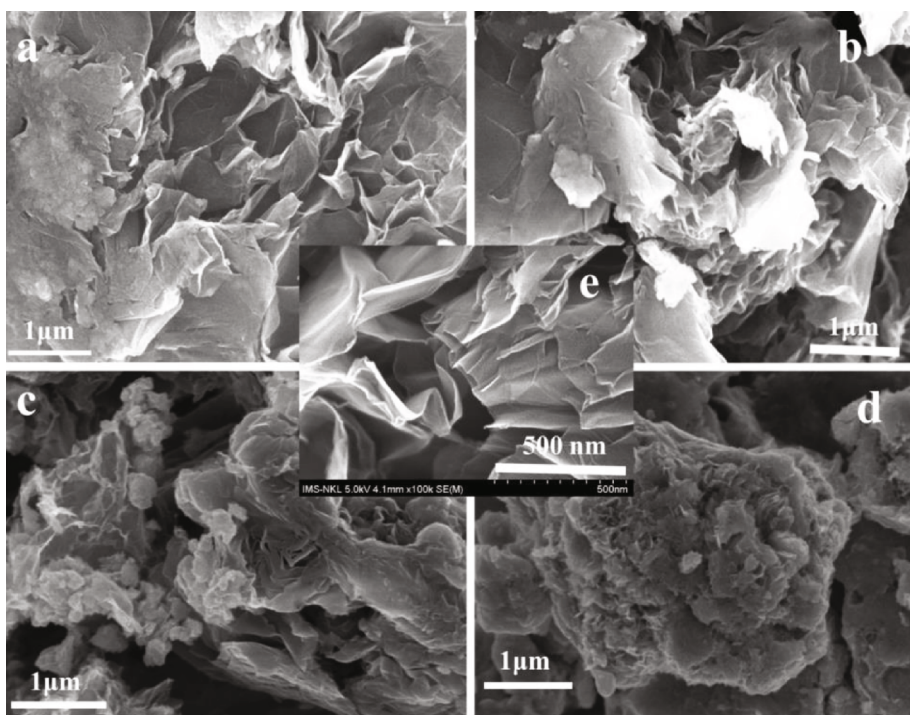

Figure 3: SEM images of MoS_2/rGO (4/1-140°C) (a), MoS_2/rGO (4/1-160°C) (b), MoS_2/rGO (4/1-180°C) (c), MoS_2/rGO (4/1-200°C) (d), and rGO (e).

The effect of the hydrothermal temperature on the photocatalytic activity of the MoS_2/rGO composites is shown in the photodegradation of RhB (Figure 4). For the single MoS_2, the RhB decomposition efficiency is only 25.9% after 4 h under visible light irradiation. In contrast, the MoS_2/rGO composites exhibited higher catalytic activities and in the order MoS_2/rGO (4/1-180°C) > MoS_2/rGO (4/1-200°C) > MoS_2/rGO (4/1-160°C) > MoS_2/rGO (4/1-140°C), in which decomposition efficiency for MoS_2/rGO (4/1-180°C) reaches 80.0% (Figure 4(a)).

Additionally, in order to evaluate the kinetics of photocatalytic progress, the Langmuir-Hinshelwood model has been applied [34]. Figure 4(b) displays the linear relationship of ln (C_o/C) versus the irradiation time, indicating that the photodegradation of RhB fits well with the pseudo-first-order kinetic model according to the equation: ln (C_o/C) =

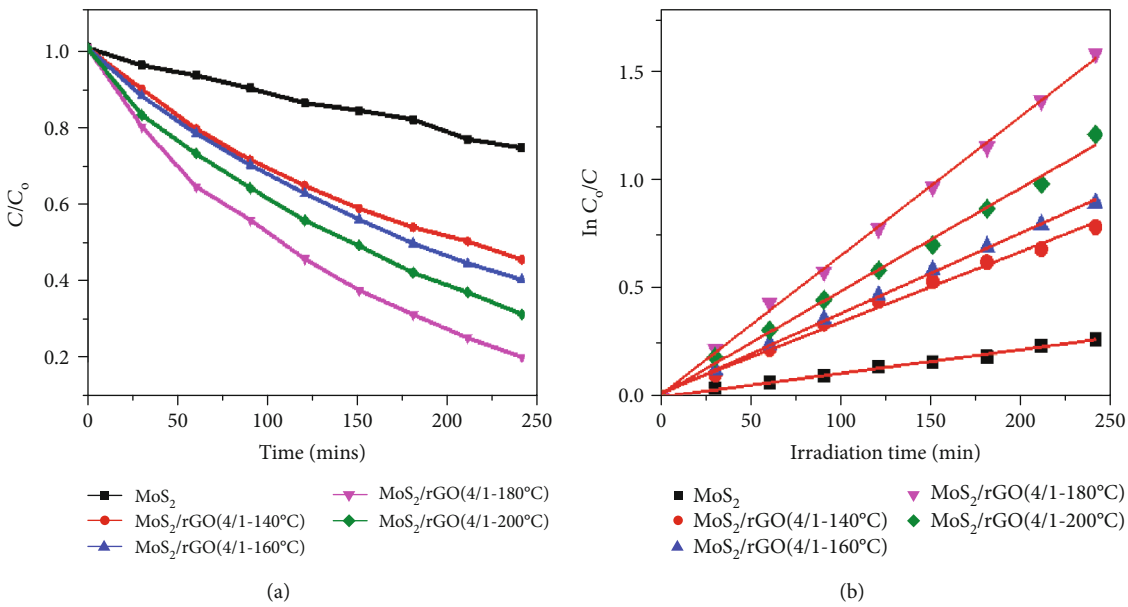

Figure 4: Effect of the hydrothermal temperature on the photocatalytic activity of the MoS_2/rGO composites in RhB decomposition (a) and their kinetic models (b).

Table 1: Rate constant of the photocatalytic degradation of RhB on the MoS_2/rGO composites at different hydrothermal temperatures.

Samples	MoS_2	MoS_2/rGO (4/1-140°C)	MoS_2/rGO (4/1-160°C)	MoS_2/rGO (4/1-180°C)	MoS_2/rGO (4/1-200°C)
Rate constant k_{app} (min^{-1})	0.00121	0.0033	0.00378	*0.00652*	0.00484
Correlation coefficients (R^2)	0.994	0.991	0.998	*0.998*	0.994

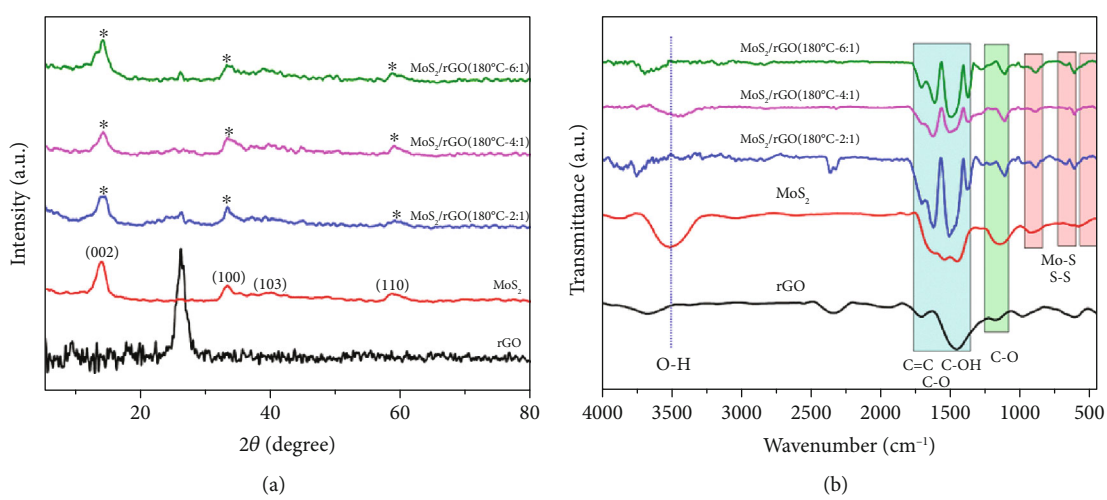

Figure 5: X-ray diffraction patterns (a) and IR spectra (b) of rGO, MoS_2, and MoS_2/rGO (180°C-x) composites with x = 2/1, 4/1, and 6/1.

$k.t$, where C is the equilibrium concentration of RhB (mg/L), C_o is the initial concentration of RhB before irradiation (mg/L), t is the reaction time (min), and k (min^{-1}) is the reaction rate constant. The obtained data are summarized in Table 1.

As observed in Table 1, MoS_2/rGO (4/1-180°C) performs the highest k value (0.00652 min^{-1}), which is about 5.3 times higher than that of the pure MoS_2. This observation is consistent with the above statement that MoS_2/rGO-180°C has more favourable hybrid structure and morphology as well as better light-harvesting ability than the remaining composites. Therefore, the hydrothermal condition of 180°C is considered to be the most appropriate, allowing the creation of more active MoS_2/rGO composites, reducing the

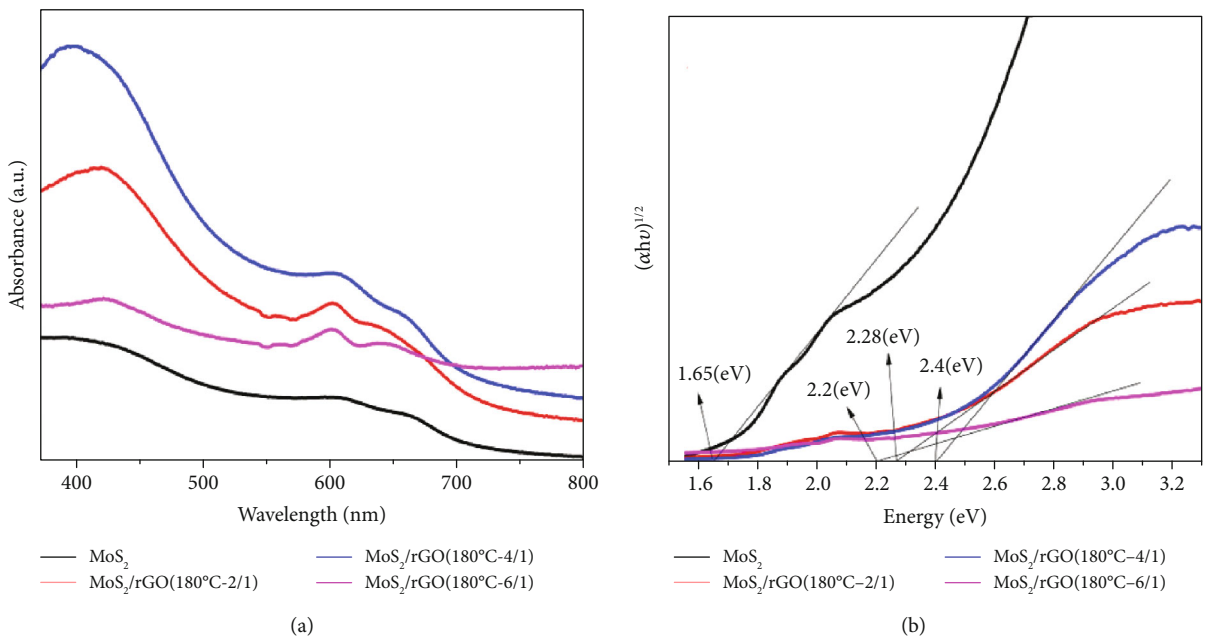

Figure 6: UV-Vis diffuse reflectance spectra of MoS_2 and MoS_2/rGO (180°C-x) composites with $x = 2/1$, 4/1, and 6/1.

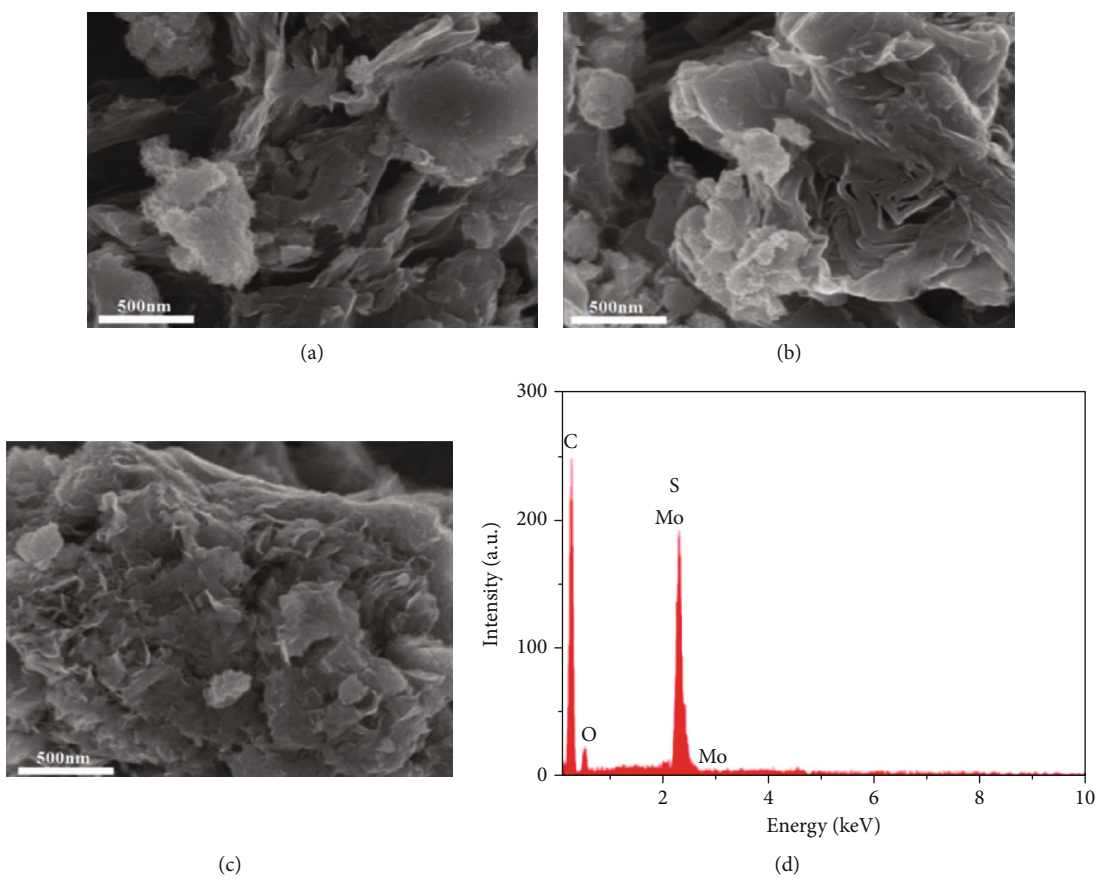

Figure 7: SEM images of MoS_2/rGO (180°C-x) with $x = 2/1$ (a); $x = 4/1$ (b); $x = 6/1$ (c), and EDX of MoS_2/rGO (180°C-4/1) (d).

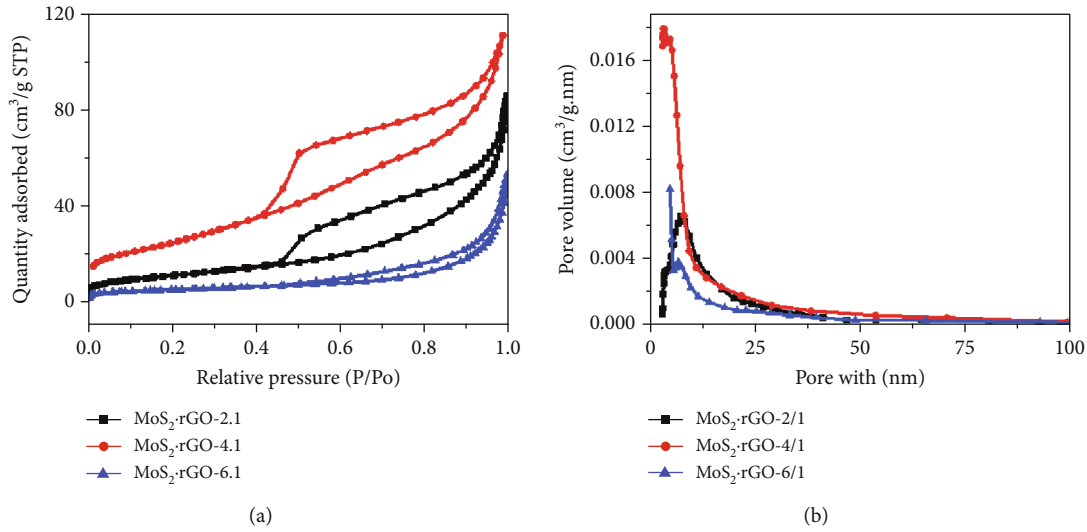

Figure 8: N_2 adsorption-desorption isotherms and pore-size distribution curves of MoS_2/rGO (180°C-x) with x = 2/1, 4/1, and 6/1.

Table 2: The characteristic parameters of MoS_2/rGO (180°C-x) with x = 2/1, 4/1, and 6/1 obtained from the BET method.

Parameter	MoS_2/rGO (180°C-2/1)	MoS_2/rGO (180°C-4/1)	MoS_2/rGO (180°C-6/1)
Specific surface area (m^2/g)	36.3	88.1	30.6
Total pore volume (cm^3/g)	0.156802	0.174731	0.158113
Pore diameter (nm)	7.8–12.8	5.4–7.4	10.1–12.1

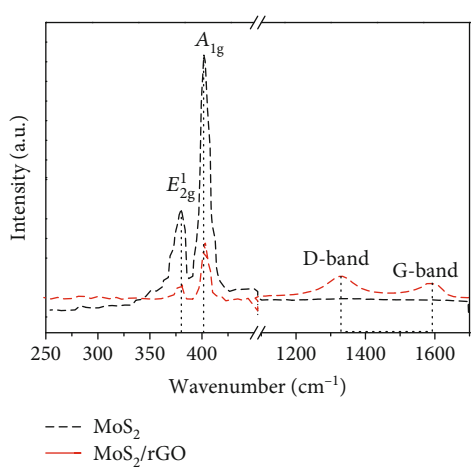

Figure 9: Raman spectra of MoS_2 and MoS_2/rGO (180°C-4/1).

recombination rate of photogenerated electron-hole pairs in the single MoS_2.

3.2. Effect of the Ratio of MoS_2 to rGO. Further investigation on the MoS_2 supported on rGO sheets substrate, the XRD patterns, and FT-IR spectra of selected samples with different mass MoS_2/rGO ratios are displayed in Figure 5.

As can be illustrated in Figure 5(a), the XRD patterns of the MoS_2/rGO composites exhibit characteristic peaks at 2θ = 14.1; 33.6; 39.84; and 58.1° corresponding to the (002), (100), (103), and (110) planes, respectively, which are well agreed with the 2H hexagonal phase of MoS_2 [26]. The increase of MoS_2/rGO mass ratio led to the gradually increase in intensity of MoS_2-related peaks, which could be clearly observed at the (002) lattice plane. Among the three composites, the pattern of the sample with ratio of 4/1 (MoS_2/rGO (4/1-180°C)) presents the most obtuse peak, indicating clear integration between graphene and MoS_2 nanosheets toward an uniform heterojunction.

The chemical bonding characteristics of the composites with various MoS_2/rGO ratios are displayed in Figure 5(b). The typical peaks of Mo-S, S-S, C-OH, CO, OH, and C=C functional groups at different wavenumbers (as mentioned in Section 3.1) all appeared in the composites. For MoS_2/rGO (4/1-180°C), however, the intensity of these peaks reduced significantly, suggesting a robust structure with intimate contact between the MoS_2 and rGO in the composite.

The optical absorption capacity of MoS_2 and the MoS_2/rGO composites was investigated by UV-Vis DRS. As shown in Figure 6(a), similar to the results obtained in changing the hydrothermal temperature, changes in the ratios of precursors lead to changes in the optical absorption intensity of the materials. Moreover, a dramatic shift in the absorption peak of the visible light region to around 700 nm appeared in all the composites. Moreover, the main peak systems of both MoS_2 and rGO present in these composites, which is consistent with previous reports [32]. This feature is favorable for increasing the light absorption ability as well as extending the optically active region of the composites to the low energy region (inherently abundant in the

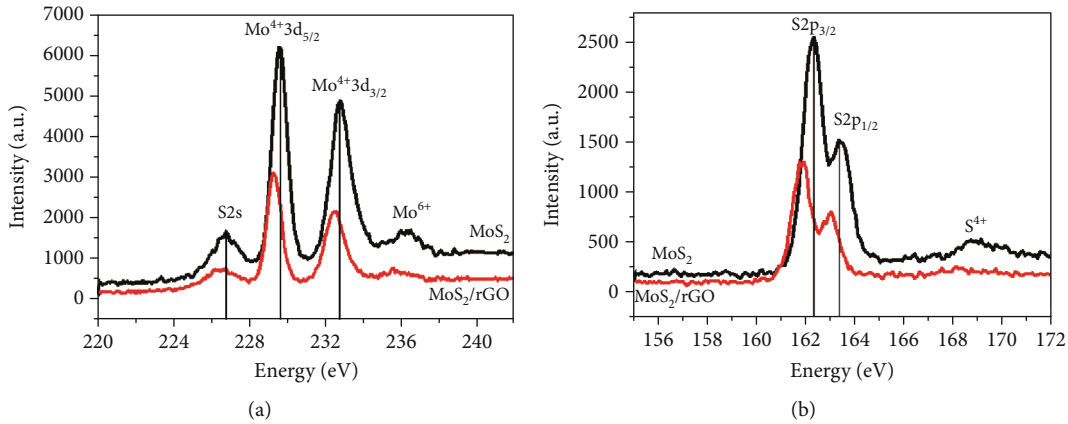

Figure 10: XPS spectra of Mo3d (a) and S2p (b) for MoS_2 and MoS_2/rGO (180°C-4/1).

sunlight region) (as shown in Figure 6(b)). Consequently, it is proved that the combination of intercalated MoS_2 nanosheets and rGO layers plays an important role in increasing the photosensitivity of the materials.

The morphology of the materials with different ratios of MoS_2 is given in the SEM images. Figures 7(a)–7(c) display different surface structure morphology of the composites. Accordingly, the MoS_2 flakes appeared on rGO relatively little in MoS_2/rGO (2/1-180°C) (Figure 7(a)). Nevertheless, when increasing the ratio to 4/1 (Figure 7(b)), rGO was covered by a large number of MoS_2 flakes. With further increase in the ratio to 6/1 (Figure 7(c)), the layers of MoS_2 flakes appear more densely and tend to agglomerate together into large bulks. On the other hand, the EDX analysis of MoS_2/rGO (180°C-4/1) indicates that the atomic ratio of Mo to S is approximately 1 : 2, in accordance with the bonding properties of MoS_2 in the material structure (as shown in Figure 7(d)).

The specific surface area and porosity of the MoS_2/rGO (180°C-x) composites were confirmed by the BET analysis as illustrated in Figure 8. The hysteresis phenomenon and the hysteresis loops as shown in Figure 8(a) could be assigned to a type-IV isotherm (according to IUPAC classification), suggesting their mesoporous structure. The results in Table 2 show that the specific surface area of MoS_2/rGO-4/1 was higher than that of MoS_2/rGO-2/1 and MoS_2/rGO-6/1. This is in agreement with the aforementioned discussion of the SEM images, which may contribute to a significant enhancement in the photocatalytic efficiency of the material. The appropriate ratio of MoS_2 and rGO in MoS_2/rGO-2/1 and MoS_2/rGO-4/1 could provide a sufficient content of rGO framework assuring the better dispersion of MoS_2 nanosheets. This leads to prevent components' nanosheets from recollapse then help enlarge their surface area. However, at higher content of MoS_2 (MoS_2/rGO-6/1), the insufficient rGO framework may cause the restacking of excess MoS_2. Therefore, the specific surface area of MoS_2/rGO-6/1 is the lowest value among three samples.

The Raman spectra of MoS_2 and a representative composite MoS_2/rGO (180°C-4/1) shown in Figure 9 exhibit two characteristic peaks located at wavenumbers of between 378 and 404 cm^{-1}, corresponding to the in-plane E^1_{2g} and out-of-plane A_{1g} vibration modes of the hexagonal phase of MoS_2 crystal [34]. An energy value difference between them corresponding to 26 cm^{-1} reflects the multilayer structure of MoS_2 [35]. It is worth mentioning that the intensity of peaks at about 380 cm^{-1} (internal vibration of Mo-S bond) and 405 cm^{-1} (out-of-plane vibration of "S" element in Mo-S bond) of MoS_2/rGO (180°C-4/1) is much lower than that of the single MoS_2 that is suitable for the 2H-MoS_2 phase [36].

The intensity of the E^1_{2g} peak is lower than that of the A_{1g} peak, indicating that the crystal structure of the obtained materials contains significant defect sites and side structures [23]. This observation is expected to enhance their photocatalytic activity. In addition, values at 1330 and 1590 cm^{-1} can be related to D and G breathing vibrations, respectively, corresponding to the defects and sp^2 hybrid carbon atoms in the MoS_2/rGO composite [37]. This parameter indicates the presence of rGO integrated into MoS_2 to form a composite structure during the hydrothermal process. On the other hand, the I_D/I_G peak intensity ratio of 1.41 for MoS_2/rGO (180°C-4/1) is lower than that for rGO ($I_D/I_G = 1.72$), indicating a decrease in size and then density of the defect sites on the rGO surface in the composite compared to single rGO [23, 37].

To distinguish the existing forms of Mo and S in MoS_2 and MoS_2/rGO (4/1-180°C), X-ray photoelectron spectroscopy was performed. Figure 10(a) exhibits the binding energy values of S2s, $Mo^{4+}3d_{5/2}$, $Mo^{4+}3d_{3/2}$, and Mo^{6+} at photoelectron peaks of 226.7, 229.2, 232.5, and 235.5 eV, respectively [38]. In which the peaks of $Mo^{4+}3d_{5/2}$, $Mo^{4+}3d_{3/2}$, and S2s reflect the presence of the S-Mo-S bond in MoS_2. The binding energy of 235.5 eV corresponds to Mo^{6+} in the MoO_3 or MoO_4^{2-} compounds. The existence of this peak may come from the oxidation of Mo^{4+} to Mo^{6+} in the calcination process for preparing MoS_2. In addition, the results in Figure 10(b) show that the binding energy values at 161.9 and 163 eV can be assigned to $S^{2-}2p_{3/2}$ and $S^{2-}2p_{1/2}$ levels of the S^{2-} species in the composite [39]. All binding energy values at peaks of Mo3d and S2p in the composite shifted compared to that in single MoS_2 material, as described clearly in Figure 10. This shows that, in the hydrothermal process, there is an interaction of interlayer stacking between the

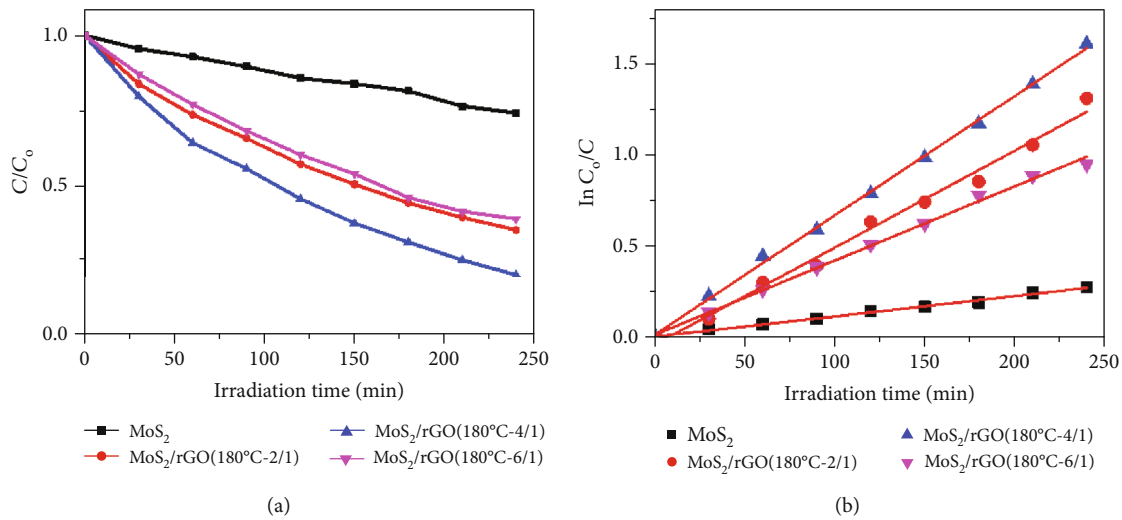

Figure 11: The change in C/C_o (a) and ln C_o/C as a function of the irradiation time for MoS_2 and MoS_2/rGO composites under the illumination of the compact light (60 W–220 V).

Table 3: Kinetic data of MoS_2/rGO samples with different ratios.

Samples	MoS_2	MoS_2/rGO (180°C-2/1)	MoS_2/rGO (180°C-4/1)	MoS_2/rGO (180°C-6/1)
Rate constant k_{app} (min^{-1})	0.00121	0.0053	*0.00652*	0.0041
Correlation coefficients (R^2)	0.994	0.988	*0.998*	0.995

MoS_2 layers on the rGO nanosheets in forming composites. Furthermore, the slight shift of Mo3d and S2p signal in the MoS_2/rGO composite to lower binding energy could be an evidence for the electrons transfer from MoS_2 to rGO which is expected to accelerate the separation of photoinduced electrons and holes.

These changes in the composite structure with different MoS_2/rGO ratios also have significant effects on the photocatalytic activity of the material in the degradation of MB (Figure 11). The results show that all the MoS_2/rGO composites exhibit a much higher catalytic activity compared to the sole component, MoS_2. Upon increasing the MoS_2 loading, the light absorption intensity of the composites increases, leading to boosting catalytic efficiency. Particularly, as the MoS_2/rGO ratio increased from 2/1 to 4/1, the degradation of RhB increased to approximately 80%. However, when this ratio increased to 6/1, photocatalytic degradation tended to decrease. This is attributed to that when the MoS_2 content overloads, it leads to aggregation on the surface of the rGO (as observed in the SEM image), which reduce the number of active sites and the light-harvesting ability in the visible region as well as the electron-hole transportation process. Therefore, the overloading of MoS_2 could limit the photocatalytic efficiency of the materials. Similar to the process of investigating the effects of temperature, the degradation of RhB in the composites with various ratios fits well with the pseudo-first-order kinetic model of Langmuir-Hinshelwood. The obtained data in Table 3 show that MoS_2/rGO (180°C-4/1) has a higher constant rate than the other samples. This can be explained by the synergistic effect between MoS_2 and rGO, which enhanced the photocatalytic performance of the materials. Among the composites, MoS_2/rGO (180°C-4/1) displayed the most excellent efficiency of RhB degradation.

4. Conclusion

In this work, the MoS_2/rGO composites were synthesized *via* a hydrothermal method using MoS_2 and rGO as precursors. The impacts of hydrothermal temperature and mass ratio of MoS_2 to rGO on surface morphology, crystallographic phase, and optical property were investigated. The efficiency for RhB photodegradation of the optimal interfacially assembled MoS_2/rGO composites can reach approximately 80%, which is three times higher than that of the single component MoS_2. This observation is due to the reduction in electron-hole pair recombination and the enhancement in visible light harvesting. Therefore, this current work revealed that the optimized MoS_2/rGO composites could be a promising candidate for the photodegradation of persistent toxic organic compounds in aqueous solutions.

Data Availability

The data used to support the findings of this study are included within the article.

Conflicts of Interest

The authors declare that there are no conflicts of interest regarding the publication of this paper.

Acknowledgments

This work was financially supported by the Vietnam Ministry of Science and Technology (Grant no. NĐT.52.KR/19).

References

[1] Q. T. H. Ta, E. Cho, A. Sreedhar, and J.-S. Noh, "Mixed-dimensional, three-level hierarchical nanostructures of silver and zinc oxide for fast photocatalytic degradation of multiple dyes," *Journal of Catalysis*, vol. 371, pp. 1–9, 2019.

[2] H. Abu Hasan, M. H. Muhammad, and N. '. I. Ismail, "A review of biological drinking water treatment technologies for contaminants removal from polluted water resources," *Journal of Water Process Engineering*, vol. 33, article 101035, 2020.

[3] Q. V. Thi, M. S. Tamboli, Q. Thanh Hoai Ta, G. B. Kolekar, and D. Sohn, "A nanostructured MOF/reduced graphene oxide hybrid for enhanced photocatalytic efficiency under solar light," *Materials Science and Engineering B*, vol. 261, article 114678, 2020.

[4] A. Sreedhar, I. N. Reddy, Q. T. Hoai Ta, G. Namgung, E. Cho, and J.-S. Noh, "Facile growth of novel morphology correlated Ag/Co-doped ZnO nanowire/flake- like composites for superior photoelectrochemical water splitting activity," *Ceramics International*, vol. 45, no. 6, pp. 6985–6993, 2019.

[5] M. N. Chong, B. Jin, C. W. K. Chow, and C. Saint, "Recent developments in photocatalytic water treatment technology: a review," *Water Research*, vol. 44, no. 10, pp. 2997–3027, 2010.

[6] R. Ameta, S. Benjamin, A. Ameta, and S. C. Ameta, "Photocatalytic Degradation of Organic Pollutants: A Review," in *Materials Science Forum*, vol. 734, pp. 247–272, Trans Tech Publications Ltd, 2013.

[7] D. N. Thoai, Q. T. Hoai Ta, T. T. Truong, H. van Nam, and G. van Vo, "Review on the recent development and applications of three dimensional (3D) photothermal materials for solar evaporators," *Journal of Cleaner Production*, vol. 293, article 126122, 2021.

[8] Q. T. H. Ta, G. Namgung, and J.-S. Noh, "Facile synthesis of porous metal-doped ZnO/g-C_3N_4 composites for highly efficient photocatalysts," *Journal of Photochemistry and Photobiology A: Chemistry*, vol. 368, pp. 110–119, 2019.

[9] A. Sreedhar, I. N. Reddy, Q. T. Hoai Ta, T. H. Phuong Doan, J. Shim, and J.-S. Noh, "Unveiling the impact of interfacially engineered selective V_2O_5 nanobelt bundles with flake- like ZnO and Co-ZnO thin films for multifunctional visible-light water splitting and toxic gas sensing," *Journal of Power Sources*, vol. 478, article 229081, 2020.

[10] Z. Shayegan, C.-S. Lee, and F. Haghighat, "TiO_2 photocatalyst for removal of volatile organic compounds in gas phase - a review," *Chemical Engineering Journal*, vol. 334, pp. 2408–2439, 2018.

[11] C. B. Roxlo, M. Daage, A. F. Ruppert, and R. R. Chianelli, "Optical absorption and catalytic activity of molybdenum sulfide edge surfaces," *Journal of Catalysis*, vol. 100, no. 1, pp. 176–184, 1986.

[12] D. James and T. Zubkov, "Photocatalytic properties of free and oxide-supported MoS_2 and WS_2 nanoparticles synthesized without surfactants," *Journal of Photochemistry and Photobiology A: Chemistry*, vol. 262, pp. 45–51, 2013.

[13] S. Li, Y. Li, L. Shao, and C. Wang, "Direct Z-scheme N-doped TiO2/MoS2Heterojunction photocatalyst for photodegradation of methylene blue under simulated sunlight," *ChemistrySelect*, vol. 6, no. 2, pp. 181–186, 2021.

[14] Y. Fu, Z. Ren, J. Wu et al., "Direct Z-scheme heterojunction of ZnO/MoS_2 nanoarrays realized by flowing-induced piezoelectric field for enhanced sunlight photocatalytic performances," *Applied Catalysis B: Environmental*, vol. 285, article 119785, 2021.

[15] Y. Chen, F. Su, H. Xie et al., "One-step construction of S-scheme heterojunctions of N-doped MoS_2 and S-doped g-C_3N_4 for enhanced photocatalytic hydrogen evolution," *Chemical Engineering Journal*, vol. 404, article 126498, 2021.

[16] E.-J. Yu, H. C. Kim, H. J. Kim et al., "Anisotropic heteronanocrystals of Cu_2O-2D MoS_2 for efficient visible light driven photocatalysis," *Applied Surface Science*, vol. 538, article 148159, 2021.

[17] L. Zhang, L. Sun, S. Liu, Y. Huang, K. Xu, and F. Ma, "Effective charge separation and enhanced photocatalytic activity by the heterointerface in MoS_2/reduced graphene oxide composites," *RSC Advances*, vol. 6, no. 65, pp. 60318–60326, 2016.

[18] S. Min and G. Lu, "Sites for high efficient photocatalytic hydrogen evolution on a limited-layered MoS_2 cocatalyst confined on graphene sheets—the role of graphene," *Journal of Physical Chemistry C*, vol. 116, no. 48, pp. 25415–25424, 2012.

[19] N. M. Julkapli and S. Bagheri, "Graphene supported heterogeneous catalysts: an overview," *International Journal of Hydrogen Energy*, vol. 40, no. 2, pp. 948–979, 2015.

[20] R. R. Nair, P. Blake, A. N. Grigorenko et al., "Fine structure constant defines visual transparency of graphene," *Science*, vol. 320, no. 5881, p. 1308, 2008.

[21] S. P. Lonkar and A. A. Abdala, "Applications of graphene in catalysis," *Journal of Thermodynamics & Catalysis*, vol. 5, article 100132, 2014.

[22] S. Pei and H.-M. Cheng, "The reduction of graphene oxide," *Carbon*, vol. 50, no. 9, pp. 3210–3228, 2012.

[23] D. B. Nimbalkar, H. H. Lo, P. V. R. K. Ramacharyulu, and S. C. Ke, "Improved photocatalytic activity of RGO/MoS2nanosheets decorated on TiO2nanoparticles," *RSC advances*, vol. 6, no. 38, pp. 31661–31667, 2016.

[24] T. T. Trang Phan, T. T. Truong, H. T. Huu et al., "Visible light-driven Mn-MoS_2/rGO composite photocatalysts for the photocatalytic degradation of rhodamine B," *Journal of Chemistry*, vol. 2020, Article ID 6285484, 10 pages, 2020.

[25] Q. T. H. Ta, G. Namgung, and J.-S. Noh, "Synthesis of Ag@rGO/gC_3N_4 layered structures and their application to toxic gas sensors: effect of Ag nanoparticles," *Electronic Materials Letters*, vol. 15, no. 6, pp. 750–759, 2019.

[26] J. Prasad, A. K. Singh, K. K. Haldar, V. Gupta, and K. Singh, "Electromagnetic interference shielding effectiveness in 3D flower-like MoS_2-rGO/gadolinium-doped nanocomposites," *Journal of Alloys and Compounds*, vol. 788, pp. 861–872, 2019.

[27] X. Guo, Y. Hou, R. Ren, and J. Chen, "Temperature-dependent crystallization of MoS_2 nanoflakes on graphene nanosheets for electrocatalysis," *Nanoscale Research Letters*, vol. 12, no. 1, article 2248, pp. 479–479, 2017.

[28] D. Wang, X. Zhang, Y. Shen, and Z. Wu, "Ni-doped MoS_2 nanoparticles as highly active hydrogen evolution electrocatalysts," *RSC Advances*, vol. 6, no. 20, pp. 16656–16661, 2016.

[29] C. Koventhan, V. Vinothkumar, S.-M. Chen et al., "Efficient hydrothermal synthesis of flake-like molybdenum disulfide

for selective electrochemical detection of metol in water real samples," *International Journal of Electrochemical Science*, vol. 15, pp. 7390–7406, 2020.

[30] J. Wang, F. Sun, S. Yang et al., "Robust ferromagnetism in Mn-doped MoS_2 nanostructures," *Applied Physics Letters*, vol. 109, no. 9, article 092401, 2016.

[31] M. Murugan, M. R. Kumar, A. Alsalme, A. Alghamdi, and R. Jayavel, "Synthesis and property studies of molybdenum disulfide modified reduced graphene oxide (MoS_2-rGO) nanocomposites for supercapacitor applications," *Journal of Nanoscience and Nanotechnology*, vol. 17, no. 8, pp. 5469–5474, 2017.

[32] L. Zou, R. Qu, H. Gao et al., "MoS_2/RGO hybrids prepared by a hydrothermal route as a highly efficient catalytic for sonocatalytic degradation of methylene blue," *Results in Physics*, vol. 14, article 102458, 2019.

[33] Y. Du, J. Wang, Y. Zou et al., "Synthesis of molybdenum disulfide/reduced graphene oxide composites for effective removal of Pb(II) from aqueous solutions," *Scientific Bulletin*, vol. 62, no. 13, pp. 913–922, 2017.

[34] F. A. Aisien, N. A. Amenaghawon, and E. F. Ekpenisi, "Photocatalytic decolourisation of industrial wastewater from a soft drink company," *Journal of Engineering and Applied Science*, vol. 9, pp. 11–16, 2013.

[35] Y. Zhong, T. Shi, Y. Huang et al., "Three-dimensional MoS_2/-graphene aerogel as binder-free electrode for Li-ion battery," *Nanoscale Research Letters*, vol. 14, no. 1, article 2916, pp. 85–88, 2019.

[36] Y. Zhou, G. Liu, X. Zhu, and Y. Guo, "Ultrasensitive NO_2 gas sensing based on rGO/MoS_2 nanocomposite film at low temperature," *Sensors and Actuators B: Chemical*, vol. 251, pp. 280–290, 2017.

[37] M. Choi, S. K. Koppala, D. Yoon, J. Hwang, S. M. Kim, and J. Kim, "A route to synthesis molybdenum disulfide-reduced graphene oxide (MoS_2-RGO) composites using supercritical methanol and their enhanced electrochemical performance for Li-ion batteries," *Journal of Power Sources*, vol. 309, pp. 202–211, 2016.

[38] W. Qin, T. Chen, L. Pan et al., "MoS_2-reduced graphene oxide composites via microwave assisted synthesis for sodium ion battery anode with improved capacity and cycling performance," *Electrochimica Acta*, vol. 153, pp. 55–61, 2015.

[39] N. Tronganh, Y. Yang, F. Chen et al., "SiO_2-assisted synthesis of layered MoS_2/reduced graphene oxide intercalation composites as high performance anode materials for Li-ion batteries," *RSC Advances*, vol. 6, no. 78, pp. 74436–74444, 2016.

Hindawi
Journal of Nanomaterials
Volume 2021, Article ID 5527519, 17 pages
https://doi.org/10.1155/2021/5527519

Research Article

Novel Eco-Friendly Synthesis of Biosilver Nanoparticles as a Colorimetric Probe for Highly Selective Detection of Fe (III) Ions in Aqueous Solution

Nguyen Le Nhat Trang,[1] Van-Tuan Hoang,[1] Ngo Xuan Dinh,[1] Le Thi Tam,[2] Van Phan Le,[3] Dong Thi Linh,[4] Doan Manh Cuong,[5] Nguyen Tien Khi,[1] Nguyen Ha Anh,[1] Pham Tuyet Nhung,[1] and Anh-Tuan Le[1,6]

[1]*Phenikaa University Nano Institute (PHENA), Phenikaa University, Hanoi 12116, Vietnam*
[2]*Advanced Institute for Science and Technology (AIST), Hanoi University of Science and Technology (HUST), 01 Dai Co Viet Street, Hai Ba Trung, Ha Noi 10000, Vietnam*
[3]*College of Veterinary Medicine, Vietnam National University of Agriculture (VNUA), Trau Quy-Gia Lam, Hanoi, Vietnam*
[4]*Department of Physics, Thai Nguyen University of Technology, Thai Nguyen City, Vietnam*
[5]*Department of Electronics and Communication, University of Information and Communication Technology (ICTU), Thai Nguyen City, Vietnam*
[6]*Faculty of Materials Science and Engineering (MSE), Phenikaa University, Hanoi 12116, Vietnam*

Correspondence should be addressed to Nguyen Le Nhat Trang; trang.nguyenlenhat@phenikaa-uni.edu.vn and Anh-Tuan Le; tuan.leanh@phenikaa-uni.edu.vn

Received 3 February 2021; Revised 19 April 2021; Accepted 29 April 2021; Published 8 June 2021

Academic Editor: Duong Tuan Quang

In this work, an eco-friendly approach for the synthesis of biogenic silver nanoparticles (bio-AgNPs) using botanical extracts in combination with an electrochemical process was carried out. We employed three types of plant extracts, including green tea leaf (GTE), grapefruit peel (GP), and mangosteen peel (MP) extracts to successfully synthesize the bio-AgNPs and optimized the experimental conditions aiming to get the highest synthetic yield. The formation of bio-AgNPs was monitored by UV-Vis spectroscopy via a surface plasmon resonance (SPR) band at about 420–430 nm. Transmission electron microscope (TEM) showed their spherical shape with the size range within 23–55 nm. While X-ray diffraction (XRD) analysis described in detail the crystalline structure of the bio-AgNPs with a face-centered cubic crystal lattice of metallic silver. The chemical bonding and elemental compositions of the bio-AgNPs were determined by Fourier Transform Infrared (FTIR) spectroscopy, in which organic compounds in the natural extracts not only acted as effective reductants but also capping agents for the fabricated bio-AgNPs. The prepared bio-AgNPs exhibited high stability and excellent dispersion for about four months. Based on the linear relationship between obtained SPR band intensity of bio-AgNP GTE in the presence of Fe (III) and concentration of Fe (III) ions, our bio-AgNP GTE can be used to develop a highly selective colorimetric sensor for the determination of Fe (III) ions within a linear range from 1 to 25 μM. According to that, the limit of detection (LOD) was recorded at approximately 0.532 μM, and the quantitative limit (LOQ) was calculated to be 1.77 μM. A detection mechanism was proposed through redox reactions between bio-AgNP GTE and Fe (III) ions. More interestingly, this method was successfully applied for the determination of Fe (III) ions in a lake water sample with percentage recovery of 107-150% and high reproducibility (RSD = 1.49%).

1. Introduction

Nanoscience is an emerging multidisciplinary field facilitating the design development, improvement, and potential application of nanomaterials. Metallic nanoparticles (NPs) exhibit many unique features such as high aspect and surface area/volume ratios, novel electromagnetic, chemical, and optical properties compared to those of the bulk metal [1–3]. Among them, AgNPs have been regarded as promising candidates for various studies in nanoscience due to their unique properties including antibacterial [4, 5], antifungal [6, 7], antiviral [8], antioxidant [9, 10], and anticancer [11] activities contributing to developing applications in wound healing, dentistry, and biomedicine [6, 12–16]. Besides, AgNPs have also been reported as a new generation of catalysts for organic chemistry [17] and highly sensitive bio/-chemosensors [18]. Those attractive applications lead to a growing demand for novel fabrication types of AgNPs.

The AgNPs in different sizes and shapes have been synthesized for several years by a series of various techniques, for example, physical, chemical, and biological ones [19]. Even though some physical and chemical methods have been successfully reported for producing the AgNPs in aqueous stable state in controlled sizes and shapes [20–24], many of them have required extreme synthetic conditions such as high temperature and pressure, which might be expensive and tedious for material costs. Moreover, the use and release of hazardous chemicals and solvents are potential risks for the environment and human health [25, 26]. Hence, there is a growing need to investigate alternative approaches which are more environmentally and economically feasible to synthesize these NPs. Biogenic methods of fabrication of AgNPs involving bacteria, fungi, or plant extracts might answer this demand. In recent years, plant extracts have been the most favorable. Stems, leaves, roots, flowers, or fruits of plant species have been employed to synthesize functional nanomaterials applying green chemistry technology [27–30]. In comparison to other biological routes, plants exhibit more accessible availability, more convenient preparation, better cost-effectiveness, and more comfortable scaling up production [31–33]. Besides, in the presence of plant extracts, the rate of metal ion reduction is also higher compare to that of microorganisms [33]. In general, various metabolites and reductive biomolecules (e.g., polyphenols, tannic acids, flavonoids, and terpenoids) in the plant extracts act as bioreductants to reduce Ag^+ ions into metallic Ag^0 simultaneously. They also play the role of stabilizers to prevent the conglomeration of bio-AgNPs [27, 34]. Furthermore, using polyphenols, flavonoids, terpenoids, amino acids, vitamins, etc. from plant extracts as capping agents can improve the characteristics of newly fabricated NPs [15, 35, 36], which is promising to develop advanced technological applications.

Previously, bio-AgNPs have been synthesized by using different plant extracts as reducing agents. Aloe vera leaf extract (*Aloe vera*) was employed to prepare bio-AgNPs with the size of 70–192 nm from $AgNO_3$ solution using the hydrothermal method [37]. In 2013, Geethalakshmi and Sadara described the one-step synthesis of bio-AgNPs based on incubation of aqueous solutions containing $AgNO_3$ and a solution of saponin isolated from *Trianthema decandra*. They obtained the NPs rapidly with the size of 17.9–59.6 nm [38]. Besides, tea leaf extract has been a popular candidate to develop different methods on this approach. Many kinds of evenly dispensed bio-AgNPs with the various diameters (from 20 to 90 nm) have been prepared using this kind of extract [39–42]. In a recent study, Sökmen et al. were successful in designing to generate the bio-AgNPs with green tea extract in citric acid 0.1 M. The bio-AgNPs of about 15 nm in diameter were obtained in a microwave-assisted production system after the addition of $AgNO_3$ solution [39]. More recently, spherical bio-AgNPs were produced from $AgNO_3$ using green tea extracts in a basalt medium. The newly fabricated NPs exhibited low toxicity to mammalian cells but antibacterial effects on several pathogenic bacteria [42]. Those studies resulted in successful biogenic manufacture of AgNPs with excellent applications; however, they still involved several chemicals, especially silver salts ($AgNO_3$) in excess, which is a source of Ag^+ that is toxic to mammalian cells [43], so it is harmful to human and also the ecosystem. Thus, researchers still keep trying to investigate more "green" methods for the synthesis of bio-AgNPs.

From an analytical point of view, iron (Fe) is essential for living bodies in all biological kingdoms. It is necessary for many physiological processes such as oxygen transportation, electron transfer, and regulation of cell growth and differentiation [44, 45]. However, at the evaluated level, it becomes toxic as excess free iron in cells, which can produce reactive oxygen species (ROS) arising from interconverting between Fe^{3+} and Fe^{2+}. Moreover, there is no active mechanism to excrete ion from the body. As a result, excess iron often leads to the damage of different organs, especially the heart, liver, and bone [46]. Nowadays, an increasing amount of ferric ion from domestic, agricultural, and industrial activities has been accumulated in the aqueous ecosystem, while water treatment plants are unable to eliminate it completely. As a result, even our drinking water and food source have been polluted with ferric ions. The World Health Organization (WHO) has set the "Guidelines for Drinking-Water Quality" of Fe (III) ions as 2 mg/mL (36 μM) [47]. Hence, it is pertinent to develop a sensitive method to determine Fe (III) ions in aqueous systems, biological, or food specimens [48]. Definitely, Fe (III) ions can be detected and quantified accurately by routine analytical techniques including atomic absorption spectroscopy (AAS), in-mass mass spectrometry, and inductively bonded plasma emission spectroscopy and liquid chromatography high performance (HPLC) [49–54]. However, these methods require expensive instruments, technical expertise, and elaborate sample preparation. Recently, the colorimetric detection method using plasmonic NPs has attracted the attention of global researchers due to its simplicity, high sensitivity, and fast response. Moreover, this method is capable to be developed into a compact and portable sensing system for practical applications. On the other hand, gold and silver have been known as noble metal NPs possessing impressive optical properties, which have been the most-used materials for this approach of Fe (III) detection. The gold nanoparticle was employed in a 2011 study to detect Fe^{3+} in the linear range of 10 μM–60 μM and

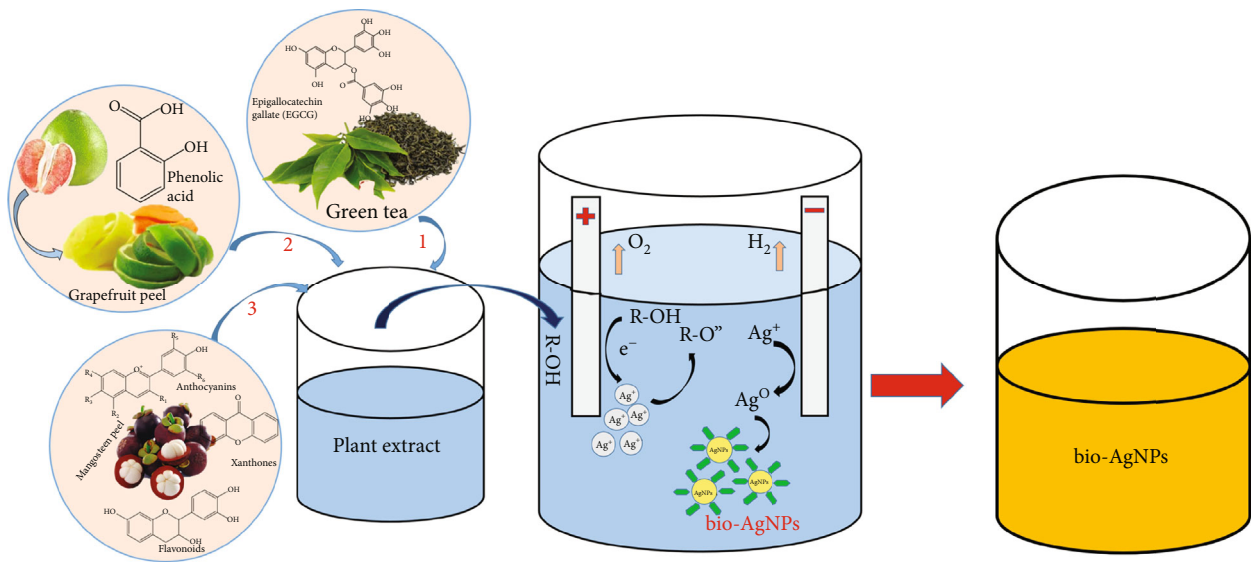

Figure 1: Extraction process combined with the electrochemical method to fabricate bio-AgNPs from plant extracts.

detection limit LOD = 5.6 μM [55]. In 2015, Gao et al. fabricated and utilized N-acetyl-L-cysteine stabilized AgNPs for detecting Fe (III) ions in the linear concentration range from 80 nM to 80 μM, corresponding to LOD = 80 nM [56].

In this study, we proposed a new method to synthesize a bio-AgNP solution using extracts from three natural plant sources including green tea leaves, grapefruit peel, and mangosteen peel in combination with an electrochemical technique using a metallic silver bar to produce Ag^+ ion source. This is a new "green" technology that is highly efficient in generating metallic nanomaterials in controlled shapes and sizes and can be easily scaled up for a large amount of products. The conventional electrochemical synthesis of AgNPs was performed by allowing an electric current to flow between two electrodes (cathode and anode) in an electrolyte solution. Here, we used plant extracts as electrolyte solutions. *Epigallocatechin gallate* in green tea leaves [40, 41]; *phenolic acid* in grapefruit peel [57]; and four main phenolic compounds including *xanthones*, *flavonoids*, *anthocyanins*, and *tannins* in mangosteen peel [58, 59] played the roles of reducing agents to reduce Ag^+ ions into Ag^0 as well as a surface stabilizer to help the newly synthesized nanoparticles to be well-dispersed and stable in the aqueous environment. The whole experiments were carried out under ambient conditions, using natural plant extracts as alternatives for metal salts and organic solvents. Therefore, this method is more simple, eco-friendly, and high cost-effective to synthesize the bio-AgNPs. The fabricated bio-AgNPs were characterized via different techniques, for instance, transmission electron microscopy (TEM), X-ray diffraction (XRD), and Fourier Transform Infrared (FTIR) spectroscopy to determine their size, shape, and composition. According to that, to take advantage of the potential optical properties of these novel bio-AgNPs, the development of colorimetric sensing systems has been more focused, so here, we described a bio-AgNP-based ultrasensitive detection of Fe^{3+} ion in aqueous solutions. By adding Fe (III) ions, the color of the bio-AgNP solution rapidly changed and the color difference could be observed by the naked eye. It is undeniable that the bio-AgNP solution is an ideal probe for a simple, fast, sensitive, and environmentally and economically effective method of Fe (III) detection.

2. Experimental Procedures

2.1. Chemicals. Two silver rods with a height of 70 mm and a diameter of 2 mm are used as electrodes. Ammonium hydroxide (NH_4OH, 25%), nitric acid (HNO_3, 63%), sulfuric acid (H_2SO_4, 98%), hydrochloric acid (HCl, 37%), iron (III) nitrate ($Fe(NO_3)_3$, 99%), copper (II) sulfate ($CuSO_4$,99%), potassium carbonate (K_2CO_3, 99%), zinc nitrate($Zn(NO_3)_2$, 99%), nickel (II) nitrate ($Ni(NO_3)_2$, 99%), cobalt (II) chloride ($CoCl_2$, 99%), and sodium chloride (NaCl, 99%) were obtained from Shanghai Chemical Reagent.

2.2. Preparation of Plant Extracts. Three kinds of botanical extracts from the green tea leaf, grapefruit peel, and mangosteen peel were prepared. Raw materials (with the weight mentioned below) were collected and washed by water and, then, dried naturally under shade. Next, they were cut into fine pieces. After that, each kind of plant material was immersed in 100 mL distilled water at 80°C. The mixture was incubated at 60°C for 20 minutes upon constant stirring to extract organic compounds from plant materials. From each mixture, 80 mL of plant extract was obtained and diluted using 420 mL of distilled water for the following experiments.

2.3. Electrochemical Synthesis for Bio-AgNPs Combined with Plant Extracts. The proposed process for the synthesis of bio-AgNPs is based on a two-electrode setup system in combination with the controlled addition of natural plant extracts (see Figure 1). The electrochemical experiments were carried out in a 500 mL beaker filled with diluted botanical extracts as described in the part of experimental procedures. Two rods of bulk Ag (70 mm in height × 2 mm in diameter) were

employed as the anode and the cathode and placed vertically face-to-face 3 nm apart. The two electrodes were mechanically polished and washed with distilled water to eliminate oxides on the surface. Electrolysis was performed at room temperature upon magnetic stirring. The voltage and time for the electrochemical process will be mentioned below. During electrolysis, the solution color gradually changed from yellow to finally to yellowish-brown, suggesting the formation of bio-AgNPs.

2.4. Optimization of Experimental Conditions for Electrochemical Synthesis of Bio-AgNPs Using Plant Extracts. To optimize the electrochemical synthesis of bio-AgNPs with the presence of plant extracts, three factors, including the amount of extract, reaction time, and DC voltage setup during electrolysis, were investigated to evaluate their effects on the fabrication of bio-AgNPs.

With group 01, electrochemical synthetic bio-AgNPs using green tea extract (bio-AgNP GTE), the weight of dry green tea was varied from 0.5 to 2 g, and the extract was employed for electrolysis in 30 minutes at a constant voltage of 12 V. After obtaining the optimal amount of green tea, this amount of botanical material was used to conduct the following experiments during varied periods of fabrication time, from 15 to 45 minutes, at a voltage of 12 V (Table S1).

With group 02, electrochemical synthesis of bio-AgNPs using grapefruit peel extract (bio-AgNP GP) was also performed under different experimental conditions. First, from fresh grapefruit peel with the weight in a range from 2.5 to 4.5 g, the extracts were prepared as an electrolyte for electrolysis in 30 minutes at the voltage of 12 V. The optimal amount of grapefruit peel was then applied for other electrochemical syntheses in 30 minutes, in which the DC voltage was the variable (6–16 V). Finally, using the optimal amount and voltage, electrolysis was carried out in different periods (20–45 minutes) to optimize this factor (Table S2).

Similarly, for group 03, electrochemical synthesis of bio-AgNPs using mangosteen peel extract (bio-AgNP MP), we also conducted experiments to evaluate the influence of amount, voltage, and reaction time, on the formation of bio-AgNPs. First, fresh mangosteen peel weighted from 3 to 11 g was employed for the preparation of electrolyte solutions for electrolysis performed in 30 minutes at a constant voltage of 12 V. Second, different voltages (8–16 V) were applied in the electrochemical process using the optimal plant exact as an electrolyte in 30 minutes. Finally, reaction time was also optimized using the same strategy, in which it varied in the range from 15 to 45 minutes (Table S3).

2.5. Colorimetric Detection of Fe (III) Ions. 0.5 mL of diluted bio-AgNP GTE, GP, and MP into 10 mL using 9.5 mL of distilled water was used as a primary testing sample. 1 mL of Fe (III) ion solution in the various concentrations ranges from 1 to 25 μM was introduced into the above solution. The mixtures were then shaken in 20 minutes using a shaker before the corresponding absorbance spectra were recorded by UV-Vis spectrophotometer. The experiment was repeated three times.

The LOD and LOQ were calculated through the following equations (Eqs. 1 and 2):

LOD = 3S/b,(1)

LOQ = 10S/b,(2)

where S is the standard deviation of the blank solution and b is the slope of the analytical curve.

2.6. Characterization Techniques. A Bruker D5005 X-ray diffractometer using Cu-K_a radiation (λ = 0.154056 nm) under a voltage of 40 kV and a current of 30 mA was employed to investigate the crystalline structure of the synthetic samples. The morphology and size of the bio-AgNPs were studied using a JEOL JEM 1010 transmission electron microscope (TEM) at an acceleration voltage of 80 kV and the Fourier transform infrared (FTIR, JASCO 6100) spectroscopy was obtained with the KBr pellet technique in the 4000–400 cm^{-1} spectral region and a resolution of 2 cm^{-1}, respectively. The value of pH was measured by pH meters PH1200, Horiba, Japan. The UV-Vis absorbance spectra were recorded using an HP 8453 spectrophotometer, and 10 mm path length quartz cuvettes were used for the measurement.

3. Result and Discussion

3.1. Research on the Formation of Bio-AgNPs through the Electrolysis Method in the Presence of Plant Extracts

3.1.1. Optimization of the Electrochemical Process for the Synthesis of Bio-AgNPs Using Plant Extracts. The color change of the botanical extract solutions during electrolysis is the first signal of the successful syntheses of bio-AgNPs. In the experiments using the green tea extract or the grapefruit peel extract, the solutions gradually turned from pale yellow to yellowish. With the samples using mangosteen peel extract, the solution color changed from red to yellow-brown. The color change before and after synthesis can be considered to the Surface Plasmon Resonance (SPR) property of bio-AgNPs [60]. The UV-visible spectra of bio-AgNPs were examined after each experiment of synthesis. The value of λ_{max} was determined and compared to investigate the optimal conditions for the electrochemical synthesis of bio-AgNPs. As mention in the part of experimental procedures, we examined three factors, including the amount of extract, reaction time, and DC voltage.

With group 01, as-synthesized bio-AgNPs using green tea extract (bio-AgNP GTE), the first parameter studied was the weight of green tea. Reactions were independently performed employing different amounts of dry green tea in the range from 0.5 to 2 g. As illustrated in Figure S1a, an SPR band was easily seen in the range of 420–450 nm for the bio-AgNPs synthesized using different amounts of green tea, which is consistent with the characteristic range of λ_{max} for AgNPs [60]. Moreover, the intensity of the SPR band of bio-AgNP GTE increased with an increase in the weight of the raw botanical material, corresponding to the darker color of the solution towards yellowish-brown. Nevertheless, when using 2 g of green tea, after electrolysis, the solutions turned greenish-gray and the intensity of the SPR band significantly decreased, in comparison to other

samples. It may be explained by the aggregation of formed bio-AgNPs in the solution.

From visual observation of the UV-Vis spectra as well as the color of the solution after electrolysis, the most appropriate weight of green tea was found that should be used for extraction and biogenic synthesis of bio-AgNP GTE. Using 1 g of green tea for the synthesis, we obtained a sharp SPR band at 420 nm, corresponding to the yellowish-brown color of the solution. Furthermore, increasing the mass of green tea from 0.5 to 1 g resulted in the rise in SPR intensity, as well as a red-shift, which is attributed to increasing the grain size of bio-AgNPs. It was also confirmed by the characteristic color change of bio-AgNPs. Therefore, we propose that the optimal amount of green tea for the preparation of bio-AgNPs is 1 g in this study.

Employing the optimal mass of green tea, we examined the influence of electrochemical time on the synthesis by performing the bio-synthesis in different reaction times to find the most appropriate one. As shown in Figure S1b, lengthening the reaction time led to the increase of the SPR band, corresponding to the change of the color toward brown. After 45 minutes of electrolysis, the SPR band reached the highest intensity with the sharpest peak at 420 nm. This improvement might be due to the increase in the concentration of NPs in the solution. In consequence, the optimal conditions for electrochemical synthesis of bio-AgNPs using green tea extract are using 1 g green tea for extraction. The electrolysis should be carried out in 45 minutes at a constant voltage of 12 V.

Concerning Group 02 of as-synthesized bio-AgNPs using grapefruit peel extract (bio-AgNP GP), we investigated all three factors to optimize the conditions for the biosynthesis. Different amounts of fresh grapefruit peel were employed for extraction, and the extracts were then used as an electrolyte solution for electrolysis. An SPR band of about 430 nm, which is characteristic of bio-AgNPs, was observed in every sample. Moreover, the intensity of the SPR band of bio-AgNP GP was enhanced by adding more grapefruit peel, from 2 g to 4.5 g, corresponding to the color change from yellow-brown to dark-brown (Figure S2a). Among those UV-Vis spectra, the sample using 2.5 g grapefruit peel exhibited the sharpest SPR peak without broadband within 500–600 nm region and yellowish-brown color, showing the uniform formation of bio-AgNP GP. Therefore, this amount of grapefruit peel was chosen for the following experiments.

Similarly, different DC voltage and reaction times were also examined. To evaluate the effects of applied voltage on the bio-AgNP formation, we applied the variation of electrolytic voltage in the range of 6–16 V (Figure S2b). At low voltage such as 6 V and 8 V, there was no characteristic band for bio-AgNP GP. At higher voltage, from 10 V, we started observing absorption bands. However, at the voltage of 10 V, 14 V, and 16 V, the absorption spectra showed a band at around 400 nm and a large shoulder at about 500 nm, while at the voltage of 12 V, a sharp band was observed at 430 nm, which is characteristic for bio-AgNPs. Therefore, it was evident that 12 V is the optimal voltage for the electrochemical synthesis of bio-AgNPs using grapefruit peel.

Figure S2c demonstrates the effect of the electrochemical time tested on the electrochemical synthesis at 12 V, using the extract from 2.5 g grapefruit peel as an electrolyte. Although lengthening the reaction time resulted in the increase in the intensity of the absorption bands in UV-Vis spectra, only the spectrum of the sample of 30 minutes exhibited the characteristic SPR band for bio-AgNP GP at 430 nm. Thus, the optimal reaction time for electrochemical synthesis of bio-AgNP using grapefruit peel extract is 30 minutes.

To sum up, the optimal experimental condition for the synthesis of bio-AgNPs from grapefruit peel extracts through the electrochemical process is the usage of 2.5 g grapefruit peel for extraction, an electrolytic voltage of 12 V, and a reaction time of 30 minutes.

A similar sequence of experiments was performed using mangosteen peel extract as the electrolyte solution for the electrochemical synthesis of bio-AgNPs MP to optimize those three factors. Several amounts of fresh mangosteen peel, from 3 to 11 g, were employed for extraction. Being different from the other extracts, the color of mangosteen peel extract is red in color, so during the electrochemical synthesis, the color gradually switched from red to reddish-brown and then dark brown. However, the SPR band at about 420 nm further confirmed the formation of bio-AgNP MP (Figure 2(a)). The increase in weight of the fresh mangosteen peel led to an increase in the intensity of the SPR band of bio-AgNP MT. Moreover, a red-shift was recorded in the UV-Vis spectra of bio-AgNP MP synthesized using a larger amount of mangosteen peel extract compared to the one using a lower amount. It might be due to the increase in particle size, exhibiting via the darker color of the bio-AgNP MP solution. Using 5 g of mangosteen peel, we obtained a sharp SPR band at 420 nm. Using a larger amount of peel such as 7 or 9 g did not significantly improve the band intensity. Employing 11 g of mangosteen peel led to a rise in the intensity of the SPR band; however, the appearance of a shoulder at around 510 nm might correspond to the aggregation of AgNP MP in the solution. Therefore, 5 g of mangosteen peel was chosen as the optimal mass of botanical material for the following experiments.

Voltage is also an important factor that impacts the formation of bio-AgNP MP during electrochemical synthesis. As shown in Figure 2(b), starting from 10 V, a SPR band was observed at around 420 nm. Clearly, the increase in the voltage led to improve significantly intensity of the SPR band. Compared to the other voltages, the sample using 12 V and 14 V for electrolysis exhibits a sharp band without any large shoulder. We select the voltage of 12 V for the following experiments.

Reaction time is the last parameter that we studied to optimize experimental conditions for electrochemical synthesis of bio-AgNPs using mangosteen peel extracts. Figure 2(c) demonstrates that the intensity of the SPR band increased with the lengthening of reaction time as longer reaction time might have allowed more Ag^+ to come into the solution and be reduced to Ag^0 to form metallic NPs. After 30 minutes of electrolysis, the solution obtaining exhibited a sharp SPR band at 420 nm. Extending the reaction time to 40 minutes did not significantly improve the intensity of

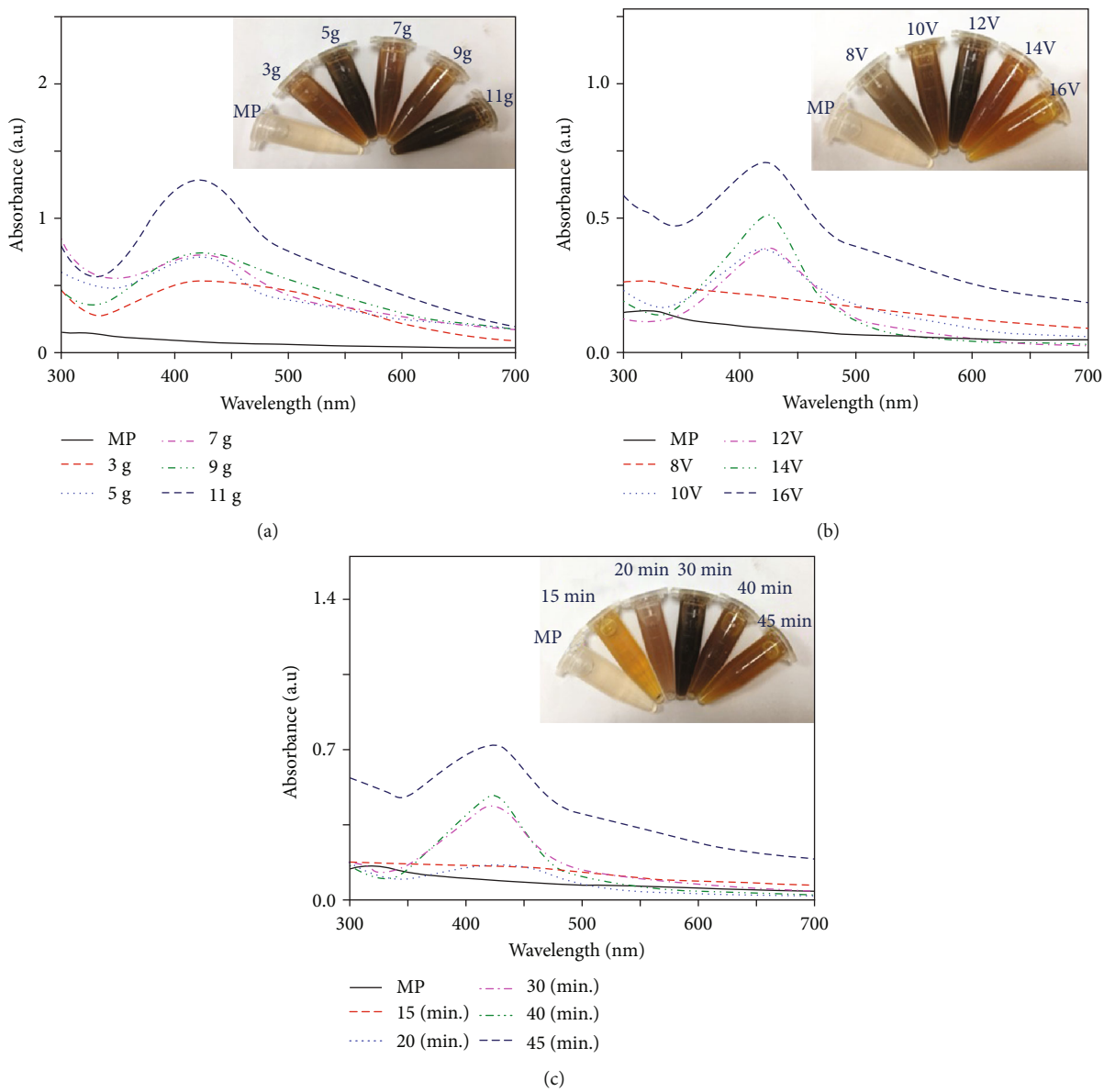

Figure 2: UV-Vis spectrum of bio-AgNP MP using mangosteen peel extracts synthesized at different masses of mangosteen peel (a), the applied DC voltage (b), and time of synthesis reaction (c), respectively. Insert pictures of bio-AgNP MP with different experimental conditions.

the band. After 45 minutes, the intensity increased but the appearance of a shoulder at about 520 nm might be a signal of aggregation. Furthermore, the color of the sample after 30 minutes of electrolysis was the darkest, which might correspond to the highest concentration of bio-AgNP MP. Hence, the reaction time of 30 minutes was regarded as the most appropriate one for this kind of synthesis.

In summary, to synthesize bio-AgNP MP using mangosteen peel extracts through electrochemical technique, 5 g of the fresh peel should be used for extraction, and the electrolysis should be carried out in 30 minutes at a constant voltage of 12 V.

3.1.2. A Mechanism for the Formation of these Bio-AgNPs. The results obtained from the investigation for optimal experimental conditions suggested that the formation of bio-AgNPs was substantially influenced by the mass of the raw botanical materials. We expected that it also affects the composition of the fabricated bio-AgNPs.

Green tea leaf extract contains several water-soluble phenolic compounds such as catechin (C), epicatechin (EC), epigallocatechin (EGC), and epigallocatechin gallate (EGCG) [40]. In particular, catechins are the main phenols in green tea, which allows the silver ions to be strongly reduced and thus to form AgNPs [40]. The phenolic configuration and catechin content, as well as the quantitative extraction of the extract, can be determined by HPLC analysis as previously reported [61]. Based on the above results, a possible mechanism of the bio-AgNP formation in green tea extract was proposed in Figure 3. Upon application of voltage, OH^-

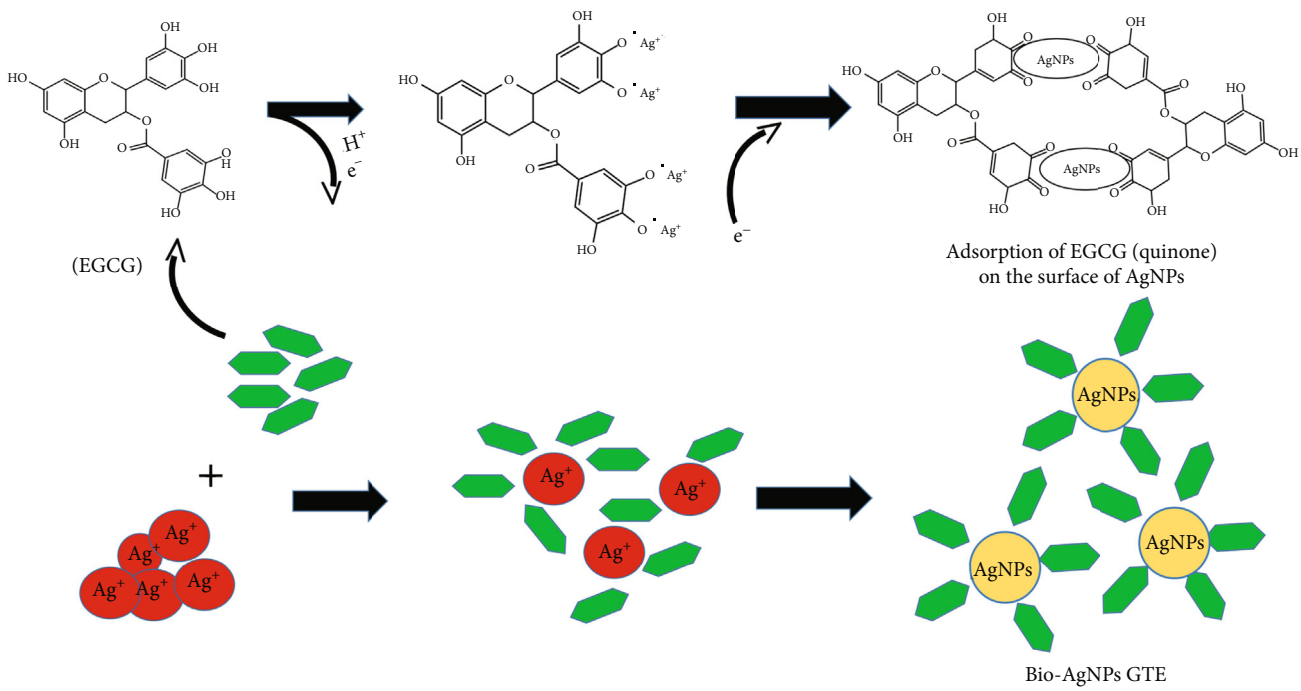

Figure 3: Mechanism of forming bio-AgNP GTE from green tea extract.

ions and Ag^+ ions were formed on the surface of the cathode and anode at the same time. Silver ions migrated from the anode migrate to the cathode, a part of Ag^+ ions was reduced to Ag^0. EGCG presents as the most-seen catechin, and it is also the most active component in green tea. EGCG consists of multiple phenolic hydroxyls, so it tends to eject the phenolic photon strongly. Hence, the presence of poly –OH groups in the structure explains why EGCG can transfer the photon to Ag^+ easily to form stable EGCG-AgNPs [41] (see Figure 3).

Figure 3 illustrates the possible mechanism of bio-AgNP GTE formation during the electrochemical process in the presence of EGCG from green tea extract. The first reaction represented proton ejection (one electron one-step oxidation-reduction mechanism), leading to the formation of Ag^0 and EGCG radical. In the following reaction, EGCG radical is immediately converted to a stable quinone. Ag^0 atoms aggregated together to form clusters, and then, they grow into bio-AgNPs. These NPs were coated by the phenolic compound EGCG to achieve a steady-state of NPs.

Grapefruit peel extract contains phenolic acid, while mangosteen peel extract contains several kinds of phenolic compounds. Thus, the formation of bio-AgNP MP also occurred in a similar mechanism as the flexible –OH groups of these polyphenolic compounds transfer their proton to reduce Ag^+ to Ag^0. Silver atom then aggregated together and became NPs coated by the phenolic compounds in the extracts (Figure S3).

3.1.3. Characterization Studies and Stability of Bio-AgNPs at the Optimum Conditions. Once bio-AgNPs were prepared using green tea extracts under the optimal conditions, the successful fabrication of bio-AgNPs was confirmed by TEM, XRD, and UV-Vis spectroscopy analyses, respectively. TEM images (Figure 4(a)—the inset) show the encapsulation of organic compounds in the plant extracts around the bio-AgNP GTE as well as the size and shape of the NPs. These images indicate that the bio-AgNP GTE were spherical in the size range of 20-30 nm, and they are evenly distributed within the shell of EGCG. The bio-AgNP GTE were dried and employed for XRD measurement (Figure 4(a)). The diffraction peaks at 38.1°, 44.4°, 63.8°, and 76.7° matched well to the (111), (200), (220), and (311) crystalline planes of the pure face-centered cubic (fcc) silver structure, respectively, which agrees with the reference JCPDS PDF 04-0783. In addition, no characteristic diffraction peaks of other phases (e.g., Ag_2O and AgOH) were detected in the two patterns, indicating high crystallinity of prepared bio-AgNP GTE. Also, XRD analysis further confirmed the formation of single-phase bio-AgNP GTE with high purity. Using the Debye-Scherrer equation, the average crystalline size of the bio-AgNP GTE was calculated to be approximately 23 nm, in accordance with TEM images.

The presence of polyphenols from green tea extracts on the NPs surface (Figure 4(b)) was demonstrated by Fourier-transform infrared (FTIR) spectroscopy data of bio-AgNP GTE. The broad and intense band at 3420 cm^{-1} were presented in the spectrum of bio-AgNP GTE, which was similar to that of the green tea extract. This peak was associated with the O–H elongated vibrations assigned -OH groups from polyphenols in green tea extracts such as catechins [62]. The band at 2913 cm^{-1} corresponded to elongated oscillations C-H and CH_2 of hydrocarbons [42]. The peak of 1630 cm^{-1} involved a prolonged C=O oscillation of the conjugate bonded to ketone, quinones, carboxylic acids, and esters [41, 42]. At 1392 cm^{-1}, there was a C-N elongated vibration of

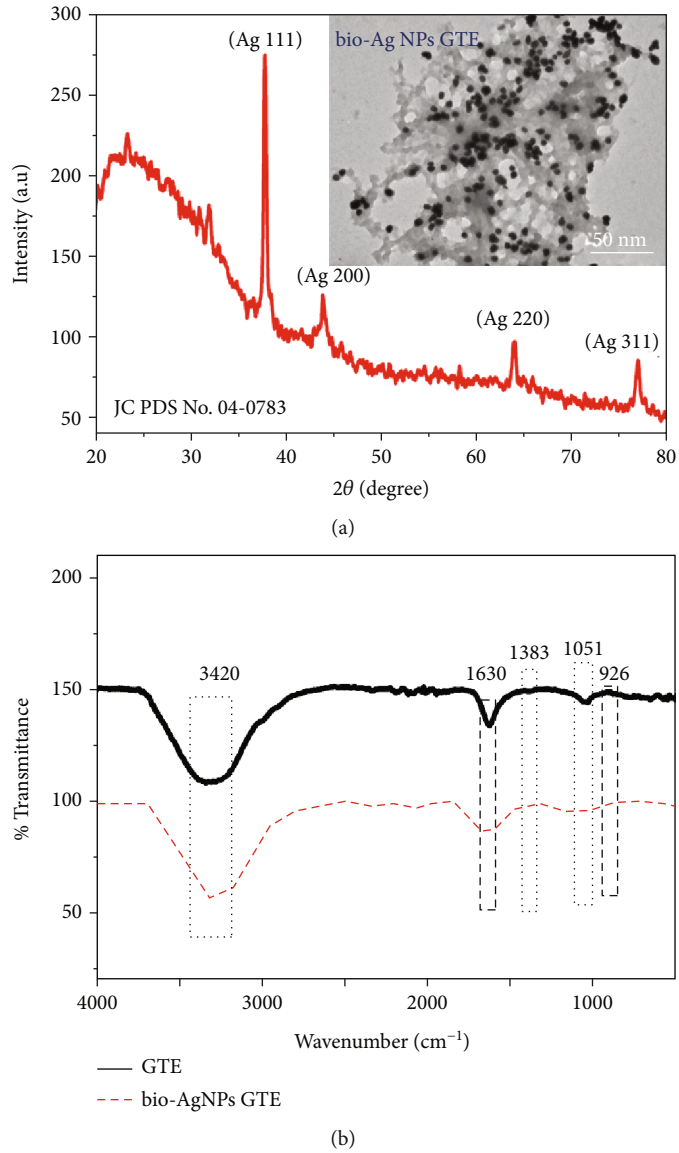

Figure 4: (a) XRD spectrum (inset: TEM image of bio-AgNP GTE). (b) FTIR spectrum of bio-AgNP GTE synthesized with green tea extract.

aromatic amines, indicating the presence of water-soluble EGCG. Furthermore, the band located at 1044 cm^{-1} was associated with C-O-C elongated vibration [63]. Most of the obtained results agreed with previous reports [64–66] and demonstrated the presence of the polyphenol in green tea extract as a protective agent on the bio-AgNP GTE surface, which also helped NPs to be well-dispersed in the aqueous environment.

Two other types of bio-AgNPs synthesized using grapefruit peel and mangosteen peel extracts were also characterized through XRD spectroscopy (Figure S4). Figure S4a demonstrates the XRD measurement of bio-AgNP GP prepared using grapefruit extract with diffraction peaks at 37.9°, 43.9°, 63.8°, 76.67°, and 82.7°, corresponding to (111), (200), (220), (311), and (222) crystalline planes of the pure fcc of bulk Ag (JCPDS PDF 04-0783). Besides, the Debye-Scherrer equation was used to determine the average crystal size of the formed bio-AgNPs in the range of 26 nm. Figure S4b shows the XRD data of bio-AgNP MP synthesized with mangosteen peel extract. Four diffraction peaks at 38°, 44.2°, 64°, and 76.6° were suitable for the (111), (200), (220), and (311) crystalline planes of the fcc silver structure, in accordance to JCPDS PDF 04-0783. The average crystal size of bio-AgNP MP was determined approximately 55 nm by using the Debye-Scherrer equation. In addition, no characteristic diffraction peaks of Ag_2O or AgOH were observed in the XRD results of all types of bio-AgNPs. These newly fabricated bio-AgNPs were confirmed to possess a face-centered cubic structure and high purity.

The stability of three types of bio-AgNPs synthesized using green tea, grapefruit peel, and mangosteen peel extract was also examined via visual observation and UV-Vis spectroscopy. Two months after synthesis, SPR bands of these bio-AgNPs showed an increase in intensity (Figure 5). This can be explained that the phytochemical compounds in the

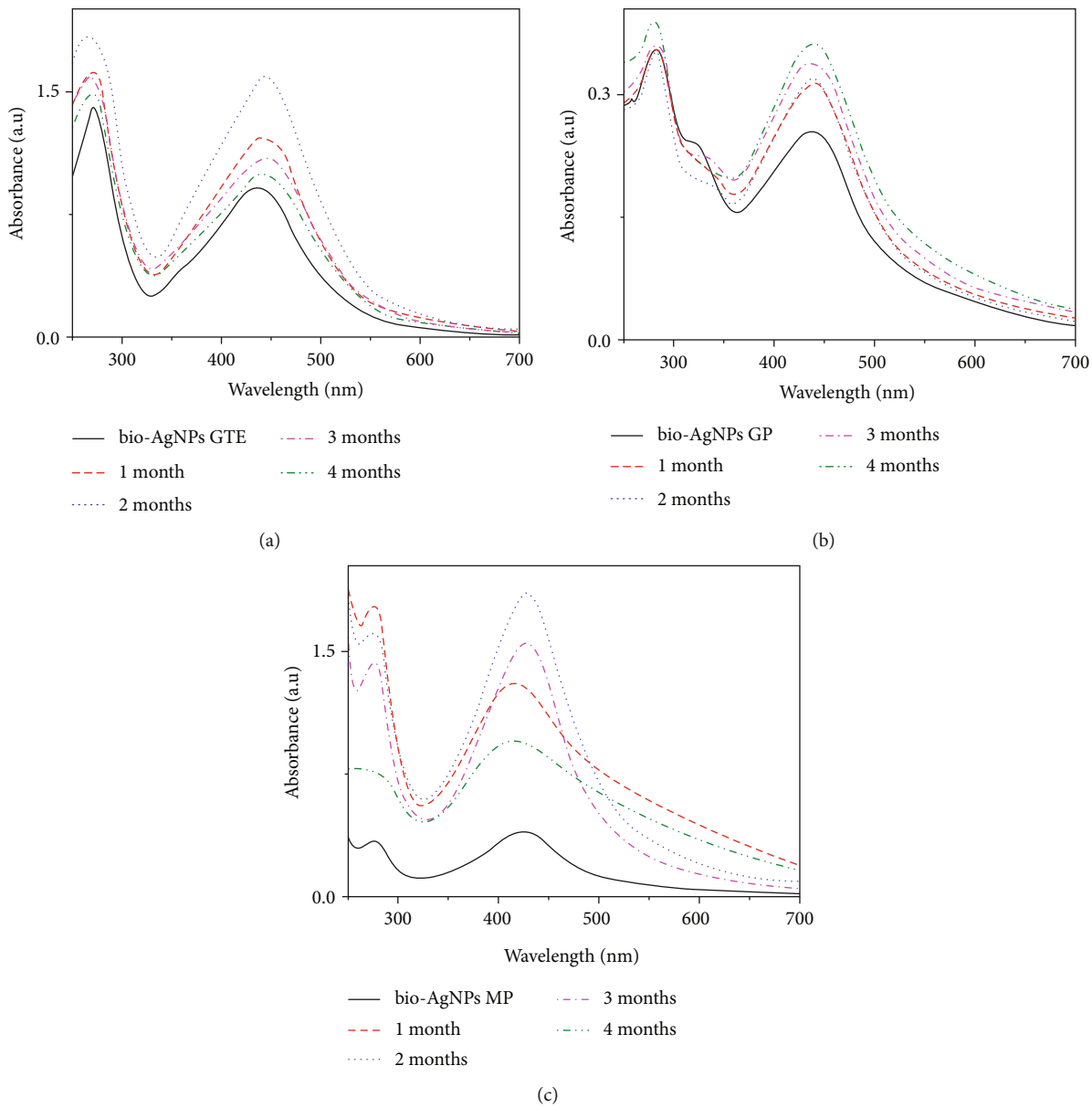

Figure 5: UV-Vis spectroscopy monitoring the stability of bio-AgNPs synthesized from green tea extract (a), grapefruit peel (b), and mangosteen peel (c) over time.

plant extracts were weak reducing agents, so Ag^+ formed by the electrochemical process was not completely reduced to Ag^0. Therefore, during this storage period, the reduction continued occurring, resulting in the enhanced concentration of bio-AgNPs, which caused the rise in absorption intensity. Two months later, the intensity of the SPR band of bio-AgNPs prepared using green tea and mangosteen peel extract tend to gradually decrease, corresponding to the faded color of the solutions. The reduction might stop. In addition, a sedimentation phenomenon was observed as NPs started aggregated. The percentage increase in the absorption intensity of bio-AgNPs over storage time was calculated in Table S4. Concerning bio-AgNPs fabricated with grapefruit peel extracts, even four months after synthesis, the SPR band intensity continued increasing, which could be the result of the continuous reduction.

3.2. Research on the Applicability of Bio-AgNPs towards Colorimetric Detection of Fe (III) Ions in Aqueous Solution. The bio-AgNPs synthesized from plant extracts were used with an aim to detect the colorimetric of metal ions. 1 mL of 25 μM Fe (III) ion was added to 10 mL of diluted bio-AgNP solutions (as described in the part of the experimental procedures). After being well-shaken, the color change of the solutions was observed by the naked eye. Besides, the obtained results from UV–visible spectroscopy exhibited the differences in their SPR band. By naked eye, it can see that only the bio-AgNP GTE synthesized from green tea extract showed the obvious color change in adding of Fe (III) ion, namely, the solution color of the bio-AgNP GTE changed from yellow to nearly colorless due to the agglomeration of created NPs. This change was then confirmed by UV-Vis absorption spectra with a drop-off in intensity along with a

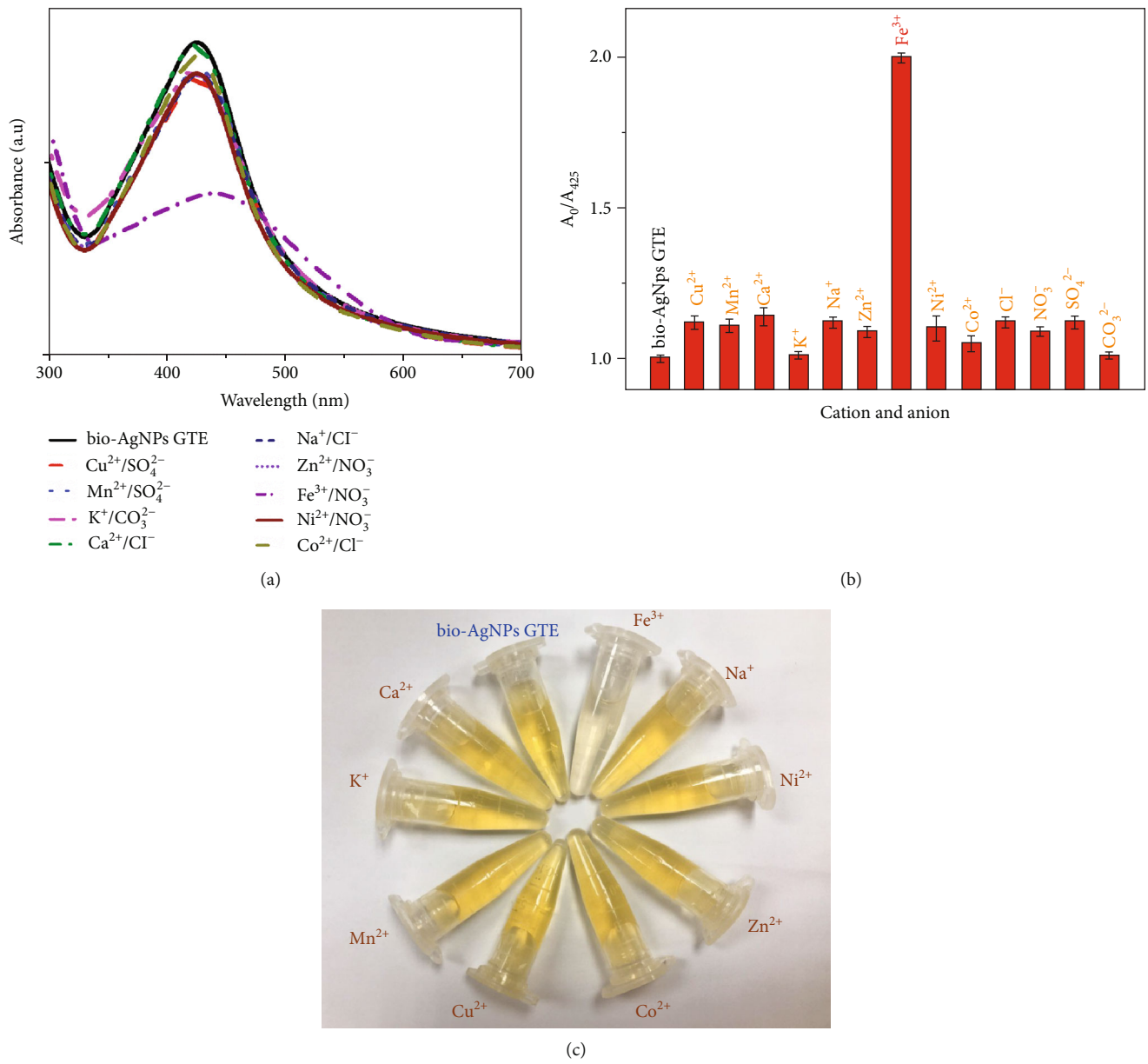

Figure 6: UV-Vis absorption spectra (a) of bio-AgNP GTE in the addition of 10^{-4} M ions (Co^{2+}, Cu^{2+}, Ca^{2+}, Zn^{2+}, Ni^{2+}, K^{+}, Na^{+}, Mn^{2+}, NO_3^-, Cl^-, and SO_4^{2-}) and 10 μM Fe (III) ions. (b) Comparison of the absorbance rate A_0/A_{425} of the bio-AgNP GTE with different ions. (c) A visual representation of the color change by using different ions.

red-shift of the SPR band (Figure S5a). In contrast, for bio-AgNP GP and bio-AgNP MP solutions, they did not exhibit any color change or shifting of absorption band when Fe (III) ions were added (Figure S5b, c). Hence, we chose the sample of bio-AgNP GTE for the following experiments to evaluate its selectivity of sensing metal ions.

3.2.1. Colorimetric Detection of Fe (III) Ions. In order to evaluate the selectivity of the colorimetric sensor, which was developed by bio-AgNP GTE for the detection of Fe (III) ions, we investigated the colorimetric response in the presence of a large amount of various interfering cations including (Co^{2+}, Cu^{2+}, Ca^{2+}, Zn^{2+}, Ni^{2+}, K^{+}, Na^{+}, and Mn^{2+}) and anion (NO_3^-, Cl^-, and SO_4^{2-}) with 10-fold excess concentrations. The change in UV-Vis spectra of bio-AgNP GTE solution with and without adding a pair of above cations and anions (10^{-4} M) were shown in Figure 6(a). It is evident that only the sample containing Fe (III) ions exhibited a significant band change as described above. Figure 6(b) compares the absorption rate (A_0/A_{425}) after adding different ions into the bio-AgNP GTE solution (A_0 and A_{425} represent the SPR peak intensities of bio-AgNP GTE solution and bio-AgNP GTE solution in the addition of ions, respectively, Table S5). This fact was reconfirmed by visual observation in Figure 6(c) as only the solution with the presence of Fe (III) ions was colorless with the aggregation of NPs, while

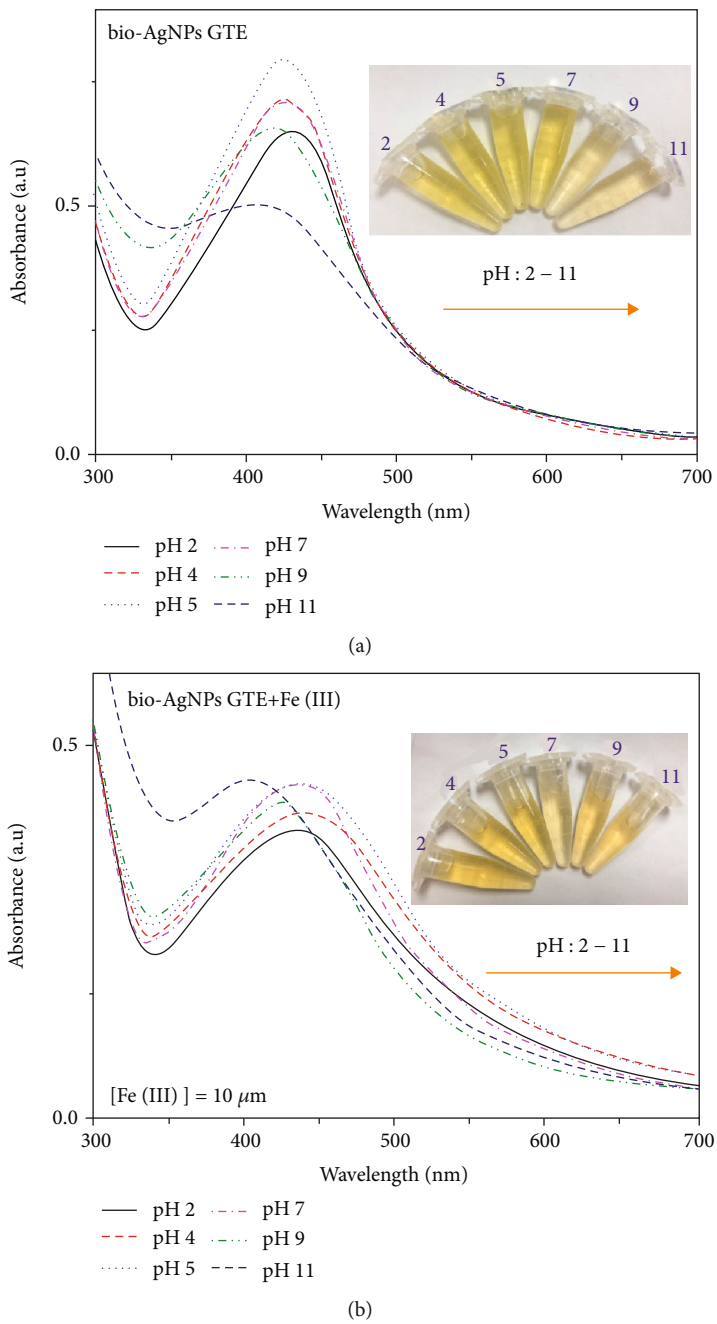

Figure 7: UV-Vis absorption spectra of bio-AgNP GTE without (a) and with (b) the presence of 10 μM Fe (III) ions in the pH range from 2 to 11. Inset (a) picture of bio-AgNP GTE with a pH between 2 and 11. Insert (b) picture of bio-AgNP GTE with a pH range of 2 to 11 in the presence of 10 μM Fe (III) ions.

the others remained yellow. These results state that the proposed bio-AgNP GTE-based colorimetric sensor is highly selective to Fe (III) ions.

The bio-AgNP-based colorimetric sensors were highly dependent on the pH of the solution. In the present study, the pH value can affect the interaction of Fe (III) ions with bio-AgNP GTE as well as the state of the functional groups surrounding the NPs. Therefore, different sets of experiments were performed using nitric acid (HNO_3) and NH_4OH to adjust pH in the range from 2 to 11. The UV-Vis absorption spectra of bio-AgNP GTE solution were observed in the absence and presence of 10 μM Fe (III) (see Figure 7). When without adding Fe (III), bio-AgNP GTE solutions were bright yellow at the pH in the range of 2–7. These samples also showed an SPR band at 425 nm. With high intensities of the SPR band, the bio-AgNP GTE exhibited high stability in the pH range of 4 to 7. Whereas, when the pH was larger than 7, the oxidation of bio-AgNP GTE occurred leading to a blue-shift of the plasmon peak, along with that the color of the solutions faded and turned into light reddish-yellow.

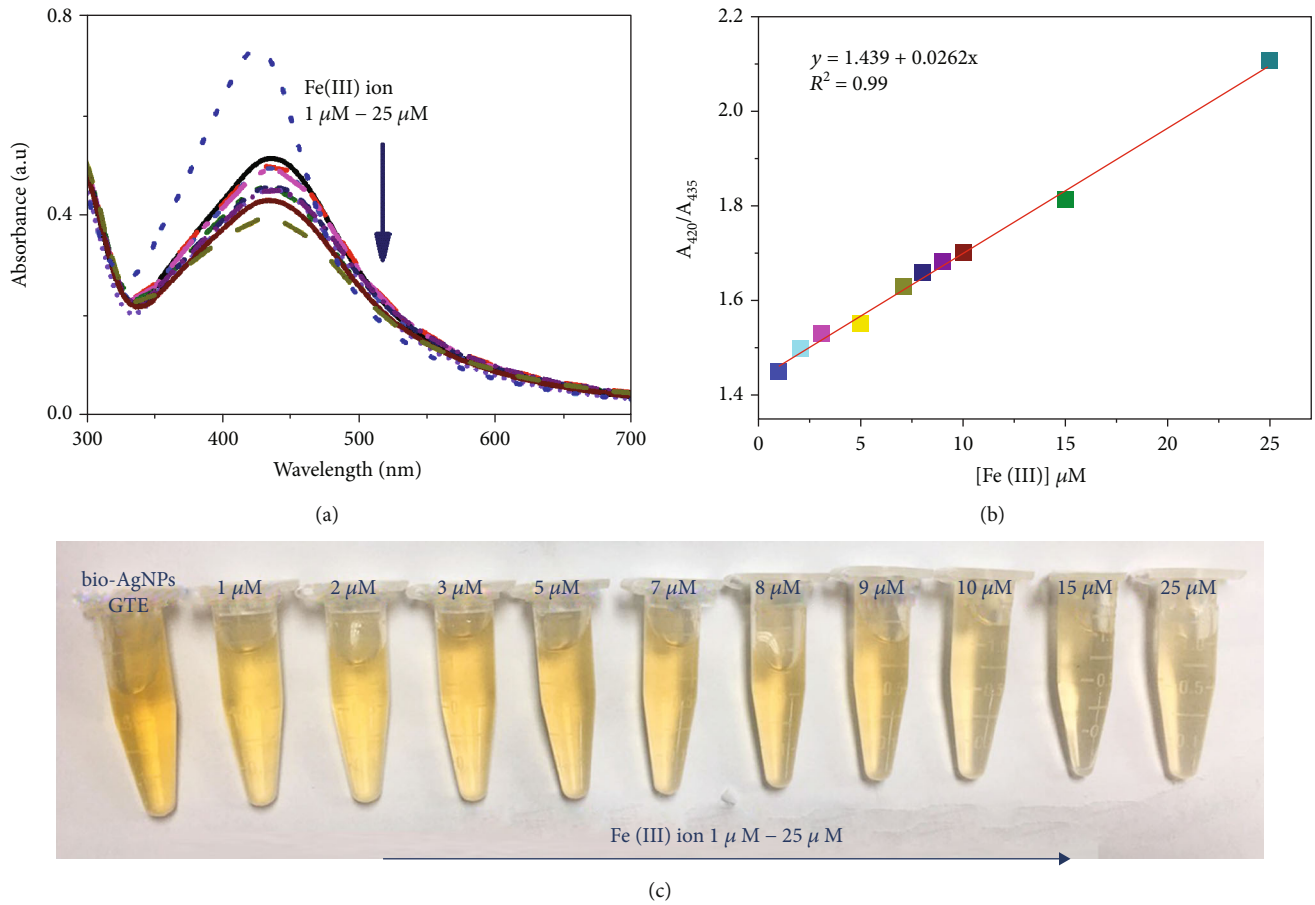

Figure 8: Spectroscopy absorption UV-Vis (a) and photographic image (c) of bio-AgNP GTE in the presence of Fe (III) ions at various concentrations determined at pH 7 (1-25 μM). (b) The plot of absorbance ratio (A_{420}/A_{435}) against the Fe (III) concentration range of 1-25 μM and its linear calibration curve (A_{420} and A_{435} is the absorbance of the ion bio-AgNP GTE with/without adding Fe (III) ions, respectively).

In the presence of Fe (III) ions, the color change was the most obvious at pH 7, and the change of absorbance (ΔA) was also largest at this pH value. Therefore, the suitable pH value for effective detecting Fe (III) ions using bio-AgNP GTE solution was 7.

To evaluate in more detail the analytical performance of the bio-AgNP GTE-based colorimetric sensor for the detection of Fe (III) ion in water samples, the sensitivity was assessed by investigating some important parameters including linear range, LOD, and LOQ values. The sensitivity for detection of Fe (III) ion was determined by adding different amounts of Fe (III) ions within the bio-AgNP GTE solution. The changes in absorption spectra were recorded through UV-Vis results (Figure 8(a)). In which, it observed the decrease in intensity of the SPR band when increasing Fe (III) concentration in the bio-AgNP GTE solution, along with a slight blue-shift as well as the expansion of the SPR band. Figure 8(b) depicts the linear relationship between the absorption rate (A_{420}/A_{435}) and the Fe (III) ions concentration within the range from 1 to 25 μM (Figure 8(c)) (A_{420} and A_{435} denote the SPR peak intensities of bio-AgNP GTE with and without Fe (III) ions, respectively) with the linear regression equation of $A_{420}/A_{435} = 0.0262\, C_{[Fe3+]} + 1.439$ and correlation coefficient of 0.99. The LOD of the bio-AgNP GTE-based colorimetric sensor was 0.532 μM, and the LOQ was estimated to be 1.77 μM.

Table 1 summarizes several reported methods relating to the detection of Fe (III) ions to compare with the one that we propose in this work. It is obvious that the bio-AgNP GTE-based colorimetric sensor has to be not the best one, but its LOD is still lower than several others. More importantly, it is a sensing system which was developed by the most "green" process with a completely plant-routed coating agent. Moreover, this system could detect Fe (III) ions within a relatively wide linear range and a low LOD that is competitive compared to other colorimetric sensors. More importantly, the LOD 0.532 μM obtained by bio-AgNP GTE-based colorimetric sensor is much lower than the value reported by WHO guidance for *Drinking-Water Quality* ~36 μM. This sensing platform can open up new opportunities to develop an ultra-sensitive colorimetric probe to detect Fe (III) ions in aqueous systems.

To evaluate the practical applicability of the newly-developed colorimetric sensor, we employed the bio-AgNP GTE-based colorimetric sensor to detect Fe (III) in water collected from Van Quan Lake, Hanoi, Vietnam. Before starting

Table 1: Comparison of the proposed method using bio-AgNP GTE with some other methods investigated in the literature for detection of Fe (III) ions.

Functional nanomaterials	Capping agent	Detection mechanism	Linear range	LOD (M)	Ref.
AgNPs 6.55 ± 1.0 nm	N-acetyl-L-cysteine-stabilized	Colorimetric sensor	0.08-80 μM	80 nM	[56]
ZnSe quantum dots 4, 1 ± 0, 2 nm	Thioglycolic acid	Colorimetric sensor	0-50 mM	2.2 mM	[51]
AuNPs (26-30 nm)	Pyrophosphate ($P_2O_7^4$ -AuNPs)	Colorimetric sensor	10-60 μM	5.6 μM	[55]
AuNPs 100 nm	Cetyltrimethylammonium bromide (CTAB)	Raman spectroscopic	100-10000 ppb	100 ppb	[67]
Graphitic carbon 9 nm		Fluorescent sensor	2 nM-5 μM	2 nM	[68]
Graphene quantum dots. (GQDs) 3 nm	(1-butyl-3-methylimidazolium hexafluorophosphate ($BMIMPF^6$)	Fluorescent sensor	0-400 μM	7.22 μM	[69]
Graphene quantum dots (GQDs) 3.8 nm	Nitrogen-doped (N-GQDs)	Fluorescent sensor	1-1945 μM	90 nM	[70]
Graphene quantum dots (GQDs) (2-4 nm)	p-toluenesulfonate S-GQDs	Fluorescent sensor	0.01-0.70 μM	4.2 nM	[71]
Bio-AgNP GTE 23 nm	Epigallocatechin gallate (EGCG)	Colorimetric sensor	1-25 μM	0.532 μM	This work

the detection, the lake water samples were pretreated through Whatman® Grade 1 filter paper (11 μm) to filter out the large impurities. After that, different volumes of Fe (III) ion solution were added into the treated water sample and analyzed with the standard method. Figure S6 demonstrates that the SPR band of bio-AgNP GTE decreased when the concentration of Fe (III) ion increased. Lake water contained various microorganisms and minerals that might have affected the detection of Fe (III), but the bio-AgNP GTE-based sensor still exhibited high sensitivity.

Figure S7 presents the linear relationship as revealed by the obtained SPR intensity *vs.* Fe (III) concentration. The good linearity demonstrates the effective ability to sense Fe (III) ions in lake water. The impressive results were summarized in Table 2. The recoveries achieved about 107 to 150 with a relative standard deviation (RSD) within 1.49%. For the direct addition of only lake water, there is not a significant change in the absorption spectrum of the bio-AgNP GTE solution, so the concentration of Fe (III) in lake water is extremely low. These results demonstrate that our prepared bio-AgNP GTE-based colorimetric sensor possesses high practical applicability for Fe (III) ion detection in lake water, and it is promising to determine Fe (III) ions in other sources of real water.

3.2.2. Sensing Mechanism of Fe (III) Ions Using Bio-AgNP GTE Probe. In general, fluorescent NPs such as Au, Ag NPs are employed to detect some transition metal ions as such metal ions can interact with the NPs and quench their fluorescence [72, 73]. Besides, nonfluorescent NPs are used to generate colorimetric sensors to detect metal ions due to the changes in SPR band (i.e., intensity and red- or blue-shift) in the addition of metal ions. These changes might be due to

Table 2: Analysis of Fe (III) ions using bio-AgNP GTE-based colorimetric sensor in lake water.

Added (μM)	Determined (μM)	Recovery (%)	RSD (%)^n
2	3	150	0.7
8	8.6	107.5	0.42
14	16.1	115	1.49

the dissolution, the aggregation of NPs, and even be the formation of new core-shell NPs [74].

To observe the existence of bio-AgNP GTE in the solution after adding Fe (III) ions, FTIR measurement and UV-Vis absorption spectra were used. Based on the FTIR spectrum, we see that there was a fluctuation of the -OH group at about 3400 cm^{-1} leading to the OH elongation band. The expansion of the absorption peaks was considered to the absorption of water into a prepared sample. The maximum stretching vibration at ~1630 cm^{-1} was assigned to C=O. Besides, the sharp absorption peaked at ~1051 cm^{-1} related to C-O-C elongated oscillation (Figure S8) [42]. Measurements showed no synthetic AgNPs formed after Fe (III) ions were added.

Based on the obtained results, a redox mechanism for colorimetric detection of bio-AgNP GTE (see Figure 9) was proposed. In the previous studies, they have shown the possibility of a redox reaction between bio-AgNP and Fe (III) ions [45, 51, 56]. When Fe (III) ions were added to the bio-AgNP solution, a redox reaction occurred between Ag^0 and Fe^{3+} ions, so bio-AgNP were oxidized and decomposed while Fe^{3+} ions were reduced to Fe^{2+} ions or Fe^0 atoms. This mechanism could explain the decrease of SPR band intensity of bio-AgNP GTE solution depending on Fe (III) concentration. The partial oxidation of bio-AgNP

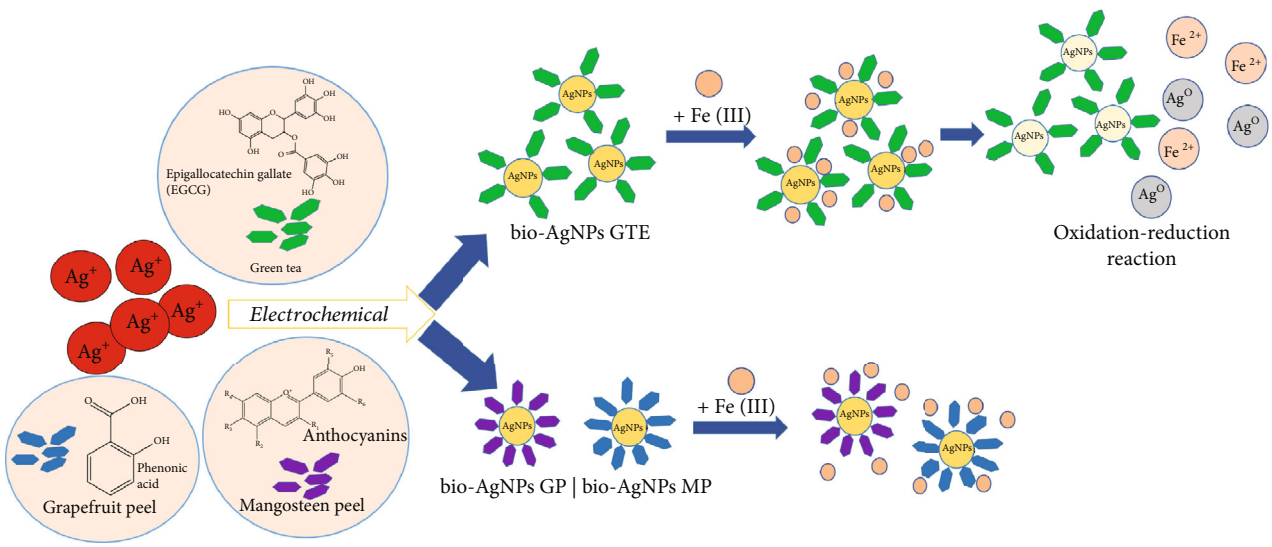

Figure 9: Possible mechanism of detecting Fe (III) ions using bio-AgNP GTE.

GTE in the low Fe (III) concentration might break the steady-state of the NPs, so they aggregated together and grew larger clusters, which resulted in the red-shift in absorption spectra and the agglomeration of NPs as described above.

Although Fe (III) ions were introduced to all of the three types of NPs synthesized using plant extracts in the same conditions, only bio-AgNP GTE solution became colorless. We assume that it might be due to the difference in the stabilizing agents of these bio-AgNPs. The phenolic acids in grapefruit peel or xanthones flavonoids, anthocyanins, and tannins in the mangosteen peel might have coated more tightly and seamlessly around the NPs, so it is more difficult for Fe (III) ions to interact with Ag^0 and degrade the NPs. As a result, Fe (III) ions do not discolor the bio-AgNP solutions prepared using these extracts.

4. Conclusions

In summary, the bio-AgNPs have successfully synthesized by a simple, cost-effective, and environmentally friendly method combining the electrochemical method and using natural extracts (green tea, grapefruit peel, and mangosteen peel) without using any additive chemicals. Inside, natural plant extracts played an important role as an effective reductant for Ag^+ ions as well as a great stabilizer for created bio-AgNPs for long-term storage. The influencing factors of various parameters such as input volume, electrochemical voltage, and fusion time have been optimized. As a result, we gave a data set of optimal parameters for each biosilver NPs synthesized from different extracts. Under optimal conditions, the obtained bio-AgNP-green tea was used as a colorimetric sensor for the most effective detection of Fe (III) ions. In the presence of Fe (III) ions, bio-AgNP GTE solution occurred color change from yellow to colorless while reducing absorption intensity and peak fluid absorption to long wavelength. The sensor has determined that the detection limit for Fe (III) ions was 0.532 μM and the LOQ was estimated to be 1.77 μM in the linear range 1-25 μM. The method was tested for the detection of Fe (III) ions in lake water with a percentage recovery of 107-150% and RSD = 1.49%.

Data Availability

Data are available on request.

Conflicts of Interest

The authors declare that they have no conflicts of interest.

Acknowledgments

This research was supported by the National Foundation for Science and Technology Development (NAFOSTED) through a fundamental research project (103.02.2019.01). We also thank the collaborative supports with XRD, TEM, UV-Vis, Electrochemical Synthesis measurements from the Institute of Materials Science-VAST, NIHE-Ministry of Health, and NEB Lab at the Phenikaa University Nano Institute (PHENA), respectively.

Supplementary Materials

Table S1: technical specifications for manufacturing bio-AgNP samples using green tea extract. Table S2: technical specifications for manufacturing bio-AgNP samples using grapefruit peel extract. Table S3: technical specifications for manufacturing bio-AgNP samples using grapefruit peel extract. Table S4: table showing the percentage (%) increase in the absorption intensity of bio-AgNP over time compared to the sample after synthesis. Table S5: the absorbance rate A_0/A_{425} of the bio-AgNP GTE with different ions. Figure S1: UV-vis absorption spectrum of bio-AgNPs synthesized using different amounts of green tea for 30 minutes, at 12 V (a). (b) Different time of electrolysis from 15 to 45 minutes using 1 g of green tea at a constant voltage of 12 V. Inset pictures show the color change of the reaction solutions. Figure

S2: UV-vis spectrum of bio-AgNPs using grapefruit peel extracts synthesized at different masses of grapefruit peel (a), the applied DC voltage (b), and time of synthesis reaction (c), respectively. Inset pictures of glass vitals of reaction solutions. Figure S3: mechanism of forming silver nanoparticles from grapefruit peel extract. Figure S4: XRD spectrum of bio-AgNPs synthesized from grapefruit peel extract (a) and mangosteen peel extract (b). Figure S5: UV-vis spectrum of bio-AgNPs synthesized from three extracts of green tea (a), grapefruit peel (b), and mangosteen peel (c) in the presence of Fe (III) ions. Inset images show the color change of the solution after the addition of Fe (III) ions. Figure S6: UV-vis absorption spectroscopy and photo of bio-AgNP GTE in the presence of Fe (III) ions at a determined concentration at a concentration of 1 μM, 8 μM, and 14 μM measuring sensor with lake water sample. (The experiment was repeated 3 times with the same conditions). Figure S7: the linear relationship between the SPR band intensity and the concentration of Fe (III) ions using bio-AgNP GTE sensor measured with lake water sample (A_{425} and A_{440} is the absorbance of the ion bio-AgNP GTE in the absence and presence of corresponding Fe (III) ions, respectively). Figure S8: FTIR spectra of bio-AgNP GTE spectrum with Fe (III) ion addition. *(Supplementary Materials)*

References

[1] G. Cao, *Nanostructures and Nanomaterials*, Published by Imperial College Press and Distributed by World Scientific Publishing Co., 2004.

[2] V. V. Mody, R. Siwale, A. Singh, and H. R. Mody, "Introduction to metallic nanoparticles," *Journal of Pharmacy & Bioallied Sciences*, vol. 2, no. 4, pp. 282–289, 2010.

[3] I. Díez and R. H. A. Ras, "Fluorescent silver nanoclusters," *Nanoscale*, vol. 3, no. 5, pp. 1963–1970, 2011.

[4] V. Ahluwalia, S. Elumalai, V. Kumar, S. Kumar, and R. S. Sangwan, "Nano silver particle synthesis using *Swertia paniculata* herbal extract and its antimicrobial activity," *Microbial Pathogenesis*, vol. 114, pp. 402–408, 2018.

[5] X. Yan, B. He, L. Liu et al., "Antibacterial mechanism of silver nanoparticles in Pseudomonas aeruginosa: proteomics approach," *Metallomics*, vol. 10, no. 4, pp. 557–564, 2018.

[6] M. Konop, T. Damps, A. Misicka, and L. Rudnicka, "Certain aspects of silver and silver nanoparticles in wound care: a minireview," *Journal of Nanomaterials*, vol. 2016, Article ID 7614753, 10 pages, 2016.

[7] A. U. Khan, M. Khan, and M. M. Khan, "Antifungal and antibacterial assay by silver nanoparticles synthesized from aqueous leaf extract of Trigonella foenum-graecum," *Bionanoscience*, vol. 9, no. 3, pp. 597–602, 2019.

[8] S. Galdiero, A. Falanga, M. Vitiello, M. Cantisani, V. Marra, and M. Galdiero, "Silver nanoparticles as potential antiviral agents," *Molecules*, vol. 16, no. 10, pp. 8894–8918, 2011.

[9] Z. Bedlovičová, I. Strapáč, M. Baláž, and A. Salayová, "A brief overview on antioxidant activity determination of silver nanoparticles," *Molecules*, vol. 25, no. 14, p. 3191, 2020.

[10] C. Balagna, S. Perero, E. Percivalle, E. V. Nepita, and M. Ferraris, "Virucidal effect against coronavirus SARS-CoV-2 of a silver nanocluster/silica composite sputtered coating," *Open Ceramics*, vol. 1, p. 100006, 2020.

[11] Z. A. Ratan, M. F. Haidere, M. Nurunnabi et al., "Green chemistry synthesis of silver nanoparticles and their potential anticancer effects," *Cancers*, vol. 12, no. 4, p. 855, 2020.

[12] P. Yin, H. Li, C. Ke et al., "Intranasal Delivery of Immunotherapeutic Nanoformulations for Treatment of Glioma Through in situ Activation of Immune Response [Corrigendum]," *International Journal of Nanomedicine*, vol. Volume 15, pp. 8873-8874, 2020.

[13] K. B. Narayanan and N. Sakthivel, "Green synthesis of biogenic metal nanoparticles by terrestrial and aquatic phototrophic and heterotrophic eukaryotes and biocompatible agents," *Advances in Colloid and Interface Science*, vol. 169, no. 2, pp. 59–79, 2011.

[14] M. Rai, K. Kon, A. Ingle, N. Duran, S. Galdiero, and M. Galdiero, "Broad-spectrum bioactivities of silver nanoparticles: the emerging trends and future prospects," vol. 98, no. 5, pp. 1951–1961, 2014.

[15] S. Ahmed, M. Ahmad, B. L. Swami, and S. Ikram, "A review on plants extract mediated synthesis of silver nanoparticles for antimicrobial applications: a green expertise," *Journal of Advanced Research*, vol. 7, no. 1, pp. 17–28, 2016.

[16] X. Zhang, Z. Liu, W. Shen, and S. Gurunathan, "Silver nanoparticles: synthesis, characterization, properties, applications, and therapeutic approaches," vol. 17, no. 9, p. 1534, 2016.

[17] X.-Y. Dong, Z.-W. Gao, K.-F. Yang, W.-Q. Zhang, and L.-W. Xu, "Nanosilver as a new generation of silver catalysts in organic transformations for efficient synthesis of fine chemicals," *Catalysis Science & Technology*, vol. 5, no. 5, pp. 2554–2574, 2015.

[18] A. Loiseau, V. Asila, G. Boitel-Aullen, M. Lam, M. Salmain, and S. Boujday, "Silver-based plasmonic nanoparticles for and their use in biosensing," *Biosensors*, vol. 9, no. 2, p. 78, 2019.

[19] M. Yusuf, "Silver nanoparticles: synthesis and applications," in *Handbook of Ecomaterials*, pp. 2343–2356, Springer Nature, 2019.

[20] M. N. Nadagouda, T. F. Speth, and R. S. Varma, "Microwave-assisted green synthesis of silver nanostructures," *Accounts of Chemical Research*, vol. 44, no. 7, pp. 469–478, 2011.

[21] J. Pulit, M. Banach, and Z. Kowalski, "Chemical Reduction as the Main Method for Obtaining Nanosilver," *Journal of Computational and Theoretical Nanoscience*, vol. 10, no. 2, pp. 276–284, 2013.

[22] K. Ranoszek-Soliwoda, E. Tomaszewska, E. Socha et al., "The role of tannic acid and sodium citrate in the synthesis of silver nanoparticles," *Journal of Nanoparticle Research*, vol. 19, no. 8, p. 273, 2017.

[23] S. M. Landage, "Synthesis of nanosilver using chemical reduction methods," *International Journal of Advanced Research in Engineering and Applied Sciences*, vol. 3, no. 5, pp. 14–22, 2014.

[24] M. Xing, L. Ge, M. Wang, Q. Li, X. Li, and J. Ouyang, "Nanosilver particles in medical applications: synthesis, performance, and toxicity," *International journal of nanomedicine*, vol. 9, pp. 2399–2407, 2014.

[25] A. B. Seabra and N. Durán, "Nanotoxicology of metal oxide nanoparticles," *International Journal of Nanomedicine*, vol. 5, no. 2, pp. 934–975, 2015.

[26] S. Prabhu and E. K. Poulose, "Silver nanoparticles: mechanism of antimicrobial action, synthesis, medical applications, and toxicity effects," *International Nano Letters*, vol. 2, no. 1, pp. 32–41, 2012.

[27] A. K. Mittal, Y. Chisti, and U. C. Banerjee, "Synthesis of metallic nanoparticles using plant extracts," *Biotechnology Advances*, vol. 31, no. 2, pp. 346–356, 2013.

[28] P. Rauwel, S. Küünal, S. Ferdov, and E. Rauwel, "A review on the green synthesis of silver nanoparticles and their morphologies studied via TEM," *Advances in Materials Science and Engineering*, vol. 2015, Article ID 682749, 9 pages, 2015.

[29] V. V. Makarov, A. J. Love, O. V. Sinitsyna, S. S. Makarova, and I. V. Yaminsky, "Green' nanotechnologies: synthesis of metal nanoparticles using plants," vol. 6, no. 20, pp. 35–44, 2014.

[30] P. Singh, Y. Kim, D. Zhang, and D. Yang, "Biological synthesis of nanoparticles from plants and microorganisms," *Trends in Biotechnology*, vol. 34, no. 7, pp. 588–599, 2016.

[31] P. Agarwal, V. K. Bairwa, S. Kachhwaha, and S. L. Kothari, "Green synthesis of silver nanoparticles using callus extract of Capsicum annuum L. and their activity against microorganisms," *International Journal of Nanotechnology and Application*, vol. 4, no. 5, pp. 1–8, 2014.

[32] M. Rafique, I. Sadaf, M. S. Rafique, and M. B. Tahir, "A review on green synthesis of silver nanoparticles and their applications," *Artificial Cells, Nanomedicine, and Biotechnology*, vol. 45, no. 7, pp. 1272–1291, 2017.

[33] G. Gahlawat and A. R. Choudhury, "A review on the biosynthesis of metal and metal salt nanoparticles by microbes," *RSC Advances*, vol. 9, no. 23, pp. 12944–12967, 2019.

[34] P. C. Nagajyothi, S. E. Lee, M. An, and K. D. Lee, "Green synthesis of silver and gold nanoparticles using Lonicera Japonica flower extract," *Bulletin of the Korean Chemical Society*, vol. 33, no. 8, pp. 2609–2612, 2012.

[35] A. Ebrahiminezhad, A. Zare-Hoseinabadi, A. K. Sarmah, S. Taghizadeh, Y. Ghasemi, and A. Berenjian, "Plant-mediated synthesis and applications of iron nanoparticles," *Molecular Biotechnology*, vol. 60, no. 2, pp. 154–168, 2018.

[36] J. Y. Song and B. S. Kim, "Rapid biological synthesis of silver nanoparticles using plant leaf extracts," *Bioprocess and Biosystems Engineering*, vol. 32, no. 1, pp. 79–84, 2009.

[37] P. Tippayawat, N. Phromviyo, P. Boueroy, and A. Chompoosor, "Green synthesis of silver nanoparticles in aloe vera plant extract prepared by a hydrothermal method and their synergistic antibacterial activity," *PeerJ*, vol. 4, p. e2589, 2016.

[38] R. Geethalakshmi and D. V. L. Sarada, "Characterization and antimicrobial activity of gold and silver nanoparticles synthesized using saponin isolated from *Trianthema decandra* L.," *Industrial Crops and Products*, vol. 51, pp. 107–115, 2013.

[39] M. Sökmen, S. Y. Alomar, C. Albay, and G. Serdar, "Microwave assisted production of silver nanoparticles using green tea extracts," *Journal of Alloys and Compounds*, vol. 725, pp. 190–198, 2017.

[40] S. Hussain and Z. Khan, "Epigallocatechin-3-gallate-capped Ag nanoparticles: preparation and characterization," *Bioprocess and Biosystems Engineering*, vol. 37, no. 7, pp. 1221–1231, 2014.

[41] Q. Sun, X. Cai, J. Li, M. Zheng, Z. Chen, and C. P. Yu, "Green synthesis of silver nanoparticles using tea leaf extract and evaluation of their stability and antibacterial activity," *Colloids and Surfaces A: Physicochemical and Engineering Aspects*, vol. 444, pp. 226–231, 2014.

[42] W. R. Rolim, M. T. Pelegrino, B. de Araújo Lima et al., "Green tea extract mediated biogenic synthesis of silver nanoparticles: Characterization, cytotoxicity evaluation and antibacterial activity," *Applied Surface Science*, vol. 463, pp. 66–74, 2019.

[43] D. Zhan, X. Li, A. B. Nepomnyashchii, M. A. Alpuche-Aviles, F. R. F. Fan, and A. J. Bard, "Characterization of Ag^+ toxicity on living fibroblast cells by the ferrocenemethanol and oxygen response with the scanning electrochemical microscope," *Journal of Electroanalytical Chemistry*, vol. 688, pp. 61–68, 2013.

[44] J. Xu, Y. Zhou, S. Liu, M. Dong, and C. Huang, "Low-cost synthesis of carbon nanodots from natural products used as a fluorescent probe for the detection of ferrum(iii) ions in lake water," *Analytical Methods*, vol. 6, no. 7, pp. 2086–2090, 2014.

[45] V. Kumar, S. Mohan, D. K. Singh, D. K. Verma, V. K. Singh, and S. H. Hasan, "Photo-mediated optimized synthesis of silver nanoparticles for the selective detection of Iron(III), antibacterial and antioxidant activity," *Materials Science and Engineering: C*, vol. 71, pp. 1004–1019, 2017.

[46] K. Lertsuwan, K. Nammultriputtar, S. Nanthawuttiphan et al., "Differential effects of Fe2+ and Fe3+ on osteoblasts and the effects of 1,25(OH)2D3, deferiprone and extracellular calcium on osteoblast viability under iron-overloaded conditions," *PLoS One*, vol. 15, no. 5, pp. e0234009–e0234023, 2020.

[47] V. K. Gupta, N. Mergu, and L. K. Kumawat, "A new multifunctional rhodamine-derived probe for colorimetric sensing of Cu(II) and Al(III) and fluorometric sensing of Fe(III) in aqueous media," *Sensors and Actuators B: Chemical*, vol. 223, pp. 101–113, 2016.

[48] C. R. Lohani and K. H. Lee, "The effect of absorbance of Fe^{3+} on the detection of Fe^{3+} by fluorescent chemical sensors," *Sensors and Actuators B: Chemical*, vol. 143, no. 2, pp. 649–654, 2010.

[49] A. Kamal, N. Kumar, V. Bhalla, M. Kumar, and R. K. Mahajan, "Rhodamine-dimethyliminocinnamyl based electrochemical sensors for selective detection of iron (II)," *Sensors and Actuators B: Chemical*, vol. 190, pp. 127–133, 2014.

[50] X. Chen, Q. Zhao, W. Zou, Q. Qu, and F. Wang, "A colorimetric Fe3+ sensor based on an anionic poly(3,4-propylenedioxythiophene) derivativeA colorimetric Fe3+ sensor based on an anionic poly(3,4-propylenedioxythiophene) derivative," *Sensors and Actuators B: Chemical*, vol. 244, pp. 891–896, 2017.

[51] X. Xing, Y. Yang, T. Zou et al., "Thioglycolic acid-capped ZnSe quantum dots as nanoprobe for cobalt(II) and iron(III) via measurement of grey level, UV-vis spectra and dynamic light scattering," *Microchimica Acta*, vol. 186, no. 7, pp. 26–31, 2019.

[52] C. Chen, X. Zhang, P. Gao, M. Hu, and M. Hu, "A water stable europium coordination polymer as fluorescent sensor for detecting Fe^{3+}, CrO_4^{2-}, and $Cr_2O_7^{2-}$ ions," *Journal of Solid State Chemistry*, vol. 258, pp. 86–92, 2018.

[53] K. S. Rao, T. Balaji, T. P. Rao, Y. Babu, and G. R. K. Naidu, "Determination of iron, cobalt, nickel, manganese, zinc, copper, cadmium and lead in human hair by inductively coupled plasma-atomic emission spectrometry," *Spectrochimica Acta Part B: Atomic Spectroscopy*, vol. 57, no. 8, pp. 1333–1338, 2002.

[54] M. Soylak and A. Aydin, "Determination of some heavy metals in food and environmental samples by flame atomic absorption spectrometry after coprecipitation," *Food and Chemical Toxicology*, vol. 49, no. 6, pp. 1242–1248, 2011.

[55] S. P. Wu, Y. P. Chen, and Y. M. Sung, "Colorimetric detection of Fe3+ ions using pyrophosphate functionalized gold nanoparticles," *Analyst*, vol. 136, no. 9, pp. 1887–1891, 2011.

[56] X. Gao, Y. Lu, S. He, X. Li, and W. Chen, "Colorimetric detection of iron ions (III) based on the highly sensitive plasmonic response of the *N*-acetyl-l-cysteine-stabilized silver nanoparticles," *Analytica Chimica Acta*, vol. 879, pp. 118–125, 2015.

[57] B. Singh, J. P. Singh, A. Kaur, and N. Singh, "Phenolic composition, antioxidant potential and health benefits of citrus peel," *Food Research International*, vol. 132, article 109114, 2020.

[58] K. N. Mahmud and Z. A. Zakaria, "Pyrolytic products from oil palm biomass and its potential applications," in *Valorisation of Agro-industrial Residues–Volume II: Non-Biological Approaches*, pp. 225–236, Springer, Cham, 2020.

[59] A. S. Zarena and K. Udaya Sankar, "Xanthones enriched extracts from mangosteen pericarp obtained by supercritical carbon dioxide process," *Separation and Purification Technology*, vol. 80, no. 1, pp. 172–178, 2011.

[60] K. S. Siddiqi, A. Husen, and R. A. K. Rao, "A review on biosynthesis of silver nanoparticles and their biocidal properties," *Journal of nanobiotechnology*, vol. 16, no. 1, p. 14, 2018.

[61] G. Serdar, E. Demir, S. Bayrak, and M. Sökmen, "New approaches for effective microwave assisted extraction of caffeine and catechins from green tea," *International Journal of Secondary Metabolite*, vol. 3, no. 1, pp. 3–13, 2016.

[62] R. D. Rivera-Rangel, M. P. González-Muñoz, M. Avila-Rodriguez, T. A. Razo-Lazcano, and C. Solans, "Green synthesis of silver nanoparticles in oil-in-water microemulsion and nanoemulsion using geranium leaf aqueous extract as a reducing agent," *Colloids and Surfaces A: Physicochemical and Engineering Aspects*, vol. 536, pp. 60–67, 2018.

[63] B. Banumathi, B. Vaseeharan, P. Suganya et al., "Toxicity of Camellia sinensis-Fabricated Silver Nanoparticles on Invertebrate and Vertebrate Organisms: Morphological Abnormalities and DNA Damages," *Journal of Cluster Science*, vol. 28, no. 4, pp. 2027–2040, 2017.

[64] D. Kumar, G. Kumar, and V. Agrawal, "Green synthesis of silver nanoparticles using Holarrhena antidysenterica (L.) Wall. bark extract and their larvicidal activity against dengue and filariasis vectors," *Parasitology Research*, vol. 117, no. 2, pp. 377–389, 2018.

[65] S. S. K. Kamal, P. K. Sahoo, J. Vimala, M. Premkumar, S. Ram, and L. Durai, "A novel green chemical route for synthesis of silver nanoparticles using Camellia sinensis," *Acta Chimica Slovenica*, vol. 57, no. 4, pp. 808–812, 2010.

[66] L. O. Cinteza, C. Scomoroscenco, S. Voicu et al., "Chitosan-stabilized ag nanoparticles with superior biocompatibility and their synergistic antibacterial effect in mixtures with essential oils," *Nanomaterials*, vol. 8, no. 10, p. 826, 2018.

[67] S. Thatai, P. Khurana, S. Prasad, and D. Kumar, "A new way in nanosensors: gold nanorods for sensing of Fe(III) ions in aqueous media," *Microchemical Journal*, vol. 113, pp. 77–82, 2014.

[68] Y. L. Zhang, L. Wang, H. C. Zhang et al., "Graphitic carbon quantum dots as a fluorescent sensing platform for highly efficient detection of Fe3+ ions," *RSC Advances*, vol. 3, no. 11, pp. 3733–3738, 2013.

[69] A. Ananthanarayanan, X. Wang, P. Routh et al., "Facile synthesis of graphene quantum dots from 3D graphene and their application for Fe3+ sensing," *Advanced Functional Materials*, vol. 24, no. 20, pp. 3021–3026, 2014.

[70] J. Ju and W. Chen, "Synthesis of highly fluorescent nitrogen-doped graphene quantum dots for sensitive, label-free detection of Fe (III) in aqueous media," *Biosensors & Bioelectronics*, vol. 58, pp. 219–225, 2014.

[71] S. Bian, C. Shen, H. Hua et al., "One-pot synthesis of sulfur-doped graphene quantum dots as a novel fluorescent probe for highly selective and sensitive detection of lead(II)," *RSC Advances*, vol. 6, no. 74, pp. 69977–69983, 2016.

[72] C. Guo and J. Irudayaraj, "Fluorescent Ag clusters via a protein-directed approach as a Hg(II) ion sensor," *Analytical Chemistry*, vol. 83, no. 8, pp. 2883–2889, 2011.

[73] X. Yuan, T. J. Yeow, Q. Zhang, J. Y. Lee, and J. Xie, "Highly luminescent Ag+ nanoclusters for Hg2+ ion detection," *Nanoscale*, vol. 4, no. 6, pp. 1968–1971, 2012.

[74] M. Annadhasan, T. Muthukumarasamyvel, V. R. Sankar Babu, and N. Rajendiran, "Green synthesized silver and gold nanoparticles for colorimetric detection of Hg 2+, Pb 2+, and Mn 2+ in aqueous medium," *ACS Sustainable Chemistry & Engineering*, vol. 2, no. 4, pp. 887–896, 2014.

Hindawi
Journal of Nanomaterials
Volume 2021, Article ID 5532477, 10 pages
https://doi.org/10.1155/2021/5532477

Research Article

Rapid Detection of Tebuconazole Based on Aptasensor and Aggregation of Silver Nanoparticles

Phuoc Long Truong,[1,2] **Vo Thi Cam Duyen**,[1,2] **and Vo Van Toi**[1,2]

[1]*School of Biomedical Engineering, International University, Ho Chi Minh City 700000, Vietnam*
[2]*Vietnam National University, Ho Chi Minh City 700000, Vietnam*

Correspondence should be addressed to Phuoc Long Truong; tplong@hcmiu.edu.vn

Received 2 March 2021; Revised 27 April 2021; Accepted 16 May 2021; Published 2 June 2021

Academic Editor: Mai Duy Hien

Tebuconazole is a triazole fungicide used in agriculture to treat pathogenic fungi. It is listed as a possible carcinogen and it shows a potential risk for the environment at very low concentration. Therefore, the detection and monitoring of tebuconazole in food and environment play an important role. The current methods for the analysis of tebuconazole employ gas-liquid chromatography (GLC) and high-performance liquid chromatography (HPLC) after sample extraction with organic solvents and column cleaning. Besides the advantages of these methods such as efficiency, repeatability, and accuracy, they are still time-consuming and costly. Herein, we report a simple, sensitive platform for the fast detection of pesticides with a low cost. The detection technique exploits a pesticide-specific DNA aptamer as the bioreceptor of an optical biosensor. Instead of trying to capture the pesticide on the sensor surface, our method allows the DNA aptamers, which are adsorbed on the nanoparticle's surface, to detach from the nanoparticles when interacting with the pesticide. This leads to the pesticide-induced aggregation and the change of the absorption spectrum of metallic nanoparticles upon high-salt concentrations, which can be monitored with unaided eye or absorbance measurement. Using tebuconazole as a model analyte for detection of pesticide, the designed aptasensor showed a high sensitivity and selectivity with a detection limit of ~10 nM and reaction time within ~20 min. In the case of tebuconazole detection in spiked rice samples, the average recoveries were in the range of 89.90–110.86% with the relative standard deviations (RSD) of 3.11–4.32%. These results indicate that our sensing platform can be exploited for the rapid detection of pesticides in real samples.

1. Introduction

Pesticides are crop protection products which play an important role in modern agriculture because of their ability to protect seeds and crops against insects, fungi, weeds, and other pests. Besides preventing crop loss and enhancing productivity, pesticides are also potentially toxic to humans [1, 2]. They may cause environmental pollution and severe impairment of human health including cancer disease, effects on reproduction, and immune and nervous systems. The increasing globalization of agri-food production and consumption is now becoming more elongated. Food moves from country to country more frequently and in shorter time frames. As a result, contaminated foods have often been consumed before being approved by authorities. In order to minimize the health hazards caused by pesticides, governments and international organizations try to regulate the maximum residues level in agri-products and foodstuffs [3, 4].

Tebuconazole is a fungicide of the triazole group which treats pathogenic fungi on a plant by inhibiting ergosterol biosynthesis, an important component of fungal cell membranes, resulted in inhibition of growth and spore formation [5]. It is used in a wide range of crops such as cereals, nuts, grapes, and vegetables, and it is proved to be effective against powdery mildew, loose smuts, rusts of legume, and nonlegume crops. In soil, tebuconazole has a half-life ranging from 49 to 610 days under aerobic conditions [6]. Regular use of tebuconazole in agriculture leads to its accumulation in soils and, subsequently, can cause risks for surface water, groundwater, and soil ecosystems [7]. According to the United

States Environmental Protection Agency (US EPA), tebuconazole is listed as a possible carcinogen with a rating of C, and it has the potential to affect the endocrine system of different species by interacting with the steroidogenesis pathway [8].

Pesticide residues are a great concern for the public, and the monitoring of these chemical residues in water and foodstuffs is one of the most important steps in minimizing potential hazards to consumers. The standard methods for detection of pesticide residues are performed by various techniques such as gas-liquid chromatography (GLC), gas chromatography–mass spectrometry (GC-MS), and high-performance liquid chromatography (HPLC) after sample extraction with organic solvents and column cleaning [9]. Other methods such as immunoassays, electrochemical assays, and capillary gas chromatography are widely used for fast detection. These methods are sensitive and reliable, but each of them still has its shortcomings for food safety control such as complexity, high cost, time consumption including prerequisite sample pretreatment with the toxic organic reagents, inability for on-site testing, solution instability, and short storage time for testing [10, 11]. For these reasons, there is now a great need of cost-efficient, rapid, and accurate detection methodologies.

In recent years, the progress in the field of nanomaterials has been made it possible to develop new sensors to overcome the disadvantages of the previous methods [11]. Among metallic nanoparticles, gold and silver nanoparticles (AuNPs and AgNPs) are of great interest due to their intrinsically strong surface plasmon resonance (SPR) absorptions, distance-dependent optical properties, high extinction coefficients, easy synthesis, and good biocompatibility [12]. The unique properties of noble metallic nanoparticles make them ideal probes for colorimetric assays to probe target analytes with the naked eye or with low-cost portable apparatus [13, 14]. The colorimetric assays have been developed by exploiting the color changes associated with the aggregation of nanoparticles, and they have been proved to be very useful in the determination of various analytes due to their outstanding analytical performances such as simplicity, sensitivity, specificity, rapidity, and on-site analysis with minimal reagent volumes. The sensing mechanism is based on the peak shift of absorption spectra of metallic nanoparticles due to the analyte-induced aggregation of the nanoparticles via the various interactions [15, 16]. For sensing applications, metallic nanoparticles are usually required to conjugate with thiolated receptors. However, the immobilization is a time-consuming process, and it is needed to optimize the amount of receptors loaded on the nanoparticle surface before sensing applications. In the case of AgNPs, the surface functionalization process that is time-consuming usually leads to the chemical degradation and oxidization of metal surface [12]. Recently, the electrostatic interaction between nonthiolated DNA and noble metallic nanoparticles has been exploited for biosensing [17, 18]. In this case, DNA can be loaded on the nanoparticles in a short time at neutral pH. The advent of aptamers, which are short, single-stranded DNA or RNA (ssDNA or ssRNA) molecules, called "artificial antibodies" has enabled the study of metallic nanoparticles for colorimetric aptasensors [12, 19]. The aptamers loading on the nanoparticle surface make colorimetric assays more sensitive because the aggregation of nanoparticles is prevented in a high concentration of salt [20]. Currently, AuNPs are often used as sensing elements to develop colorimetric biosensors due to their chemical stability. As colorimetric assays, AgNPs are favored over AuNPs because they are cheaper and easier to synthesize and have higher extinction coefficients relative to AuNPs of the same size. Moreover, AgNPs have a stronger surface-enhanced Raman scattering (SERS) effect and surface plasmon resonance (SPR) absorption [21, 22]. Up to now, there are very few reports that described the use of AgNPs as colorimetric probes for the detection of fungicide. Therefore, the development of a simple colorimetric and spectrophotometric method with silver nanoparticles for rapid and on-site detection of tebuconazole has a great significance.

Herein, we report a simple, sensitive platform for the fast detection of pesticides with a low cost. The detection method exploits a pesticide-specific DNA aptamer as the recognition element of optical nanosensors. Instead of trying to capture pesticide on the sensor surface, our method allows the ssDNA aptamers, which are adsorbed on the silver nanoparticle's surface, to detach from the silver nanoparticles when interacting with pesticide. This leads to pesticide-induced aggregation of the silver nanoparticle upon high-salt concentrations, which can be monitored with unaided eye or simple absorbance measurement. Using tebuconazole as a model analyte for the detection of pesticides, the aptasensor could detect the tebuconazole with a detection limit as low as 10 nM and the reaction time within 20 min. With regard to demonstrating the sensitivity and specificity of the aptasensor, this sensing platform shows a great potential application for the fast and on-site detection of pesticides in real samples.

2. Materials and Methods

2.1. Chemicals and Materials. Silver nitrate ($AgNO_3$, 99%), Tebuconazole (99%), sodium citrate dihydrate ($Na_3C_6H_5O_7{\cdot}2H_2O$), phosphate buffer saline pH 7.4 (PBS buffer), and sodium borohydride ($NaBH_4$, 98%) were obtained from Sigma-Aldrich, Inc. (USA). Acetone, ethanol, methanol, sodium chloride, nitric acid, and hydrochloric acid were purchased from Xilong Scientific Co. (China). The ssDNA aptamer of tebuconazole (5′CGTACGGAATTCGC TAGCAGCGTCCACGAGTGTGGTGTGGAT CCGAGC TCCACGTG-3′) [19] was obtained from PHUSA Biochem Co. (Vietnam). Other chemicals and essential reagents used were of AR grade. All glassware was intensively cleaned with freshly prepared aqua regia (3 : 1 HCl/HNO_3) and rinsed thoroughly with ultrapure water before use. Ultrapure water was used to prepare all chemical solutions.

2.2. Synthesis and Characterization of Silver Nanoparticles. Colloidal solution of citrate-capped silver nanoparticles (AgNPs) was prepared by reducing an aqueous solution of silver nitrate with a mixture of two reducing agents, trisodium citrate and sodium borohydride [23, 24]. In brief, 1 mL of 100 mM $AgNO_3$ is added drop-wise to 99 mL of a vigorously stirred ice-cold solution containing 1 mM $NaBH_4$

and 0.30 mM trisodium citrate. The resulting solution was centrifuged for 15 min at 14000 rpm in order to remove the excess of $NaBH_4$, and the precipitation was redispersed in 2 mM trisodium citrate. Then, the colloidal solution was filtered by a 0.22 μm filter to eliminate aggregated nanoparticles. The morphology of citrate-capped AgNPs was characterized by UV-Vis spectrophotometer (Jasco V-730, Japan) and transmission electron microscopy (TEM; JEM-1400, USA).

2.3. pH Effect on the Stability of Silver Nanoparticles. pH is a key factor that affects the stability of nanoparticles. Hence, in order to assure that the nanoparticle aggregation is caused by the presence of the target analyte, we investigated the effect of pH on the stability of the silver colloidal solution. Briefly, the colloidal solution was centrifuged for 15 min at 14000 rpm, and the precipitation was redispersed in the solution with the pH in the range from 3 to 12. The stability of colloidal nanoparticles was checked by the naked eye and UV-Vis spectrophotometer.

2.4. Effect of Solvents on Silver Nanoparticles. Solvents were used to stabilize silver nanoparticles and dissolve reactants as well as analytes. To determine the stability of silver nanoparticles with respect to solvents, the silver nanoparticles were redispersed in distilled water, PBS buffer (pH 7.4), and organic solvents such as trisodium citrate (2 mM), methanol, ethanol, and acetone. The stability of colloidal nanoparticles was recorded by the naked eye and UV-Vis spectrophotometer after 1-hour incubation.

2.5. Optimal Concentration of ssDNA Aptamer for Detection of Tebuconazole. Our sensing is platform based on the principle that silver nanoparticles and pesticides bind competitively to ssDNA aptamer. The ssDNA aptamer was absorbed on the nanoparticle's surface, and it stabilizes the nanoparticles against aggregation when adding salt with high concentration [19]. Its concentration directly influences on the sensitivity of the colorimetric assay. Therefore, it is needed to determine an optimal amount of DNA aptamer for the bioassay. In this study, ssDNA aptamer-wrapped silver nanoparticles were prepared based on the previous studies with modification [25, 26]. Firstly, ssDNA aptamer was fully dehybridized and stretched by heating to 95°C for 2 min. Then, ssDNA aptamer was diluted into various concentrations (0, 5, 10, 20, 30, 40, 50, 60, and 70 pmol/μL). Next, 7 μL of different concentrations of ssDNA aptamer was thoroughly mixed with 350 μL AgNPs and incubated for 30 min at room temperature following the addition of 350 μL PBS pH 7.4. Subsequently, 35 μL of 1.7 M NaCl was slowly added and mixed with the above solution and incubating for 10 min. The stability of ssDNA aptamer-wrapped AgNPs was observed by the unaided eye and UV-Vis spectrophotometer. The minimum concentration of ssDNA aptamer that can stabilize the colloidal solution of silver nanoparticles was selected for biosensing.

2.6. Assay for Detection of Tebuconazole. 350 μL of DNA aptamer wrapped AgNPs was mixed with 350 μL of various concentrations of tebuconazole (0, 25, 50, 100, 150, 250, 500, and 750 nM) and incubated for 10 min at room temperature. After adding 35 μL of 1.7 M NaCl into the incubated mixture, the color change and spectra response of DNA aptamer wrapped AgNPs with tebuconazole were observed by the naked eye and/or an UV-Vis spectrophotometer. To ensure the specificity of the DNA aptamer, a series of other pesticides were examined under the same procedure. These pesticides were as follows: difenoconazole, hexaconazole, thiophanate-methyl, mancozeb, azoxystrobin, and carbendazim.

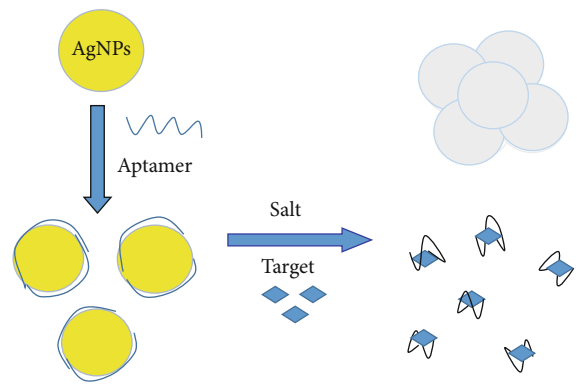

Figure 1: Experimental scheme depicting the experimental processes.

2.7. Application to Spiked Rice Samples. To assess the feasibility of sensing platform in real samples, the sensing platform was applied to detect tebuconazole in the spiked rice samples. The spiked rice samples were prepared based on the previous report with minor modification [27]. In brief, 2 g of rice flour was spiked with various concentrations of tebuconazole (50, 100, and 250 nM), respectively, and incubated at room temperature for 30 min for better absorbance of the pesticide in the matrix. Next, the spiked samples were mixed with 4 mL of acetonitrile and 1 mL distilled water, followed by ultrasonic extraction for 30 min and centrifugation at 5000 rpm for 15 min. Then, the supernatant was collected and evaporated at 40°C. The residue was diluted with water for further analysis. Then, the tebuconazole was detected using the aptasensor above.

3. Results and Discussion

The sensing mechanism of the proposed platform is based on the adsorption of the single-stranded DNA (ssDNA) on the metallic nanoparticles in a colloidal solution [28]. ssDNA is capable to uncoil its bases to make them exposed to the nanoparticle's surface. The electrostatic interaction between the positively charged bases of ssDNA and the negative charge of nanoparticles helps attach the ssDNA on the nanoparticle surface. Therefore, ssDNA can stabilize the nanoparticle against aggregation via electrostatic repulsion when adding salt with high concentration [25]. In this study, we used DNA aptamer as a specific recognition element and bare AgNPs as a signal transducer element. As illustrated in Figure 1, our detection method is based on the principle that

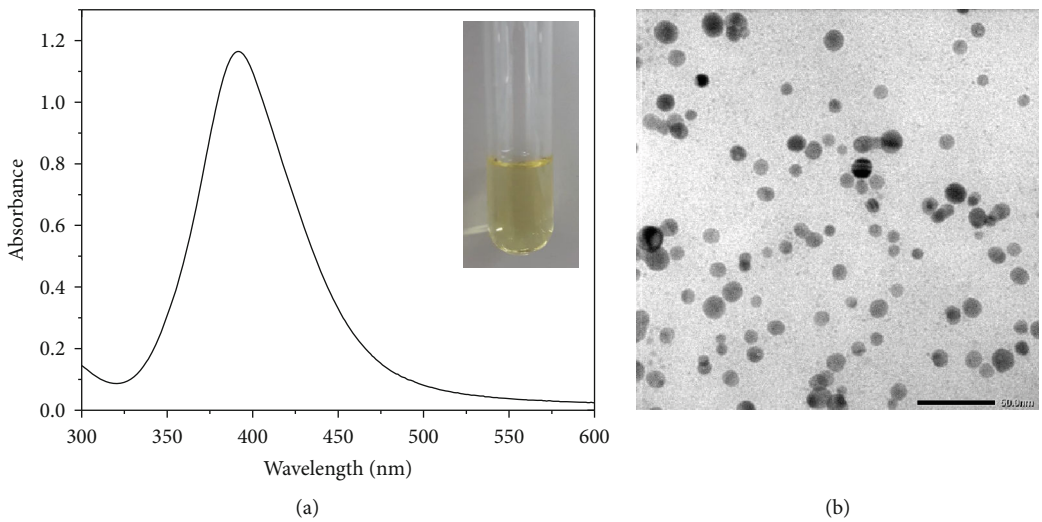

Figure 2: (a) UV-Vis absorption spectrum of Ag nanoparticles. (b) Size and morphology of Ag nanoparticles with a diameter of ~12 nm (TEM).

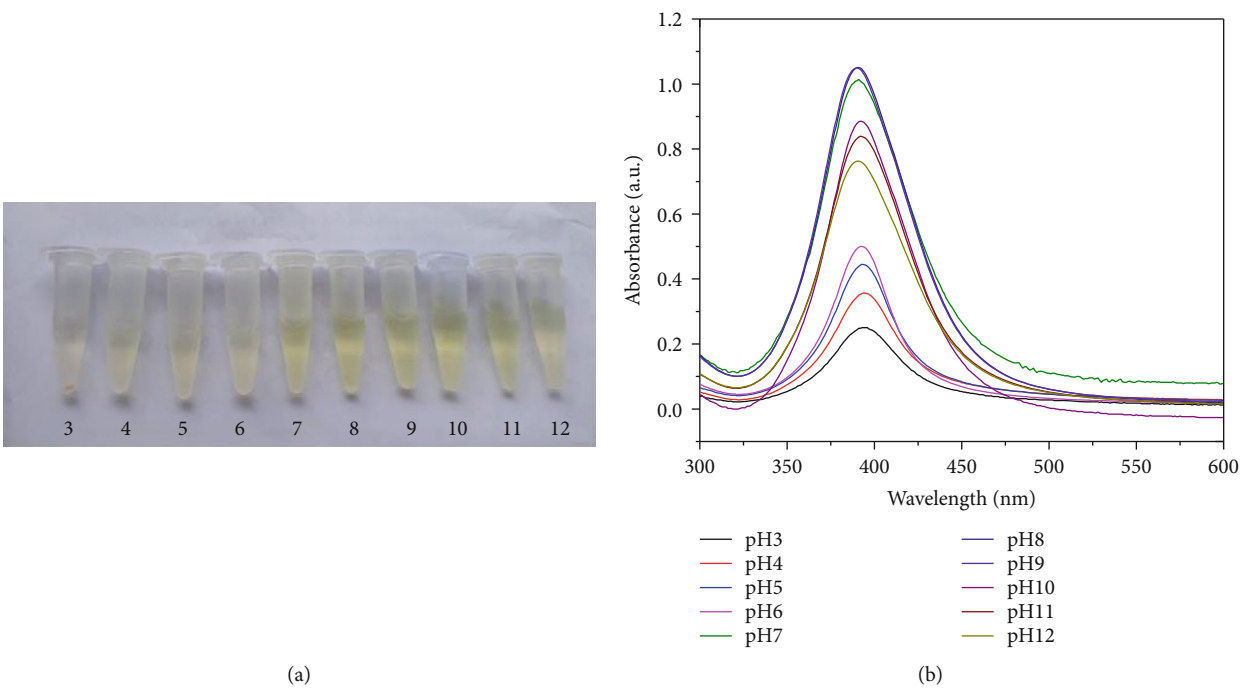

Figure 3: (a) The color of colloidal solution of silver nanoparticles in solvents with different pH values. (b) UV-Vis spectra of silver nanoparticles in solutions with different pH values.

target pesticide and AgNPs bind competitively to DNA aptamer. The DNA aptamer was absorbed on the nanoparticle's surface, and it stabilizes the nanoparticles against aggregation via the electrostatic repulsion when adding salt with high concentration [29]. The electrostatic repulsion helps prevent the strong van der Waals attraction and enhances the stability of metallic nanoparticles. The conformation of DNA aptamer changes from a randomly coiled structure to a folded 3D structure when adding target pesticide that made DNA aptamers detach from the nanoparticle surface. This transition resulted in the subsequent aggregation of the nanoparticles when adding a high concentration of salt. This leads to the changes of the UV-Vis absorption spectrum and the characteristic color change of colloidal silver.

The first step in this study involved the synthesis of the colloidal silver nanoparticles using the classical chemical synthesis method. The silver nitrate was reduced by sodium borohydride and trisodium citrate to form AgNPs, and the remaining citrate helps stabilize AgNPs. The reaction occurs

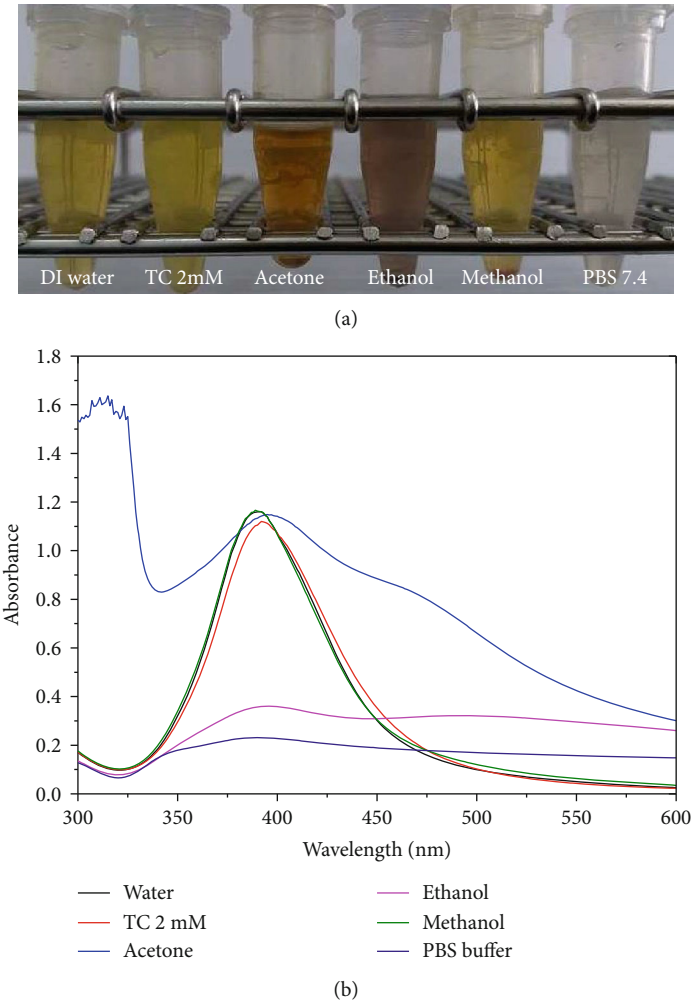

Figure 4: (a) The visual color changes of colloidal silver in various solvents. (b) UV-Vis spectra of silver nanoparticles in various solvents.

at room temperature with very fast rate [23, 30]. This method yielded pale yellow colored aqueous dispersion of silver nanoparticles with a diameter of ~12 nm, as revealed by UV-Vis spectrophotometer and transmission electron microscopy (TEM). The silver nanoparticles were nearly spherical in shape and had a size dispersion of only a few nanometers, and the wavelength of surface plasmon resonance (SPR) occurred at 393 nm (Figure 2). The concentration of citrate-capped silver nanoparticles was ~2.0 nM calculated based on Beer-Lambert law and the average diameter of silver nanoparticles [24].

It is well-known that the applications of the silver nanoparticles in assays depend on their stability, especially for those based on the aggregation of noble metal nanoparticles [31]. Silver nanoparticles prepared in this research are relatively stable and well dispersed in solution because of the negative charge of the citrate layer on the nanoparticle surface. The electrostatic repulsions among neighboring nanoparticles due to negative surface charge keep them remain dispersed in solution. pH is one of the critical factors that affect the stabilization of the nanoparticles. Hence, we investigated the effect of pH in the range from 3 to 12. Figure 3 shows the visual observation and UV-Vis spectra of colloidal solution of silver nanoparticles with different pH values. At pH<7, the silver nanoparticles were unstable, and the color of nanosilver solutions was changed from yellow to yellowish indicating aggregation of the nanoparticles. These observations were supported by the UV-Vis spectra of colloidal silver nanoparticles. The UV-Vis spectrum showed a significant decrease in the absorbance at 393 nm, and the absorbance further decreased when decreasing pH of the colloidal solution. This is because citrate is fully protonated at acidic pH values, and hence, the number of negative charge on the silver nanoparticle surface is reduced. The decrease in negative surface charges results in the aggregation of the nanoparticles. For the silver colloidal solution with the pH in the alkaline region, the decrease in the peak absorbance was much less than that of the acidic pH region. This indicated that the solution was more stabilized in the alkaline pH region. The reason is that the citrate is fully deprotonated, and there are more negative charges that result in repulsion among silver nanoparticles, and hence, little or no aggregation was observed. At a pH range of 7-9, there was almost no change in the peak absorbance that indicated no aggregation of the

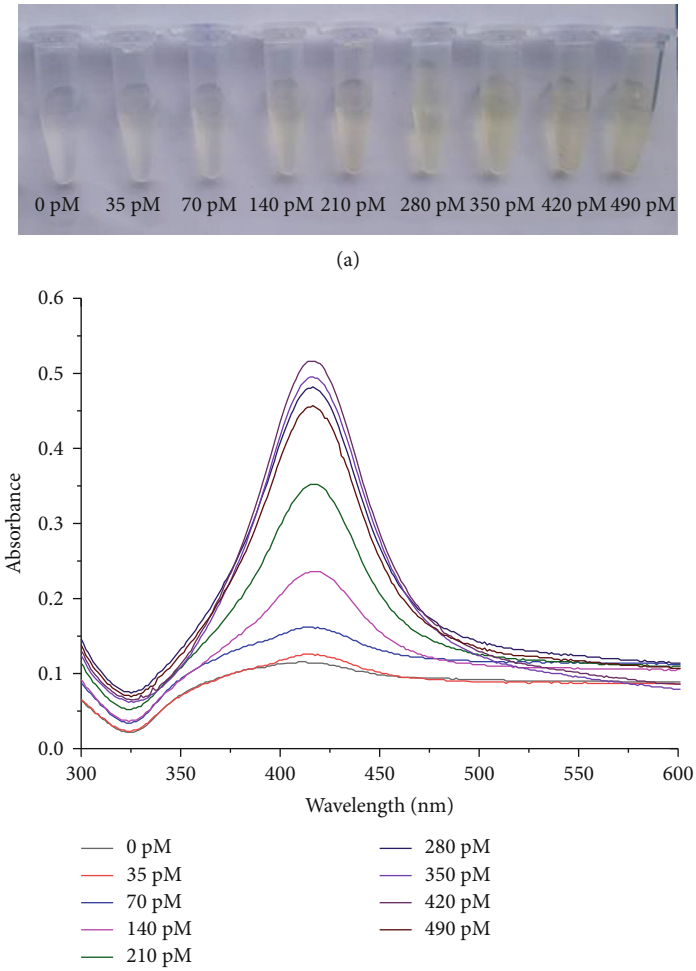

Figure 5: (a) The color change of colloidal solution of silver nanoparticles stabilized by different amounts of DNA aptamer. (b) UV-Vis spectra of colloidal silver nanoparticles stabilized by different amounts of DNA aptamer after salt addition.

silver nanoparticles. Therefore, this pH range was chosen for further studies.

Solvent is one of the most important factors that affect the stability of the colloidal solution. The changing of the dielectric environment of silver nanoparticles is very important as it relates to the ability to process metal nanoparticles in various solutions for applications [32]. Furthermore, solvents can have an effect on the solubility and stability of pesticides. To determine the effect of solvents on colloidal silver, the silver nanoparticles were centrifuged and redispersed in various solvents. The stability of silver nanoparticle was evaluated by the color change of the colloidal solution and UV-Vis spectrum after one-hour incubation. As demonstrated in Figure 4, three solvents (PBS pH 7.4, ethanol, and acetone) significantly turned the solution color and the UV-Vis spectrum of silver colloids that indicate the aggregation of silver nanoparticles. In the case of water, trisodium citrate, and methanol, the silver nanoparticles are nicely redispersed, and all 3 solvents had little to no effect on the solution color and the UV-Vis spectrum of silver nanoparticles. That is because these solvents provide solvation and driving forces that prevent the aggregation of silver nanoparticles. In this research, ultrapure water and sodium citrate solution with a concentration of 2 mM were used as solvents to dilute the stock solutions of pesticides and disperse silver nanoparticles.

As mentioned above, DNA aptamer was used as a recognition factor and the AgNPs was used as a signal transducer element. Hence, the aptamer amount and the ratio of DNA aptamer and AgNPs in the assays directly affect the sensitivity of the sensor. It should be noted that the electrostatic interaction between AgNPs and the bases of DNA is a key factor to cause aptamer to stick on the nanoparticle's surface. For this reason, the DNA amount used for these assays directly relates to the length of DNA aptamer and its sequence. To identify an optimal ratio of DNA aptamer to AgNPs at which the aptamer–AgNPs remains stable in the absence of target pesticide after addition of high-level salt, different amounts of DNA aptamer were examined. As shown in Figure 5, DNA could protect the AgNPs from the aggregation in solutions with high salinity. In the presence of 280 pmol of DNA, the silver colloid could keep stable in a solution containing a high concentration of salt. With the

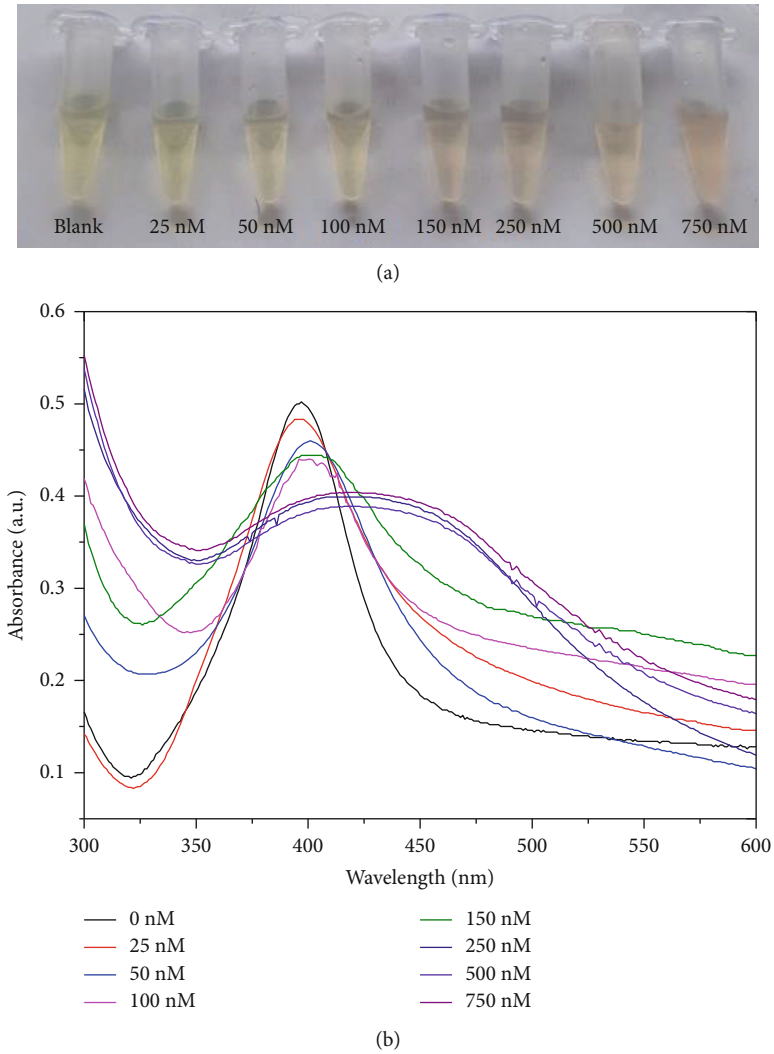

Figure 6: (a) Colorimetric response of DNA aptamer modified AgNPs as a function of tebuconazole concentration. (b) UV-Vis spectral response of aptasensor in the presence of various amounts of tebuconazole.

lower amount of DNA aptamer, the absorbance of AgNPs at 393 nm gradually decreased, and the color of silver solutions was changed from yellow to yellowish indicating aggregation of the nanoparticles. With the higher amount of DNA aptamer, the colloidal solutions of nanoparticles maintain its original yellow color, and the absorbance of AgNPs at 393 nm indicated no aggregation of the nanoparticles. The successful fabrication of the aptamer-wrapped AgNPs was confirmed by the measurement of the zeta potential of nanoparticles. The zeta potential of citrate-capped AgNPs was -42.35 ± 3.10 mV ($n = 3$) due to the presence of citrate on the nanoparticle surface. After modification, the zeta potential of the aptamer-wrapped AgNPs was -38.22 ± 1.70 mV ($n = 3$). This indicates that the AgNPs were stabilized by ssDNA aptamer. Hence, the optimal ratio of DNA aptamer and AgNPs used for detection of tebuconazole was 280 pM/350 μL AgNPs with a concentration of ~2.0 nM.

After optimizing the reaction conditions, the sensitivity of the proposed DNA aptasensor was investigated. For pesticide analysis, different concentrations of tebuconazole ranging from 0 to 750 nM were incubated with DNA aptamer wrapped AgNPs, and the color change and spectra response were recorded. As illustrated in Figure 6, in the presence of tebuconazole, DNA aptamers bind to tebuconazole and form a structured complex, resulting in the aggregation of AgNPs after salt addition that leads to the characteristic color change from yellow to pink (Figure 6(a)). With the increase of tebuconazole concentration, the UV-Vis spectra of AgNPs showed that the characteristic absorbance at 393 nm decreased, while the absorbance band ~450 nm increased progressively which indicated the aggregation of AgNPs (Figure 6(b)). In this study, the absorbance ratio (A450/A393) was used to evaluate the tebuconazole-induced aggregation level of DNA aptamer-wrapped AgNPs and the sensitivity of aptasensor. Figure 7(a) demonstrates the relationship between the absorbance ratio (A450/A393) and tebuconazole concentrations, and the ratio was found to be linear in the concentration range of 25 nM to 250 nM. The linear regression equation for detection of tebuconazole

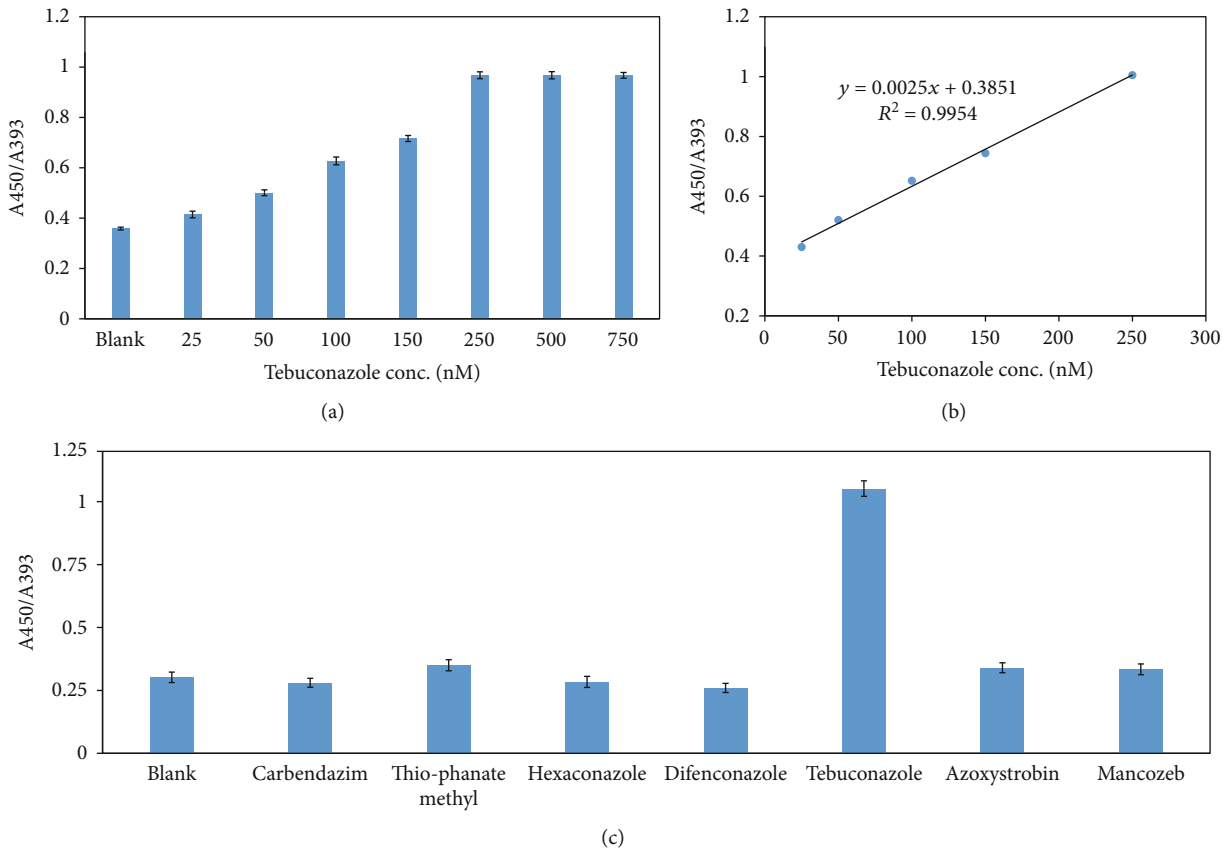

Figure 7: (a) The response of absorbance ratio (A450/A393) for the various concentrations of tebuconazole ranging from 0 to 750 nM. (b) The linear scale of the calibration curve describing the relation between absorbance ratio (A450/A393) and concentrations of tebuconazole. (c) Specificity of aptasensor in the presence of different pesticides.

was $y = 0.0025x + 0.3851$ ($R^2 = 0.9954$), where y and x are the ratio of A_{450}/A_{393} and tebuconazole concentration (nM), respectively (Figure 7(b)). The detection limit was calculated based on the formula $3\alpha/s$, where α is the standard deviation of the plank sample and s is the slope of the linear scale of the calibration curve. Therefore, the detection limit of this aptasensor is ~10 nM, which is about two orders of magnitude lower than the maximum residue limit (MRL) of tebuconazole in agri-products (Nos. EU 750/2010 and 50/2016/TT-BYT) [33, 34]. Moreover, in comparison with other assays for detection of tebuconazole that require expensive reagents, costly instrumentation, sample pretreatment with the toxic organic reagents such as immunoassay [35, 36], liquid chromatography (LC) with UV detection (LC–UV) [37], and capillary gas chromatography with nitrogen phosphorus detection (GC–NPD) [38], this sensing platform shows its advantages in terms of simplicity, experimental cost, time for analysis, and ability for on-site testing.

To ensure the observed absorbance ratio of A450/A393 from the specific interaction of tebuconazole and aptamer–AgNPs, the specificity of the aptasensor was investigated on a series of interfering pesticides such as difenoconazole, hexaconazole, thiophanate-methyl, mancozeb, azoxystrobin, and carbendazim at concentrations which were larger than the concentration of the saturation response of aptasensor.

Table 1: Detection of tebuconazole in spiked rice samples.

Spiked concentration (nM)	Found concentration (nM)	Recovery (%)	RSD (%)
50	55.43	110.86	3.65
100	89.90	89.9	3.11
250	248.40	99.36	4.32

As shown in Figure 7(c), the absorbance ratio of A450/A393 in the presence of tebuconazole was much larger than those of other pesticides. This result indicated that this sensing platform could be used for the detection of pesticides with high specificity.

To evaluate the efficacy of the proposed aptasensor for the analysis of complex samples, spiked rice samples were tested. As demonstrated in Table 1, the average recoveries were in the range of 89.90–110.86%; the relative standard deviations (RSD) were 3.11–4.32%. The recovery results are in good agreement with those obtained from gas-liquid chromatography (GLC) and liquid chromatography–mass spectrometry. These results confirmed the reliability and practicability of the proposed sensing platform for the simple and fast detection of tebuconazole in real samples as well.

4. Conclusions

In summary, we developed a simple aptasensor for the fast detection of tebuconazole fungicide at a low cost based on the aggregation of AgNPs. This approach is suitable for on-site detection because the aggregation of the nanoparticle is very fast and easy to visualize through the color and state of the resultant solution. Using tebuconazole as a model for the detection of pesticides, the plasmonic aptasensor could detect as low as 10 nM with a reaction time of ~20 min and the plotted calibration curve in the concentration range of 25 to 250 nM. Moreover, the tebuconazole was successfully detected in spiked rice samples with the average recoveries ranging from 89.90 to 110.86% and the relative standard deviations (RSD) of 3.11–4.32%. The above results show that the proposed aptasensor can detect tebuconazole with high sensitivity and selectivity. In addition, the tebuconazole induced color change of aptamer-modified AgNPs from yellow to pink enables visual detection of tebuconazole in real applications.

Data Availability

All data used to support the findings of this study are included within the article.

Conflicts of Interest

The authors have no conflicts of interest.

Acknowledgments

This research is funded by the Vietnam National University Ho Chi Minh City (VNU-HCM) under grant number NCM2020-28-01.

References

[1] S. Armenta, G. Quintas, S. Garrigues, and M. De la Guardia, "Mid-infrared and Raman spectrometry for quality control of pesticide formulations," *TrAC Trends in Analytical Chemistry*, vol. 24, no. 8, pp. 772–781, 2005.

[2] A. Nougadère, J. C. Reninger, J. L. Volatier, and J. C. Leblanc, "Chronic dietary risk characterization for pesticide residues: a ranking and scoring method integrating agricultural uses and food contamination data," *Food and Chemical Toxicology*, vol. 49, no. 7, pp. 1484–1510, 2011.

[3] A. Pop, F. Manea, A. Flueras, and J. Schoonman, "Simultaneous voltammetric detection of carbaryl and paraquat pesticides on graphene-modified boron-doped diamond electrode," *Sensors*, vol. 17, no. 9, p. 2033, 2017.

[4] X. Liu, X. Wang, J. Xu, F. Dong, W. Song, and Y. Zheng, "Determination of tebuconazole, trifloxystrobin and its metabolite in fruit and vegetables by a Quick, Easy, Cheap, Effective, Rugged and Safe (QuEChERS) method using gas chromatography with a nitrogen–phosphorus detector and ion trap mass spectrometry," *Biomedical Chromatography*, vol. 25, no. 10, pp. 1081–1090, 2011.

[5] N. T. Sehnem, P. Souza-Cruz, M. D. C. R. Peralba, and M. A. Z. Ayub, "Biodegradation of tebuconazole by bacteria isolated from contaminated soils," *Journal of Environmental Science and Health Part B*, vol. 45, no. 1, pp. 67–72, 2009.

[6] B. Muñoz-Leoz, E. Ruiz-Romera, I. Antigüedad, and C. Garbisu, "Tebuconazole application decreases soil microbial biomass and activity," *Soil Biology and Biochemistry*, vol. 43, no. 10, pp. 2176–2183, 2011.

[7] R. Norková, J. J. Dytrtová, M. Jakl, and D. Schröder, "Formation of tebuconazole complexes with cadmium (II) investigated by electrospray ionization mass spectrometry," *Water, Air, & Soil Pollution*, vol. 223, no. 5, pp. 2633–2640, 2012.

[8] R. Noguerol-Pato, R. M. González-Rodríguez, C. González-Barreiro, B. Cancho-Grande, and J. Simal-Gándara, "Influence of tebuconazole residues on the aroma composition of Mencía red wines," *Food Chemistry*, vol. 124, no. 4, pp. 1525–1532, 2011.

[9] M. L. Xu, Y. Gao, X. X. Han, and B. Zhao, "Detection of pesticide residues in food using surface-enhanced Raman spectroscopy: a review," *Journal of Agricultural and Food Chemistry*, vol. 65, no. 32, pp. 6719–6726, 2017.

[10] E. Watanabe, S. Miyake, and Y. Yogo, "Review of enzyme-linked immunosorbent assays (ELISAs) for analyses of neonicotinoid insecticides in agro-environments," *Journal of Agricultural and Food Chemistry*, vol. 61, no. 51, pp. 12459–12472, 2013.

[11] G. Aragay, F. Pino, and A. Merkoçi, "Nanomaterials for sensing and destroying pesticides," *Chemical Reviews*, vol. 112, no. 10, pp. 5317–5338, 2012.

[12] M. Sabela, S. Balme, M. Bechelany, J.-M. Janot, and K. Bisetty, "A review of gold and silver nanoparticle-based colorimetric sensing assays," *Advanced Engineering Materials*, vol. 19, 2017.

[13] J. V. Rohit and S. K. Kailasa, "5-Sulfo anthranilic acid dithiocarbamate functionalized silver nanoparticles as a colorimetric probe for the simple and selective detection of tricyclazole fungicide in rice samples," *Analytical Methods*, vol. 6, no. 15, pp. 5934–5941, 2014.

[14] J.-S. Lee, A. K. R. Lytton-Jean, S. J. Hurst, and C. A. Mirkin, "Silver nanoparticle– oligonucleotide conjugates based on DNA with triple cyclic disulfide moieties," *Nano Letters*, vol. 7, no. 7, pp. 2112–2115, 2007.

[15] H. Jans and Q. Huo, "Gold nanoparticle-enabled biological and chemical detection and analysis," *Chemical Society Reviews*, vol. 41, no. 7, pp. 2849–2866, 2012.

[16] R. Elghanian, J. J. Storhoff, R. C. Mucic, R. L. Letsinger, and C. A. Mirkin, "Selective colorimetric detection of polynucleotides based on the distance-dependent optical properties of gold nanoparticles," *Science*, vol. 277, no. 5329, pp. 1078–1081, 1997.

[17] S. Abbasian, A. Moshaii, M. Nikkhah, and N. Farkhari, "Adsorption of DNA on colloidal Ag nanoparticles: effects of nanoparticle surface charge, base content and length of DNA," *Colloids and Surfaces B: Biointerfaces*, vol. 116, pp. 439–445, 2014.

[18] N. Farkhari, S. Abbasian, A. Moshaii, and M. Nikkhah, "Mechanism of adsorption of single and double stranded DNA on gold and silver nanoparticles: investigating some important parameters in bio-sensing applications," *Colloids and Surfaces B: Biointerfaces*, vol. 148, pp. 657–664, 2016.

[19] V. T. Nguyen, Y. S. Kwon, J. H. Kim, and M. B. Gu, "Multiple GO-SELEX for efficient screening of flexible aptamers," *Chemical Communications*, vol. 50, no. 72, pp. 10513–10516, 2014.

[20] J. Wang, L. Wang, X. Liu et al., "A gold nanoparticle based aptamer target binding readout for ATP assay," *Advanced Materials*, vol. 19, no. 22, pp. 3943–3946, 2007.

[21] X. Xu, J. Wang, F. Yang, K. Jiao, and X. Yang, "Label-free colorimetric detection of small molecules utilizing DNA oligonucleotides and silver nanoparticles," *Small*, vol. 5, no. 23, pp. 2669–2672, 2009.

[22] S. K. Menon, N. R. Modi, A. Pandya, and A. Lodha, "Ultrasensitive and specific detection of dimethoate using ap-sulphonato-calix [4] resorcinarene functionalized silver nanoprobe in aqueous solution," *RSC Advances*, vol. 3, no. 27, pp. 10623–10627, 2013.

[23] G. L. Wang, X. Y. Zhu, H. J. Jiao, Y. M. Dong, and Z. J. Li, "Ultrasensitive and dual functional colorimetric sensors for mercury (II) ions and hydrogen peroxide based on catalytic reduction property of silver nanoparticles," *Biosensors and Bioelectronics*, vol. 31, no. 1, pp. 337–342, 2012.

[24] D. Paramelle, A. Sadovoy, S. Gorelik, P. Free, J. Hobley, and D. G. Fernig, "A rapid method to estimate the concentration of citrate capped silver nanoparticles from UV-visible light spectra," *Analyst*, vol. 139, no. 19, pp. 4855–4861, 2014.

[25] M. Ramezani, N. M. Danesh, P. Lavaee, K. Abnous, and S. M. Taghdisi, "A novel colorimetric triple-helix molecular switch aptasensor for ultrasensitive detection of tetracycline," *Biosensors and Bioelectronics*, vol. 70, pp. 181–187, 2015.

[26] W. H. Wu, M. Li, Y. Wang et al., "Aptasensors for rapid detection of Escherichia coli O157: H7 and Salmonella typhimurium," *Nanoscale Research Letters*, vol. 7, no. 1, p. 658, 2012.

[27] N. Fahimi-Kashani and M. R. Hormozi-Nezhad, "Gold-nanoparticle-based colorimetric sensor array for discrimination of organophosphate pesticides," *Analytical Chemistry*, vol. 88, no. 16, pp. 8099–8106, 2016.

[28] H. Li and L. Rothberg, "Colorimetric detection of DNA sequences based on electrostatic interactions with unmodified gold nanoparticles," *Proceedings of the National Academy of Sciences*, vol. 101, no. 39, pp. 14036–14039, 2004.

[29] Y. Wang, J. Wang, F. Yang, and X. Yang, "Spectrophotometric determination of cysteine with gold nanoparticles stabilized with single-stranded oligonucleotides," *Analytical Sciences*, vol. 26, no. 5, pp. 545–549, 2010.

[30] S. Preciado-Flores, D. A. Wheeler, T. M. Tran et al., "SERS spectroscopy and SERS imaging of Shewanella oneidensis using silver nanoparticles and nanowires," *Chemical Communications*, vol. 47, no. 14, pp. 4129–4131, 2011.

[31] R. C. Doty, T. R. Tshikhudo, M. Brust, and D. G. Fernig, "Extremely stable water-soluble Ag nanoparticles," *Chemistry of Materials*, vol. 17, no. 18, pp. 4630–4635, 2005.

[32] M. A. H. Muhammed, F. Aldeek, G. Palui, L. Trapiella-Alfonso, and H. Mattoussi, "Growth of in situ functionalized luminescent silver nanoclusters by direct reduction and size focusing," *ACS Nano*, vol. 6, no. 10, pp. 8950–8961, 2012.

[33] "EU pesticide database," https://eurlex.europa.eu/legalcontent/EN/ALL/?uri=CELEX:32010R0750.

[34] "Vietnam. Maximum residue limits for pesticides in food. 50/2016/TT-BYT," https://www.fas.usda.gov/data/vietnam-moh-revises-mrls-pesticides-foods.

[35] Y. Wang, J. Xu, Y. Qiu et al., "Highly specific monoclonal antibody and sensitive quantum dot beads-based fluorescence immunochromatographic test strip for tebuconazole assay in agricultural products," *Journal of Agricultural and Food Chemistry*, vol. 67, no. 32, pp. 9096–9103, 2019.

[36] X. Chen, Z. Li, F. Sun et al., "An innovative hapten and monoclonal antibody-based immunoassay for determining tebuconazole residues in aqueous samples," *Food and Agricultural Immunology*, vol. 30, no. 1, pp. 677–691, 2019.

[37] T. Miyauchi, M. Mori, and K. Ito, "Application of solid-phase extraction to quantitatively determine cyproconazole and tebuconazole in treated wood using liquid chromatography with UV detection," *Journal of Chromatography A*, vol. 1063, no. 1-2, pp. 137–141, 2005.

[38] Z. Deng, J. Hu, D. Qin, and H. Li, "Simultaneous analysis of hexaconazole, myclobutanil, and tebuconazole residues in apples and soil by SPE clean-up and GC with nitrogen–phosphorus detection," *Chromatographia*, vol. 71, no. 7-8, pp. 679–684, 2010.

Hindawi
Journal of Nanomaterials
Volume 2021, Article ID 6648704, 16 pages
https://doi.org/10.1155/2021/6648704

Research Article

Single-Atom Ni Heterogeneous Catalysts Supported UiO-66 Structure: Synthesis and Catalytic Activities

Le Thi Hoa,[1] Le Thi Thanh Nhi,[1,2] Le Van Thanh Sơn,[3] Nguyen Le My Linh,[4] Ho Van Minh Hai,[1] and Dinh Quang Khieu[1]

[1]*University of Sciences, Hue University, 49000, Vietnam*
[2]*Duy Tan University, 50000, Vietnam*
[3]*University of Education and Science, The University of Da Nang, 50000, Vietnam*
[4]*University of Education, Hue University, 49000, Vietnam*

Correspondence should be addressed to Ho Van Minh Hai; hvmhai@hueuni.edu.vn and Dinh Quang Khieu; dqkhieu@hueuni.edu.vn

Received 16 December 2020; Revised 20 January 2021; Accepted 20 April 2021; Published 19 May 2021

Academic Editor: Ovidiu Ersen

Herein, the single-atom Ni site heterogeneous catalysts supported by the UiO-66 structure (University of Oslo-66 metal organic framework) were successfully synthesized by a postsynthetic metalation method, where Ni ions are covalently attached to the missing-linker defect sites at zirconium oxide clusters ($Zr_6O_4(OH)_4$) in as-prepared UiO-66 structure, $[Zr_6O_4(OH)_4(BDC)(DMF)_{10}(OH)_{10}]$ (BDC (benzene-1,4-dicarboxylate), DMF (dimethylformamide)). The structure properties of the catalysts were characterized using powder X-ray diffraction (PXRD), Fourier transform infrared (FT-IR), scanning electron microscopy (SEM), transmission electron microscopy (TEM), energy-dispersive X-ray spectroscopy (EDX), N_2 adsorption-desorption isotherms (BET), thermogravimetric analysis (TGA), X-ray photoelectron spectroscopy (XPS), and photoluminescence spectroscopy (PL). It was found that single-atom Ni heterogeneous catalysts supported by the UiO-66 structure, UiO-66/Ni1.0 $[Zr_6O_4(OH)_4(C_8H_4O_4)(DMF)_{10}(OH)_8Ni_2(OH)_2(Cl)_2]$, showed a sphere-like morphology with a high specific surface area as well as good thermal stability. Specifically, the as-prepared UiO-66/Ni1.0 exhibited the excellent catalytic activity and stability for 4-nitrophenol reduction in terms of low activation energy ($E_a = 23.15\,\mathrm{kJ\,mol^{-1}}$), high turnover frequency (76.19 molecules g^{-1} min^{-1}), and high apparent rate constant ($k_{app} = 0.956\,\mathrm{min^{-1}}$). In addition, methylene blue (MB) was also chosen as the organic dye model for catalytic reduction reaction. The k_{app} and TOF for the reduction of MB using UiO-66/Ni1.0 were 0.787 min^{-1} and 33.89×10^{20} molecules g^{-1} min^{-1}, respectively.

1. Introduction

Nitroaromatic compounds, especially 4-nitrophenol (4-NP), are extensively employed in the fields of pigments, pharmaceuticals, dyes, explosives, plastics, pesticides, wood, or leather preservative [1–7]. However, 4-nitrophenol (4-NP), known as the toxic and highly hazardous contaminants, is found in agricultural and industrial wastewaters [8–10]. This compound released from above industrial sectors can impact negatively on the ecological system and pose serious environmental pollution. It is worth noting that the exposure of 4-NP would threaten human health such as damage to the nervous central system, blood system, and primary organs [11–13]. In addition to this, methylene blue (MB), known as organic dye, is broadly studied because of its many potential applications in industries such as printing, textile, paper, paints, and plastics [14]. It is noticeable that methylene blue is also a high-toxicity carcinogenic organic compound and can be a cause of water environmental pollution [15, 16].

Due to this reason, it is necessary to develop the simple, efficient method for removal of these organic compounds in wastewaters. Recently, many various technologies such as adsorption, photocatalytic degradation, chemical oxidation, and membrane filtration have been applied to remove these

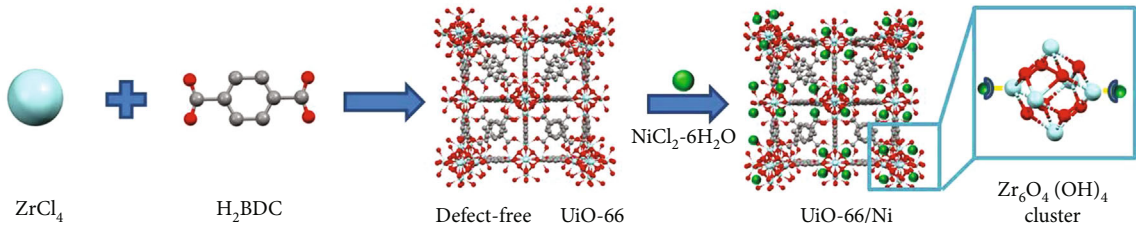

Scheme 1: The scheme of the formation process of the UiO-66/Ni catalyst. Atom label: C: grey; O: red; Zr: sky blue; Ni: green (H atoms are omitted for clarity).

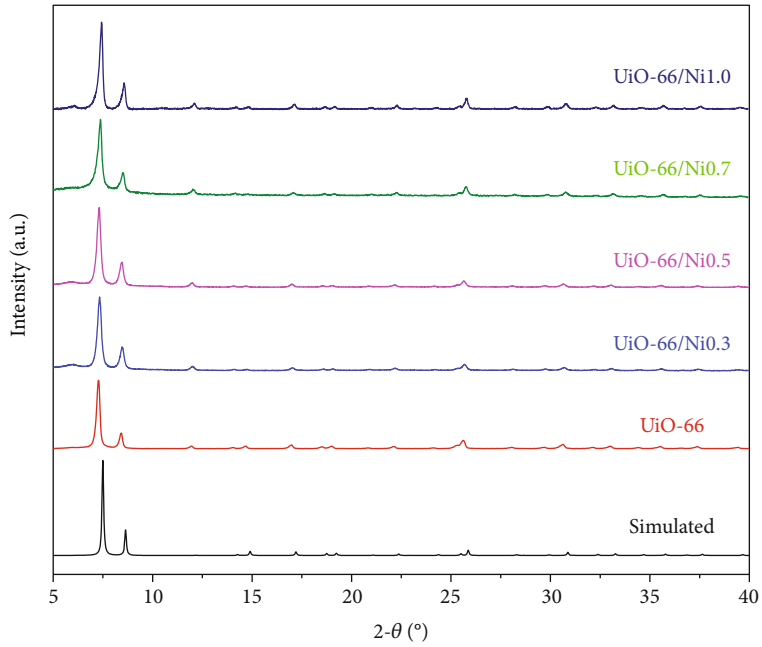

Figure 1: PXRD patterns of UiO-66 and UiO-66/Nix ($x = 0.3, 0.5, 0.7$, and 1.0).

compounds with the aim of reducing the risks [17–20]. In particular, the catalytic reduction can be considered as an effective and facile route to remove these organic pollutants [21–24]. Thus, many efforts have been devoted to the design of the suitable catalyst structure, which can significantly improve the reduction efficiency, providing excellent catalytic sustainability and recoverability.

Metal oxides, metal nanoparticles, and metal complexes can be employed as promising candidates in a wide range of heterogeneous catalytic fields [25–27]. The active metal sites are normally located at crystal corners, edges, and facets which exhibit the diverse catalytic properties [28]. Among these above-mentioned heterogeneous metal catalysts, metal complexes are known as single-site heterogeneous catalysts which have attracted increasing attention in recent years [29–32]. These exposed identical site-isolated metal centers can easily bond and react with reactant molecules in solution. In order to synthesize single-site heterogeneous catalysts, one of the simplest methods is to anchor catalytically active metal atoms, cations, or complexes directly to high surface area solid supports.

Metal-organic frameworks (MOFs) are known as porous material, and the crystalline structure consists of a metal cluster connected by organic linker molecules [33–36]. The abundance of MOFs' structure was derived from the diverse combination of metal clusters and organic components which has been intensively investigated for a wide range of application such as gas adsorption, catalysis, energy storage, sensing, and drug delivery [37–40]. Recently, many works have demonstrated that the existence of missing-linker defects on MOFs has significantly influenced the material properties [41–43]. In this case, an outstanding example is UiO-66 which has attracted considerable attention due to its chemical, mechanical, and thermal stability [44]. The crystal structure of UiO-66 consists of zirconium oxide clusters ($Zr_6O_4(OH)_4$) connected to six benzene-1,4-dicarboxylate (H_2BDC) linkers, leading to the formation of the 3D framework. However, the UiO-66 structure has been identified to contain defect sites at zirconium oxide clusters, where a linker is missed such as water and hydroxide [45–47]. By utilizing the postsynthetic metalation method, the UiO-66 structure with a high surface provides a highly tunable platform to design single-site heterogeneous catalysts.

In this study, we report a simple route to synthesize the single-site heterogeneous catalyst UiO-66/Ni, where Ni atoms are to anchor to the missing-linker defect sites at

Table 1: Elemental composition of as-prepared UiO-66 and UiO-66/Ni analyzed by EDX.

Samples	Atom (%)						
	C	O	Zr	Ni	Cl	Ni/Zr ratio	Ni/Cl ratio
UiO-66	60.96	35.91	3.12	—	—	—	—
UiO-66/Ni0.3	51.27	44.49	3.77	0.18	0.3	0.048	1.333
UiO-66/Ni0.5	50.03	46.58	3.03	0.2	0.16	0.066	1.250
UiO-66/Ni0.7	55.91	40.85	2.79	0.23	0.22	0.082	1.045
UiO-66/Ni1.0	54.59	42.14	2.78	0.24	0.24	0.086	1.000

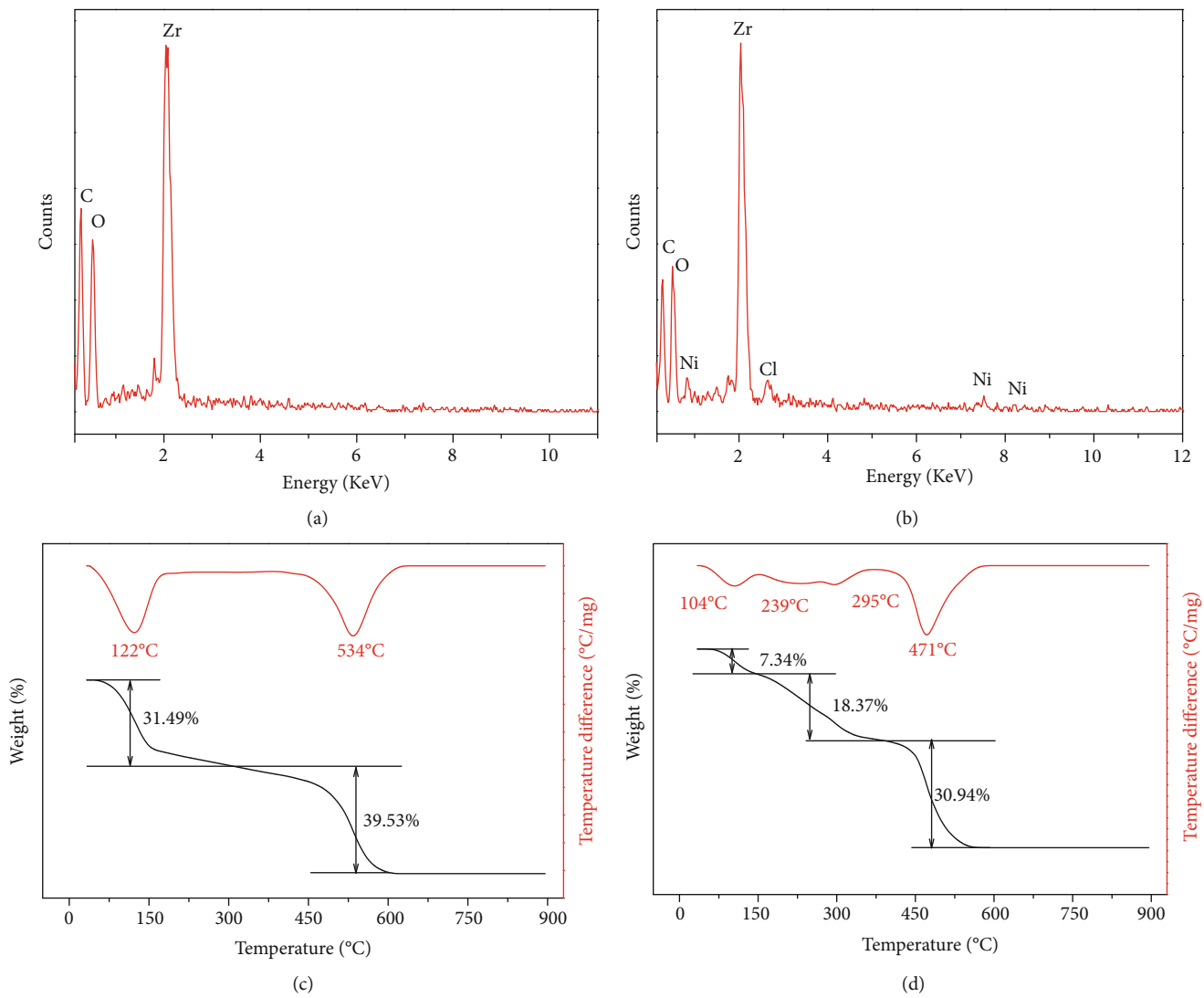

Figure 2: Energy-dispersive X-ray (EDX) spectra and the TG-DTA diagrams of UiO-66 (a, c) and UiO-66/Ni1.0 (b, d).

zirconium oxide clusters ($Zr_6O_4(OH)_4$) in the as-prepared UiO-66 structure, $Zr_6O_4(OH)_4(C_8H_4O_4)$ $(DMF)_{10}(OH)_{10}$. By this strategy, active Ni sites can be inherently located at the pore surfaces with the host as-prepared UiO-66 frameworks well retained, which will significantly enhance the free diffusion of reactant molecules. Thus, single-atom Ni site heterogeneous catalysts exhibit the highly efficient reduction catalysis toward 4-nitrophenol and methylene blue.

2. Experiment

2.1. Materials. Zirconium tetrachloride ($ZrCl_4$, 99%), 1,4-benzenedicarboxylic acid (H_2BDC, 97%), N,N′-dimethylformamide (DMF, 99%), nickel(II) chloride hexahydrate ($NiCl_2{\cdot}6H_2O$, 97.0%) methanol (CH_3OH, 99%), and 4-nitrophenol ($C_6H_5NO_3$, 99%) were used without further purification and purchased from the Merck Company, Germany.

2.2. Instrumental Characterization. Powder X-ray diffraction (PXRD) analysis was carried out on a D8 Advanced Bruker anode X-ray diffractometer with CuKα ($\lambda = 1.5406$ Å) radiation. The morphology of the samples was observed by scanning electron microscopy (Hitachi S-4800). The transmission electron microscopy (TEM) images were obtained using a JEOL JEM-2100 transmission electron microscope at 200 kV. Fourier transformation infrared analyses were recorded on a Shimadzu IRPrestige-21 (Japan). Nitrogen adsorption/desorption isotherms were measured using a Micromeriti CMS 2020 volumetric adsorption analyzer system. The samples were degassed by heating under vacuum at 393 K for 24 h. The specific surface area of the samples was calculated using the Brunauer–Emmett–Teller (BET) model. X-ray photoelectron spectroscopy (XPS) was recorded with a Kratos Analytical spectrometer. All binding energies were referenced to the contaminant C 1s peak (at 284.6 eV) of adventitious carbon. Thermogravimetric analysis (TGA) was carried out using a TG-DTA instrument (DTG-60H Shimadzu) under atmospheric pressure at a heating rate of 10°C min^{-1}. Photoluminescence spectroscopy (PL) was measured at room temperature with a photoluminescence spectrophotometer (Horiba FL3). The concentration of 4-nitrophenolate was measured using a UV-vis spectrophotometer (V-630 Jasco) at λ_{max} 400 nm.

2.3. Synthesis of Materials

2.3.1. Synthesis of UiO-66. In a typical process, $ZrCl_4$ (0.53 g, 2.274 mmol) and H_2BDC (0.38 g, 2.287 mmol) were dissolved into N,N′-dimethylformamide (60 mL) to form homogeneous solution at room temperature. Next, the obtained solution was transferred into a Teflon-lined autoclave and maintained at 120°C for 36 h. The white solids were then collected and washed with N,N′-dimethylformamide and methanol, respectively. Finally, the resulting products were dried at 60°C for 24 h in the oven to obtain UiO-66.

2.3.2. Synthesis of UiO-66/Ni. UiO-66/Ni was synthesized by a postsynthetic metalation method [48]. As-prepared UiO-66 (0.1 g) was transferred into a glass vial, which contained 10 mL of N,N′-dimethylformamide. After sonication for 1 min, a certain amount of $NiCl_2{\cdot}6H_2O$ (0.3, 0.5, 0.7, and 1.0 mmol) was added into the suspension solution. Then, the vial was sealed, heated, and maintained at 90°C for 24 h. The slight blue solids were collected and washed with N,N′-dimethylformamide and methanol, respectively. The final products of UiO-66/Ni were finally dried at 60°C for 24 h in the oven and named UiO-66/Nix (x: 0.3, 0.5, 0.7, and 1.0).

2.4. Catalytic Activity of UiO-66/Ni. The reduction reaction of 4-nitrophenol with the presence of $NaBH_4$ solution was used to evaluate the catalytic activity of the UiO-66/Ni catalyst. In this study, the reaction process was performed in a quartz cuvette, and UV-vis spectroscopy was intermittently recorded at room temperature. Initially, 3.0 mL of aqueous 4-NP solution 20 mg L^{-1} and 5.0 mg of $NaBH_4$ were alternately transferred into a quartz cuvette. The obtained solution mixture color changed immediately to deep yellow. Then, 5.0 mg of UiO-66/Ni was dispersed in 1.0 mL of deionized water with the assistance of sonication for 1 hour to yield a stable suspension. Subsequently, 5 μL of the obtained UiO-66/Ni dispersion liquid (5 mg mL^{-1}) was dropped into the above yellow solution. UV-vis absorption spectroscopy was recorded to determine the reaction progress. 4-NP conversion was calculated as the following equation:

$$\text{Conversion}(\%) = \frac{C_0 - C_t}{C_0} \times 100\%, \quad (1)$$

where C_0 is the initial concentration of 4-NP and C_t is the concentration of 4-NP at time t. The catalytic reduction of methylene blue (MB) by $NaBH_4$ with the presence of the UiO-66/Ni catalyst was also investigated similarly to the procedure for the catalytic reduction of 4-NP.

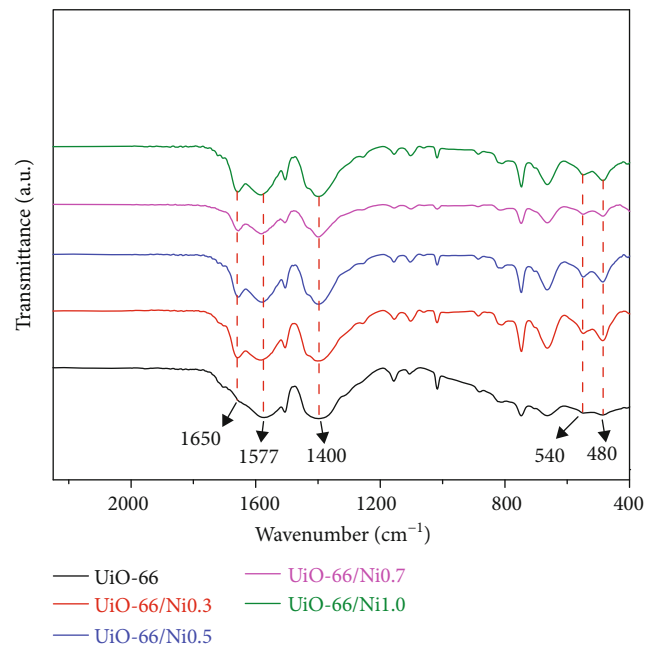

Figure 3: The Fourier transform infrared spectra (FTIR) of as-prepared UiO-66 and UiO-66/Nix.

3. Results and Discussion

3.1. Characterization of Materials. Scheme 1 illustrates the schematic diagram of the formation process of UiO-66/Ni. Firstly, UiO-66 is synthesized by a one-step solvothermal method. Then, nickel single atoms are introduced onto the UiO-66 framework through a postsynthetic metalation method. The crystal structure description of as-synthesized UiO-66 is shown in Scheme 1. As can be seen, the UiO-66 exhibits face-centered-cubic crystal structure, and the structure symmetry was identified as the Fm-3m space group. Each zirconium metal is coordinated to 8 oxygen atoms which belong to four H_2BDC linkers, and six of them connect together, leading to the formation of the $Zr_6O_4(OH)_4$ metal center. It is noticeable that each $Zr_6O_4(OH)_4$ metal center is connected to six H_2BDC linkers to create the 3D framework

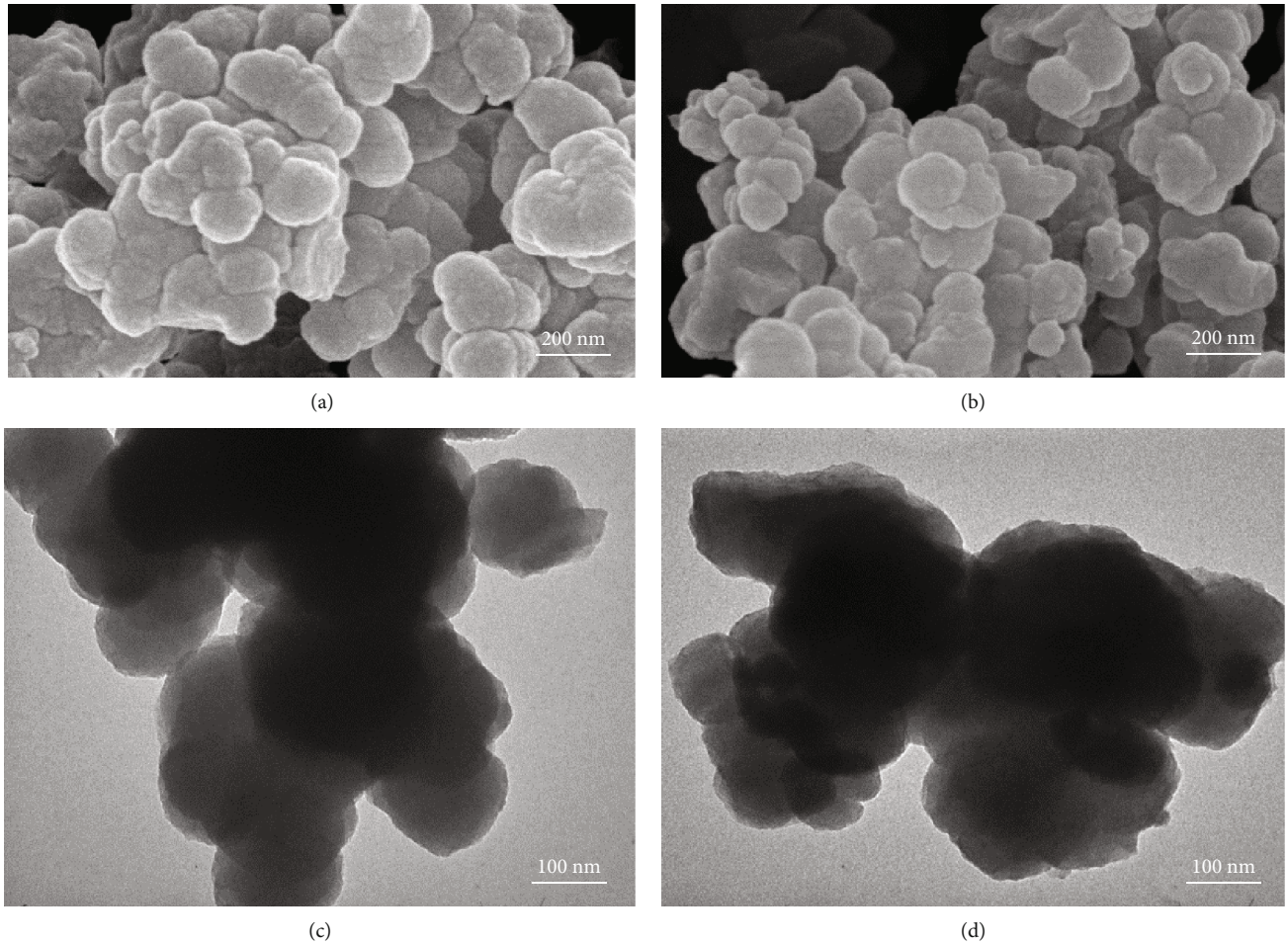

Figure 4: SEM and TEM images of UiO-66 (a, c) and UiO-66/Ni1.0 (b, d).

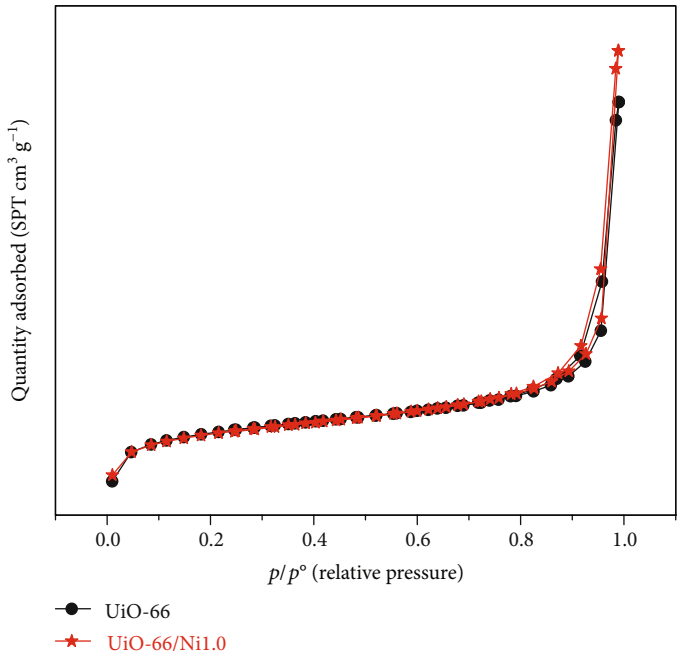

Figure 5: N_2 adsorption-desorption isotherms of as-prepared UiO-66 and UiO-66/Ni1.0.

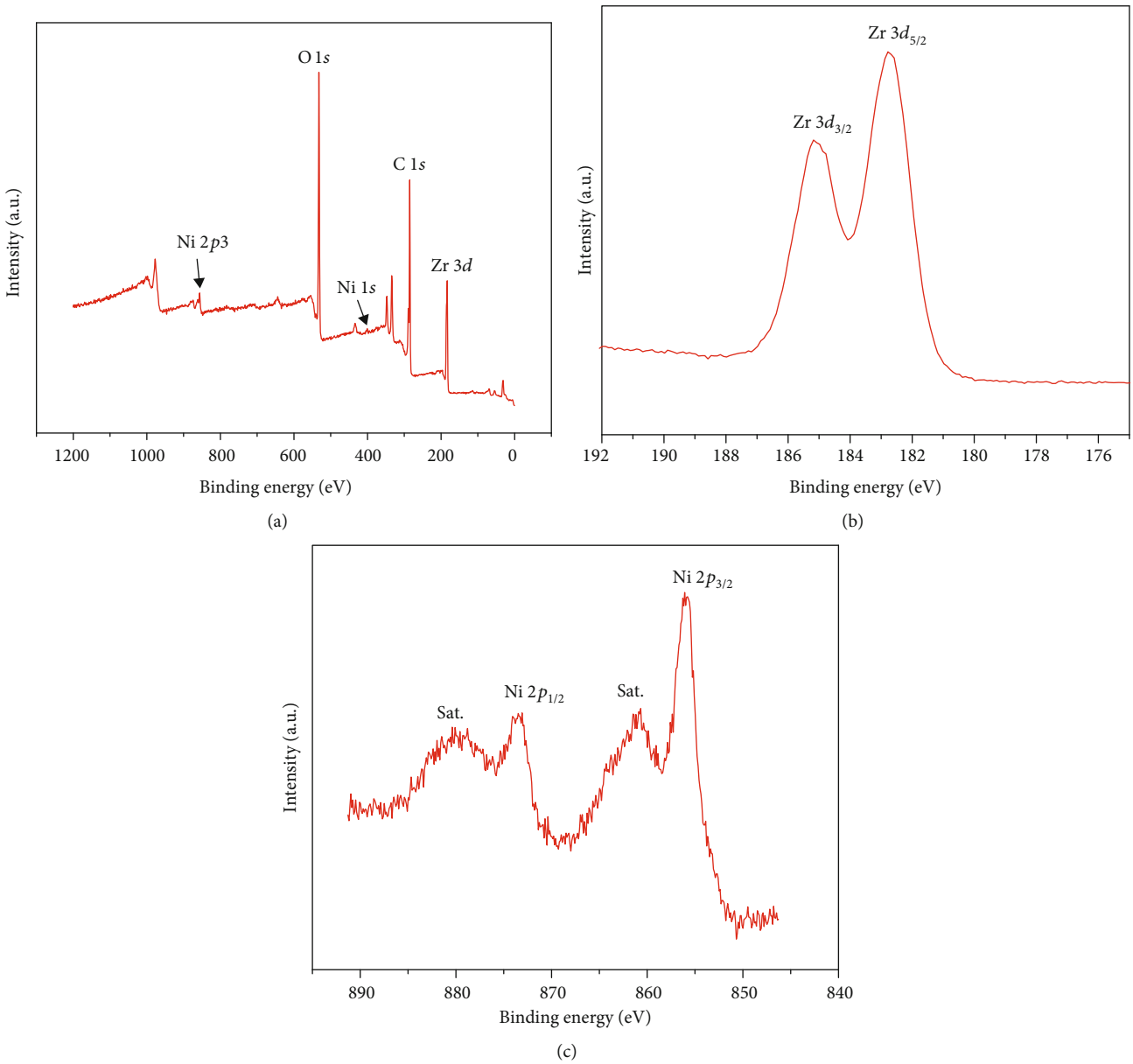

Figure 6: XPS survey scan of UiO-66/Ni1.0 (a) and core scan spectra of (b, c) C1s, O1s, Ni 2p, and Zr 3d.

with the high degree of network connection. This can be explained for its high stability in most chemical solvent and stable up to 500°C in air atmosphere [49]. It is worth noting that the UiO-66 structure demonstrated the existence of linker vacancies which are located in terminate -OH/OH_2 groups of the $Zr_6O_4(OH)_4$ metal center. The amount of defect sites depends on the synthetic protocol. In this study, the stoichiometric formula of the as-prepared UiO-66 was hypothesized as follows: $Zr_6O_4(OH)_4(C_8H_4O_4)_x(DMF)_{12-2x}(OH)_{12-2x}$. Hydroxide groups and DMF can be used for charge balancing and completing the coordination clusters of the $Zr_6O_4(OH)_4$ metal center. Then, as-prepared UiO-66 was immersed in solution of $NiCl_2{\cdot}6H_2O$ in DMF at 90°C for 24 h with the aim of anchoring Ni atoms at the oxygen atoms of -OH/OH_2 groups, leading to the formation of the UiO-66/Ni structure.

The structure and crystal phase of the as-prepared UiO-66 and UiO-66/Ni with different concentrations of the nickel precursor were determined by the PXRD analysis, as shown in Figure 1. It is clearly seen that all of the diffraction peaks of UiO-66 and UO-66/Ni were well matched with the simulated PXRD pattern of hydroxylated UiO-66, indicating that the as-prepared UiO-66 was successfully synthesized with a high degree of crystallinity. It is noticeable that the characteristic diffraction peaks of NiO and other nickel atom contained compound nanoparticles not observed in Figure 1. This result can be explained to be the reason for its low degree of crystallinity and very low proportion and quantum size.

The PXRD patterns of Ni single-atom-supported UiO-66 show that the crystalline structure of as-prepared UiO-66 did not change after metalation of the nickel atoms with their

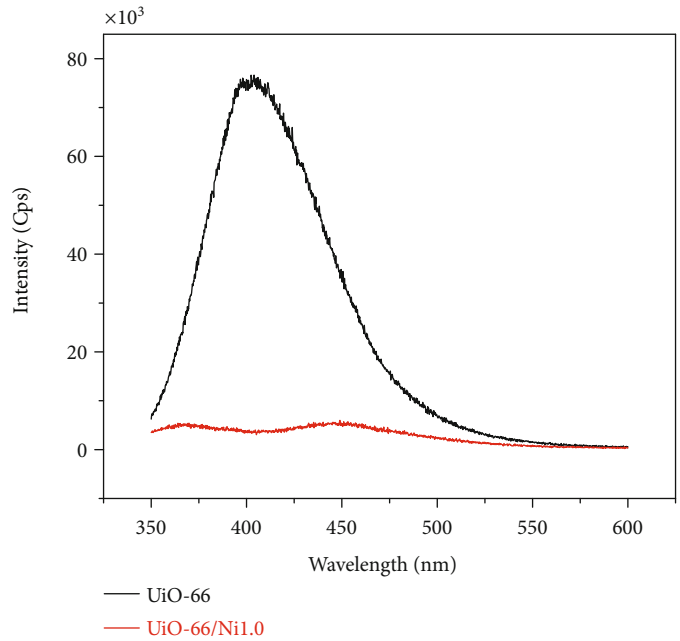

Figure 7: Fluorescence spectra of the UiO-66 and UiO-66/Ni1.0.

framework, demonstrating that the chemical structure of the as-prepared UiO-66 with the presence of nickel atoms cannot be destroyed. However, it is difficult to obtain the structure of the Ni single-atom site using the single X-ray diffraction patterns. Thus, in order to investigate the existence of a nickel single atom in the as-prepared UiO-66 structure, the EDX analysis of the as-prepared UiO-66 and UiO-66/Nix ($x = 0.3, 0.5, 0.7$, and 1.0) samples was performed and is shown in Table 1 and Figures 2(a) and 2(b). These results show that the incorporation of Ni atoms in the UiO-66 structure can be controlled by the amount of $NiCl_2{\cdot}6H_2O$ used in the synthesis. The Ni·:·Zr atomic ratio increased with the increase in the amount of the $NiCl_2{\cdot}6H_2O$ precursor from 0.3 to 0.5 mmol and remained constant from 0.7 to 1.0 mmol, demonstrating that the number of defect sites is limited in the as-synthesized UiO-66 structure.

TG-DTA analysis of UiO-66 and UiO-66/Ni1.0 catalysts was also performed to investigate the amount of the missing-linker defects in the UiO-66 structure. As can be seen in Figure 2(c), 31.49% weight loss in the range of 100 to 150°C corresponded to DMF, CH_3OH, and H_2O solvent within the pores of the UiO-66 structure. The second step weight loss of 39.68% after 300°C was attributed to the coordinated ligand with Zi^{4+} cation to form the UiO-66 structure such as H_2BDC and missing-linker defects (-OH/OH_2). The final thermal deposition product of UiO-66 began at 610°C, corresponding to ZrO_2. The actual stoichiometric formula weight of as-prepared UiO-66 was calculated by varying the value of x. It was found that the value x of 1 was closely consistent with the calculated weight loss of 39.78%, corresponding that each $Zr_6O_4(OH)_4$ is coordinated to 1 molecule of H_2BDC, 10 molecules of DMF, and 1 molecule of the OH^- group. Hence, the stoichiometric formulae of the as-prepared UiO-66 can be described as follows: $Zr_6O_4(OH)_4(C_8H_4O_4)(DMF)_{10}(OH)_{10}$.

Figure 2(d) illustrates the TG-DTA analysis of the nickel single-atom-incorporated UiO-66 structure (UiO-66/Ni1.0). Similarly, 7.34% of weight loss at 104°C was due to solvent molecules within the pores of the UiO-66/Ni1.0 structure. Then, the composition process of UiO-66/Ni1.0 samples experiences two steps of weight loss of 38.46% prior to the formation of the final ZrO_2 and NiO products. It is worth noting that the molar ratio of Ni : Cl of about 1 was calculated by energy-dispersive X-ray spectroscopic (EDX) analysis of these samples of UiO-66/Ni, indicating that Cl^- anion can be seen as a ligand coordinating to Ni^{2+} cation. The stoichiometric formula of the UiO-66/Ni1.0 was also hypothesized as follows: $Zr_6O_4(OH)_4(C_8H_4O_4)(DMF)_{10}(OH)_{10-2x}Ni_xOH_x(Cl)_x$. The result suggested that the value x of 2 was closely consistent with the TG calculated value (49.31%). Hence, the stoichiometric formula of the UiO-66 after metalation with nickel single atoms can be described as follows: $Zr_6O_4(OH)_4(C_8H_4O_4)(DMF)_{10}(OH)_8Ni_2(OH)_2(Cl)_2$. This result shows that the ratio of Zr_6/Ni was closely consistent with elemental composition of the as-prepared UiO-66/Ni sample which was determined by EDX analysis.

Figure 3 illustrates the FTIR spectra of as-prepared UiO-66 and the samples of UiO-66/Nix ($x = 0.3, 0.5, 0.7$, and 1.0). The peaks in the regions of 1650 and 1577 cm^{-1} are attributed to the symmetric stretching vibrations of the carboxylate group which are coordinated with a zirconium center during the deprotonation. Specifically, the peak of the band at 1400 cm^{-1} is associated with C-O root in C-OH of carboxylic acid. The presence of the band at 746 and 659 cm^{-1} corresponded to the stretch vibration of Zr-O clusters and O-H of defect sites where Ni atoms are coordinating to -OH/OH_2

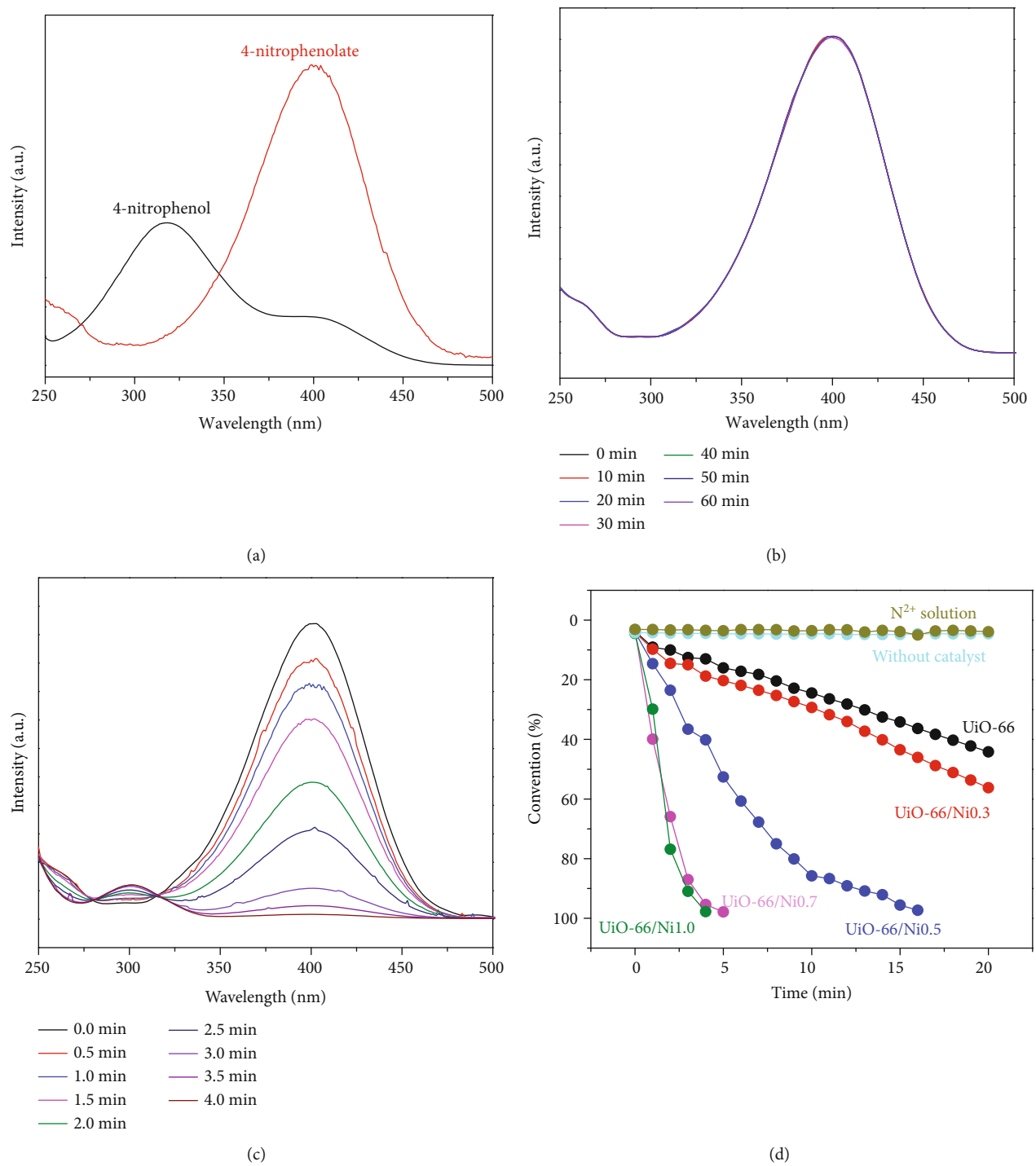

Figure 8: UV-vis spectra of 4-NP solution before and after adding $NaBH_4$ (a); the time-dependent successive reduction of 4-NP with $NaBH_4$ without catalyst (b); reduction of 4-NP in the presence of UiO-66/Ni1.0 (c); 4-NP conversion (%) of different catalysts (d).

species on UiO-66. The small peaks at 540 and 480 cm^{-1} can be attributed to the symmetric and asymmetric stretching vibrations of Zr-(OC). It can be clearly observed that the positions of each peak in all samples are well matched together, demonstrating that the incorporation of Ni single atoms does not change the chemical structure of UiO-66 and Ni single atoms that are coordinated to -OH/OH_2 species on defect-free UiO-66 structure.

The morphology of as-prepared UiO-66 and UiO-66/Ni1.0 was clearly observed by using SEM images, as shown in Figures 4(a) and 4(b). The SEM images represented that the as-prepared UiO-66 before and after the incorporation of Ni single atoms were sphere-like particles with uniform size and smooth surface.

In order to further investigate the morphology of the samples and the existence of impurity nanoparticles on the

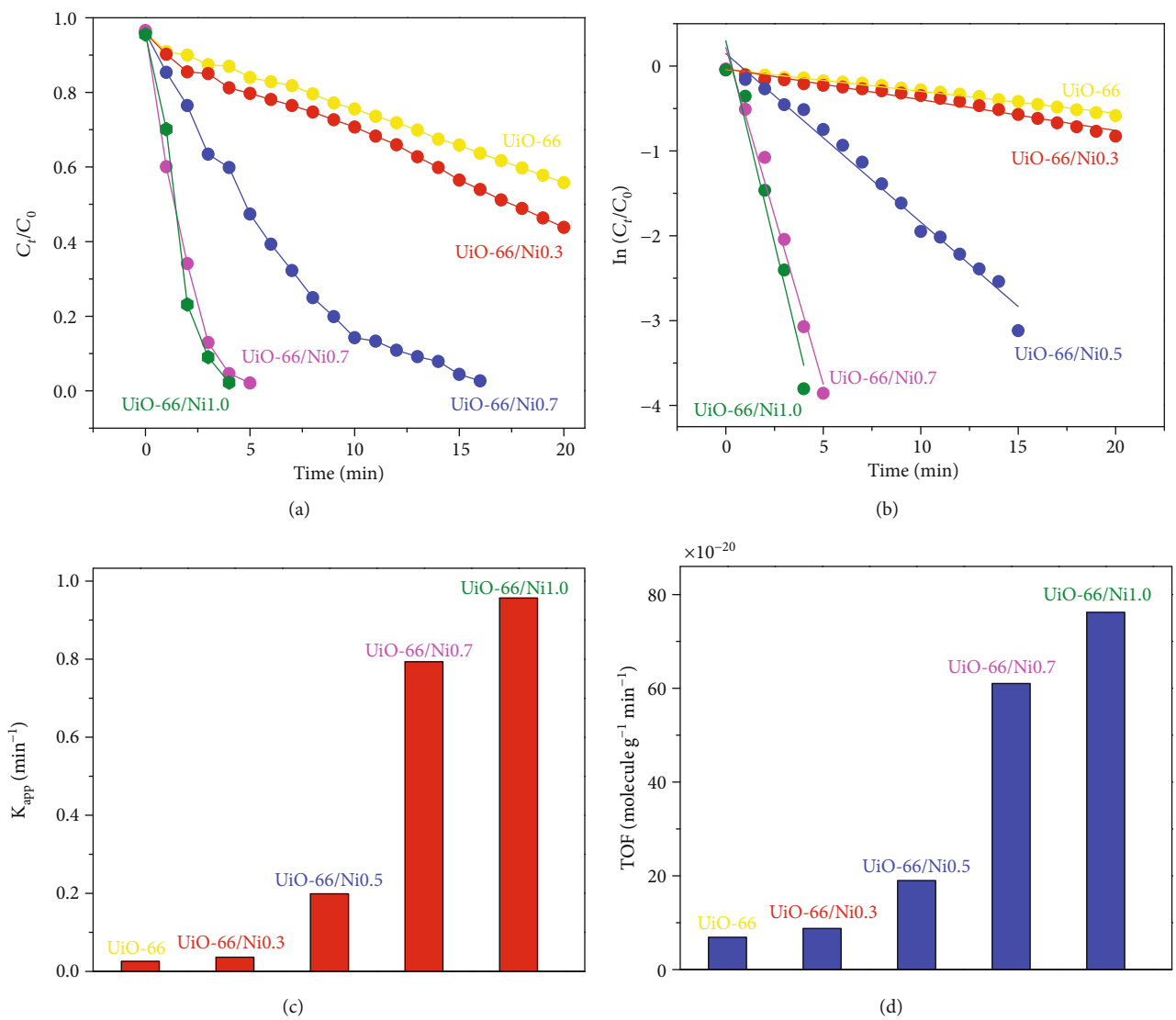

FIGURE 9: Plots of C_t/C_0 (a) and ln C_t/C_0 (b) vs. reaction time and the k_{app} (c) and TOF values (d) of different catalysts.

UiO-66 surface, the TEM images were observed and are exhibited in Figures 4(c) and 4(d). It can be clearly seen that the Ni or NiO nanoparticle formation did not occur on the surface of the UiO-66 structure, which is consistent with the results of XRD patterns of both UiO-66 and UiO-66/Ni1.0.

The nitrogen adsorption-desorption isotherms of the samples of defect-free UiO-66 and UiO-66/Ni1.0 are illustrated in Figure 5. Two isotherms of UiO-66 and UiO-66/Ni1.0 have the similar shape, exhibited typical type I with a H4 hysteresis loop, and possessed mesoporous structure [50].

The pore size distributions and the BET-specific surface area for the samples were obtained by using desorption data by the BJH method. The pore sizes for the samples do not change considerably, about 4.4 and 4.8 nm, respectively.

The specific surface area of as-prepared UiO-66 was 855.06 $m^2\ g^{-1}$. After metalation with Ni single atoms, the S_{BET} of UiO-66/Ni1.0 catalysts is slightly decreased, about 10 $m^2\ g^{-1}$ compared to that of as-synthesized UiO-66. These results evidenced that the as-prepared UiO-66 structure is unchangeble after metalation with the Ni single atoms.

The chemical composition and the chemical state of the elements in the sample UiO66/Ni1.0 were determined by using XPS spectra and are presented in Figure 6. As the extensive scan data in Figure 6(a), all the peaks corresponding to the Zr, Ni, O, and C elements have been detected. In addition, the high-resolution spectrum of the sample shows two peaks at 182.74 and 185.03 eV, which could be attributed to Zr $3d_{5/2}$ and Zr $3d_{3/2}$ of zirconium in the $Zr_6O_4(OH)_4$ metal center (Figure 6(b)). The bending energy of Ni $2p_{3/2}$ and Ni $2p_{1/2}$ was 855.28 eV and 872.48 eV, respectively. The energy binding distance of Ni $2p_{3/2}$ and Ni $2p_{1/2}$ peaks was around 17 eV, indicating that Ni2p belongs to the Ni(II) oxidation state in the UiO-66/Ni structure [51]. Those results demonstrated that Ni single-atom metalation with the UiO-66 structure was successfully synthesized via chemical bonding.

Table 2: k_{app} and TOF values for the reduction of 4-NP with different catalysts (the concentration of the catalyst was 8.33 mg L^{-1}).

No.	Samples	TOF[a] × 10^{-20} (molecule $g^{-1}min^{-1}$)	k_{app} (min^{-1})	R^2
1	UiO-66	6.89	0.026	0.991
2	UiO-66/Ni0.3	8.76	0.036	0.975
3	UiO-66/Ni0.5	18.96	0.198	0.985
4	UiO-66/Ni0.7	61.03	0.794	0.983
5	UiO-66/Ni1.0	76.19	0.956	0.964

[a]Turnover frequency (TOF) = (molecule of reacted organic substrate/mass of catalyst) × reaction time (min^{-1}).

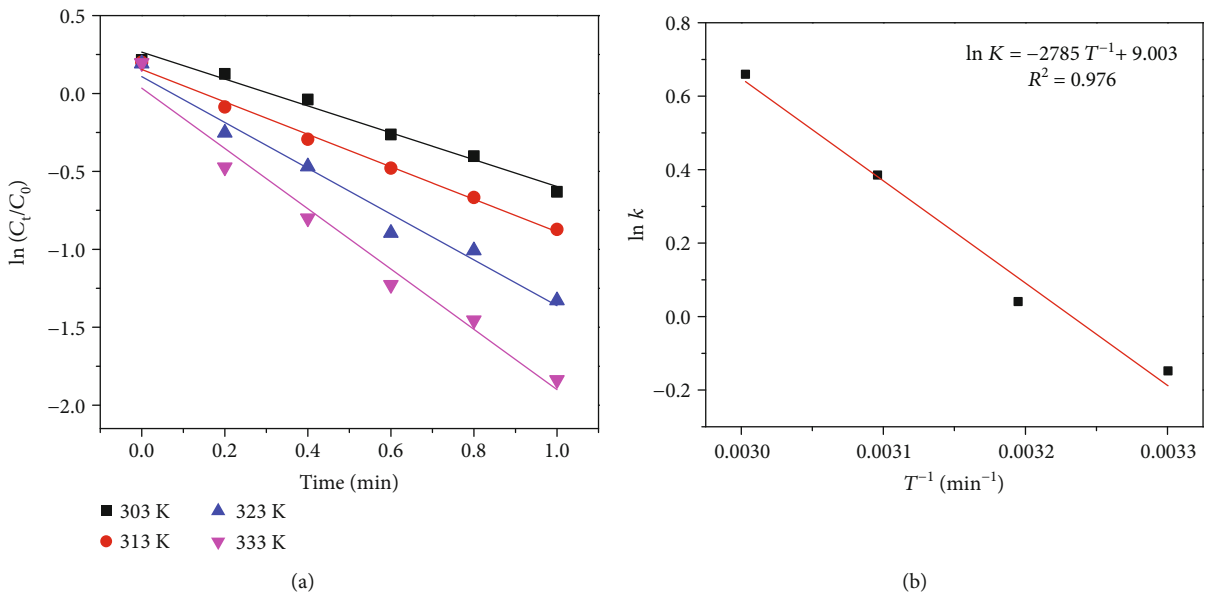

Figure 10: Plot of ln (C_t/C_0) vs. time (a). Arrhenius plot of ln K vs. $1/T$ for the catalytic reduction of 4-NP using the UiO-66/Ni1.0 catalyst at different temperatures (b).

In order to evaluate the transfer of photogenerated electrons, the photoluminescence quenching of UiO-66 and Ni-supported UiO-66 (UiO-66/Ni1.0) was carried out and is shown in Figure 7. The maximum emission wavelength was observed at 402 nm for UiO-66 when the excitation wavelength was 300 nm. For UiO-66 with the presence of Ni atoms, the fluorescence was completely quenched, indicating that the existence of Ni in the UiO-66 structure plays a vital role in retarding recombination of photoinduced hole-electron pairs.

Table 3: Thermodynamic parameters of the catalytic reduction of 4-NP at different temperatures.

T (K)	k_{app} (min^{-1})	R^2	E_a (kJ mol^{-1})
303	0.862	0.987	23.15
313	1.042	0.994	
323	1.470	0.979	
333	1.934	0.977	

3.2. Reduction of 4-Nitrophenol Using UiO-66/Ni as a Catalyst

3.2.1. Catalytic Reduction of 4-Nitrophenol. The reduction reaction of 4-nitrophenol with the presence of $NaBH_4$ solution was used to investigate the catalytic activity of the UiO-66/Ni catalyst.

The catalytic performance of single-atom Ni-supported UiO-66 was investigated using the model of reduction reaction of 4-nitrophenol (4-NP) to 4-aminophenol (4-AP) by $NaBH_4$ solution. It is clear that the maximum adsorption peak of 4-NP was observed at 317 nm and shifted to 400 nm with the presence of $NaBH_4$ solution (Figure 8(a)). This can be explained by an increase in alkalinity upon addition of $NaBH_4$, leading to the formation of 4-nitrophenolate ions which corresponds to a color change from light yellow to deep yellow. As can be seen in Figure 8(b), the maximum adsorption peak at 400 nm remained steady over 60 min after the addition of $NaBH_4$, demonstrating that the reduction reaction of 4-NP did not occur with the absence of the catalyst. After the addition of 5 μL of the UiO-66/Ni1.0 dispersion liquid, the intensity of characteristic adsorption peak at 400 nm decreased significantly over the reaction process, while the novel maximum adsorption peak was observed at 300 nm and the deep yellow of solution mixture was changed

Table 4: Comparison of the activity of various catalysts for the reduction performance toward 4-nitrophenol.

Catalyst	Type	$C_{4\text{-NP}}$ (mM)	$C_{catalyst}$ (mg mL^{-1})	Time (min)	K_{app} (min^{-1})	Ref
Au@[Na]-HAMS	Yolk-shell mesoporous	5.217	1.739	15	0.310	[59]
Pd/C	Nanoparticles	1.67	0.0024 mM	8	0.529	[60]
Co-Ni double hydroxide	2D graphene-like	0.129	0.323	6	0.669	[61]
Co@C	Porous prisms	0.1	0.02	4	0.660	[62]
Pt/Co_3O_4-CeO_2	Mesoporous	0.0958	0.0479	4	0.678	[63]
Ca/Co_3O_4	Mesopore	3.5×10^{-3}	0.08	41.67	0.230	[64]
MoS_2/SnO_2	Hierarchical heterojunction	0.1	0.5	13	0.252	[65]
Pt@Ag	Core-shell nanoparticles	0.1	0.016	8	0.355	[66]

into colorless solution within 4 min, corresponding to the formation of the product of 4-AP (Figure 8(c)).

Figure 8(d) shows the convention of reduction reactions toward 4-NP at different times without a catalyst and the presence of the as-prepared UiO-66 and UiO-66/Nix ($x = 0.3, 0.5, 0.7$, and 1.0) catalyst, respectively. The 4-NP convention with the presence of $NaBH_4$ without a catalyst or 0.01 M Ni^{2+} remained stable over 20 min, approximately 5% indicating that $NaBH_4$ without UiO-66/Ni or NaBH4 with Ni^{2+} could not reduce 4-NP. This result means that UiO-66/Ni plays an important role as a heterogeneous catalyst for 4-NP reduction. However, in the presence of the as-prepared UiO-66 catalyst, the reduction of 4-NP into the corresponding 4-AP took 20 min for the conversion of 44%; this figure was 56% for UiO-66/Ni0.3. It is noticeable that it took around 9 min for UiO-66/Ni0.5 for 99% conversion, while the UiO-66/Ni0.7 and UiO-66/Ni1.0 catalysts needed only 3 min and 4 min, respectively, to complete the reduction of 4-NP. The results demonstrated that the presence of nickel single-atom-supported UiO-66 structure plays a crucial role in the excellent catalytic performance toward 4-NP reduction. Specifically, the optimal amount of the $NiCl_2{\cdot}6H_2O$ precursor, introduced in the UiO-66 structure, was 1.0 mmol (UiO-66/Ni1.0 catalyst) indicating the best catalytic performance.

Figure 9(a) illustrates the plot of C_t/C_0 versus reaction time of each catalyst, where C_t and C_0 represent the concentration of 4-NP at the time of t and 0 min, respectively. The catalytic performance of all as-prepared samples was monitored by UV-vis spectrometry at the interval time of 1 min. The plots of ln (C_t/C_0) versus reaction time for the reduction of 4-NP are shown in Figure 9(b). The excess of concentration of $NaBH_4$ can be considered a constant during the reaction progress. Thus, the pseudo-first-order kinetics was employed to investigate the reduction reaction of 4-NP. The linear fit with a coefficient of determination very close to unity also supports the assumption of the pseudo-first-order kinetics. The apparent rate constant values (k_{app}) were found to be 0.026, 0.036, 0.198, 0.794, and 0.95 min^{-1} for the UiO-66, UiO-66/Ni0.3, UiO-66/Ni0.5, UiO-66/Ni0.7, and UiO-66/Ni1.0 catalysts, respectively, using the following equation:

$$-\frac{dC_t}{dt} = k_{app}C_t, \quad (2)$$

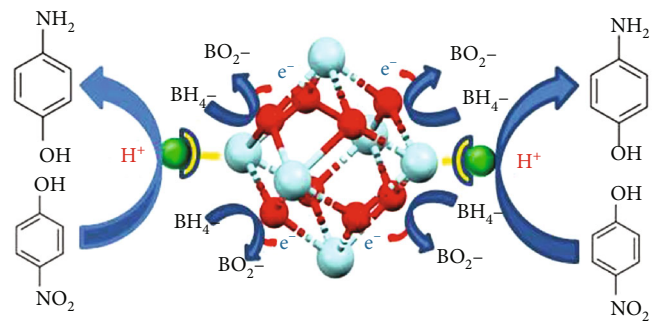

Scheme 2: Proposed mechanism for the reduction of 4-nitrophenol using the UiO-66/Ni1.0 catalyst.

where C_t was the concentration of 4-NP at time t and k_{app} was the apparent rate constant.

The detailed results are represented in Table 1 and Figure 9(c). The apparent rate constant values (k_{app}) increase significantly with an increase in the amount of Ni in the UiO-66 structure. The UiO-66/Ni1.0 catalyst showed the highest k_{app} compared to as-prepared UiO-66 and different UiO-66/Nix ($x = 0.3, 0.5$, and 0.7). The TOF values were calculated, and the results are shown in Figure 9(d) and Table 2. The catalytic reduction reaction toward 4-nitrophenol was also evaluated by using the TOF values. As can be seen in Figure 9(d) and Table 2, the TOF values were calculated to be 6.89×10^{20}, 8.76×10^{20}, 18.96×10^{20}, 61.03×10^{20}, and 76.19×10^{20} molecules g^{-1}min^{-1} for UiO-66, UiO-66/Ni0.3, UiO-66/Ni0.5, UiO-66/Ni0.7, and UiO-66/Ni1.0, respectively. The increase in the TOF value can be attributed to the increased amount of active nickel catalyst sites which are present in UiO-66 network and the facile diffusion routes of the reactant molecules to the active sites in porous structure.

In order to determine the apparent activation energy (E_a) of the reduction reaction of 4-NP using UiO-66/Ni1.0 as the catalyst, the reaction kinetics was conducted over the temperature range of 303-343 K (Figure 10). The extraction of the apparent activation energy E_a from the Arrhenius equation (3) is determined to be 23.15 kJ mol^{-1} for the UiO-66/Ni1.0 catalyst (Table 3).

$$\ln k_{app} = \ln A - \frac{E_a}{RT}. \quad (3)$$

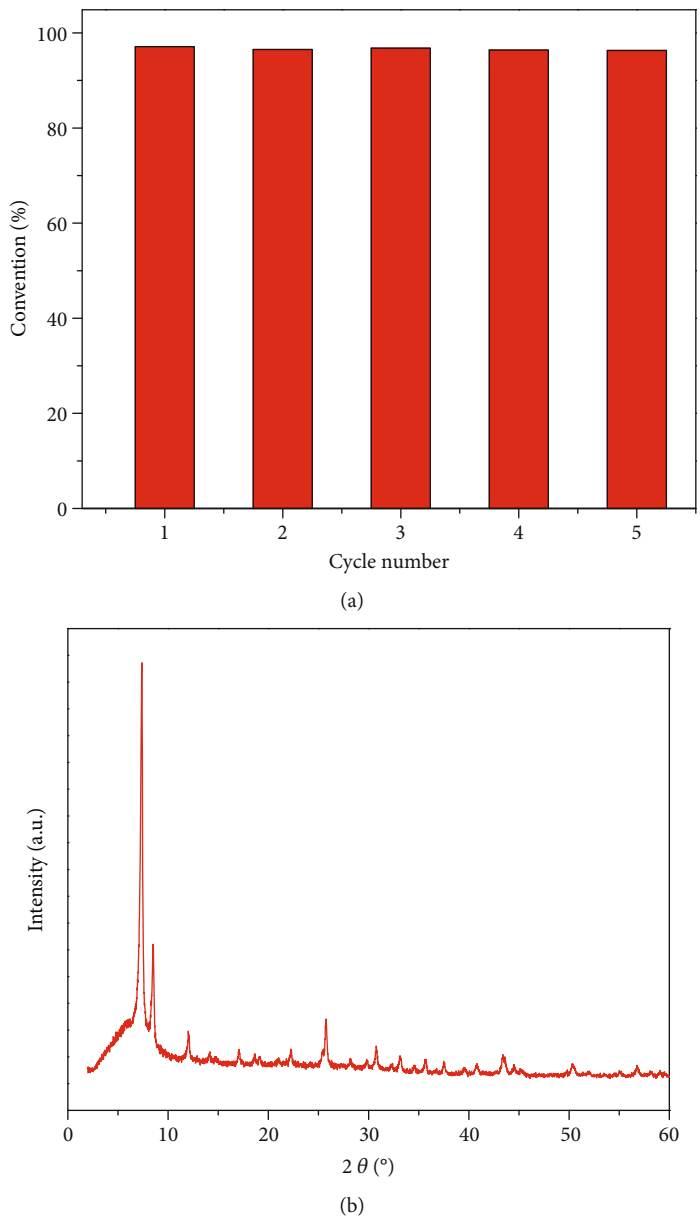

Figure 11: Recyclability of the 4-nitrophenol reduction reaction using the UiO-66/Ni1.0 catalyst (a) and XRD patterns of the 5th reused UiO-66/Ni1.0 catalyst (b).

The obtained results show that the UiO-66/Ni1.0 catalyst can significantly decrease the activation energy and increase the apparent rate constants of 4-NP catalytic reduction.

The comparison of the various catalysts in previously published papers for the reduction performance toward 4-nitrophenol is listed in Table 4. It is clear that the UiO-66/Ni1.0 catalyst exhibits the highest catalytic activity for 4-NP reduction. For example, k_{app} is 0.529 min^{-1} for Pd/C NPs, 0.660 min^{-1} for porous prisms Co@C NPs, and 0.335 min^{-1} for core-shell nanoparticles Pt@Ag, which are lower than 0.956 of UiO-66/Ni1.0.

3.2.2. The Mechanism of the 4-Nitrophenol Reduction Reaction Using the UiO-66/Ni1.0 Catalyst. The excellent catalytic performance of the UiO-66/Ni1.0 can be ascribed to the high activity of the nickel single-atom-supported UiO-66 network and the excellent permeability of the porous structure. In this study, the mechanism of the 4-nitrophenol reduction reaction can be described in Scheme 2.

Initially, the 4-nitrophenol can easily penetrate and diffuse into the inner pore spaces of the UiO-66/Ni1.0 catalytic structure. Then, 4-nitrophenol molecules were rapidly absorbed on the Ni(II) active sites which are present in the UiO-66 structure, thanks to the high electrical transport of the Ni(II) active sites, which can facilitate the electron transfer from BH_4^- to 4-NP and reduce the activation energy. At last, 4-AP can be formed efficiently through the hydrogenation reduction of 4-NP and diffused conveniently from the nanoporous structure via the abundant mesopores.

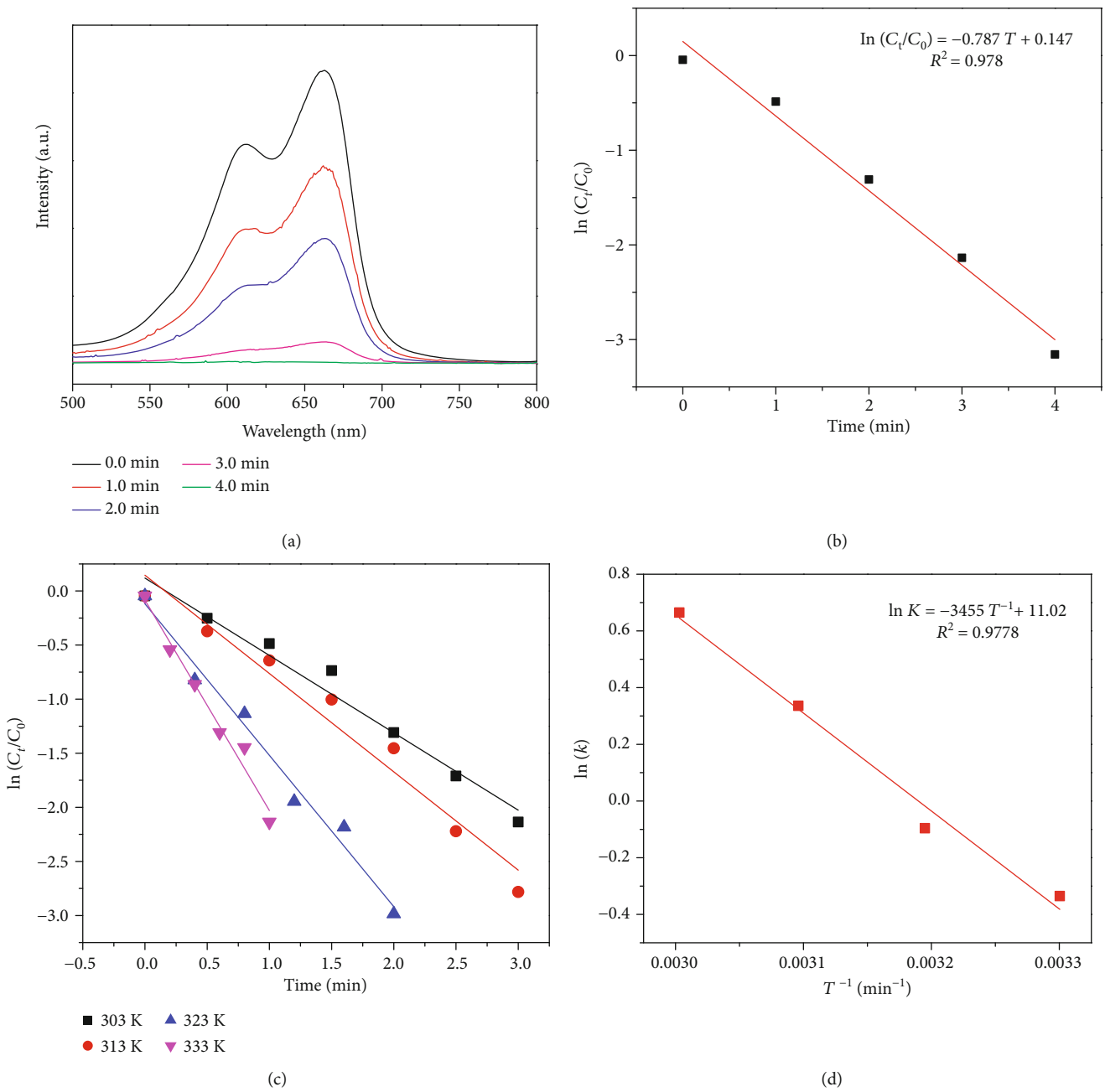

Figure 12: UV-vis absorption spectrum changes in MB solution catalyzed by UiO-66/Ni1.0 (a); plot of $\ln(C_t/C_0)$ vs. time corresponding to (a) (b); plot of $\ln(C_t/C_0)$ vs. time (c); Arrhenius plot (a) of $\ln k$ vs. $1/T$ for the catalytic reduction of MB in the presence of UiO-66/Ni1.0 at different temperatures (d).

3.2.3. Recyclability of the UiO-66/Ni1.0 Catalyst. The recyclability of the catalyst plays an important role in the heterogeneous catalytic reaction. In order to evaluate the recyclability of the catalyst, 5 cycles of 4-nitrophenol catalytic reduction were performed with the UiO-66/Ni1.0 catalyst. As can be seen in Figure 11(a), during the 5 cycles, the conversion of 4-nitrophenol was more than 95% within 4 min of the reaction process. The XRD pattern of the 5th reused UiO-66/Ni1.0 catalyst is shown in Figure 11(b). The intensity of the characteristic peak after the 5th recycle indicates that the UiO-66/Ni1.0 preserved the high degree of crystallinity of the UiO-66 framework. The results show that the UiO-66/Ni1.0 catalyst possesses the excellent stability and recyclability of the UiO-66/Ni.

3.3. Catalytic Performance of UiO-66/Ni1.0 for MB. To further evaluate the catalytic performance of UiO-66/Ni1.0, the catalytic reduction of MB in the presence of $NaBH_4$ as the reduction agent was also investigated and is shown in Figure 12 and Table 5.

In the presence of 5μL of the obtained UiO-66/Ni dispersion liquid (5 mg mL^{-1}), the color of MB solution with the

Table 5: Thermodynamic parameters of the catalytic reduction of MB at different temperatures.

T (K)	k_{app} (min^{-1})	R^2	E_a (kJ mol^{-1})
303	0.715	0.973	28.72
313	0.909	0.967	
323	1.399	0.983	
333	1.944	0.978	

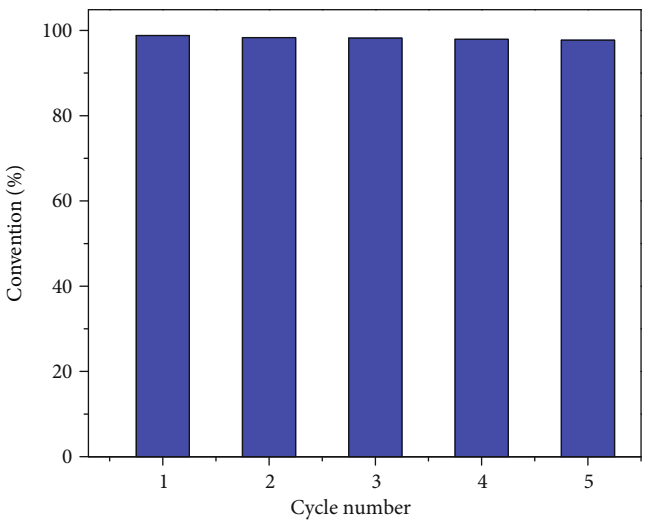

Figure 13: Recyclability of the MB reduction reaction using the UiO-66/Ni1.0 catalyst.

intensity of the characteristic adsorption peak at 664 nm disappeared swiftly within 4 min (Figure 12(a)). The MB decolorization kinetics followed the pseudo-first-order kinetics model (Figure 12(b)). Moreover, the k_{app} and TOF for the reduction of MB using UiO-66/Ni1.0 at room temperature are 0.787min^{-1} and 33.89×10^{20} molecules g^{-1} min^{-1}, respectively. The apparent activation energy E_a is determined to be 28.72 kJ mol^{-1} (Table 5 and Figure 12(d)). The apparent kinetic rate constant for MB decolorization is found to be several ten to hundred times greater than those for photocatalysts in previous publications [52–54] and is much higher than that for MB decolorization with $NaBH_4$ as a reduction agent on the CuNPs@Gelatin catalyst [55], Fe_3O_4/SiO_2/Au/por-SiO_2 catalyst [56], Ag/PSNM nanocomposite spheres [57], and Ag, Au nanoparticles [58]. These results show that UiO-66/Ni exhibits excellent catalytic performance for the hydrogenation of MB.

Similarly, the recyclability of the synthesized catalyst for the purpose of MB degradation was also assessed. The MB reduction reaction was repeated for five cycles, and the convention remained almost constant, more than 97% within 4 min, as can be seen in Figure 13.

4. Conclusion

In this research, a novel single-atom Ni heterogeneous catalyst-supported UiO-66 structure has been successfully synthesized through a postsynthetic metalation method. This structure possesses the well-defined active site with a high specific surface area, where single Ni atoms are anchored to the oxygen atoms of -OH/OH_2 capping the defect sites on the Zr oxide clusters of UiO-66. The as-synthesized catalyst was employed to investigate the reduction reaction of 4-nitrophenol or methylene blue with the presence of $NaBH_4$. It was found that this catalyst exhibits excellent catalytic activity and high stability. It is expected that this research would pave the way for the construction of other single-site heterogeneous catalysts for wide applications.

Data Availability

The data used to support the findings of this study are available from the corresponding author upon request.

Conflicts of Interest

The authors declare that they have no conflicts of interest.

Acknowledgments

This work was supported by Hue University under Decision DHH 2020-01-170.

References

[1] P. K. Arora, A. Srivastava, and V. P. Singh, "Bacterial degradation of nitrophenols and their derivatives," *Journal of Hazardous Materials*, vol. 266, pp. 42–59, 2014.

[2] Y. Li, W. P. Hsieh, R. Mahmudov, X. Wei, and C. P. Huang, "Combined ultrasound and Fenton (US-Fenton) process for the treatment of ammunition wastewater," *Journal of Hazardous Materials*, vol. 244-245, pp. 403–411, 2013.

[3] Z. Fang, J. Chen, X. Qiu, X. Qiu, W. Cheng, and L. Zhu, "Effective removal of antibiotic metronidazole from water by nanoscale zero- valent iron particles," *Desalination*, vol. 268, no. 1–3, pp. 60–67, 2011.

[4] Y. Yuan, B. Lai, and Y. Y. Tang, "Combined Fe^0/air and Fenton process for the treatment of dinitrodiazophenol (DDNP) industry wastewater," *Chemical Engineering Journal*, vol. 283, pp. 1514–1521, 2016.

[5] B. Petrova, B. Tsyntsarski, T. Budinova, N. Petrov, L. F. Velasco, and C. O. Ania, "Activated carbon from coal tar pitch and furfural for the removal of p-nitrophenol and m-aminophenol," *Chemical Engineering Journal*, vol. 172, no. 1, pp. 102–108, 2011.

[6] Z. Xiong, B. Lai, Y. Yuan, J. Cao, P. Yang, and Y. Zhou, "Degradation of *p* -nitrophenol (PNP) in aqueous solution by a micro-size Fe^0/O_3 process (mFe^0/O_3): Optimization, kinetic, performance and mechanism," *Chemical Engineering Journal*, vol. 302, pp. 137–145, 2016.

[7] S. Chiron, L. Comoretto, E. Rinaldi, V. Maurino, C. Minero, and D. Vione, "Pesticide by-products in the Rhone delta (Southern France). The case of 4-chloro-2-methylphenol and of its nitroderivative," *Chemosphere*, vol. 74, no. 4, pp. 599–604, 2009.

[8] Z. I. Bhatti, H. Toda, and K. Furukawa, "*p* -Nitrophenol degradation by activated sludge attached on nonwovens," *Water Research*, vol. 36, no. 5, pp. 1135–1142, 2002.

[9] C. Qiu, X. Li, H. Wang et al., "Investigation of the synergistic effects for *p* -nitrophenol mineralization by a combined process of ozonation and electrolysis using a boron-doped diamond anode," *Journal of Hazardous Materials*, vol. 280, pp. 644–653, 2014.

[10] B. Lai, Y. H. Zhang, R. Li, Y. X. Zhou, and J. Wang, "Influence of operating temperature on the reduction of high concentration *p* -nitrophenol (PNP) by zero valent iron (ZVI)," *Chemical Engineering Journal*, vol. 249, pp. 143–152, 2014.

[11] G. Eichenbaum, D. Kirkland, P. O'Neill et al., "Assessment of the genotoxic and carcinogenic risks of *p* -nitrophenol when it is present as an impurity in a drug product," *Regulatory Toxicology and Pharmacology*, vol. 55, no. 1, pp. 33–42, 2009.

[12] E. Fernandes Silva, A. S. Varela Junior, T. F. Cardoso et al., "Reproductive toxicology of 2,4 dinitrophenol in boar sperm," *Toxicology in Vitro*, vol. 35, pp. 31–35, 2016.

[13] J. Chen, M. Song, Y. Li, Y. Zhang, K. Taya, and C. M. Li, "The effect of phytosterol protects rats against 4-nitrophenol-induced liver damage," *Environmental Toxicology and Pharmacology*, vol. 41, pp. 266–271, 2016.

[14] E. Forgacs, T. Cserháti, and G. Oros, "Removal of synthetic dyes from wastewaters: a review," *Environment International*, vol. 30, no. 7, pp. 953–971, 2004.

[15] B. K. Ghosh, S. Hazra, B. Naik, and N. N. Ghosh, "Preparation of Cu nanoparticle loaded SBA-15 and their excellent catalytic activity in reduction of variety of dyes," *Powder Technology*, vol. 269, pp. 371–378, 2015.

[16] J. K. Ahmed and M. Ahmaruzzaman, "A facile synthesis of Fe_3O_4-charcoal composite for the sorption of a hazardous dye from aquatic environment," *Journal of Environmental Management*, vol. 163, pp. 163–173, 2015.

[17] I. Ali, "New generation adsorbents for water treatment," *Chemical Reviews*, vol. 112, no. 10, pp. 5073–5091, 2012.

[18] J. N. Tiwari, N. H. le, K. C. Kemp et al., "Reduced graphene oxide-based hydrogels for the efficient capture of dye pollutants from aqueous solutions," *Carbon*, vol. 56, pp. 173–182, 2013.

[19] T. Zhu, J. S. Chen, and X. W. D. Lou, "Highly efficient removal of organic dyes from waste water using hierarchical NiO spheres with high surface area," *Journal of Physical Chemistry C*, vol. 116, no. 12, pp. 6873–6878, 2012.

[20] M. Panizza and G. Cerisola, "Direct and mediated anodic oxidation of organic pollutants," *Chemical Reviews*, vol. 109, no. 12, pp. 6541–6569, 2009.

[21] O. A. Zelekew and D. H. Kuo, "Synthesis of a hierarchical structured NiO/NiS composite catalyst for reduction of 4-nitrophenol and organic dyes," *RSC Advances*, vol. 7, no. 8, pp. 4353–4362, 2017.

[22] R. J. Tayade, T. S. Natarajan, and H. C. Bajaj, "Photocatalytic degradation of methylene blue dye using ultraviolet light emitting diodes," *Industrial & Engineering Chemistry Research*, vol. 48, no. 23, pp. 10262–10267, 2009.

[23] J. A. Laszlo, "Regeneration of dye-saturated quaternized cellulose by bisulfite-mediated borohydride reduction of dye azo groups: an improved process for decolorization of textile wastewaters," *Environmental Science & Technology*, vol. 31, no. 12, pp. 3647–3653, 1997.

[24] J. Liu, J. Yang, H. Ma et al., "Facile synthesis of carbon-doped mesoporous anatase TiO2for the enhanced visible-light driven photocatalysis," *Chemical Communications*, vol. 50, no. 90, pp. 13971–13974, 2014.

[25] Z. Li and Q. Xu, "Metal-nanoparticle-catalyzed hydrogen generation from formic acid," *Accounts of Chemical Research*, vol. 50, no. 6, pp. 1449–1458, 2017.

[26] Q. Yang, Q. Xu, and H. L. Jiang, "Metal–organic frameworks meet metal nanoparticles: synergistic effect for enhanced catalysis," *Chemical Society Reviews*, vol. 46, no. 15, pp. 4774–4808, 2017.

[27] R. H. Crabtree, "Deactivation in homogeneous transition metal catalysis: causes, avoidance, and cure," *Chemical reviews*, vol. 115, no. 1, pp. 127–150, 2015.

[28] Q. Wang and D. Astruc, "State of the art and prospects in metal-organic framework (MOF)-based and MOF-derived nanocatalysis," *Chemical Reviews*, vol. 120, no. 2, pp. 1438–1511, 2020.

[29] L. Liu and A. Corma, "Metal catalysts for heterogeneous catalysis: from single atoms to nanoclusters and nanoparticles," *Chemical Reviews*, vol. 118, no. 10, pp. 4981–5079, 2018.

[30] Z. Liang, C. Qu, D. Xia, R. Zou, and Q. Xu, "Atomically dispersed metal sites in MOF-based materials for electrocatalytic and photocatalytic energy conversion," *Angewandte Chemie International Edition*, vol. 57, no. 31, pp. 9604–9633, 2018.

[31] L. Jiao and H. L. Jiang, "Metal-organic-framework-based single-atom catalysts for energy applications," *Chem*, vol. 5, no. 4, pp. 786–804, 2019.

[32] Y. Wang, J. Mao, X. Meng, L. Yu, D. Deng, and X. Bao, "Catalysis with two-dimensional materials confining single atoms: concept, design and applications," *Chemical reviews*, vol. 119, no. 3, pp. 1806–1854, 2019.

[33] B. F. Hoskins and R. Robson, "Design and construction of a new class of scaffolding-like materials comprising infinite polymeric frameworks of 3D-linked molecular rods. a reappraisal of the zinc cyanide and cadmium cyanide structures and the synthesis and structure of the diamond-related frameworks [N(CH3)4][CuIZnII(CN)4] and CuI[4,4',4",4'"-tetracyanotetraphenylmethane]BF4.xC6H5NO2," *Journal of the American Chemical Society*, vol. 112, no. 4, pp. 1546–1554, 1990.

[34] S. KITAGAWA, S. MATSUYAMA, M. MUNAKATA, and T. EMORI, "Synthesis and crystal structures of novel one-dimensional polymers, $[\{M(bpen)X\}_\infty][M = Cu^l, X = PF_6^-; M = Ag^l, X = ClO_4^-; bpen = trans-1,2bis(2-pyridyl)ethylene]and[\{Cu(bpen)(CO)(CH_3CN)PF_6\}_\infty]$," *Journal of the Chemical Society, Dalton Transactions*, vol. 11, no. 11, pp. 2869–2874, 1991.

[35] D. Riou and G. Férey, "Hybrid open frameworks (MIL-*n*). Part 3 crystal structures of the HT and LT forms of MIL-7: a new vanadium propylenediphosphonate with an open-framework. Influence of the synthesis temperature on the oxidation state of vanadium within the same structural type," *Journal of Materials Chemistry*, vol. 8, no. 12, pp. 2733–2735, 1998.

[36] H. C. Zhou, J. R. Long, and O. M. Yaghi, "Introduction to metal-organic frameworks," *Chemical Reviews*, vol. 112, no. 2, pp. 673-674, 2012.

[37] O. K. Farha, I. Eryazici, C. D. Malliakas et al., "*De novo* synthesis of a metal -organic framework material featuring ultrahigh surface area and gas storage capacities," *Nature Chemistry*, vol. 2, no. 11, pp. 944–948, 2010.

[38] G. Lu and J. T. Hupp, "Metal–organic frameworks as sensors: a ZIF-8 based Fabry-Pérot device as a selective sensor for chemical vapors and gases," *Journal of the American Chemical Society*, vol. 132, no. 23, pp. 7832-7833, 2010.

[39] J. R. Li, R. J. Kuppler, and H. C. Zhou, "Selective gas adsorption and separation in metal-organic frameworks," *Chemical Society Reviews*, vol. 38, no. 5, pp. 1477–1504, 2009.

[40] N. C. Thacker, Z. Lin, T. Zhang, J. C. Gilhula, C. W. Abney, and W. Lin, "Robust and porous β-diketiminate-functionalized metal-organic frameworks for earth-abundant-metal-catalyzed C-H amination and hydrogenation," *Journal of the American Chemical Society*, vol. 138, no. 10, pp. 3501–3509, 2016.

[41] H. Furukawa, Y. B. Zhang, J. Jiang et al., "Water adsorption in porous metal-organic frameworks and related materials," *Journal of the American Chemical Society*, vol. 136, no. 11, pp. 4369–4381, 2014.

[42] Z. Fang, J. P. Dürholt, M. Kauer et al., "Structural complexity in metal-organic frameworks: simultaneous modification of open metal sites and hierarchical porosity by systematic doping with defective linkers," *Journal of the American Chemical Society*, vol. 136, no. 27, pp. 9627–9636, 2014.

[43] B. Tu, Q. Pang, D. Wu, Y. Song, L. Weng, and Q. Li, "Ordered vacancies and their chemistry in metal-organic frameworks," *Journal of the American Chemical Society*, vol. 136, no. 41, pp. 14465–14471, 2014.

[44] Q. Zhao, W. Yuan, J. Liang, and J. Li, "Synthesis and hydrogen storage studies of metal–organic framework UiO-66," *International Journal of Hydrogen Energy*, vol. 38, no. 29, pp. 13104–13109, 2013.

[45] H. Wu, V. Krungleviciute, M. Tyagi et al., "Unusual and highly tunable missing-linker defects in zirconium metal-organic framework UiO-66 and their important effects on gas adsorption," *Journal of the American Chemical Society*, vol. 135, no. 28, pp. 10525–10532, 2013.

[46] L. Valenzano, S. Chavan, S. Bordiga et al., "Disclosing the complex structure of UiO-66 metal organic framework: a synergic combination of experiment and theory," *Chemistry of Materials*, vol. 23, no. 7, pp. 1700–1718, 2011.

[47] S. Øien, H. Reinsch, S. Svelle et al., "Detailed structure analysis of atomic positions and defects in zirconium metal-organic frameworks," *Crystal Growth & Design*, vol. 14, no. 11, pp. 5370–5372, 2014.

[48] K. Manna, Z. Lin, F. X. Greene et al., "Chemoselective single-site Earth-abundant metal catalysts at metal-organic framework nodes," *Nature Communications*, vol. 7, no. 1, pp. 1–11, 2016.

[49] S. Kim, J. Lee, S. Jeoung, H. R. Moon, and M. Kim, "Surface-deactivated core–shell metal–organic framework by simple ligand exchange for enhanced size discrimination in aerobic oxidation of alcohols," *Chemistry–A European Journal*, vol. 26, no. 34, pp. 7568–7572, 2020.

[50] Y. He, "UiO-66-NDC (1,4-naphthalenedicarboxilic acid) as a novel fluorescent probe for the selective detection of Fe^{3+}," *Journal of Solid State Chemistry*, vol. 285, article 121206, 2020.

[51] M. C. Biesinger, B. P. Payne, L. W. M. Lau, A. Gerson, and R. S. C. Smart, "X-ray photoelectron spectroscopic chemical state quantification of mixed nickel metal, oxide and hydroxide systems," *Surface and Interface Analysis: An International Journal devoted to the development and application of techniques for the analysis of surfaces, interfaces and thin films*, vol. 41, no. 4, pp. 324–332, 2009.

[52] A. Houas, H. Lachheb, M. Ksibi, E. Elaloui, C. Guillard, and J. M. Herrmann, "Photocatalytic degradation pathway of methylene blue in water," *Applied Catalysis B: Environmental*, vol. 31, no. 2, pp. 145–157, 2001.

[53] D. Caschera, T. de Caro, B. Cortese et al., "Fabrication of Eu-TiO_2 NCs functionalized cotton textile as a multifunctional photocatalyst for dye pollutants degradation," *Applied Surface Science*, vol. 427, pp. 81–91, 2018.

[54] W. Wang, K. Xiao, L. Zhu, Y. Yin, and Z. Wang, "Graphene oxide supported titanium dioxide & ferroferric oxide hybrid, a magnetically separable photocatalyst with enhanced photocatalytic activity for tetracycline hydrochloride degradation," *RSC Advances*, vol. 7, no. 34, pp. 21287–21297, 2017.

[55] A. Musa, M. B. Ahmad, M. Z. Hussein, M. I. Saiman, and H. A. Sani, "Effect of gelatin-stabilized copper nanoparticles on catalytic reduction of methylene blue," *Nanoscale Research Letters*, vol. 11, no. 1, p. 438, 2016.

[56] J. Ge, Q. Zhang, T. Zhang, and Y. Yin, "Core-satellite nanocomposite catalysts protected by a porous silica shell: controllable reactivity, high stability, and magnetic recyclability," *Angewandte Chemie*, vol. 47, no. 46, pp. 8924–8928, 2008.

[57] G. Liao, Q. Li, W. Zhao, Q. Pang, H. Gao, and Z. Xu, "_In-situ_ construction of novel silver nanoparticle decorated polymeric spheres as highly active and stable catalysts for reduction of methylene blue dye," *Applied Catalysis A: General*, vol. 549, pp. 102–111, 2018.

[58] V. S. Suvith and D. Philip, "Catalytic degradation of methylene blue using biosynthesized gold and silver nanoparticles," *Spectrochimica Acta Part A: Molecular and Biomolecular Spectroscopy*, vol. 118, pp. 526–532, 2014.

[59] X. Fang, M. F. Hsieh, M. Chen et al., "Hollow mesoporous aluminosilica spheres with perpendicular pore channels as catalytic nanoreactors," *ACS Nano*, vol. 6, no. 5, pp. 4434–4444, 2012.

[60] F. Paquin, J. Rivnay, A. Salleo, N. Stingelin, and C. Silva-Acuña, "Multi-phase microstructures drive exciton dissociation in neat semicrystalline polymeric semiconductors," *Journal of Materials Chemistry C*, vol. 3, no. 41, pp. 10715–10722, 2015.

[61] J. M. Song, J. Zhang, D. Ling et al., "A facile synthesis of graphene-like cobalt–nickel double hydroxide nanocomposites at room temperature and their excellent catalytic and adsorption properties," *Journal of Nanoparticle Research*, vol. 16, no. 2, article 2269, 2014.

[62] H. Li, L. Chi, C. Yang, L. Zhang, F. Yue, and J. Wang, "MOF derived porous Co@C hexagonal-shaped prisms with high catalytic performance," *Journal of Materials Research*, vol. 31, no. 19, pp. 3069–3077, 2016.

[63] Q. Wang, Y. Zhang, Y. Zhou et al., "Preparation of platinum nanoparticles immobilized on ordered mesoporous Co_3O_4–CeO_2 composites and their enhanced catalytic activity," *RSC Advances*, vol. 6, no. 71, pp. 67173–67183, 2016.

[64] B. M. Mogudi, P. Ncube, N. Bingwa, N. Mawila, S. Mathebula, and R. Meijboom, "Promotion effects of alkali- and alkaline earth metals on catalytic activity of mesoporous Co_3O_4 for 4-nitrophenol reduction," *Applied Catalysis B: Environmental*, vol. 218, pp. 240–248, 2017.

[65] X. Q. Qiao, D. F. Hou, D. S. Li et al., "Tunable MoS_2/SnO_2P–N heterojunctions for an efficient trimethylamine gas sensor and 4-nitrophenol reduction catalyst," *ACS Sustainable Chemistry & Engineering*, vol. 6, no. 9, pp. 12375–12384, 2018.

[66] Z. S. Lv, X. Y. Zhu, H. B. Meng, J. J. Feng, and A. J. Wang, "One-pot synthesis of highly branched core-shell nanoparticles as a recyclable catalyst with dramatically boosting the catalytic performance for 4-nitrophenol reduction," *Journal of Colloid and Interface Science*, vol. 538, pp. 349–356, 2018.

Hindawi
Journal of Nanomaterials
Volume 2021, Article ID 5570866, 14 pages
https://doi.org/10.1155/2021/5570866

Research Article

Effect of NH_3 Alkalization and MgO Promotion on the Performance of Ni/SBA-15 Catalyst in Combined Steam and Carbon Dioxide Reforming of Methane

Phan H. Phuong,[1,2] Luu C. Loc,[1,2,3,4] Nguyen Tri,[3,4] Nguyen P. Anh,[3] and Ha C. Anh[1,2,4]

[1]*Vietnam National University Ho Chi Minh City, Linh Trung Ward, Thu Duc District, Ho Chi Minh City, Vietnam*
[2]*Ho Chi Minh City University of Technology (HCMUT), 268 Ly Thuong Kiet Street, Ho Chi Minh City, Vietnam*
[3]*Institute of Chemical Technology, Vietnam Academy of Science and Technology, Ho Chi Minh City, Vietnam*
[4]*Graduate University of Science and Technology, Vietnam Academy of Science and Technology, Hanoi, Vietnam*

Correspondence should be addressed to Luu C. Loc; lcloc@ict.vast.vn

Received 8 January 2021; Revised 30 March 2021; Accepted 17 April 2021; Published 17 May 2021

Academic Editor: Nguyen Duc Cuong

In this work, 31.4 wt.% Ni/SBA-15 (Ni/SBA-15) nonpromoted and alkalized with ammonia solution and by MgO promoter catalysts were prepared and used for combined steam and CO_2 reforming of CH_4 (bireforming). Effect of concentration of ammonia solution ($NH_{3(aq)}$) (10–25 vol.%) and Mg content (3–12 wt.%) on the properties of the Ni/SBA-15 catalysts was investigated by low-angle and powder X-ray diffraction (XRD), N_2-BET isothermal adsorption, SEM, TEM, EDS mapping, H_2-TPR, and CO_2-TPD methods. The performance of the catalysts in bireforming was assessed in the temperature range of 550–800°C. The enhancement of dispersion of NiO particles, reducibility, and basicity of alkalized Ni/SBA-15 catalysts were responsible for improving the catalytic performance of this catalyst. The results revealed that the Ni/SBA-15 treated with 15-25% $NH_{3(aq)}$ solution and promoted with 3-9% Mg exhibited high activity for CH_4 conversion. Meanwhile, Ni6Mg/SBA-15 showed the highest CO_2 conversion. Among tested catalysts, Ni/SBA-15-20NH_3 and Ni9Mg/SBA-15 samples had an almost equal activity with a CH_4 conversion of nearly 97% and a CO_2 conversion of about 84% at 700°C thanks to its moderate affinity with both CO_2 and CH_4. However, the H_2/CO ratio of the product mixture remained at 2.02 on the Ni/SBA-15-20NH_3 catalyst and almost 1 on the Ni9Mg/SBA-15 sample. These results might be related to the fact that the alkalization of the Ni/SBA-15 catalyst by $NH_{3(aq)}$ solution had an advantage over using MgO because side reactions were unlikely to occur.

1. Introduction

The rapid increase in emissions of major greenhouse gases such as CO_2 and CH_4 in the last decade has seriously affected climate change and the living environment in the world. Besides, syngas, the variable mixture of carbon monoxide and hydrogen, is an important intermediate for downstream processes in the chemical industry. Including many benefits for producing syngas from available natural gas reservoirs, along with the consumption of two main greenhouse gases, bireforming of CH_4 using CO_2 and H_2O (reaction (1)) is the most suitable method with extensive application in the chemical industry [1]:

$$3CH_4 + CO_2 + 2H_2O \longrightarrow 4CO + 8H_2, \quad \Delta H_{298} = +220\,\text{kJ/mol} \tag{1}$$

The bireforming process (BRM) (reaction (1)) consists of two reactions: dry reforming (DRM) (reaction (2)) and steam reforming (SRM) (reaction (3)):

$$CH_4 + CO_2 \rightleftharpoons 2CO + 2H_2, \quad \Delta H_{298} = +247.3\,\text{kJ/mol} \quad (2)$$

$$CH_4 + H_2O \rightleftharpoons CO + 3H_2, \quad \Delta H_{298} = +206.3\,\text{kJ/mol} \quad (3)$$

As can be seen from reactions (1) and (2), the enthalpy at 298 K of DRM is +247.3 kJ/mol, 1.122 times higher than BRM. This means that, as an endothermic reaction, the combined CO_2 and steam reforming of methane (Equation (1)) consumes less energy than DRM (Equation (2)). Furthermore, this combination shows the most desirable stoichiometry of H_2 and CO, completely suitable for the Fischer-Tropsch synthesis process. By feeding CO_2 and steam simultaneously, the products' ratio can be controlled by adjusting the $CH_4/CO_2/H_2O$ ratio of the feedstock [2]. Moreover, one of the disadvantages of steam reforming methane is the generation of large amounts of CO_2 in the side reaction

$$CO + H_2O \rightleftharpoons CO_2 + H_2, \quad \Delta H^o_{298K} = -41\,\text{kJ/mol} \quad (4)$$

In a bireforming reaction, this problem was overcome. In addition, adding H_2O to the dry reforming reaction (2), to create a bireforming reaction (1), has limited coke deposition—the biggest disadvantage of CO_2 reforming of methane, thanks to reaction (5) [3]:

$$C + H_2O \rightleftharpoons CO + H_2, \quad \Delta H^o_{298K} = +131.3\,\text{kJ/mol} \quad (5)$$

For these reasons, presently, bireforming is receiving great attention for converting natural gas into synthetic gas.

Metals in the VIII B group, especially Ni, Ru, Rh, Pd, Ir, and Pt, have been reported to be highly active in CH_4 reforming processes. Despite higher activity and stability, the usage of noble metals is not preferred due to their high cost and less availability. Among other transition metals, Ni possesses high reactivity towards conversion of hydrocarbons [4], photocatalytic water splitting [5], and the hydrogen and the oxygen evolution reaction [6]. In general, supported Ni catalysts are commercially used in steam reforming of CH_4 because of the cheap price and good performance compared to the ones with noble metals [7, 8]. However, coke formation and metal sintering have been making this process inapplicable commercially until recently. Hence, metal dispersing and coke resistance improvement of Ni-based catalyst has been attracting attention.

In our previous study [9], nanosized NiO/SBA-15 catalysts with NiO crystallite size in the range of 12.9 to 18.3 nm were successfully prepared. In this catalytic system, there are 5–6 nm NiO particles dispersed inside the pores and the NiO particles of 20–50 nm distributed on the surface of SBA-15 when Ni content was 23.5–39.2 wt.%. Dispersion of metallic sites into the pores could prevent Ni from sintering and metal loss during reaction. The high dispersion of NiO in the Ni/SBA-15 catalyst is caused by the unique properties of SBA-15 such as uniform pores with large diameters (5.3–6.0 nm), high porosity, and high specific surface area (613 m^2/g). The reduced catalysts have high activity in bireforming reaction, reaching 86% CH_4 and 77% CO_2 converted at 700°C or 90.5% and 80%, respectively, at 800°C. The catalysts work stably for hundreds of hours due to the presence of weak and strong Lewis basic sites which limit coke formation and increase CO_2 adsorption. Similarly, Zhang et al. [10] reported that 12.5% NiO/SBA-15 catalyst had CH_4 and CO_2 conversion at 800°C of 89% and 85%, respectively, and could remain its activity over 600 hours time-on-stream (TOS) in CO_2 methane reforming. As a result, SBA-15 is believed to be potential support for nickel catalyst in the methane bireforming process.

Deactivation of Ni/SBA-15 catalyst in dry reforming of CH_4 has been addressed to coke deposition rather than sintering of Ni particles [10]. One of the most important factors affecting coke deposition during the reaction is the basicity of catalysts [11]. Coke formation could be reduced or even inhibited when the active metal is dispersed on the metal oxide support with Lewis basic sites. Many studies show that the addition of alkali and alkaline earth metals could change the nature of supports, leading to a reduction of coke formation and an increase of CO_2 adsorption [12]. For example, adding a basic Lewis promoter such as alkali metal oxides (Na_2O, K_2O), alkaline earth (CaO, MgO), or weak base (NH_4OH) reduces coke deposition and metal sintering of Ni/Al_2O_3, Ni/SiO_2, and NiO/SBA-15 catalysts [12–14].

Danilova et al. [15] suggested that the structural similarity of NiO and MgO led to the formation of a solid solution in the form of a thin layer, surrounding the Ni particles that increased catalyst stability and reduced carbon deposition. Wang et al. [16] demonstrated that in the MgO-modified Ni/SBA-15 catalyst synthesized by the coimpregnation method, the MgO particles covered the walls of channels of SBA-15. Besides, the catalyst basicity increased and the Ni dispersion was improved, leading to an enhancement in chemical adsorption of CO_2. As a result, the activity and the coke resistance of the catalyst in the dry reforming reaction were improved. In addition, Alipour et al. [17] reported that adding MgO to the nickel catalyst promoted the catalyst reducibility that enhanced CH_4 conversion and coke resistance. NiO-MgO bonding was useful in preventing Ni particle sintering; carbon deposits and these facts have been accepted in many studies [15, 18, 19].

Recently, another promoter considered to be examined was NH_4OH. Previous researches used NH_4OH as a pH controller for some processes [20, 21], but NH_4OH could also be used as a promoter thanks to its basicity to enhancing some characteristics of the catalyst. This property was believed to reduce the acidic sites which would improve catalyst activity, limit coke formation, and stabilize catalyst. Modification of SBA-15 by attaching the $-NH_2$ group to its structure improved the structural stability and increased content of amino as well as basic sites [22]. Hao et al. [23] indicated that alkalization increased catalytic activity and coke resistance of the supported Co/Al_2O_3 catalyst.

However, to the best of our knowledge, the impact of treatment with aqueous NH_3 step in catalyst preparation or promoting catalysts by MgO on the activity of Ni/SBA-15 catalyst in bireforming has not been carried out so far. In our previous investigation [9], it was reported that NiO/SBA-15 catalyst contained 31.4 mass% Ni (Ni/SBA-15), exhibiting higher activity than other Ni/SBA-15 samples. The conversion of CH_4 and CO_2 on this catalyst in

bireforming (BRM) reached 90% and 76%, respectively, at 700°C. In this study, the effect of NH_3 alkalization or promotion by MgO on catalytic activity of Ni/SBA-15 catalyst in BRM reaction was investigated and optimized.

2. Materials and Methods

SBA-15 was prepared by the method described in the work [9]. To prepare SBA-15 alkalized with ammonia solution (SBA-15-NH_3), 2 grams of SBA-15 was put into beakers containing 50 ml $NH_{3(aq)}$ solution with various concentrations, 10%, 15%, 20%, and 25% in volume, respectively. These mixtures were then placed in an autoclave at 160°C for 10 h. After that, they were washed with distilled water and dried at 120°C for 2 h.

Then, NiO supported on SBA-15-NH_3 catalysts were prepared by impregnating $Ni(NO_3)_2$ solution on SBA-15-NH_3 according to the procedure described in reported work [9]. The Ni content in the catalysts was fixed at 31.4 wt.% (or 40 wt.%NiO). The obtained samples were calcined in air at 800°C for 0.5 h and symbolized as follows, Ni/SBA-15-*a* NH_3, where *a* represents concentration of ammonia solution used in preparation of alkalized SBA-15 support. Meanwhile, NiO supporting SBA-15 promoted by MgO catalysts were formed by using coimpregnation of $Ni(NO_3)_{2(aq)}$ and $Mg(NO_3)_{2(aq)}$ solution on support SBA-15. The amount of $Mg(NO_3)_{2(aq)}$ solution used is varied to obtain samples with different Mg contents (3–12 wt.%). After that, the samples were calcined at 800°C for 0.5 h and were denoted as Ni*b* Mg/SBA-15, where *b* performs Mg content. All the samples were then reduced *in situ* in 40 mol% H_2/N_2 gas mixture (3 L/h) at 800°C for 2 h before reaction.

The physicochemical properties of the catalysts were studied by several methods such as XRD (Bruker D2 Phaser powder diffractometer), N_2-BET isothermal adsorption (Nova Station B, Quantachrome NovaWin Instrument), scan electron microscopy (FE–SEM JEOL 7401 instrument), transmission electron microscopy (TEM on the TEM JEM 1400 of JEOL USA instrument), EDS mapping on JEOL JST-IT 200 instrument, hydrogen temperature-programmed reduction (H_2-TPR), and the carbon dioxide temperature-programmed desorption (CO_2-TPD). Both H_2-TPR and CO_2-TPD were carried out on a microreactor with a sample of 50 mg using a Gas Chromatograph GOW-MAC 69-350 with a thermal conductivity detector (TCD). The activity of catalysts for bireforming was tested in a microflow reactor under atmospheric pressure at a temperature of 550–800°C as described in detail in our previous paper [9]. Briefly, a catalyst sample of 0.2 grams, the feed flow rate of 6 L/h, CH_4 concentration in feed of 3 mol.%, and the molar ratio of $CH_4 : CO_2 : H_2O$ in feed of 3 : 1.2 : 2.4 was used in the investigation.

3. Results and Discussion

3.1. Physicochemical Characteristics of Catalysts. The properties of bare SBA-15 support are showed detailed in our previous paper [9]. Briefly, three intensive main diffraction peaks at 2θ of 0.90°, 1.60°, and 1.84°, indexed as the (100), (110), and (200) reflections, respectively, appearing in the low-angle XRD pattern (Figure 1(a)), prove that two-dimensional, ordered hexagonal mesostructure SBA-15 was successfully prepared [24]. The SEM image (Figure 1(b)) showed that SBA-15 was prepared in a porous cocoon diameter of hundred nm. N_2 adsorption-desorption profiles of the synthesized SBA-15 are presented in Figure 1(c). According to the IUPAC classification, the profile of the sample belonged to the IV type isotherm curve with the H1 hysteresis loop in a P/P_0 range of 0.45–0.7, which was a characteristic of mesoporous materials. Hysteresis was observed for reasonably large pores ($d \geq 4$ nm), and these pores showed capillary condensation and evaporation at values for $P/P_0 >$ 0.45 [25]. The H1 type hysteresis of obtained SBA-15 indicated the well-organized materials, associating with the presence of cylindrical pores. Moreover, the small inclination of hysteresis indicated that the obtained pores were uniform. This result was further confirmed by the TEM image of synthesized SBA-15 reported in our previous paper [26]. The diameter of the channels of SBA-15, determined from the N_2 adsorption isotherms (Figure 1(d)) and TEM analysis [26], was approximately 6.08 nm. The specific surface area and pore volume of the synthesized SBA-15, determined from the N_2 adsorption isotherm, were 639.1 $m^2 \cdot g^{-1}$ and 0.65 $cm^3 \cdot g^{-1}$, respectively. Therefore, NiO were easily dispersed into the channel system of SBA-15, as indicated in Figure 2(a').

The reducibility of supports was characterized by the H_2-TPR method. It was found from Figure 1(e) that there were no reduction peaks for SBA-15 and NH_3-treated SBA-15 supports in the temperature range from 100 up to 900°C. The basicity of supports and catalysts was evaluated via CO_2-TPD characterization. It was reported that there were three CO_2-TPD peaks observed in the temperature ranges of 100–200, 300–400, and 600–800°C, attributed to weak, moderate, and strong basic sites, respectively [27]. The two CO_2-TPD peaks of SBA-15 and SBA-15-NH_3 at 100–200°C and 500–700°C were attributed to weak and strong basic sites, respectively. The same result was reported by Zhang et al. [27]. The presence of weak basic sites (100–200°C) and strong basic sites (600–700°C) on SBA-15 was explained as follows. At the heating temperature of 550°C for 2 hours, there still existed H_2O and Cl^- ions in the structure of SBA-15, which were Lewis bases. The CO_2-TPD pattern of the ammonia-treated support, SBA-15-NH_3, was similar, including the characteristic peaks for weak and strong basic sites. Heating ammonia in glass tubes at various temperatures, Perman and Atkinson found that decomposition began under the most favourable circumstances at 500°C [28]. Then, on the alkalized support, there existed NH_3, which almost did not dissociate to N_2 and H_2 at drying temperature 120°C for 2 hours, providing additional Lewis basic sites.

The wide-angle XRD patterns of the obtained catalysts are indicated in Figure 3. The spreading peak located at about 20-25° was accredited to the silica frameworks belonging to SBA-15 support for all catalysts [29]. The XRD patterns of NH_3-modified SBA-15 supported NiO (Figure 3(a)), and MgO-promoted NiO/SBA-15 catalysts (Figure 3(b)) showed that all catalysts exhibited diffraction peaks with high

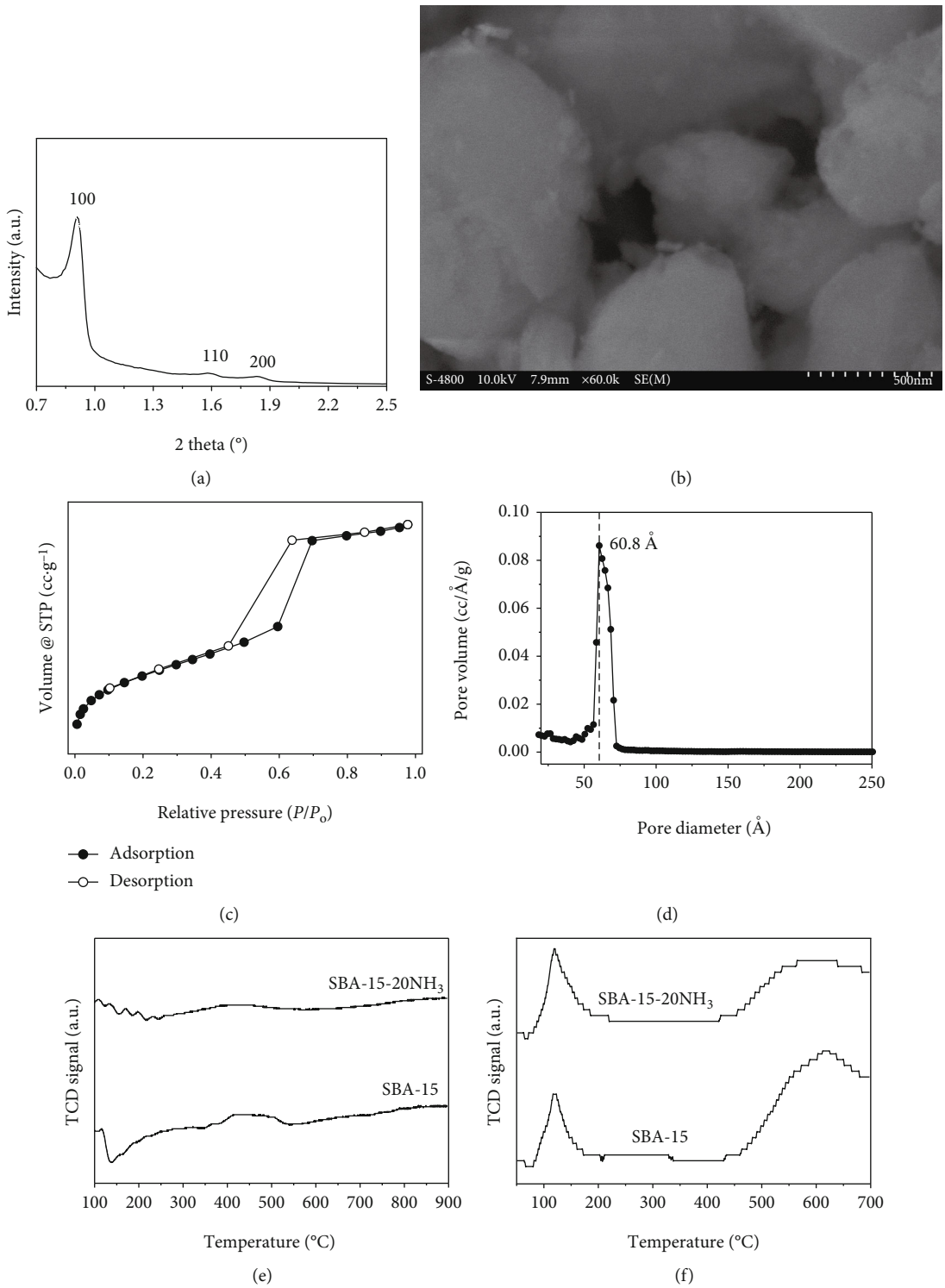

Figure 1: The narrow-angle XRD pattern (a) [9] and physicochemical properties of synthesized SBA-15 support: SEM image (b), N_2 isotherm (c), pore distribution (d), H_2-TPR profiles (e), and CO_2-TPD pattern (f).

intensity at $2\theta = 37.3^\circ$, 43.2°, 62.9°, 76°, and 79.3° corresponding to (101), (200), (220), (311), and (222) plans of a face-center cubic crystalline NiO structure in all catalysts [30]. Moreover, all of the peaks were highly apparent at high intensity. This meant that NiO appeared as a high-crystalline state. Besides, the peaks for the NiO phase in alkalized catalysts were more intense than that of the bare catalyst, Ni/SBA-15. It was proposed that NiO particles were not dispersed homogeneously over the mesopores of SBA-15 for alkalized samples [31]. Based on XRD patterns, the average crystallite

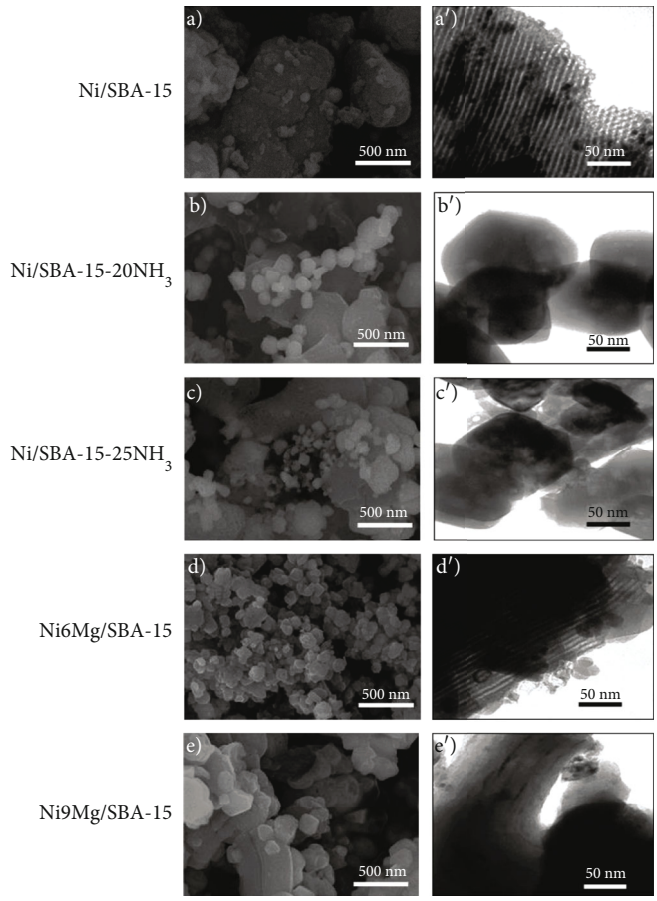

Figure 2: SEM images (a–e) and TEM images (a'–e') of the catalysts.

size of NiO (d_{cry}) could be calculated through the Scherrer equation [32] at $2\theta = 43.2°$, which is shown in Table 1. As seen, the size of NiO crystals increased from 18.4 nm in non-promoted catalyst to 18.5-21 nm in the MgO-promoted ones and to 30–40 nm in ammonia-alkalized samples (Table 1). In particular, no characteristic peaks of MgO crystallites were detected in all samples containing 3–12% Mg. This fact suggested a high dispersion of Mg oxides on mesoporous silica or a formation of Ni-Mg-O solid solution [33].

On the SEM image of the nonmodified sample Ni/SBA-15 catalyst (Figure 2(a)), the SBA-15 cocoon diameter of 200-400 nm and spherical particle size of ten nm sticking on the cocoon surface were found. The highly ordered hexagonal structure of the SBA-15 was clearly observed on the TEM image of this catalyst (Figure 2(a')). In addition, the nanosized NiO particles in the channels of SBA-15 and some large clusters on the outer surfaces were shown in the TEM image of the Ni/SBA-15 sample (Figure 2(a')). This meant that the size of inside NiO particles was around 6 nm and of outside NiO bulk was almost ten nm.

The cocoon shape of SBA-15 was still observed on SEM images of all alkalized samples (Figures 2(b)–2(e)). It could be seen from Figures 2(b) and 2(c) that, for NH_3-alkalized Ni/SBA-15 samples, cocoons had smaller size and are less porous than nonmodified Ni/SBA-15 and some particles had been broken down. The SEM image of the MgO-promoted samples (Figures 2(d) and 2(e)) was characterized by many bright spherical particles with size of 10-50 nm appearing on the surface of SBA-15 cocoons. In addition, the ordered mesostructure was still observed on the TEM images (Figures 2(d') and 2(e')) of these samples. On the TEM image of the MgO-promoted samples, besides the dark particles being similar to those of the Ni/SBA-15 sample (Figure 2(a')), the light-colored particles were also observed. Both types of particles appeared both in the structural channel and on the outer surface of SBA-15 support. This proved the existence of particles with different compositions on the NiMg/SBA-15 catalyst. Specifically, dark-colored particles could be assigned to NiO while light-colored particles were responsible for the MgO or the NiO-MgO mixture. Meanwhile, as depicted in Figures 2(b') and 2(c'), the ordered mesoporous structure was not observed on TEM images of NH_3-alkalized Ni/SBA-15 samples. This was possibly due to the damage of thin pore walls of SBA-15 support in ammonia solution. On the TEM image of the NH_3-modified samples (Figures 2(b') and 2(c')), the light-colored particles, assigned to NiO particles distributed in the porous structure of the material and the dark color thin layer, which might be derived from NH_3, could be seen.

EDS mapping of catalysts (Figure 4) indicated an evenly and highly dispersed form of all species on all catalysts. The elemental composition indicated in the EDS mapping to

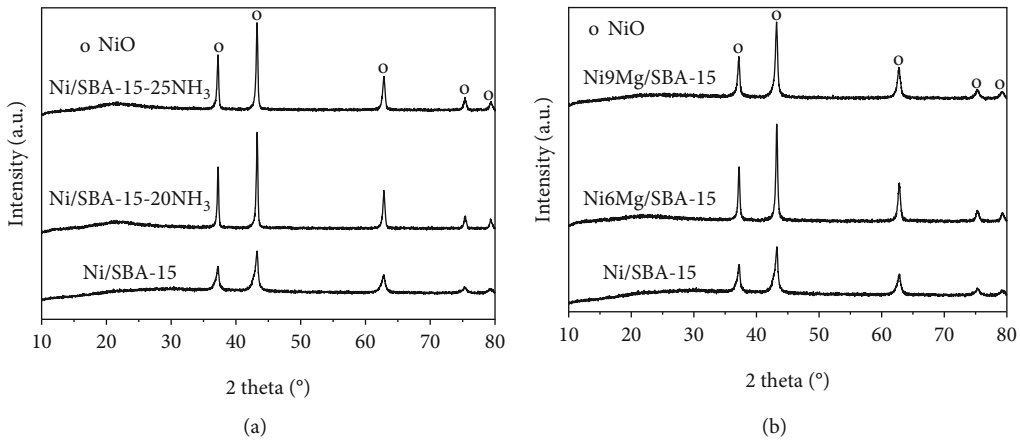

Figure 3: XRD patterns of NiO/SBA-15 catalysts alkalized with $NH_{3(aq)}$ (a) and NiO/SBA-15 catalysts promoted by MgO (b).

Table 1: The structural properties of the catalysts.

Catalysts	S_{BET} [a] (m^2/g)	d_{pore} [a] (nm)	V_{pore} [a] (cm^3/g)	d_{cry} [b] (nm)	T_{max} [c] (°C)	m_{Ni^o} [c] (a.u.)	m_{CO_2} [d] (a.u.)
Ni/SBA-15	232.6	6.08	0.29	18.35	369, 450, and 620	1	1
Ni/SBA-15-15NH_3	—	—	—	—	340	1.8	1.2
Ni/SBA-15-20NH_3	24.89	2.50	0.02	40.8	331	1.8	1
Ni/SBA-15-25NH_3	27.42	2.54	0.02	30.0	330	1.9	1.2
Ni3Mg/SBA-15	—	—	—	—	392, 788	0.89	1
Ni6Mg/SBA-15	36.5	2.14	0.02	21.0	385, 760	0.73	2
Ni9Mg/SBA-15	27.5	1.64	0.01	18.5	360, 440, and 586	1.07	4

[a]BET surface (S_{BET}), average pore diameter (d_{pore}), and total pore volume (V_{pore}) were obtained from N_2 adsorption isotherm analysis. [b]NiO crystal size (d_{cry}) was obtained from XRD patterns at $2\theta = 43.2°$. [c]The maximal reduction temperature (T_{max}) and the number of reduced Ni^o(m_{Ni^o}), based on H_2 consumption, were obtained from H_2-TPR results. [d]The desorbed CO_2 amount (m_{CO_2}) was obtained from the results of CO_2-TPD results of activated samples.

some extent was matched with the loading value, proving that the method of catalysts' preparation was suitable. On the Ni/SBA-15 catalyst, the elemental content of Si (28.4%) was approximate to the loading value (28.0%) while the oxygen content was slightly higher (46.8% vs. 40%) and of Ni was slightly lower (24.8 vs. 31.4%). This might be related to the formation of some large clusters on the outer surfaces of the catalyst, as seen in the TEM image, reducing the Ni content. Meanwhile, the Ni content of the two alkalinized catalysts was higher than the calculated value, demonstrating the positive effect of the alkalization on Ni dispersion. The highest Ni content was achieved on the MgO-modified catalyst (Ni6Mg/SBA-15), reaching 40.6% (compared to 31.4% calculated value). This fact showed that Mg was a highly effective additive for improving Ni dispersion. In this sample, the Mg content was approximate to the expected value (5.3% vs. 6.0%) although MgO was not detected on the XRD pattern (Figure 3(b)). This fact proved that highly dispersed MgO was successfully introduced into SBA-15. Meanwhile, the content of Si and O in this sample was lower than the calculated values, respectively, 20.1 vs. 26.7% and 34.0% vs. 39.3%. This might be related to the highest density of active metal particles on the SBA-15 surface as found on the TEM image of sample Ni6Mg/SBA-15 (Figure 2(d)). On the $NH_{3(aq)}$-treated catalyst (Ni/SBA-15-20NH_3), the elemental composition of the EDS mapping was the most matched with the calculated values. Specifically, the components of Si, O, and Ni are 25.1% vs. 28%, 39.9% vs. 40.6%, and 32.3% vs. 31.4%, respectively. In particular, the content of N in this sample was determined to be 2.7%, proving that N was included in the Ni/SBA-15 catalyst. This was explained as follows. Although NH_3 was almost completely dissociated to N_2 and H_2 at 650°C on supported nickel catalysts [34], a small residual of ammonia was found even at 700°C and 800°C in calcination [35].

The alkalization of Ni/SBA-15 with NH_3 and with MgO promoter led to a sharp decrease in pore diameter, pore volume, and specific surface area. In particular, the specific surface area value dropped from 232.6 m^2/g of Ni/SBA-15 to 25–37 m^2/g, the pore diameter decreased from 6 nm to 2 nm, and the pore volume fell from 0.29 to 0.01–0.02 cm^3/g (Table 1). A sharp decrease in pore diameter and pore volume might be related to coverage of the channel walls of SBA-15 by MgO particles [16] and attachment of NH_3 residual to the structural channel of support as seen on TEM images. Consequently, the specific surface area of the catalysts was drastically reduced. However, the pore diameter of the alkalized catalysts was still being favourable for the diffusion of CH_4 and CO_2 into the pores, as their kinetic diameter was 0.38 and 0.44 nm, respectively. Besides, as seen from SEM images,

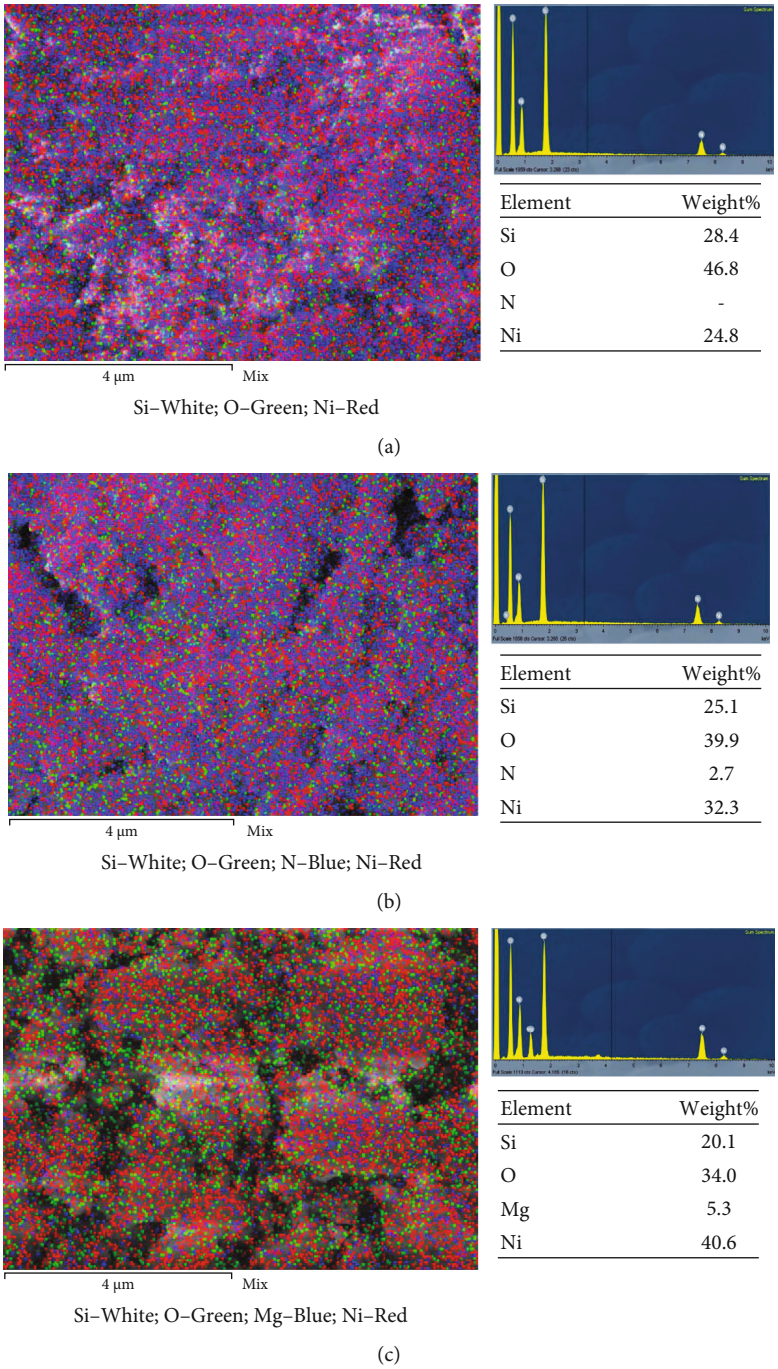

(a)

Element	Weight%
Si	28.4
O	46.8
N	-
Ni	24.8

(b)

Element	Weight%
Si	25.1
O	39.9
N	2.7
Ni	32.3

(c)

Element	Weight%
Si	20.1
O	34.0
Mg	5.3
Ni	40.6

Figure 4: EDS mapping of catalysts: Ni/SBA-15 (a), Ni/SBA-15-20NH_3 (b), and Ni6Mg/SBA-15 (c).

Ni6Mg/SBA-15 showed the smallest size. Consequently, this sample had the highest specific surface area among the alkalized catalysts.

H_2-TPR profiles of the Ni/SBA-15 catalysts modified by $NH_{3(aq)}$ or MgO are depicted in Figure 5. The H_2-TPR pattern of the Ni/SBA-15 catalyst showed three reduction peaks. The former strongest peak is at $T_{max,1} = 372°C$, assigned to the reduction of free, bulky NiO [36, 37]. The second very weak reduction peak is at $T_{max,2} = 450°C$, representing the reduction of the weak interacted NiO-support species, and the third one is at $T_{max,3} = 620°C$, being attributed to the reduction of some forms of Ni^{2+} ions strongly interacting with support [27] and/or reduction of small clusters of Ni^{2+} in pores [38]. Compared to the Ni/SBA-15 catalyst, the NH_3-modified samples presented the shifting of the first reduction peak towards lower temperature, $T_{max,1}$ = 330-355°C, while the other two reduction peaks almost disappeared. This was consistent with the fact that only one type of active phase particle was observed on the TEM image (Figures 2(b') and 2(c')). Besides, the higher the

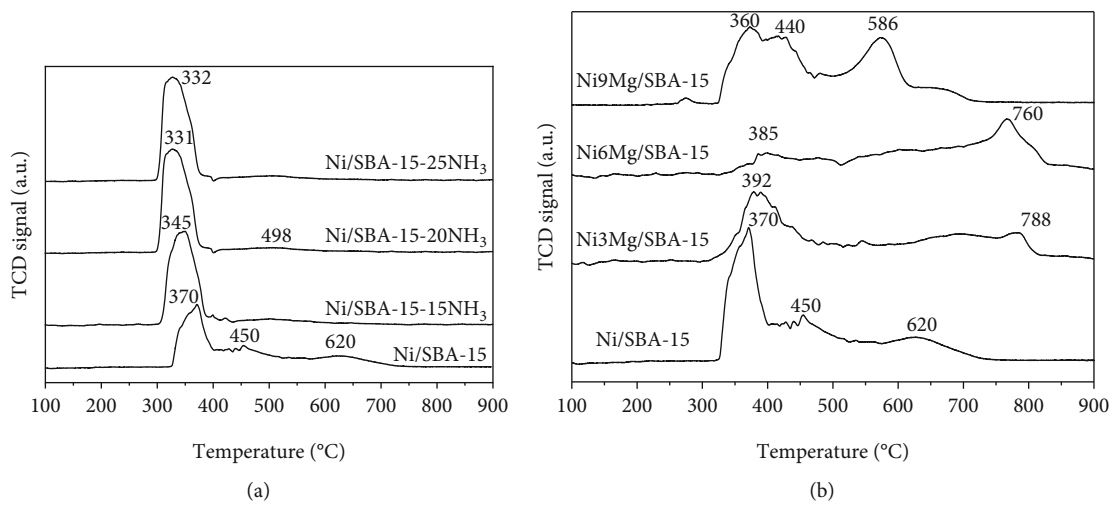

Figure 5: H_2-TPR profiles of NiO/SBA-15 catalysts alkalized with $NH_{3(aq)}$ (a) and NiO/SBA-15 catalysts promoted by MgO (b).

concentration of NH_3 solution, the more shift of reduction peaks towards the lower temperature was observed. Moreover, the area of the lower temperature reduction peak increased about doubles when nonmodified and modified catalysts were compared. That means the alkalization of SBA-15 with $NH_{3(aq)}$ solution led to an enhancement of reducibility of the Ni/SBA-15 catalyst, whereby the catalytic activity should be improved.

The characteristics of the H_2-TPR pattern of NiMg/SBA-15 catalysts (Figure 5(b)) were dependent on the MgO loading content. When the low-Mg content (3–6%) was added, the H_2-TPR profiles of NiMg/SBA-15 catalysts showed two reduction peaks. The shifting of the first reduction peak towards higher temperature ($T_{max,1}$ = 392 and 385°C) compared to the Ni/SBA-15 sample demonstrated an enhancement on the metal-support interactions [39]. The second peak in the H_2-TPR profile, at 760–788°C, was attributed to the reduction of some forms of Ni^{2+} ions deeply located in the MgO lattice which exhibited a strong interaction [27]. The area ratio of the second reduction peak to the first reduction peak rose with the increase of MgO loading content. This indicated that the more MgO added to the catalyst, the more the number of interacted NiO-MgO species formed. Meanwhile, the H_2-TPR pattern of the Ni9Mg/SBA-15 sample consists of three reduction peaks centered at 360, 440, and 586°C. There was no reduction peak above 700°C while a reduction peak at around 600°C appeared on the TPR profile of the Ni9Mg/SBA-15 catalyst. This new reduction peak could be assigned to the strong interaction of NiO with bare MgO [13], which formed when the loading MgO was in excess. The catalysts alkalized with NH_3 solution showed a higher number of reduced Ni^o as compared to the catalysts modified by the MgO additive. This might be related to the fact that the catalysts alkalized with NH_3 solution had a homogeneous dispersion of the elements throughout the catalyst since the elemental composition from EDS data was well matched with the calculated value.

The profiles of CO_2-TPD of modified Ni/SBA-15 catalysts are illustrated in Figure 6. Compared with the support (Figure 1(f)), the intensity of the CO_2 desorption peak (Figure 5), corresponding to strong basic sites, was much lower. This could be explained by the high calcination temperature of the catalyst (800°C) while the heating temperature of the SBA-15 support was 550°C and the drying temperature of the NH_3-treated SBA-15 was 120°C. The intense dehydration and Cl^- ion evaporation at the calcination temperature of 800°C resulted in a decrease in the number of Lewis basic sites in the Ni/SBA-15 and NiMg/SBA-15 catalysts. As previously reported, NH_3 was almost completely dissociated from hydrogen and nitrogen at 700°C [35] or 1100°C [40]. Furthermore, the dissociation of NH_3 to N_2 and H_2 was strongly promoted by the Ni catalyst. For example, on the Ni/TiO_2 catalyst, 30% NH_3 was dissociated at 550°C, and almost 100% NH_3 was decomposed at 650°C [34]. These processes led to lowering the basicity of the NH_3-treated catalyst as compared to the corresponding support.

There were two CO_2 desorption peaks in the temperature range of 100–350°C and 400–700°C in all Ni/SBA-15 catalysts. The first peak could be assigned to weak and moderate basic sites while the second one was addressed to strong basic sites. It could be seen that, unlike the support, the majority of basic sites in these catalysts were weak and moderate. Treating NiO/SBA-15 catalysts with $NH_{3(aq)}$ as well as promoting with MgO favoured the presence of weak and moderate basic sites. It followed from Table 1 that the alkalization led to an increase in basic site density. The basicity of the $NH_{3(aq)}$-treated samples on the one hand does not change much when the concentration of $NH_{3(aq)}$ solution changes on the other hand; it is lower than that of the NiMg/SBA-15 catalyst. This may be related to the fact that most of ammonia was dissociated into hydrogen and nitrogen at calcination temperature, and there remained only a small amount of NH_3 residue in the catalysts, as seen in EDS mapping data.

3.2. Catalytic Performance for Bireforming. Figures 7(a) and 7(b) show the activity of Ni/SBA-15 catalysts treated with different $NH_{3(aq)}$ solutions in CH_4 bireforming. It could be seen that both CH_4 and CO_2 conversion increased when raising

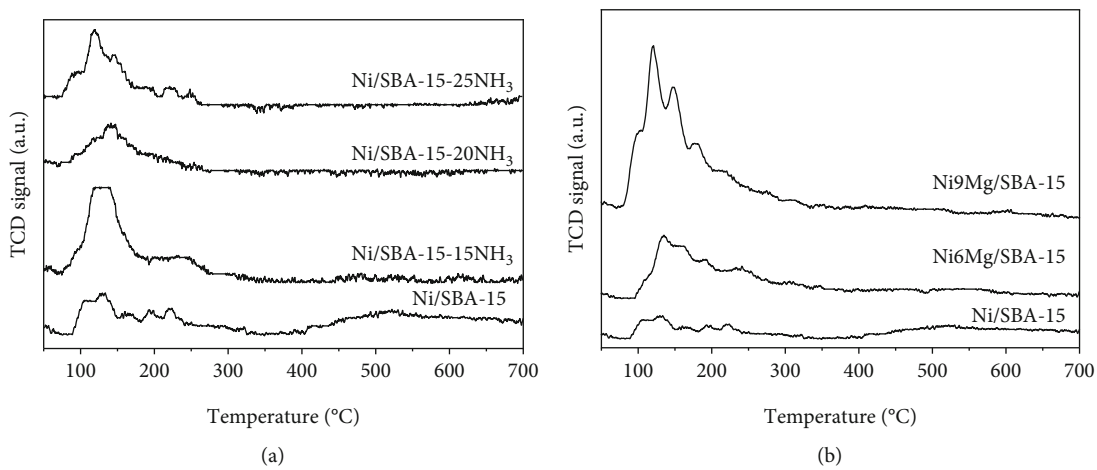

Figure 6: CO_2-TPD pattern of NiO/SBA-15 catalysts alkalized with $NH_{3(aq)}$ (a) and NiO/SBA-15 catalysts promoted by MgO (b).

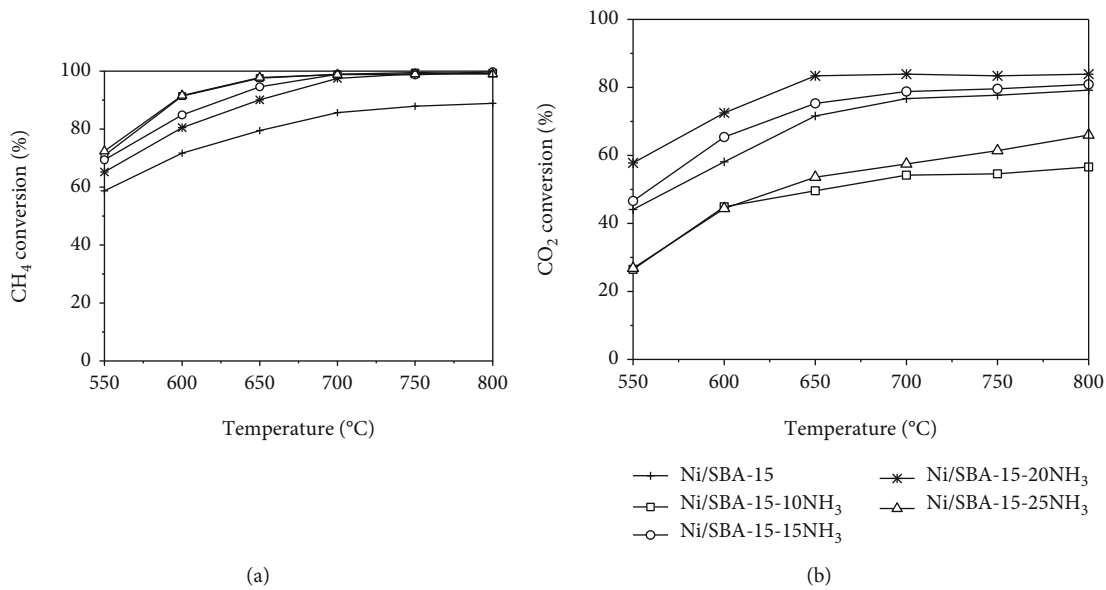

Figure 7: The conversion of CH_4 (a) and CO_2 (b) of NiO/SBA-15 catalysts treated with $NH_{3(aq)}$ at different reaction temperatures.

the reaction temperature. This was evident because bireforming (1) is a strongly endothermic reaction. In general, catalysts showed higher CH_4 conversion than CO_2 conversion. It may be related to the occurrence of the Water Gas Shift (WGS) reaction (4) in methane reforming conditions, producing additional CO_2 [41].

As it was followed from Figures 7 and 8, conversion of CH_4 on modified Ni/SBA-15 catalysts was higher than that on the nonpromoted one over the range of reaction temperature. This might be related to the alkalization of SBA-15 resulting in an increase in NiO dispersion, reducibility, and density of basic sites, as seen in Table 1. Besides, it has been found that the CH_4 conversion of NH_3-modified catalysts was higher than that of the MgO-modified samples. This result could be explained by the higher number of reduced $Ni^0(m_{Ni^0})$ in the NH_3-modified catalysts when two groups of modified catalysts were compared. From the data in Figure 8, it could be seen that by increasing the content of MgO additive from 0 to 9%, the CH_4 conversion increased, reaching the maximum value of 96.4% at the content of 9% Mg. However, when Mg content was continually raised to 12%, the conversion of CH_4 slightly decreased.

The magnitude order of the amount of reduced Ni^0, based on H_2-TPR (Table 1), was in the following order:

$$\begin{aligned} &\text{Ni/SBA-15-25NH}_3 > \text{Ni/SBA-15-20NH}_3 \\ &\quad \approx \text{Ni/SBA-15-15NH}_3 > \text{Ni9Mg/SBA-15} \\ &\quad > \text{Ni/SBA-15} > \text{Ni3Mg/SBA-15} > \text{Ni6Mg/SBA-15} \end{aligned} \tag{6}$$

From order (6), it could be seen that four catalysts with the highest number of reduced Ni^0 (Ni/SBA-15-25 NH_3, Ni/SBA-15-20 NH_3, Ni/SBA-15-15 NH_3, and Ni9Mg/SBA-15) were also the samples with the highest CH_4 conversion

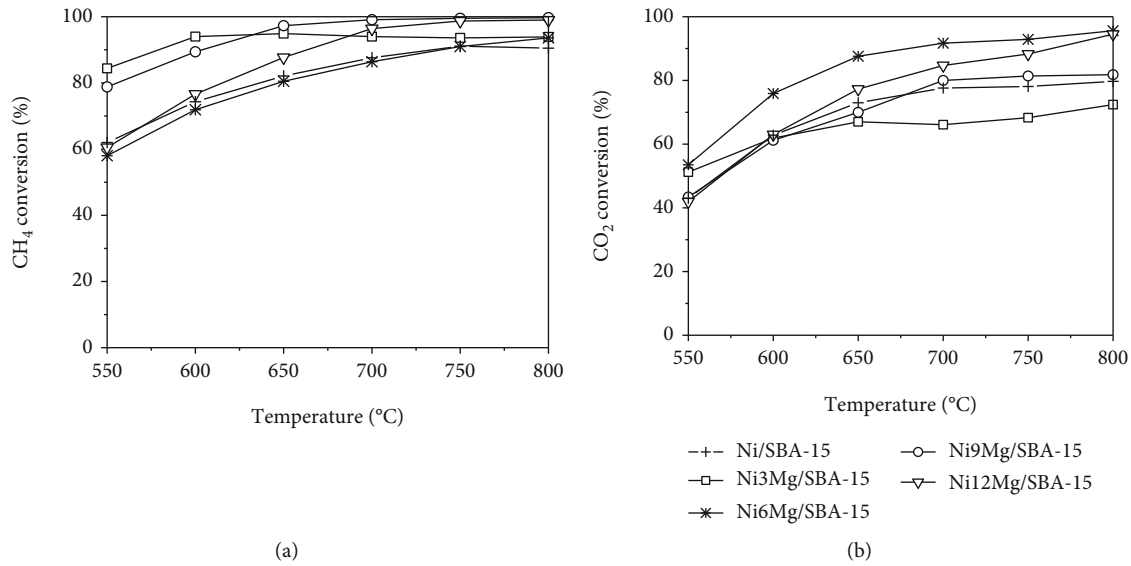

Figure 8: The conversion of CH_4 (a) and CO_2 (b) of NiO/SBA-15 catalysts promoted by MgO at different reaction temperatures.

(Figure 9). The catalysts treated with 15-25% NH_3 had approximately the same and highest value of CH_4 conversion among the catalysts, reaching 98-99% at 700°C because the number of reduced Ni^o of these three catalysts is approximate and the highest. Similarly, in the MgO-promoted catalyst group, the highest CH_4 conversion of the Ni9Mg/SBA-15 sample was due to its highest reducibility. This implied that CH_4 was activated by reduced Ni^o sites, having the higher reducibility catalyst; the higher activity in CH_4 oxidation is reached.

From the obtained results in Table 1, it is possible to order the catalysts based on their basicity as follows:

$$\begin{aligned}&\text{Ni9Mg/SBA-15} > \text{Ni6Mg/SBA-15} > \text{Ni/SBA-15-25 NH}_3\\&\quad > \text{Ni/SBA-15-15 NH}_3 \approx \text{Ni/SBA-15-20 NH}_3\\&\quad \approx \text{Ni3Mg/SBA-15} \approx \text{Ni/SBA-15}\end{aligned} \tag{7}$$

Among the samples, 9% Mg-promoted catalyst showed the highest density of basic sites, and ranked second is the catalyst with 6% Mg, based on the peak area of the TPD pattern. These samples are also the two catalysts with the highest activity in CO_2 conversion. The enhanced basicity was advantageous as CO_2 adsorption affinity could be improved, which in turn affected the CO_2 conversion and stability [42]. However, the dependence of CO_2 conversion on alkalized catalysts with different $NH_{3(aq)}$ solutions was complex (Figure 7(b)). Specifically, CO_2 conversion on the two catalysts alkalized with 15% and 20% $NH_{3(aq)}$ solution was higher than that on the nonalkalized one. In contrast, the catalysts were alkalized with the most dilute (10%) or most concentrated (25%) $NH_{3(aq)}$ solution, exhibiting a lower CO_2 conversion compared to the nonalkalized one. In addition, it should be noted that the catalysts alkalized with 10% and 25% $NH_{3(aq)}$ solution possessed the highest CH_4 conversion and the lowest CO_2 conversion (Figure 7). However, at 700°C and higher, CH_4 conversion was almost the same on the three NH_3-promoted catalysts, reaching over 98%.

It could be observed from Figure 9 that, in most cases, the H_2/CO molar ratio of the product mixture was higher than the theoretical value (which was 2) because of the WGS reaction (4), consuming CO and generating an additional amount of H_2. It was worth noting that when the $NH_{3(aq)}$ concentration or the MgO loading content increased, the H_2/CO ratio decreased and might become less than 2. In addition to the main reaction (1), several side reactions might be involved in the process. The contribution of side reactions in the composition of reaction products was dependent on feed composition and conversion [43] as well as the using catalyst. Some side reactions such as Reverse Water Gas Shift (RWGS) and methane dry reforming (2) reduced the H_2/CO ratio. Alkalization of Ni/SBA-15 catalyst could be able to increase the CO_2 adsorption that would lead to an enhancement of these reactions.

In particular, the Ni/SBA-15-25NH_3 sample has a very low CO_2 conversion although it also has high basicity. The highest CH_4 conversion and the lowest CO_2 conversion obtained on this sample might be related to its highest reducibility, promoting the CH_4 reforming by steam according to Equation (6), with the result of CO_2 additional generation:

$$CH_4 + 2H_2O \rightleftharpoons CO_2 + 4H_2, \quad \Delta H_{298} = +690\,\text{kJ/mol} \tag{8}$$

Further, although possessing higher basicity than Ni6Mg/SBA-15, the Ni9Mg/SBA-15 sample exhibits a slightly lower CO_2 conversion. Additionally, two samples with the highest basicity of the two alkalized catalyst groups (Ni/SBA-15-25NH_3 and Ni9Mg/SBA-15) also expressed the lowest value of mol ratio H_2/CO among the studied catalysts. This is explained as follows. When the samples are treated with a too high loading alkalizing agent, they possess high base properties that enhanced CO_2 adsorption, promoting dry reforming (2), generating more CO. CO in turn activates

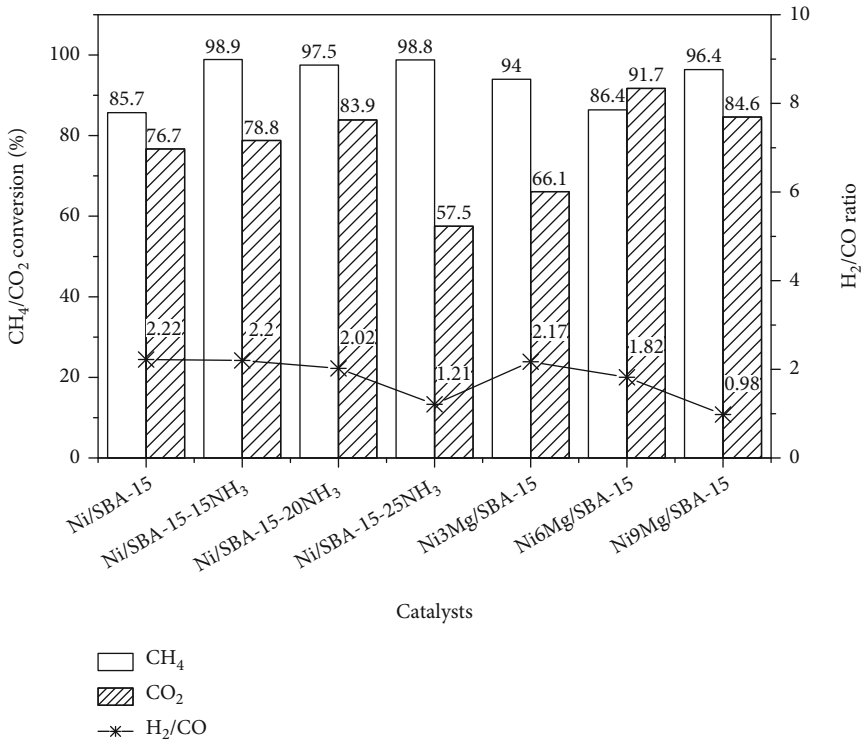

Figure 9: The conversion of CH_4 and CO_2 and the mole ratio H_2/CO at reaction temperatures of 700°C over the catalysts.

the WGS reaction (4), which in result reduces the H_2/CO ratio on the one hand and on the other hand reduces CO_2 conversion. The value of the H_2/CO ratio and the CO_2 conversion depends on the catalyst properties. On the Ni/SBA-15-25NH_3 sample, the WGS reaction (4) was stronger, so the CO_2 conversion was lower, and the $H_2 : CO$ ratio > 1. Conversely, on the Ni9Mg/SBA-15 catalyst, the dry reforming (2) is relatively stronger than WGS reaction (4), so the CO_2 conversion remains quite high, while the ratio H_2/CO~1. In general, excessive alkalization can also lead to disadvantages for the catalysts. Besides, the previous report [44] indicated that excessive basicity of the catalyst itself is detrimental to catalytic activity as it will stimulate a higher extent of the CO_2 dissociation ($CO_2 \rightarrow C + O_2$) and thereupon deactivate the catalyst.

Hence, in order to obtain the highest yield of synthetic gas, it was necessary to select a catalyst with optimal adsorption capacity for these two reactants. Comparison of the two highly active catalysts, Ni/SBA-15-20NH_3 and Ni9Mg/SBA-15, showed that they had an equally high activity with a CH_4 conversion of nearly 97% and a CO_2 conversion of almost 84% at 700°C. However, the H_2/CO ratio obtained remained at 2.02 on the Ni/SBA-15-20NH_3 catalyst and almost 1 on the Ni9Mg/SBA-15 sample. These facts proved that the alkalization of the Ni/SBA-15 catalyst by $NH_{3(aq)}$ solution had an advantage over using MgO because side reactions were unlikely to occur.

As shown in Table 2, there are three main groups of Ni-based catalysts for the BRM reaction based on three supports including Al_2O_3 [14, 49–52, 56], CeO_2 [45, 50, 51], and SBA-15 [9, 42, 52]. In general, the highest value of CH_4 conversion reached on all three groups is

Table 2: Comparison of the CH_4 and CO_2 conversion in CSCRM: reaction temperature (T), CH_4 conversion (X_{CH_4}), and CO_2 conversion (X_{CO_2}).

Catalysts	T (°C)	X_{CH_4} (%)	X_{CO_2} (%)	Refs.
5Ni/Al_2O_3	900	58	—	[45]
5Ni/CeO_2		73	—	
6.67Ni/α-Al_2O_3	700	92	64	[46]
6.67Ni/(MgO-Al_2O_3) (1 : 2)	800	100	67	[47]
6.67Ni/(BaO-Al_2O_3) (1 : 2)		100	78	
6.67Ni/(CaO-Al_2O_3) (1 : 2)		100	58	
Ni/MgO–Al_2O_3	800	93	—	[13]
	700	83	71	
15Ni/$MgAl_2O_4$	850	74	35	[48]
15Ni/CeO_2–ZrO_2/$MgAl_2O_4$		80	41	
15Ni–CeO_2–ZrO_2/$MgAl_2O_4$		81	44	
Ni–Ce/θ-Al_2O_3	850	80	47	[49]
Ni/$MgAl_2O_4$ (MgO/Al_2O_3 = 3/7)		85	47	
Ni–Ce/$MgAl_2O_4$(3)		86	58	
7.87Ni/CeO_2-NR	700	89	67	[50]
	800	96	72	
7.87Ni0.3V/CeO_2-NR	700	96	75	[51]
31.4Ni/SBA-15	700	86	77	[9]
	800	90.5	80	
10Ni/SBA-15	850	98	85	[42]
10Ni3MgO/SBA-15		92	85	
10Ni/Ce-SBA-15	800	78	60	[52]
31.4Ni/SBA-15-20NH_3	700	97	84	This work
31.4Ni9Mg/SBA-15		96	85	

approximately the same, ranging from 86 to 92% at 700°C. Meanwhile, the CO_2 conversion under the same reaction conditions is lower (64-77%). In particular, two groups of Ni catalysts supported on Al_2O_3 and CeO_2 show low CO_2 conversion and do not exceed 67% at 700°C [46, 50], while this value reached 77% on the Ni/SBA-15 catalyst [9]. Furthermore, the promotion of the Ni/Al_2O_3 catalyst by alkali metal additives [13, 47–49] or CeO_2 [48, 49] or Zr [48] did not significantly improve the activity, and the CO_2 conversion did not exceed 78% at 700°C [47]. Meanwhile, for the Ni/CeO_2 catalyst, vanadium additive shows its promoting role, since the conversion of CH_4 and CO_2 at 700°C was raised from 89% to 96% and from 67% to 75%, respectively [51], as 0.3%V was added to the Ni/CeO_2 catalyst. The special feature of the Ni/SBA-15 [9] compared with Ni/Al_2O_3 [46] and Ni/CeO_2 [50] catalysts is that it has high conversion of both CH_4 and CO_2. These values reach 86% and 77% at 700°C, respectively [9]. In comparison with other Ni-based catalysts, Ni/SBA-15-20NH_3 and Ni9Mg/SBA-15 catalysts in this study showed outstanding activity in bireforming of CH_4. Typically, CH_4 conversion on these two samples was almost 97% at 700°C, and CO_2 conversion was nearly 84%, much higher than this value on others.

4. Conclusion

On the one hand, the alkalization of Ni/SBA-15 by NH_3 solution and with MgO promoter led to a sharp decrease in pore diameter, pore volume, and specific surface area, but on the other hand, this modification significantly enhanced the dispersion of NiO particles, reducibility, and basicity of catalysts. As a result, performance of alkalized Ni/SBA-15 catalysts in methane reforming was improved. MgO acted as a highly effective additive for improving the Ni dispersion and enhancing the metal-support parent and the basicity, but it had slight effect on reducibility. Therefore, the Ni/SBA-15 catalyst promoted by MgO exhibited high activity in CO_2 conversion. Meanwhile, the NH_3 treatment led to a homogeneous dispersion of the elements throughout the catalyst. So, the catalyst reducibility as well as CH_4 conversion was improved strongly. However, the excessive alkalization of the catalyst was not favourable in BRM due to strong adsorption of CO_2 and stimulation of side reactions that reduced the H_2/CO ratio. The results revealed that the Ni/SBA-15 treated with 15-25% $NH_{3(aq)}$ solution and promoted with 3-9% Mg exhibited high activity for CH_4 conversion while Ni6Mg/SBA-15 showed the highest CO_2 conversion. Among tested catalysts, Ni/SBA-15-20NH_3 and Ni9Mg/SBA-15 samples showed better catalytic activity. At 700°C, conversion of CH_4 and CO_2 reached 97% and 84%, respectively, on these catalysts, which were higher than the values on the others. However, the Ni/SBA-15-20NH_3 sample showed an advantage in limiting side reactions since the H_2/CO ratio was obtained at a theoretical value.

Data Availability

The data used to support the findings of this study are included within the article.

Conflicts of Interest

The authors declare that there are no conflicts of interest regarding the publication of this paper.

Acknowledgments

This research is funded by Viet Nam National University Ho Chi Minh City (VNU-HCM) under grant number C-2019-20-21.

References

[1] C. Song, "Global challenges and strategies for control, conversion and utilization of CO_2 for sustainable development involving energy, catalysis, adsorption and chemical processing," *Catalysis Today*, vol. 115, no. 1-4, pp. 2–32, 2006.

[2] V. R. Choudhary and A. M. Rajput, "Simultaneous carbon dioxide and steam reforming of methane to syngas over NiO-CaO catalyst," *Industrial & Engineering Chemistry Research*, vol. 35, no. 11, pp. 3934–3939, 1996.

[3] V. Subramani, P. Sharma, L. Zhang, and K. Liu, "Catalytic steam reforming technology for the production of hydrogen and syngas," in *Hydrogen and Syngas Production and Purification Technologies*, K. Liu, C. Song, and V. Subramani, Eds., pp. 14–126, Wiley, 2009.

[4] D. Wang, L. Jin, B. Wei, J. Lv, Y. Li, and H. Hu, "Oxidative catalytic cracking and reforming of coal pyrolysis volatiles over NiO," *Energy & Fuels*, vol. 34, no. 6, pp. 6928–6937, 2020.

[5] C.-C. Hu and H. Teng, "Structural features of p-type semiconducting NiO as a co-catalyst for photocatalytic water splitting," *Journal of Catalysis*, vol. 272, no. 1, pp. 1–8, 2010.

[6] X. Li, Y. Wang, J. Wang et al., "Sequential electrodeposition of bifunctional catalytically active structures in MoO_3/Ni–NiO composite electrocatalysts for selective hydrogen and oxygen evolution," *Advanced Materials*, vol. 32, no. 39, p. 2003414, 2020.

[7] H.-S. Roh, K.-W. Jun, S.-C. Baek, and S.-E. Park, "A highly active and stable catalyst for carbon dioxide reforming of methane: Ni/Ce–ZrO_2/θ-Al_2O_3," *Catalysis Letters*, vol. 81, no. 3/4, pp. 147–151, 2002.

[8] G. Zhang, L. Hao, Y. Jia, and Y. Zhang, "CO_2 reforming of CH_4 over efficient bimetallic Co-Zr/AC catalyst for H_2 production," *International Journal of Hydrogen Energy*, vol. 40, no. 37, pp. 12868–12879, 2015.

[9] P. H. Phuong, L. C. Loc, H. T. Cuong, and N. Tri, "Effect of NiO loading and thermal treatment duration on performance of Ni/SBA-15 catalyst in combined steam and CO_2 reforming of CH_4," *Materials Transactions*, vol. 59, no. 12, pp. 1898–1902, 2018.

[10] M. Zhang, S. Ji, L. Hu, F. Yin, C. Li, and H. Liu, "Structural characterization of highly stable Ni/SBA-15 catalyst and its catalytic performance for methane reforming with CO_2," *Chinese Journal of Catalysis*, vol. 27, no. 9, pp. 777–781, 2006.

[11] M. A. Soria, C. Mateos-Pedrero, A. Guerrero-Ruiz, and I. Rodríguez-Ramos, "Thermodynamic and experimental study of combined dry and steam reforming of methane on Ru/ ZrO_2-La_2O_3 catalyst at low temperature," *International Journal of Hydrogen Energy*, vol. 36, no. 23, pp. 15212–15220, 2011.

[12] H.-S. Roh and K.-W. Jun, "Carbon dioxide reforming of methane over Ni catalysts supported on Al_2O_3 modified with La_2O_3, MgO, and CaO," *Catalysis Surveys from Asia*, vol. 12, no. 4, pp. 239–252, 2008.

[13] H.-S. Roh, K. Y. Koo, J. H. Jeong et al., "Combined reforming of methane over supported Ni catalysts," *Catalysis Letters*, vol. 117, no. 1-2, pp. 85–90, 2007.

[14] J. Juan-Juan, M. C. Román-Martínez, and M. J. Illán-Gómez, "Effect of potassium content in the activity of K-promoted Ni/Al_2O_3 catalysts for the dry reforming of methane," *Applied Catalysis A: General*, vol. 301, no. 1, pp. 9–15, 2006.

[15] M. M. Danilova, Z. A. Fedorova, V. A. Kuzmin, V. I. Zaikovskii, A. V. Porsin, and T. A. Krieger, "Combined steam and carbon dioxide reforming of methane over porous nickel based catalysts," *Catalysis Science & Technology*, vol. 5, no. 5, pp. 2761–2768, 2015.

[16] N. Wang, X. Yu, K. Shen, W. Chu, and W. Qian, "Synthesis, characterization and catalytic performance of MgO-coated Ni/SBA-15 catalysts for methane dry reforming to syngas and hydrogen," *International Journal of Hydrogen Energy*, vol. 38, no. 23, pp. 9718–9731, 2013.

[17] Z. Alipour, M. Rezaei, and F. Meshkani, "Effect of alkaline earth promoters (MgO, CaO, and BaO) on the activity and coke formation of Ni catalysts supported on nanocrystalline Al_2O_3 in dry reforming of methane," *Journal of Industrial and Engineering Chemistry*, vol. 20, no. 5, pp. 2858–2863, 2014.

[18] E. Ruckenstein and Y. H. Hu, "Methane partial oxidation over NiO/MgO solid solution catalysts," *Applied Catalysis A: General*, vol. 183, no. 1, pp. 85–92, 1999.

[19] Y.-H. Wang, H.-M. Liu, and B.-Q. Xu, "Durable Ni/MgO catalysts for CO_2 reforming of methane: activity and metal-support interaction," *Journal of Molecular Catalysis A: Chemical*, vol. 299, no. 1-2, pp. 44–52, 2009.

[20] S. J. H. Rad, M. Haghighi, A. A. Eslami, F. Rahmani, and N. Rahemi, "Sol-gel vs. impregnation preparation of MgO and CeO_2 doped Ni/Al_2O_3 nanocatalysts used in dry reforming of methane: Effect of process conditions, synthesis method and support composition," *International Journal of Hydrogen Energy*, vol. 41, no. 11, pp. 5335–5350, 2016.

[21] K. Selvarajah, N. H. H. Phuc, B. Abdullah, F. Alenazey, and D.-V. N. Vo, "Syngas production from methane dry reforming over Ni/Al_2O_3 catalyst," *Research on Chemical Intermediates*, vol. 42, no. 1, pp. 269–288, 2016.

[22] L. You, F. Yuan, and F. Ma, "Synthesis of mesoporous NH2-SBA-15 by a simple and efficient strategy," *Russian Journal of Physical Chemistry A*, vol. 89, no. 12, pp. 2298–2303, 2015.

[23] Z. Hao, Q. Zhu, Z. Jiang, and H. Li, "Fluidization characteristics of aerogel Co/Al_2O_3 catalyst in a magnetic fluidized bed and its application to CH_4-CO_2 reforming," *Powder Technology*, vol. 183, no. 1, pp. 46–52, 2008.

[24] S. N. Bukhari, C. Y. Chin, H. D. Setiabudi, and D.-V. N. Vo, "Tailoring the properties and catalytic activities of Ni/SBA-15 via different TEOS/P123 mass ratios for CO_2 reforming of CH_4," *Journal of Environmental Chemical Engineering*, vol. 5, no. 4, pp. 3122–3128, 2017.

[25] M. S. M. d. Oliveira, L. Bieseki, A. E. V. d. Alencar, T. P. Braga, and S. B. C. Pergher, "Incorporating aluminum into the structure of SBA-15 by adjusting the pH and adding NaF," *Materials Research*, vol. 22, no. 3, 2019.

[26] B. M. Q. Phan, Q. L. M. Ha, N. P. Le et al., "Influences of various supports, γ-Al_2O_3, CeO_2, and SBA-15 on HDO performance of NiMo catalyst," *Catalysis Letters*, vol. 145, no. 2, pp. 662–667, 2015.

[27] H. Zhang, M. Li, P. Xiao, D. Liu, and C. J. Zou, "Structure and catalytic performance of Mg-SBA-15-supported nickel catalysts for CO_2 Reforming of methane to syngas," *Chemical Engineering & Technology*, vol. 36, no. 10, pp. 1701–1707, 2013.

[28] E. P. Perman, G. A. S. Atkinson, and W. Ramsay, "The decomposition of ammonia by heat," *Proceedings of the Royal Society of London*, vol. 74, no. 497-506, pp. 110–117, 1905.

[29] H. Li, J. Ren, X. Qin, Z. Qin, J. Lin, and Z. Li, "Ni/SBA-15 catalysts for CO methanation: effects of V, Ce, and Zr promoters," *RSC Advances*, vol. 5, no. 117, pp. 96504–96517, 2015.

[30] H. Setiabudi, N. Razak, F. Suhaimi, and F. Pauzi, "CO_2 reforming of CH_4 over Ni/SBA-15: influence of Ni-loading methods," *Malaysian Journal of Catalysis*, vol. 1, 2016.

[31] C. C. Chong, L. P. Teh, and H. D. Setiabudi, "Syngas production via CO2 reforming of CH4 over Ni-based SBA-15: promotional effect of promoters (Ce, Mg, and Zr)," *Materials Today Energy*, vol. 12, pp. 408–417, 2019.

[32] A. L. Patterson, "The Scherrer formula for X-ray particle size determination," *Physical review*, vol. 56, no. 10, pp. 978–982, 1939.

[33] A. J. Vizcaíno, A. Carrero, and J. A. Calles, "Ethanol steam reforming on Mg- and Ca-modified Cu-Ni/SBA-15 catalysts," *Catalysis Today*, vol. 146, no. 1-2, pp. 63–70, 2009.

[34] K. Okura, K. Miyazaki, H. Muroyama, T. Matsui, and K. Eguchi, "Ammonia decomposition over Ni catalysts supported on perovskite-type oxides for the on-site generation of hydrogen," *RSC Advances*, vol. 8, no. 56, pp. 32102–32110, 2018.

[35] T. Saika, M. Nakamura, T. Nohara, and S. Ishimatsu, "Study of hydrogen supply system with ammonia fuel," *JSME International Journal Series B Fluids and Thermal Engineering*, vol. 49, no. 1, pp. 78–83, 2006.

[36] D. Xu, W. Li, Q. Ge, and H. Xu, "A novel process for converting coalmine-drained methane gas to syngas over nickel-magnesia solid solution catalysts," *Fuel Processing Technology*, vol. 86, no. 9, pp. 995–1006, 2005.

[37] T. Yoshida, T. Tanaka, H. Yoshida, T. Funabiki, and S. Yoshida, "Study on the dispersion of nickel ions in the NiO– MgO system by X-ray absorption fine structure," *The Journal of Physical Chemistry*, vol. 100, no. 6, pp. 2302–2309, 1996.

[38] D. Li, L. Zeng, X. Li et al., "Ceria-promoted Ni/SBA-15 catalysts for ethanol steam reforming with enhanced activity and resistance to deactivation," *Applied Catalysis B: Environmental*, vol. 176-177, pp. 532–541, 2015.

[39] Z. Bian, Z. Li, J. Ashok, and S. Kawi, "A highly active and stable Ni–Mg phyllosilicate nanotubular catalyst for ultrahigh temperature water-gas shift reaction," *Chemical Communications*, vol. 51, no. 91, pp. 16324–16326, 2015.

[40] A. H. White and W. Melville, "The decomposition of ammonia at high temperatures," *Journal of the American Chemical Society*, vol. 27, no. 4, pp. 373–386, 1905.

[41] S. Wang, G. Q. M. Lu, and G. J. Millar, "Carbon dioxide reforming of methane to produce synthesis gas over metal-supported catalysts: state of the art," *Energy & Fuels*, vol. 10, no. 4, pp. 896–904, 1996.

[42] B. Huang, X. Li, S. Ji, B. Lang, F. Habimana, and C. Li, "Effect of MgO promoter on Ni-based SBA-15 catalysts for combined

steam and carbon dioxide reforming of methane," *Journal of Natural Gas Chemistry*, vol. 17, no. 3, pp. 225–231, 2008.

[43] M. M. B. Quiroga and A. E. C. Luna, "Kinetic analysis of rate data for dry reforming of methane," *Industrial & Engineering Chemistry Research*, vol. 46, no. 16, pp. 5265–5270, 2007.

[44] S. Das, M. Sengupta, J. Patel, and A. Bordoloi, "A study of the synergy between support surface properties and catalyst deactivation for CO_2 reforming over supported Ni nanoparticles," *Applied Catalysis A: General*, vol. 545, pp. 113–126, 2017.

[45] N. Laosiripojana, D. Chadwick, and S. Assabumrungrat, "Effect of high surface area CeO2 and Ce- ZrO2 supports over Ni catalyst on CH4 reforming with H2O in the presence of O2, H2, and CO2," *Chemical Engineering Journal*, vol. 138, no. 1-3, pp. 264–273, 2008.

[46] P. H. Phuong, L. C. Loc, D. N. Tin et al., "Combined steam and CO_2 reforming of CH_4 over NiO/αAl2O_3 catalysts promoted with MgO and V_2O_5," *Vietnam Journal of Chemistry*, vol. 55, no. 5e34, pp. 181–185, 2017.

[47] P. H. Phuong, L. C. Loc, P. T. Sang, and N. Tri, "Combined steam and CO_2 reforming of CH_4 over nickel catalysts based on Al_2O_3–MO (M= Mg, Ca, Ba)," *Vietnam Journal of Science and Technology*, vol. 55, 2018.

[48] J. W. Bae, A. R. Kim, S.-C. Baek, and K.-W. Jun, "The role of CeO_2–ZrO_2 distribution on the Ni/$MgAl_2O_4$ catalyst during the combined steam and CO_2 reforming of methane," *Reaction Kinetics, Mechanisms and Catalysis*, vol. 104, no. 2, pp. 377–388, 2011.

[49] S.-C. Baek, J.-W. Bae, J. Y. Cheon, K.-W. Jun, and K.-Y. Lee, "Combined steam and carbon dioxide reforming of methane on Ni/$MgAl_2O_4$: effect of CeO_2 promoter to catalytic performance," *Catalysis Letters*, vol. 141, no. 2, pp. 224–234, 2011.

[50] L. C. Loc, P. H. Phuong, D. Putthea, N. Tri, N. T. T. Van, and H. T. Cuong, "Effect of CeO_2 morphology on performance of NiO/CeO_2 catalyst in combined steam and CO_2 reforming of CH_4," *International Journal of Nanotechnology*, vol. 15, no. 11/12, pp. 968–982, 2018.

[51] P. H. Phuong, L. C. Loc, N. Tri et al., "Effect of V_2O_5 promoter on characteristics and performance of NiO/CeO_2 catalyst in methane bi-reforming," *Advances in Natural Sciences: Nanoscience and Nanotechnology*, vol. 11, no. 4, 2020.

[52] J. S. Tan, H. T. Danh, S. Singh, Q. D. Truong, H. D. Setiabudi, and D.-V. N. Vo, "Syngas production from CO2reforming and CO_2-steam reforming of methane over Ni/Ce-SBA-15 catalyst," *IOP Conference Series: Materials Science and Engineering*, vol. 206, 2017.

Hindawi
Journal of Nanomaterials
Volume 2021, Article ID 5565169, 7 pages
https://doi.org/10.1155/2021/5565169

Research Article

The Resistive Switching Behavior of Al/Chitosan-Graphene Oxide/FTO Structure

Hau Huu Do Ho,[1,2] Trung Minh Le,[1,2] and Ngoc Kim Pham [1,2]

[1]*Faculty of Materials Science and Technology, University of Science, Ho Chi Minh City, Vietnam*
[2]*Vietnam National University, Ho Chi Minh City, Vietnam*

Correspondence should be addressed to Ngoc Kim Pham; phamkngoc@hcmus.edu.vn

Received 19 February 2021; Revised 12 March 2021; Accepted 18 March 2021; Published 7 April 2021

Academic Editor: Nguyen Duc Cuong

Resistive random access memory (RRAM) is emerging as a new class of nonvolatile memory that offers promising electronic properties and simple metal-insulator-metal (MIM) structures for sandwich layers, such as organics, inorganics, and hybrid materials. Hybrid structures have attracted much interest recently because of their advantageous properties. The combination of chitosan (CS) and graphene oxide (GO) acts as switching layers in the Al/CS-GO/FTO RRAM structure it is studied with bipolar switching behavior at approximately 10^2 ON/OFF ratios during 100 cycles. This hybrid interaction is identified by shifts in the D, G, and 2D bands using Raman spectroscopy. The conduction mechanism is proposed to be a space-charge-limited conduction (SCLC) mechanism and trap-assisted tunneling conduction mechanism in the ON and OFF states, respectively. The trapped and detrapped electrons move through the trap sites with external electric fields, and this movement is responsible for the switching mechanism of the CS-GO nanocomposite memory device.

1. Introduction

There has been a recent rapid increase in the field of nanotechnology, particularly in memory storage devices [1]. Increased demands for information-storage have required the development of new technologies to meet these demands. Resistive random access memory (RRAM) is one candidate for next-generation information storage due to its high speed, long retention time with low power consumption, and simple structure [2, 3]. Different materials such as organics, inorganics, transition metal dichalcogenides, metal-organic frameworks, and hybrid materials [4–12] have been utilized in RRAM devices to demonstrate their potential applications in data storage.

Environmentally friendly materials such as chitin/chitosan, cellulose, alginate, and carbohydrate polymers [13] have recently received much attention due to their biodegradability, antibacterial properties, protein affinity, and biocompatibility [1, 14]. Chitosan is a component of the protective shell of marine crustaceans, such as crabs, shrimps, and crayfish. Chitosan is composed of bonded $\beta(1\longrightarrow4)$-2-amino-2-deoxy-D-glucopyranoses and $\beta(1\longrightarrow4)$-2-acetamido-2-deoxy-D-glucopyranoses [1]. It is chemically flexible because there are three types of functional groups in the polymers, which are amines, acetamides, and both primary and secondary hydroxyl groups. With these advantages, the use of chitosan is increasing [1]. Currently, chitosan is sold as a white powder that can be dissolved in dilute organic acids, such as acetic, lactic, hydrochloric, formic, or succinic acid [15]. However, it is a poor conductor so it is necessary to add a conductive filler in data storage applications [16].

Two-dimensional graphene oxide (GO) nanosheets have recently been synthesized from graphite. It has an advantageous chemical structure that leads to improved mechanical properties, biological compatibility, water superiority, low cost, lightweight, and excellent durability [17, 18]. Therefore, GO has been focused on changing the thickness and control the number of functional groups with organic compounds. This opens it as a promising biomaterial that is available in nature.

We studied resistive memory devices in capacitor-like Ag/CS-GO/FTO structures in a previous report where the CS-GO nanocomposites acted as the memory layer [19]. The devices showed a bipolar resistive-switching effect under

an external electric field with an endurance of 10^3 and an ON/OFF ratio of 10^2. We have changed the top electrode from Ag to Al to demonstrate the stability of the resistive switching behavior of the CS-GO nanocomposites. The Al/CS-GO/FTO structure was fabricated using a CS-GO nanoblend to act as a switching layer to improve the stability and conductivity. The GO was used to enhance the resistive switching behavior and CS to make it more environmentally friendly. The electrical conductivity and resistive switching mechanisms of Al/CS-GO/FTO were also analyzed. This study is aimed at improving our understanding of resistive switching in CS-GO for RRAM applications.

2. Experimental Procedure

2.1. Materials. The 4-10% edge-oxidized GO powders were supplied by Sigma Aldrich (average of 15-20 sheets). The CS powders (MW = 100,000-300,000, degree of deacetylation of 76%) and acetic acid (99.5% purity) were purchased from Acros and used to synthesize the CS-GO nanocomposite. The commercial FTO-coated glass (MTI, USA) with a resistance of 12 Ω was used for device fabrication.

2.2. Fabrication of Devices. A 0.5 mg/mL (~0.05% wt/*v*) GO solution was prepared in deionized water and stirred for six hours. The CS powder was dissolved in acetic acid to create a 2% wt/*v* solution and stirred for 12 hours. These two solutions were mixed at a 1 : 1 ratio and stirred for one hour at 60°C to create a homogeneous solution.

The CS-GO thin film was coated on an FTO substrate by spin coating at 3000 rpm for 60 seconds and then heat-treated at 50°C to evaporate the solvent. The membrane was annealing for 12 hours to improve the stability. Finally, the Al electrode was deposited by evaporation using a shadow mask with a target-substrate spacing of 10 cm (Figure 1).

2.3. Analysis Technique. A semiconductor characterization system (Keithley 2400) and probe station were used to perform current-voltage measurements. A bias sweep sequence of $0\,V \longrightarrow -7\,V \longrightarrow 0\,V \longrightarrow 7\,V \longrightarrow 0\,V$ was applied to the memory device. Raman spectra (Labram 300, Horiba) were used to analyze scattering oscillations in the CS, GO, and CS-GO nanocomposites. The morphology of GO was studied by using the transmission electron microscopy technique with a JEOL JEM-2100F system. The X-ray photoelectron spectroscopy (XPS) was conducted for the chemical state analysis by the Thermo Fisher Scientific (UK) system with a monochromated source of Al K_α ($h\nu$ = 1486.6 eV).

3. Results and Discussion

3.1. Structural Characteristics. Figure 2 shows the Raman spectra of CS, CS-GO, and GO. Three peaks were observed in the GO spectrum and labeled as D band at ~1329 cm^{-1}, G band at ~1570 cm^{-1}, and 2D band at ~2656 cm^{-1} [8, 9]. The D band is attributed to defects and disturbances in the hexagonal graphite layers, which is characteristic of the in-plane stretching motion of sp^2 carbon atoms [10]. The G-band appeared due to defects, deformations, doping, and temperature. It was used to detect the reactions of graphene-based materials [8]. The 2D band was used to characterize changes in the number of GO layers. The 2D peak of CS-GO shifted from 2656 cm^{-1} to 2682 cm^{-1} in the GO and CS-GO spectra, which showed the change in the GO layer as it was embedded into the CS matrix [11]. The features of both CS and GO were detected in the CS-GO spectrum. The bands D, G, and 2D of CS-GO are all higher compared to GO. Shifts from 2656 cm^{-1} to 2682 cm^{-1} for band 2D, 1329 cm^{-1} to 1336 cm^{-1} for band D, and 1570 cm^{-1} to 1586 cm^{-1} for band G indicate the physical and chemical interactions between the GO and CS functional groups [12].

3.2. Surface Morphology. Figure 3 shows TEM images of the GO morphology at a scale of 200 nm and 100 nm. It is observed that the GO has various size clusters and fairly evenly dispersed. Uncontrolled temperature or oxidation could be responsible for the irregular shapes and uneven particle size [20]. GO was distributed into a thin flat sheet on a surface and folds to create wrinkles [21]. The solid graphene sheets are affected by structural disturbances, possibly due to the laminated thin layers and crumpled sheets involved during exfoliation in a reducing and saponification medium with the removal of oxygen alternating other functional groups between layers [20].

3.3. Elemental Composition and Oxidation States of ZnO NPs. X-ray electron spectroscopy (XPS) was used to determine the chemical states of various elements and the presence of functional groups. The scan spectrum showed that the main elements are carbon and oxygen (Figure 4(a)). The peaks identified in the GO spectrum at ~284.4 eV and ~531.8 eV are the C 1s and O 1s excitations, respectively. Figure 4(b) shows the convoluted C 1s peak, including different binding energies of 284.5, 284.8, 286.5, 287.5, and 288.9 eV. These peaks correspond to different functional groups of sp^2 C=C (42.9%) and sp^3 C-C (47.6%) in the aromatic rings, along with C-O (4.7%), C=O (1.2%), and O=C-OH (3.6%) [22]. The convoluted O 1s peak (Figure 4(c)) shows two peaks at binding energies of 533.1 and 533.4 eV, which are assigned to C-O bonds (66.4%) and C=O bonds (33.6%), respectively [23]. These two peaks correspond to the oxygen in the surface hydroxyl groups of GO. The atomic ratio of carbon to oxygen (C/O) was determined from XPS to be 20, which indicates that there are oxygen vacancies in the surface of GO layers. These vacancies can act as traps that support the electrical conduction and resistive switching mechanism of the memory device.

3.4. Resistive Switching Characteristics. A bias sweep in a sequence of $0\,V \longrightarrow -7\,V \longrightarrow 0\,V \longrightarrow 7\,V \longrightarrow 0\,V$ was applied to the devices. The *I-V* characteristics are shown in Figure 5 with a current threshold of 0.5 mA applied to prevent the breakdown of the device [24]. The device was initially in a high-resistance state (HRS) with no bias applied. The high conductivity ON state was achieved by applying negative voltage. The current increased gradually with increasing negative voltage and jumped quickly at approximately -3 V, converting the device to a low-resistance state (LRS). This transition from HRS to LRS is referred to as the

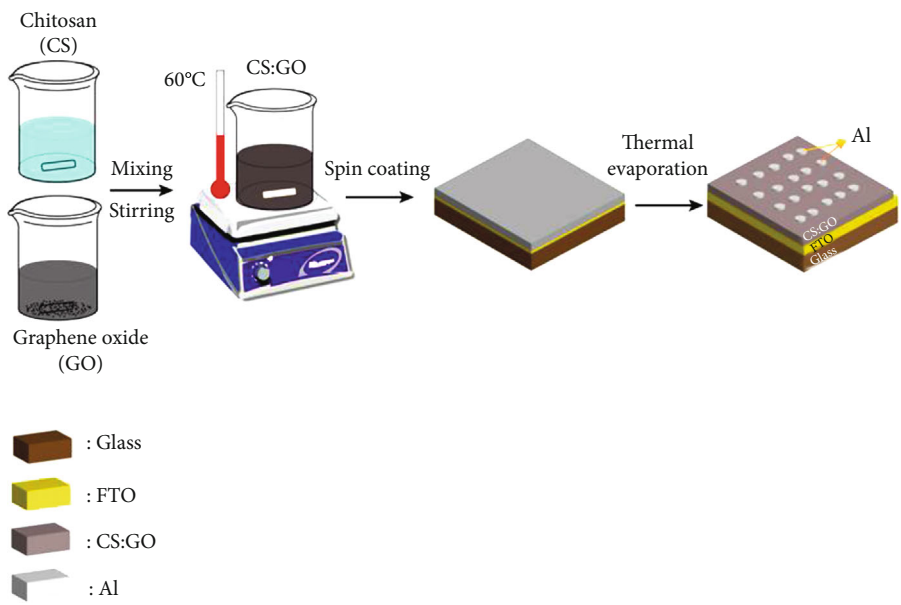

Figure 1: Schematic diagram of the fabrication process of the Al/CS-GO/FTO device.

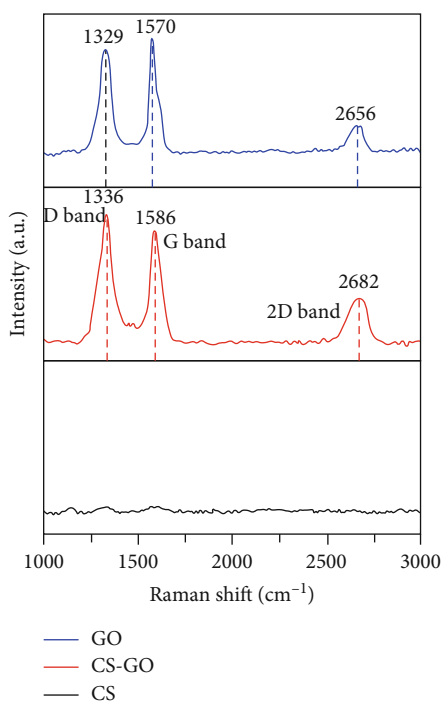

Figure 2: Raman spectra of the CS, CS-GO, and GO.

"writing" process or the SET process, and this state was retained during the voltage sweep back from -7 V to 0 V. The current dropped suddenly around +1 V when applying a positive voltage, which indicates the resistive switching from LRS to HRS and referred to as the "erase" process or RESET process. These results show that the clockwise bipolar resistive switching behavior with the SET state was due to the negative voltage, and the positive voltage was specified as the RESET state.

Figures 6(a) and 6(b) show the endurance and cumulative probability performance of the Al/CS-GO/FTO structure at $V_{\text{read}} = -0.5$ V. The switching behavior was maintained with an "ON/OFF" ratio of approximately 10^2 during 100 cycles. However, both stages fluctuate little. The variation of the operating voltages is shown in Figure 6(c). The SET voltages ranged from -3 V to -4 V while the RESET voltages ranged from 0.7 V to 1.5 V between devices. The RESET voltage deviates less compared to the SET voltage in each device. The SET and RESET voltages are in the opposite polarities so we classify this memory device as a bipolar resistive switch. This bipolar behavior avoids confusion during the operation.

The experimental I-V curve was converted to the J-E plot shown in Figure 7 to understand the conduction mechanism in the process of the Al/CS-GO/FTO device. The plot of J versus E from 0 V to -7 V is consistent with a space-charge-limited conduction (SCLC) mechanism as shown in Figure 7(a) with three distinct curves of either ohmic ($I \sim V$), space-charge-trap-filled limit (V_{TFL}) ($I \sim V^n$ with $n > 2$), or Child's ($I \sim V^2$), which are given by equations (1)-(3) [25–27]:

$$J_{\text{ohmic}} = qn_o\mu\frac{V}{d}, \tag{1}$$

$$J_{\text{TFL}} = \frac{9}{8}\mu\varepsilon\theta\frac{V^2}{d^3}, \tag{2}$$

$$J_{\text{Child}} = \frac{9}{8}\mu\varepsilon\frac{V^2}{d^3}. \tag{3}$$

Ohmic conduction was observed in the voltage range from 0 V to -3 V, corresponding to a slope of approximately one ($I \sim V^{1.27}$). This can be attributed to thermally generated carriers that are more dominant than injected carriers in the dielectric layer [27]. Alternatively, the current was the dominant control in the trap-filled limit with a slope of $I \sim V^{120}$

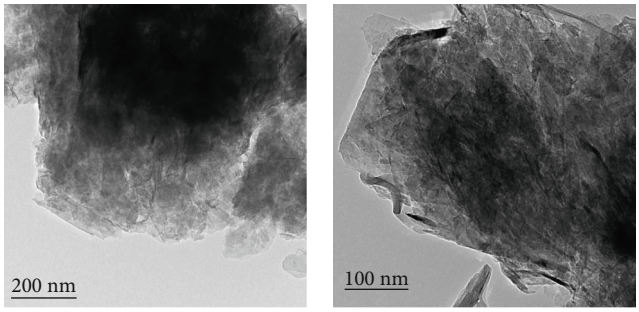

(a) (b)

Figure 3: TEM images of the GO sheets at a scale of (a) 200 nm and (b) 100 nm.

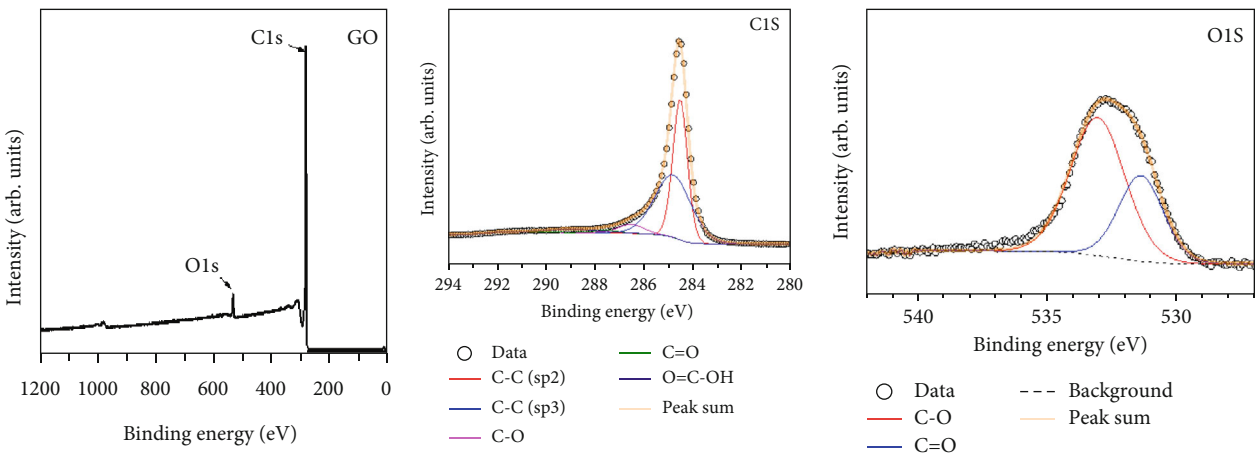

(a) (b) (c)

Figure 4: The X-ray photoelectron survey spectrum of GO (a), the convoluted C 1s high-resolution spectrum (b), and the convoluted O 1s spectrum of GO (c).

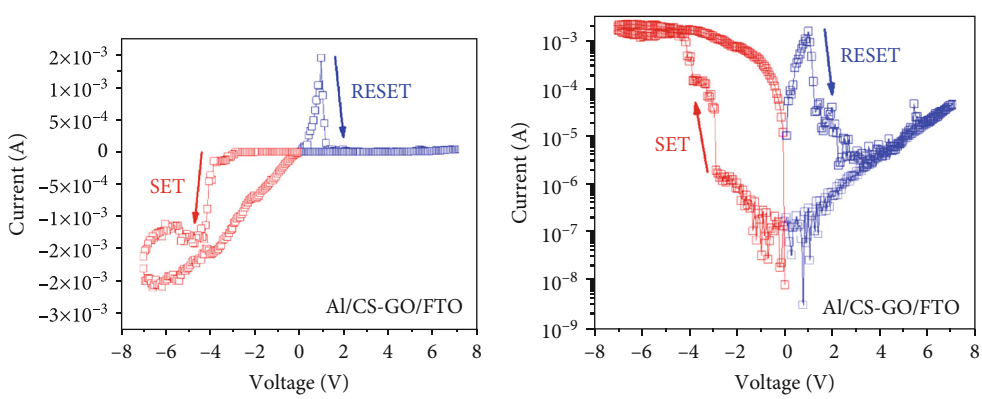

(a) (b)

Figure 5: A linear (a) and semilog (b) plot of the typical current-voltage (I-V) characteristics of an Al/CS-GO/FTO device.

because of the free movement of the carriers in the dielectric layer after all traps are filled [26]. The slope decreased gradually to $I \sim V^2$ due to the accumulation of a space-charge layer in the dielectric layer from -3.5 V to -4 V [28].

The current was consistent with variable-range hopping (VRH) in the back sweep from -7 V to 0 V, which is shown in Figure 7(b). The relationship between J versus E is given by

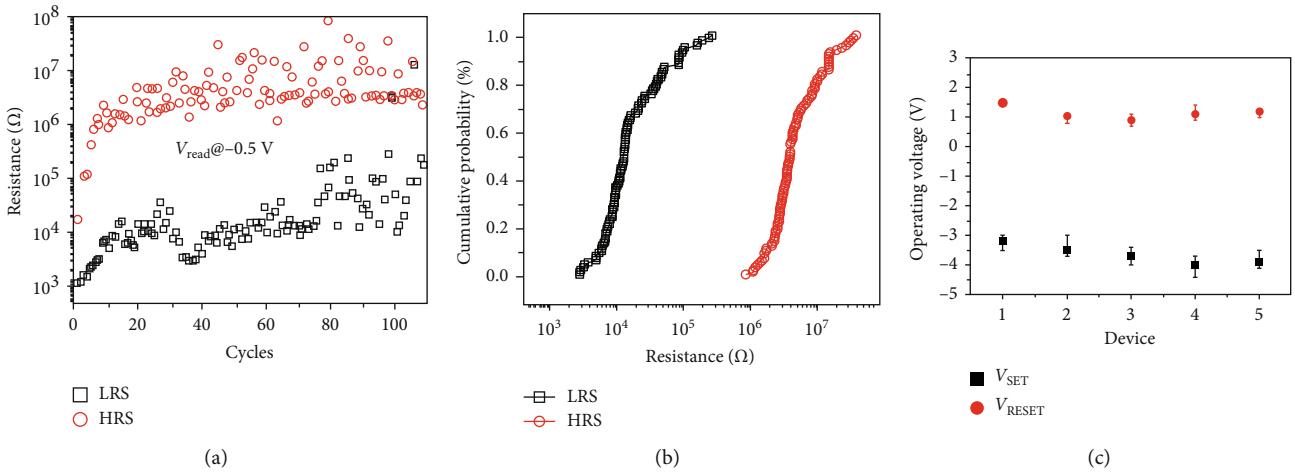

Figure 6: The endurance performance (a) and cumulative probability test (b) at 100 cycles under $V_{read} = -0.5$ V. The variation of operating voltages in five devices of Al/CS-GO/FTO (c).

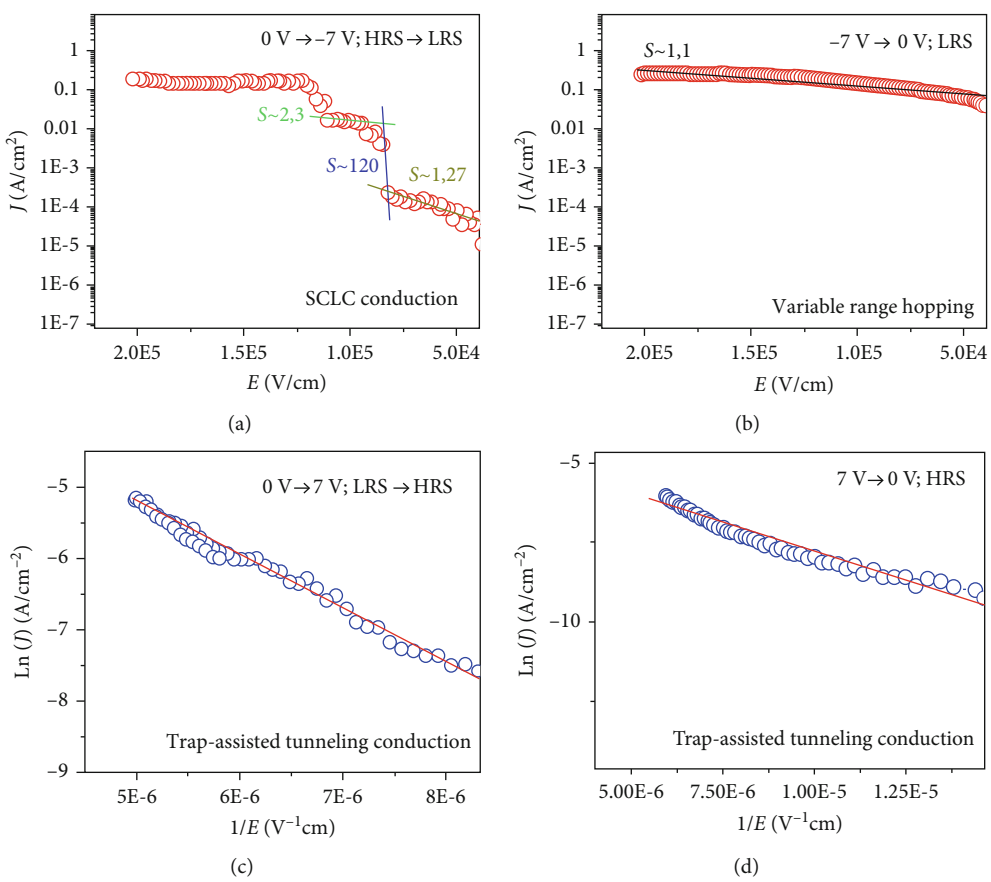

Figure 7: The electrical conduction mechanism of the Al/CS-GO/FTO structure in SCLC conduction (a), variable range hopping (b), and trap-assisted tunneling conduction (c, d).

$$J_{VRH} = \sigma_0 \exp\left(\frac{-T_0}{T}\right)^{1/4} E. \quad (4)$$

Here, σ_0 is the electrical conductivity at T_0. The temperatures T_0 and T are the absolute temperatures, and all other variables are the same as defined previously. The slope $J \sim E$ about 1.1 is likely influenced by the hopping of electrons in the thin-film layer through traps localized in the charge-carrier states [25].

The current dropped abruptly at V_{reset} of 1 V during the reverse voltage from 0 V to 7 V. The current at HRS is

predominantly controlled by trap-assisted tunneling conduction as represented by

$$J_{\mathrm{TAT}} = A \exp\left(\frac{-8\pi\sqrt{2qm^*}}{3hE}\varphi_T^{3/2}\right). \quad (5)$$

Here, A is a constant, m^* is effective mass of an electron, h is Planck's constant, and φ_T is the energy of the electron traps. All other variables are the same as defined before.

Based on these results, we proposed that the resistive switching mechanism in Al/CS-GO/FTO is due to the charge trapping and detrapping process at the defect sites in composite CS-GO. GO usually has many structural defects due to the manufacturing process [29] including oxygen vacancies as shown in the XPS spectra, which act as trapping positions in the CS-GO matrix. Injected electrons from the Al electrode to CS-GO may undergo two processes simultaneously when a negative voltage is initially applied. First, some electrons move freely by hopping between trapped positions into the matrix heading to the FTO electrode. Second, the other electrons are held in trapped positions. There is subsequently an increase in the number of electrons that move directly to the bottom electrode without any resistance forming a continuous current when all traps are filled. This switched the device to the ON state with a high conductivity current. Electrons injected from the FTO electrode still move freely in a dielectric layer when the positive voltage is applied until the voltage is high enough to disrupt the conducting channels which switched the device to the ON state.

4. Conclusion

In summary, we have successfully combined CS and GO in an Al/CS-GO/FTO structure with bipolar along with repeatable and reliable reversible resistive switching abilities. The CS-GO acts as a switching layer with an ON/OFF ratio of ~10^2 over 100 cycles. The conduction mechanism which was related to SCLC, Ohm's law, VRH, and trap-assisted tunneling conduction mechanisms were demonstrated to exist in the bias sweeps. The resistive switching was activated by trapping/detrapping electrons in the CS-GO layer under the external electric field due to the existence of oxygen vacancies in GO. This CS-GO hybrid material shows promise as an environmentally friendly memory device.

Data Availability

Data is available within the article.

Conflicts of Interest

There are no conflicts of interest to declare.

Acknowledgments

This research is funded by Viet Nam National University Ho Chi Minh City (VNU-HCM) under grant number C2018-18-27.

References

[1] K. Pieklarz, M. Tylman, and Z. Modrzejewska, "Applications of chitosan–graphene oxide nanocomposites in medical science: a review," *Progress on Chemistry and Application of Chitin and its Derivatives*, vol. 23, pp. 5–24, 2018.

[2] T. C. Chang, K. C. Chang, T. M. Tsai, T. J. Chu, and S. M. Sze, "Resistance random access memory," *Materials Today*, vol. 19, no. 5, pp. 254–264, 2016.

[3] F. Zahoor, T. Z. Azni Zulkifli, and F. A. Khanday, "Resistive random access memory (RRAM): an overview of materials, switching mechanism, performance, multilevel cell (mlc) storage, modeling, and applications," *Nanoscale Research Letters*, vol. 15, no. 1, p. 90, 2020.

[4] H. Wang and X. Yan, "Overview of resistive random access memory (RRAM): materials, filament mechanisms, performance optimization, and prospects," *physica status solidi (RRL) - Rapid Research Letters*, vol. 13, no. 9, p. 1900073, 2019.

[5] Z. Shen, C. Zhao, Y. Qi et al., "Advances of RRAM devices: resistive switching mechanisms, materials and bionic synaptic application," *Nanomaterials*, vol. 10, no. 8, p. 1437, 2020.

[6] L. Zhu, J. Zhou, Z. Guo, and Z. Sun, "An overview of materials issues in resistive random access memory," *Journal of Materials*, vol. 1, no. 4, 295 pages, 2015.

[7] S. Munjal and N. Khare, "Multilevel resistive and magnetization switching in Cu/CoFe2O4/Pt device: coexistence of ionic and metallic conducting filaments," *Applied Physics Letters*, vol. 113, no. 24, article 243501, 2018.

[8] A. Nife and O. F. T. O. Device, "Forming free resistive switching characteristics," in *AIP Conference Proceedings*, p. 020171, Greece, 2020.

[9] J. Molina-Reyes and L. Hernandez-Martinez, "Understanding the resistive switching phenomena of stacked Al/Al2O3/Al thin films from the dynamics of conductive filaments," *Complexity*, vol. 2017, 10 pages, 2017.

[10] D. Filatov, I. Kazantseva, D. Antonov et al., "Conductive atomic force microscopy study of the resistive switching in yttria- stabilized zirconia films with Au nanoparticles," *Scanning*, vol. 2018, 9 pages, 2018.

[11] S. Munjal and N. Khare, "Electroforming free controlled bipolar resistive switching in Al/CoFe2O4/FTO device with self-compliance effect," *Applied Physics Letters*, vol. 112, no. 7, article 073502, 2018.

[12] S. Munjal and N. Khare, "Compliance current controlled volatile and nonvolatile memory in Ag/CoFe2O4/Pt resistive switching device," *Nanotechnology*, vol. 32, no. 18, p. 185204, 2021.

[13] V. K. Thakur, M. K. Thakur, P. Raghavan, and M. R. Kessler, "Progress in green polymer composites from lignin for multifunctional applications: a review," *ACS Sustainable Chemistry & Engineering*, vol. 2, no. 5, pp. 1072–1092, 2014.

[14] A. Ali and S. Ahmed, "A review on chitosan and its nanocomposites in drug delivery," *International Journal of Biological Macromolecules*, vol. 109, pp. 273–286, 2018.

[15] M. H. Periayah, A. S. Halim, and A. Z. M. Saad, "Chitosan: a promising marine polysaccharide for biomedical research," *Pharmacognosy Reviews*, vol. 10, no. 19, pp. 39–42, 2016.

[16] A. Barra, N. M. Ferreira, M. A. Martins et al., "Eco-friendly preparation of electrically conductive chitosan - reduced graphene oxide flexible bionanocomposites for food packaging

and biological applications," *Composites Science and Technology*, vol. 173, pp. 53–60, 2019.

[17] J. Ahmed, M. Mulla, Y. A. Arfat, and T. Lidia Arockia Thai, "Mechanical, thermal, structural and barrier properties of crab shell chitosan/graphene oxide composite films," *Food Hydrocolloids*, vol. 71, pp. 141–148, 2017.

[18] N. Raeis-Hosseini and J. S. Lee, "Resistive switching memory using biomaterials," *Journal of Electroceramics*, vol. 39, no. 1-4, pp. 223–238, 2017.

[19] K. My Tran, D. Phuc Do, H. Nam Vu et al., "Experimental combined theoretical study on chemical interactions of graphene oxide with chitosan and its resistive-switching effect," *Materials Science and Engineering: B*, vol. 262, article 114788, 2020.

[20] M. Aziz, F. S. Abdul Halim, and J. Jaafar, "Preparation and characterization of graphene membrane electrode assembly," *Jurnal Teknologi*, vol. 69, no. 9, pp. 11–14, 2014.

[21] A. K. Mishra and S. Ramaprabhu, "Functionalized graphene sheets for arsenic removal and desalination of sea water," *Desalination*, vol. 282, pp. 39–45, 2011.

[22] Y. E. Shin, Y. J. Sa, S. Park et al., "An ice-templated, pH-tunable self-assembly route to hierarchically porous graphene nanoscroll networks," *Nanoscale*, vol. 6, no. 16, pp. 9734–9741, 2014.

[23] Y. Feng, N. Feng, Y. Wei, and G. Zhang, "An in situ gelatin-assisted hydrothermal synthesis of ZnO-reduced graphene oxide composites with enhanced photocatalytic performance under ultraviolet and visible light," *RSC Advances*, vol. 4, no. 16, pp. 7933–7943, 2014.

[24] W. Y. Chang, Y. C. Lai, T. B. Wu, S. F. Wang, F. Chen, and M. J. Tsai, "Unipolar resistive switching characteristics of ZnO thin films for nonvolatile memory applications," *Applied Physics Letters*, vol. 92, no. 2, pp. 1–4, 2008.

[25] E. W. Lim and R. Ismail, "Conduction mechanism of valence change resistive switching memory: a survey," *Electronics*, vol. 4, no. 3, pp. 586–613, 2015.

[26] B. T. Phan, C. Jung, T. Choi, and J. Lee, "Trap-controlled space-charge-limited current conduction in the Cr-doped SrTiO3 thin films deposited by using pulsed laser deposition," *Journal of the Korean Physical Society*, vol. 51, no. 92, pp. 664–668, 2007.

[27] F. C. Chiu, "A review on conduction mechanisms in dielectric films," *Advances in Materials Science and Engineering*, vol. 2014, 18 pages, 2014.

[28] M. A. Lampert, "Simplified theory of space-charge-limited currents in an insulator with traps," *Physics Review*, vol. 103, no. 6, pp. 1648–1656, 1956.

[29] S. C. Ray, "Application and uses of graphene oxide and reduced graphene oxide," in *Applications of Graphene and Graphene-Oxide Based Nanomaterials*, pp. 39–55, Elsevier, 2015.

Hindawi
Journal of Nanomaterials
Volume 2021, Article ID 5533620, 12 pages
https://doi.org/10.1155/2021/5533620

Research Article

Prussian Blue Analogues of $A_2[Fe(CN)_6]$ (A: Cu^{2+}, Co^{2+}, and Ni^{2+}) and Their Composition-Dependent Sorption Performances towards Cs^+, Sr^{2+}, and Co^{2+}

Lan Ha Thi Le,[1,2] Son An Nguyen,[2] Trung Dinh Nguyen,[2] Van Cam Thi Le,[3] Hai Van Cao,[2] Ngoc Bao Nguyen,[2] and Thao Phuong Thi Le[2]

[1]*Tran Phu High School, Da Lat, Vietnam*
[2]*Department of Physics and Nuclear Engineering, Dalat University, Da Lat, Vietnam*
[3]*Department of Environmental Sciences and Engineering, Hallym University, Chuncheon, Republic of Korea*

Correspondence should be addressed to Son An Nguyen; sonna@dlu.edu.vn

Received 10 January 2021; Revised 5 March 2021; Accepted 18 March 2021; Published 27 March 2021

Academic Editor: Duong Tuan Quang

Investigation in radioactive contaminant removal from aqueous solutions has been considered essential upon unexpected nuclear accidents. In this report, we have successfully prepared Prussian blue analogues (PBAs) with different substituted cations ($A_2[Fe(CN)_6]$ (A: Cu^{2+}, Co^{2+}, and Ni^{2+})). The synthesized PBAs were characterized and employed for the removal of Cs^+, Sr^{2+}, and Co^{2+} as sorption models, which are commonly found in radioactive waste. Sorption examinations reveal that $Cu_2[Fe(CN)_6]$ has the highest sorption capacity towards Cs^+, Sr^{2+}, and Co^{2+} compared with those of $Co_2[Fe(CN)_6]$ and $Ni_2[Fe(CN)_6]$. This is mainly attributed to the cation-exchange ability of substituted metal within the framework of PBAs. The sorption mechanism is qualitatively and quantitatively supported by infrared spectroscopy (IR) and total reflection X-ray fluorescence spectroscopy analysis (TXRF). In addition, it was found that Cs^+ is adsorbed most effectively by PBAs due to the size matching between Cs^+ ions and the channel windows of PBAs. These findings are important for the design of sorbents with suitable ion-exchange capacity and selectivity toward targeted radioactive wastes.

1. Introduction

Increasing demand for nuclear power plants (NPP) has caused a large amount of highly radioactive waste, which brings with it the risk of severe impact on humans and the environment in the event of a nuclear accident [1]. Real-time monitoring and removal of such contaminants are considered an important task upon a NPP shutdown [2, 3]. Radioactive nuclides with long half-life, e.g., ^{137}Cs (30.2 years) [4–6], ^{90}Sr (28.8 years) [7], and ^{60}Co (5.3 years) [8], are the primary species produced in the nuclear reactions and are potentially discharged into the environment during an accident, such as the explosion at the Fukushima Daiichi power plant in 2011 [9]. The isotopes ^{137}Cs and ^{90}Sr can be found in radioactive nuclide-contaminated areas, primarily in the aqueous phase, whereas ^{60}Co is found as an impurity in the stainless steel used in nuclear reactors. ^{60}Co is also used as a gamma ray source in radiotherapy or used as a disinfectant in the food industry [10]. Thus far, a variety of techniques, e.g., precipitation, extraction, ion-exchange, and adsorption [11–14] have been extensively developed to remove radioactive nuclides from aqueous solutions. Of great interest is the combination of adsorption- and ion-exchange-based approaches because the combined techniques can considerably enhance removal efficiency and selectivity towards the targeted radioactive waste rather than the coexisting competitors or inhibitors [15]. Therefore, it is highly desirable to develop advanced materials with a high degree of porosity and well-established pore size distribution and controllable ion-exchange capability for improved removal efficiency.

In recent years, there have been several classes of porous inorganic materials that match the aforementioned standards, such as clays [16], zeolites [17], and Prussian blue (PB) and Prussian blue analogues (PBAs) [18–20]. In particular, PB and/or PBAs are constructed via coordination bonds between transition metals (e.g., Fe^{2+}, Fe^{3+}, Cu^{2+}, Co^{2+}, and Ni^{2+}) and CN^- ligands. In particular, PBAs can be synthesized in a facile and cost-effective manner. Such materials often exhibit high porosity, excellent thermal, and radiation stability [21], which render them highly applicable in many fields, including information/energy storage [22], biomedicine [23], and dye [24] or radioactive waste removal. In addition, PBAs have been regarded as one of the most efficient and selective adsorbents for cesium ions. The selective cesium adsorption is attributable to the size matching between PBAs (3.2 Å) and cesium ions (3.25 Å) [25]. Although a number of publications have demonstrated adsorption performance of PBAs towards individual radioactive nuclides Cs^+, Sr^{2+}, and Co^{2+}(Table 1), there is few research comparing the adsorption capacity of Cs^+, Sr^{2+}, and Co^{2+}ions and the correlation between PBA compositions and adsorption activities.

Herein, we successfully synthesized different PBAs, including A_2 $[Fe(CN)_6]$ (A: Cu^{2+}, Co^{2+}, and Ni^{2+}) and compared theirs adsorption performances with Cs^+, Sr^{2+}, and Co^{2+} ions. It was found that the substitution of the transition metal ions used (Cu^{2+}, Co^{2+}, and Ni^{2+}) in the framework of PBAs led to improved adsorption capacity and selectivity. Total reflection X-ray fluorescence spectroscopy analysis (TXRF) provides quantitative evidence with respect to the adsorption mechanism of the obtained PBAs.

2. Materials and Methods

2.1. Materials. Standard solutions (Cs^+ (1000 mg/L), Sr^{2+} (1000 mg/L), Co^{2+} (1000 mg/L)), CsCl (99.99%, Meck), $SrCl_2$ (99.99%, Meck), $CoCl_2$ (99.99%, Meck), $K_4[Fe(CN)_6]$ (99.99%, Meck), $CoCl_2{\cdot}6H_2O$ (99.99%, Meck), $CuCl_2{\cdot}2H_2O$ (99.99%, Meck), and $NiSO_4{\cdot}6H_2O$ (99.99%, Meck) were used as received. pH was adjusted using HNO_3 (0.01–0.1 N) and NaOH (0.01–0.1 N).

2.2. Synthesis of $A_2[Fe(CN)_6]$. The synthetic protocol for $A_2[Fe(CN)_6]$ (A = Co, Ni, and Co) was slightly modified from previous Therefore reports [26–29]. For the synthesis of $Cu_2[Fe(CN)_6]$, a 250 mL of 0.05 M $K_4[Fe(CN)_6]$ solution was slowly added to a 750 mL of 0.15 M $CuCl_2$ solution. The reaction mixture was stirred at 1200 rpm and sonicated, prior to heating to 60°C for 4 h. Upon reaction completion, the product was purified by repeated washing with water and centrifugation and dried at 70°C. For the synthesis of $Co_2[Fe(CN)_6]$ and $Ni_2[Fe(CN)_6]$, a $CoCl_2$ or $NiSO_4$ solution was, respectively, used in place of $CuCl_2$ in the aforementioned procedure. The other reaction conditions remained unchanged, unless stated otherwise.

2.3. Adsorption Performance of $A_2[Fe(CN)_6]$ towards Cs^+, Sr^{2+}, and Co^{2+}. For the sake of safety, Cs^+, Sr^{2+}, and Co^{2+} used in this study were stable isotopes. A series of reaction flasks containing 50 mL of Cs^+, Sr^{2+}, and Co^{2+}solutions with concentrations of 0.1 mg/L, 1 mg/L, 10 mg/L, 30 mg/L, 50 mg/L, 70 mg/L, 100 mg/L, 150 mg/L, 200 mg/L, 250 mg/L, 300 mg/L, 350 mg/L, 400 mg/L, 450 mg/L, 500 mg/L, 550 mg/L, and 600 mg/L were prepared. To the above solutions, 0.1 g of the *as*-synthesized $A_2[Fe(CN)_6]$ was added. The pH was adjusted to 7.0, and the mixture was sealed and shaken at 270 times/min for 24 hours at 25°C in order to reach equilibrium. After adsorption completion, the adsorbent was separated by centrifugation (8500 rpm, 10 min), and the remaining solution was filtered through a 220 nm filter for further analysis with TXRF.

The adsorption capacity of $A_2[Fe(CN)_6]$ toward Cs^+, Sr^{2+}, and Co^{2+} is calculated using the following formula:

$$q = \frac{V \times (C_i - C_e)}{B}, \quad (1)$$

where q is the adsorption capacity of the adsorbent material (mg/g adsorbent), C_i and C_e are the concentrations of adsorbate (i.e., Cs^+, Sr^{2+}, and Co^{2+}) before and after adsorption, respectively, V is the volume of the solution, and B is the mass of the adsorbent used.

Langmuir and Freundlich models were used to assess the adsorption performance of $A_2[Fe(CN)_6]$.

$$\text{Langmuir adsorption equation } q_e = \frac{Q_m \times b \times C_e}{1 + bC_e}, \quad (2)$$

where q_e is the amount of Cs^+, Sr^{2+}, and Co^{2+} ions adsorbed by the material (mg/g), Q_m is the maximum adsorption capacity for Cs^+, Sr^{2+}, and Co^{2+} ions, C_e is the initial concentration at a point of adsorption (mg/L), and rate constant b is the adsorption/desorption.

$$\text{Freundlich adsorption equation } q_e = K \times C_e^{1/n}, \quad (3)$$

where q_e is the amount of Cs^+, Sr^{2+}, and Co^{2+} ions adsorbed by the material (mg/g), and K and n are the adsorption constant at equilibrium.

2.4. TXRF Analyses of the Samples and Cs^+, Sr^{2+}, and Co^{2+} Solution prior to and after Adsorption. After adsorption completion, the adsorbents were washed several times with distilled water and dried at 60°C. The sample elemental contents were analyzed by total reflection X-ray fluorescence (TXRF) to monitor the change in the composition of the material before and after the reaction. The content of Cs^+, Sr^{2+}, and Co^{2+} before and after adsorption remaining in the solution was also measured by TXRF.

2.5. Characterizations. Crystalline structures of $A_2[Fe(CN)_6]$ were investigated by powder X-ray diffraction (PXRD) performed with a Bruker D8 Advance diffractometer using Cu Kα radiation (wavelength 1.541 Å) in focused beam and in the range 10-80°. The morphologies and elemental composition of $A_2[Fe(CN)_6]$ were characterized using field emission transmission electron microscopy (FE-TEM; JEM 2100-Jeol, Japan) and energy dispersive X-ray spectroscopy (EDS; JEM 2100-Jeol, Japan). Gas adsorption isotherms at

Table 1: Comparison of the adsorption capacity of Cs^+, Sr^{2+}, and Co^{2+} ions on different adsorbent materials.

Adsorbent	pH	Maximum adsorption capacity ($mg\ g^{-1}$)	References
Cs^+ ion			
Copper hexacyanoferrate (CuHCF)	7.0	155.60	This research
Cobalt hexacyanoferrate (CoHCF)	7.0	154.46	This research
Nickle hexacyanoferrate (NiHCF)	7.0	120.31	This research
Copper ferrocyanide functionalized mesoporous silica	7.7	17.1	[37]
Zeolite A	6.0	208.7	[38]
Magnetic PB/GO	7.0	55.6	[39]
Montmorillonite-iron oxide composite	6.5	52.6	[25]
Conjugate adsorbent	7.0	77.7	[40]
Ammonium molybdophosphate-polyacrylonitrile	6.5	81.3	[41]
Cs^+-imprinted polymer nanoparticle	9.0	50.0	[42]
Poly(AAc-co-B18C6Am) hydrogels	6.0	74.6	[6]
Prussian blue/Fe_3O_4	7.0	280.82	[43]
CuHCF-cellulose hydrogel	7.0	309	[44]
CuHCF/MWCNT	7.0	310	[44]
MOF/KNiFC	5.0	153	[45]
Sr^{2+} ion			
Copper hexacyanoferrate(CuHCF)	7.0	59.95	This research
Cobalt hexacyanoferrate(CoHCF)	7.0	32.73	This research
Nickle hexacyanoferrate (NiHCF)	7.0	29.17	This research
Amorphous zirconium phosphates	11.4	134.2	[46]
Zr-MOF	7.0	7.548	[47]
Zirconium phosphate on active carbon	6.0	2.9	[22]
ZrO_2-TiO_2	9.0	28.01	[48]
Zirconium phosphate	1.0	34	[49]
Fower-like α-ZrP	4.0	293.43	[50]
Titanate nanofibers	7.0	55.2	[51]
PAN-zeolite	7.0	44.43	[52]
Carboxymethylated cellulose	4.0	108.7	[53]
Graphene oxide	6.5	23.83	[54]
ZrP-SO_3H	4.0	183.21	[55]
Nb-doped WO_3	7.0	54.39	[54]
Co^{2+}ion			
Copper hexacyanoferrate (CuHCF)	7.0	62.08	This research
Nickle hexacyanoferrate (NiHCF)	7.0	32.34	This research
MWCNT/IO		10.61	[56]
Silica SBA-15		181.67	[57]
SiO_2/Nb_2O_5/ZnO		0.518	[58]
Ordered micro- and mesoporous/SiO_2		8.43	[59]
Magnetite-based nanocomposites		43.292	[60]
GO-NH_2		116.35	[61]

77 K are obtained using TriStar II-Micromeritics, America. The IR spectra of the samples were recorded in the 399-4000 cm^{-1} range using KBr pellets on a Nicolet iS10 (Thermo Scientific, America). The composition of the material before and after the reaction was analyzed using total reflection X-ray fluorescence (TXRF) S2 Picofox Bruker.

3. Results and Discussion

$A_2[Fe(CN)_6]$ (A: Cu, Co, and Ni) was readily synthesized by precipitating Cu^{2+}, Co^{2+}, and Ni^{2+} salt with $K_4[Fe(CN)_6]$ aqueous solution at 60°C for 4 h. The chemical reactions for $A_2[Fe(CN)_6]$ are as follows:

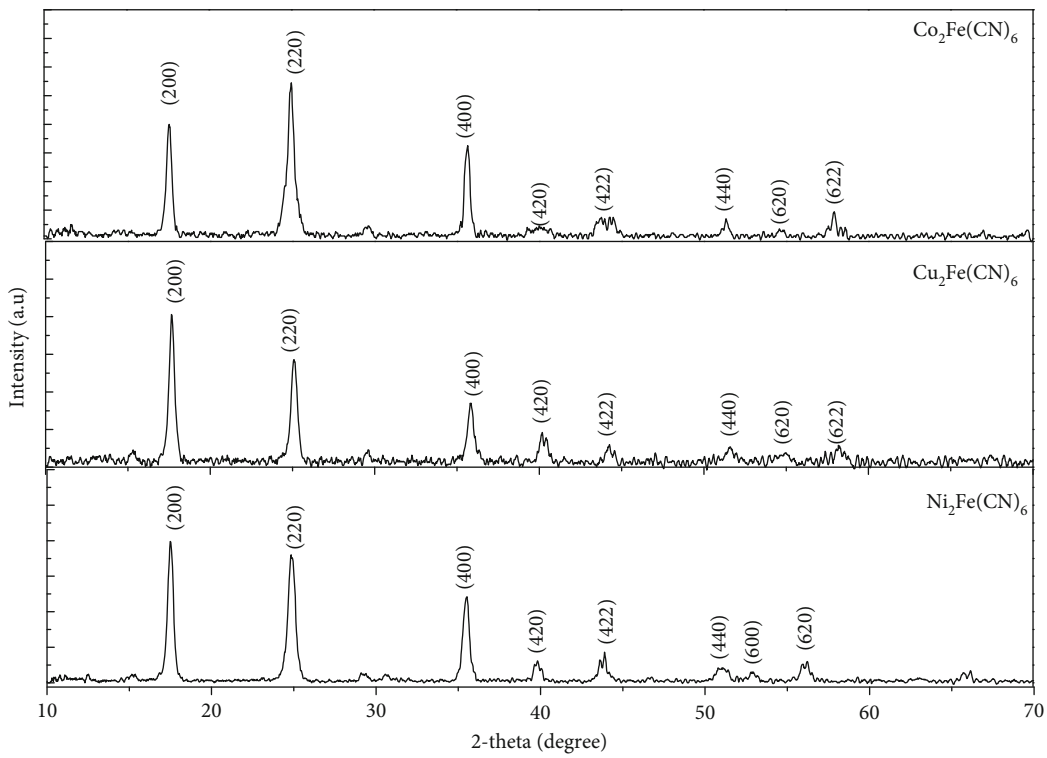

Figure 1: PXRD of $A_2[Fe(CN)_6]$ (A: Co, Cu, Ni).

Table 2: Typical parameters estimated from XRD patterns of $Cu_2[Fe(CN)_6]$, $Co_2[Fe(CN)_6]$, and $Ni_2[Fe(CN)_6]$.

Sample	A (Å)	The average crystallite size D (Å)	Unit cell volume V (Å^3)
$Cu_2Fe(CN)_6$	9.92 ± 0.1	142.3	1003.9
$Co_2Fe(CN)_6$	10.22 ± 0.2	309.6	1022.5
$Ni_2Fe(CN)_6$	10.26 ± 0.2	166.6	1032.5

Table 3: BJH pore size and BET surface areas of $Cu_2[Fe(CN)_6]$, $Co_2[Fe(CN)_6]$, and $Ni_2[Fe(CN)_6]$.

	$Cu_2Fe(CN)_6$	$Co_2Fe(CN)_6$	$Ni_2Fe(CN)_6$
BJH pore size (nm)	22.105	34.9401	34.0211
BET surface area (m^2/g)	5.857	63.9561	59.0432

$$\begin{aligned} 2NiSO_4 + K_4\left[Fe(CN)_6\right] &\rightarrow Ni_2\left[Fe(CN)_6\right] + 2K_2SO_4 \\ 2CuCl_2 + K_4\left[Fe(CN)_6\right] &\rightarrow Cu_2\left[Fe(CN)_6\right] + 4KCl \\ 2CoCl_2 + K_4\left[Fe(CN)_6\right] &\rightarrow Co_2\left[Fe(CN)_6\right] + 4KCl \end{aligned} \quad (4)$$

Crystalline properties of the *as*-synthesized $A_2[Fe(CN)_6]$ were examined using PXRD, and the data are shown in Figure 1. $Ni_2[Fe(CN)_6]$, $Co_2[Fe(CN)_6]$, and $Cu_2[Fe(CN)_6]$ exhibit a high degree of crystallinity with a set of diffraction peak characteristic for the PBA family (JCPDS 77-1161) [26, 30, 31]. The respective lattice constant estimated from the PXRD data for $Cu_2[Fe(CN)_6]$, $Co_2[Fe(CN)_6]$, and $Ni_2[Fe(CN)_6]$ is 9.92 ± 0.1 Å, 10.22 ± 0.2 Å, and 10.26 ± 0.2 Å, respectively (Table 2). Although the estimated lattice constants show a slight deviation, presumably due to the size difference among the metal ions, these results are highly consistent with the lattice constant of the face-centered cubic (Pm3m) of PBAs previously reported [26]. The specific surface area of $A_2[Fe(CN)_6]$ was also characterized using N_2 isotherm adsorption at 77 K, and the results were tabulated in Table 3. The surface area of $Co_2Fe\ (CN)_6$ and $Ni_2Fe\ (CN)_6$ is around 60 m^2 g^{-1}, which are tenfold higher than that of $Cu_2Fe\ (CN)_6$. This could be attributed to the slight aggregation of $Cu_2Fe(CN)_6$ as seen by TEM.

The particle size and morphological properties of $A_2[Fe(CN)_6]$ were examined using transmission electron microscopy (TEM) (Figure 2). $Co_2Fe\ (CN)_6$ shows pseudo-spherical particles with the size varying between 25 and 55 nm (Figure 2(a)). For $Cu_2[Fe(CN)_6]$, the particles are formed from the aggregation of smaller subparticles, resulting in a wider spectrum of distribution. Among the synthesized PBAs, $Ni_2[Fe(CN)_6]$ shows the smallest size, ranging from 15 nm to 35 nm. Essentially, the elemental composition of $A_2[Fe(CN)_6]$ was confirmed using X-ray energy dispersion spectroscopy (EDX) (Figure 3). The data show that the elements Co, Cu, and Ni were uniformity distributed throughout the examined area in $Co_2[Fe(CN)_6]$, $Cu_2[Fe(CN)_6]$, and $Ni_2[Fe(CN)_6]$, respectively. This further confirms the successful synthesis of $A_2[Fe(CN)_6]$.

Infrared spectroscopy (IR) is used to investigate the characteristic bonding information within the structure of $A_2[Fe(CN)_6]$ (Figure 4). In addition to a vibrational band at

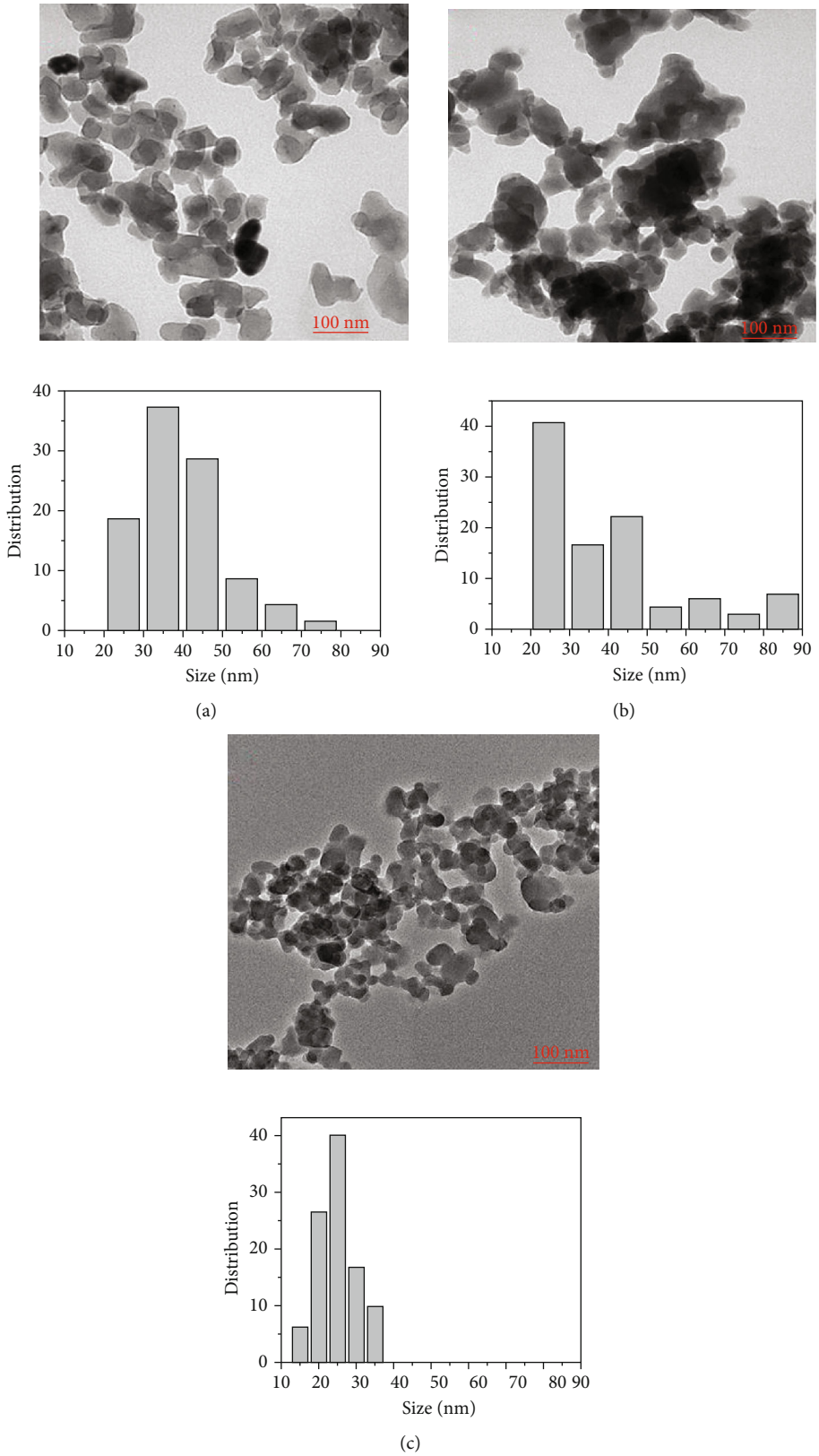

Figure 2: TEM images and the corresponding particle size distribution of (a) $Co_2[Fe(CN)_6]$, (b) $Cu_2[Fe(CN)_6]$, and (c) $Ni_2[Fe(CN)_6]$.

590 cm^{-1} and 3450 cm^{-1} corresponding to Fe-C bond [32, 33] and bending mode of H_2O [34], all of the $A_2[Fe(CN)_6$ exhibit a characteristic peak assigned to the C-N bonding located at around 2000 cm^{-1}, which belongs to the CN^- ligand. Principally, the peak position of C-N vibration is indirectly indicative of the bond strength between metal cation and CN^-

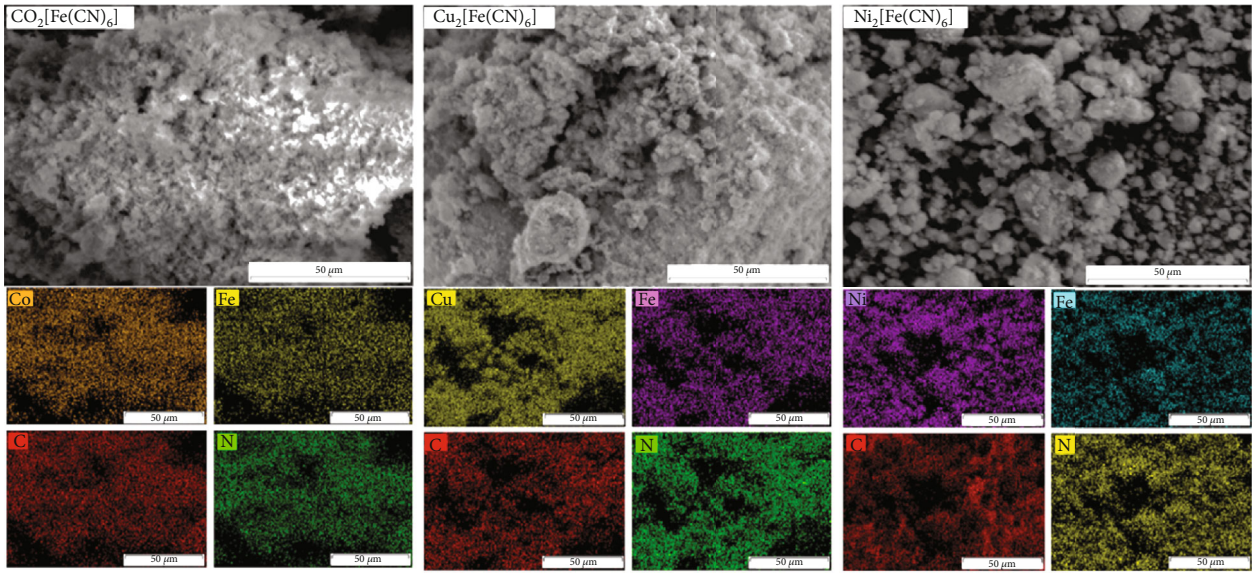

Figure 3: SEM images and the corresponding elemental mapping by EDX of $A_2[Fe(CN)_6]$.

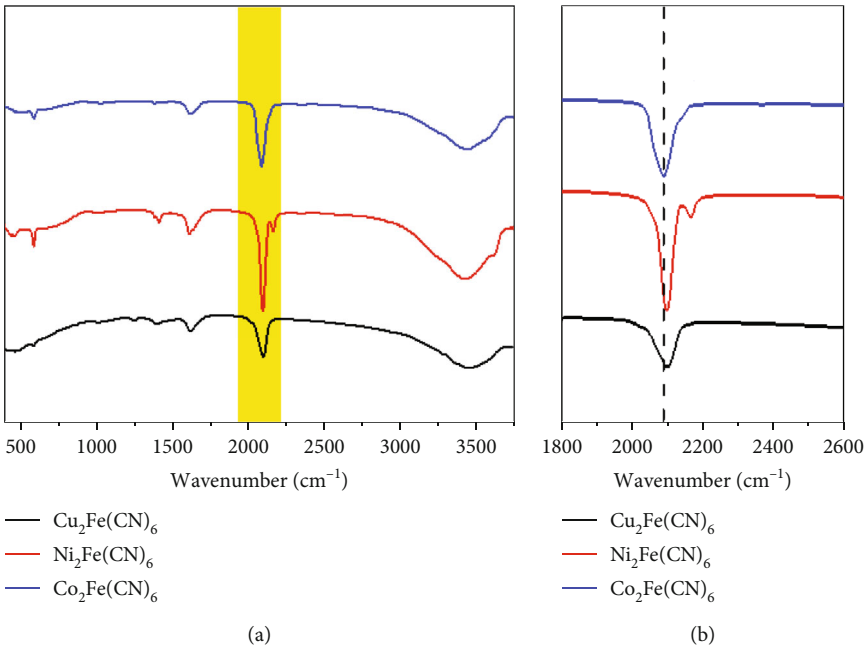

Figure 4: FT-IR spectra of (a) $Cu_2[Fe(CN)_6]$, $Ni_2[Fe(CN)_6]$, and $Co_2[Fe(CN)_6]$ exhibit a characteristic peak of C-N around 2000 cm^{-1}. (b) The location of the C-N vibration peak in $Cu_2[Fe(CN)_6]$, $Ni_2[Fe(CN)_6]$, and $Co_2[Fe(CN)_6]$ is at 2099 cm^{-1}, 2097 cm^{-1}, and 2088 cm^{-1}, respectively.

ligands. It is observed that the location of C-N vibration peak in $Cu_2[Fe(CN)_6]$ is at 2099 cm^{-1}, which is slightly higher than those of $Ni_2[Fe(CN)_6]$ (2097 cm^{-1}) and $Co_2[Fe(CN)_6]$ (2088 cm^{-1}), revealing that the contribution of π-back bonding to the antibonding orbital of CN^- ligand from Cu^{2+} is less significant than those from Ni^{2+} and Co^{2+}. In other words, Cu^{2+} within the framework of $Cu_2[Fe(CN)_6]$ binds less strongly to CN ligand than Ni^{2+} and Co^{2+} do in $Ni_2[Fe(CN)_6]$ and $Co_2[Fe(CN)_6]$. This is an important evidence as it is explicitly correlated with the ion-exchange capacity of $A_2[Fe(CN)_6]$ discussed later.

The adsorption isotherms of $A_2[Fe(CN)_6]$ towards Cs^+, Sr^{2+}, and Co^{2+} were examined at 25°C and pH 7 (Figures 5 and 6). The parameters of the isothermal adsorption of Cs^+, Sr^{2+}, and Co^{2+} ions on $A_2[Fe(CN)_6]$ estimated from Langmuir and Freudlich models are shown in Table 4. It is interesting to note that $Cu_2[Fe(CN)_6]$ shows much higher maximum adsorption capacity (Qm) towards Cs^+ (155.60 mg g-1), Sr^{2+} (59.95 mg g-1), and Co^{2+} (62.08 mg g-1) than those of $Ni_2[Fe(CN)_6]$ (120.31, 29.17, and 32.34 for Cs^+, Sr^{2+}, and Co^{2+}, respectively) and $Co_2[Fe(CN)_6]$ (154.46 and 59.95 for Cs^+ and Sr^{2+}, respectively).

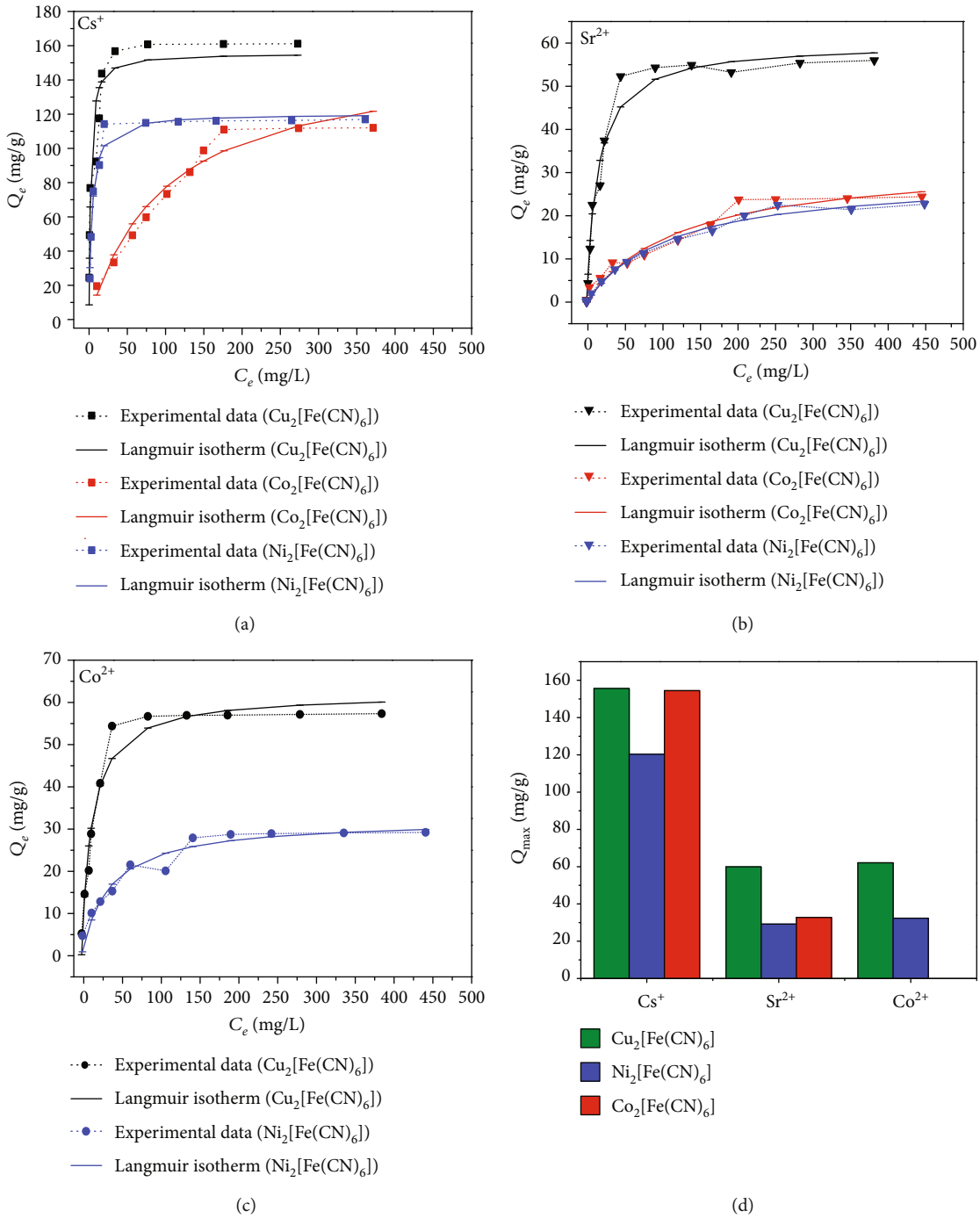

Figure 5: The Langmuir isotherm model fitted for the adsorption of (a) Cs^+, (b) Sr^{2+}, and (c) Co^{2+} on $A_2[Fe(CN)_6]$ at pH 7. (d) The maximum adsorption capacity of Cs^+, Sr^{2+}, and Co^{2+} ions of $A_2[Fe(CN)_6]$ estimated from their corresponding Langmuir model.

Considering crystallographic similarity among the structures of $Cu_2[Fe(CN)_6]$, $Ni_2[Fe(CN)_6]$, and $Co_2[Fe(CN)_6]$, the difference in adsorption capacity can be associated with the ion-exchange capability of the metal nodes in the framework of $A_2[Fe(CN)_6]$. More specifically, the metal nodes that bond less strongly to the CN^- ligand are more likely to participate in ion-exchange with adsorbate (i.e., Cs^+, Sr^{2+}, and Co^{2+}). In order to further understand the sorption mechanism, TXRF was used to investigate the solution composition before and after sorption (Figure 7). Figures 7(a)–7(c), respectively, demonstrate the change in the peak intensity of Cs^+ (4.3 keV), Sr^{2+} (14.2 keV), and Co^{2+} (6.93 keV) in the solution before and after adding $Cu_2[Fe(CN)_6]$, $Ni_2[Fe(CN)_6]$, and $Co_2[Fe(CN)_6]$ into the solution. As seen, after the sorption reaches equilibrium, the peak intensity corresponding to Cs^+, Sr^{2+}, and Co^{2+} decreases, revealing the sorption process of those cations by $A_2[Fe(CN)_6]$. Interestingly, the peak located at 8.05 keV, which is assigned to Cu K_α, is clearly observed after the sorption process in all solutions (Figures 7(d)–7(f)); however, we could not observe

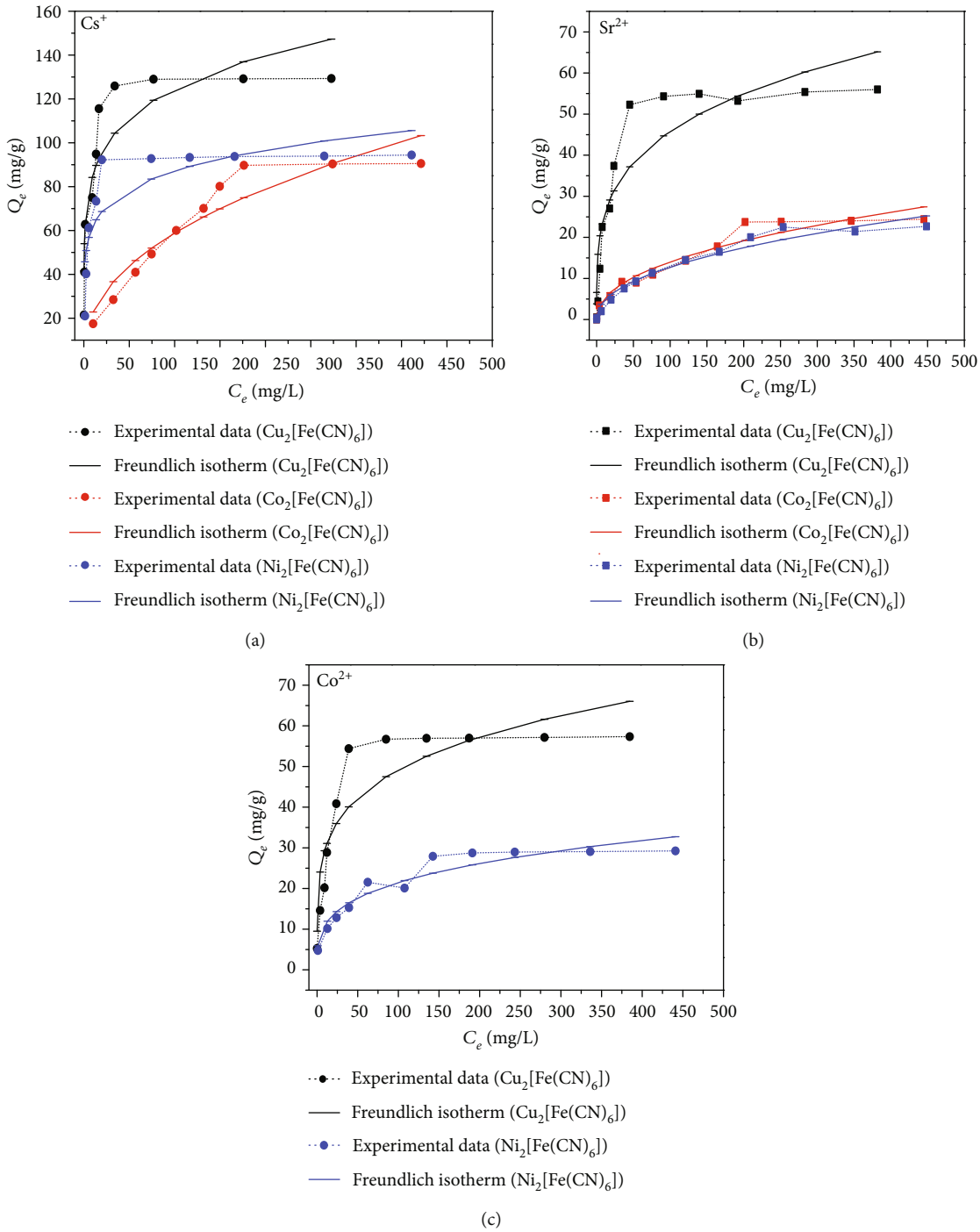

Figure 6: The Freundlich isotherm model fitted for the adsorption of (a) Cs^+, (b) Sr^{2+}, and (c) Co^{2+} on $A_2[Fe(CN)_6]$ at pH 7.

any peaks corresponding to those of Ni^{2+} or Co^{2+}. These data imply that only Cu^{2+} cations within the framework of $Cu_2[Fe(CN)_6]$ meaningfully participate in the sorption via ion exchanging with the adsorbates. This is in concert with the IR data in which Cu^{2+} binds less strongly to CN^- ligands, thus readily subjected to readily ion exchange with Cs^+, Sr^{2+}, and Co^{2+}. Ion-exchange-based sorption for removal of radioactive waste was also previously reported for PBAs [35]. In addition, among the tested cations, Cs^+ was found to be the most effectively adsorbed PBAs. This is mainly attributed to the size similarity between Cs^+ cation (3.25 Å) [25] and the channel window of PBAs (3.2 Å), while the size of Sr^{2+} (4.12 Å) and Co^{2+} (4.23 Å) [36] is comparably larger than the window size. These are important points as these findings can allow for the potential design of adsorbent with designed ion-exchange capacity, so that we could further control the sorption process as well as enhance the selectivity.

Table 4: Adsorption isothermal parameters of Cs^+, Sr^{2+}, andCo^{2+} by $A_2[Fe(CN)_6]$ extract from Langmuir and Freundlich models.

Ion	Adsorbent material	Langmuir			Freundlich		
		Q_m (mg/g)	K_L (L/mg)	R^2	K_F (mg/g)	n	R^2
Cs^+	$Cu_2[Fe(CN)_6]$	155.60	0.996	0.927	62.69	6.797	0.907
	$Co_2[Fe(CN)_6]$	154.46	0.010	0.954	9.44	2.269	0.890
	$Ni_2[Fe(CN)_6]$	120.31	0.272	0.973	53.49	6.570	0.708
Sr^{2+}	$Cu_2[Fe(CN)_6]$	59.95	0.068	0.980	13.65	3.804	0.871
	$Co_2[Fe(CN)_6]$	32.73	0.008	0.961	1.79	2.233	0.953
	$Ni_2[Fe(CN)_6]$	29.17	0.009	0.989	1.58	2.204	0.965
Co^{2+}	$Cu_2[Fe(CN)_6]$	62.08	0.078	0.961	18.03	4.585	0.827
	$Ni_2[Fe(CN)_6]$	32.34	0.028	0.935	5.81	3.523	0.914

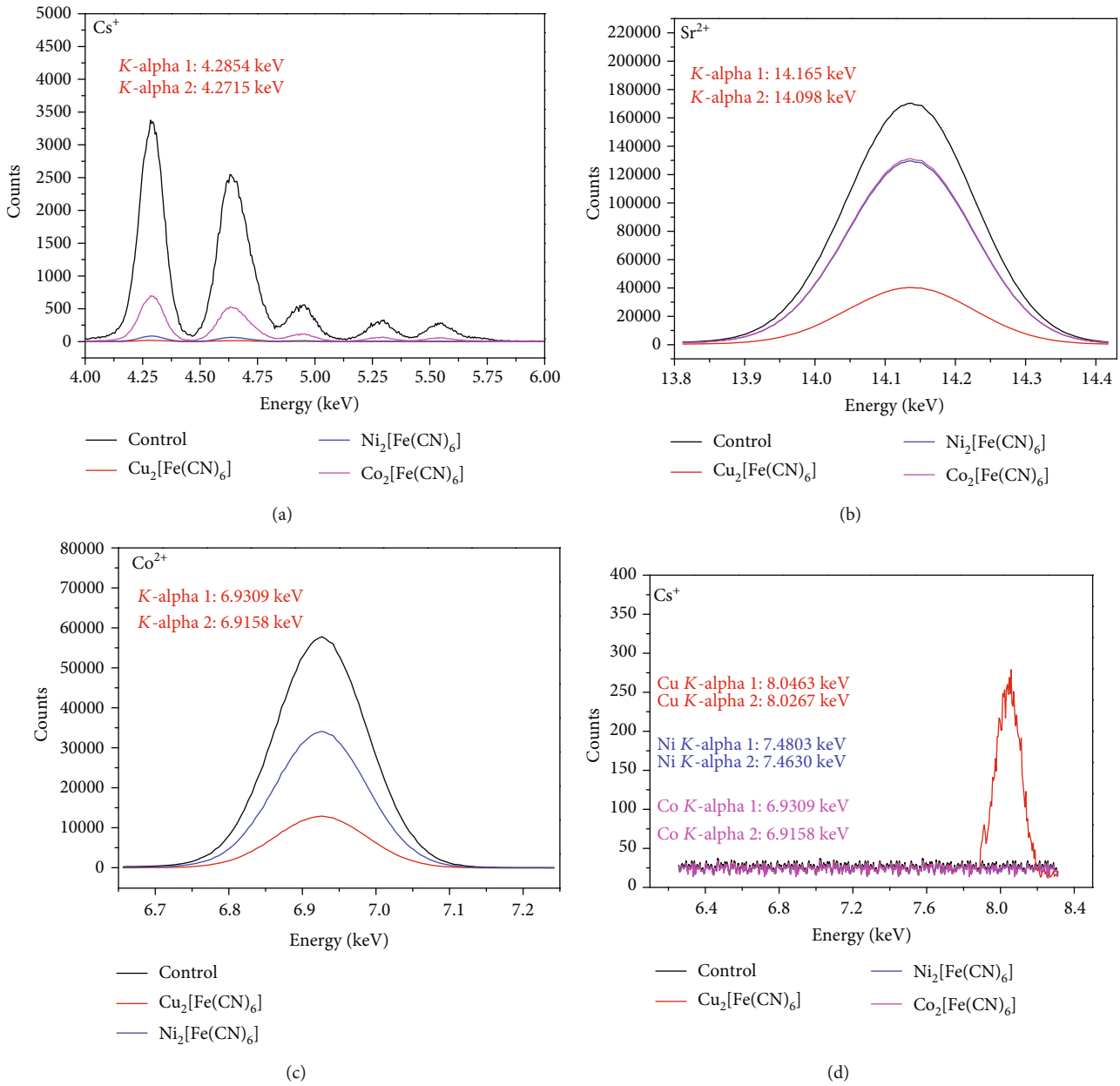

Figure 7: Continued.

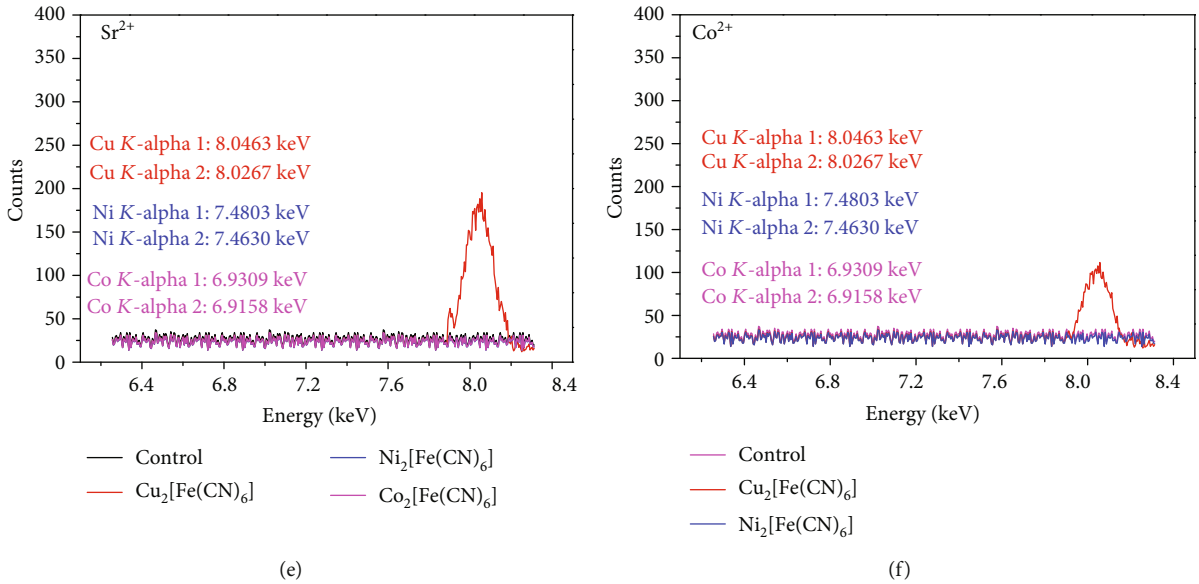

Figure 7: TXRF spectra analyzing the composition of the waste solution before and after adsorption by $A_2[Fe(CN)_6]$.

4. Conclusions

Prussian blue analogues (PBAs) with different substituted cations ($A_2[Fe(CN)_6]$ (A: Cu^{2+}, Co^{2+}, and Ni^{2+})) were successfully synthesized and applied for the removal of Cs^+, Sr^{2+}, and Co^{2+}, which are commonly found in radioactive waste. It was found that $Cu_2[Fe(CN)_6]$ exhibits the highest sorption capacity towards Cs^+, Sr^{2+}, and Co^{2+} compared with those of $Co_2[Fe(CN)_6]$ and $Ni_2[Fe(CN)_6]$. IR and TXRF data reveal that the cation-exchange ability of substituted metal within the framework of PBAs has a significant impact on the sorption performance of PBAs. In addition, the similarity between the Cs^+ size and the channel window size of PBAs leads to a preferential sorption of Cs^+ over Sr^{2+} and Co^{2+}.

Data Availability

The data has been provided by the DaLat University.

Conflicts of Interest

The authors declare that they have no conflicts of interest.

References

[1] J. Jewell, "Ready for nuclear energy?: An assessment of capacities and motivations for launching new national nuclear power programs," *Energy Policy*, vol. 39, no. 3, pp. 1041–1055, 2011.

[2] Anonymus, *Radiological Characterization of Shut Down Nuclear Reactors for Decommissioning Purposes*, Atomic Energy Agency, 1998.

[3] M. Laraia, "Introduction to nuclear decommissioning: definitions and history," in *Nuclear Decommissioning*, Elsevier, 2012.

[4] M. Xing, S. Zhuang, and J. Wang, "Efficient removal of Cs(I) from aqueous solution using graphene oxide," *Progress in Nuclear Energy*, vol. 119, article 103167, 2020.

[5] H.-M. Yang, K. S. Hwang, C. W. Park, and K.-W. Lee, "Sodium-copper hexacyanoferrate-functionalized magnetic nanoclusters for the highly efficient magnetic removal of radioactive caesium from seawater," *Water Research*, vol. 125, pp. 81–90, 2017.

[6] H.-R. Yu, J.-Q. Hu, Z. Liu et al., "Ion-recognizable hydrogels for efficient removal of cesium ions from aqueous environment," *Journal of Hazardous Materials*, vol. 323, no. Part B, pp. 632–640, 2017.

[7] A. M. Emara, F. H. El-Sweify, S. F. Abo-Zahra, A. I. Hashim, and T. E. Siyam, "Removal of Cs-137 and Sr-90 from reactor actual liquid waste samples using a new synthesized bionanocomposite-based carboxymethylcellulose," *Radiochimica Acta*, vol. 107, no. 8, pp. 695–711, 2019.

[8] G. L. Brownell and C. J. Maletskos, "Half-Life ofFe55andCo60," *Physical Review*, vol. 80, no. 6, pp. 1102-1103, 1950.

[9] M. Manolopoulou, E. Vagena, S. Stoulos, A. Ioannidou, and C. Papastefanou, "Radioiodine and radiocesium in Thessaloniki, northern Greece due to the Fukushima nuclear accident," *Journal of Environmental Radioactivity*, vol. 102, no. 8, pp. 796-797, 2011.

[10] D. Kim, A. Jo, H.-M. Yang, B.-K. Seo, K.-W. Lee, and T. S. Lee, "Colorimetric detection and removal of radioactive co ions using sodium alginate-based composite beads," *Journal of Hazardous Materials*, vol. 326, pp. 69–76, 2017.

[11] C. A. Kozlowski, J. Kozlowska, W. Pellowski, and W. Walkowiak, "Separation of cobalt-60, strontium-90, and cesium-137 radioisotopes by competitive transport across polymer inclusion membranes with organophosphorous acids," *Desalination*, vol. 198, no. 1-3, pp. 141–148, 2006.

[12] C. A. Kozlowski, W. Walkowiak, and W. Pellowski, "Sorption and transport of Cs-137, Sr-90 and co-60 radionuclides by polymer inclusion membranes," *Desalination*, vol. 242, no. 1-3, pp. 29–37, 2009.

[13] B. Ma, S. Oh, W. S. Shin, and S.-J. Choi, "Removal of Co^{2+}, Sr^{2+} and Cs^+ from aqueous solution by phosphate-modified montmorillonite (PMM)," *Desalination*, vol. 276, no. 1-3, pp. 336–346, 2011.

[14] P. Sylvester and A. Clearfield, "The removal of strontium and cesium from simulated Hanford groundwater using inorganic

ion exchange materials," *Solvent Extraction and Ion Exchange*, vol. 16, no. 6, pp. 1527–1539, 1998.

[15] A. Nilchi, H. Atashi, A. H. Javid, and R. Saberi, "Preparations of PAN-based adsorbers for separation of cesium and cobalt from radioactive wastes," *Applied Radiation and Isotopes*, vol. 65, no. 5, pp. 482–487, 2007.

[16] A. F. Seliman, Y. F. Lasheen, M. A. E. Youssief, M. M. Abo-Aly, and F. A. Shehata, "Removal of some radionuclides from contaminated solution using natural clay: bentonite," *Journal of Radioanalytical and Nuclear Chemistry*, vol. 300, no. 3, pp. 969–979, 2014.

[17] T. Kubota, S. Fukutani, T. Ohta, and Y. Mahara, "Removal of radioactive cesium, strontium, and iodine from natural waters using bentonite, zeolite, and activated carbon," *Journal of Radioanalytical and Nuclear Chemistry*, vol. 296, no. 2, pp. 981–984, 2013.

[18] N. R. de Tacconi, K. Rajeshwar, and R. O. Lezna, "Metal hexacyanoferrates: electrosynthesis, in situ characterization, and applications," *Chemistry of Materials*, vol. 15, no. 16, pp. 3046–3062, 2003.

[19] T. Vincent, C. Vincent, Y. Barré, Y. Guari, G. le Saout, and E. Guibal, "Immobilization of metal hexacyanoferrates in chitin beads for cesium sorption: synthesis and characterization," *Journal of Materials Chemistry A.*, vol. 2, no. 26, pp. 10007–10021, 2014.

[20] J. Wang, S. Zhuang, and Y. Liu, "Metal hexacyanoferrates-based adsorbents for cesium removal," *Coordination Chemistry Reviews*, vol. 374, pp. 430–438, 2018.

[21] M. S. Denton, M. J. Manos, and M. G. Kanatzidi, "Highly selective removal of cesium and strontium utilizing a new class of inorganic ion specific media–92670," *Northwestern University, Department of Chemistry*, vol. 2145, pp. 60208–63113, 2009.

[22] B. Aguila, D. Banerjee, Z. Nie, Y. Shin, S. Ma, and P. K. Thallapally, "Selective removal of cesium and strontium using porous frameworks from high level nuclear waste," *Chemical Communications*, vol. 52, no. 35, pp. 5940–5942, 2016.

[23] L. Catala and T. Mallah, "Nanoparticles of Prussian blue analogs and related coordination polymers: from information storage to biomedical applications," *Coordination Chemistry Reviews*, vol. 346, pp. 32–61, 2017.

[24] A. Nowak-Król and F. Würthner, "Progress in the synthesis of perylene bisimide dyes," *Organic Chemistry Frontiers*, vol. 6, no. 8, pp. 1272–1318, 2019.

[25] X. Liu, G.-R. Chen, D.-J. Lee et al., "Adsorption removal of cesium from drinking waters: a mini review on use of biosorbents and other adsorbents," *Bioresource Technology*, vol. 160, pp. 142–149, 2014.

[26] S. Adak, L. L. Daemen, M. Hartl, D. Williams, J. Summerhill, and H. Nakotte, "Thermal expansion in 3 *d* -metal Prussian Blue Analogs-a survey study," *Journal of Solid State Chemistry*, vol. 184, no. 11, pp. 2854–2861, 2011.

[27] S. Ayrault, B. Jimenez, E. Garnier, M. Fedoroff, D. J. Jones, and C. Loos-Neskovic, "Sorption Mechanisms of cesium on $Cu^{II}{}_{2-}Fe^{II}(CN)_6$and $Cu^{II}{}_3[Fe^{III}(CN)_6]_2$hexacyanoferrates and their relation to the crystalline structure," *Journal of solid state Chemistry*, vol. 141, no. 2, pp. 475–485, 1998.

[28] S. N. Ghosh, "Infrared spectra of the Prussian blue analogs," *Journal of Inorganic and Nuclear Chemistry*, vol. 36, no. 11, pp. 2465-2466, 1974.

[29] K. Itaya, I. Uchida, and V. D. Neff, "Electrochemistry of polynuclear transition metal cyanides: Prussian blue and its analogues," *Accounts of Chemical Research*, vol. 19, no. 6, pp. 162–168, 1986.

[30] L. Hu, P. Zhang, Q. W. Chen, J. Y. Mei, and N. Yan, "Room-temperature synthesis of Prussian blue analogue $Co_3[Co(CN)_6]_2$ porous nanostructures and their CO_2 storage properties," *RSC Advances*, vol. 1, pp. 1574–1578, 2011.

[31] S. Xu, X. Qian, and G. Li, "Size and morphology-controlled $Ni_2[Fe(CN)_6]\bullet x\ H_2O$ Prussian Blue analogue fabricated via a hydrothermal route," *Materials Research Bulletin*, vol. 43, no. 1, pp. 135–140, 2008.

[32] F. Karadas, H. el-Faki, E. Deniz, C. T. Yavuz, S. Aparicio, and M. Atilhan, "CO_2 adsorption studies on Prussian blue analogues," *Microporous and Mesoporous Materials*, vol. 162, pp. 91–97, 2012.

[33] J. Lejeune, J.-B. Brubach, P. Roy, and A. Bleuzen, "Application of the infrared spectroscopy to the structural study of Prussian blue analogues," *Comptes Rendus Chimie*, vol. 17, no. 6, pp. 534–540, 2014.

[34] X. Li, J. Liu, A. I. Rykov et al., "Excellent photo-Fenton catalysts of Fe-Co Prussian blue analogues and their reaction mechanism study," *Applied Catalysis B: Environmental*, vol. 179, pp. 196–205, 2015.

[35] J. Liu, X. Li, A. I. Rykov et al., "Zinc-modulated Fe–Co Prussian blue analogues with well-controlled morphologies for the efficient sorption of cesium," *Journal of Materials Chemistry A*, vol. 5, no. 7, pp. 3284–3292, 2017.

[36] E. R. Nightingale Jr., "Phenomenological theory of ion solvation. Effective radii of hydrated ions," *The Journal of Physical Chemistry*, vol. 63, no. 9, pp. 1381–1387, 1959.

[37] T. Sangvanich, V. Sukwarotwat, R. J. Wiacek et al., "Selective capture of cesium and thallium from natural waters and simulated wastes with copper ferrocyanide functionalized mesoporous silica," *Journal of Hazardous Materials*, vol. 182, no. 1-3, pp. 225–231, 2010.

[38] A. M. El-Kamash, "Evaluation of zeolite A for the sorptive removal of Cs^+ and Sr^{2+} ions from aqueous solutions using batch and fixed bed column operations," *Journal of Hazardous Materials*, vol. 151, no. 2-3, pp. 432–445, 2008.

[39] H. Yang, L. Sun, J. Zhai, H. Li, Y. Zhao, and H. Yu, "*In situ* controllable synthesis of magnetic Prussian blue/graphene oxide nanocomposites for removal of radioactive cesium in water," *Journal of Materials Chemistry A*, vol. 2, no. 2, pp. 326–332, 2014.

[40] M. R. Awual, T. Yaita, T. Taguchi, H. Shiwaku, S. Suzuki, and Y. Okamoto, "Selective cesium removal from radioactive liquid waste by crown ether immobilized new class conjugate adsorbent," *Journal of Hazardous Materials*, vol. 278, pp. 227–235, 2014.

[41] N. L. Torad, M. Hu, M. Imura, M. Naito, and Y. Yamauchi, "Large Cs adsorption capability of nanostructured Prussian blue particles with high accessible surface areas," *Journal of Materials Chemistry*, vol. 22, no. 35, pp. 18261–18267, 2012.

[42] M. Shamsipur and H. R. Rajabi, "Flame photometric determination of cesium ion after its preconcentration with nanoparticles imprinted with the cesium-dibenzo-24-crown-8 complex," *Microchimica Acta*, vol. 180, no. 3-4, pp. 243–252, 2013.

[43] J. Jang and D. S. Lee, "Magnetic Prussian blue nanocomposites for effective cesium removal from aqueous solution," *Industrial & Engineering Chemistry Research*, vol. 55, no. 13, pp. 3852–3860, 2016.

[44] Y. Kim, Y. K. Kim, S. Kim, D. Harbottle, and J. W. Lee, "Nanostructured potassium copper hexacyanoferrate-cellulose hydrogel for selective and rapid cesium adsorption," *Chemical Engineering Journal*, vol. 313, pp. 1042–1050, 2017.

[45] S. Naeimi and H. Faghihian, "Performance of novel adsorbent prepared by magnetic metal-organic framework (MOF) modified by potassium nickel hexacyanoferrate for removal of Cs^+ from aqueous solution," *Separation and Purification Technology*, vol. 175, pp. 255–265, 2017.

[46] Y. JIAN, W.-J. MU, N. LIU, and S.-M. PENG, "Removal of Sr^{2+} ions by ta-doped hexagonal WO_3: zeta potential measurements and adsorption mechanism determination," *Acta Physico-Chimica Sinica*, vol. 32, no. 8, pp. 2052–2058, 2016.

[47] Y. Zhu, T. Shimizu, T. Kitajima et al., "Synthesis of robust hierarchically porous zirconium phosphate monolith for efficient ion adsorption," *New Journal of Chemistry*, vol. 39, no. 4, pp. 2444–2450, 2015.

[48] L. Nagy, G. Török, N. Vajda, and I. Gerlei, *Preparation of Zirconium-Phosphate on Support Material and its Application for the Sorption of some Radioactive Ions*, Mitteilungsblatt der Chemischen Gesellschaft der Deutschen Demokratischen Republik, Beiheft, 1979.

[49] H. Tel, Y. Altaş, M. Eral, Ş. Sert, B. Çetinkaya, and S. İnan, "Preparation of ZrO_2 and ZrO_2-TiO_2 microspheres by the sol- gel method and an experimental design approach to their strontium adsorption behaviours," *Chemical Engineering Journal*, vol. 161, no. 1-2, pp. 151–160, 2010.

[50] W. Mu, Q. Yu, R. Zhang et al., "Controlled fabrication of flower-like α-zirconium phosphate for the efficient removal of radioactive strontium from acidic nuclear wastewater," *Journal of Materials Chemistry A*, vol. 5, no. 46, pp. 24388–24395, 2017.

[51] T. M. Nenoff, J. E. Miller, S. G. Thoma, and D. E. Trudell, "Highly selective inorganic crystalline ion exchange material for Sr^{2+} in acidic solutions," *Environmental Science & Technology*, vol. 30, no. 12, pp. 3630–3633, 1996.

[52] S. Sungworawongpana and S. Pengprecha, "Calcination effect of diatomite to chromate adsorption," *Procedia Engineering*, vol. 8, pp. 53–57, 2011.

[53] H. Faghihian, M. Iravani, M. Moayed, and M. Ghannadi-Maragheh, "Preparation of a novel PAN-zeolite nanocomposite for removal of Cs^+ and Sr^{2+} from aqueous solutions: Kinetic, equilibrium, and thermodynamic studies," *Chemical Engineering Journal*, vol. 222, pp. 41–48, 2013.

[54] B. Liu, W. Mu, X. Xie et al., "Enhancing the adsorption capacity of Sr^{2+} and Cs^+ onto hexagonal tungsten oxide by doped niobium," *RSC Advances*, vol. 5, no. 20, pp. 15603–15611, 2015.

[55] W. Mu, S. du, Q. Yu et al., "Highly efficient removal of radioactive ^{90}Sr based on sulfonic acid-functionalized α-zirconium phosphate nanosheets," *Chemical Engineering Journal*, vol. 361, pp. 538–546, 2019.

[56] M. U. Ibezim-Ezeani, F. A. Okoye, and O. Akaranta, "Studies on the ion exchange properties of modified and unmodified orange mesocarp extract in aqueous solution," *International Archive of Applied Science & Technolgy*, vol. 1, pp. 33–40, 2010.

[57] W. Guo, R. Chen, Y. Liu et al., "Preparation of ion-imprinted mesoporous silica SBA-15 functionalized with triglycine for selective adsorption of Co(II)," *Colloids and Surfaces A: Physicochemical and Engineering Aspects*, vol. 436, pp. 693–703, 2013.

[58] A. Rámila, B. Muñoz, J. Pérez-Pariente, and M. Vallet-Regí, "Mesoporous MCM-41 as drug host system," *Journal of Sol-Gel Science and Technology*, vol. 26, no. 1/3, pp. 1199–1202, 2003.

[59] J. Andersson, J. Rosenholm, S. Areva, and M. Lindén, "Influences of material characteristics on ibuprofen drug loading and release profiles from ordered micro- and mesoporous silica matrices," *Chemistry of Materials*, vol. 16, no. 21, pp. 4160–4167, 2004.

[60] S. Tizro and H. Baseri, "Removal of cobalt ions from contaminated water using magnetite based nanocomposites: effects of various parameters on the removal efficiency," *Journal of Water and Environmental Nanotechnology*, vol. 2, no. 3, pp. 174–185, 2017.

[61] F. Fang, L. Kong, J. Huang et al., "Removal of cobalt ions from aqueous solution by an amination graphene oxide nanocomposite," *Journal of Hazardous Materials*, vol. 270, pp. 1–10, 2014.

Hindawi
Journal of Nanomaterials
Volume 2021, Article ID 5586622, 12 pages
https://doi.org/10.1155/2021/5586622

Research Article

On the Optical Stark Effect of Excitons in InGaAs Prolate Ellipsoidal Quantum Dots

Le Thi Ngoc Bao,[1] **Duong Dinh Phuoc**,[2] **Le Thi Dieu Hien**,[1,2] **and Dinh Nhu Thao**[2]

[1]*Hue University of Sciences, Hue University, 77 Nguyen Hue Street, Hue City, Vietnam*
[2]*Hue University of Education, Hue University, 34 Le Loi Street, Hue City, Vietnam*

Correspondence should be addressed to Le Thi Ngoc Bao; ltnbao@hueuni.edu.vn and Dinh Nhu Thao; dnthao@hueuni.edu.vn

Received 8 January 2021; Revised 22 February 2021; Accepted 27 February 2021; Published 24 March 2021

Academic Editor: Mai Duy Hien

In this paper, we study the exciton absorption spectra in InGaAs prolate ellipsoidal quantum dots when a strong pump laser resonant with electron quantized levels is active. Our obtained results by renormalized wavefunction theory show that, under suitable conditions, the initial exciton absorption peak is split into two new peaks as the evidence of the existence of the three-level optical Stark effect of excitons. We have suggested an explanation of the origin of the effect as well as investigating the effect of pump field energy, size, and geometric shape of the quantum dots on effect characteristics. The comparison with the results obtained in the spherical quantum dots implies the important role of geometric shape of the quantum structures when we examine this effect.

1. Introduction

One of the low dimensional structures recently attracting much interest from researchers is the semiconductor quantum dots [1–4], which are structures that confine carriers in all three spatial dimensions. Quantum dot structures have many interesting applications, such as producing artificial atoms and molecules [5], single-electron transistors [6], and quantum dot lasers [7]. In recent years, there has seen many studies on optical properties in quantum dots with different shapes, for example, cylindrical, cubic, and spherical quantum dots [8–12]. These studies show that optical properties of quantum dots are highly dependent on external fields and size of quantum dots. It is worth mentioning that the shape of quantum dots also makes a huge difference to the optical properties of quantum dots [13]. Therefore, quantum dots are expected to create even more breakthrough applications in the future.

The optical Stark effect of excitons is one of the unique optical properties of bulk materials in general and low dimensional structures in particular. The optical Stark effect of excitons occurs due to the coupling of the two exciton states under the excitation of near resonant beam [14]. Scientists divided this effect into two types as follows. First, two-level optical Stark effect arises when a pump laser of strong intensity couples exciton ground state and an exciton excited state in the quantum system [14, 15]. Second, three-level optical Stark effect is the result of a couple of two excited states of exciton under the control of a pump laser beam of lower intensity [16, 17]. The latter has received more attention from researchers because they are more likely to occur and have better potential application. In general, optical Stark effect has potential applications in manufacturing ultrafast optical switching of future optical devices [11, 18], optical modulators [19], mesoporous hybrid multifunctional system [20], and optically controlled field-effect transistors [21]. The optical Stark effect of excitons in quantum dots has also been of interest in both experimental and theoretical research [11, 22–24] but mainly for spherical quantum dots. The investigation of this effect in a more complicated and more practical shaped quantum dot structures, such as ellipsoidal quantum dots, has not been carried out in detail.

In this paper, we study theoretically the three-level optical Stark effect of excitons in InGaAs prolate ellipsoidal

quantum dots. We applied the renormalized wavefunction method to investigate the dependence of the exciton absorption spectra on the external fields, size, and shape of quantum dot, when there exists the optical Stark effect of excitons. In addition, the effects of the pump laser energy, size, and geometric shape of quantum dots on the behavior of the effect are also clarified. The article includes the following main sections: Section 2 presents model and theory, Section 3 presents the main results and discussion, and conclusions are presented in Section 4.

2. Model and Theory

2.1. Wavefunctions and Energy Levels of Electron and Hole in Prolate Ellipsoidal Quantum Dots. In this section, we present the wavefunctions and energy levels of electron and hole in prolate ellipsoidal quantum dots. We consider a prolate ellipsoidal quantum dot with rotational symmetry around the z axis, with a and c are its semi-axes along the xOy plane and stay in the z-direction, respectively, in which x, y, and z are the coordinates in Cartesian coordinate system with its origin at the ellipsoidal symmetry center (Figure 1). Simply put, we assume that prolate ellipsoidal quantum dot is set under the effect of an infinite potential of the form [25–29]

$$U\left(\vec{r}\right) = \begin{cases} 0, & \text{where} \quad 0 < S\left(\vec{r}_i\right) < 1, \\ \infty, & \text{where} \quad S\left(\vec{r}_i\right) \geq 1, \end{cases} \tag{1}$$

where $S(\vec{r}_i)$ depends on parameters a and c which are semi-axes of the ellipsoidal quantum dot, as follows

$$S\left(\vec{r}_i\right) = \frac{x^2 + y^2}{a^2} + \frac{z^2}{c^2}, \tag{2}$$

with $c > a$, and the surface of the prolate ellipsoidal quantum dot has the shape as in Figure 1.

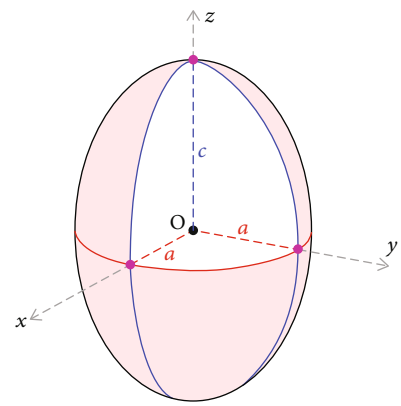

Figure 1: Illustration of a prolate ellipsoidal quantum dot [30].

To conveniently examine the prolate ellipsoidal quantum dots, in this study, we use the prolate spheroidal coordinates

$$\begin{cases} x = f\sqrt{\left(\xi^2 - 1\right)\left(1 - \eta^2\right)}\cos\varphi, \\ y = f\sqrt{\left(\xi^2 - 1\right)\left(1 - \eta^2\right)}\sin\varphi, \\ z = f\xi\eta, \end{cases} \tag{3}$$

where $1 \leq \xi < +\infty$, $-1 \leq \eta \leq +1$, and f is the parameter. The envelope wavefunctions of electron (hole) in prolate ellipsoidal quantum dot then has the following form [25–29]

$$\Psi\left(\vec{r}\right) = \Psi_{nlm}^{e,h}(\xi, \eta, \varphi) = A_{nlm} J_{lm}^{(1)}(h, \xi) S_{lm}^{(1)}(h, \eta) e^{im\varphi}, \tag{4}$$

where $n = 1, 2, 3, \cdots$, $l = 0, 1, 2, 3, \cdots$, $m = -l, \cdots, 0, \cdots, +l$, $J_{lm}^{(1)}(h, \xi)$, and $S_{lm}^{(1)}(h, \eta)$ are prolate radial and prolate angular spheroidal functions of the first kind, respectively, and A_{nlm} is the normalization coefficient

$$A_{nlm} = \sqrt{\frac{\chi^3}{2\pi c^3 e^3 \int_1^{\bar{\xi}} \int_{-1}^{+1} \left(\xi^2 + \eta^2\right) J_{lm}^{(1)*}(h, \xi) S_{lm}^{(1)*}(h, \eta) J_{lm}^{(1)}(h, \xi) S_{lm}^{(1)}(h, \eta) d\xi d\eta}}, \tag{5}$$

where the ellipsoidal aspect ratio is defined as

$$\chi = \frac{c}{a}, \tag{6}$$

and e is the ellipsoidal eccentricity

$$e = \sqrt{1 - \frac{1}{\chi^2}}. \tag{7}$$

The quantized energy levels of electron (hole) are determined as follows

$$\varepsilon_{nlm}^{e,h} = \frac{\hbar^2 k_{nlm}}{2m_{e,h}^*}, \tag{8}$$

where $m_{e,h}^*$ is the effective mass of electron (hole) and

$$h = f\sqrt{k_{nlm}}. \tag{9}$$

The values of h are determined from the boundary condition

$$J_{lm}^{(1)}\left(h, \bar{\xi}\right) = 0, \tag{10}$$

where

$$\bar{\xi} = \frac{1}{\sqrt{1-(1/\chi^2)}} = \frac{1}{e}, \tag{11}$$

and

$$f = \frac{c}{\bar{\xi}} = c \cdot e. \tag{12}$$

The values of the parameter h depend on the values of the indices n, l, and m. When $h \to 0$ (or $f \to 0$), the prolate ellipsoidal quantum dot becomes the spherical quantum dot; therefore, $\chi \to 1$. In that condition, the envelope wavefunction of electron (hole) in quantum dot looks like the following form [31]

$$\Psi_{nlm}^{S(e,h)}(r,\theta,\varphi) = \sqrt{\frac{2}{R^3}} \frac{j_l(\chi_{nl}(r/R))}{j_{l+1}(\chi_{nl})} Y_{lm}(\theta,\varphi), \tag{13}$$

where $Y_{lm}(\theta,\varphi)$ is the spherical harmonic function, $j_l(r)$ is the spherical Bessel function of order l (l is a non-negative integer, $l = 0, 1, 2 \cdots$), and χ_{nl} is its nth zero. The expression of the quantized energy levels of electron (hole) corresponding to wavefunctions (13) is

$$E_{nl}^{S(e,h)} = \frac{\hbar^2 \chi_{nl}^2}{2m_{e,h}^* R^2}. \tag{14}$$

In Eqs. (13) and (14), the indices n, l, and m are principle, orbital, and azimuthal quantum numbers, respectively. However, for ellipsoidal quantum dots, since its spherical symmetry no longer exists, so the index l in the wavefunction and energy expressions of the particle in Eqs. (4) and (8) no longer represent the orbital quantum numbers. However, in this paper, we still use the set of indices n, l, and m in Eqs. (4) and (8) in order to have a one-to-one correspondence between prolate ellipsoidal and spherical quantum dot when $\chi \to 1$ [26]. The volume of prolate ellipsoidal quantum dot of semi-axes a and c is determined as follows [32]

$$V = \frac{4}{3}\pi a^2 c = \frac{4}{3}\pi a^3 \chi = \frac{4}{3}\pi R_S^3, \tag{15}$$

where $R_s = a\sqrt[3]{\chi}$ is the radius of a sphere with the same volume.

In the effective mass approximation and envelope-function theory, the total wavefunction of electrons (holes) in a prolate ellipsoidal quantum dot with an infinite potential has the following form

$$\Lambda_{nlm}^{e,h}\left(\vec{r}\right) = u_{c,v}\left(\vec{r}\right)\Psi_{nlm}^{e,h}\left(\vec{r}\right), \tag{16}$$

where $\vec{r} = (\xi, \eta, \varphi)$ and $u_{c,v}(\vec{r})$ are the periodic Bloch functions in conduction and valence band.

As we set the zero energy at the top of the valence band, the expression of the quantized energy levels of electron and hole is then determined as follows

$$E_{nlm}^e = E_g + \frac{\hbar^2 k_{nlm}}{2m_e^*}, \tag{17}$$

and

$$E_{nlm}^h = \frac{\hbar^2 k_{nlm}}{2m_h^*}, \tag{18}$$

where E_g is the bandgap of the semiconductor.

2.2. Intersubband Optical Transition. In this paper, we study the three-level optical Stark effect of excitons in prolate ellipsoidal quantum dots. Thus, we need to examine a three-level system of exciton and thus result in a three-level diagram of electron and hole, which consist of the lowest level E_{100}^h corresponding to the first quantized state of the hole in the valence band $|0\rangle$, and the other two levels have the energy of E_{100}^e and E_{110}^e corresponding to two lowest quantized states of the electrons in the conduction band $|1\rangle$ and $|2\rangle$ as illustrated in Figure 2.

When the electromagnetic field is not so strong, we can omit higher-order term, and using some gauges and approximations, the electron-electromagnetic field interaction Hamiltonian then can be written as follows [31, 33]

$$\hat{H}_{\text{int}} = -\frac{q}{m_0}\frac{A_x e^{-i\omega_x t}}{i\omega_x}\vec{n}\cdot\hat{\vec{p}} \equiv \hat{V}_x e^{-i\omega_x t}, \tag{19}$$

in which we set

$$\hat{V}_x = -\frac{q}{m_0}\frac{A_x}{i\omega_x}\vec{n}\cdot\hat{\vec{p}}, \tag{20}$$

where q, m_0, and $\vec{p}$ are the bare mass, the charge, and the momentum of the particle, respectively; A_x and ω_x are, respectively, magnitude and frequency of the laser, with x clarifying if that is a pump or probe laser; and $\vec{n}$ is the unit vector pointing to the wave propagation direction.

In order to investigate the three-level optical Stark effect of excitons in prolate ellipsoidal quantum dots, we need to examine two optical transitions, which are the intersubband transition between electron levels under a strong pump laser and the interband transition between two lowest levels of hole and electron under a probe laser. In this section, we examine the matrix element for the optical intersubband transition between electron levels E_{100}^e and E_{110}^e under the effect of pump laser. The two quantized states of electrons are defined as follows

$$\begin{cases} |1\rangle \equiv \Lambda_{100}^e\left(\vec{r}\right) = u_c\left(\vec{r}\right)\Psi_{100}^e\left(\vec{r}\right), \\ |2\rangle \equiv \Lambda_{110}^e\left(\vec{r}\right) = u_c\left(\vec{r}\right)\Psi_{110}^e\left(\vec{r}\right). \end{cases} \tag{21}$$

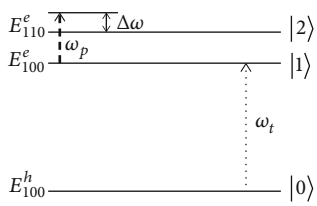

Figure 2: Three-level energy diagram of electron and hole. E^h_{100} is the lowest energy level of the hole corresponding to state $|0\rangle$; E^e_{100} and E^e_{110} are the two lowest energy levels of electrons corresponding to states $|1\rangle$ and $|2\rangle$; ω_p and ω_t are frequency of the pump or probe laser, respectively; $\Delta\omega$ is pump laser detuning.

The matrix element for an intersubband transition between two electron quantized levels defined as follows

$$v_{21} = \langle 2 \mid \widehat{H}_{\text{int}} \mid 1 \rangle = \langle 2 \mid \widehat{V}_p \mid 1 \rangle e^{-i\omega_p t} \equiv V_{21} e^{-i\omega_p t}, \tag{22}$$

in which

$$V_{21} = -\frac{qA_p}{m_0 i\omega_p} \langle 2 \mid \widehat{V} \mid 1 \rangle = -\frac{qA_p}{m_0 i\omega_p} \left\langle \Psi^e_{110}\left(\vec{r}\right) \mid \vec{n}\,\widehat{\vec{p}} \mid \Psi^e_{100}\left(\vec{r}\right) \right\rangle, \tag{23}$$

where A_p and ω_p are the magnitude and frequency of the pump laser. Equation (23) can be rewritten as follows

$$V_{21} = \frac{qA_p}{m_0 i\omega_p} \frac{m^*_e}{i\hbar} (E^e_{110} - E^e_{100}) \left\langle \Psi^e_{110}\left(\vec{r}\right) \mid \vec{n}\,\vec{r} \mid \Psi^e_{100}\left(\vec{r}\right) \right\rangle. \tag{24}$$

From Eq. (4), we have

$$\begin{cases} \Psi^e_{110}\left(\vec{r}\right) = A_{110} J^{(1)}_{10}(h,\xi) S^{(1)}_{10}(h,\eta) e^{i0\varphi} = A_{110} J^{(1)}_{10}(h,\xi) S^{(1)}_{10}(h,\eta), \\ \Psi^e_{100}\left(\vec{r}\right) = A_{100} J^{(1)}_{00}(h,\xi) S^{(1)}_{00}(h,\eta) e^{i0\varphi} = A_{100} J^{(1)}_{00}(h,\xi) S^{(1)}_{00}(h,\eta). \end{cases} \tag{25}$$

Choosing polarization vector along the z axis, while replacing Eq. (25) into Eq. (24), and performing some additional calculations, we have the expression of V_{21} as follows

$$V_{21} = \frac{qA_p}{m_0 i\omega_p} \frac{m^*_e}{i\hbar} A^*_{110} A_{100} (E^e_{110} - E^e_{100}) 2\pi f^4 \times \\ \times \int_1^{\bar{\xi}} \int_{-1}^{+1} \xi\eta\left(\xi^2 - \eta^2\right) J^{(1)*}_{10}(h,\xi) S^{(1)*}_{10}(h,\eta) J^{(1)}_{00}(h,\xi) S^{(1)}_{00}(h,\eta) d\xi d\eta. \tag{26}$$

From there, we have the expression of matrix element for an intersubband transition between two electron quantized levels as follows

$$v_{21} = V_{21} e^{-i\omega_p t} = \frac{qA_p e^{-i\omega_p t}}{m_0 i\omega_p} \frac{m^*_e}{i\hbar} A^*_{110} A_{100} (E^e_{110} - E^e_{100}) 2\pi f^4 \times \\ \times \int_1^{\bar{\xi}} \int_{-1}^{+1} \xi\eta\left(\xi^2 - \eta^2\right) J^{(1)*}_{10}(h,\xi) S^{(1)*}_{10}(h,\eta) J^{(1)}_{00}(h,\xi) S^{(1)}_{00}(h,\eta) d\xi d\eta. \tag{27}$$

2.3. The Exciton Absorption Spectra

2.3.1. Without the Present of the Pump Laser. According to the selection rules for interband transitions in quantum dots, interband transitions only occur within the lowest energy levels of hole and electron. First, we consider the condition in which pump laser is absent; the matrix element for an interband transition of exciton only exists an allowed transition between two levels E^h_{100} and E^e_{100}. This is an interband transition with the initial and final states described as follows

$$\begin{cases} |0\rangle = u_v\left(\vec{r}\right) \Psi^h_{100}\left(\vec{r}\right) e^{-(i/\hbar)E^h_{100} t}, \\ |1\rangle = u_c\left(\vec{r}\right) \Psi^e_{100}\left(\vec{r}\right) e^{-(i/\hbar)E^e_{100} t}. \end{cases} \tag{28}$$

Under the effects of probe laser, matrix element for an interband transition between two quantized levels of electron and hole is

$$T_{10} = \langle 1 \mid \widehat{H}_{\text{int}} \mid 0 \rangle. \tag{29}$$

Replacing $\widehat{H}_{\text{int}}$ from Eq. (19) into Eq. (29), we have the expression of matrix element for an interband transition without pump laser effect as follows

$$T_{10} = -\frac{eA_t p_{cv}}{m_0 i\omega_t} e^{i/\hbar\left(E^e_{100} - E^h_{100} - \hbar\omega_t\right)t}, \tag{30}$$

where A_t and ω_t are the magnitude and frequency of the probe laser, respectively; p_{cv} is the polarization matrix element between conduction and valence band and has the form of

$$p_{cv} = \left\langle u_c\left(\vec{r}\right) \mid \vec{n}\,\widehat{\vec{p}} \mid u_v\left(\vec{r}\right) \right\rangle. \tag{31}$$

The absorption spectra of the excitons are defined using the expression of the transition rates (or the absorption probabilities in a unit of time). According to Fermi's golden rule, the expression of transition rates is defined as [34]

$$\mathrm{W} = \frac{2\pi}{\hbar} \left|T_{fi}\right|^2 \delta\left(E_f - E_i - \hbar\omega_t\right), \tag{32}$$

where T_{fi} is the matrix element for interband transition between initial i and final f states and E_i and E_f are the corresponding energy levels of initial i and final f states.

From Eqs. (30) and (32), we get the expression of transition rates as follows

$$W_0 = \frac{2\pi}{\hbar}\left(\frac{qA_t p_{cv}}{m_0\omega_t}\right)^2 \delta\left(E^e_{100} - E^h_{100} - \hbar\omega_t\right). \quad (33)$$

Applying "Lorentz line" function [35]

$$\delta(x) = \frac{1}{\pi}\cdot\frac{\Gamma}{x^2+\Gamma^2}, \quad (34)$$

Eq. (33) can be rewritten as follows

$$W_0 = \frac{2}{\hbar}\left(\frac{qA_t p_{cv}}{m_0\omega_t}\right)^2 \frac{\Gamma}{\left(E^{\text{dot}}_g - \hbar\omega_t\right)^2 + \Gamma^2}, \quad (35)$$

where

$$E^{\text{dot}}_g = E^e_{100} - E^h_{100}, \quad (36)$$

and Γ is the phenomenological linewidth of absorption peak.

2.3.2. With the Presence of the Pump Laser. Under the effect of a strong pump laser resonating with the energy distance between the two quantized levels of the electron, the wavefunctions of electron are renormalized by the pump laser effect and can be described as

$$\Lambda^e_{\text{mix}}\left(\vec{r}, t\right) = \sum_{l=0}^{1} c_l(t)\Lambda^e_{1l0}\left(\vec{r}\right)\exp\left(-\frac{i}{\hbar}E^e_{1l0}t\right), \quad (37)$$

where coefficients $c_l(t)$ $(l = \overline{0,1})$ are determined through the time-dependent Schrodinger equation and have the following form [12]

$$\begin{cases} c_0(t) = \dfrac{1}{2\Omega_R}\left(\alpha_1 e^{i\alpha_2 t} + \alpha_2 e^{-i\alpha_1 t}\right), \\ c_1(t) = -\dfrac{V_{21}}{2\Omega_R}\left(e^{i\alpha_1 t} - e^{-i\alpha_2 t}\right), \end{cases} \quad (38)$$

where

$$\hbar\omega_{21} = E^e_{110} - E^e_{100}, \quad (39)$$

and

$$\begin{cases} \alpha_1 = \Omega_R - \dfrac{\Delta\omega}{2}, \\ \alpha_2 = \Omega_R - \dfrac{\Delta\omega}{2}, \\ \Omega_R = \left[\left(\dfrac{\Delta\omega}{2}\right)^2 + \dfrac{|V_{21}|^2}{\hbar^2}\right]^{1/2}, \\ \Delta\omega = \omega_p - \omega_{21}. \end{cases} \quad (40)$$

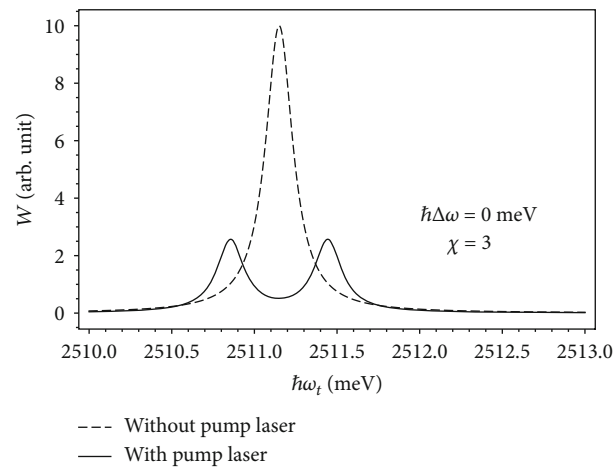

Figure 3: The dependence of transition rate on the photon energy of probe laser in a prolate ellipsoidal quantum dot with the ellipsoidal aspect ratio $\chi = 3$ (corresponding to the length of the semi-major axis $c = 75$ Å) in two cases: in the absence of the pump laser (dashed line) and in the presence of the pump laser (solid line) with the detuning $\hbar\Delta\omega = 0$ meV.

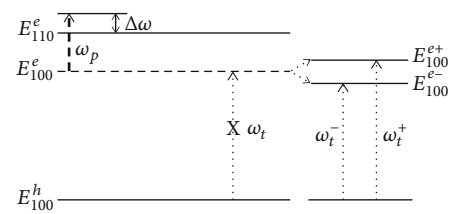

Figure 4: The scheme of splitting of the energy levels of electrons under the effect of a strong pump laser resonant with two electron levels.

Replacing coefficients $c_0(t)$ and $c_1(t)$ from Eq. (38) into Eq. (37), we get the expression of the renormalized wavefunction of electron under pump laser effect as follows

$$\Lambda^e_{\text{mix}}\left(\vec{r}, t\right) = \frac{1}{2\Omega_R}\left(\alpha_1 e^{i\alpha_2 t} + \alpha_2 e^{-i\alpha_1 t}\right)e^{-(i/\hbar)E^e_{100}t}\Lambda^e_{100}\left(\vec{r}\right) - \frac{V_{21}}{2\hbar\Omega_R}\left(e^{i\alpha_1 t} - e^{-i\alpha_2 t}\right)e^{-(i/\hbar)E^e_{110}t}\Lambda^e_{110}\left(\vec{r}\right), \quad (41)$$

where V_{21} is the quantity given in Eq. (26). Then, Eq. (41) can be rewritten as follows

$$\Lambda^e_{\text{mix}}\left(\vec{r}, t\right) = \frac{1}{2\Omega_R}\left(\alpha_1 e^{-(i/\hbar)(E^e_{100}-\hbar\alpha_2)t} + \alpha_2 e^{-(i/\hbar)(E^e_{100}+\hbar\alpha_1)t}\right)\Lambda^e_{100}\left(\vec{r}\right) - \frac{V_{21}}{2\hbar\Omega_R}\left(e^{-(i/\hbar)(E^e_{110}-\hbar\alpha_1)t} - e^{-(i/\hbar)(E^e_{110}+\hbar\alpha_2)t}\right)\Lambda^e_{110}\left(\vec{r}\right). \quad (42)$$

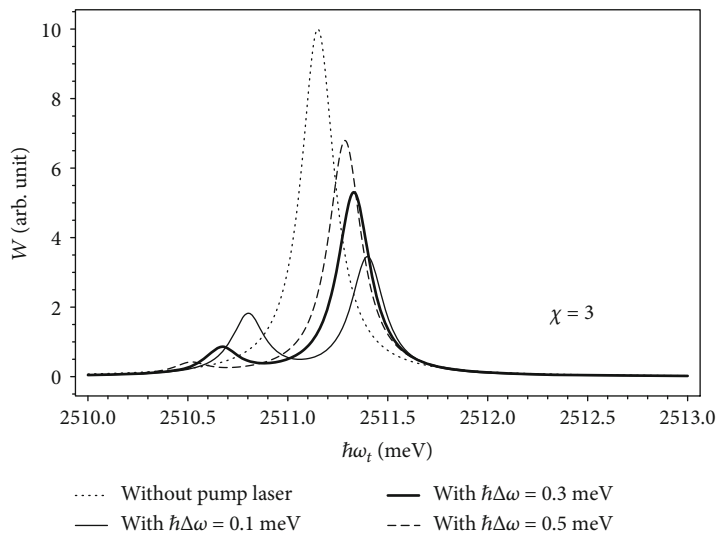

Figure 5: The dependence of transition rate on the photon energy of probe laser in a prolate ellipsoidal quantum dot with the value of the ellipsoidal aspect ratio is $\chi = 3$ without the pump laser effect (dotted line) and with the pump laser effect, with different detunings $\hbar\Delta\omega = 0.1$ meV (solid line), $\hbar\Delta\omega = 0.3$ meV (thick solid line), and $\hbar\Delta\omega = 0.5$ meV (dashed line).

Therefore, the energy spectrum of electron corresponding to wavefunction given in Eq. (42) is expanded to four levels as follows

$$\begin{cases} E_{100}^{e+} = E_{100}^{e} + \hbar\alpha_1, \\ E_{100}^{e-} = E_{100}^{e} - \hbar\alpha_2, \end{cases} \tag{43}$$

and

$$\begin{cases} E_{110}^{e+} = E_{110}^{e} + \hbar\alpha_2, \\ E_{110}^{e-} = E_{110}^{e} - \hbar\alpha_1. \end{cases} \tag{44}$$

From Eqs. (43) and (44), we can rewrite the renormalized wavefunctions of the electron under the pump laser effect in Eq. (42) as follows

$$\begin{aligned} \Lambda_{\text{mix}}^{e}\left(\vec{r}, t\right) = {} & \frac{1}{2\Omega_R}\left(\alpha_1 e^{-(i/\hbar)E_{100}^{e-}t} + \alpha_2 e^{-(i/\hbar)E_{100}^{e+}t}\right)\Lambda_{100}^{e}\left(\vec{r}\right) \\ & - \frac{V_{21}}{2\hbar\Omega_R}\left(e^{-(i/\hbar)E_{110}^{e-}t} - e^{-(i/\hbar)E_{110}^{e+}t}\right)\Lambda_{110}^{e}\left(\vec{r}\right). \end{aligned} \tag{45}$$

In order to define the three-level optical Stark effect of exciton in prolate ellipsoidal quantum dots, the pump laser intensity must be significantly stronger than the probe laser. At the same time, the detuning of the pump laser to the electron levels must be much smaller than the frequency of the pump laser and band gap of active material in quantum dots

$$\Delta\omega \ll \omega_p \ll \frac{E_g}{\hbar}. \tag{46}$$

The matrix element for the interband transition between the hole state and the electron superposition state specified by the renormalized wavefunction under the effect of the probe laser when the system is irradiated by a strong resonant pump laser is defined as follows

$$\begin{aligned} T_{\text{mix},0} &= \left\langle \Lambda_{\text{mix}}^{e}\left(\vec{r}, t\right) \mid \widehat{H}_{\text{int}} \mid \Lambda_{100}^{h}\left(\vec{r}, t\right)\right\rangle \\ &= -\frac{qA_t e^{-i\omega_t t}}{m_0 i\omega_t}\left\langle \Lambda_{\text{mix}}^{e}\left(\vec{r}, t\right) \mid \widehat{\vec{n}\,\vec{p}} \mid \Lambda_{100}^{h}\left(\vec{r}, t\right)\right\rangle, \end{aligned} \tag{47}$$

or

$$T_{\text{mix},0} = -\frac{qA_t p_{cv}}{m_0 i\omega_t}\left[\frac{1}{2\Omega_R}\left(\alpha_1 e^{i\alpha_2 t} + \alpha_2 e^{-i\alpha_1 t}\right)\right]^{*} e^{(i/\hbar)\left(E_g^{\text{dot}} - \hbar\omega_t\right)t}. \tag{48}$$

Next, we perform the similar calculation as in the previous section for the pump laser inactivity; the expression of transition rate for interband transition between the hole state and the electron superposition state when the system is irradiated by a resonant pump laser has following formula

$$\begin{aligned} \text{W} = {} & \frac{2\pi}{\hbar}\left(\frac{eA_t p_{cv}}{m_0\omega_t}\right)^2 \left[\left(\frac{\alpha_1}{2\Omega_R}\right)^2 \delta\left(E_g^{\text{dot}} - \hbar\omega_t - \hbar\alpha_2\right)\right. \\ & \left. + \left(\frac{\alpha_2}{2\Omega_R}\right)^2 \delta\left(E_g^{\text{dot}} - \hbar\omega_t + \hbar\alpha_1\right)\right]. \end{aligned} \tag{49}$$

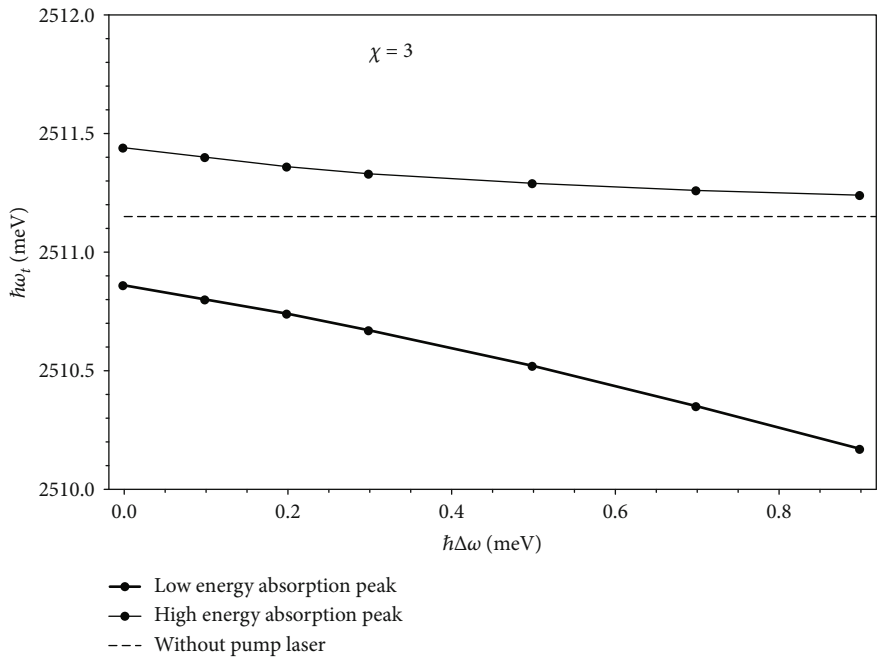

Figure 6: The dependence of the photon energy of probe laser on the pump laser detuning of low-energy absorption peak (thick solid line), high-energy absorption peak (solid line), and original absorption peak in the absence of the pump laser (dashed line) in prolate ellipsoidal quantum dots, when $\chi = 3$ (corresponding to the length of the semi-major axis $c = 75$ Å).

Applying "Lorentz line" function, the approximated form of the transition rate with pump laser effect can be rewritten as

$$W = \frac{2}{\hbar}\left(\frac{eA_t p_{cv}}{m_0\omega_t}\right)^2 \left[\left(\frac{\alpha_1}{2\Omega_R}\right)^2 \frac{\Gamma}{\left(E_g^{\text{dot}} - \hbar\omega_t - \hbar\alpha_2\right)^2 + \Gamma^2} + \left(\frac{\alpha_2}{2\Omega_R}\right)^2 \frac{\Gamma}{\left(E_g^{\text{dot}} - \hbar\omega_t + \hbar\alpha_1\right)^2 + \Gamma^2}\right]. \tag{50}$$

3. Results and Discussion

To clarify the results obtained above, in this section, we perform the calculation for transition rate in $In_{0.53}Ga_{0.47}As/In_{0.52}Al_{0.48}As$ prolate ellipsoidal quantum dots in two cases: without and with the pump laser. The parameters used in the calculation are as follows. The effective mass of electron and hole in the dot material $In_{0.53}Ga_{0.47}As$ are $m_e = 0.042\, m_0$ and $m_h = 0.052 m_0$; the band gap of the dot material is $E_g = 750$ meV [36]; the pump laser amplitude was chosen to be $A_p = 4 \times 10^4$ V/cm, and the linewidth was chosen as the $\Gamma = 0.1$ meV. In addition, since this paper examines prolate ellipsoidal quantum dot structure. This is a low dimensional structure, so the length of the major axis $2c$ and minor axis $2a$ must be selected to be smaller the bulk exciton Bohr radius in the dot material $In_{0.53}Ga_{0.47}As$. Thus, we have selected the length of the semi-major axis as $a = 25$ Å to do the calculation in this section, while the length of the semi-minor axis will depend on the selected value of χ ($c = \chi \cdot a$).

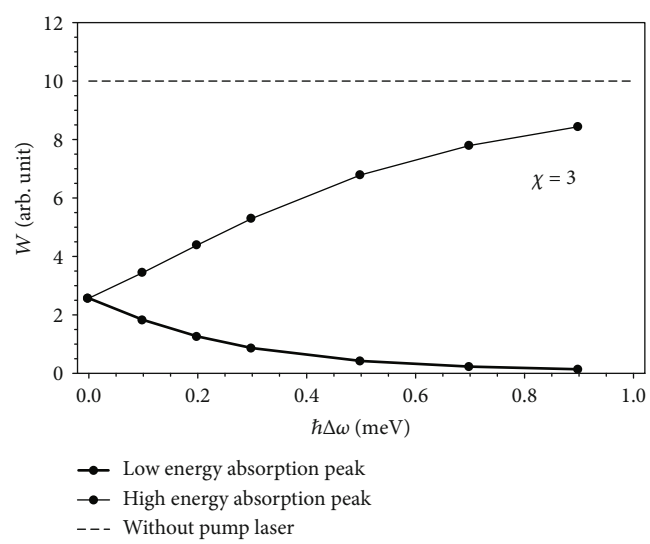

Figure 7: The dependence of transition rate on the pump laser detuning of low-energy absorption peak (thick solid line), high-energy absorption peak (solid line), and original absorption peak in the absence of the pump laser (dashed line) in prolate ellipsoidal quantum dot when the ellipsoidal aspect ratio $\chi = 3$ (corresponding to the length of the semi-major axis $c = 75$ Å).

In Figure 3, we depict the dependence of transition rate on the photon energy of the probe laser in a prolate ellipsoidal quantum dot with the value of the ellipsoidal aspect ratio of $\chi = 3$ in two conditions: without the pump laser effect (dashed line) and with the pump laser effect (solid line).

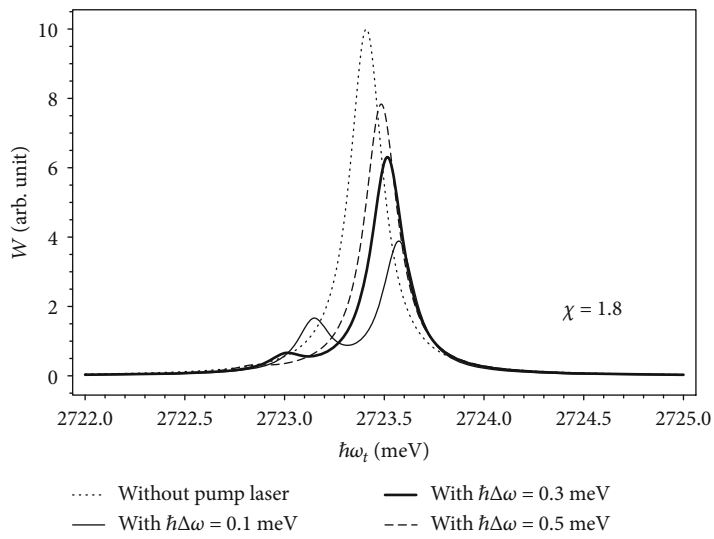

Figure 8: The dependence of transition rate on the photon energy of probe laser in a prolate ellipsoidal quantum dot with the ellipsoidal aspect ratio $\chi = 1.8$ (corresponding to the length of the semi-major axis of $c = 45$ Å) in the absence of the pump laser (dotted line) and in the presence of the pump laser with different detunings $\hbar\Delta\omega = 0.1$ meV (solid line), $\hbar\Delta\omega = 0.3$ meV (thick solid line), and $\hbar\Delta\omega = 0.5$ meV (dashed line).

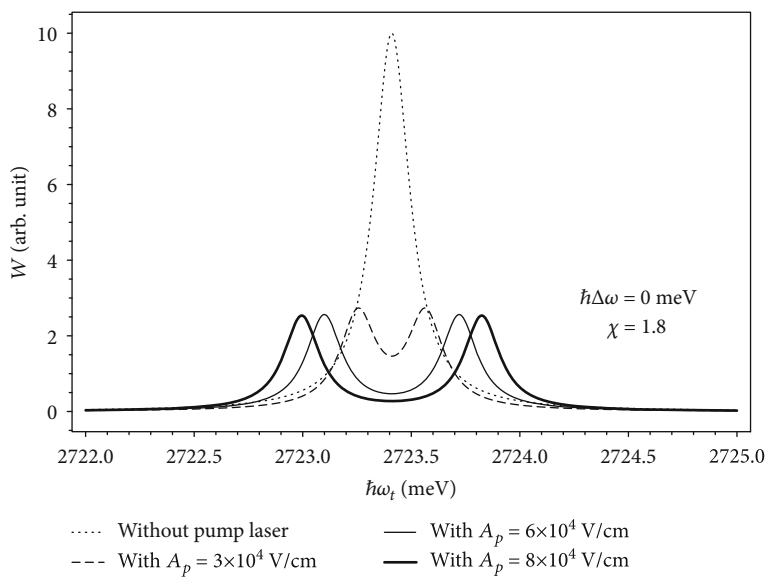

Figure 9: The dependence of transition rate on the photon energy of probe laser in a prolate ellipsoidal quantum dot in the absence of the pump laser (dotted line) and in the presence of the pump laser with different amplitude of pump laser $A_p = 3 \times 10^4$ V/cm (dashed line), $A_p = 6 \times 10^4$ V/cm (solid line), and $A_p = 8 \times 10^4$ V/cm (thick solid line) when $\chi = 1.8$ and the pump laser detuning $\hbar\Delta\omega = 0$ meV.

From the figure, we can see that, without the pump laser, the absorption spectra of excitons includes only one absorption peak. However, when the system is irradiated by a strong pump laser exactly resonant with the energy distance between the two quantized levels of the electron, the graph appeared two distinct equal peaks in the exciton absorption spectra. These two vertices are bilaterally symmetrical with respect to the original peak when the pump laser does not operate. Moreover, we found that the exciton absorption intensity is drastically reduced in the presence of a laser field. This reduction is the consequence of the conservation of the electronic transition rate as discussed in Ref. [11]. In short, the above results demonstrate the existence of the three-level optical Stark effect of exciton in the prolate ellipsoidal quantum dots. In addition, comparing the results found in the prolate ellipsoidal and spherical quantum dots [11], we find that they are similar. The reason is given to the fact that both prolate ellipsoidal and spherical quantum dots are quasi-zero-dimensional systems.

The existence of the two distinct peaks in the absorption spectra of excitons under the effect of a strong pump laser resonating with the energy distance between the two

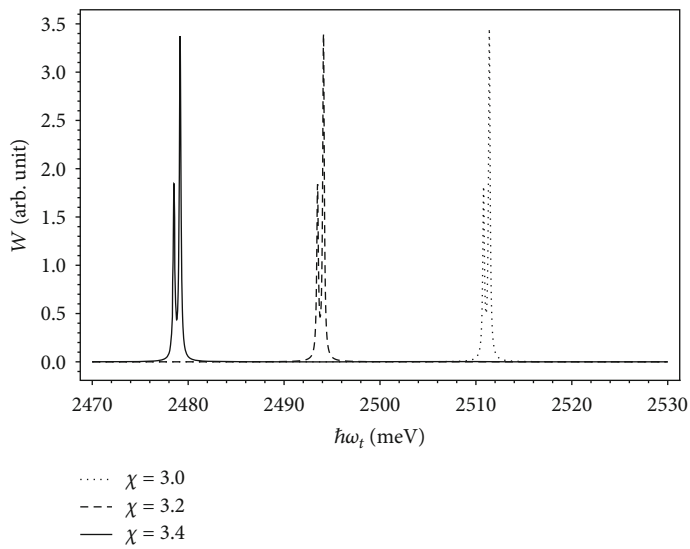

Figure 10: The dependence of transition rate on the photon energy of probe laser with the different ellipsoidal aspect ratios $\chi = 3$ (or $c = 75$ Å) (dotted line), $\chi = 3.2$ (or $c = 80$ Å) (dashed line), and $\chi = 3.4$ (or $c = 85$ Å) (solid line) in the presence of the pump laser with detuning $\hbar\Delta\omega = 0.1$ meV.

quantized levels of the electron can be explained in Figure 4. From Figure 4, we see that when the pump laser is active, the initial electron levels are split into sub-levels. For example, two new levels E_{100}^{e+} and E_{100}^{e-} are separated from the initial level E_{100}^{e}, and two sub-levels E_{110}^{e+} and E_{110}^{e-} are split from the initial level E_{110}^{e}, determined according to Eqs. (43) and (44). Thus, when we use the probe laser, we find two interband transitions from hole level E_{100}^{h} to two sub-levels of electron E_{100}^{e+} and E_{100}^{e-}, obeying the selection rules of the interband transitions in quantum dots. This means in the absorption spectrum of excitons there appear two new absorption peaks of excitons. These two peaks are located symmetrically on both sides of the original peak according to the energy conservation law.

To better reveal the strong effect of the pump laser detuning on the absorption spectrum of excitons, we investigated the dependence of the transition rate according to the photon energy of probe laser when the ellipsoidal aspect ratio $\chi = 3$ in the absence of the pump laser (dotted line) and in the presence of the pump laser with different detunings $\hbar\Delta\omega = 0.1$ meV (thin solid line), $\hbar\Delta\omega = 0.3$ meV (thick solid line), and $\hbar\Delta\omega = 0.5$ meV (dashed line) as shown in Figure 5. From Figure 5, we can see that in the presence of the pump laser, all absorption spectra of excitons contain two absorption peaks of excitons in the absorption spectra. The heights of two absorption peaks of excitons are different and depend on the pump laser detuning. When the pump laser detuning changes, the height of two exciton absorption peaks will also change, the more the detuning increases, the higher the height of one peak increases while the height of the other peak decreases. As the detuning increases, one absorption peak tends to move towards the original peak (which is the peak in the inactivity of the pump laser); the other is far from the position of the original peak, and this is clearly shown in Figure 6. From Figure 6, we also find that the more the detuning, the more redshifted two peaks. In addition, the detuning

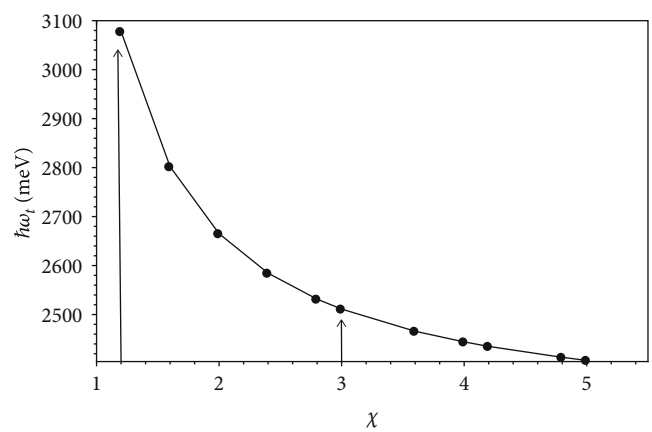

Figure 11: The dependence of the photon energy of probe laser on the ellipsoidal aspect ratio χ in the absence of the pump laser.

of the pump laser also strongly influences the transition rate of two absorption peaks as shown in Figure 7.

From Figure 7, we see that when the pump laser detuning is increased, the transition rate of the high-energy absorption peak increases and approaches to the transition rate of original peak when the pump laser was not active, while the transition rate of low-energy absorption peak decreases and approaching to zero. At the same time, the transition rate of these two absorption peaks depends monotonously on the pump laser detuning.

Similar to Figure 5, we also examine the dependence of the transition rate according to the photon energy of probe laser when $\chi = 1.8$ as shown in Figure 8. Comparing Figure 5 with Figure 8, we found that the height of the low-energy absorption peak depends very sensitive on the value of χ. With the same $\hbar\Delta\omega = 0.3$ meV value, when $\chi = 3$, the height of the low-energy absorption peak is still clearly observed, but with $\chi = 1.8$, the height of the low-energy

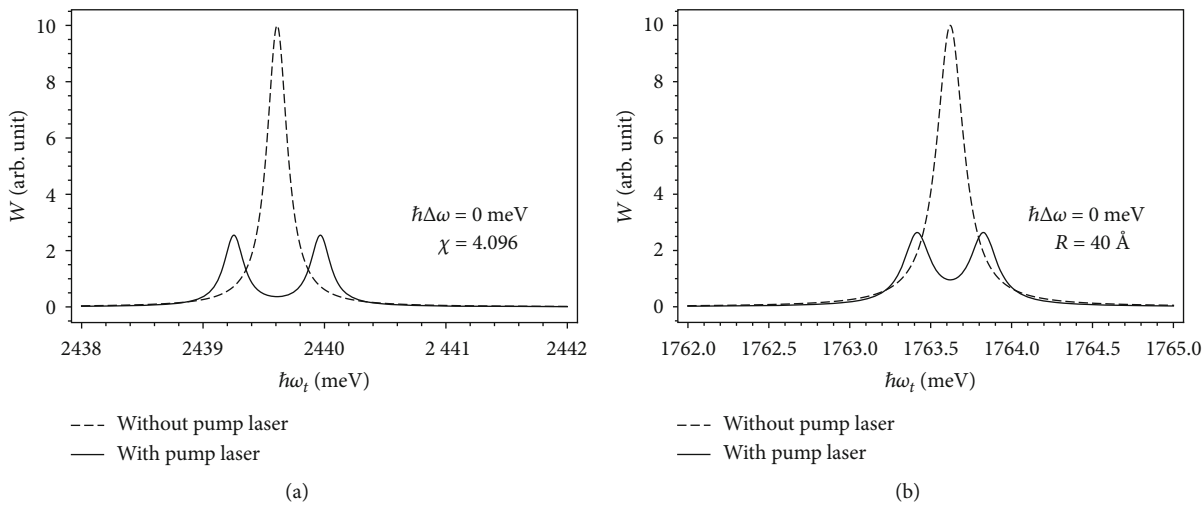

Figure 12: The dependence of exciton absorption spectra on the photon energy of probe laser in the prolate ellipsoidal quantum dot (a) with the length of the semi-minor axis $a = 25$ Å, $\chi = 4.096$ (corresponding to the length of the semi-major axis $c = 102.4$ Å) and spherical quantum dot (b) with radius $R = 40$ Å with the same volume.

absorption peak is very small. As the value of χ decreases, the low-energy absorption peak will almost disappear, and the high-energy absorption peak will reach the original peak. In addition, the location of these two exciton absorption peaks is also strongly dependent on the amplitude of pump laser as shown in Figure 9. In addition, in the case $\hbar\Delta\omega > 0$ as presented in Figures 5 and 8, after being split (and decreasing peak intensity), the second peak intensity increases with the detuning and tends to return as in the case of no pump laser. This phenomenon can be explained as follows. When the detuning increases, the pump laser is hard to make an intraband transition between two electron levels (indicated by thick dashed arrow in Figure 4), that means it is hard to connect those two electron levels to become one big degeneracy electron level. Hence, under effect of strong electric field of the pump laser, the symmetry of the initial electron levels (as well as the symmetry of this big degeneracy electron level) is hard to be broken, and hence, the initial electron levels are hard to be split into sublevels. This is the reason why we see one large splitting peak near the original peak (in the case of no pump laser), while another splitting peak nearly disappears. Therefore, when we probe the exciton spectrum, the second peak intensity increases with the detuning and tends to return as in the case of no pump laser, and if the detuning is large enough, we will see only one peak in the spectrum.

Figure 9 illustrates the absorption spectra of excitons in a prolate ellipsoidal quantum dot in the absence of the pump laser (dotted line) and in the presence of the pump laser with different amplitude of pump laser $A_p = 3 \times 10^4$ V/cm (dashed line), $A_p = 6 \times 10^4$ V/cm (solid line), and $A_p = 8 \times 10^4$ V/cm (thick solid line) when $\chi = 1.8$ and the pump laser detuning $\hbar\Delta\omega = 0$ meV. From Figure 9, we find that when increasing the amplitude of the pump laser, the distance between the two exciton absorption peaks also increases, but these two peaks are located symmetrically on both sides of the original peak according to energy conservation law. In other words, the optical Stark effect can be controlled using the strong pump laser.

Next, we examine the effect of the χ value on the exciton absorption spectra. Figure 10 describes the dependence of transition rate on the photon energy of probe laser with the different ellipsoidal aspect ratios $\chi = 3$ (dotted line), $\chi = 3.2$ (dashed line), and $\chi = 3.4$ (solid line) in the presence of the pump laser with detuning $\hbar\Delta\omega = 0.1$ meV. In all three cases, we can see two exciton absorption peaks, which again confirm the existence of the excitonic optical Stark effect in this structure. Besides, when χ was increased, both absorption peaks moved quickly to the lower energy region, corresponding to a red shift in the absorption spectrum. Therefore, changing the optical properties of prolate ellipsoidal quantum dot structures will become easier to control and more flexible by changing only two parameters semi-minor axis and semi-major axis of this quantum dot structure. This is one of the advantages of ellipsoidal quantum dot structures compared to spherical quantum dots.

To further investigate the properties of absorption spectra of interband transitions in prolate ellipsoidal quantum dots, we continue examining the shift of the photon energy of probe laser as a function of the ellipsoidal aspect ratio χ in the case of the pump laser is not switched on (Figure 11). As shown in Figure 11, we see a red shift in the absorption spectra when increasing the ellipsoidal aspect ratio χ as mentioned in Figure 10. In particular, the strongest shift occurs in the range of $1.2 < \chi < 3$, and weaker displacement appears when $\chi > 3$. This clearly shows the characteristic quantum size effect of quantum dot structures in general and of prolate ellipsoidal quantum dots in particular. We think the result will be very useful for experimental studies in choosing the wavelength of probe laser to match the size of the quantum dots to study the existence of the optical Stark effect.

Lastly, we compare the exciton absorption spectra in the prolate ellipsoidal quantum dot (Figure 12(a)) and the spherical quantum dot (Figure 12(b)) [11] with the same volume.

Derived from Eq. (15), we consider the prolate ellipsoidal quantum dot in case $a = 25$ Å and $\chi = 4.096$, which show the same volume as the spherical quantum dot with radius $R = 40$ Å. From Figure 12, we can see that, although two structures have the same volume, the exciton absorption spectra in two quantum dots of different shapes are completely different. This means that the exciton absorption spectra, or in other words, the optical Stark effect of exciton not only depends on the pump laser detuning and size of quantum dots but also very sensitive on geometric shapes of quantum dots. The reason for the difference between the exciton absorption spectra of two quantum dot structures can be explained as follows. The shape of the quantum dots as well-known strongly affects the wavefunctions and the energy spectra of particles. Hence, the wavefunctions and the energy spectra of particles in quantum dots of different shapes are really distinct from others, though the quantum dots have the same volume. It leads to a change of the electronic transitions in those structures, resulting in a variation in the exciton absorption spectra. Moreover, because the renormalized wavefunction method is a quantum mechanical based approach, so our theory can be easily applied for the other low-dimensional structures as long as we can determine energy levels and wavefunctions of particles. In fact, we have applied our theory to the similar problems in QDs of various shapes as well as in quantum wires and quantum wells [11, 12, 37, 38].

4. Conclusion

To sum up, in this study, we have investigated the characteristics of the exciton absorption spectra in the InGaAs/InAlAs prolate ellipsoidal quantum dot through calculating the transition rate of the interband transition using the renormalized wavefunction theory. The results show that when the two quantized energy levels of electrons are coupled by a polarized pump field, one initial absorption peak of exciton is split into distinct absorption peaks as an evidence of the existence of the three-level optical Stark effect. This is the consequence of the splitting of the electron quantized levels due to the effect of the strong resonant pump laser. We also find analytical expressions for the electron splitting levels and attempt to explain the mechanism of effect generation. Another important result is that the exciton absorption spectra are not only strongly affected by the energy of the pump laser but also depend strongly on geometric shapes of quantum dots. Specifically, with the same volume, the exciton absorption spectra in the spherical quantum dots and the prolate ellipsoidal quantum dots are completely different. Furthermore, when we increase the ellipsoidal aspect ratio of the prolate ellipsoidal quantum dots, a clear red shift in the optical absorption spectra was observed. The existence of two parameters of semi-minor axis and semi-major axis in the prolate ellipsoidal quantum dot structures makes the ability to control optical properties of the ellipsoidal quantum dots easier and more flexible than the spherical quantum dots. This is one of the advantages of the ellipsoidal quantum dot structures compared to the spherical quantum dots. We believe that the interesting features in the optical absorption spectra in the prolate ellipsoidal quantum dots when the optical Stark effect occurs have the great potential application to the development of computing devices and quantum information.

Data Availability

The material data used to support the findings of this study are included within the article.

Conflicts of Interest

The authors declare that they have no conflicts of interest.

Acknowledgments

This research is funded by Vietnamese Ministry of Education and Training (MOET) under grant number B-2020-DHH-06.

References

[1] A. D. Yoffe, "Semiconductor quantum dots and related systems: electronic, optical, luminescence and related properties of low dimensional systems," *Advances in Physics*, vol. 50, no. 1, pp. 1–208, 2001.

[2] H.-L. Wu, X.-B. Li, C.-H. Tung, and L.-Z. Wu, "Semiconductor quantum dots: an emerging candidate for CO_2 Photoreduction," *Advanced Materials*, vol. 31, no. 36, article 1900709, 2019.

[3] J. Owen and L. Brus, "Chemical synthesis and luminescence applications of colloidal semiconductor quantum dots," *Journal of the American Chemical Society*, vol. 139, no. 32, pp. 10939–10943, 2017.

[4] Y. Li, S. He, X. Luo, X. Lu, and K. Wu, "Strong spin-selective optical stark effect in lead halide perovskite quantum dots," *The Journal of Physical Chemistry Letters*, vol. 11, no. 9, pp. 3594–3600, 2020.

[5] W. Wegscheider, G. Schedelbeck, M. Bichler, and G. Abstreiter, "Atomically precise quantum dots fabricated by two-fold cleaved edge overgrowth: from artificial atoms to molecules," *Physica E*, vol. 3, no. 1-3, pp. 103–111, 1998.

[6] L. Zhuang, L. Guo, and S. Y. Chou, "Silicon single-electron quantum-dot transistor switch operating at room temperature," *Applied Physics Letters*, vol. 72, no. 10, pp. 1205–1207, 1998.

[7] M. Grundmann, "How a quantum-dot laser turns on," *Applied Physics Letters*, vol. 77, no. 10, pp. 1428–1430, 2000.

[8] Q. Ye, R. Tsu, and E. H. Nicollian, "Resonant tunneling via microcrystalline-silicon quantum confinement," *Physical Review B*, vol. 44, no. 4, pp. 1806–1811, 1991.

[9] V. A. Harutyunyan, E. M. Kazaryan, A. A. Kostanyan, and H. A. Sarkisyan, "Interband transitions in cylindrical layer quantum dot: influence of magnetic and electric fields," *Physica E*, vol. 36, no. 1, pp. 114–118, 2007.

[10] C.-H. Liu and B.-R. Xu, "Theoretical study of the optical absorption and refraction index change in a cylindrical quantum dot," *Physics Letters A*, vol. 372, no. 6, pp. 888–892, 2008.

[11] D. N. Thao, L. T. N. Bao, D. D. Phuoc, and N. H. Quang, "A theoretical study of the optical Stark effect in InGaAs/InAlAs quantum dots," *Semiconductor Science and Technology*, vol. 32, no. 2, article 025014, 2017.

[12] D. N. Thao and L. T. N. Bao, "Quantum beat of excitons in spherical semiconductor quantum dots," *Superlattices and Microstructures*, vol. 146, article 106675, 2020.

[13] L. Liang and W. Xie, "Influence of the shape of quantum dots on their optical absorptions," *Physica B*, vol. 462, pp. 15–17, 2015.

[14] E. Garmire, A. A. Maradudin, and K. K. Rebane, *Laser Optics of Condensed Matter (Volume 2 The Physics of Optical Phenomena and Their Use as Probes of Matter)*, Springer Science +Business Media, LLC, 1991.

[15] D. Fröhlich, C. Neumann, B. Uebbing, and R. Wille, "Experimental investigation of three-level optical stark effect in semiconductors," *Physica Status Solidi B: Basic Solid State Physics*, vol. 159, no. 1, pp. 297–307, 1990.

[16] D. Song, F. Wang, G. Dukovic et al., "Measurement of the optical Stark effect in semiconducting carbon nanotubes," *Applied Physics A*, vol. 96, no. 2, pp. 283–287, 2009.

[17] S. Efumi, Y. Uchibori, J. Ishihara, and K. Miyajima, "Observation of optical Stark effect between 1*s* -2*p* exciton levels in CuCl single crystal," *Journal of Physics: Conference Series*, vol. 1220, no. 1, article 012022, 2019.

[18] A. V. Trifonov, I. Y. Gerlovin, I. V. Ignatiev et al., "Multiple-frequency quantum beats of quantum confined exciton states," *Physical Review B*, vol. 92, no. 20, article 201301, 2015.

[19] Y. Rong, Y. Huo, E. T. Fei et al., "High speed optical modulation in Ge quantum wells using quantum confined stark effect," *Frontiers of Optoelectronics*, vol. 5, no. 1, pp. 82–89, 2012.

[20] M. Gogoi, P. Deb, D. Sen, S. Mazumder, and A. Kostka, "Enhanced quantum confined stark effect in a mesoporous hybrid multifunctional system," *Solid State Communications*, vol. 187, pp. 48–52, 2014.

[21] J. T. Liu, F. H. Su, H. Wang, and X. H. Deng, "The influence of the optical Stark effect on chiral tunneling in graphene," *A Letters Journal Exploring the Frontiers of Physics*, vol. 95, article 24003, 2011.

[22] T. Unold, K. Mueller, C. Lienau, T. Elsaesser, and A. D. Wieck, "Optical Stark effect in a quantum dot: ultrafast control of single exciton polarizations," *Physical Review Letters*, vol. 92, no. 15, article 157401, 2004.

[23] S. I. Pokutnyi, L. Jacak, J. Misiewicz, W. Salejda, and G. G. Zegrya, "Stark effect in semiconductor quantum dots," *Journal of Applied Physics*, vol. 96, no. 2, pp. 1115–1119, 2004.

[24] L. Zhang, B. Lv, H. Yang et al., "Quantum-confined stark effect in the ensemble of phase-pure CdSe/CdS quantum dots," *Nanoscale*, vol. 11, no. 26, pp. 12619–12625, 2019.

[25] V. I. Boichuk, V. B. Hol'skyi, R. Y. Kubay, and R. I. Lukin, "The electron energy spectrum in an ellipsoidal quantum dot with regard for finite band gap at the interface," *Ukrainian Journal of Physics*, vol. 53, no. 6, pp. 574–578, 2008.

[26] G. Cantele, D. Ninno, and G. Iadonisi, "Confined states in ellipsoidal quantum dots," *Journal of Physics: Condensed Matter*, vol. 12, pp. 9019–9036, 2000.

[27] G. Cantele, D. Ninno, and G. Iadonisi, "Calculation of the infrared optical transitions in semiconductor ellipsoidal quantum dots," *Nano Letters*, vol. 1, no. 3, pp. 121–124, 2001.

[28] G. Cantele, G. Piacente, D. Ninno, and G. Iadonisi, "Optical anisotropy of ellipsoidal quantum dots," *Physical Review B*, vol. 66, no. 11, article 113308, 2002.

[29] G. Iadonisi, G. Cantele, V. Marigliano Ramaglia, and D. Ninno, "Electronic and optical properties of semiconductor nanostructures," *Physica Status Solidi (b)*, vol. 237, no. 1, pp. 320–340, 2003.

[30] https://en.wikipedia.org/wiki/Spheroid.

[31] L. Bányai and S. W. Koch, *Semiconductor Quantum Dots*, World Scientific, Singapore, 1st ed. edition, 1993.

[32] F. Dujardin, E. Feddi, and E. Assaid, "Excitonic binding energy in prolate and oblate spheroidal quantum dots," *Superlattices and Microstructures*, vol. 114, pp. 296–304, 2018.

[33] A. Jorio, R. Saito, G. Dresselhaus, and M. S. Dresselhaus, *Raman Spectroscopy in Graphene Related Systems*, Wiley-VCH Verlag GmbH & Co. KGaA, Weinheim, 2011.

[34] F. Schwabl, *Quantum Mechanics*, Springer, Springer-Verlag Berlin Heidelberg, 4th ed. edition, 2007.

[35] V. Balakrishnan, "All about the Dirac delta function(?)," *Resonance*, vol. 8, no. 8, pp. 48–58, 2003.

[36] H. Asai and Y. Kawamura, "Intersubband absorption inIn0.53Ga0.47As/In0.52Al0.48As multiple quantum wells," *Physical Review B*, vol. 43, no. 6, pp. 4748–4759, 1991.

[37] L. T. N. Bao and D. N. Thao, "Theoretical investigation of quantum beat of excitons in GaAs/AlGaAs quantum wells," in *The 42nd Vietnam National Conference on Theoretical Physics (NCTP-42)*, Cantho, Vietnam, 2017.

[38] D. N. Thao, D. D. Phuoc, L. T. N. Bao, L. T. D. Hien, T. P. T. Linh, and N. T. L. Thuy, "Three-level optical Stark effect of excitons in GaAs cylindrical quantum wires," *Journal of Nanomaterials*, vol. 2021, Article ID 5594256, 10 pages, 2021.

Hindawi
Journal of Nanomaterials
Volume 2021, Article ID 5530709, 6 pages
https://doi.org/10.1155/2021/5530709

Research Article

Gold Nanoparticles Modified a Multimode Clad-Free Fiber for Ultrasensitive Detection of Bovine Serum Albumin

Vu Thi Huong,[1,2] Nguyen Tran Truc Phuong,[1,2] Nguyen Tien Tai,[1,2] Nguyen Thuy An,[1,2] Vu Dinh Lam,[3] Do Hung Manh,[4] Tran Thi Kim Chi,[4] Ngoc Xuan Dat Mai,[2,5] Viet-Duc Phung,[6,7] and Nhu Hoa Thi Tran[1,2]

[1]*Faculty of Materials Science and Technology, University of Science, Ho Chi Minh City, Vietnam*
[2]*Vietnam National University Ho Chi Minh City, Vietnam*
[3]*Graduate University of Science and Technology, Vietnam Academy of Science and Technology, Hanoi, Vietnam*
[4]*Institute of Materials Science, Vietnam Academy of Science and Technology, Hanoi, Vietnam*
[5]*Center for Innovative Materials and Architectures (INOMAR), Ho Chi Minh City, Vietnam*
[6]*Faculty of Environmental and Chemical Engineering, Duy Tan University, Da Nang 550000, Vietnam*
[7]*Future Materials and Devices Laboratory, Duy Tan University, Ho Chi Minh City 700000, Vietnam*

Correspondence should be addressed to Viet-Duc Phung; phungvietduc2021@gmail.com and Nhu Hoa Thi Tran; ttnhoa@hcmus.edu.vn

Received 1 February 2021; Revised 22 February 2021; Accepted 5 March 2021; Published 18 March 2021

Academic Editor: Nguyen Duc Cuong

Gold nanoparticles (Au NPs) were almost chosen as the first option for biological and biosensor applications due to their enhancement and their outstanding properties. The combining of optical fiber with localized surface plasmon resonance (LSPR) for forming a biosensor is widely used in diagnosis. In this work, we report a fiber optical biosensor based on LSPR of Au NPs for the detection of bovine serum albumin (BSA) protein. BSA was functionalized on Au NPs immobilized fiber optic sensing head (length of 1 cm) via methanesulfonic acid (MSA) by carboxylic binding. It is the binding between the analytes with the surface-modified Au NPs that caused refractive index changes in the sensing medium led to changes in optical power at the output of the sensor. The detection limit of the LSPR fiber biosensor was found to be 0.18 ng/mL for the BSA detection with the low coefficient of variation (CV) at under 1%. We have demonstrated the effectiveness of combining multimode fiber with Au NPs to generate the biosensor as the label-free sensor that can be a feasible tool for highly sensitive, rapid response time, stable, and miniaturized point-of-care analytical systems.

1. Introduction

Gold nanoparticles (Au NPs) with unique properties such as excellent compatibility, intense light scattering/absorption, high surface area to volume ratios, highly selective interoperability through electrostatic interaction, stable structure, and nontoxic have become the first choice among plasmonic nanoparticles for biological and biosensor applications [1–3]. Au NPs also have a special phenome that is localized surface plasmon resonance (LSPR), which was widely studied recently in sensing platforms due to its great advantages [4–6]. It provides compact, label-free, highly sensitive, and stable biosensing for the detection of biological molecules [7, 8]. LSPR is a phenomenon in metallic nanostructures related to the resonance of free-electron waves in a metal. The incident light could be in resonance with the oscillations of the surface electron at an excitation frequency, resulting in the collective oscillation of the surface plasmons, and it is called an LSPR mode [9].

It is due to the unique optical properties and surface chemistries that Au NPs were used as the promising nanomaterial in numerous different types of sensors such as surface-enhanced Raman scattering (SERS), fluorescence, electrochemical, and fiber optical-based LSPR sensor.

Therein, the combining of optical fiber with the LSPR phenomenon helps to enhance the light-matter interaction that provided a sensor type with enhanced sensitivity, fast response, higher stability, more affordable, compact size, and lower limit of detect sensor than that others [10, 11]. The basic principle of this sensor relies on the altar reflective index of ambient dielectrics around the sensing region and does not require the labeling of the target molecules.

In this work, Au NPs were synthesized via the seed-mediated growth method for the fabrication of the LSPR-based optical biosensor for the detection of a standard protein in biosensor experiments that is bovine serum albumin (BSA). Mercaptosuccinic acid (MSA) with carboxylic acid (−COOH) groups was modified on the sensing surface via Au NP thiol bond and was utilized for the immobilization of BSA. The properties of Au NPs were tracked through the spectroscopic measurements including UV-visible spectroscopy, powder X-ray diffraction (PXRD), and field emission scanning electron microscope (FESEM). Moreover, Fourier-transform infrared spectroscopy (FTIR) and water contact angles (WCAs) were used to confirm the presence of surface functional groups. We achieved a low limit of detection (LOD) of 0.18 ng/mL for BSA detection. This result in this study can be compared to be 5284 times better than Peng et al.'s work [12] about optical biosensors based on surface plasmon polaritons for detecting BSA and 20 times better than that Tran et al.'s [13] about optical fiber biochemical sensors. This result proved the effective combining between the optical properties of Au NPs and optical devices, unfolded potentials in biological analysis, and biosensor application.

2. Experimental Section

2.1. Materials and Reagents. Gold(III) chloride trihydrate ($HAuCl_4{\cdot}3H_2O$, 99.9%), (3-aminopropyl)triethoxysilane (APTES, 99%), Mercaptosuccinic acid (MSA, 97%), sodium citrate tribasic dihydrate ($HOC(COONa)(CH_2COONa)_2{\cdot}2H_2O$, Na_3Ctr, 99%), phosphate-buffered saline (PBS), and bovine serum albumin (BSA) were all supplied by Sigma-Aldrich Co., MO, USA. Ethanol (C_2H_5OH, 99.8%) was obtained from Fisher Ltd. (UK), and glycerol ($C_3H_8O_3$, 99%) was provided by Duksan Pure Chemicals Co. (Ltd., Korea). Sodium hydroxide (NaOH, 96%) was purchased from Guangdong Guanghua Sci-Tech Co., Ltd. (China).

2.2. Synthesis of Gold Nanoparticles. Gold nanoparticles were synthesized by the seed-mediated growth method utilizing citrate reduction of gold(III) chloride trihydrate. Deionized (DI) water was used for all preparations. The seed nanoparticles were made by adding Na_3Ctr rapidly into a round bottom storage flask containing the mixture of 200 μL of NaOH 1 M and 100 mL of $HAuCl_4$ 1 mM at 100°C under vigorous stirring. The solution was stirred stably for 15 minutes and stored at 4°C. Then, the resulting Au seeds were grown by adding 3.377 mL seed into 36.22 mL DI water, 0.176 mL Na_3Ctr, and 0.227 mL of $HAuCl_4{\cdot}3H_2O$ 1 mM. The reaction was conducted in an ultrasonic bath at RT for 40 minutes. The final product was preserved in glass vials and stored at 4°C for further use.

2.3. Surface Modification of Fiber Core for BSA Detection. Multimode optical fibers have been used for the construction of this type of sensor for a number of reasons as follows. It is suitable for a wide variety of luminescent sources so it can be expanded for more applications. The larger core makes it easier to denature the surface for sensor application. It is easier to adjust and introduce light to the multimode fiber so it is easier to experiment.

The clad-free fiber (Multimode, NA 0.37, JFTLH-Polymicro Technologies) with the length of 1 cm core sensing has been fabricated by removing part middle of the plastic buffer layer with a soldering machine (ATC−2450−III, ARIM, Korea), and the cladding layer with a mixture of acetone and ethanol (3 : 1). After removing, the silica (SiO_2) surface of the sensor head was modified with Au NPs for the LSPR sensor; then, the carboxylic groups were created on it for BSA detection as shown in Figure 1. Briefly, the fiber core surface was silanized using 3% APTES after the generation of the hydroxyl groups (−OH) on it by an oxygen plasma machine (CUTE-1MPR, Femto Science Inc., Korea) for 2 min. Subsequently, Au NPs were immobilized on the amine-modified sample via the strong electrostatic force. The immersing time for Au NPs to be coated on the surface was investigated (4, 8, 12, and 16 hr). Finally, the clad-free fiber was carboxyl-functionalized using MSA acid solution of 0.1 mM in ethanol for 16 hr at RT, then washed with methanol several times.

2.4. Optical Setup for Biosensor Measurements. Microfluidic fabrication for real-time optical biosensor measurement was proposed and implemented. Briefly, this device is constructed from the bonding PDMS (polydimethylsiloxane, Sylgard 184, Dow Corning Co., USA) mold and clean glass together as soon as they are treated by an oxidation plasma system with the installation of a clad-free fiber inside. The PDMS mold with two ports (inlet/outlet, a diameter of 1 mm) and a straight-shaped flow channel are generated from pouring the mixture of cross-linker curing agent and silicone elastomer base (v/v, a ratio of 1 : 10) into a mold and dried at 70°C during 30 minutes in an oven.

Figure 2 shows the optical measurement system including a 5 mW He-Ne laser (632.8 nm, LASOS LGK 7628), a coupling system (NA of o.4), an aperture collimator mount (AD9.5F), a digital handheld optical power (PM 100D, Thorlabs, Newton, NJ, USA), and the peristaltic pump (Eleya, SMP-21, Japan) to inject the analyte solution into the channel of microfluidic. Two ports for injecting liquids into the channel were made from the plastic tubing (Eleya, Japan) with inner diameter : outer diameter = 1.15 : 3.2 mm.

2.5. Measurement Techniques. The gold nanoparticles were characterized utilizing UV-visible spectroscopy (V-730 visible/NIR, JASCO, Tokyo, Japan), powder X-ray diffraction (PXRD, Bruker D8 Advance diffractometer, $\lambda = 1.54178$ Å), and field emission scanning electron microscope (FESEM, Hitachi S4800, USA). The presence of the surface functional

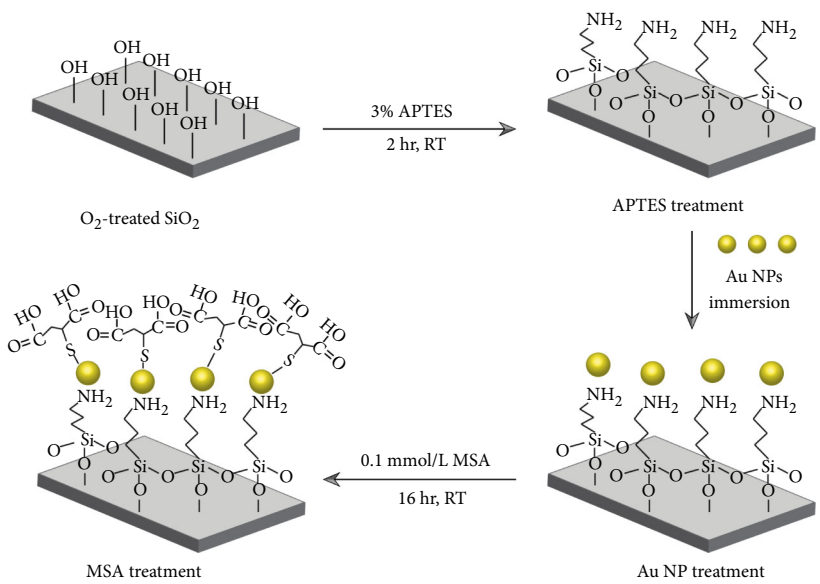

Figure 1: The illustrations of the surface modification steps for BSA detection.

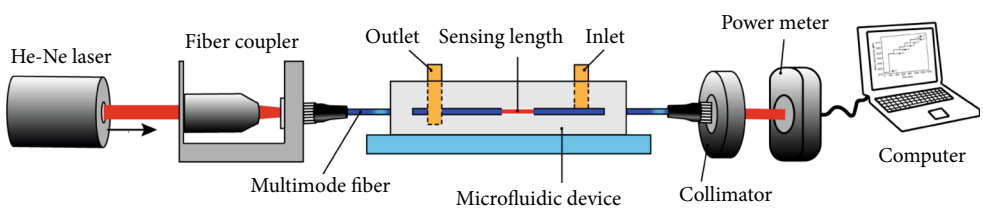

Figure 2: Diagram of the optical measurement system.

groups such as hydroxyl, carboxyl, and amino was investigated by the Fourier transform infrared spectroscopy (FTIR, Bruker Vertex 70, Germany) and water contact angles (WCAs, Phoenix 300, Surface Electro-Optics).

3. Results and Discussion

Au NPs were prepared by the seed-mediated growth method with the reduction of $HAuCl_4$ utilizing Na_3Ctr as a reducing agent. As soon as the synthesis of Au NPs is completed, the change in wavelength value and the color between Au nanoseed and Au NP solution was observed, shown in Figure 3. Briefly, a wine red color was obtained with the LSPR peak at 522.6 nm for the Au nanoseed solution. There are some disadvantages to the seed solution, such as uneven seed size and agglutination between seeds. The use of the intermediate particle development method helps to control the properties of the gold nanoparticles such as absorption size and wavelength, in addition to helping to produce single dispersed Au NPs. As the resulting Au seeds were grown, a slight redshift of the maximum absorbance peak from 522.6 nm to 524.5 nm with the change color to pink was recorded. The Au NPs formation with LSPR of 524.5 nm and the color of solution (Figure 3) implied the appearance of the spherical Au NPs, which is directed in this experiment due to the usefulness of them in bioapplications [14].

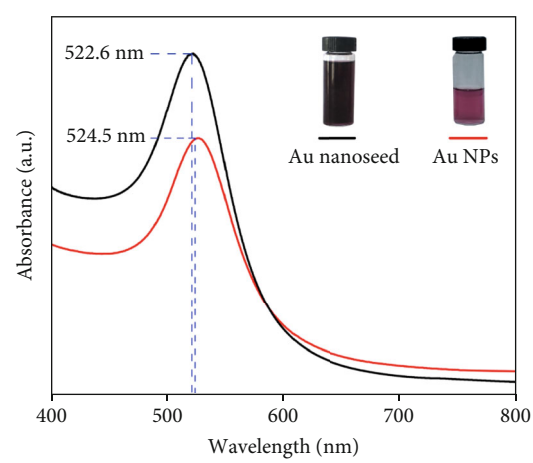

Figure 3: Wavelength shift in the UV-vis spectrum after the growth of Au NPs from Au nanoseed.

The proof of the presence of the characteristic functional group vibrations after the surface modification steps was recorded via FTIR spectroscopy and WCAs goniometry, as shown in Figure 4. In the FTIR spectrum (Figure 4(a)), the adsorption band at 450, 687, and 1140 cm^{-1} is attributed to Si-O-Si bending (δ), symmetric O-Si-O stretching (υ), and asymmetric Si-O-Si stretching (υ_{as}) vibrational, respectively [15]. The broadening in a band at 3370 to 3500 cm^{-1}

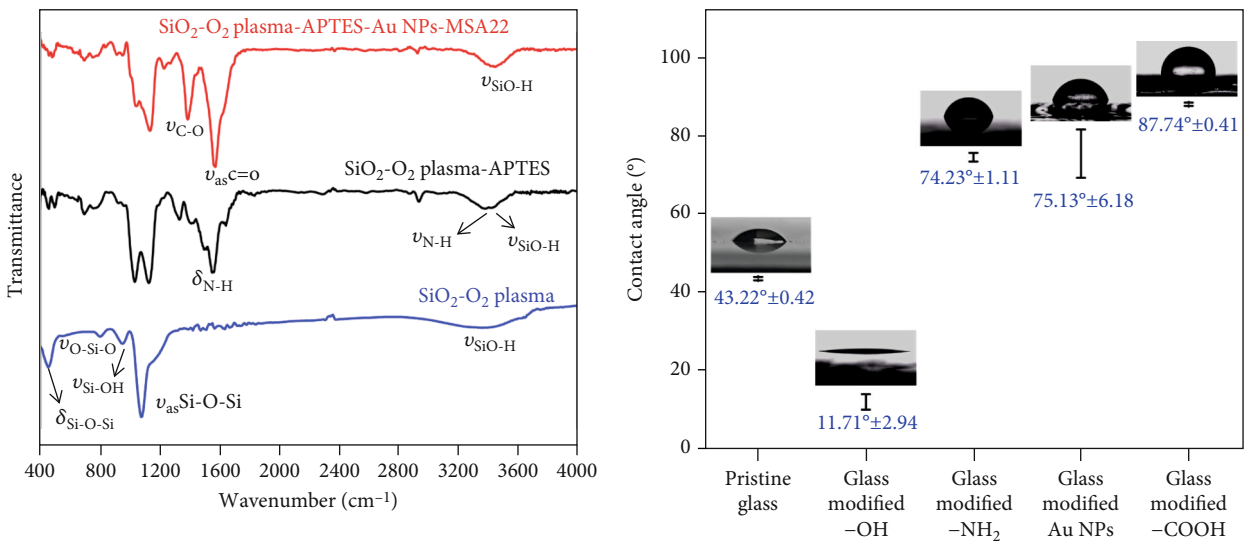

(a) (b)

Figure 4: (a) FTIR spectra and (b) WCA goniometry of the modified silica surfaces.

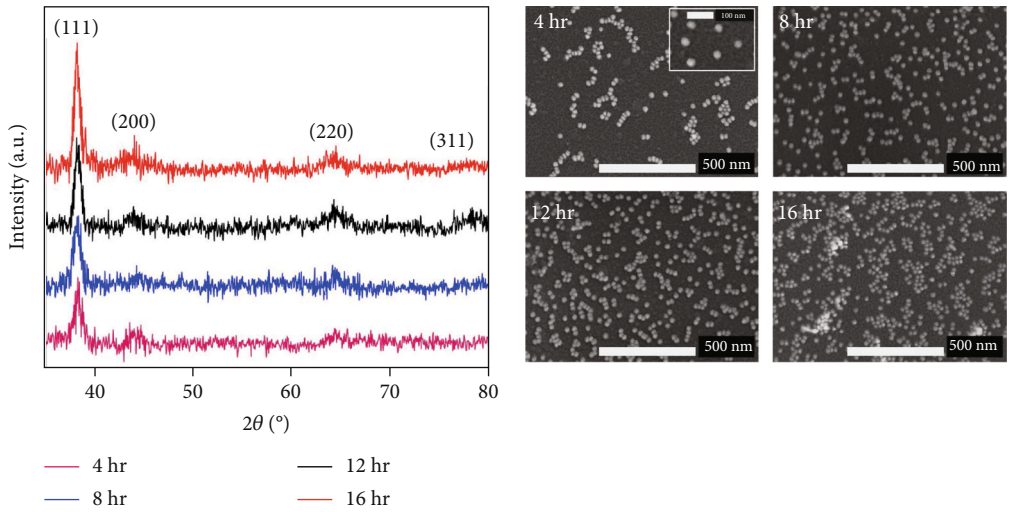

(a) (b)

Figure 5: (a) XRD spectra and (b) FESEM image of the sample at the various gold immersing times (4, 8, 12, and 16 hr).

indicated the signal of -OH groups of the Si-OH stretching vibration and retained water [16]. When modified with APTES, the IR spectrum was changed with the appearance of two peaks that is the N-H stretching and N-H bending vibrations at 3350 and 1570 cm^{-1} [17]. In the spectrum of Au NP-MSA treatment, the amine vibration disappeared and the emergence of new bands at 1603 and 1340 cm^{-1} is assigned to asymmetric C=O stretching and the C-O stretching vibration, respectively [18]. In the results of WCA measurement (Figure 4(b)), the wetting behavior of the modified surfaces (the hydrophilic or hydrophobic) was investigated. Briefly, oxygen plasma-treated pristine glass indicated hydrophilicity due to a decrease from the angle of $43.22° \pm 0.42$ to $11.71° \pm 2.94$. After APTES functionalization, the wetting angle was increased to $74.23° \pm 1.11$, implying the hydrophobic layer on the surface. Then, Au NP-coated glass was determined to be more hydrophobic than the amine-modified surface with an angle of $75.13° \pm 6.18$. After modification of Au NP-treated surface with MSA acid, the contact angle was increased sharply to $87.74° \pm 0.41$, shown to turn super hydrophobic of the surface. The presence of the characteristic functional group vibrations in FTIR results and the surface wetting change in WCAs has indicated that -OH, $-NH_2$, and -COOH groups were successfully formed on the wafer surface.

The properties of Au NPs including the shape, size, crystal structure were investigated via XRD spectra and FESEM image, as shown in Figure 5. The results show that the gold crystallines on the sample surface have the face-centered cubic (fcc) structure with (111), (200), (220), and (311)

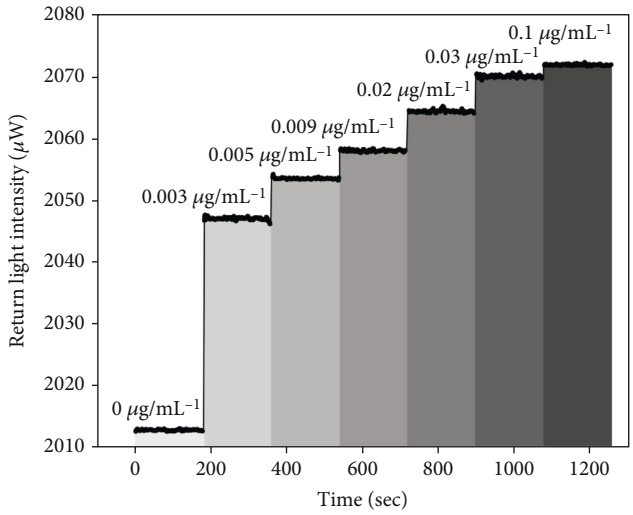

Figure 6: Time-dependent return light intensity via the optical fiber with the change of BSA concentration (from 0 to 0.1 μg/mL).

planes corresponding to 2-theta values of 38.2, 44.4, 64.5, and 77.4° at the different immersing time (4, 8, 12 and 16 hr) (Figure 5(a)) [19]. The (111) plane is the strongest intensity peak indicated that it is the preferred development orientation of Au NPs on the substrate. Furthermore, the shape of Au NPs was displayed as monodispersity spherical nanoparticles with an average diameter of 32 nm ± 3 (Figure 5(b)). Increased immersion time led to an increase in particle count and the dispersion of Au NPs on the surface. According to the investigated results in Figures 5, 12 hr is considered as the appropriate candidate for use in subsequent experiments.

In order to evaluate the optical fiber-based LSPR sensor's performance, BSA was prepared in a list of various concentrations from 0 to 0.1 μg/mL in PBS buffer solution. The BSA solution was injected into the channel of microfluidic where the sensor head was contained. It was the addition of the analyte molecule that caused a change of refractive index (RI) of the sensor medium, which led to an increase or decrease in the light intensity at the output. The basic principle of this sensor is based on the refractive index change of the sensor medium, so it can detect different proteins with different refractive indexes and give different signals. BSA molecules were easily immobilized on the Au NP-covered sensing surface via COOH groups. The refractive index (RI) was altered in the direction of increase by the increasing of BSA concentration, proved in the work of Tran et al. [13]. To determine the LOD of our optical sensor, we measured and recorded the transmittance light in output at various RI of the ambient medium with fixed input light value. The results are presented in Figure 6 showing the sequential increase response of the sensor as the concentration of BSA was increased. The average signal intensity with the error bar at each concentration was recorded for 1 min and was repeated at least 3 times. Then, the coefficient of variation (CV) was estimated to be <1%, indicating the high reproducibility. This sensor was rated highly sensitive due to the signal that varies significantly and immediately as analyte concentration changes. The LOD value (ng/mL) of this sensor was calculated as 0.18. This LOD is comparable to that of other sensors as shown in Table 1 indicating the high efficiency of the fiber optical LSPR biosensor. Our sensor therefore with this performance can be recognized as a feasible tool to be applied to biosensing.

Table 1: The performance of the sensor for detecting BSA.

Biosensor methods	Detection limit	Ref.
ELISA	0.38 ng/mL	[20]
Vis-IR spectral	0.05 mg/mL	[21]
Reverse-phase high performance liquid chromatography (RP-HPLC)	0.11 μg/mL	[22]
Two-dimensional transition metal dichalcogenides assisted optical fiber SPR biosensor	0.45 μg/mL	[23]
SPR sensor probe without optical fibers	50 ng/mL	[24]
This study	0.18 ng/mL	

4. Conclusion

In this article, an optical real-time measurement system and a biosensor device that contain the Au NP-coated fiber sensor head have been fabricated for sensor application. Au NPs have been synthesized by the seed-mediated growth method with the investigation of seed development through ultrasonic energy along with time change to find out the optimization in the properties of nanoparticles. Moreover, the process of surface denaturation of the sensor head of fiber optics with the modification of hydroxyl, amine, Au NPs, and carboxylic, respectively, for the analyte detection has been proposed. The combination of optical properties, X-ray diffraction technique, UV-vis spectroscopy, IR, and FESEM was used to follow the formation of crystal growth, absorption plasmon peak, sizes, and shapes of Au NPs. The high LOD of the LSPR sensor achieved 0.18 ng/mL for detection of BSA protein with remarkably high reproducibility. This research presented an in situ biosensor with highly sensitive in a compact format suited to the point-of-care testing.

Data Availability

The data used to support the findings of this study are included within the article.

Conflicts of Interest

The authors declare that they have no conflicts of interest.

Authors' Contributions

Vu Thi Huong and Nguyen Tran Truc Phuong contributed equally to this work.

Acknowledgments

This research is funded by the Vietnam National Foundation for Science and Technology Development (NAFOSTED) under grant number 103.03-2019.379. The authors would like to gratefully acknowledge the Vietnam National University Ho Chi Minh City, Center for Innovative Materials and Architectures (Laboratory for Optics and Sensing).

References

[1] S. Zeng, K. Yong, I. Roy, X.-Q. Dinh, X. Yu, and F. Luan, "A review on functionalized gold nanoparticles for biosensing applications," *Plasmonics*, vol. 6, no. 3, pp. 491–506, 2011.

[2] P. K. Jain, K. S. Lee, I. H. El-sayed, and M. A. El-sayed, "Calculated absorption and scattering properties of gold nanoparticles of different size, shape, and composition: applications in biological imaging and biomedicine," *Journal of Physical Chemistry B*, vol. 110, no. 14, pp. 7238–7248, 2006.

[3] K. Saha, S. Agasti, C. Kim, X. Li, and V. M. Rotello, "Gold Nanoparticles in Chemical and Biological Sensing," *Chemical Reviews*, vol. 112, no. 5, pp. 2739–2779, 2012.

[4] P. Q. T. Do, V. T. Huong, N. T. T. Phuong et al., "The highly sensitive determination of serotonin by using gold nanoparticles (Au NPs) with a localized surface plasmon resonance (LSPR) absorption wavelength in the visible region," *RSC Advances*, vol. 10, no. 51, pp. 30858–30869, 2020.

[5] L. Chau, Y. Lin, S. Cheng, and T. Lin, "Fiber-optic chemical and biochemical probes based on localized surface plasmon resonance," *Sensors and Actuators B: Chemical*, vol. 113, no. 1, pp. 100–105, 2006.

[6] J. R. L. Guerreiro, M. Frederiksen, V. E. Bochenkov, V. de Freitas, M. G. Ferreira Sales, and D. S. Sutherland, "Multifunctional biosensor based on localized surface plasmon resonance for monitoring small molecule–protein interaction," *ACS Nano*, vol. 8, no. 8, pp. 7958–7967, 2014.

[7] K. A. Willets and R. P. Van Duyne, "Localized surface plasmon resonance spectroscopy and sensing," *Annual Review of Physical Chemistry*, vol. 58, no. 1, pp. 267–297, 2007.

[8] Y. Wang, J. Zhou, and J. Li, "Construction of Plasmonic Nano-Biosensor-Based Devices for Point-of-Care Testing," *Small Methods*, vol. 1, no. 11, article 1700197, 2017.

[9] S. Unser, I. Bruzas, J. He, and L. Sagle, "Localized surface plasmon resonance biosensing: current challenges and approaches," *Sensors*, vol. 15, no. 7, pp. 15684–15716, 2015.

[10] M. Lu, H. Zhu, C. G. Bazuin, W. Peng, and J. F. Masson, "Polymer-templated gold nanoparticles on optical fibers for enhanced-sensitivity localized surface plasmon resonance biosensors," *ACS Sensors*, vol. 4, no. 3, pp. 613–622, 2019.

[11] H. Jeong, N. Erdene, J. Park, D. Jeong, H. Lee, and S. Lee, "*Real-time* label-free immunoassay of interferon-gamma and prostate-specific antigen using a Fiber-Optic Localized Surface Plasmon Resonance sensor," *Biosensors and Bioelectronics*, vol. 39, no. 1, pp. 346–351, 2013.

[12] Y. Peng, Y. Zhao, X. G. Hu, and Y. Yang, "Optical fiber quantum biosensor based on surface plasmon polaritons for the label-free measurement of protein," *Sensors and Actuators B: Chemical*, vol. 316, article 128097, 2020.

[13] N. H. T. Tran, J. Kim, T. B. Phan, S. Khym, and H. Ju, "Label-free optical biochemical sensors via liquid-cladding-induced modulation of waveguide modes," *ACS Applied Materials & Interfaces*, vol. 9, no. 37, pp. 31478–31487, 2017.

[14] P. N. Njoki, I. S. Lim, D. Mott et al., "Size correlation of optical and spectroscopic properties for gold nanoparticles," *Journal of Physical Chemistry C*, vol. 111, no. 40, pp. 14664–14669, 2007.

[15] A. M. Dattelbaum, M. L. Amweg, J. D. Ruiz, L. E. Ecke, A. P. Shreve, and A. N. Parikh, "Surfactant removal and silica condensation during the photochemical calcination of thin film silica mesophases," *Journal of Physical Chemistry B*, vol. 109, no. 30, pp. 14551–14556, 2005.

[16] A. S. Khan, H. Khalid, Z. Sarfraz et al., "Vibrational spectroscopy of selective dental restorative materials," *Applied Spectroscopy Reviews*, vol. 52, no. 6, pp. 507–540, 2017.

[17] N. Majoul, S. Aouida, and B. Bessaïs, "Progress of porous silicon APTES-functionalization by FTIR investigations," *Applied Surface Science*, vol. 331, pp. 388–391, 2015.

[18] I. M. A. Viegas, B. S. Santos, A. Fontes, G. A. L. Pereira, and C. F. Pereira, "Multivariate optimization of optical properties of CdSe quantum dots obtained by a facile one-pot aqueous synthesis," *Inorganic Chemistry Frontiers*, vol. 6, no. 6, pp. 1350–1360, 2019.

[19] M. Kamiński, K. Jurkiewicz, A. K. Burian, and A. Bródka, "The structure of gold nanoparticles: molecular dynamics modeling and its verification by X-ray diffraction," *Journal of Applied Crystallography*, vol. 53, no. 1, pp. 1–8, 2020.

[20] K. Zhang, C. Song, Q. Li, Y. Li, K. Yang, and B. Jin, "The establishment of a highly sensitive ELISA for detecting bovine serum albumin (BSA) based on a specific pair of monoclonal antibodies (mAb) and its application in vaccine quality control," *Human Vaccines & Immunotherapeutics*, vol. 6, no. 8, pp. 652–658, 2010.

[21] D. Shajari, A. Bahari, and P. Gill, "Fast and simple detection of bovine serum albumin concentration by studying its interaction with gold nanorods," *Colloids and Surfaces A: Physicochemical and Engineering Aspects*, vol. 543, pp. 118–125, 2018.

[22] M. Umrethia, V. L. Kett, G. P. Andrews, R. K. Malcolm, and A. D. Woolfson, "Selection of an analytical method for evaluating bovine serum albumin concentrations in pharmaceutical polymeric formulations," *Journal of Pharmaceutical and Biomedical Analysis*, vol. 51, no. 5, pp. 1175–1179, 2010.

[23] S. Kaushik, U. K. Tiwari, A. Deep, and R. K. Sinha, "Two-dimensional transition metal dichalcogenides assisted bio-functionalized optical fiber SPR biosensor for efficient and rapid detection of bovine serum albumin," *Scientific Reports*, vol. 9, no. 1, p. 6987, 2019.

[24] T. Akimoto, S. Wada, and I. Karube, "A surface plasmon resonance probe without optical fibers as a portable sensing device," *Analytica Chimica Acta*, vol. 610, no. 1, pp. 119–124, 2008.

Hindawi
Journal of Nanomaterials
Volume 2021, Article ID 5530606, 9 pages
https://doi.org/10.1155/2021/5530606

Research Article

Comparing Thermal Durability and Effects of Annealing Temperature on Characteristics of Hydrogen-Doped ZnO, AZO, and GZO Thin Films

Dung Van Hoang,[1,2] **Anh Tuan Thanh Pham**,[1,2] **Truong Huu Nguyen**,[1,2] **Thang Bach Phan**,[1,2,3] **and Vinh Cao Tran**[1,2]

[1]*Laboratory of Advanced Materials, University of Science, HoChiMinh City, Vietnam*
[2]*Vietnam National University, HoChiMinh City, Vietnam*
[3]*Center for Innovative Materials and Architectures, HoChiMinh City, Vietnam*

Correspondence should be addressed to Vinh Cao Tran; tcvinh@hcmus.edu.vn

Received 17 January 2021; Revised 14 February 2021; Accepted 28 February 2021; Published 18 March 2021

Academic Editor: Duong Tuan Quang

In this work, undoped, aluminum-, and gallium-doped ZnO thin films (ZnO-H, AZO-H, and GZO-H, respectively) deposited on soda-lime glass substrates by magnetron sputtering method in a gas mixture of hydrogen and argon are annealed at various temperatures in the range of 200–500°C in air to evaluate the durability of those films under annealing temperature. From photoluminescence spectra, formation of point defects, especially oxygen vacancies, when hydrogen diffuses out of the films at high annealing temperature is exhibited via a significant increase of visible emissions. We find out that carrier concentration and Hall mobility of AZO-H and ZnO-H films dramatically decrease, while those of GZO-H film are still stable as the annealing temperature increased from 200°C to 300°C. We proposed a model for interpreting the thermal durability of GZO-H film that, at an annealing temperature of 300°C, Ga^{3+} ions located at adjacent Zn sites can push hydrogen atoms, which are broken out of the antibonding sites which are perpendicular to the $\boldsymbol{c}$ -axis (AB⊥), into bond center sites paralleled to the $\boldsymbol{c}$ -axis ($BC_{//}$). The movement of hydrogen from AB⊥ to $BC_{//}$ site also gives rise to the durability of electrical properties of GZO-H films at the high annealing temperature.

1. Introduction

ZnO, a native n-type oxide semiconductor, owning a wide bandgap (3.37 eV) along with a high exciton energy of 60 meV, has been extensively investigated in recent years due to its ability for UV detectors, photoelectric electronic devices, or thin film solar cells [1, 2]. However, efficiency of those devices is strongly affected by intrinsic or extrinsic defects, which are generated during depositing, such as zinc interstitials (Zn_i), oxygen vacancies (V_O), or zinc vacancies (V_{Zn}) [1–3]. Therefore, the intrinsic or extrinsic defects are popularly investigated by researchers via simulations or experiments to depress and enhance the useless and useful defects, respectively.

Zn_i and V_O play role as donors in ZnO material [3–5]. Ghose et al. [4] proved that Zn_i and V_O can exist in different charged states. For example, the yellow emission from photoluminescence spectra is attributed to doubly charged oxygen vacancies ($V_O^{\bullet\bullet}$) ($^{\bullet}$ is the Kröger–Vink notation) or the blue luminescence is attributed to Zn_i. Lin et al. [5] also proved that Zn_i and V_O still exist in ZnO films regardless of growing in high oxygen partial pressure. Huang et al. [6] theoretically proved the migration barrier of Zn_i that has a very small value, about 0.3–0.5 eV, which could mobile down to very low temperature. Besides, those authors also showed that V_{Zn} is stable at room temperature. Apart from mentioned intrinsic defects, the un- or intentional extrinsic defects, especially defects related to hydrogen, also play a crucial role

on characteristics of ZnO thin films. Van de Walle exploded the researches related to hydrogen in ZnO [7] after the conclusion that hydrogen behaves as a shallow donor in ZnO thin films. After that, there have been numerous experimental as well as theoretical reports which proved and expanded the role of hydrogen in ZnO [8–16]. Hydrogen could be un- or intentionally incorporated into ZnO films during depositing and it could locate at H_{BC} or H_{AB} as the configuration proposed by Van de Walle [7]. Besides, hydrogen can also passivate defects like oxygen vacancy (V_O) or zinc vacancy (V_{Zn}) to create V_O-H (H_O) or V_{Zn}-H complex, respectively [9, 17–19], which improve electron mobility in ZnO thin films. However, hydrogen can easily diffuse out of ZnO thin films at low temperature, which leads to decreased electrical properties of ZnO thin films. Among those hydrogen-related defects, H_O may be the best thermal stable defect up to 475°C before diffusing out, while H_i (H_{BC}, H_{AB}) would diffuse out if the temperature is higher than 225°C [20]. Therefore, finding the method to improve or maintain the electrical properties of hydrogen and/or dopants codoped ZnO thin films under high temperature conditions is very important to widen applications of ZnO materials. Thus, this study investigates the effects of annealing temperature on durability of un-, aluminum-, or gallium-doped ZnO thin films and compares the thermal durability between them.

2. Experimental Details

2.1. Specimen Preparation. ZnO, AZO, and GZO thin films were deposited on soda-lime glass substrates by a dc magnetron sputtering on a Univex-450 system. All films were deposited in Ar-H gas from 3-inch ceramic un-, aluminum- (0.25 wt.% Al_2O_3), or gallium- (0.25 wt.% Ga_2O_3) doped ZnO targets. Prior to the deposition, the glass substrates were cleaned in dilute sodium hydroxide 1%, acetone, and distilled water by ultrasonic wave for 15 minutes at each step before plasma cleaning for 15 minutes. The vacuum chamber was evacuated to the base pressure of 6×10^{-6} Torr. The Ar-H gas was introduced into the sputtering chamber to reach the working pressure of 5×10^{-3} Torr. The hydrogen partial pressure ratio was calculated as the following expression: H_2 ratio = $pH_2/(pH_2 + pAr)$, where pH_2 and pAr are hydrogen and argon gas partial pressure, respectively. In this work, we prepared three series of ZnO-H, AZO-H, and GZO-H thin films at H_2 ratio of 1.7% and the substrate temperature of 200°C. The distance between the substrate and the target and sputtering power was fixed at 50 mm and 60 W, respectively. All films were annealed in air with temperature range of 200–500°C.

2.2. Characterizations. Hall effect measurement using the Van der Pauw method at room temperature on Ecopia HMS-3000 system was employed to investigate the electrical properties of the films. The transmission spectra of the films in the wavelength range of 300–1100 nm were obtained from a Jasco-730 UV-visible spectrophotometer. Film thickness was determined by using Dektak 6M surface profilometer. The film thickness of all films was maintained at 800 nm. The crystalline structure of the films was identified by X-ray diffraction (XRD) using CuKα radiation of Bruker D8 Advance system. The photoluminescence spectra obtained from NanoLog™ spectrofluorometer (Horiba) system by using the excitation wavelengths of 325 nm (He-Cd laser) were used to determinate the effects of annealing temperature on defects in ZnO thin films.

3. Results and Discussions

The dependence of carrier concentration (n) and electron mobility (μ) as a function of annealing temperature is illustrated in Figure 1. In Figure 1(a), for as-deposited films, n values of AZO-H and GZO-H films are higher than those of ZnO-H film, which indicates that group III elements effectively substituted for Zn atoms in ZnO lattice. The μ values for all films without undergoing annealing process are quite high in comparison with published reports for the similar materials and technique [21, 22]. Besides, in Figure 1(b), hydrogen shows the ability to improve the electron mobility for unannealed AZO-H and ZnO-H films better than unannealed GZO-H films. There are numerous experimental as well as theoretical publications reported that hydrogen not only behaves as a shallow donor, which gives rise to the increase of carrier concentration [8, 14, 23–28], but also passivates defects [29–31] such as V_O, Zn_i, or V_{Zn} in ZnO thin films.

The carrier concentration and electron mobility just insignificantly decrease for all films annealed at 200°C, which means that hydrogen-related defect complexes are not influenced at anneal temperature ≤ 200°C. With further increase of annealing temperature up to 300°C, there is a difference between ZnO-H and AZO-H films and GZO-H film in μ as seen in Figure 1(b). The μ values of ZnO-H and AZO-H films sharply drop from *ca.* 55 cm^2/Vs at 200°C to 2 cm^2/Vs and 12 cm^2/Vs at 300°C, respectively. The significant decrease of μ in ZnO-H and AZO-H films originates from the diffusion of hydrogen out of defect complexes, which gives rise to the formation of "dangling bond" type defects, as in silicon materials, inside the crystal grains or at the grain boundaries [8, 32, 33]. As mentioned above, H_i plays role as a shallow donor, therefore the diffusion of H_i out of crystal grains triggers reduction of carrier concentration in ZnO-H and AZO-H films. In addition, the n curves of ZnO-H and AZO-H films being similar to each other with the increase of annealing temperature (≤300°C) indicate that aluminum dopant has no roles in thermal resistance like gallium in ZnO materials as discussed below. Interestingly, n and μ of GZO-H film are not only still stable at annealing temperature of 300°C but also have a slight increasing trend. This implies that hydrogen and gallium interacted with each other in a certain way to keep stable the electrical properties of GZO-H film at 300°C. However, if the annealing temperature is higher than 400°C, n as well as μ has a dramatic decrease for all films, which indicates that hydrogen completely diffuses out of the host lattice, even H_O defects, and results in a large amount of defect.

XRD patterns, crystallite size, and full width at half maximum (FWHM) of ZnO-H, AZO-H, and GZO-H films as a function of annealing temperature are shown in Figure 2.

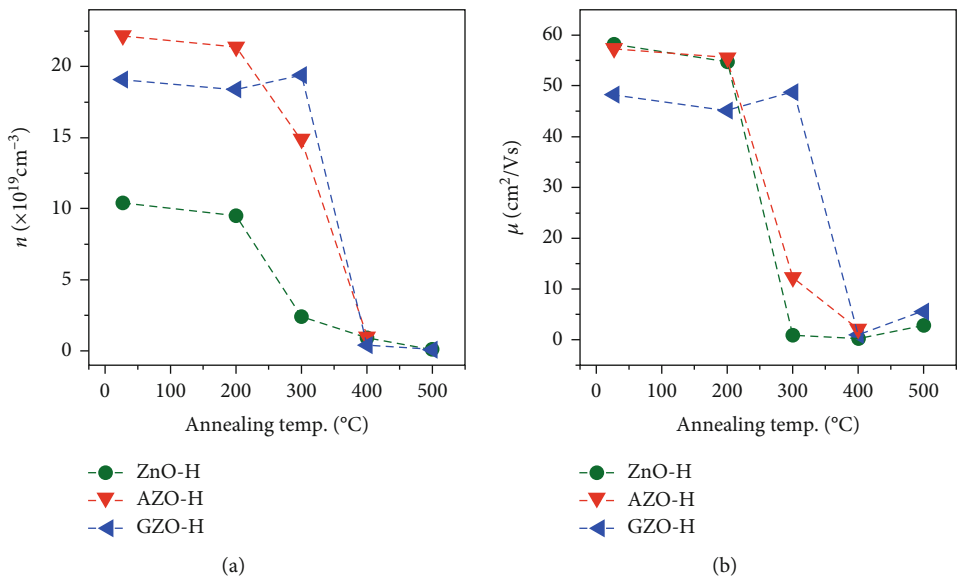

Figure 1: The variation of (a) carrier concentration and (b) electron mobility at different annealing temperatures of ZnO-H, AZO-H, and GZO-H films.

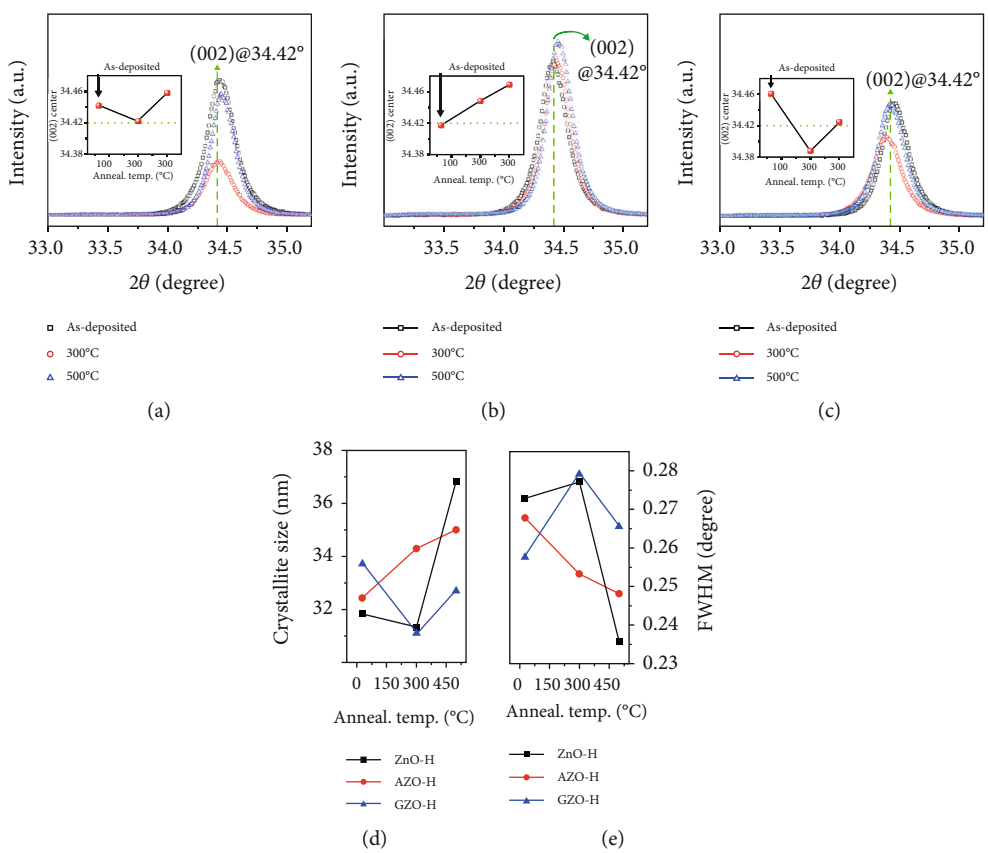

Figure 2: XRD patterns of (a) ZnO-H, (b) AZO-H, and (c) GZO-H films at different annealing temperatures. The dependence of (d) crystallite size and (e) full width at half maximum (FWHM) of ZnO-H, AZO-H, and GZO-H films on annealing temperature.

At the first glance, all films reveal a strong preferred orientation of (002) peak (JCPDS #36-1451) and the intensity of ZnO-H and GZO-H has a decrease trend, while the intensity of AZO-H films is almost unchanged as rising annealing temperature up to 300°C, which implies that there has a variation in crystal structure of these films. The recrystallisation phenomenon is observed for all films annealed at 500°C, which interprets the increase of electron mobility for all films

after being annealed at 500°C except AZO-H film which cannot be measured by Hall measurement at this temperature.

To shed light on effects of annealing temperature on the crystal structure of films, the (002) peak centers obtained from fitting these peaks based on Pearson VII function are plotted in the insets of Figures 2(a)–2(c). For ZnO-H, AZO-H, and GZO-H films without annealing treatment, the (002) peak center of AZO-H film is nearest the 2θ value of 34.42° in comparison with ZnO-H and GZO-H films, which indicates that hydrogen effectively bonds with host lattice in AZO-H film rather than in ZnO-H and GZO-H films (especially located at $BC_{//}$ site [34]) which gives rise to the significant restoration of crystal lattice and also the highest carrier concentration of AZO-H film as seen in Figure 1. However, at annealing temperature of 300°C, there has a significant decrease in the (002) peak center of ZnO-H and GZO-H films, while AZO-H film has an increase trend. Based on Bragg's equation

$$n \cdot \lambda = 2.\cdot d_{002} \cdot \sin\theta, \tag{1}$$

where n is a positive integer, λ is the wavelength of X-ray source ($\lambda_{CuK\alpha} = 0.154$ nm), and d_{002} is the interplaner spacing of the (002) plane of ZnO crystal, we reveal that the (002) peak center of ZnO-H and GZO-H films annealed at 300°C shifts towards lower 2θ angle, which means that the lattice parameter c ($c = 2d_{002}$ for hexagonal wurtzite structure of ZnO) would increase. To interpret the increase of lattice parameter c of ZnO-H and GZO-H films, we proposed some causes for this:

(1) Hydrogen atoms originated from the broken bonds of H_{AB} defects due to high temperature may move into the position between Zn-O bonds parallel c -axis. Wardle et al. [16] proved by first-principle study that the movement of hydrogen between $H_{AB}\perp$ and $H_{BC//}$ sites has relatively low barrier and they found that $H_{BC//}$ was the lowest energy structure. In addition, $H_{BC//}$ does gives rise to the increase of lattice parameter c

(2) The zinc or gallium interstitials (Zn_i or Ga_i) move into the zinc vacancies' sites (V_{Zn}—a type of electron trapping defect) which gives rise to crystal lattice restoration

(3) Oxygen interstitial (O_i) atoms move into the oxygen vacancies' sites (the existence of O_i atoms in films because of all films annealed in air ambiance). However, there is no trace of this defect in photoluminescence spectrum (discussion below) of films with annealing temperature under 300°C. Therefore, this cause may be ruled out

At annealing temperature of 300°C, the H_{AB} bonds are easy to be broken and hydrogen diffuses out of the host lattice in case of ZnO-H and AZO-H films; however, in case of GZO-H film, hydrogen is seemingly pushed by adjacent Ga^{3+} ions at Zn^{2+} site and move into the bond-center position ($H_{AB//}$). Therefore, the cause (1) interprets for the increase of the lattice parameter c, while n and μ values of GZO-H film are still stable, because H_{BC} is also considered as a shallow donor [11] and Ga_{Zn}-O-Zn-$H_{BC//}$-O complex results in the increase of lattice parameter c. The cause (2) accounts for the increase of lattice parameter c of ZnO-H film annealed at 300°C. Figure 3 is outlined to illustrate causes increasing lattice parameter c of ZnO-H and GZO-H films as elevating annealing temperature up to 300°C. However, in case of AZO-H film, the lattice parameter c monotonically decreases with further increase of annealing temperature up to 500°C, because of the hydrogen diffusion out of bond-center positions along with the small ionic radii of Al^{3+} ion ($R_{Al^{3+}} = 54$ pm) in comparison with ionic radii of Ga^{3+} ion ($R_{Ga^{3+}} = 62$ pm) and Zn^{2+} ions ($R_{Zn^{2+}} = 72$ pm) [35].

At annealing temperature of 500°C, all films have a trend of increasing lattice parameter c, because most of hydrogen in films, especially hydrogen at bond-center positions paralleled to the c-axis ($H_{BC//}$), completely diffuse out of the host lattice. Besides, Figure 2(d) shows that the crystallite size of all samples fluctuates around the value of 31–37 nm and has a slight increasing trend at high annealing temperature due to the recrystallisation phenomenon. In addition, with this large crystallite size of all films, the contribution of the boundary scattering on electrical resistivity could be omitted [36]. In addition, Figure 2(e) shows FWHM values of ZnO-H, AZO-H, and GZO-H films at various annealing temperatures. The Scherrer equation (2) is commonly used to calculate nanoscale crystallite size, and FWHM value is one of the two parameters determining the crystallite size. Bragg angle θ and FWHM are inversely proportional to crystallite size, while the variation of Bragg angle is small; thus, the crystallite size as seen in Figure 2(e) has the opposite trend with FWHM values.

$$D = \frac{K\lambda}{\beta\cos\theta}, \tag{2}$$

where D is the crystallite size (nm), K is a dimensionless shape factor, and β is FWHM.

Figure 4 shows the surface morphology of ZnO-H, AZO-H, and GZO-H films as-deposited and annealed at various temperatures. Generally, there is no significant difference in surface morphology between as-deposited films regardless of the appearance of aluminum or gallium and that annealed at 300°C or 500°C. Besides, based on SEM micrographs, it is clearly seen that the distribution of grain size for all films is homogenous on the surface and all films have the similar morphology, which indicates that films were well prepared and homogeneous.

The transmittance spectra of ZnO-H, AZO-H, and GZO-H thin films measured in wavelength range of 300–1100 nm in Figure 5 show clear and homogenous interference fringes of all films indicating the high crystalline quality and the similar film thickness, respectively. The inset in Figure 5(a) shows a red shift of all films with further increasing annealing temperature, because the decrease of n as seen in Figure 1(a) gives rise to the Burstein-Moss effect. The transmittance is larger than 82% (including film and glass substrate) when

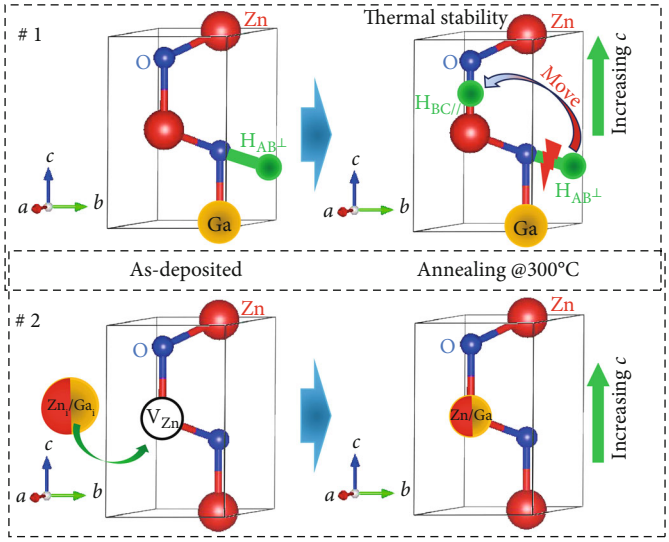

Figure 3: Illustrations of causes increasing lattice parameter c of ZnO-H and GZO-H films.

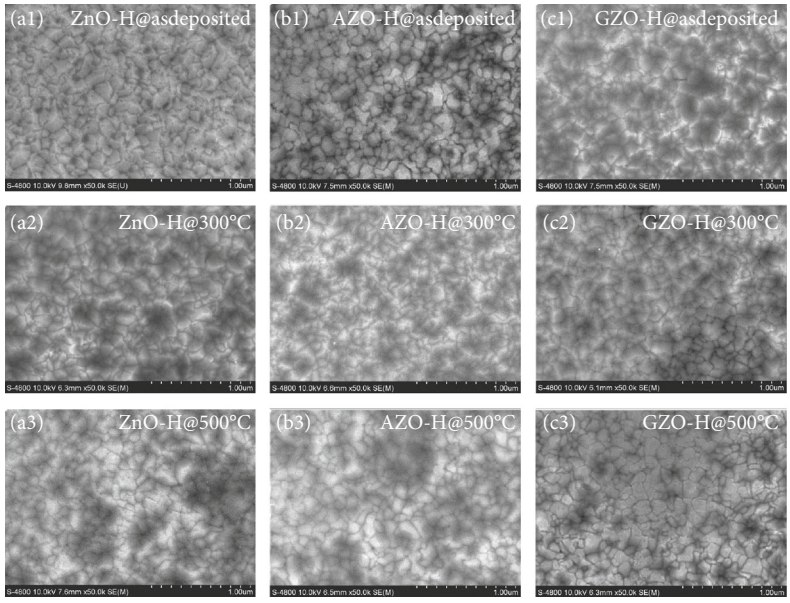

Figure 4: SEM micrographs of (a1–a3) ZnO-H, (b1–b3) AZO-H, and (c1–c3) GZO-H films prepared at different annealing temperatures.

averaged in the visible and near-infrared range from 400 to 1100 nm for all films as seen in Figure 5(b). The average transmittance of ZnO-H and AZO-H films has a decreasing trend when annealing temperature rises to 300°C. This is due to the formation of defects in host lattice generated from the broken hydrogen-related bonds as mentioned above, which gives rise to the appearance of scattering centers. However, the average transmittance of GZO-H films is almost unchanged at annealing temperature of 300°C, which is consistent with electrical properties as discussed above. With further increasing annealing temperature, the average transmittance of all films increases because of the aforementioned recrystallisation phenomenon.

Figure 6 shows the variation of the photoluminescence spectra of ZnO-H, AZO-H, and GZO-H thin films at different annealing temperatures. All films have a strong emission band in wavelength range of 375–450 nm, which is known as a featured emission band of ZnO material including near-band edge emission (NBE) [37, 38] and the transition between donor levels (such as Zn_i or H_i) and acceptor levels (V_{Zn}). The broaden emission band in wavelength range of 450–600 nm is attributed to the transition from oxygen vacancy levels to acceptor levels or valence band (VB) [37, 38]. From Figure 6, it can be clearly seen that there is a significant variation in shape of PL spectra of all films at different annealing temperatures, which indicates that annealing temperature strongly affects defect levels. In case of AZO-H films (Figure 6(b)), the PL intensity of AZO-H films significantly increases at annealing temperature of 300°C, which indicates that hydrogen is easy to cooperate with defects in AZO-H

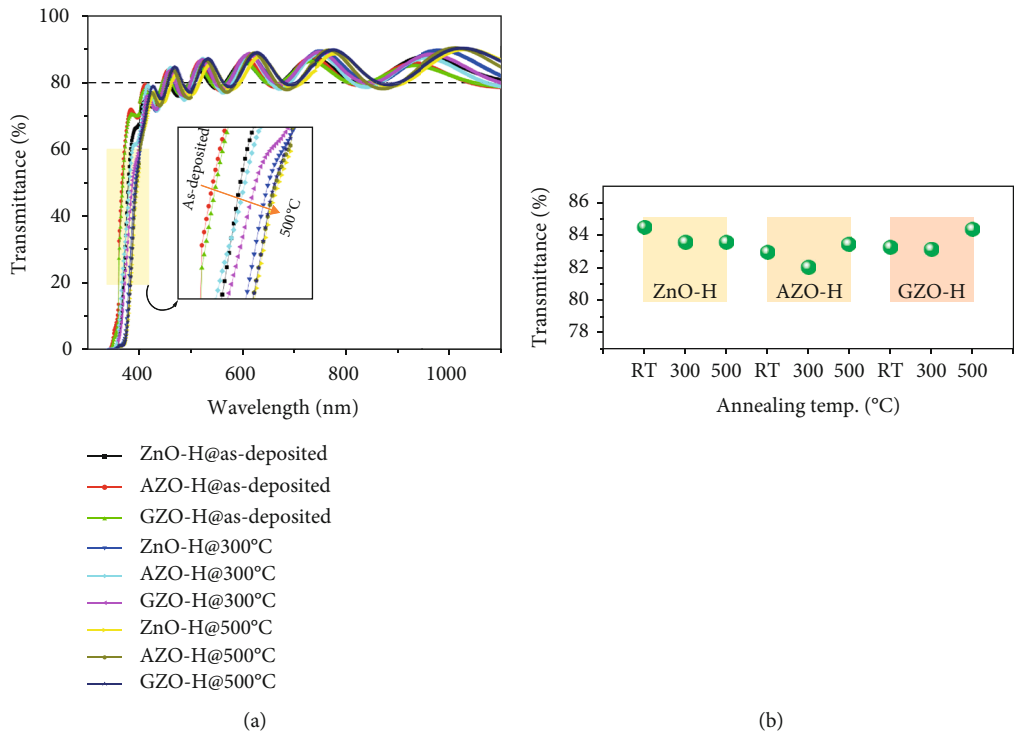

Figure 5: (a) Transmittance spectra of ZnO-H, AZO-H, and GZO-H at different annealing temperatures. (b) The dependence of the average transmittance of all films on annealing temperature.

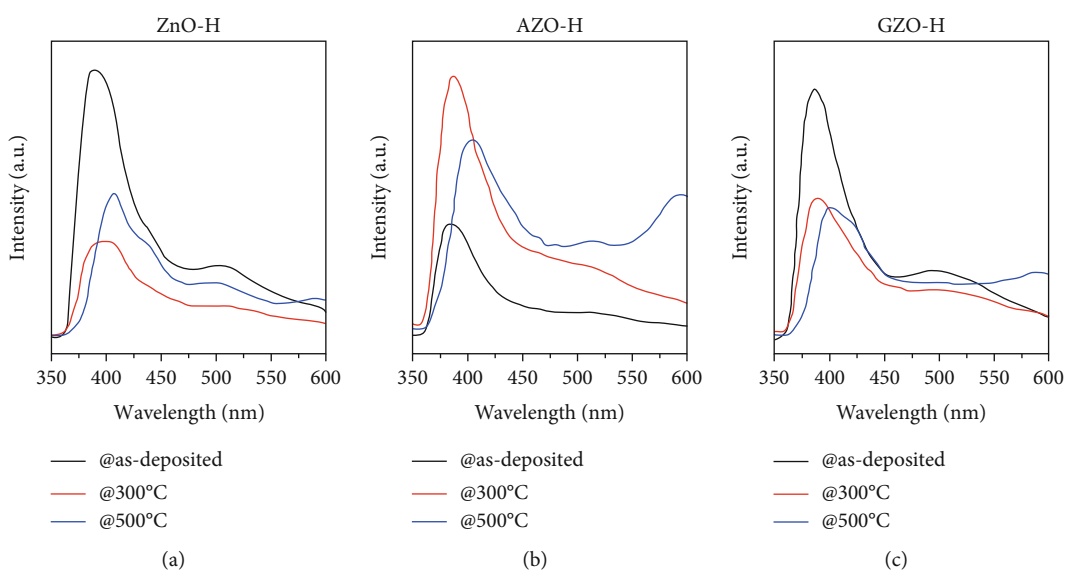

Figure 6: PL spectra of (a) ZnO-H, (b) AZO-H, and (c) GZO-H films annealed at different temperatures.

films such as H_i or V_{Zn} to effectively improve electron mobility and carrier concentration as seen in Figure 1, but these hydrogen-related bonds are easy to be broken, which results in defects. However, in the case of ZnO-H and GZO-H films, the defect-related emission has a slight variation. The intensity of all samples in wavelength range of around 600 nm strongly increases at annealing temperature of 500°C, which indicates that hydrogen diffused out of oxygen vacancy sites.

To get more details on the influence of annealing temperature on defects in ZnO-H, AZO-H, and GZO-H films, all PL spectra were deconvoluted based on Gaussian function distribution to determinate the overlapped emissions as seen in Figure 7. There are four deconvoluted emission peaks for all films. However, there is an absence or appearance of several PL peaks because of the annealing treatment. For example, for as-deposited and 300°C-annealed films (ZnO-H,

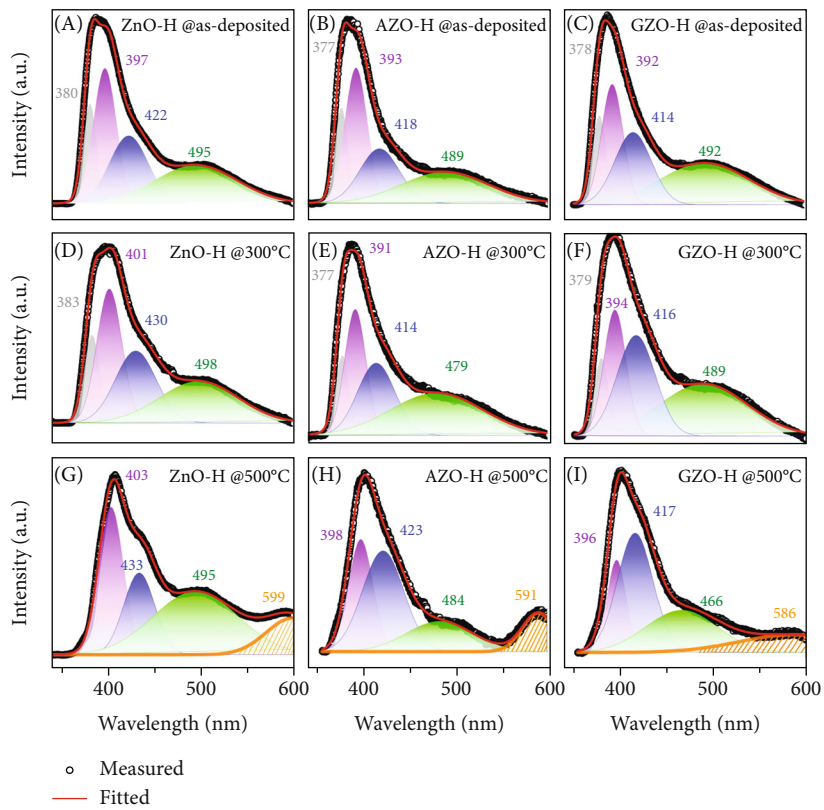

Figure 7: Deconvoluted photoluminescence spectra of (a, d, g) ZnO-H, (b, e, h) AZO-H, and (c, f, i) GZO-H films prepared at different annealing temperatures.

AZO-H, and GZO-H films), the emission peaks in the UV region (under 383 nm in this work) which is known as the transition of electrons between NBE states and VB were detected, while the yellow emission peak at around 600 nm which is attributed to the emission from conduction band (CB) to doubly charged oxygen vacancies ($V_O^{\bullet\bullet}$) appears in the films annealed at temperature of 500°C [4].

The violet region (391–403 nm) for all films (as-deposited and annealed films) is attributed to the transition from the Zn_i levels (located at 0.2 eV below the CB for a typical bandgap of 3.37 eV of ZnO) to VB or from CB to the V_{Zn} levels (located at 0.3 eV above VB) [39, 40]. For ZnO-H films, the violet emission peaks located in wavelength range of 397 nm (3.12 eV) to 403 nm (3.07 eV) are caused by the transitions from CB and NBE to V_{Zn} levels. However, for AZO-H and GZO-H films, the violet emissions fluctuate around the wavelength range of 391 nm (3.17 eV) to 398 nm (3.11 eV) which means that these emissions are well fitting with the transition of electrons from Zn_i levels to VB. The transition between Zn_i levels and VB prevails in AZO-H and GZO-H films in comparison with ZnO-H film because of the existence of Ga_i or Al_i which cannot completely substitute for Zn and behave as a shallow donor like Zn_i [41]. The near-blue emission peaks (414–433 nm and 2.99–2.86 eV, respectively) in PL spectra of ZnO-H, AZO-H, and GZO-H films (both as-deposited and annealed films) are the result of transition of electrons from Zn_i to V_{Zn} levels [3].

From the observation of the emissions in violet and near-blue regions in Figures 6 and 7, ZnO-H film has the larger red shift in comparison with GZO-H film because the broadness of V_{Zn} level relates to the broken V_{Zn}-H complexes at annealing temperature of 300°C. However, interestingly, AZO-H film has the blue shift in the violet and near-blue regions because of the narrowness of V_{Zn} levels which is caused by the formation of Al_{Zn}-V_{Zn} complex as proved by Johansen et al. [42]. The annealing temperature of 300°C is enough to break the V_{Zn}-H complex as well as gives rise to the combination of Al_{Zn} defect to the nearest V_{Zn} defect to form the Al_{Zn}-V_{Zn} complex. This complex limits the role of shallow Al_{Zn} donor because it acts as a compensating acceptor with the charge state of -1, which is consistent with the decrease of carrier concentration of AZO-H film annealed at temperature of 300°C as mentioned above.

The blue-green emission peaks (479–498 nm; 2.59–2.49 eV) are attributed to the transition of electrons from V_O^* defect (neutral oxygen vacancies formed by the $V_O^{\bullet}$ state captures an electron from CB) [3] or $V_O^{\bullet}-H$ complex to VB. Besides, the blue-green emission peaks of ZnO-H films have a red-shifted tendency, whereas those of AZO-H and GZO-H films have a blue-shifted tendency at annealing temperature of 300°C, which implies that there is an influence of Al or Ga on V_O-related defect level. From those PL results, we reveal that there is a small change in emission peaks of GZO-H films in comparison with ZnO-H and AZO-H films at

annealing temperature of 300°C, which indicates that GZO-H film is still stable at this annealing temperature and these PL results are consistent with electrical properties.

4. Conclusions

The influence of annealing temperature on electrical, optical, structural, and morphological properties of ZnO-H, AZO-H, and GZO-H films was systematically investigated to find out the thermal durability of those films. We reveal that GZO-H films are not only durable with respect to electrical properties at annealing temperature up to 300°C but also have slightly increased carrier concentration and electron mobility. Besides, we propose that Ga^{3+} ions located at adjacent Zn sites along with annealing temperature of 300°C can push hydrogen atoms into bond center sites forming $H_{BC//}$, which gives rise to the stability of electrical properties of GZO-H films. ZnO-H and AZO-H films have only thermal durability at annealing temperature up to 200°C.

Data Availability

The data that support the findings of this study are within the article and the raw data are available from the corresponding author, Vinh Cao Tran, upon reasonable request.

Conflicts of Interest

There are no conflicts of interest to declare.

Acknowledgments

This research is funded by Vietnam National University HoChiMinh City (VNU-HCM) under the grant number B2017-18-09. The Hall effect measurement was supported by the Faculty of Materials Science and Technology, University of Science, VNU-HCM.

Supplementary Materials

Graphical abstract depicting a model for briefly interpreting the thermal durability of GZO-H film can be found at the system on Journal of Nanomaterials. *(Supplementary Materials)*

References

[1] T. F. Wu, K. Zhao, B. W. Lü, Z. L. Wu, and Y. S. Wang, "Intrinsic defects in ZnO films deposited by RF sputtering," *Ferroelectrics*, vol. 528, no. 1, pp. 31–37, 2018.

[2] Y. J. Y. Onofre, S. de Castro, and M. P. F. de Godoy, "Effect of traps localization in ZnO thin films by photoluminescence spectroscopy," *Materials Letters*, vol. 188, pp. 37–40, 2017.

[3] F. Kayaci, S. Vempati, I. Donmez, N. Biyikli, and T. Uyar, "Role of zinc interstitials and oxygen vacancies of ZnO in photocatalysis: a bottom-up approach to control defect density," *Nanoscale*, vol. 6, no. 17, pp. 10224–10234, 2014.

[4] S. Ghose, T. Rakshit, R. Ranganathan, and D. Jana, "Role of Zn-interstitial defect states on d0 ferromagnetism of mechanically milled ZnO nanoparticles," *RSC Advances*, vol. 5, no. 121, pp. 99766–99774, 2015.

[5] B. Lin, Z. Fu, and Y. Jia, "Green luminescent center in undoped zinc oxide films deposited on silicon substrates," *Applied Physics Letters*, vol. 79, no. 7, pp. 943–945, 2001.

[6] G. Y. Huang, C. Y. Wang, and J. T. Wang, "First-principles study of diffusion of zinc vacancies and interstitials in ZnO," *Solid State Communications*, vol. 149, no. 5-6, pp. 199–204, 2009.

[7] C. G. Van De Walle, "Hydrogen as a cause of doping in zinc oxide," *Physical Review Letters*, vol. 85, no. 5, pp. 1012–1015, 2000.

[8] D. L. Zhu, G. J. Wang, F. Jia et al., "Study of H-related defects in Ga-doped ZnO thin films deposited by RF magnetron sputtering in Ar+H2 ambient," *Materials Technology*, vol. 32, no. 7, pp. 424–429, 2017.

[9] M. D. McCluskey and S. J. Jokela, "Defects in ZnO," *Journal of Applied Physics*, vol. 106, no. 7, article 071101, 2009.

[10] D. M. Hofmann, A. Hofstaetter, F. Leiter et al., "Hydrogen: a relevant shallow donor in zinc oxide," *Physical Review Letters*, vol. 88, no. 4, 2002.

[11] E. V. Lavrov, "Hydrogen in ZnO," *Physica B: Condensed Matter*, vol. 404, no. 23-24, pp. 5075–5079, 2009.

[12] J. Koßmann and C. Haettig, "Investigation of interstitial hydrogen and related defects in ZnO," *Physical Chemistry Chemical Physics*, vol. 14, no. 47, pp. 16392–16399, 2012.

[13] D. Gaspar, L. Pereira, K. Gehrke, B. Galler, E. Fortunato, and R. Martins, "High mobility hydrogenated zinc oxide thin films," *Solar Energy Materials and Solar Cells*, vol. 163, pp. 255–262, 2017.

[14] W. M. Kim, Y. H. Kim, J. S. Kim et al., "Hydrogen in polycrystalline ZnO thin films," *Journal of Physics D: Applied Physics*, vol. 43, no. 36, p. 365406, 2010.

[15] C. G. Van de Walle, "Hydrogen in semiconductors and insulators," *Journal of Alloys and Compounds*, vol. 446-447, pp. 48–51, 2007.

[16] M. G. Wardle, J. P. Goss, and P. R. Briddon, "First-principles study of the diffusion of hydrogen in ZnO," *Physical Review Letters*, vol. 96, no. 20, 2006.

[17] S. G. Koch, E. V. Lavrov, and J. Weber, "Interplay between interstitial and substitutional hydrogen donors in ZnO," *Physical Review B: Condensed Matter and Materials Physics*, vol. 89, no. 23, 2014.

[18] E. V. Lavrov, F. Börrnert, and J. Weber, "On the nature of hydrogen-related shallow donors in ZnO," *Physica B: Condensed Matter*, vol. 376-377, pp. 694–698, 2006.

[19] X. Li, B. Keyes, S. Asher et al., "Hydrogen passivation effect in nitrogen-doped ZnO thin films," *Applied Physics Letters*, vol. 86, no. 12, p. 122107, 2005.

[20] J. Bang and K. J. Chang, "Diffusion and thermal stability of hydrogen in ZnO," *Applied Physics Letters*, vol. 92, no. 13, p. 132109, 2008.

[21] J. Nomoto, H. Makino, and T. Yamamoto, "Carrier mobility of highly transparent conductive Al-doped ZnO polycrystalline films deposited by radio-frequency, direct-current, and radio-frequency-superimposed direct-current magnetron sputtering: Grain boundary effect and scattering in the grain bulk," *Journal of Applied Physics*, vol. 117, no. 4, p. 045304, 2015.

[22] J. Nomoto, H. Makino, and T. Yamamoto, "High-Hall-mobility Al-doped ZnO films having textured polycrystalline structure with a well-defined (0001) orientation," *Nanoscale Research Letters*, vol. 11, no. 1, p. 320, 2016.

[23] M. D. McCluskey, S. J. Jokela, and W. M. H. Oo, "Hydrogen donors in ZnO," *MRS Proceedings*, vol. 864, 2005.

[24] X. Xue, T. Wang, X. Jiang, J. Jiang, C. Pan, and Y. Wu, "Interaction of hydrogen with defects in ZnO nanoparticles – studied by positron annihilation, Raman and photoluminescence spectroscopy," *CrystEngComm*, vol. 16, no. 6, 2014.

[25] C. G. Van de Walle, "Hydrogen as a shallow center in semiconductors and oxides," *Physica Status Solidi B: Basic Research*, vol. 235, no. 1, pp. 89–95, 2003.

[26] M. D. McCluskey and S. J. Jokela, "Sources of n-type conductivity in ZnO," *Physica B: Condensed Matter*, vol. 401-402, pp. 355–357, 2007.

[27] Y. Hu, Y. Chen, J. Chen, X. Chen, and D. Ma, "Effects of hydrogen flow on properties of hydrogen doped ZnO thin films prepared by RF magnetron sputtering," *Applied Physics A*, vol. 114, pp. 875–882, 2014.

[28] M. D. Mccluskey and S. J. Jokela, "Infrared spectroscopy of hydrogen in ZnO," *MRS Proceedings*, vol. 813, 2004.

[29] J. Cho, K.-H. Yoon, M.-S. Oh, and W.-K. Choi, "Effects of H[sub 2] annealing treatment on photoluminescence and structure of ZnO:Al/Al[sub 2]O[sub 3] grown by radio-frequency magnetron sputtering," *Journal of the Electrochemical Society*, vol. 150, no. 10, p. H225, 2003.

[30] D. L. Zhu, H. F. Xiang, P. J. Cao et al., "Influence of H2 introduction on properties in Al-doped ZnO thin films prepared by RF magnetron sputtering at room temperature," *Journal of Materials Science: Materials in Electronics*, vol. 24, no. 6, pp. 1966–1969, 2013.

[31] B. L. Zhu, J. Wang, S. J. Zhu et al., "Influence of hydrogen introduction on structure and properties of ZnO thin films during sputtering and post-annealing," *Thin Solid Films*, vol. 519, no. 11, pp. 3809–3815, 2011.

[32] M. D. McCluskey, M. C. Tarun, and S. T. Teklemichael, "Hydrogen in oxide semiconductors," *Journal of Materials Research*, vol. 27, no. 17, pp. 2190–2198, 2012.

[33] M.-C. Chen, T.-C. Chang, S.-Y. Huang et al., "A low-temperature method for improving the performance of sputter-deposited ZnO thin-film transistors with supercritical fluid," *Applied Physics Letters*, vol. 94, no. 16, p. 162111, 2009.

[34] F. T. Kong, H. J. Tao, and H. R. Gong, "Interstitial hydrogen in ZnO and BeZnO," *International Journal of Hydrogen Energy*, vol. 38, no. 14, pp. 5974–5982, 2013.

[35] M.-C. Li, C.-C. Kuo, S.-H. Peng, S.-H. Chen, and C.-C. Lee, "Influence of hydrogen on the properties of Al and Ga-doped ZnO films at room temperature," *Applied Optics*, vol. 50, no. 9, pp. C197–C200, 2011.

[36] D. P. Pham, H. T. Nguyen, B. T. Phan, V. D. Hoang, S. Maenosono, and C. V. Tran, "Influence of addition of indium and of post-annealing on structural, electrical and optical properties of gallium-doped zinc oxide thin films deposited by direct-current magnetron sputtering," *Thin Solid Films*, vol. 583, pp. 201–204, 2015.

[37] A. Tiwari and P. P. Sahay, "The effects of Sn-In co-doping on the structural, optical, photoluminescence and electrical characteristics of the sol-gel processed ZnO thin films," *Optical Materials*, vol. 110, p. 110395, 2020.

[38] X. Chen, Q. Xie, and J. Li, "Significantly improved photoluminescence properties of ZnO thin films by lithium doping," *Ceramics International*, vol. 46, no. 2, pp. 2309–2316, 2020.

[39] Y. M. Hu, J. Y. Li, N. Y. Chen, C. Y. Chen, T. C. Han, and C. C. Yu, "Effect of sputtering power on crystallinity, intrinsic defects, and optical and electrical properties of Al-doped ZnO transparent conducting thin films for optoelectronic devices," *Journal of Applied Physics*, vol. 121, no. 8, p. 085302, 2017.

[40] C. H. Ahn, Y. Y. Kim, D. C. Kim, S. K. Mohanta, and H. K. Cho, "A comparative analysis of deep level emission in ZnO layers deposited by various methods," *Journal of Applied Physics*, vol. 105, no. 1, p. 013502, 2009.

[41] A. Janotti and C. G. Van de Walle, "Fundamentals of zinc oxide as a semiconductor," *Reports on Progress in Physics*, vol. 72, no. 12, p. 126501, 2009.

[42] K. M. Johansen, L. Vines, T. S. Bjørheim, R. Schifano, and B. G. Svensson, "Aluminum migration and intrinsic defect interaction in single-crystal zinc oxide," *Physical Review Applied*, vol. 3, no. 2, 2015.

Hindawi
Journal of Nanomaterials
Volume 2021, Article ID 5594256, 10 pages
https://doi.org/10.1155/2021/5594256

Research Article

Three-Level Optical Stark Effect of Excitons in GaAs Cylindrical Quantum Wires

Dinh Nhu Thao,[1] **Duong Dinh Phuoc**,[1] **Le Thi Ngoc Bao**,[2] **Le Thi Dieu Hien**,[1,2] **Tran Phan Thuy Linh**,[3] **and Nguyen Thi Le Thuy**[4]

[1]*Hue University of Education, Hue University, 34 Le Loi Street, Hue City, Vietnam*
[2]*Hue University of Sciences, Hue University, 77 Nguyen Hue Street, Hue City, Vietnam*
[3]*Faculty of Physics, Hanoi National University of Education, 136 Xuanthuy, Caugiay, Hanoi 100000, Vietnam*
[4]*Research Laboratories of Saigon Hi-Tech Park, Lot I3, Road N2, Saigon Hi-Tech Park, District 9, Ho Chi Minh City, Vietnam*

Correspondence should be addressed to Dinh Nhu Thao; dnthao@hueuni.edu.vn
and Duong Dinh Phuoc; dinhphuoc2808@gmail.com

Received 8 January 2021; Revised 25 February 2021; Accepted 3 March 2021; Published 17 March 2021

Academic Editor: Mai Duy Hien

This study looks at the three-level optical Stark effect of excitons in GaAs cylindrical quantum wires, utilizing the renormalized wave function theory. By applying the three-level model consisting of the first two electron levels connected via a powerful pump laser and the first hole level, we observe the appearance of the excitonic optical Stark effect through the appearance of two separated peaks in the exciton absorption spectra. In addition, the strong impact of the pump laser detuning and the wire radius on the optical Stark effect are also put under thorough examination. Finally, a brief guidance for experimental verification is also suggested.

1. Introduction

Low-dimensional semiconductor structures, which are the core of many semiconductor devices, have been studied for new applied fields thanks to the inventions of advanced technologies [1–12]. These devices play important roles in the fields of medicine, military, telecommunication, and many others [13–17]. The semiconductor quantum wires, one of the low-dimensional structures that possess many special properties, have drawn the attention of scientists [18–22]. These structures could be applied to create high-speed lasers [23, 24], quantum electron waveguides [25], resonant tunneling field-effect transistors [26, 27], or telecommunication networks [28]. Recently, studies of movement and interaction among electrons in the quantum wires have shown the quantum effects that can lead to various applications in the new quantum technology [29]. Nonetheless, many new physical properties of these structures, which are expected to have more breakthrough applications in the future, have been little known to researchers.

In low-dimensional semiconductor systems, scientists have observed the excitonic optical Stark effect when irradiating a strong pump laser pulse in [30, 31]. This effect resulted from the interaction between exciton states, displayed through splitting and shifting the absorption spectrum of the exciton [32–35]. Based on these properties, the researchers proposed a number of prospective applications of the excitonic optical Stark effect, such as making optical switching devices [33, 34], optical modulators [35], mesoporous hybrid multifunctional system [36], or optically controlled field-effect transistors [37]. So far, the excitonic optical Stark effect has been primarily studied on quantum wells and quantum dots [30, 31]. The existence of this effect in quantum wire structures is still under investigation.

The excitonic optical Stark effect is divided into two types. The first type is the consequence of a coupling of the exciton ground state and an exciton-excited state, e.g., the first exciton state under the effect of a strong pump laser beam called a two-level Stark effect [38]. The second type is due to a coupling of two exciton-excited states under the effect of a pump laser beam of lower intensity, known as a three-level Stark effect [38, 39]. The latter has more applicability because it is more likely to occur. The excitonic optical

Stark effect can be experimentally studied by the pump-probe technique [40, 41]. For theoretical research, methods to be deployed can be the renormalized wave function theory [42], the density matrix approach [43, 44], the finite difference method [45], the photoemission theory [46], or the non-equilibrium many body perturbation theory [47]. In our viewpoint, the renormalized wave function formulation has many advantages such as it only renormalizes the wave function of exciton, or it is easy to confirm the existence of the effect as well as to reveal its physical properties.

In this study, we investigate the three-level excitonic optical Stark effect in GaAs cylindrical quantum wires utilizing the renormalized wave function formulation. We have also successfully applied that formulation to study the excitonic quantum beats [48], a phenomenon that occurs as the consequence of the three-level excitonic optical Stark effect in the same structures of quantum wires. Therefore, both the recent report and Ref. [48] share the same starting point. Hence, we can expect to successfully study the three-level excitonic optical Stark effect in those structures. This paper is organized into three main sections, with the present section justifying the rationale and introducing the stated problem. Section 2 provides the formulation and basic equations. Section 3 presents and discusses the findings of the study, based on which, conclusions are arrived at.

2. Formulation

2.1. Wave Functions and Quantized Levels of Electron and Hole in a Cylindrical Quantum Wire. Let consider a circular cylindrical quantum wire in the cylindrical coordinates (r, φ, z). Suppose that the quantum wire is of the radius R and stays along the Oz axis, and the particles are confined in the plane Oxy by an infinite cylindrical symmetric potential,

$$U(x, y) = U(r) = \begin{cases} 0, & r \le R, \\ \infty, & r > R, \end{cases} \tag{1}$$

where r is the length from the wire axis to the considered position. The envelope wave functions describing the states of the electron and hole in the confined plane can be written as [48, 49]

$$\Psi_{mn}^{e,h}\left(\vec{r}\right) = \frac{1}{\sqrt{\pi R^2}} \frac{J_m(\chi_{mn}(r/R))}{J_{m+1}(\chi_{mn})} e^{im\varphi}, \tag{2}$$

where $\vec{r} = (r, \varphi)$ is the position vector of the particle, $J_m(r)$ are the Bessel functions of the first kind of order m ($m = 0, 1, 2, \cdots$), and χ_{mn} are its nth zero points ($n = 1, 2, \cdots$). The full wave functions of the electron and hole are presented as

$$\Lambda_{mn}^{e,h}\left(\vec{r}\right) = u_{c,v}\left(\vec{r}\right) \Psi_{mn}^{e,h}\left(\vec{r}\right), \tag{3}$$

where $u_{c,v}(\vec{r})$ is the periodic Bloch function in the first Brillouin zone and c and v signify the conduction and valence band, respectively.

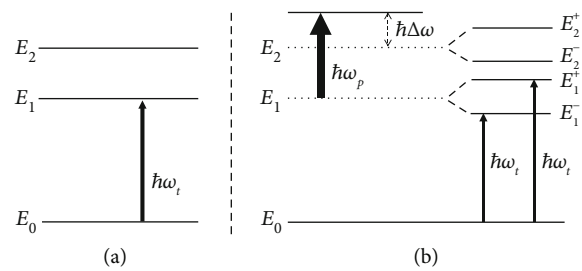

Figure 1: The three-level diagram of energy: (a) Under no pump laser, the system contains one hole level (E_0) and two electron levels (E_1 and E_2). The probe laser of photon energy $\hbar\omega_t$ detects the interband transition between the E_0 and E_1 levels (thin arrow). (b) Under the pump laser of photon energy $\hbar\omega_p$ (thick arrow), level E_1 is separated into levels E_1^- and E_1^+; level E_2 is separated into levels E_2^- and E_2^+. The probe laser of photon energy $\hbar\omega_t$ detects two interband transitions from E_0 level to E_1^- level and from E_0 level to E_1^+ level (thin arrows).

The quantized levels of the electron and hole are determined as

$$\begin{cases} \varepsilon_{mn}^{e} = E_g + \dfrac{\hbar^2 \chi_{mn}^2}{2m_e R^2}, \\ \varepsilon_{mn}^{h} = \dfrac{\hbar^2 \chi_{mn}^2}{2m_h R^2}, \end{cases} \tag{4}$$

where m_e and m_h are the effective masses of the electron and hole, respectively, and E_g is the energy gap of the wire material. Here, we set the top of the valence band as the origin for calculating the energy of the particles.

In this paper, we use a three-level energy diagram to study the excitonic optical Stark effect in the quantum wire. Therefore, we investigate a three-level model in which E_0 is the first hole level, while E_1 and E_2 are the first two electron ones (as shown in Figure 1(a)).

The energies of the particles are determined as follows [48]:

$$\begin{cases} E_0 \equiv \varepsilon_{01}^{h}, \\ E_1 \equiv \varepsilon_{01}^{e}, \\ E_2 \equiv \varepsilon_{11}^{e}, \end{cases} \tag{5}$$

with the compatible time-dependent wave functions

$$\begin{cases} \Pi_0\left(\vec{r}, t\right) = \Pi_0\left(\vec{r}\right) e^{-(i/\hbar)E_0 t}, \\ \Pi_1\left(\vec{r}, t\right) = \Pi_1\left(\vec{r}\right) e^{-(i/\hbar)E_1 t}, \\ \Pi_2\left(\vec{r}, t\right) = \Pi_2\left(\vec{r}\right) e^{-(i/\hbar)E_2 t}, \end{cases} \tag{6}$$

in which $\Pi_j(\vec{r})(j = 0, 1, 2)$ are the stationary wave functions of the particles in the quantum wire and are defined by [48]

$$\begin{cases} \Pi_0\left(\vec{r}\right) \equiv \Lambda_{01}^h\left(\vec{r}\right), \\ \Pi_1\left(\vec{r}\right) \equiv \Lambda_{01}^e\left(\vec{r}\right), \\ \Pi_2\left(\vec{r}\right) \equiv \Lambda_{11}^e\left(\vec{r}\right). \end{cases} \tag{7}$$

2.2. Electronic Wave Function and Energy Levels in the Presence of Pump Laser. To seek the evidence of the existence of the excitonic optical Stark effect in the quantum wire and study its properties, we irradiate concurrently two lasers on the system. A strong pump laser, which resonates with the energy separation between two electron levels, is utilized to stimulate the intraband transition of the electron (as indicated by the thick arrow in Figure 1(b)). Besides, a weak probe laser is utilized to identify the interband transitions among the hole level and the electron levels (as indicated by the thin arrow in Figure 1(b)). The form of the laser waves is chosen as follows:

$$\vec{E}(t) = \vec{n}A_x e^{-i\omega_x t}, \tag{8}$$

where $\vec{n}$ is the unit vector along the direction of wave propagation, the symbol x represents either the pump laser (when x is substituted by p) or the probe laser (when x is substituted by t), and ω_x and A_x are the frequency and amplitude of the corresponding laser, respectively. Accordingly, Hamiltonian that describes the interaction of the electron and the electromagnetic field accompanying the laser can be written as [50]

$$\hat{H}_{\text{int}} = -\frac{e}{m_0}\frac{A_x.e^{-i\omega_x t}}{i\omega_x}\vec{n}\,\hat{\vec{p}}, \tag{9}$$

where m_0, e, and $\vec{p}$ represent the bare mass, charge, and momentum of electron, respectively.

When the strong resonant pump laser is switched on, the wave functions of the electron are renormalized. Now, the electrons stay in a superposition state represented by the wave function

$$\begin{aligned} \Pi_{\text{mix}}^e\left(\vec{r}, t\right) = {} & \frac{1}{2\Omega_R}\left(\alpha_1 e^{-(i/\hbar)E_1^- t} + \alpha_2 e^{-(i/\hbar)E_1^+ t}\right)\Pi_1\left(\vec{r}\right) \\ & - \frac{V_{21}}{2\hbar\Omega_R}\left(e^{-(i/\hbar)E_2^- t} - e^{-(i/\hbar)E_2^+ t}\right)\Pi_2\left(\vec{r}\right), \end{aligned} \tag{10}$$

where $\Pi_1(\vec{r})$ and $\Pi_2(\vec{r})$ are the initial electron wave functions in the absence of the pump laser as given in Equation (7). When the pump laser operates, the energy spectrum of the electron are expanded to four levels in which two new levels E_1^- and E_1^+ come from the splitting of the initial level E_1, and two sublevels E_2^- and E_2^+ are detached from the initial level E_2 (as plotted in Figure 1(b)). These splitting levels are

$$\begin{cases} E_1^- = E_1 - \hbar\alpha_2, \\ E_1^+ = E_1 + \hbar\alpha_1, \end{cases} \tag{11}$$

$$\begin{cases} E_2^- = E_2 - \hbar\alpha_1, \\ E_2^+ = E_2 + \hbar\alpha_2. \end{cases} \tag{12}$$

In Equation (10), we set

$$\begin{cases} \alpha_1 = \Omega_R - \dfrac{\Delta\omega}{2}, \\ \alpha_2 = \Omega_R + \dfrac{\Delta\omega}{2}, \\ \Omega_R = \sqrt{\dfrac{\Delta\omega^2}{4} + \dfrac{|V_{21}|^2}{\hbar^2}}, \end{cases} \tag{13}$$

with $\hbar\Delta\omega$ being the pump laser detuning, which is the energy difference between the photon energy of the pump laser and the energy distance between two original electron levels E_1 and E_2, $\hbar\Delta\omega = \hbar\omega_p - (E_2 - E_1)$; please look at the left side of Figure 1(b) for a schematic view of the pump laser detuning. In addition, V_{21} is the intraband transition matrix element between those levels:

$$V_{21} = \frac{e}{m_0}\frac{A_p}{i\omega_p}\frac{m_e}{i\hbar}\frac{(E_2 - E_1)R}{J_1(\chi_{01})J_2(\chi_{11})}\int_0^1 J_0(\chi_{01}r)J_1(\chi_{11}r)r^2 dr, \tag{14}$$

where m_e is the effective mass of electron. We see that the matrix element depends not only on the parameters of the quantum wire but also on those of the pump laser.

2.3. The Absorption Spectrum of Excitons in the Absence of the Pump Laser. We will analyze the exciton absorption spectrum in quantum wires to study the excitonic optical Stark effect. In order to determine the exciton absorption spectrum, we have to calculate the transition rate through the interband transition matrix element from the level of the hole to levels of electrons. First, we will investigate the case in which the system is under no pump laser. In this case, due to the selection rules for the quantum wire structure, there is only a possible occurrence of the interband transition between the hole level E_0 and the first electron level E_1 under the excitation of a suitable probe laser, as sketched by the thin arrow in Figure 1(a). The matrix element of the interband transition between these levels is determined as follows:

$$T_{10} = \left\langle \Pi_1\left(\vec{r}, t\right)\middle|\hat{H}_{\text{int}}\middle|\Pi_0\left(\vec{r}, t\right)\right\rangle. \tag{15}$$

By substituting Equations (6) and (9) into Equation (15), we have

$$T_{10} = -\frac{eA_t}{m_0 i\omega_t} e^{(i/\hbar)(E_1-E_0-\hbar\omega_t)t} \left\langle \Pi_1\left(\vec{r}\right) \middle| \vec{n}\,\widehat{\vec{p}} \middle| \Pi_0\left(\vec{r}\right) \right\rangle. \quad (16)$$

By using Equation (7), we can rewrite Equation (16) as follows:

$$T_{10} = -\frac{eA_t}{m_0 i\omega_t} e^{(i/\hbar)(E_1-E_0-\hbar\omega_t)t} \left\langle u_c\left(\vec{r}\right) \mid \vec{n}\,\widehat{\vec{p}} \mid u_v\left(\vec{r}\right) \right\rangle \cdot \left\langle \Psi_{01}^{e}\left(\vec{r}\right) \mid \Psi_{01}^{h}\left(\vec{r}\right) \right\rangle, \quad (17)$$

or

$$T_{10} = -\frac{eA_t p_{\mathrm{cv}}}{m_0 i\omega_t} e^{(i/\hbar)(E_1-E_0-\hbar\omega_t)t}, \quad (18)$$

where ω_t and A_t are the frequency and amplitude of the probe laser, respectively, and p_{cv} is the polarization matrix element between Bloch functions of the conduction and the valence band

$$p_{cv} = \left\langle u_c\left(\vec{r}\right) \mid \vec{n}\,\widehat{\vec{p}} \mid u_v\left(\vec{r}\right) \right\rangle. \quad (19)$$

From Equation (18), in the absence of the pump laser, we find the transition rate as follows [51]:

$$W_0 = \frac{2\pi}{\hbar}\left(\frac{eA_t p_{cv}}{m_0\omega_t}\right)^2 \delta(E_1 - E_0 - \hbar\omega_t). \quad (20)$$

The transition rate can be rewritten in Lorentz's form as follows [52]:

$$W_0 = \frac{2}{\hbar}\left(\frac{eA_t p_{cv}}{m_0\omega_t}\right)^2 \frac{\Gamma}{(E_1 - E_0 - \hbar\omega_t)^2 + \Gamma^2}, \quad (21)$$

where Γ is the phenomenological linewidth of the absorption peak.

2.4. The Exciton Absorption Spectrum in the Presence of the Pump Laser. Now, we will calculate the interband transition rate when the pump laser operates. As mentioned above, under the effect of a strong resonant pump laser, the electrons are now in the superposition state specified by the renormalized wave function given in Equation (10). Then, the matrix element for the interband transition between the hole state and the electron superposition state is determined as follows:

$$T_{\mathrm{mix},0} = \left\langle \Pi_{\mathrm{mix}}^{e}\left(\vec{r}, t\right) \middle| \widehat{H}_{\mathrm{int}} \middle| \Pi_0\left(\vec{r}, t\right) \right\rangle. \quad (22)$$

Replacing Equations (6), (9), and (10) into Equation (22), we have

$$\begin{aligned} T_{\mathrm{mix},0} = -\frac{eA_t e^{-i\omega_t t}}{m_0 i\omega_t} \Bigg[& \frac{1}{2\Omega_R}\left(\alpha_1 e^{-(i/\hbar)E_1^- t} + \alpha_2 e^{-(i/\hbar)E_1^+ t}\right)^* e^{-(i/\hbar)E_0 t} \\ & \cdot \left\langle \Pi_1\left(\vec{r}\right) \middle| \vec{n}\,\widehat{\vec{p}} \middle| \Pi_0\left(\vec{r}\right) \right\rangle - \frac{V_{21}}{2\hbar\Omega_R} \\ & \cdot \left(e^{-(i/\hbar)E_2^- t} - e^{-(i/\hbar)E_2^+ t}\right)^* e^{-(i/\hbar)E_0 t} \\ & \cdot \left\langle \Pi_2\left(\vec{r}\right) \middle| \vec{n}\,\widehat{\vec{p}} \middle| \Pi_0\left(\vec{r}\right) \right\rangle \Bigg]. \end{aligned} \quad (23)$$

Notably, when the probe laser irradiates on the system, due to the selection rules for the quantum wire structure, the interband transitions can only occur among the hole level E_0 and the electron splitting levels E_1^- and E_1^+ (thin arrows in Figure 1(b)). Therefore, in Equation (23), we can omit the second term and rewrite it as follows:

$$\begin{aligned} T_{\mathrm{mix},0} = -\frac{eA_t e^{-i\omega_t t}}{m_0 i\omega_t} \Bigg[& \frac{1}{2\Omega_R}\left(\alpha_1 e^{-(i/\hbar)E_1^- t} + \alpha_2 e^{-(i/\hbar)E_1^+ t}\right)^* e^{-(i/\hbar)E_0 t} \\ & \cdot \left\langle \Pi_1\left(\vec{r}\right) \middle| \vec{n}\,\widehat{\vec{p}} \middle| \Pi_0\left(\vec{r}\right) \right\rangle \Bigg]. \end{aligned} \quad (24)$$

Substituting Equation (7) into Equation (24), we obtain

$$\begin{aligned} T_{\mathrm{mix},0} = -\frac{eA_t p_{\mathrm{cv}}}{m_0 i\omega_t} \Bigg[& \frac{1}{2\Omega_R}\left(\alpha_1 e^{(i/\hbar)(E_1^- - E_0 - \hbar\omega_t)t} + \alpha_2 e^{(i/\hbar)(E_1^+ - E_0 - \hbar\omega_t)t}\right) \\ & \cdot \left\langle \Psi_{01}^{e}\left(\vec{r}\right) \mid \Psi_{01}^{h}\left(\vec{r}\right) \right\rangle \Bigg], \end{aligned} \quad (25)$$

or

$$T_{\mathrm{mix},0} = -\frac{eA_t p_{\mathrm{cv}}}{m_0 i\omega_t} \left[\frac{\alpha_1}{2\Omega_R} e^{(i/\hbar)(E_1^- - E_0 - \hbar\omega_t)t} + \frac{\alpha_2}{2\Omega_R} e^{(i/\hbar)(E_1^+ - E_0 - \hbar\omega_t)t} \right]. \quad (26)$$

Then, we can determine the interband transition rate under the effect of a resonant pump laser as [51]

$$\begin{aligned} W = \frac{2\pi}{\hbar}\left(\frac{eA_t p_{\mathrm{cv}}}{m_0\omega_t}\right)^2 \Bigg[& \left(\frac{\alpha_1}{2\Omega_R}\right)^2 \delta(E_1^- - E_0 - \hbar\omega_t) \\ & + \left(\frac{\alpha_2}{2\Omega_R}\right)^2 \delta(E_1^+ - E_0 - \hbar\omega_t) \Bigg]. \end{aligned} \quad (27)$$

We omit the crossing terms in the above formula due to the negligible overlap of the delta functions. Then, by

applying a similar transformation as in the previous section, we get a clearer form of the transition rate as

$$W = \frac{2}{\hbar}\left(\frac{eA_t p_{cv}}{m_0\omega_t}\right)^2 \left[\left(\frac{\alpha_1}{2\Omega_R}\right)^2 \frac{\Gamma}{(E_1^- - E_0 - \hbar\omega_t)^2 + \Gamma^2} + \left(\frac{\alpha_2}{2\Omega_R}\right)^2 \frac{\Gamma}{(E_1^+ - E_0 - \hbar\omega_t)^2 + \Gamma^2}\right]. \quad (28)$$

where Γ is the linewidth of the absorption peak described in the previous section. As calculated from Fermi's golden rule, the transition rate W is the probability of transition per unit time from the initial state to the final state, so its unit is the number of transitions per unit time. In this study, however, we will consider W in the arbitrary unit for the sake of convenience.

3. Results and Discussion

In this section, we study the exciton absorption spectrum in GaAs/$Al_{0.7}Ga_{0.3}As$ cylindrical quantum wires in the absence and in the presence of the pump laser to reveal the excitonic optical Stark effect. Of course, the band offset between GaAs and $Al_{0.7}Ga_{0.3}As$ is finite, but here, in our very first work related to quantum wires, we assume quantum wires being surrounded by an infinite potential for the sake of simplicity. Therefore, we do not mention the effect of the barrier layer in the later discussion but leave it for future work. The parameters are used as follows. The pump laser is assigned an amplitude of about $A_p = 8 \times 10^6$ V/m and has a very small detuning, $\hbar\Delta\omega \ll \hbar\omega_p$. The linewidth of the absorption peak is assumed to be $\Gamma = 0.1$ meV; here, we use a monochrome probe laser. The effective masses of the electron and hole of the wire material, GaAs, are $m_e = 0.067m_0$ and $m_h = 0.51m_0$, respectively [53]; the energy gap of GaAs is $E_g = 1424$ meV [54].

First, we plot the absorption spectra of excitons in the quantum wire of the radius $R = 50\,Å$ in the absence and in the presence of a strong pump laser that resonates accurately with two levels of the electron ($\hbar\Delta\omega = 0$ meV), Figure 2. The results show that, before the pump laser operates, the absorption spectra of excitons include only one absorption peak (dashed line). By contrast, after turning on the pump laser, two distinct peaks (solid lines) arise in the exciton absorption spectra as convincing evidence of the existence of the excitonic optical Stark effect in the system. These results can be explained as follows.

Before the pump laser is switched on, according to the selection rules for the quantum wire structures, there is only one transition between the hole level and the first electron level in the absorption spectrum of excitons (the thin arrow in Figure 1(a)). Therefore, we see only one peak in the absorption spectrum. On the contrary, if there exists a resonant pump laser that can excite the intraband transition between two electron levels (as illustrated by the thick arrow in Figure 1(b)), and if the intensity of the pump laser is very strong, then it can merge those two electron levels into a single level. According to the Pauli exclusion principle, this single level allows a maximum of two states of electron, while two initial electron levels allow up to four states. In order to ensure that the system still includes the four permitted states and still satisfies the Pauli exclusion principle, each initial electron level needs to be split into two sublevels. Fortunately, under the strong electric field of the pump laser, the symmetry of the state of this single level is broken as seen in the Stark effect. Therefore, both initial electron levels are split. Consequently, when we irradiate a proper probe laser into the system, we can find two interband transitions from the hole level to two sublevels of electron (as indicated by the two thin arrows in Figure 1(b)), and thus, we can see two distinct peaks in the exciton absorption spectrum. Obviously, due to the selection rules, it is impossible that the interband transitions from the hole level to the electron sublevels split from the second quantized level of the electron will occur. Moreover, due to the symmetry between the sublevels with reference to the position of the initial electron level, the two obtained peaks have the same height (or the same transition rate) and stay symmetrical on both sides of the initial peak, which satisfies the energy conservation law. We also found that, in Figure 2, the intensity of the exciton absorption spectra in the case of without pump wave (dashed line) appears much higher than that in the presence of the pump wave (solid line). This reduction is due to the act of the conservation of the transition rate [55]. We realize that, by turning the pump laser on or off, this effect can control the system to work as an optical switching by letting the probe laser beam of certain frequency propagate through it or not.

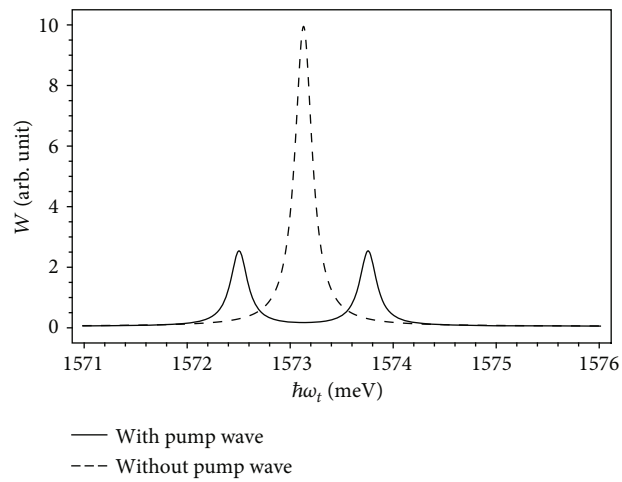

Figure 2: The exciton absorption spectra in the cylindrical quantum wire with radius $R = 50\,Å$ in the absence (dashed line) and in the presence (solid line) of the pump laser with the detuning $\hbar\Delta\omega = 0$ meV.

Now, we will thoroughly study the excitonic optical Stark effect in the quantum wires by examining the dependence of the exciton absorption spectrum on the pump laser detuning and the wire radius. First, we plot the exciton absorption spectra in the quantum wire with radius $R = 50\,Å$ with different detuning in both cases with and without the pump laser (Figure 3). We observe that in the presence of the pump laser, all excitonic absorption spectra contain two distinct spectral

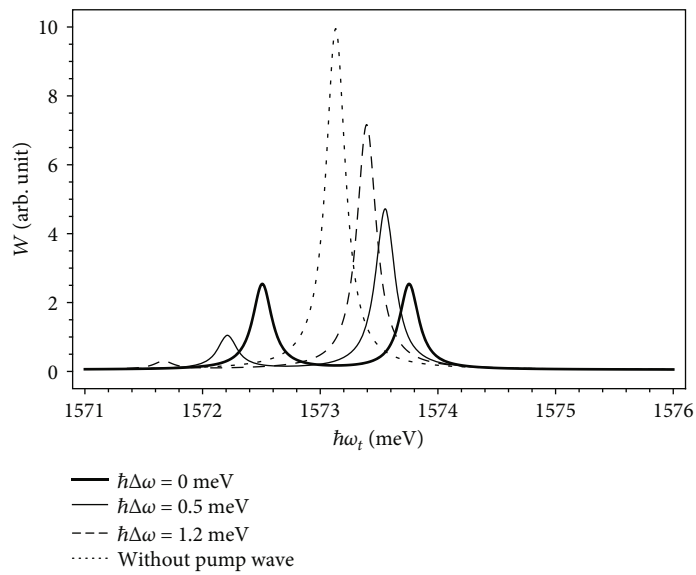

Figure 3: The exciton absorption spectra in cylindrical quantum wire of radius $R = 50\,\mathring{A}$ in the absence (dotted line) and in the presence of the resonant pump laser with specific detuning $\hbar\Delta\omega = 0$ meV (thick solid line); $\hbar\Delta\omega = 0.5$ meV (thin solid line); $\hbar\Delta\omega = 1.2$ meV (dashed line).

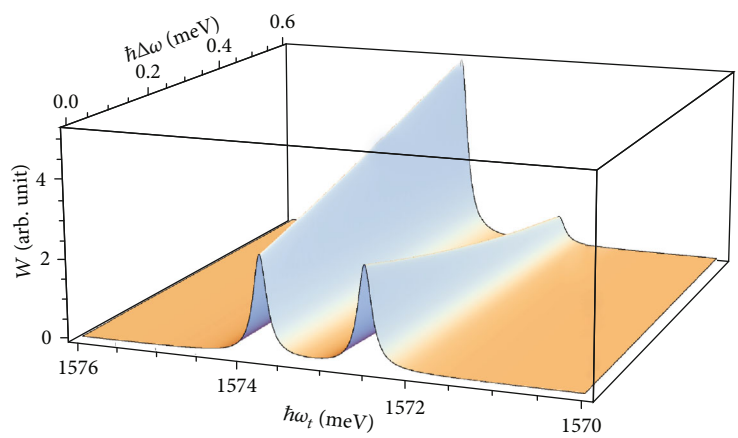

Figure 4: The exciton absorption spectra in the cylindrical quantum wire of radius $R = 50\,\mathring{A}$ as a function of the photon energy of the probe laser $\hbar\omega_t$ and the detuning $\hbar\Delta\omega$ of the pump laser.

peaks, which implies that the optical Stark effect occurs. Moreover, as we increase the detuning, the height of one peak increases and that peak moves closer to the position of the initial peak, while the other peak gets farther from the position of the initial peak and lowered, and it almost disappears when the detuning is too large (as in the case $\hbar\Delta\omega = 1.2$ meV, dashed line). The higher the difference in height of the two spectral peaks is, the greater the difference in the transition rate. Despite this, in all the cases under investigation, we can see that the total transition rate is conserved.

Figure 4 shows more clearly the change in height and position of the absorption peaks when the pump laser detuning is increased from 0 meV to 0.6 meV. It is obvious that when the detuning increases, then one peak raises its height while the other lowers to the zero value.

Next, we investigate the influence of the quantum wire radius on the excitonic optical Stark effect. Figure 5 shows the exciton absorption spectra in the quantum wires of radii $R = 45\,\mathring{A}$ (solid line), $R = 50\,\mathring{A}$ (dashed line), and $R = 55\,\mathring{A}$ (dotted line) in the presence of the pump laser with the detuning $\hbar\Delta\omega = 0.5$ meV. In all three cases, we observe the appearance of two exciton absorption peaks, which again confirmed the existence of the optical Stark effect. We can see that as the wire radius increases, the absorption spectra of excitons shift very fast to the lower energy region. This can be explained as follows. According to Equation (4), as the quantum wire radius increases, the quantized levels of the electron and hole have smaller values and they stay closer to each other. Therefore, a smaller photon energy is needed to excite the transition from the hole level to the splitting electron levels. As a result, we see that the absorption spectra of the excitons shift to a lower energy region as the wire radius becomes larger. It is worth mentioning that we have applied our theory for the other low-dimensional structures such as quantum dots and quantum wells and we have obtained the similar results [55, 56].

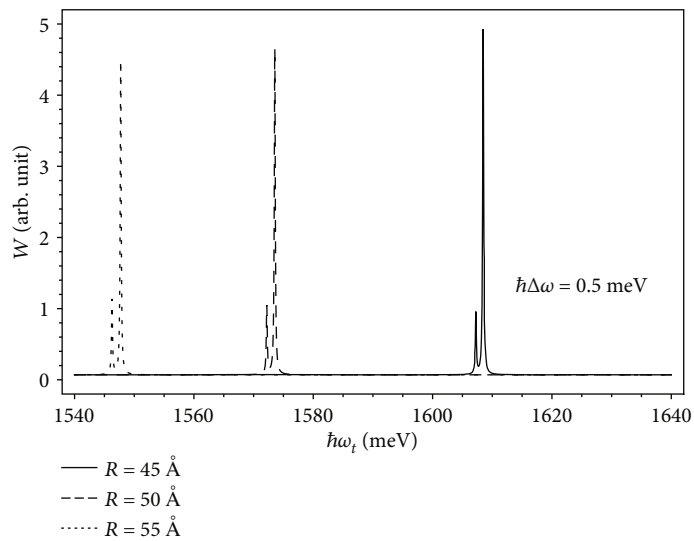

Figure 5: The absorption spectra of excitons in the cylindrical quantum wires with various radii in the presence of pump laser with the detuning $\hbar\Delta\omega = 0.5$ meV.

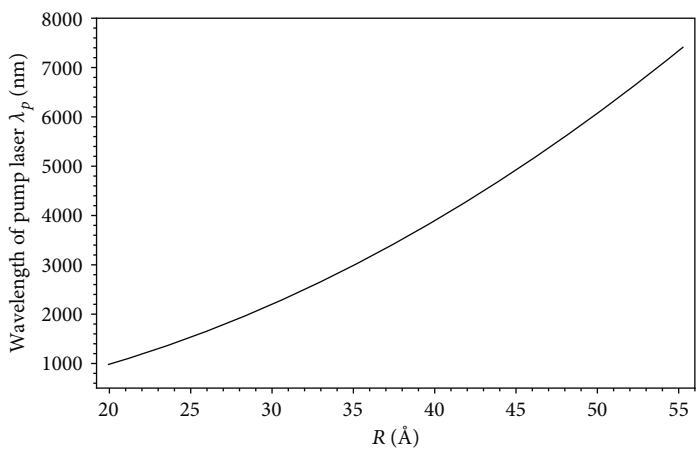

Figure 6: The wavelength of pump laser of zero detuning as a function of wire radius.

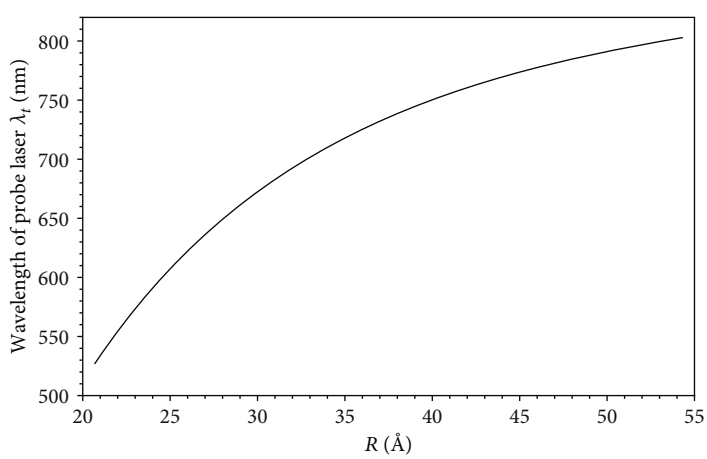

Figure 7: The wavelength of probe laser λ_t as a function of wire radius.

As an effort to provide a brief guidance for experimental verification of our results, in Figures 6 and 7, the dependence of the wavelength of pump laser λ_p and that of probe laser λ_t on the wire radius are plotted. We see that both the wavelengths increase with the wire radius as a result of the quantum size effect. However, while one curve describes a

parabolic function (Figure 6), the other shows a square root one (Figure 7).

After fabricating quantum wires, by looking at these figures, experimentalists can find the proper wavelengths of lasers and set up verification experiments. By controlling the laser's powers to fit values, the excitonic optical Stark effect is expected to occur. Also, by adjusting the other parameters, we can find the properties of the excitonic optical Stark effect.

4. Conclusions

In this work, we have studied the three-level excitonic optical Stark effect in GaAs circular cylindrical quantum wires by means of the renormalized wave function theory. The results show that, while the pump laser operates, there appear two separated spectral peaks in the excitonic absorption spectra as the indication of the excitonic optical Stark effect. Moreover, the absorption spectra of excitons shift sharply with the wire radius. Also, the heights of the two absorption peaks are very sensitive to the detuning of the pump laser.

Additionally, we have proposed an explanation for the splitting of the energy levels of the electron under the effect of the strong resonant pump laser, which leads to the formation of two new absorption peaks of the exciton. We have also tried to explain the shift of the excitonic absorption spectra as the wire radius varies. Finally, we have tried to provide a brief guidance for experimental verification of our results. We expect that these results could be confirmed by proper experiments and could have some contribution to the related fields such as making ultrafast switching devices for quantum computers.

For the sake of simplicity, here, we consider circular cylindrical quantum wires surrounded by an infinite potential. However, we believe that our model can be expanded to other quantum wires of different shapes under various potentials as long as we can determine the wave functions and energy levels of particles.

Data Availability

The material structure parameters used to support the findings of this study are included within the article.

Conflicts of Interest

The authors declare that they have no conflicts of interest.

Acknowledgments

This research is funded by the Vietnam National Foundation for Science and Technology Development (NAFOSTED) under grant number 103.01-2017.321.

References

[1] H. Cansizoglu, E. Ponizovskaya Devine, Y. Gao et al., "A new paradigm in high-speed and high-efficiency silicon photodiodes for communication-part I: enhancing photon-material interactions via low-dimensional structures," *IEEE Transactions on Electron Devices*, vol. 65, no. 2, pp. 372–381, 2018.

[2] B. Kelleher, C. Bonatto, G. Huyet, and S. P. Hegarty, "Excitability in optically injected semiconductor lasers: contrasting quantum-well- and quantum-dot-based devices," *Physical Review E*, vol. 83, no. 2, article 026207, 2011.

[3] R. D. Dupuis, "III–V semiconductor quantum-well devices grown by metalorganic chemical vapor deposition," *Proceedings of the IEEE*, vol. 101, no. 10, pp. 2188–2199, 2013.

[4] J. Y. Huang, C. Y. Lin, W.-S. Liu, and J.-I. Chyi, "Quantum control study of ultrafast optical responses in semiconductor quantum dot devices," *Optics Express*, vol. 22, no. 25, pp. 30815–30825, 2014.

[5] M. K. Yakes, N. Mahadik, S. B. Qadri et al., "Scanning probe microscopy based characterizations of III-V semiconductor quantum well devices," *Microscopy and Microanalysis*, vol. 18, no. S2, pp. 1810-1811, 2012.

[6] S. Iizuka, H. Asai, J. Hattori, K. Fukuda, and T. Mori, "Implementation of Coulomb blockade transport on a semiconductor device simulator and its application to tunnel-FET-based quantum dot devices," *Japanese Journal of Applied Physics*, vol. 59, no. SI, article SIIE02, 2020.

[7] M. G. Barseghyan, C. A. Duque, E. C. Niculescu, and A. Radu, "Intense laser field effects on the linear and nonlinear optical properties in a semiconductor quantum wire with triangle cross section," *Superlattices and Microstructures*, vol. 66, pp. 10–22, 2014.

[8] S. Saravanan, A. J. Peter, and C. W. Lee, "Laser field induced optical gain in a group III-V quantum wire," *The European Physical Journal D*, vol. 70, no. 8, p. 165, 2016.

[9] Y. K. Ezhovskii, "Chemical nanotechnology of oxide and nitride low-dimensional structures on a semiconductor matrix," *Russian MicroElectronics*, vol. 39, no. 3, pp. 182–189, 2010.

[10] H. Hardtdegen, M. Mikulics, S. Rieß et al., "Modern chemical synthesis methods towards low-dimensional phase change structures in the Ge-Sb-Te material system," *Progress in Crystal Growth and Characterization of Materials*, vol. 61, no. 2-4, pp. 27–45, 2015.

[11] F. J. Owens, *The Physics of Low Dimensional Materials*, World Scientific Publishing Company, 2017.

[12] Y. Sun, K. Liu, and Y. Zhu, "Recent progress in synthesis and application of low-dimensional silicon based anode material for lithium ion battery," *Journal of Nanomaterials*, vol. 2017, Article ID 4780905, 15 pages, 2017.

[13] K. Boeneman, D. E. Prasuhn, J. B. Blanco-Canosa et al., "Quantum dots as a FRET donor and nanoscaffold for multivalent DNA photonic wires," in *Proceedings of SPIE*, vol. 7909 of *Colloidal Quantum Dots/Nanocrystals for Biomedical Applications VI*, p. 79090R, San Francisco, CA, USA, 2011.

[14] P. Bhattacharya, A. D. Stiff-Roberts, S. Krishna, and S. Kennerly, "Quantum dot infrared detectors and sources," *International Journal of High Speed Electronics and Systems*, vol. 12, pp. 969–994, 2011.

[15] A. P. Litvin, I. V. Martynenko, F. Purcell-Milton, A. V. Baranov, A. V. Fedorov, and Y. K. Gun'ko, "Colloidal quantum dots for optoelectronics," *Journal of Materials Chemistry A*, vol. 5, no. 26, pp. 13252–13275, 2017.

[16] A. Boutramine, A. Nafidi, D. Barkissy, A. Hannour, A. Elanique, and T. E. Gouti, "Application of the transition semiconductor to semimetal in type II nanostructure

superlattice for mid-infrared optoelectronic devices," *Applied Physics A*, vol. 122, no. 4, 2016.

[17] S. G. Schirmer and P. J. Pemberton-Ross, "Fast high-fidelity information transmission through spin-chain quantum wires," *Physical Review A*, vol. 80, no. 3, article 030301, 2009.

[18] R. Castellanos, R. Franco, J. Silva-Valencia, and M. S. Figueira, "Thermoelectric transport properties of a quantum wire, coupled to a quantum dot: finite band effects," *Journal of Superconductivity and Novel Magnetism*, vol. 23, no. 1, pp. 153–155, 2010.

[19] R. Khordad, "Quantum wire with parallelogram cross section: optical properties," *Journal of Theoretical and Applied Physics*, vol. 6, no. 1, p. 19, 2012.

[20] H. Bahramiyan and R. Khordad, "The effect of electron-phonon interaction on optical properties of a triangular quantum wire," *Superlattices and Microstructures*, vol. 63, pp. 267–276, 2013.

[21] R. Khordad and H. Bahramiyan, "Effect of size distribution on the optical properties of quantum wire systems," *International Journal of Modern Physics*, vol. 28, no. 18, article 1450119, 2014.

[22] R. Khordad and H. R. Rastegar Sedehi, "Low temperature behavior of thermodynamic properties of 1D quantum wire under the Rashba spin-orbit interaction and magnetic field," *Solid State Communications*, vol. 269, pp. 118–124, 2018.

[23] D. Piester, A. A. Ivanov, A. S. Bakin, H.-H. Wehmann, and A. Schlachetzki, "Semiconductor nanostructures for quantum wire lasers," *Proceedings of SPIE*, vol. 4748, pp. 476–485, 2001.

[24] S. Arai and T. Maruyama, "GaInAsP/InP quantum wire lasers," *IEEE Journal of Selected Topics in Quantum Electronics*, vol. 15, no. 3, pp. 731–742, 2009.

[25] M. A. Grado-Caffaro and M. Grado-Caffaro, "Electron wavelength and drift mobility operators for treating quantum electron waveguides," *Optik*, vol. 125, no. 21, pp. 6543-6544, 2014.

[26] J. B. Khurgin and D. Yang, "Resonant tunneling field-effect transistor based on wave function shape modulation in quantum wires," *Journal of Applied Physics*, vol. 85, no. 6, pp. 3218–3221, 1999.

[27] D. Yang and J. B. Khurgin, "Analysis of the performance of the quantum wire resonant tunneling field-effect transistor," *Superlattices and Microstructures*, vol. 27, no. 4, pp. 245–254, 2000.

[28] S. Saravanan and A. John Peter, "Binding energy of a magneto-exciton in an InAsP quantum well wire for the potential application of telecommunication networks," *Materials Today: Proceedings*, vol. 2, pp. 4373–4377, 2015.

[29] L. Donaldson, "Quantum effects in 1D wires," *Materials Today*, vol. 19, no. 10, pp. 550-551, 2016.

[30] K. Tai, J. Hegarty, and W. T. Tsang, "Observation of optical Stark effect in InGaAs/InP multiple quantum wells," *Applied Physics Letters*, vol. 51, no. 3, pp. 152–154, 1987.

[31] T. Unold, K. Mueller, C. Lienau, T. Elsaesser, and A. D. Wieck, "Optical Stark effect in a quantum dot: ultrafast control of single exciton polarizations," *Physical Review Letters*, vol. 92, no. 15, 2004.

[32] M. Combescot and R. Combescot, "Optical Stark effect of the exciton: biexcitonic origin of the shift," *Physical Review B*, vol. 40, no. 6, pp. 3788–3801, 1989.

[33] I. M. Gadzhiyev, M. S. Buyalo, A. E. Gubenko et al., "Switching between the mode-locking and Q-switching modes in two-section QW lasers upon a change in the absorber properties due to the Stark effect," *Semiconductors*, vol. 50, no. 6, pp. 828–831, 2016.

[34] D. Ahn, "Enhancement of the Stark effect in coupled quantum wells for optical switching devices," *IEEE Journal of Quantum Electronics*, vol. 25, no. 11, pp. 2260–2265, 1989.

[35] Y. Rong, Y. Huo, E. T. Fei et al., "High speed optical modulation in Ge quantum wells using quantum confined Stark effect," *Frontiers of Optoelectronics*, vol. 5, no. 1, pp. 82–89, 2012.

[36] M. Gogoi, P. Deb, D. Sen, S. Mazumder, and A. Kostka, "Enhanced quantum confined Stark effect in a mesoporous hybrid multifunctional system," *Solid State Communications*, vol. 187, pp. 48–52, 2014.

[37] J. T. Liu, F. H. Su, H. Wang, and X. H. Deng, "The influence of the optical Stark effect on chiral tunneling in graphene," *EPL (Europhysics Letters)*, vol. 95, no. 2, article 24003, 2011.

[38] E. I. Garmire, A. I. A. Maradudin, and K. K. Rebane, *Laser Optics of Condensed Matter (Volume 2 the Physics of Optical Phenomena and Their Use as Probes of Matter)*, Springer Science+Business Media, LCC, 1991.

[39] D. Fröhlich, C. Neumann, B. Uebbing, and R. Wille, "Experimental investigation of three-level optical Stark effect in semiconductors," *Physica Status Solidi (B)*, vol. 159, no. 1, pp. 297–307, 1990.

[40] D. Song, F. Wang, G. Dukovic et al., "Measurement of the optical Stark effect in semiconducting carbon nanotubes," *Applied Physics A: Materials Science & Processing*, vol. 96, no. 2, pp. 283–287, 2009.

[41] S. Efumi, Y. Uchibori, J. Ishihara, and K. Miyajima, "Observation of optical Stark effect between *1s*- 2pexciton levels in CuCl single crystal," *Journal of Physics: Conference Series*, vol. 1220, p. 012022, 2019.

[42] N. H. Quang, "The optical Stark effect of the exciton due to dynamical coupling between quantized states of the electron and hole in quantum wells," *International Journal of Modern Physics B*, vol. 7, pp. 3405–3413, 1993.

[43] S. Zielińska-Raczyńska, G. Czajkowski, and D. Ziemkiewicz, "Quantum confined Stark effect in wide parabolic quantum wells: real density matrix approach," *The European Physical Journal B*, vol. 88, no. 12, article 338, 2015.

[44] T. Altevogt and R. Zimmermann, "Nonclassical gain in the optical Stark effect: density matrix approach," *Journal of Physics B: Atomic, Molecular and Optical Physics*, vol. 32, no. 19, pp. 4719–4728, 1999.

[45] S. Wang, Y. Kang, and C. Han, "Transverse Stark effect in the optical absorption in a square semiconducting quantum wire," *Journal of Semiconductors*, vol. 34, no. 10, article 102001, 2013.

[46] A. Rustagi and A. F. Kemper, "Coherent excitonic quantum beats in time-resolved photoemission measurements," *Physical Review B*, vol. 99, no. 12, article 125303, 2019.

[47] D. Sangalli, E. Perfetto, G. Stefanucci, and A. Marini, "An ab-initio approach to describe coherent and non-coherent exciton dynamics," *The European Physical Journal B*, vol. 91, no. 8, article 171, 2018.

[48] D. D. Phuoc, L. T. N. Bao, L. T. D. Hien, H. K. Hieu, and D. N. Thao, "A study on quantum beats of excitons in GaAs/AlGaAs circular cylindrical quantum wires," *Japanese Journal of Applied Physics*, vol. 59, no. 12, article 125003, 2020.

[49] L. Wendler and V. G. Grigoryan, "Effect of the image potential on plasmons in cylindrical quantum-well wires," *Physica Status Solidi (B)*, vol. 181, no. 1, pp. 133–159, 1994.

[50] E. Rosencher, B. Vinter, and P. G. Piva, *Optoelectronics*, Cambridge University Press, 2002.

[51] N. Zettili, *Quantum Mechanics: Concepts and Applications*, Wiley, 2nd ed edition, 2009.

[52] V. Balakrishnan, "All about the Dirac delta function (?)," *Resonance*, vol. 8, no. 8, pp. 48–58, 2003.

[53] W. Nakwaski, "Effective masses of electrons and heavy holes in GaAs, InAs, A1As and their ternary compounds," *Physica B*, vol. 210, no. 1, pp. 1–25, 1995.

[54] J. S. Blakemore, "Semiconducting and other major properties of gallium arsenide," *Journal of Applied Physics*, vol. 53, no. 10, pp. R123–R181, 1982.

[55] D. N. Thao, L. T. N. Bao, D. D. Phuoc, and N. H. Quang, "A theoretical study of the optical Stark effect in InGaAs/InAlAs quantum dots," *Semiconductor Science and Technology*, vol. 32, no. 2, article 025014, 2017.

[56] L. T. N. Bao and D. N. Thao, "Theoretical investigation of quantum beat of excitons in GaAs/AlGaAs quantum wells," in *42nd Vietnam National Conference on Theoretical Physics (NCTP-42)*, Cantho, Vietnam, 2017.

Hindawi
Journal of Nanomaterials
Volume 2021, Article ID 5582737, 7 pages
https://doi.org/10.1155/2021/5582737

Research Article

Synthesis of Hybrid Lead Iodide Perovskite Thin Film by Two-Step Method Modified with a Double Dipping Circle to Control Its Crystallization and Morphology to Improve Solar Cells' Performance

Huy Anh Dinh,[1,2] Thuy Thanh Thi Nguyen,[1,2] Le Thi Nguyen,[1,2] Hai Tri Nguyen,[1,2] Dien Minh Trinh,[1,2] Vy Anh Tran,[1,2] and Phuong Tuyet Nguyen[1,2]

[1]*Faculty of Chemistry, University of Science, Ho Chi Minh City, Vietnam*
[2]*Vietnam National University Ho Chi Minh City, Vietnam*

Correspondence should be addressed to Phuong Tuyet Nguyen; ntphuong@hcmus.edu.vn

Received 6 January 2021; Revised 29 January 2021; Accepted 2 February 2021; Published 16 February 2021

Academic Editor: Mai Duy Hien

Crystallization and morphology of perovskite film played an important role to obtain efficient performance of perovskite solar cells. This study is aimed at optimizing the fabrication of hybrid organic–inorganic lead iodide perovskite layer by a two-step method modified by a double dip coating process which enables to control the perovskite crystallization and morphology. The duration time of each circle for the step of dipping PbI_2 film to methylammonium iodide solution was varied from 90 to 240 second. The obtained perovskite films were characterized by X-ray diffraction to evaluate the transformation of PbI_2 reactant to the perovskite product and its crystallization, by scanning electron microscopy to observe its morphology. Then, the perovskite films were implemented in functional perovskite solar cell devices followed by current–voltage characterization. Results showed that the perovskite was formed via an equilibrium process which reached an optimum transformation of PbI_2 to the product after 2×150 second circle dip coating, and its morphology was smooth with the least voids. The solar cell devices fabricated at the optimum conditions achieved a comparable performance of about 14%.

1. Introduction

Organic–inorganic hybrid materials adopting perovskite structure have attracted considerable attention because of their superior properties and excellent power conversion efficiencies (PCE). The first hybrid perovskite based on $CH_3NH_3PbBr_3$ was reported by Kojima et al. with PCE value of 2.2% [1, 2]. In 2009, they obtained a PCE of 3.8% by using iodine (I) instead of bromine (Br) [2]. Later, there have been tremendous efforts to enhance the efficiency in the hybrid lead halide perovskite $CH_3NH_3PbX_3$ (X : halogen) [3–8]. Among them, Gratzel et al. reported a remarkable record on the solid-state heterojunction DSCs employing $CH_3NH_3PbI_3$ with 9.7% of PCE [4]. Recently, the PCEs of PSCs have soared to 25.2% in 2019, the highest reported to date [9]. As demonstrated in these studies, controlling the morphology of perovskite films is essential for improving the performance of PSCs. In this regard, deposition process plays an important role in the growth of perovskite crystal. In terms of fabrication processes, the solution deposition of perovskite films has been conducted through one-step and two-step approaches. One-step coating uses a solution comprising of CH_3NH_3I and PbI_2 sources, which is dissolved into a single solution, and then, it was coated on the substrate via spin-coating [4, 10, 11]. Even though the one-step deposition is simple, the challenge of obtaining the high photovoltaic performance still remains. This obstacle is largely due to the low reaction conversion, low crystallization, high pinhole density, and high series resistance [12–14].

By contrast, the two-step sequential dipping deposition pathway in fabricating the perovskite layer involves a spin-coating process to deposit lead iodide (PbI_2) onto the

substrate; then, PbI_2 film is converted into methylammonium lead iodide ($MAPbI_3$) perovskite film by dipping it in methylammonium iodide (MAI) solution followed by a heat treatment step. In 2015, Fu et al. proposed about the dissolution-recrystallization mechanism in perovskite film [15], suggesting that the reaction between PbI_2 and $MAPbI_3$ was reversible as well as the photovoltaic performance of the device was affected by this process. Later, Lou et al. [16] precisely demonstrated influence of the perovskite morphology on the device's performance through current–voltage ($J - V$) characterization. Moreover, Hsieh et al. [17] explained their experimental phenomenon based on the aforementioned mechanism and provided more evidences about the correlation of morphology evolution and crystal growth followed the dipping time, as well as their effect on the photovoltaic performance. Therefore, it is crucial to control the morphology and the transformation yield by optimizing the dipping time in order to obtain an efficient perovskite thin film for solar cell application. Recently, Gao et al. [18] reconfirmed that the soaking time is the strong factor in controlling the crystallization of $MAPbI_3$ crystal and optical properties through the UV-Vis absorbance spectra and the XRD diffraction patterns. It has been noticed that the duration of dipping time was mostly reported as total time for a whole process in literatures, and the transformation process from PbI_2 to $MAPbI_3$ perovskite occurred obviously fast [15–18]. Wei et al. demonstrated that dipping the PbI_2 film in MAI solution in a short time (less than 1 min) could form the perovskite product but just as a skin on PbI_2, but doing the same procedure in a longer time (several min) caused a fact of recrystallization of the perovskite [17]. Both situations led to low energy conversion efficiency in the solar cells. Based on all the aforementioned work, we proposed that the formation of the perovskite film should be divided into two steps including crystal nucleation and preferable oriented crystal growth. The first circle in the dipping step is aimed at creating the perovskite skin on the PbI_2 and the second circle forced to a complete transformation of the inner reactant to the product.

Herein, we report a two-step deposition method modified by a double dip coating process in perovskite film fabrication which enabled to improve the perovskite films with high crystallinity and smooth morphology. In order to evaluate the effect of dip coating treatment, we conducted experiments with different duration times of each circle (90 s, 120 s, 150 s, 180 s, and 240 s). The perovskite film was fabricated via the new modified double cycle process and characterized using various structural and electrical characterization methods. The films were then implemented in the solar cell devices which were characterized by current–voltage ($J - V$) curve measurement to evaluate their photovoltaic performance.

2. Experimental Section

2.1. Synthesis of CH_3NH_3I (MAI). MAI was prepared by following the procedure reported in literature [17]. Hydroiodic acid (57 wt. % in water, Sigma–Aldrich) was added dropwise to methylamine solution (33 wt. % in absolute ethanol, Sigma–Aldrich), and the mixture was stirred under a nitrogen flow for two hours to obtain white precipitate of MAI. The product was finally collected and dried at 45°C in a vacuum oven overnight after recrystallization in ethanol and diethyl ether at -7°C for ten hours.

2.2. Solar Cell Fabrication. Fluorine-doped tin oxide (FTO) glass (2.2 mm; 8Ω/sq; Pilkington, USA) was cleaned step by step in a detergent solution, deionized water (DI) and ethanol and acetone, rand dried by an air blower. After that, the TiO_2 compact layer (c-TiO_2) was spin-coated onto the FTO substrate with a solution of 0.15 M titanium diisopropoxide bis(acetylacetonate) (75 wt% in isopropanol) (Sigma-Aldrich, Germany) and annealed at 500°C for 30 min. The c-TiO_2|FTO film was pretreated in a 40 mM $TiCl_4$ (≥98%, Fluka, Japan) solution at 70°C in an oven for 30 min and annealed at 500°C in 30 min. Next, a 200 nm thick mesoporous TiO_2 layer (m-TiO_2) was deposited on top of the c-TiO_2 layer by spin-coating with an ethanol-diluted commercial TiO_2 paste 30 NR (Dyesol, Australia), then calcinated from 325°C to 500°C for 2 h. The m-TiO_2|c-TiO_2|FTO substrate was treated again with $TiCl_4$ solution as aforementioned.

The perovskite film was then fabricated on the top of m-TiO_2 layer with the first step of loading the 1.5 M PbI_2 (Sigma–Aldrich, Germany) solution dissolved in a mixture solvent of DMF : DMSO (9 : 1) by spin-coating. Following the conventional two-step procedure, the wet PbI_2 layer was heated at 70°C for 10 min before dipping the whole substrate into the MAI solution in *iso*-propanol (9.5 mg/mL) to form the perovskite $MAPbI_3$ films, followed by a spin-coating to dry out the solvent on the surface. The dipping step was repeated two times until the perovskite film changed to dark brown; after that, it was heated on the hot plate at 120°C for 20 min. The dipping duration time for each circle was varied between 90, 120, 150, 180, and 240 seconds. It should be noted that the fabrication of PbI_2 and perovskite film was performed in ambient conditions with humidity controlled at around 30–40%.

The hole transport material (HTM) solution was prepared by dissolving 75 mM spiro-OMeTAD, 25 mM Li-TFSI, and 120 mM 4-*tert*-butylpyridine in chlorobenzene. All of these chemicals and the above solvents were purchased from Sigma–Aldrich, Germany, and used as received. Then, the HTM solution was spin-coated onto the hybrid perovskite film, and finally, a 80–100 nm gold layer was thermally evaporated on the spiro-OmeTAD-coated film to form the back contact layer. The size of one device was 1.5 × 8.7 mm. The perovskite device fabrication process was summarized in Scheme 1 with a photo of the final real device.

2.3. Material and Device Characterization. Morphology of perovskite films were obtained by field emission scanning electron microscopes (FE-SEM), operated at an accelerating voltage of 5 kV (SU-8010, Hitachi Japan). The powder X-ray diffraction (XRD) patterns of the samples were acquired using a D2 Bruker diffractometer operating at 40 kV and 150 mA, equipped with Cu $K_{\alpha 1}$ radiation source ($\lambda = 1.5406$ nm Å). The 2θ angular domain varied between 10° and 45°,

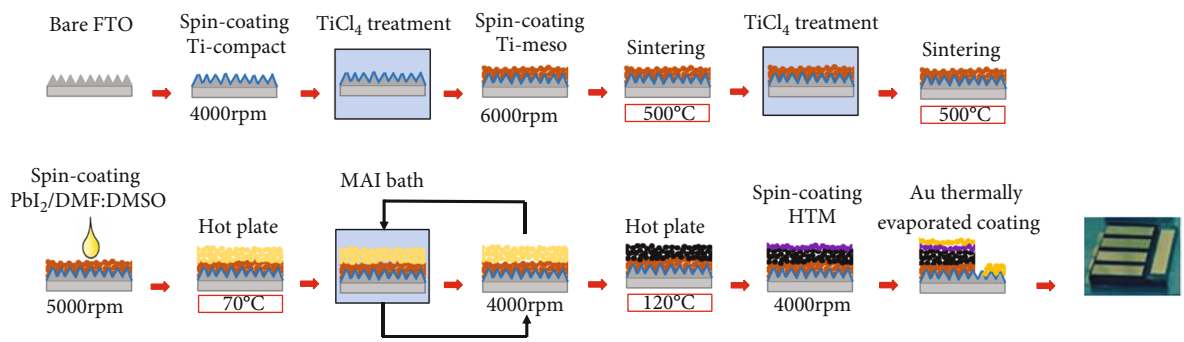

Scheme 1: The process of perovskite solar cell fabrication by two-step procedure modified double dip coating step (rpm: round per minute) with the final real device.

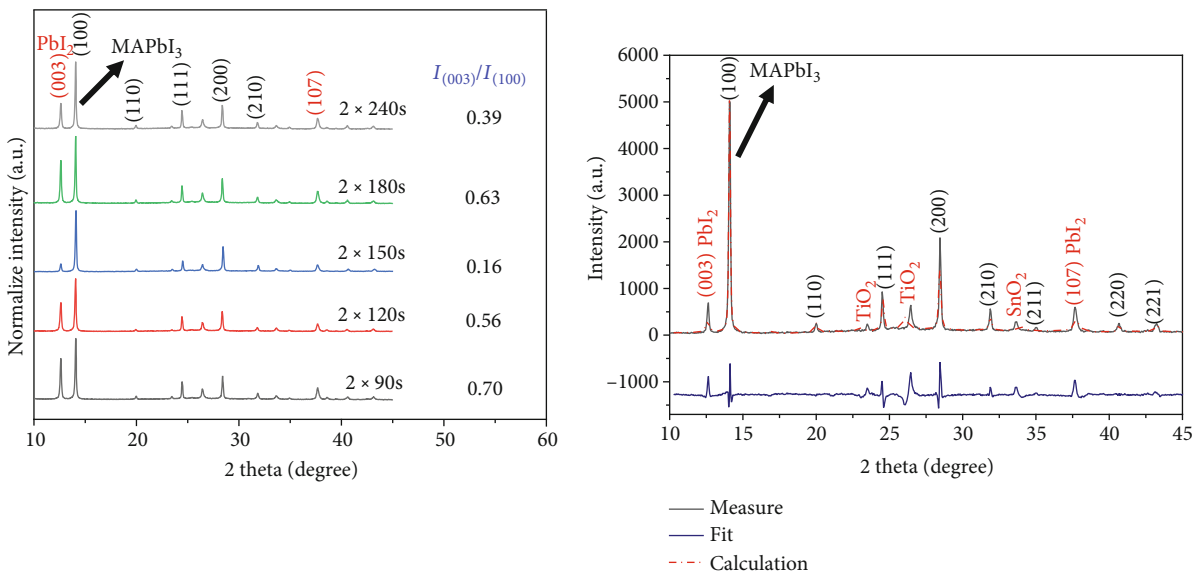

(a) (b)

Figure 1: (a) XRD patterns of $MAPbI_3$ films obtained at different conditions of dipping time $n_{dipping}$ × dipping time $t_{dipping}$. The right column gives the intensity ratios between PbI_2 (003) and $MAPbI_3$ (100). (b) Profile matching of the XRD pattern recorded on 2 × 150 s dipping condition. The structure of $MAPbI_3$ is indexed in the space group Pm-3 m, $a = b = c = 6.2673$ Å.

with a step of 0.02° and acquisition time of 0.25 s/step, and the profile matching were performed on the recorded XRD patterns, using FullProf Suite (Cu_α K-alpha1 radiation ($\lambda = 1.5406$ nm Å). Furthermore, the crystallite sizes were calculated by applying Debye-Scherrer's equation: $D_p = K\lambda/(B\ \cos\theta)$ from the XRD pattern, and the FWHM was calculated by OriginPro software.

The current–voltage (J – V) curve were measured by a Keithley 2400 digital source meter under AM 1.5G illumination and at an intensity of 100 mW cm^{-2} (Peccel Technologies, PEC-L15), while the step scan was controlled at 10 mV and the delay time was 50 ms.

3. Results and Discussion

Figure 1 shows the XRD diagram of the perovskite films fabricated at different dipping times and the fitted XRD pattern of the 2 × 150 s sample which reached to the highest transformation of PbI_2 to the perovskite product. From the XRD patterns, the crystallite size of the perovskite, calculated by Debye–Scherrer's equation, and the conversion of PbI_2 layer to $MAPbI_3$ by dipping the PbI_2 film into MAI solution was shown in Table 1.

Table 1: The ratio between integrated peak PbI_2 (003) and $MAPbI_3$ (100) and the calculated crystallite sizes of $MAPbI_3$ fabricated at various dipping times.

	2 × 90 s	2 × 120 s	2 × 150 s	2 × 180 s	2 × 240 s
I_{PbI_2}/I_{MAPbI_3} (*)	0.70	0.56	0.16	0.63	0.39
Crystallite size (nm)	58.90	57.06	58.08	61.05	60.71

(*) $I_{PbI_2(003)}/I_{MAPbI_3(100)}$ was calculated based on the integrated peak of PbI_2 (003) and the integrated peak of $MAPbI_3$ (100).

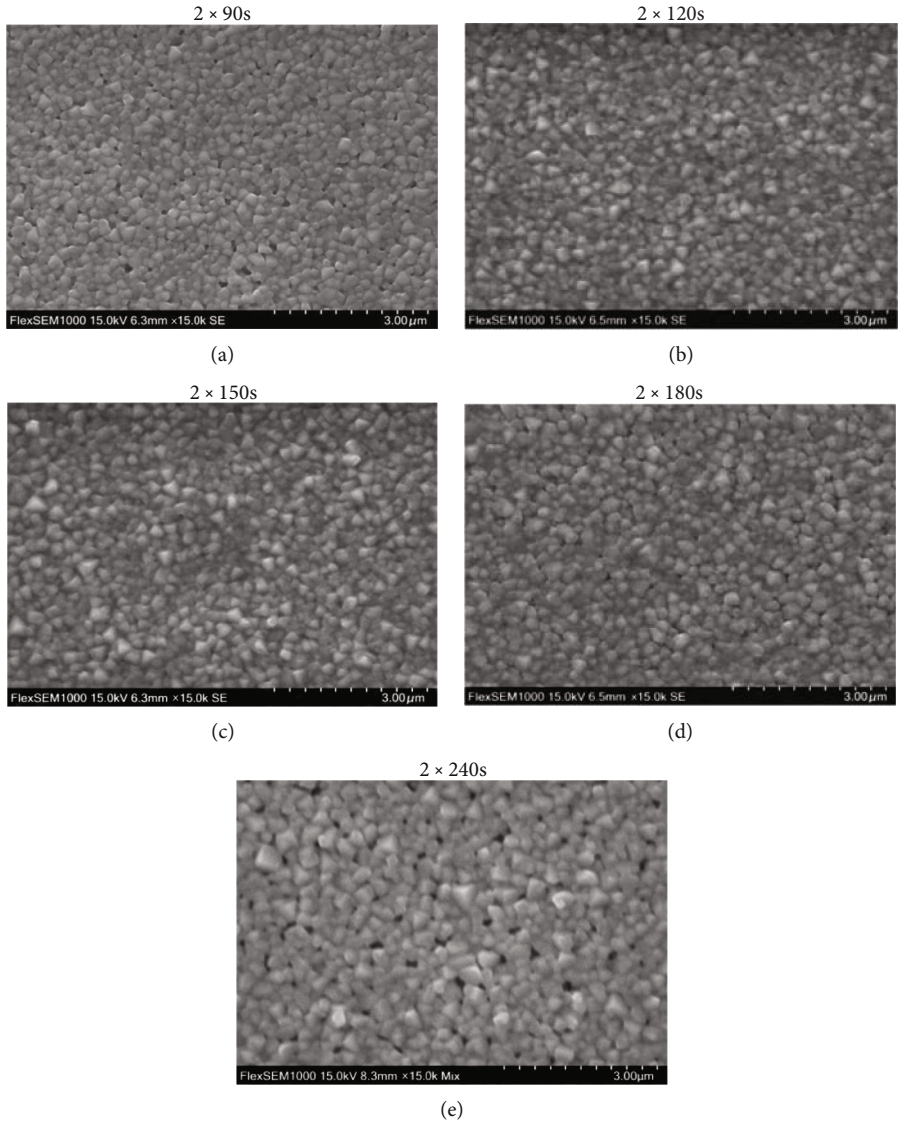

Figure 2: Scanning electron microscopy (SEM) images of the $MAPbI_3$ film fabricated at different preparation conditions: (a) 2 × 90 s, (b) 2 × 120 s, (c) 2 × 150 s, (d) 2 × 180 s, and (e) 2 × 240 s.

The formation of perovskite layer during the dipping process could be realized by the color changing of PbI_2 film from yellow to brown, then dark brown. We have noticed that during the single-dipping process of PbI_2 thin film to MAI solution, the color of PbI_2 film was changed slightly from yellow to a mixture of orange and brown. However, the color of the samples conducted under double dipping condition changed into brown, indicating the improvement of $MAPbI_3$ formation yield. As shown in the XRD pattern in Figure 1(a), five preferable peaks located at 14.11°, 20.02°, 24.58°, 28.46°, and 31.9° are indexed as the $MAPbI_3$ cubic phase of (100), (110), (111), (200), and (210) lattice planes, respectively [19]. However, the residual PbI_2 are observed in the XRD diffraction pattern of all samples, due to the presence of mainly (003) lattice planes at 12.7°. Moreover, as shown in Figure 1(b), some small diffraction peaks are observed at 23.48°, 26.45°, and 33.68°, which attributed to the presence of TiO_2 and SnO_2 in the sample during the synthesis approach on FTO | TiO_2 substrate [20].

Dissolution:

$$CH_3NH_3PbI_3(s) + I^- \rightarrow CH_3NH_3+ + PbI_4^{2-}$$

$$PbI_2 + 2I^- \rightarrow PbI_4^{2-}$$

Recrystallization:

$$PbI_4^- + CH_3NH_3^+ \rightarrow CH_3NH_3PbI_3 + I^-$$

Scheme 2: The proposed mechanism of dissolution–recrystallization process of perovskite film fabricated by a two-step dipping process explains the formation of voids and defects on the perosvkite film and the large grain size of perovskite crystals [17].

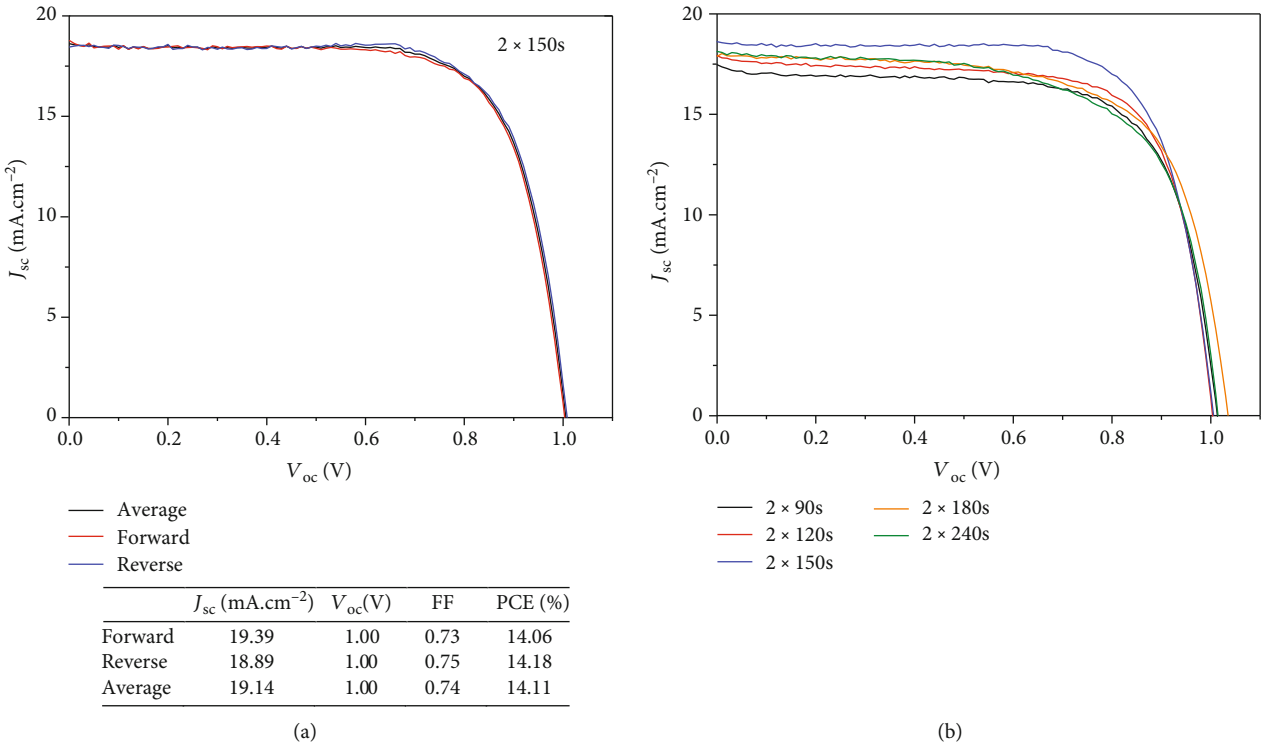

	J_{sc} (mA.cm^{-2})	V_{oc}(V)	FF	PCE (%)
Forward	19.39	1.00	0.73	14.06
Reverse	18.89	1.00	0.75	14.18
Average	19.14	1.00	0.74	14.11

Figure 3: (a) $J - V$ curve of the best performance cell at 2×150 s condition measured under AM 1.5G illumination at 100 mW cm^{-2} with forward and reverse scanning. (b) $J - V$ curves of the best devices fabricated at various dipping times.

The ratio of $PbI_2/MAPbI_3$ is found to decrease significantly from 0.7 to 0.16 when the dipping time per circle was varied from 90 s to 150 s, but then increases to 0.63 when the dipping time was prolonged to 180 s. It indicates that the reaction between PbI_2 and MAI is a reversible process, and the highest conversion of PbI_2 is obtained at 2×150 s dipping time. The results in Table 1 also clearly show that the average crystal size (D) increases when varying the reaction time from 90 s to 240 s.

In order to study the influence of the dipping time on the growth of the $MAPbI_3$ grain size as well as the dissolution-recrystallization process on the $MAPbI_3$ surface, the SEM analysis of fabricated perovskite film was examined at different conditions. After reaction at 2×90 s, the surface morphology of crystallites $MAPbI_3$ are covered in regularly shaped grains ~100 nm in diameter (Figure 2(a)), and the holes are observed on the perovskite film. After 2×120 s and 2×150 s dipping in MAI solution, the perovskite films are composed of regularly grains with size of 150–300 nm which can cover all holes and defects on the perovskite surface (Figures 2(b) and 2(c)). However, the SEM image of the samples obtained at 2×180 s and 2×240 s provides average grain sizes of 150–300 nm and 150–400 nm, respectively (Figures 2(d) and 2(e)) as well as the presence of holes on the surface even though the duration time was prolonged. This observation might be explained by the dissolution–recrystallization process of $MAPbI_3$, which was reported to occur not only on the layer of perovskite film but also inside of the perovskite grains, due to the oversaturation of I^- ion [15, 17]. Hence, the formed $MAPbI_3$ will react with an excess amount of I^- ion in $MAPbI_3$ solution and generated to lead polyiodide complex (PbI_4^{2-}) as well as the unconverted PbI_2. Accordingly, PbI_4^{2-} will react with $CH_3NH_3^+$ ion and recrystallize to grow the perovskite grain, as shown in Scheme 2.

The impact of the double dipping process on the photovoltaic performance of the PSCs is shown in Figure 3 and Table 2. The $J - V$ curves under forward and reverse scanning (Figure 3(a)) are reproducible indicating that the device works reasonably well under the measurement conditions, and it performs stable photovoltaic properties. The same observation was obtained for all the devices fabricated at various conditions. When the dipping time is increased from 2×90 to 2×240 s, the short-circuit density (J_{sc}) increases gradually and then decreases, reaching a highest value (19.01 mA.cm^{-2}) at 2×150 s, which exhibits the balance between the conversion of PbI_2 to $MAPbI_3$ and dissolution process (Table 2). The fill factor of these solar cells keeps almost constant from 0.73 at 2×90 s to 0.71 at 2×150 s and then decreased significantly to 0.66 at 2×180 s and 0.68 at 2×240 s. Besides, the results show that the overall conversion efficiency increases dramatically from 12.8% at 2×90 s to 13.4% at 2×150 s, then reduces to 11.8% at 2×180 s. These results imply that the double dipping process enhances the conversion of PbI_2 to $MAPbI_3$ and its morphology, which are important factors to improve the electrical optical properties of the perovskite. The solar cell devices prepared at 2×150 s double dip coating process, which is

Table 2: Photovoltaic performance parameters of the solar cell devices assembled at different dipping times.

Dipping time	J_{sc} (mA.Cm^{-2})	V_{oc} (V)	FF	η (%)
2 × 90 s	17.23 ± 0.64	1.03 ± 0.02	0.73 ± 0.03	12.86 ± 0.62
2 × 120 s	17.55 ± 0.60	1.00 ± 0.01	0.71 ± 0.03	12.37 ± 0.64
2 × 150 s	19.01 ± 0.65	1.00 ± 0.01	0.71 ± 0.04	13.43 ± 0.86
2 × 180 s	17.90 ± 0.19	1.01 ± 0.01	0.66 ± 0.01	11.81 ± 0.39
2 × 240 s	17.6 ± 0.51	1.01 ± 0.02	0.68 ± 0.01	12.30 ± 0.33

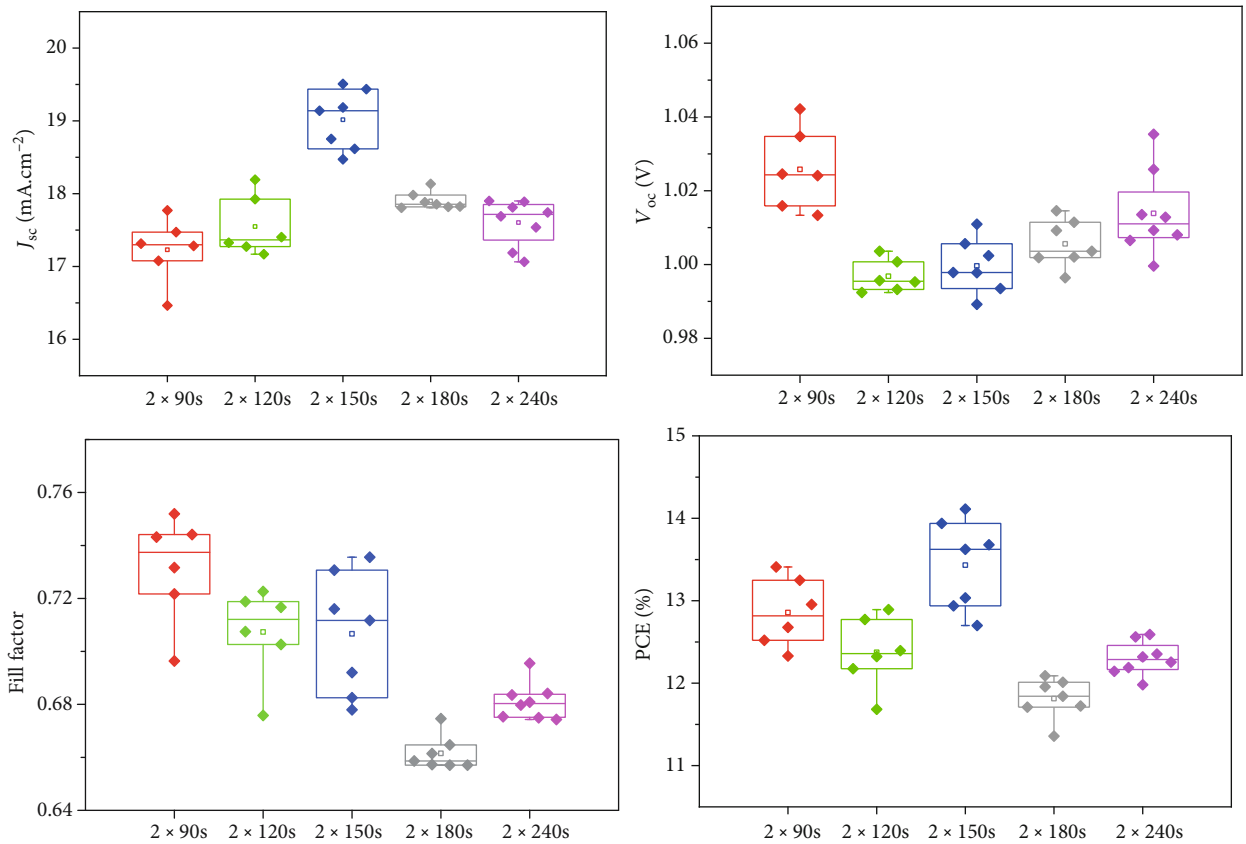

Figure 4: The statistical analysis of current density (J_{sc}), open circuit voltage (V_{oc}), fill factor, and power conversion efficiency (PCE) of all the solar cell devices fabricated at different double dipping conditions.

optimized conditions, show impressive photovoltaic performance of 14%. The results are comparable among reported ones focused on the perovskite material of $MAPbI_3$ in literature [15–20].

It can be clearly seen in Figure 4 that the 2 × 150 s solar cells could reach the optimum efficiency mostly due to the record of J_{sc} values which is mainly affected by the formation of the perovskite film. The high quality of the perovskite layer determined by the high transformation yield of the reactant PbI_2 to $MAPbI_3$ and smooth morphology of the perovskite film with no defects and high crystallinity is the key factor to optimize the performance of the solar cells. The double dipping process shows to be a suitable method to control the formation of the $MAPbI_3$ perovskite. The first circle helped to create perovskite on the surface and the nucleus crystal inside. The second circle improved the crystallization of the product deep inside the film. With the optimum duration time for each circle at 150 s, the perovskite could form at the maximum yield, and the dissolution as well as the recrystallization on the surface did not have adequate time to occur, leading to a smooth morphology with no voids and no defects.

4. Conclusion

The present work focused on the optimization of the two-step process modified by double dipping circle to produce

high superior hybrid lead iodide perovskite solar cells. The $MAPbI_3$ surface layer with high crystallinity and fewer defects was successfully prepared via an equilibrium transformation of PbI_2 at optimized dipping time. XRD analysis revealed the impact of the dipping time onto the conversion of PbI_2 to $MAPbI_3$, which is an important factor to achieve a reasonable device performance. SEM images exhibited the different morphology features of the $MAPbI_3$ layer prepared from different dipping times. SEM results implied the influence of the double dipping process on the morphology of $MAPbI_3$, and longer dipping time caused more holes and defects on its surface. Finally, an optimized cyclic dipping process at 2×150 s leads to a flawless and high crystallinity $MAPbI_3$ layer, which can present an outstanding performance of the perovskite solar device of about 14%.

Data Availability

The data used to support the findings of this study are included within the article.

Conflicts of Interest

The authors declare that they have no conflicts of interest.

Authors' Contributions

Huy Anh Dinh and Thuy Thanh Thi Nguyen have the same contribution as the first authors.

Acknowledgments

This research is funded by the Vietnam National University HoChiMinh City (VNU-HCM) under grant number C2019-18-19. The authors are grateful to Prof. Tzu-Chien Wei for his instrument support and Dr. Bao-Long Hoang Nguyen for his discussion.

References

[1] T. K. Kojima, A. Y. Shirai, and T. Miyasaka, *Abstract#397, 210th ECS Meeting, Pennington, N.J*, Electrochemical Society, Cancun, Mexico, 2006.

[2] A. Kojima, K. Teshima, Y. Shirai, and T. Miyasaka, "Organometal halide perovskites as visible-light sensitizers for photovoltaic cells," *Journal of the American Chemical Society*, vol. 131, no. 17, pp. 6050-6051, 2009.

[3] J.-H. Im, C.-R. Lee, J.-W. Lee, S.-W. Park, and N.-G. Park, "6.5% efficient perovskite quantum-dot-sensitized solar cell," *Nanoscale*, vol. 3, no. 10, pp. 4088–4093, 2011.

[4] H. S. Kim, C. R. Lee, J. H. Im et al., "Lead Iodide Perovskite Sensitized All-Solid-State Submicron Thin Film Mesoscopic Solar Cell with Efficiency Exceeding 9%," *Scientific reports*, vol. 2, no. 1, p. 591, 2012.

[5] L. Etgar, P. Gao, Z. Xue et al., "Mesoscopic CH3NH3PbI3/-TiO2Heterojunction Solar Cells," *Journal of the American Chemical Society*, vol. 134, no. 42, pp. 17396–17399, 2012.

[6] M. M. Lee, J. Teuscher, T. Miyasaka, T. N. Murakami, and H. J. Snaith, "Efficient hybrid solar cells based on meso-superstructured organometal halide perovskites," *Science*, vol. 338, no. 6107, pp. 643–647, 2012.

[7] J.-Y. Jeng, Y.-F. Chiang, M.-H. Lee et al., "CH3NH3PbI3 perovskite/fullerene planar-heterojunction hybrid solar cells," *Advanced Materials*, vol. 25, no. 27, pp. 3727–3732, 2013.

[8] C. Mu, J. Pan, S. Feng, Q. Li, and D. Xu, "Quantitative Doping of Chlorine in Formamidinium Lead Trihalide (FAPbI 3– x Cl x) for Planar Heterojunction Perovskite Solar Cells," *Advanced Energy Materials*, vol. 7, p. 1601297, 2017.

[9] N.-G. Park, "Research direction toward scalable, stable, and high efficiency perovskite solar cells," *Advanced Energy Materials*, vol. 10, no. 13, p. 1903106, 2020.

[10] W. Zhang, M. Saliba, D. T. Moore et al., "Ultrasmooth organic–inorganic perovskite thin-film formation and crystallization for efficient planar heterojunction solar cells," *Nature communications*, vol. 6, no. 1, p. 6142, 2015.

[11] Q. Wei, W. Zi, Z. Yang, and D. Yang, "Photoelectric performance and stability comparison of MAPbI3 and FAPbI3 perovskite solar cells," *Solar Energy*, vol. 174, pp. 933–939, 2018.

[12] M. Wang, Y. Feng, J. Bian, H. Liu, and Y. Shi, "A comparative study of one-step and two-step approaches for MAPbI3 perovskite layer and its influence on the performance of mesoscopic perovskite solar cell," *Chemical Physics Letters*, vol. 692, pp. 44–49, 2018.

[13] B. A. Al-Asbahi, S. M. H. Qaid, M. Hezam, I. Bedja, H. M. Ghaithan, and A. S. Aldwayyan, "Effect of deposition method on the structural and optical properties of CH3NH3PbI3 perovskite thin films," *Optical Materials*, vol. 103, p. 109836, 2020.

[14] J.-H. Im, H.-S. Kim, and N.-G. Park, "Morphology-photovoltaic property correlation in perovskite solar cells: one-step versus two-step deposition of CH3NH3PbI3," *APL Materials*, vol. 2, no. 8, article 081510, 2014.

[15] Y. Fu, F. Meng, M. B. Rowley et al., "Solution growth of single crystal methylammonium lead halide perovskite nanostructures for optoelectronic and photovoltaic applications," *Journal of the American Chemical Society*, vol. 137, no. 17, pp. 5810–5818, 2015.

[16] Y. Luo, F. Meng, E. Zhao, Y.-Z. Zheng, Y. Zhou, and X. Tao, "Fine control of perovskite-layered morphology and composition via sequential deposition crystallization process towards improved perovskite solar cells," *Journal of Power Sources*, vol. 311, pp. 130–136, 2016.

[17] T.-Y. Hsieh, C.-K. Huang, T.-S. Su, C.-Y. Hong, and T.-C. Wei, "Crystal growth and dissolution of methylammonium lead iodide perovskite in sequential deposition: correlation between morphology evolution and photovoltaic performance," *ACS Applied Materials & Interfaces*, vol. 9, no. 10, pp. 8623–8633, 2017.

[18] H. Gao, X. Meng, Y. Du, and X. Gao, "Fabrication and characterization of perovskite CH3NH3PbI3 films via two-step sol-gel process: impact of soaking time of PbI2," *Thin Solid Films*, vol. 682, pp. 37–43, 2019.

[19] T. Baikie, Y. Fang, J. M. Kadro et al., "Synthesis and crystal chemistry of the hybrid perovskite (CH3NH3)PbI3 for solid-state sensitised solar cell applications," *Journal of Materials Chemistry A*, vol. 1, no. 18, pp. 5628–5641, 2013.

[20] Y. Ando, Y. Ohishi, K. Suzuki, A. Suzuki, and T. Oku, "Rietveld refinement of the crystal structure of perovskite solar cells using CH3NH3PbI3 and other compounds," in , Article ID 020003*AIP Conference Proceedings*, vol. 1929, Tokyo, Japan, 2018.

Hindawi
Journal of Nanomaterials
Volume 2021, Article ID 6655375, 11 pages
https://doi.org/10.1155/2021/6655375

Research Article

Investigating the Anti-Inflammatory Activity of Curcumin-Loaded Silica-Containing Redox Nanoparticles

Khoa Minh Le,[1,2] Nhu-Thuy Trinh,[1,2] Vinh Dinh-Xuan Nguyen,[1,2] Tien-Dat Van Nguyen,[1,2] Thu-Ha Thi Nguyen,[1,2] Toi Van Vo,[1,2] Tuan Quoc Tran,[2,3] Dai-Nghiep Ngo,[2,3] and Long Binh Vong[1,2]

[1]*School of Biomedical Engineering, International University, 700000 Ho Chi Minh, Vietnam*
[2]*Vietnam National University Ho Chi Minh City (VNU-HCMC), 700000 Ho Chi Minh, Vietnam*
[3]*Faculty of Biology and Biotechnology, University of Science, 700000 Ho Chi Minh, Vietnam*

Correspondence should be addressed to Long Binh Vong; vblong@hcmiu.edu.vn

Received 6 December 2020; Revised 6 January 2021; Accepted 19 January 2021; Published 31 January 2021

Academic Editor: Duong Tuan Quang

Chronic inflammation is considered as one of the challenging diseases, and overproduction of reactive oxygen species (ROS) is strongly related to the onset of chronic inflammation. Therefore, antioxidant and anti-inflammatory approaches are particularly becoming suitable treatment and prevention of inflammation. Curcumin (CUR), a main component of turmeric extract, is well known as an effective agent in both antioxidant and anti-inflammatory activities; however, there are still some limitations of its use including poor water solubility, low bioavailability, and oxidation by ROS. Nanotechnology has been used as a drug delivery system, which is a promising approach in overcoming the aforementioned drawbacks of CUR; hence, it improves the antioxidant and anti-inflammatory effects of conventional medications. In this research, silica-containing redox nanoparticles (siRNP) were designed with the size of several tens of nanometers, prepared by self-assembly of an amphiphilic block copolymer consisting of drug absorptive silica moiety and ROS-scavenging nitroxide radical moiety in the hydrophobic segment. CUR was simply encapsulated into siRNP through the dialysis method, creating CUR-loaded siRNP (CUR@siRNP), which significantly improved the water solubility of CUR. The efficient antioxidant activity and anti-inflammatory effect of CUR@siRNP *in vitro* were also improved via 2,2-diphenyl-1-picrylhydrazyl assay and lipopolysaccharide-induced macrophage cell line activation, respectively. Oral administration of CUR@siRNP showed improvement in pharmacokinetic profile *in vivo* including AUC and C_{max} values as compared to free CUR. Furthermore, the anti-inflammatory effect of nanoformulation was investigated in the colitis mouse model induced by dextran sodium sulfate.

1. Introduction

According to the World Health Organization (WHO), chronic inflammation is considered one of the greatest threats to other chronic diseases. Inflammation acts as a vital part of the immune system's response to injury and infection, by which the immune system detects and eliminates harmful stimuli while initiating wound healing [1]. Prolonged inflammation, or chronic inflammation, is characterized for long-term persistence from months, years to even decades. Moreover, chronic inflammation is strongly related to many challenging diseases, such as cancer, heart disease, diabetes, and Alzheimer's disease [2]. The discovery of reactive oxygen species (ROS) features its active roles in many pathways, including oxidative stress, which progressed chronic inflammation. It has been reported that oxidative stress or overproduced ROS accumulatively induces chronic inflammation as both signalling molecules and inflammatory mediators [3]. ROS are defined as highly reactive oxygen radicals, such as superoxide (O_2^-) or hydroxyl radical ($OH^\bullet$), which display various reactivity. Due to a single electron on the outer shell, ROS are unstable and may react with adjacent molecules to maintain electrical homeostasis [4]. Endogenous ROS accumulation activates thioredoxin, which interacted protein (TXNIP) complex [4]. The complex detached, enabling TXNIP to bind with NLRP3 inflammasome. Furthermore,

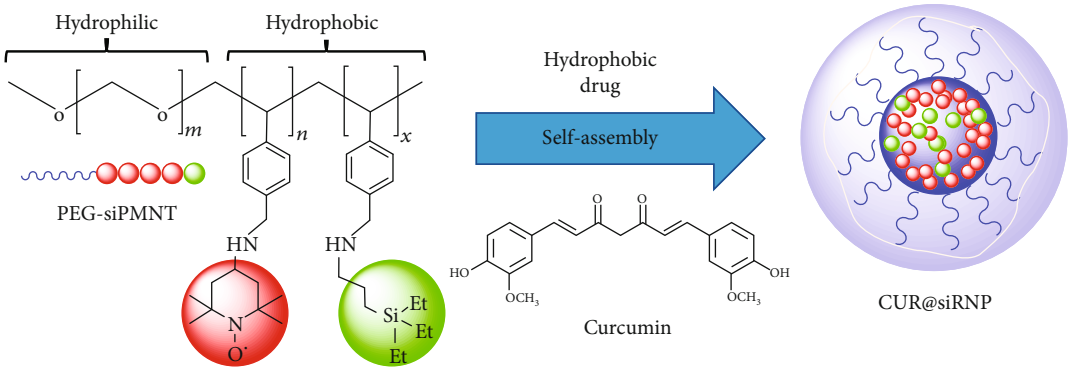

Figure 1: The self-assembly of curcumin-loaded silica-containing redox nanoparticle (CUR@siRNP).

the combination of NLRP3, apoptosis-associated speck-like protein, and caspase-1 proteins activated NLRP3 to induce production of IL-1β and IL-18, both are secreted by inflammatory cells, then promoting inflammation. ROS oxidizes crucial signalling protein in inflammation sites, i.e., tyrosine phosphatase, which results in endothelial dysfunction and tissue injury. Also, oxidative stress disrupts interendothelial junction, while inducing inflammatory cell migration across endothelial barriers to assist pathogen clearance. Hence, these consequences cause damage to biomolecules and severe tissue injury, resulting in inflammatory diseases.

Curcumin (CUR), a polyphenolic component of turmeric extract, has been mainly used as a commercial dietary additive and supplement. In addition, CUR enhances physiological antioxidant mechanism, while preventing essential inflammatory molecules, therefore, downregulating inflammation altogether [5]. Despite all of the advantages, its clinical application has been impeded by many drawbacks. CUR is great insoluble in water, poor absorption, rapid metabolism, short biological half-life, and spontaneous oxidative degradation caused by ROS leading to its low bioavailability [6, 7]. In order to improve CUR solubility, many approaches have been considered. One attempt by adding adjuvants, a combination of CUR and other bioenhancers, such as piperine, quercetin, or silibinin was used to enhance cellular absorption. This increment of pharmacokinetics is made possible by albumin-binding interactions [8]. Unfortunately, some bioenhancers showed toxicity in experimental animals. Alternately, the search for developed drug delivery nanotechnologies is perceived as a highlight approach. Nanoparticles have shown promising drug solubility enhancement properties and cell-specific distribution, hence, improving therapeutic effect [9]. There have been versatile forms and nanoparticle structures, including liposomes, dendrimers, and solid lipid nanoparticles developed for biomedical applications. The greatest challenge in nanoparticle-based pharmaceutical engineering is designing a stable and controlled release drug delivery system [10]. Conventional drug delivery systems faced coherent drawbacks, such as low drug loading capacity, low durability, and adverse side-effects. These have been used as a nanocarrier for CUR to overcome its aforementioned drawbacks. The first attempt was from Kanai et al. (2011), who used a nanoparticle formulation called THERACURMIN to illustrate the improvement in bioavailability in human subjects [11]. Tai et al. (2019) recently formulated curcumin-loaded liposomal nanoparticles (Cur-LP) with the same objective. In order to improve drug bioavailability, the research coated liposome nanoparticles with high molecular weight chitosan to enhance stability and maintain the release capacity of Cur-LP [12]. Nevertheless, various designed nanoparticles shared common concerns: they exhibited low stability, whereas the release profile was inconsistent and uncontrollable. In addition, their loading capacity was barely insufficient due to the instability, which leads to poor therapeutic effect. Finally, nanoparticle cytotoxicity still remained as a great struggle, with complex nanocarrier may engage unwanted immune responses, therefore, it adversely effects on overall health [13]. A designed silica-containing redox nanoparticle (siRNP) was previously developed to enhance therapeutic drugs with low bioavailability. siRNP was formed from self-assembled amphiphilic polymer (PEG-siPMNT, polyethylene glycol-*b*-poly (4-[2,2,6,6-tetramethyl piperidine-1-oxyl] aminomethyl styrene) composed of hydrophilic PEG segment and hydrophobic segment consisting of a ROS-scavenging moiety and a silica moiety for stability encapsulation (Figure 1) [14, 15]. This represents a self-assembly micelle structure, where the hydrophobic drug is captured within the core of the nanocarrier [15]. The objective of this study was to investigate the bioavailability and anti-inflammatory effects of CUR-loaded siRNP (CUR@siRNP) compared to free CUR. The results showed that CUR@siRNP significantly improved the water solubility and bioavailability of CUR after oral administration. Consequently, CUR@siRNP exhibited a promising antioxidant and anti-inflammatory effects *in vitro* of RAW 264.7 cell activation and *in vivo* of dextran sodium sulfate- (DSS-) induced colitis model in mice.

2. Materials and Methods

2.1. Synthesis of Nanoparticles. The synthesis of silica-containing redox polymer (PEG-siPMNT) was described in the previous study [14]. siRNP and CUR@siRNP were synthesized through dialysis of PEG-siPMNT polymer against distilled water. Briefly, 0.5 mL PEG-siPMNT (60 mg/mL) was well-mixed with 0.5 mL dimethylformamide (DMF, FUJIFILM Wako Chemicals—Japan) to prepare siRNP. The solution was transferred into the dialysis membrane and

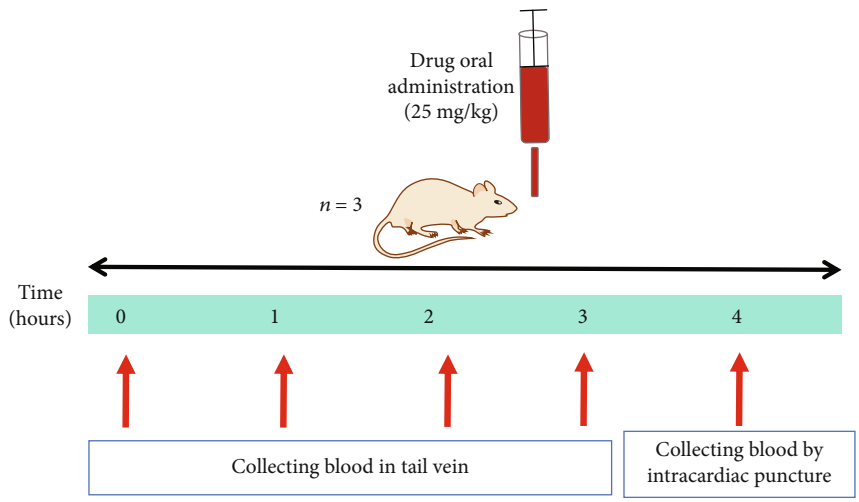

Figure 2: Timeline for blood sample collection of the CUR-treated group and the CUR@siRNP-treated group (25 mg/kg) for the pharmacokinetic experiment.

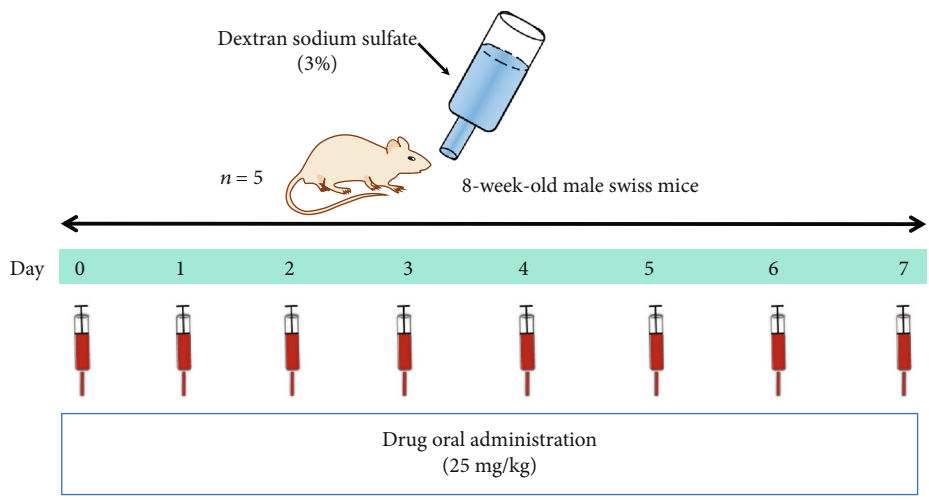

Figure 3: The oral administration of CUR and CUR@siRNP (25 mg/kg) in a colitis mouse model induced by dextran sodium sulfate (DSS).

Table 1: Disease activity index (DAI) scores [18, 19].

Stool consistency	Feces bleeding	Weight loss
		0 = no weight loss
0 = formed	0 = normal colour	1 = 1% – 5% weight loss
1 = mild soft	1 = brown colour stool	2 = 6% – 10% weight loss
2 = very soft	2 = reddish colour stool	3 = 11% – 15% weight loss
3 = watery	3 = bloody stool	4 = ≥16% weight loss

proceeded the dialysis for 24 h with occasional water change. CUR@siRNP was prepared by a similar method, whereas CUR (Tokyo Chemical Industry, Japan) was encapsulated via the hydrophobic interaction and the drug absorption feature of silica core of siRNP [15]. In such, 1.5 mg of CUR was fully dissolved in 0.5 mL of DMF. Next, 0.5 mL of PEG-siPMNT (60 mg/mL) and 14 μL of tetraethyl orthosilicate (TEOS—St. Louis, MO, USA) were added to the mixture. Obtained substance was dialyzed against water for 24 h with an occasional water change.

2.2. Characteristics of CUR@siRNP

2.2.1. Particle Size. The particle size of CUR@siRNP was analyzed by dynamic light scattering (DLS) using Zetasizer ZS (Malvern, UK). The CUR@siRNP samples were diluted in water or PBS, and the measurement was performed with an angle of 173° at 25°C.

2.2.2. Measurement of Encapsulation Efficiency and Loading Capacity. CUR concentration presented in the siRNP was measured at 450 nm and expressed in terms of encapsulation efficiency (EE) and loading capacity (LC). CUR standard curve was constructed with serial dilution of CUR in DMSO solution (0, 10, 20, 40, 50, and 60 μg/mL). CUR@siRNP was diluted with distilled water, and all samples were measured at 450 nm using UV-VIS spectrophotometer (Thermo Fisher

Table 2: Histological scores [20, 21].

Crypt architecture	Cellular infiltration	Goblet cell depletion
0 = normal	0 = normal	
1 = minimal crypt distortion	1 = minimal cellular infiltration	0 = absent
2 = moderate crypt distortion	2 = moderate cellular infiltration	1 = present
3 = severe crypt distortion	3 = dense cellular infiltration	

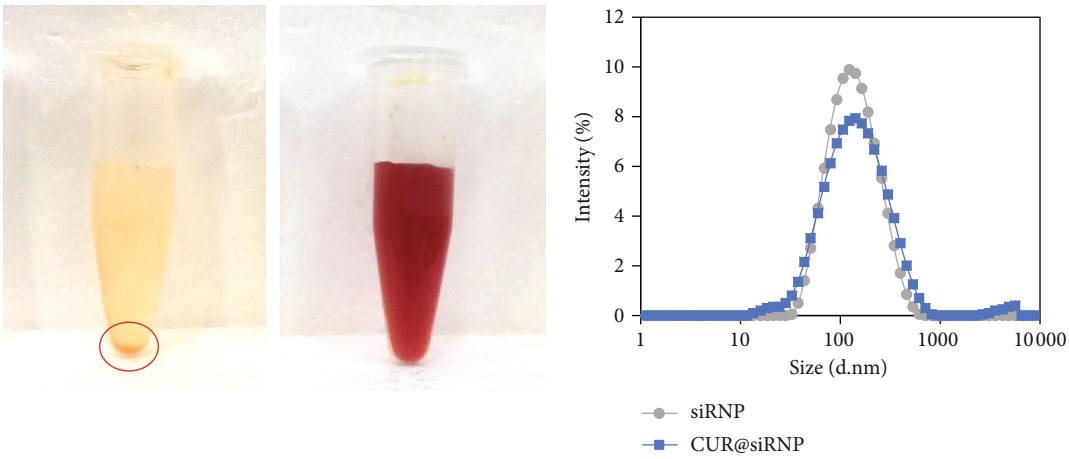

(a) (b)

Figure 4: Characterization of CUR@siRNP. (a) The solubility of CUR (left) and CUR@siRNP (right) in water (at 1 mg/mL concentration of CUR). The red circle indicates the insoluble curcumin particles. (b) The size distribution of siRNP and CUR@siRNP was measured by DLS.

Table 3: Summary of the size of siRNP and CUR@siRNP, including encapsulation efficiency (EE) and loading capacity (LC) of CUR@siRNP.

Sample	Size (nm)	PdI	EE (%)	LC (%)
siRNP	122±1	0.26	—	—
CUR@siRNP	142 ± 1	0.30	74.3 ± 5.1	7.4 ± 0.5

Scientific). The EE and LC were calculated using the given formulas:

$$\text{EE}\,(\%) = \frac{\text{The mass of drug encapsulated}}{\text{Initial drug mass}}\ \text{x}\ 100\%,$$
$$\text{LC}\,(\%) = \frac{\text{The mass of drug encapsulated}}{\text{Initial polymer mass}}\ \text{x}\ 100\%. \quad (1)$$

2.3. Investigation of CUR@siRNP Bioactivities

2.3.1. Antioxidant Assay. Antioxidant activity of CUR@siRNP was determined using the radical scavenging ability towards 2,2-diphenyl-1-picrylhydrazyl (DPPH—Sigma Aldrich, St. Louis, MO, USA). In this study, 50 μL of CUR in DMSO, siRNP, and CUR@siRNP in various concentrations (0, 2, 5, 8, and 10 μg/mL) were well-mixed with 150 μL of DPPH solution (40 μg/mL). Other samples treated with vitamin C served as the positive control, while distilled water acted as the negative control. All samples were incubated for 30 minutes in dark condition at room temperature. The optical density (OD) of tested samples was measured at 517 nm afterward, and the percentage of DPPH scavenging capacity (SC) was calculated via the following equation:

$$\text{SC}\,(\%) = \frac{(\text{OD}_{\text{blank}} - \text{OD}_{\text{sample}})}{\text{OD}_{\text{blank}}} \times 100\%, \quad (2)$$

Measurements were repeated in triplicate.

2.3.2. Nitric Oxide (NO) Assay. Nitric oxide (NO) assay was assessed by Griess test to determine the NO concentration, which acts as an anti-inflammatory substance in the physiological environment. The gaseous NO was measured to employ a 2-step diazotization reaction. Briefly, dinitrogen trioxide (N_2O_3) was secreted from the acid-catalyzed formation of nitrous acid from nitrite reacts with sulfanilamide to produce diazonium ions. When they are combined with *N*-(1-naphthyl) ethylenediamine, they yield a chromophoric azo product that shows strong absorbance at 540 nm [16, 17]. In this study, RAW 264.7 cells (ATTC, USA) were seeded in 24-well plates at a density of 5×10^5 cells per well in 400 μL of DMEM media (Sigma Aldrich, St. Louis, MO) containing 5% fetal bovine serum (Sigma Aldrich, St. Louis, MO) and 1% antibiotics (penicillin/streptomycin/neomycin; Invitrogen, Carlsbad, CA), and the cells were incubated for 24 h at a humidified atmosphere of 5% CO_2 at 37°C. Then, 50 μL of samples (siRNP, CUR@siRNP, CUR@si-nRNP, and CUR in DMSO 10%) was added at the concentration of 100 μL/mL. Next, 50 μL of lipopolysaccharide (LPS; Sigma Aldrich, St. Louis, MO) was added. After 12 h, 50 μL of

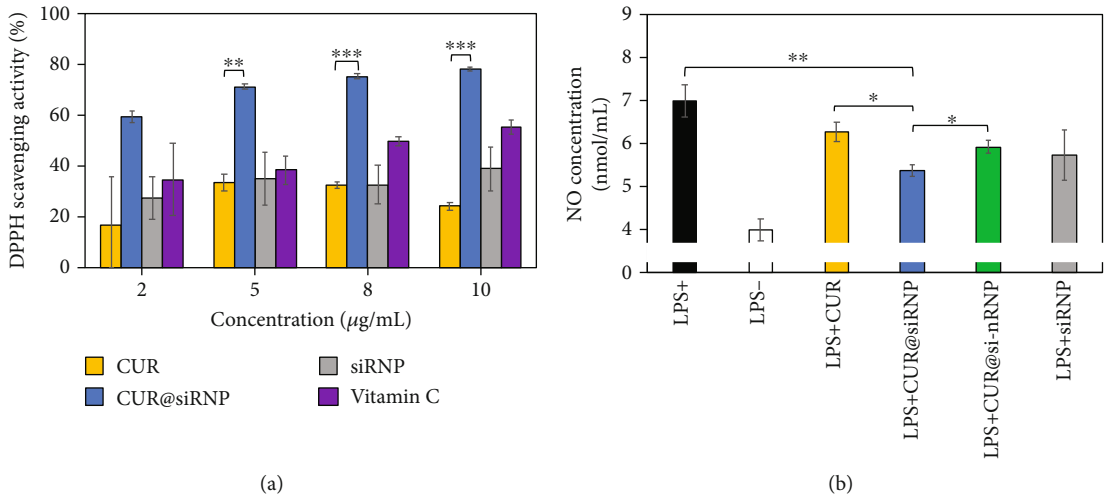

Figure 5: Bioactivities of CUR@siRNP. (a) The antioxidant activity of CUR, CUR@siRNP, and siRNP using DPPH assay. Vitamin C served as the positive control, while distilled water (DW) acted as the negative control. (b) The anti-inflammatory effect of CUR (curcumin in DMSO 10%), CUR@siRNP, CUR@si-nRNP, and siRNP via NO assay in the LPS-induced RAW 264.7 macrophage activation. Data are expressed as mean ± SD, $n = 3$, $^{*}p < 0.05$, $^{**}p < 0.01$, and $^{***}p < 0.001$.

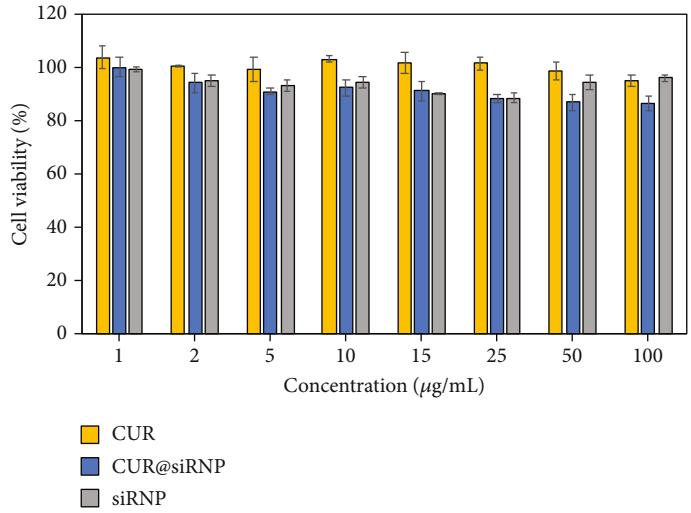

Figure 6: Cell viability of BAEC was determined by MTT assay. The concentration in the horizontal axis indicates the concentration of CUR, while the concentration of siRNP was 10 times higher than the concentration of CUR. Data are expressed as mean ± SD and $n = 3$.

Table 4: Table of pharmacokinetic parameters.

Pharmacokinetic parameter	Formulation	
	CUR	CUR@siRNP
Dose (mg/kg)	25	25
AUC (μg.h/mL)*	1.34 ± 0.09	2.79 ± 0.11
C_{max} (μg/mL)	0.69 ± 0.14	1.74 ± 0.08
T_{max} (h)	0.5	0.5
K_e (1/h)	0.71 ± 0.53	0.62 ± 0.14
$t_{1/2}$ (h)	1.34 ± 0.76	1.55 ± 0.25
V_d (mL/g)	37.01 ± 22.48	14.86 ± 2.61
Cl (mL/h)**	18.77 ± 0.98	8.98 ± 0.34

supernatant was collected and well-mixed with 50 μL Griess reagent containing 2% sulfanilamide, 0.2% N-(1-naphthylethylenediamine) dihydrochloride, and 5% acid phosphoric. The absorbance of each well was determined spectrophotometrically at a bandwidth of 540 nm. NO concentration was calculated using NO calibration curve constructed with $NaNO_2$ dilution. The wells without LPS acted as the negative control, while wells with no addition of samples were served as the positive control.

2.4. Cytotoxicity Evaluation. The cytotoxicity, based on cell metabolic activity alteration, was evaluated using 3-(4,5-dimethylthiazol-2-yl)-2,5-diphenyltetrazolium bromide (MTT; St. Louis, MO) assay. The yellow pigment of MTT was being reduced by living cells to purple formazan. Formazan particles are mostly insoluble in water; hence, a

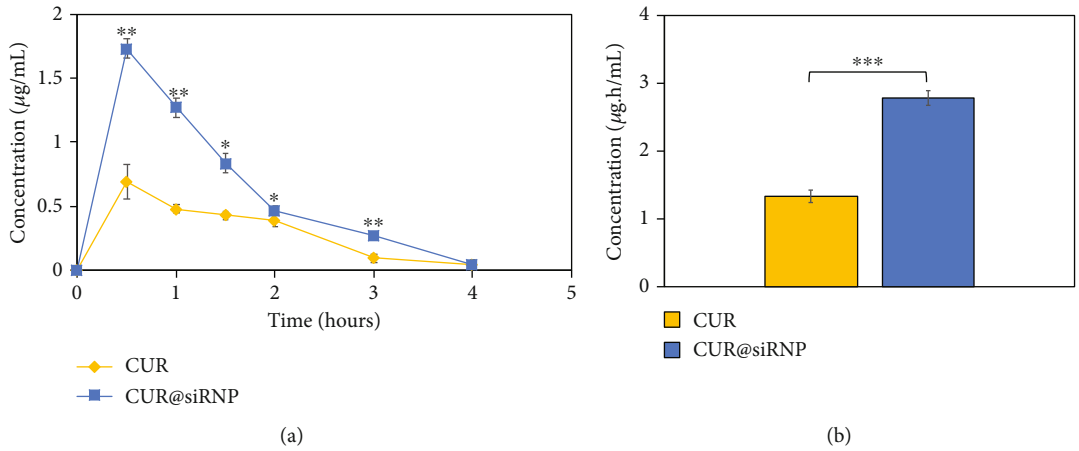

Figure 7: (a) Amount of curcumin in the plasma after oral administration of CUR (free curcumin) or CUR@siRNP. (b) AUC of curcumin in the plasma after oral administration of CUR (free curcumin) or CUR@siRNP. Data are expressed as mean ± SD, $n = 3$, $^{*}p < 0.05$, $^{**}p < 0.01$, and $^{***}p < 0.001$.

solubilization buffer was added to dissolve formazan particles. The absorbance of the solution was measured at 540 nm for the quantification of formazan, which is proportional to living cells. In this research, an MTT assay was performed on bovine aortic endothelial cells (BAEC from JCRB Cell Bank, Japan). BAEC was seeded in a 96-well plate, containing approximately 5×10^3 cells. After 24 h incubation, 10 μL of CUR, siRNP, and CUR@siRNP with various concentrations was added. The wells were incubated for another 24 h, and 5 μL of MTT solution was added to each well afterward. After 4 h incubation, 50 μL solubilization buffer was added to each well and left incubating overnight. The absorbance of each well was measured at 540 nm.

2.5. Pharmacokinetics of CUR@siRNP In Vivo. The 30 g adult male Swiss mice (Institute of Drug Quality Control Ho Chi Minh City) were acclimated at least 3 days before the experiments, and the mice were provided with free access to food and water. The animal experimental protocol was approved by the School of Biomedical Engineering, International University Ho Chi Minh. The mice were divided randomly into two groups (3 mice per group): CUR-treated group (CUR in carboxymethyl cellulose 0.5%) and CUR@siRNP-treated group. All groups were administered by oral gavage at a single dose of 25 mg/kg (Figure 2). The mice were anesthetized for collecting blood in heparin sodium-coated tube, and the plasma was obtained by centrifugation. Then, 50 μL of plasma and 100 μL mixture of acetonitrile and methanol (1 : 1) were added and vortexed for a minute. The mixtures were centrifuged at 11,200 g at 4°C for 10 min. CUR concentration in the supernatant was determined by fluorescence intensity with excitation and emission wavelengths of 425 nm and 597 nm, respectively. The plasma was frozen and stored at −80°C until further use. Pharmacokinetic parameters were estimated using the model-independent method. The terminal elimination rate constant (K_e) was estimated by a linear regression analysis of the terminal portion of the log-linear blood concentration-time profile of CUR. The terminal elimination half-life ($t_{1/2}$) was calculated from K_e using the formula $T_{1/2} = 0.693/K_e$. The maximum observed plasma concentration (C_{max}) and the time taken to reach it (T_{max}) were obtained from the curve plotting CUR concentration with time. The area under each drug concentration time curve (AUC, (ug.h)/mL) to the last data point was calculated by the linear trapezoidal rule and extrapolated to time infinity by the addition of C_{last}/K_e, where C_{last} is the concentration of the last measured plasma sample. The apparent body clearance (Cl) was calculated using the equation Cl = Dose/AUC. The apparent volume of distribution (V_d) was calculated by the equation V_d = Dose/(K_e.AUC).

2.6. Therapeutic Effect of CUR@siRNP in Colitis Mouse Model Induced by DSS. Colitis in mice was induced by 3% (wt/vol) dextran sodium sulfate (DSS, 5,000 Daltons; Fujifilm Wako Pure Chemicals, Osaka, Japan) supplemented in the drinking water for 7 d. The mice were randomized divided into 4 groups: healthy group, DSS-injured group, CUR-treated group, and CUR@siRNP-treated group. The equivalent doses of drugs (25 mg/kg) were orally administered daily during the 7 days of DSS treatment (Figure 3). The body weight changes were measured daily, while visible stool consistency and feces bleeding were assessed in the sacrifice day. Disease activity index (DAI) is the summation of stool consistency index (0–3), feces bleeding index (0–3), and weight loss index (0–4) (Table 1). After 7 days of treatment, the mice were sacrificed after anesthesia with xylazine (6 mg/kg) and zoletil (5 mg/kg). Then, the entire colon (from the cecum to the rectum) was collected. Colon length was measured and gently washed with physiological saline. After that, 1 cm of the middle section was used for histologic assessment. The histological score of the colon was evaluated using a microscope. Moreover, the histological score is the summation of crypt architecture (0–3), cellular infiltration (0–3), and goblet cell depletion (absent–0, present–1) (Table 2).

2.7. Statistical Analysis. All experiments were conducted at least thrice, and the data represent the mean ± SEM.

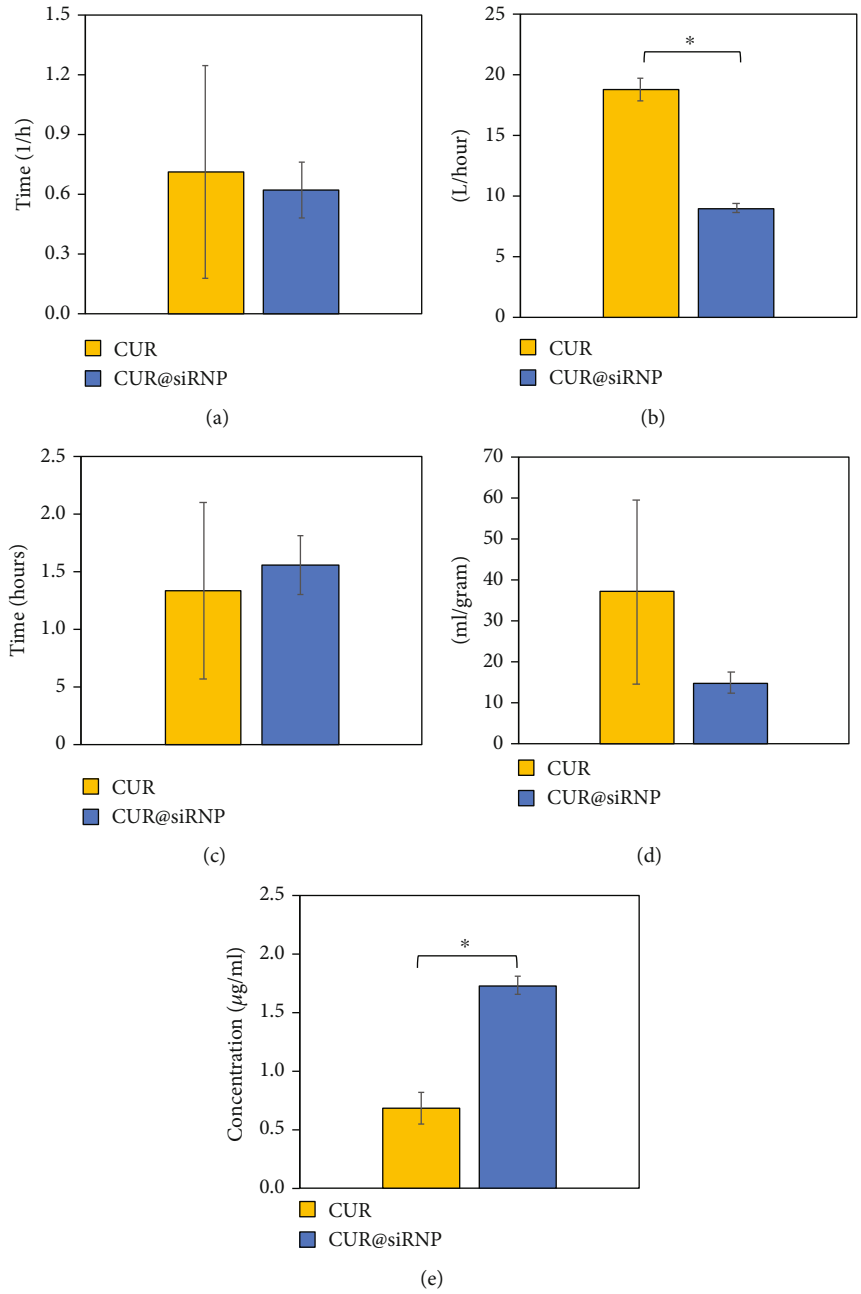

Figure 8: The comparison of pharmacokinetic parameters between CUR (free curcumin) and CUR@siRNP. (a) Elimination rate. (b) Clearance. (c) Half-life. (d) Volume distribution. (e) Maximum concentration. Data are expressed as mean ± SD, $n = 3$, and $^{*}p < 0.01$.

Statistical comparisons were performed using one-way analysis of variance (ANOVA) followed by Student's t-test using Microsoft Excel. The results were analyzed and considered statistically significant differences when $p < 0.05$ using a two-tailed t-test.

3. Results and Discussion

3.1. Characteristics of CUR@siRNP. CUR is an antioxidant substance with extremely poor solubility in an aqueous solution (<8 μg/mL) [22]; hence, the CUR sample remained insoluble in water, evidenced by small particle accumulated at the bottom of the centrifuge tube (Figure 4(a), left). Meanwhile, the CUR@siRNP solution had dark-brown colour without any precipitation (Figure 4(a), right), indicating the improvement of CUR solubility in water. As the colour became darker, it may be due to the change in particle size. Next, the size of CUR@siRNP was evaluated by DLS measurement. As shown in Figure 4(b) and Table 3, siRNP size slightly increased from 122 ± 1 nm to 142 ± 1 nm in the CUR@siRNP sample, implying that CUR was successfully encapsulated within the siRNP. In this study, CUR@siRNP size was under 200 nm, which is preferable to a complex drug delivery device to be efficient to achieve the enhanced

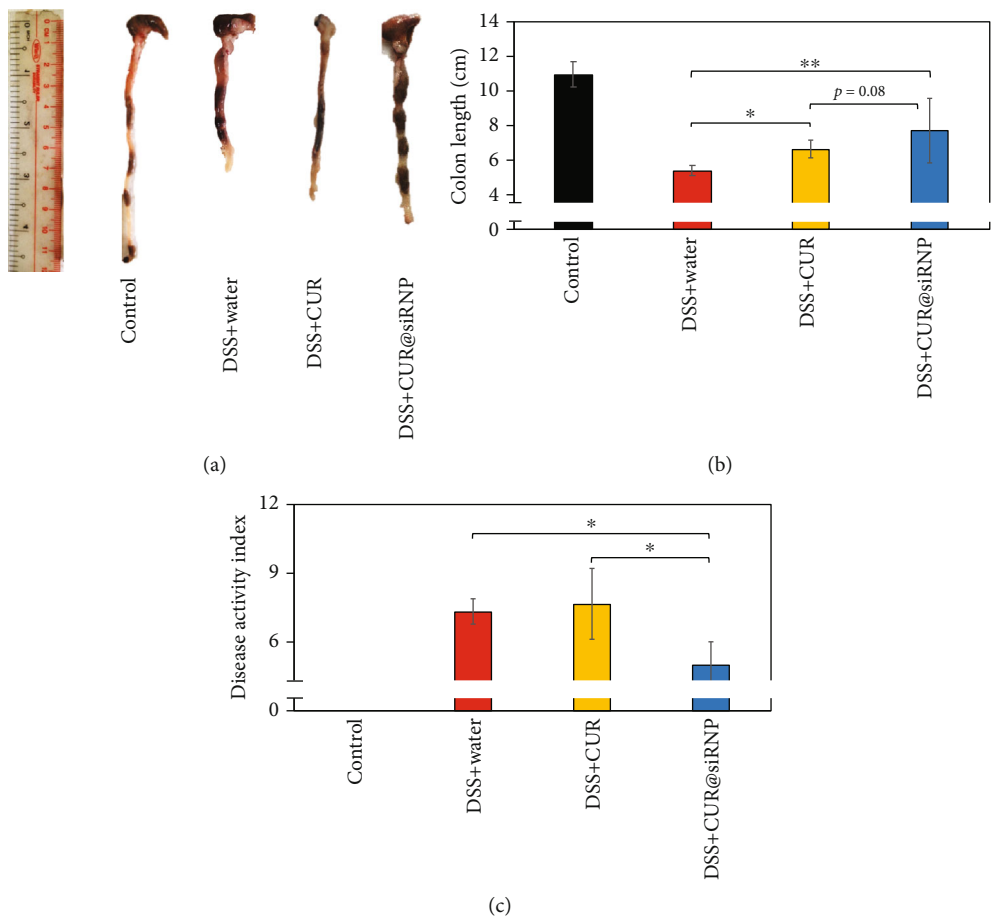

Figure 9: The therapeutic effect of CUR@siRNP in colitis mice. (a) The colon of mice after 7 days of treatment. (b) Changes in colon length. (c) Changes in DAI. DAI is the summation of stool consistency index (0–3), feces bleeding index (0–3), and weight loss index (0–4). Data are expressed as mean ± SD, $n = 5$, $^{*}p < 0.05$, and $^{**}p < 0.01$.

permeability and retention effect for the passive targeting in the inflammatory tissue [23]. In addition, monodispersity was observed with a low PDI (polydispersity index) value (<0.3), suggesting a narrow size distribution of siRNP and CUR@siRNP. Next, the encapsulation efficiency (EE) and drug loading capacity (LC) of CUR@siRNP were measured using UV-VIS spectrophotometer. In this study, the EE and LC of CUR@siRNP were 70% and 7%, respectively (Table 3). The use of siRNP helps increase CUR solubility, enabling it to overcome biological barriers that are especially easier to absorb by intestinal epithelial cells.

3.2. Bioactivities of CUR@siRNP. CUR is a natural antioxidant agent; however, due to low bioavailability, it exerted a low antioxidant effect by scavenging DPPH radical (Figure 5(a)). Meanwhile, siRNP contains both ROS scavenging moiety of nitroxide radical (TEMPO) and a drug absorptive moiety of silica for protection against oxidative damage while enhancing stability of CUR through oral delivery. It has been reported that nitroxide radical TEMPO strongly scavenges superoxide and hydroxyl radicals [24, 25], which are higher generated in the inflammatory tissues. Therefore, siRNP acts as not only a nanocarrier but also as a ROS scavenging agent to increase the antioxidant activity of CUR. At 10 μg/mL concentration, the CUR@siRNP sample had the highest DPPH scavenging activity (78.2%) compared to both CUR (24.4%) and siRNP (39.1%), suggesting that the synergistic effect was observed. This result indicated siRNP is an ideal nanocarrier for CUR, by enhancing CUR's natural antioxidant profile. Next, we investigated the anti-inflammatory activity *in vitro* using the RAW 264.7 cell model. NO is considered as a biomarker for proinflammatory due to the activation by macrophages. In this assay, NO was stimulated by RAW 264.7 cells due to the introduction of LPS *in vitro* (Figure 5(b)). The level of NO is inversely proportional to the anti-inflammatory activities of the added samples. Both CUR and siRNP showed the effect to suppress the NO level in LPS-activated macrophage cells. Interestingly, CUR@siRNP demonstrated a significant inhibition in NO level as compared to CUR and siRNP alone. These results indicated that CUR@siRNP presents higher antioxidant and anti-inflammatory activity *in vitro* as compared to free CUR.

3.3. Drug Cytotoxicity. After evaluating the antioxidant and anti-inflammatory activities of CUR@siRNP *in vivo*, the cytotoxicity was investigated using MTT assay against BAEC cell line. As shown in Figure 6, at low concentration, CUR@siRNP showed no significant difference in cell viability than

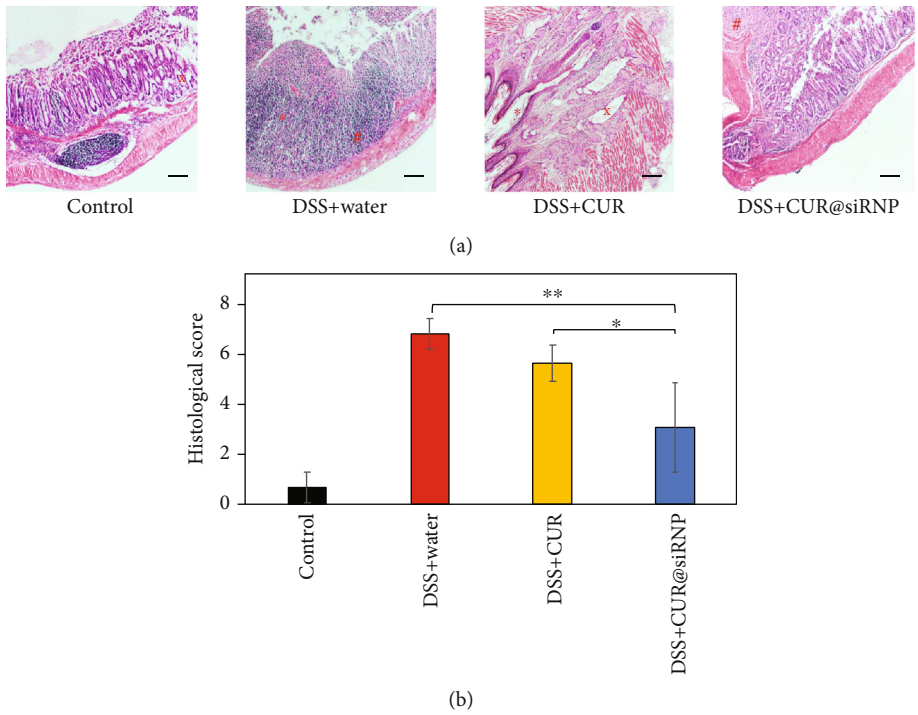

Figure 10: The histological assessment of colon after treatment. (a) Histology of 7 μm thick colonic sections by hematoxylin and eosin staining. Scale bar = 100 μm. *: distortion of crypt architecture. $^{\#}$: cellular infiltration. ^{x}: goblet cell depletion. (b) Histological score of colon section after 7 days of DSS treatment. Data are expressed as mean ± SD, $n = 5$, $^{*}p < 0.05$, and $^{**}p < 0.01$.

CUR and siRNP-treated cells. At higher concentrations, both CUR@siRNP and siRNP demonstrated a slight toxicity than free CUR. However, all CUR@siRNP and siRNP obtained 86% or more in cell viability even at high concentration (100 μg/mL), which suggested a low toxicity of CUR@siRNP against BAEC cell. It should be noticed that the concentration of siRNP was 10 times higher than the concentration of CUR. Several nanomaterials have been reported with high toxicity via inducing the generation of ROS [26]. Our previous study suggested that ROS scavenging nanoparticle could suppress the toxicity of the nanomaterial itself [27]. Therefore, CUR@siRNP was shown with low cytotoxicity, while promoting beneficial biological effects of CUR, which is highly desirable and promising as an anti-inflammatory therapeutic approach.

3.4. Pharmacokinetics of CUR@siRNP In Vivo. Since CUR@siRNP significantly improved the solubility of CUR, we continue to evaluate the bioavailability of orally administered CUR@siRNP *in vivo* mouse model (Figure 2). In this study, the pharmacokinetics was evaluated, and the basic parameters were typically shown in Table 4. The pharmacokinetic properties of CUR and CUR@siRNP were presented as follows.

Values reported as mean ± S.D. ($n = 3$). AUC: area under the plasma concentration–time curve; $C_{\max}$: peak concentration; $T_{\max}$: time to reach peak concentration; K_e: constant of elimination; $t_{1/2}$: mean half-life; V_d: apparent volume of distribution; Cl: clearance. Significant difference of CUR@siRNP versus CUR ($^{*}p < 0.05$ and $^{**}p < 0.01$).

Area Under Curve (AUC): the AUC of CUR was quite low (1.34 ± 0.09 μg.h/mL), indicating an extremely low drug absorption and internalization in the bloodstream via the intestine after oral administration. Meanwhile, the AUC value of CUR@siRNP was significantly higher (2.79 ± 0.11 μg.h/mL), which demonstrated the concentration of drugs in the bloodstream over time had been greatly improved compared to CUR aqueous suspension ($p < 0.001$) (Figures 7(a) and 7(b)).

To compare the retention of CUR and CUR@siRNP, the pharmacokinetic parameters were also described in Table 4 and Figure 8.

C_{max} and T_{max}: after the oral administration, both drugs were adsorbed quickly and achieved the highest plasma drug concentration after 0.5 h. While the maximum concentration of CUR was only 0.69 ± 0.14 μg/mL, which was quite low, the concentration of CUR@siRNP was increased 2.8-fold (1.74 ± 0.078 μg/mL) at max, indicating siRNP has improved the absorption of CUR into the bloodstream.

Elimination rate (K_e) and half-life ($t_{1/2}$): coefficients indicate the rate of elimination of the drug and the time it takes for the drug concentration to be half of its highest concentration. The elimination rate of CUR@siRNP was improved, showing that the CUR in nanoparticles eliminated slower than the CUR sample. At the same time, the $t_{1/2}$ of CUR@siRNP was increased up to 1.5 h. It suggested that the siRNP could improve the elimination time of CUR in mice, enhancing the effects of CUR in treatment.

Clearance: this feature indicates the elimination of the drug from the body. The clearance level was 18.77 ± 0.98

(mL/h) for the CUR-treated mice, which suggested that the drug digests out very quickly. CUR@siRNP clearance level was 8.98 ± 0.34 (mL/h), which was smaller and decreased 1.7-fold compared to CUR. It demonstrated that the drug was excreted slowly, staying in the body in a long period, and may exert the drug effect for a longer time. These data indicated that CUR@siRNP not only could improve the level of CUR in the bloodstream after oral administration but also prolonged the retention of CUR, which is anticipated the higher therapeutic treatment *in vivo* model.

3.5. Therapeutic Effect of CUR@siRNP in Colitis Mouse Model Induced by DSS. It was confirmed that the antioxidant and anti-inflammatory activities and pharmacokinetics profile of CUR@siRNP were remarkably improved compared to free CUR. Next, we evaluated the therapeutic anti-inflammatory effect *in vivo* using the DSS-induced colitis mouse model. DSS-induced colitis is a well-known model of inflammation in the colon, characterized by high disease activity index (DAI) and shortening colon length after 7 d treatment of DSS [24]. The shortening of colon length is an indicator of inflammation in DDS-induced colitis mice. As the result, the colon length of DSS-treated mice was significantly shortened (5.3 ± 0.3 cm), while the healthy control group was 10.9 ± 0.8 cm, indicating that the DSS-treated mice formed severe colitis (Figures 9(a) and 9(b)). Both mice treated with CUR and CUR@siRNP showed a significant improvement in colon length as compared to DSS-induced colitis mice ($^{*}p < 0.05$ and $^{**}p < 0.01$, respectively). Although the colon length of the CUR@siRNP-treated group (7.7 ± 1.2 cm) was longer than the CUR-treated group (6.6 ± 0.5 cm), a significant difference was not observed ($p = 0.08$). This result suggested that the CUR@siRNP was effectively suppressed the inflammation and preserved the colon length. In addition, the disease activity index (DAI), which is the sum of body weight loss, stool consistency, and bleeding, was evaluated. The DAI of the CUR@siRNP-treated group was the lowest compare to other treated groups, showing that siRNP improved its therapeutic effect of CUR (Figure 9(c)). More specifically, the CUR@siRNP-treated group reduced the bleeding in the colon and diarrhea levels of colitis mice. Therefore, it demonstrated that oral administration of CUR@siRNP could suppress the inflammatory damage in colitis mice.

Finally, the histology was examined to evaluate the therapeutic effect of CUR@siRNP in DSS-induced colitis mice. When the histology of colitis tissue was examined, moderate crypt distortion and cellular infiltration were shown in mice treated with DSS (Figure 10(a)). While treatment with CUR did not show any effect at all, the CUR@siRNP-treated mice showed less crypt architecture damage and cellular infiltration. Therefore, the histological score of the CUR@siRNP-treated group showed a significant difference compared to other groups (Figure 10(b)), indicating the improvement of therapeutic effect of CUR@siRNP on treating the inflammation in colitis mice. These results suggested that siRNP could enhance the anti-inflammatory efficacy of CUR not only by improving the bioavailability and distribution of CUR but also by its ROS scavenging activity.

4. Conclusions

In this study, siRNP was utilized to deliver CUR for a better inflammatory therapeutic effect. Possessing ROS scavenging feature, siRNP significantly improved not only the solubility and but also the antioxidant and anti-inflammatory activities of CUR. Additionally, oral administration of CUR@siRNP increased the concentration of CUR in blood and suppressed the CUR clearance significantly, resulting in a better pharmacokinetic profile of CUR *in vivo*. Consequently, CUR@siRNP effectively improved disease activity index and colonic injury in the DSS-induced colitis model mice, indicating that siRNP demonstrates a great potential in bioavailability improvement of various hydrophobic drugs. Further investigation and development are needed to show a firm demonstration of CUR@siRNP potential in treating chronic inflammation.

Data Availability

The data used to support the findings of this study are available from the corresponding author upon request.

Conflicts of Interest

The authors have no competing financial interests to declare.

Acknowledgments

This work was supported by the Vietnam National University Ho Chi Minh City (VNU-HCM) under grant number C2019-18-24. The authors also would like to thank Prof. Yukio Nagasaki and Ms. Hao Thi Tran for kindly giving the polymer.

References

[1] L. Ferrucci and E. Fabbri, "Inflammageing: chronic inflammation in ageing, cardiovascular disease, and frailty," *Nature Reviews. Cardiology*, vol. 15, no. 9, pp. 505–522, 2018.

[2] D. Furman, J. Campisi, E. Verdin et al., "Chronic inflammation in the etiology of disease across the life span," *Nature Medicine*, vol. 25, no. 12, pp. 1822–1832, 2019.

[3] S. J. Forrester, D. S. Kikuchi, M. S. Hernandes, Q. Xu, and K. K. Griendling, "Reactive oxygen species in metabolic and inflammatory signaling," *Circulation Research*, vol. 122, no. 6, pp. 877–902, 2018.

[4] M. Mittal, M. R. Siddiqui, K. Tran, S. P. Reddy, and A. B. Malik, "Reactive oxygen species in inflammation and tissue injury," *Antioxidants & Redox Signaling*, vol. 20, no. 7, pp. 1126–1167, 2014.

[5] J. Trujillo, Y. I. Chirino, E. Molina-Jijón, A. C. Andérica-Romero, E. Tapia, and J. Pedraza-Chaverrí, "Renoprotective effect of the antioxidant curcumin: recent findings," *Redox Biology*, vol. 1, no. 1, pp. 448–456, 2013.

[6] Y. He, Y. Yue, X. Zheng, K. Zhang, S. Chen, and Z. Du, "Curcumin, inflammation, and chronic diseases: how are they linked?," *Molecules*, vol. 20, no. 5, pp. 9183–9213, 2015.

[7] S. Thangavel, T. Yoshitomi, M. K. Sakharkar, and Y. Nagasaki, "Redox nanoparticles inhibit curcumin oxidative degradation and enhance its therapeutic effect on prostate cancer," *Journal of Controlled Release*, vol. 209, pp. 110–119, 2015.

[8] C. Moorthi and K. Kathiresan, "Curcumin–piperine/curcumin–quercetin/curcumin–silibinin dual drug-loaded nanoparticulate combination therapy: a novel approach to target and treat multidrug-resistant cancers," *Journal of Medical Hypotheses and Ideas*, vol. 7, no. 1, pp. 15–20, 2013.

[9] S. Gelperina, K. Kisich, M. D. Iseman, and L. Heifets, "The potential advantages of nanoparticle drug delivery systems in chemotherapy of tuberculosis," *American Journal of Respiratory and Critical Care Medicine*, vol. 172, no. 12, pp. 1487–1490, 2005.

[10] E. M. Pridgen, F. Alexis, and O. C. Farokhzad, "Polymeric nanoparticle drug delivery technologies for oral delivery applications," *Expert Opinion on Drug Delivery*, vol. 12, no. 9, pp. 1459–1473, 2015.

[11] M. Kanai, A. Imaizumi, Y. Otsuka et al., "Dose-escalation and pharmacokinetic study of nanoparticle curcumin, a potential anticancer agent with improved bioavailability, in healthy human volunteers," *Cancer Chemotherapy and Pharmacology*, vol. 69, no. 1, pp. 65–70, 2012.

[12] K. Tai, M. Rappolt, L. Mao, Y. Gao, X. Li, and F. Yuan, "The stabilization and release performances of curcumin-loaded liposomes coated by high and low molecular weight chitosan," *Food Hydrocolloids*, vol. 99, p. 105355, 2020.

[13] C. Mohanty, M. Das, and S. K. Sahoo, "Emerging role of nanocarriers to increase the solubility and bioavailability of curcumin," *Expert Opinion on Drug Delivery*, vol. 9, no. 11, pp. 1347–1364, 2012.

[14] L. B. Vong, S. Kimura, and Y. Nagasaki, "Newly designed silica-containing redox nanoparticles for oral delivery of novel TOP2 catalytic inhibitor for treating colon cancer," *Advanced Healthcare Materials*, vol. 6, no. 20, article 1700428, 2017.

[15] T.-H. T. Nguyen, N.-T. Trinh, H. N. Tran et al., "Improving silymarin oral bioavailability using silica-installed redox nanoparticle to suppress inflammatory bowel disease," *Journal of Controlled Release*, 2020.

[16] J. N. Sharma, A. Al-Omran, and S. S. Parvathy, "Role of nitric oxide in inflammatory diseases," *Inflammopharmacology*, vol. 15, no. 6, pp. 252–259, 2007.

[17] M. B. Grisham, G. G. Johnson, and J. R. Lancaster Jr., "Quantitation of nitrate and nitrite in extracellular fluids," *Methods in Enzymology*, vol. 268, pp. 237–246, 1996.

[18] L. B. Vong, T. Tomita, T. Yoshitomi, H. Matsui, and Y. Nagasaki, "An orally administered redox nanoparticle that accumulates in the colonic mucosa and reduces colitis in mice," *Gastroenterology*, vol. 143, no. 4, pp. 1027–1036.e3, 2012.

[19] L. B. Vong, T. Yoshitomi, K. Morikawa, S. Saito, H. Matsui, and Y. Nagasaki, "Oral nanotherapeutics: effect of redox nanoparticle on microflora in mice with dextran sodium sulfate-induced colitis," *Journal of Gastroenterology*, vol. 49, no. 5, pp. 806–813, 2014.

[20] J. J. Kim, M. S. Shajib, M. M. Manocha, and W. I. Khan, "Investigating intestinal inflammation in DSS-induced model of IBD," *JoVE (Journal of Visualized Experiments)*, no. 60, article e3678, 2012.

[21] H. Laroui, S. A. Ingersoll, H. C. Liu et al., "Dextran sodium sulfate (DSS) induces colitis in mice by forming nano-lipocomplexes with medium-chain-length fatty acids in the colon," *PLoS One*, vol. 7, no. 3, article e32084, 2012.

[22] K. Suresh and A. Nangia, "Curcumin: pharmaceutical solids as a platform to improve solubility and bioavailability," *Cryst Eng Comm*, vol. 20, no. 24, pp. 3277–3296, 2018.

[23] R. Singh and J. W. Lillard Jr., "Nanoparticle-based targeted drug delivery," *Experimental and Molecular Pathology*, vol. 86, no. 3, pp. 215–223, 2009.

[24] M. Lewandowski and K. Gwozdzinski, "Nitroxides as antioxidants and anticancer drugs," *International Journal of Molecular Sciences*, vol. 18, no. 11, p. 2490, 2017.

[25] A. M. Samuni, W. DeGraff, M. C. Krishna, and J. B. Mitchell, "Nitroxides as antioxidants: tempol protects against EO9 cytotoxicity," *Molecular and Cellular Biochemistry*, vol. 234/235, no. 1, pp. 327–333, 2002.

[26] R. P. Singh and P. Ramarao, "Accumulated polymer degradation products as effector molecules in cytotoxicity of polymeric nanoparticles," *Toxicological Sciences*, vol. 136, no. 1, pp. 131–143, 2013.

[27] L. B. Vong, M. Kobayashi, and Y. Nagasaki, "Evaluation of the toxicity and antioxidant activity of redox nanoparticles in zebrafish (*Danio rerio*) embryos," *Molecular Pharmaceutics*, vol. 13, no. 9, pp. 3091–3097, 2016.

Hindawi
Journal of Nanomaterials
Volume 2021, Article ID 8871067, 9 pages
https://doi.org/10.1155/2021/8871067

Research Article

Synthesis, Characterization, and Photocatalytic Activity of g-C_3N_4/GaN-ZnO Composite

Nguyen Ha Trang,[1] Tran Thi Viet Ha,[1] Nguyen Minh Viet,[2] and Nguyen Minh Phuong[3]

[1]*Master's Program in Environmental Engineering, VNU Vietnam Japan University, Hanoi, Vietnam*
[2]*Key Laboratory of Advanced Material for Green Growth, Faculty of Chemistry, VNU University of Science, Hanoi, Vietnam*
[3]*Faculty of Chemistry, VNU Hanoi University of Science, Hanoi, Vietnam*

Correspondence should be addressed to Tran Thi Viet Ha; ttv.ha@vju.ac.vn

Received 17 September 2020; Revised 8 December 2020; Accepted 18 December 2020; Published 11 January 2021

Academic Editor: Nguyen Duc Cuong

Recently, photocatalysis process has shown great potential as a low-cost, environmentally friendly, and sustainable method for the water/wastewater treatment. Among that, g-C_3N_4 is one of the most promising photocatalyst and widely used for a variety of applications. In spite of some unique features such as strong reduction ability, active under visible light, nontoxic, and high stability, g-C_3N_4 photocatalytic capability under visible light is limited due to fast recombination rate of reactive charges. To deal with this issue, in this study, g-C_3N_4 is combined with GaN-ZnO for reducing the recombination rate of charge carriers and increasing the active sites. The g-C_3N_4/GaN-ZnO composite was characterized by several methods such as SEM, EDX, XRD, FT-IR, UV-Vis, and BET. It is also observed that the composite with outstanding features can work effectively under visible light; thus, it is likely to be widely applied in environment treatment, especially in antibiotic residue with more than 90% of tetracycline was decomposed after 3 hours.

1. Introduction

The development of the industry now depends strongly on fossil fuels which will be exhausted in the future. Therefore, renewable energy sources are considered as an excellent alternative fuel source with advantages such as being available and being clean energy, without affecting the environment when exploited. Among them, solar energy is a popular renewable energy source today. The use of sunlight-based environmental treatment techniques has become one of the most potential and environmentally friendly techniques. Another concern is the water pollution caused by textile dyes, organic contaminants, and especially antibiotic residues. Antibiotics are defined as compounds or substances that destroy or inhibit the growth of bacteria. They are compounds used in animal husbandry and to prevent or to treat infections for human health; sometimes, they are used as food preservatives. During wastewater treatment, the partial or incomplete metabolism and also the ineffective removal of antibiotics have created the way for antibiotics to enter the environment including water, sediment, and soil through discharging wastewater. These pollutants have a big impact on the life of species and environmental pollution. Therefore, the removal of these pollutants is necessary. In recent years, a sustainable treatment technology by using semiconductor photocatalytic has been introduced because of various potential such as a low-cost, environmental friendly, and suitable for water/wastewater industry. The advantage of this technology is to oxidize and remove the organic compounds and microorganisms in water. Varieties of techniques have been applied to degradation those organic contaminants including many kind of photocatalyst (g-C_3N_4, TiO_2, ZnO,...) which is known as one of the most promising technology [1–5].

In chemistry, photocatalysis is the acceleration of a photoreaction in the presence of a catalyst. Therefore, to achieve an ideal photocatalyst, semiconductor photocatalysts need to have a suitable band gap to utilize sufficient solar energy. The graphite carbon nitride (g-C_3N_4) is known as a metal-free polymer and a conjugative π structure material. This material

has many ideal properties, such as unique electric, optical, structural, and physicochemical properties; these properties already make g-C_3N_4-based materials become the ideal substance for catalytic and energy applications [6, 7]. This is a promising nonmetallic photocatalyst in the decomposition of pollutant organic matter in visible light and the analysis of water into hydrogen and oxygen. However, the using of these photocatalyts are still faced with some drawbacks, for example, the absorption of visible light is ineffective and the quick recombination of electron-hole [8]. To improve the photocatalytic performance of g-C_3N_4, various studies were conducted, including nonmetallic g-C_3N_4 doping. The doping of g-C_3N_4 by various elements such as B, C, P, and S [2, 9] has been successfully conducted; resulting in photocatalytic activity of the materials is greatly improved. The doping of g-C_3N_4 by nonmetallic elements has become a concerned topic of research, opening up a new field of research, preparing materials that have good photocatalytic effect under visible light which meet the practical requirements. In addition to enhance the photocatalytic activity by doping a nonmetal in the lattice, the addition of a metal or metal oxide on the surface of g-C_3N_4 has also been of interest recently. Among the metals, Ag is most concerned by the acceptable price and the ability to increase the activity of Ag nanoparticles. In this case, Ag acts both as a photosensitive agent to increase the ability to absorb visible light and to exhibit a surface plasmon effect [10]. The first SnO_2/g-C_3N_4 material was synthesized. The material consists of two components: g-C_3N_4 with a low specific surface area and SnO_2 nanoparticles with a large surface area. In this composite, SnO_2 nanoparticles dispersed well into g-C_3N_4. The interaction between the two components is very strong; this is confirmed by the band gap energy and network parameters. The synergistic interaction between the two components in the SnO_2/g-C_3N_4 material is due to the contribution of the π-π conjugate effect in g-C_3N_4, resulting in a significant improvement in the process of electron separation, creating from the interaction between the contact surfaces and the two components. On the other hand, nanometer-sized SnO_2 particles will increase the surface area of the material, thereby increasing photon efficiency. As a consequence, this material is an active photocatalytic, greatly increasing the decomposition of methyl orange (MO) under visible light irradiation. Optimum optical efficiency of up to >90% indicates that photocatalytic capacity is much higher than separate g-C_3N_4 and SnO_2 components [11]. Therefore, the modification of g-C_3N_4 to create new material with high photocatalytic efficiency is necessary.

Besides, GaN–ZnO solid solution is a homogeneous phase with a lattice structure, consisting of two GaN and ZnO members dissolved in solid-state. Normally, GaN is a solvent (with a higher content), while ZnO is a solute (with a lower content). In the following years, many of these scientists' works were also published in world-renowned journals on the separation of GaN-ZnO solid solutions. Since 2005, Domen [12] and colleagues have published a large number of works on GaN–ZnO solid solutions in world-famous magazines. Initially, the authors successfully synthesized the nano-sized RuO2-doped GaN–ZnO solid solution and used it as a photocatalyst material to effectively separate water in visible light. This is one of the first publications on analyzing water under visible light on an oxynitride photocatalyst as a GaN–ZnO solid solution doped with nano-sized RuO_2. In contrast to conventional nonoxide photocatalysts, such as CdS, the GaN–ZnO solid solution is a fairly stable material in the photocatalytic reaction [12]. In another study [3], the author showed nano-dispersed Rh-/-Cr_2O_3 particles (core/-shell) on GaN-ZnO as a catalyst for separation of pure water. Rh-Cr_2O_3-/-GaN-ZnO material has good photocatalytic ability in visible light area. Cr_2O_3 shell prevents the formation of H_2 and O_2 from water on Rh nanoparticles, allowing to destroy the chemical balance of the water separation reaction, whereby the photocatalytic reaction efficiency increases significantly. The core/shell structure enhances H_2 release compared to bare Rh nanoparticles. From these studies, it can be seen that the GaN–ZnO solid solution has a special and very attractive property in the field of photocatalyst. However, concentrated works are applied in the field of water separation to produce hydrogen. Although there are many advantages in photocatalysis, the solid solution of GaN–ZnO is still rarely applied in the treatment of toxic organic substances in water. Therefore, the task of the research is to study the modification of this material to treat organic matter polluting the water environment. This is not only of scientific significance but also of high practical value.

Recently, the combination of two types of materials is GaN–ZnO and graphite carbon nitrite g-C_3N_4 have been tested as photocatalysts [13]. Compared to other photocatalysts, GaN–ZnO and g-C_3N_4 have many advantages such as low band gap energy, activating in visible light, high surface area, and durable and can be synthesized in large quantities. In this paper, the g-C_3N_4/GaN-ZnO composite photocatalyst was synthesized by a simple method and has shown a significantly improved photocatalytic activity for tetracycline (TC) degradation.

2. Materials and Methods

2.1. Sample Preparation. All chemicals used in this work were analytical grade without further purification from Merck, Germany. Deionized (DI) water was used for the preparation of all required solutions.

The urea was calcinated to obtain g-C_3N_4. 5 g of urea was put in a crucible, sealed with aluminum foil (to prevent the sublimation of precursors as well as enhance the condensation to form g-C_3N_4), then place the crucible into the furnace. The samples were heated at temperatures of 550°C in 3 hours. Finally, the furnace was naturally cooled to room temperature. The obtained polymer g-C_3N_4 is a light yellow powder with different color intensity depending on the heat regime. The samples of synthetic g-C_3N_4 materials are denoted g-C_3N_4-T, where T is the heating temperature (550°C).

The GaN-ZnO powder sample was synthesized by adding 2 g of Ga_2O_3 and ZnO with molar ratio of 1 : 1 and 2 g of urea into an agate mortar and grind finely. The mixture was put into a porcelain boat, placed a ceramic boat in the middle of the quartz tube, and then put into a horizontal furnace. The mixture was calcinated in a stream of argon gas at

temperature of 900°C for 4 hours. The products are denoted GaN-ZnO-T, where T is the heating temperature (900°C).

The composite of g-C_3N_4/GaN-ZnO was synthesized by adding 0.15 g of GaN-ZnO synthesized sample above and 1.05 g of urea into an agate mortar and grind finely. Then, the mixture was put into a crucible, covered with layers of aluminum foil, and put into a furnace. The sample was calcinated at 550°C for 3 hours.

2.2. Characterization. X-ray diffractometer (XRD, Rigaku Miniflex II, Japan) is used to study the crystal structure, evaluate the crystallization level, and detect the strange crystal phase of the material. Fourier-transform infrared spectroscopy (FTIR) (Jasco 6100, Japan) is used for characterizing chemical bonds of materials. Energy dispersive X-ray (EDX) is to analyze the chemical elements of materials from Jeol EDS System. The image of sample surface is recorded by Scanning Electron Microscope (SEM) (Jeol JSM 7500FA, Japan), the signals used by a scanning electron microscope to produce an image result from interactions of the electron beam with atoms at various depths within the sample. Brunauer–Emmett–Teller (BET) (Jeol, Japan) is used to determine the surface area and the pore volume, and Diffuse Reflectance UV-vis Spectrum (UV-Vis-DRS) is to determine the band gap energy of materials.

2.3. Photocatalytic Activity Evaluation. Photocatalytic activities of g-C_3N_4/GaN-ZnO samples were evaluated by TC degradation in aqueous solution under visible light of 60 W lamp irradiation. TC stock solution (1000 mg/L) was prepared weekly using distilled deionized water and stored in dark at 4°C. The pH is adjusted by 1 mol/L of H_2SO_4 or NaOH, and C_0 and Ct are the concentrations of TC before and after photocatalytic reaction. The degradation of TC is considered through the decrease in its concentration versus irradiation time. The sample solutions were taken after 30 minutes. The TC solution obtained at times is diluted to the appropriate concentration, then measured based on the calibration curve to deduce the concentration of TC. They were analyzed using UV-Visible spectrophotometer with detection at 357 nm to take absorbance and from that take their concentration based on a calibration curve.

The removal efficiency of TC concentrations was calculated according to the differences between the initial and final concentrations. All the experiments were carried out at least three times, and the average values were calculated. The error between two experiments will not be greater than 10%.

3. Results and Discussions

3.1. Catalyst Characterization. The XRD patterns of g-C_3N_4, GaN-ZnO, and their synthesized composites are shown in Figure 1. The characteristic peaks appeared at 13.2° and 27.3° correspond to interlayer stacking of aromatic segments and tri-striazine units of pure g-C_3N_4 sample assigned to (100) and (002) planes [13, 14]. For GaN–ZnO material, the figure of XRD pattern shows that the peaks appear at $2\theta = 32.39$, 34.67, 36.42, 48.14, 57.74, 63.47, and 68.99 are typical diffraction patterns of GaN–ZnO solid solution,

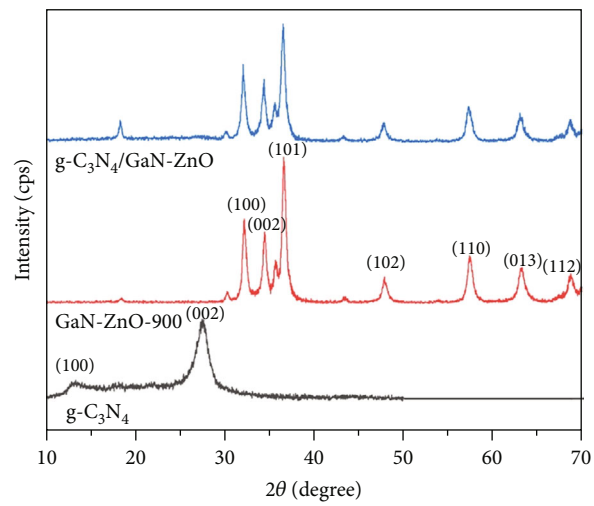

Figure 1: XRD patterns for gC_3N_4, GaN-ZnO, and gC_3N_4/GaN-ZnO composite.

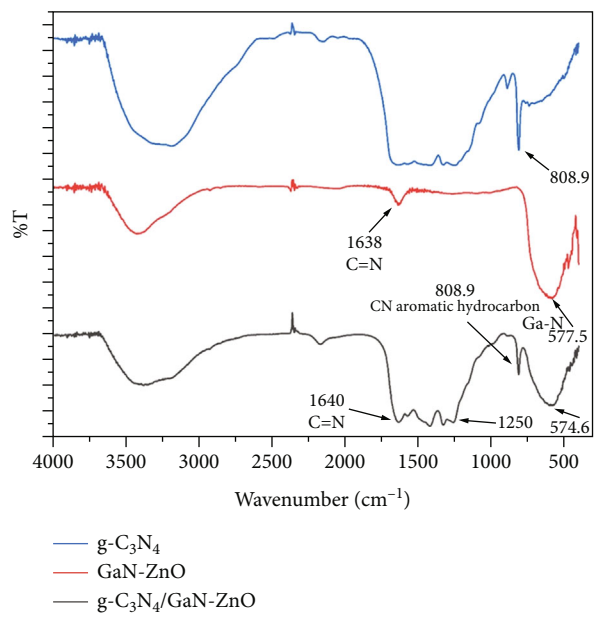

Figure 2: FT-IR spectrum for gC_3N_4, GaN-ZnO, and g-C_3N_4/GaN-ZnO composite.

corresponding to (100), (002), (101), (102), (110), (013), and (112) planes [13, 15]. Between peak of (002) and (101), there also appeared one extra strange peak thought to be of $ZnGa_2O_4$ spinene.

The g-C_3N_4/GaN-ZnO powder composites have diffraction peaks at 18.2, 32.3, 34.67, 36.42, 48.14, 57.74, 63.47, and 68.99°, which prove that the composites were successfully prepared.

IR spectra of the composites are showed in Figure 2. The IR spectrum appears almost all peaks of g-C_3N_4 and GaN-ZnO. At 808 cm^{-1} and some peaks in the range of 1250-1650 cm^{-1} are typical peaks for valence fluctuations of C-N bonds inside and outside the aromatic ring and the oscillation of the C=N bond. The broad absorption bands at

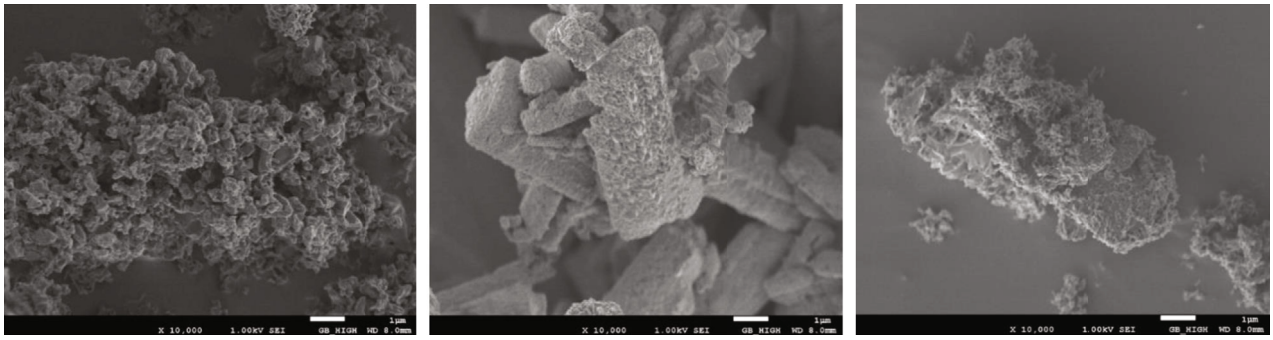

Figure 3: SEM image of g-C_3N_4, GaN-ZnO, and composite g-C_3N_4/GaN-ZnO.

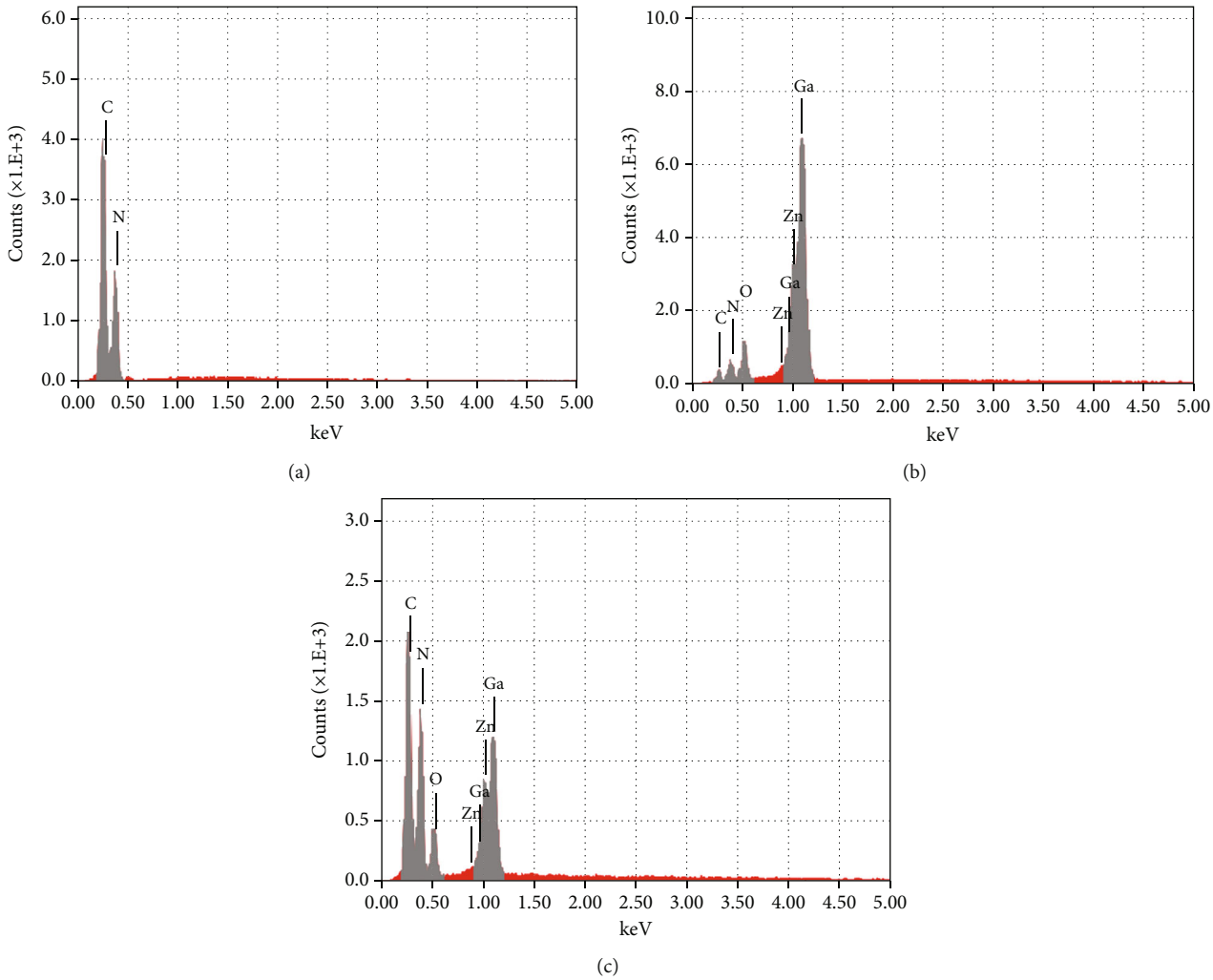

Figure 4: EDX spectra of g-C_3N_4 (a), GaN-ZnO (b), and g-C_3N_4/GaN-ZnO composite (c) materials.

3332.39–3186.8 cm^{-1} are oscillations of secondary and primary amines. These results are similar to previous reports [1, 11, 16]. When comparing the spectra of the composite and GaN-ZnO material, a wide absorption band at the number of waves above 3426 cm^{-1} and about 1638 cm^{-1} is the oscillation of -OH of physical absorbing water [15, 17]. The peak at the number of waves 494.6 cm^{-1} is the valence oscillation of the Zn–O bond [18]. In particular, the peak at 577 cm^{-1} of the solid solution featured for the bond of Ga-N was also discovered [17]. This proves that there are g-C_3N_4 and GaN-ZnO in the composite model.

Figure 3 shows the SEM images of GaN-ZnO and g-C_3N_4/GaN-ZnO material samples. The pure g-C_3N_4 catalyst sample is mainly in the form of low-porosity blocks. The GaN-ZnO samples had a clear shape of particles, while the g-C_3N_4/GaN-ZnO composite materials were blurred and no clear delineation between particles; the particles are covered by a thin film, which is thought to be of g-C_3N_4. The size of

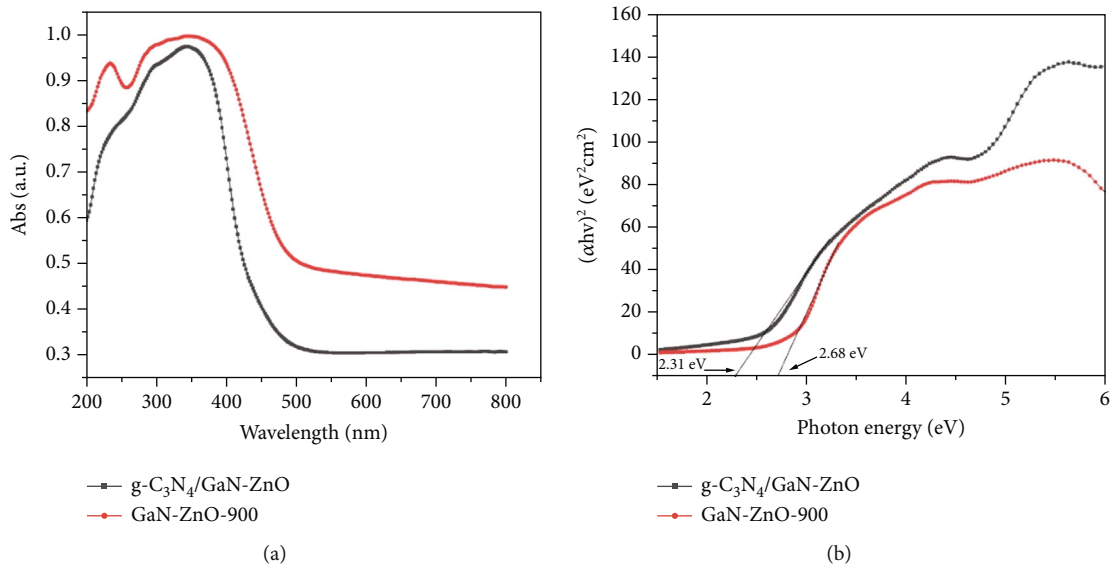

Figure 5: (a) UV-Vis-DRS spectra of GaN-ZnO and g-C_3N_4/GaN-ZnO (b). The energy band gap of GaN-ZnO and g-C_3N_4/GaN-ZnO.

the spherical particles is approximately 200 nm which is beneficial to enhance the photocatalytic efficiency of the synthesized material.

Elemental composition of g-C_3N_4/GaN-ZnO material samples characterized by EDX method is shown in Figure 4. This obtained result shows that the Ga, N, Zn, and O are detected with the percentage of mass of 30.65%, 6.00%, 7.99%, and 4.00%, respectively, while the element N content is still very low in the GaN-ZnO material sample. However, elemental element N significantly increased in the composite g-C_3N_4/GaN-ZnO material (21.64%). Figure 4(c) also indicates the appearance of C in the composite sample with the proportion of mass is 11.04%. This proves that there is an addition of element N into composite materials; the presence of element C in this spectrum further confirms the formation of composite materials from two components, g-C_3N_4 and GaN-ZnO. In particular, in this composite material sample, there is no presence of elements other than the constituent elements from the precursor materials. This further illustrates that the sample is not containing impurity, and the formation of composites is very good.

In addition, the optical properties of the material are determined by UV–Vis–DRS spectra; the results are shown in Figure 5. It can be noticed that the absorption peak and the light absorption edge of all materials are located in the visible light region (Vis region). From the results of UV-Vis-DRS spectroscopy, the band gap energy of GaN-ZnO and g-C_3N_4/GaN-ZnO composite was also determined in Figure 5(b). The band gap energy of GaN-ZnO and g-C_3N_4/GaN-ZnO composite was determined to be 2.68 eV and 2.31 eV. The band gap energy of g-C_3N_4 is 2.70 eV as reported in previous articles. Thus, the band gap energy of g-C_3N_4/GaN-ZnO composite is significantly lower than that of g-C_3N_4 and GaN-ZnO materials.

The BET surface areas and porous structures of g-C_3N_4, GaN-ZnO, and composite g-C_3N_4/GaN-ZnO are showed in Figure 6. In this figure, a type IV adsorption isotherm of the composite sample was showed with a hysteresis loop in the range ($P/P0$) of 0.6–1.0. The surface area and pore volume (Table 1) of g-C_3N_4 were 35.96 m^2/g and 0.114 cm^2/g,

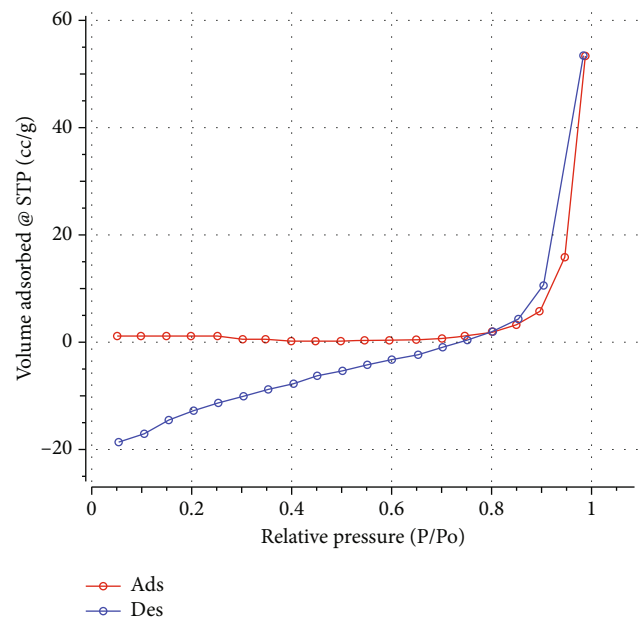

Figure 6: Nitrogen adsorption–desorption isotherm of composite g-C_3N_4/GaN-ZnO.

Table 1: Specific surface area, pore volume, and average pore radius.

Sample	Specific surface area (m^2/g)	Pore volume (cm^2/g)	Pore radius (nm)
g-C_3N_4	35.96	0.114	13.21
GaN-ZnO	2.787	0.014	5.840
g-C_3N_4/GaN-ZnO	9.515	0.075	13.21

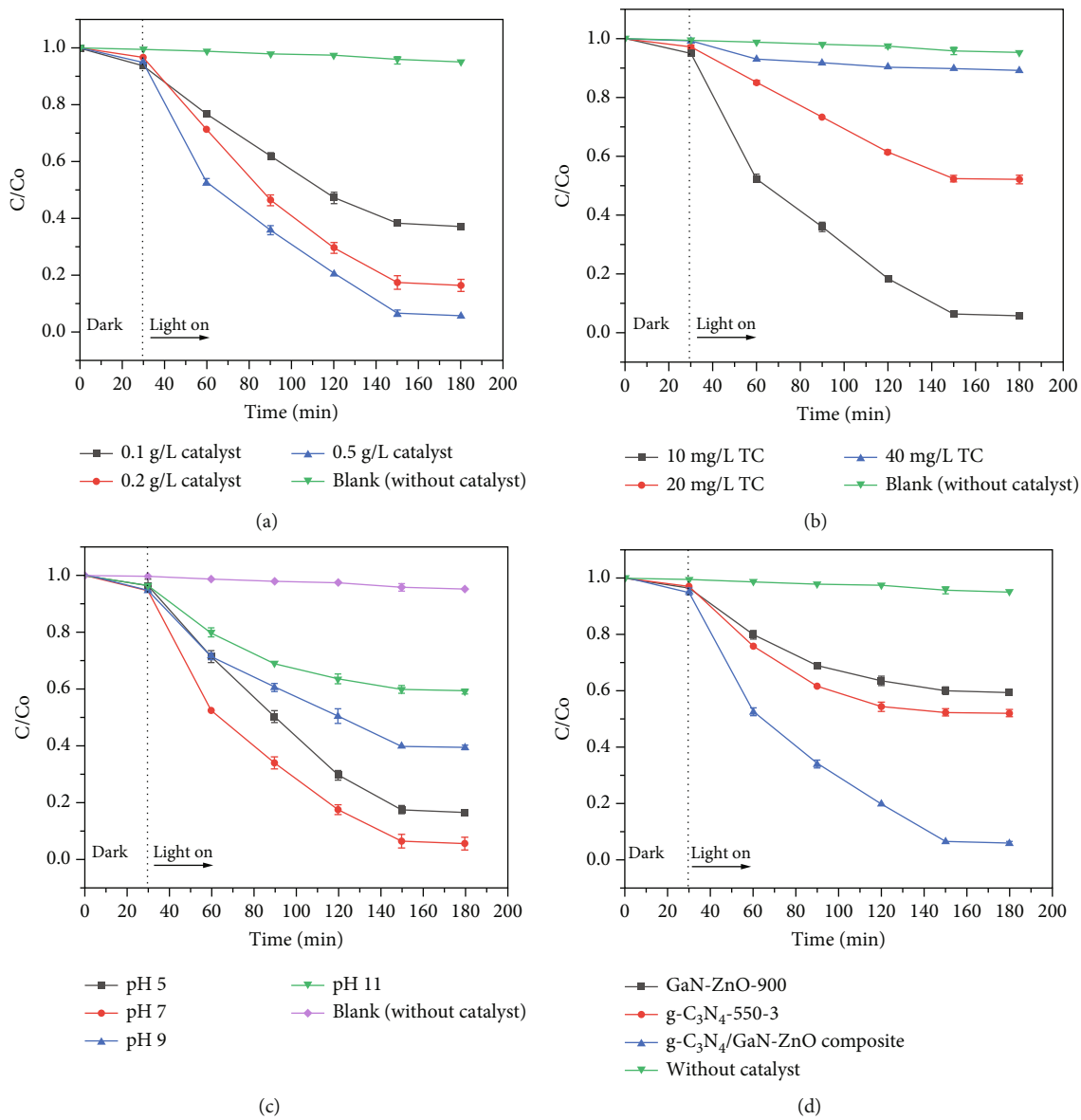

Figure 7: Degradation of TC under (a) various catalyst dosage, (b) various concentrations of TC, (c) initial pH, and (d) different materials.

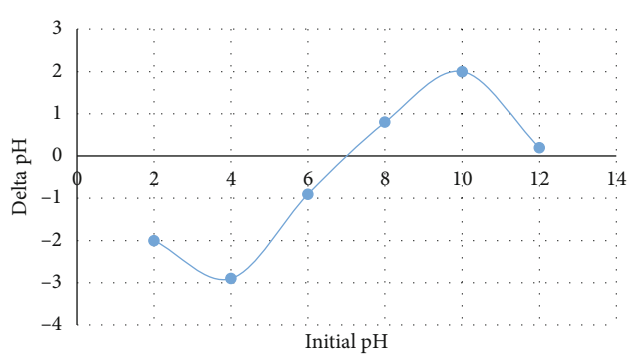

Figure 8: The plot of initial pH value versus delta pH value.

greater than GaN-ZnO and composite g-C_3N_4/GaN-ZnO (2.787 m^2/g, 0.014 cm^2/g and 9.515 m^2/g, and 0.075 cm^2/g, respectively). In the comparison of g-C_3N_4, the specific surface area of composite g-C_3N_4/GaN-ZnO was decreased, which is believed due to the presence of GaN-ZnO layers on the g-C_3N_4 surface. However, the surface area of composite g-C_3N_4/GaN-ZnO is not a main factor. Therefore, the improved photocatalytic performance is not influenced by the specific surface area. The increasing of photocatalytic activity of the composite materials is attributed to the more efficient separation of the photo-generated electron–hole pairs.

3.2. Photocatalytic Activity. In order to evaluate the effect of catalyst dosage, initial concentration, and initial pH on the removal efficiency, TC degradation experiments were conducted in various catalyst g-C_3N_4/GaN-ZnO weight (0.01, 0.02, and 0.05 g) and concentrations of TC (10, 20, and 40 mg/L) in the range of pH 5–11. Figure 7 shows the effect of catalyst dosage, initial concentration, and pH on the

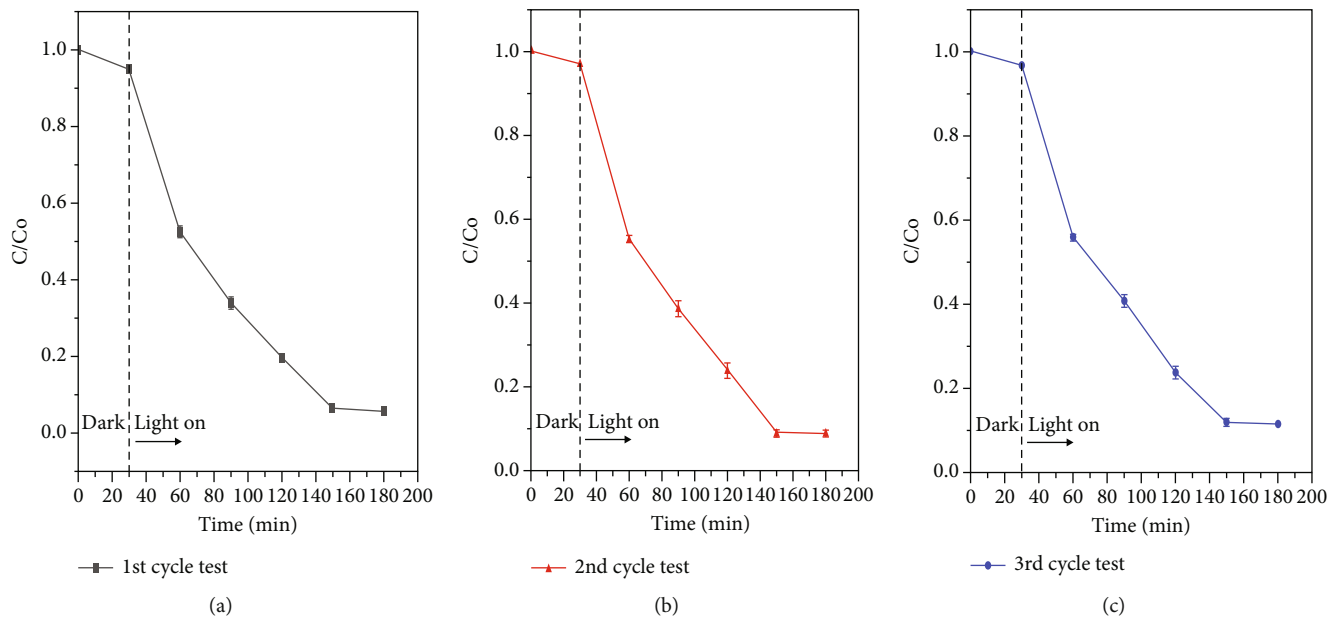

Figure 9: Cycling test for the degradation of TC by g-C_3N_4/GaN-ZnO composite.

removal efficiency of TC. After 30 min in the dark condition, only 5% of TC was absorbed on the surface of synthesized catalyst.

The results showed that the removal efficiency increased with the increasing of catalyst weight (Figure 7(a)). After 180 min of reaction time, 94.3% of TC was degraded by using appearance by using 0.05 g of catalyst. This result reflects the high removal efficiency at higher amount of catalyst. When the number of material particles increase, there are an increasing the number of photon and dye molecules absorbed. Therefore, the surface area of nanoparticles provides more active site to produce radicals for the reaction.

In Figure 7(b), the irradiation of TC solution with the initial concentrations of 10, 20, and 40 mg/L for 180 min leads to degradation of 94.5, 48.3, and 12.1% of TC. The degradation efficiency of TC decreased with the increasing initial concentration of the interest solution. These results can come from the reason that at higher concentrations, the concentration of intermediate products increases, and the hydroxyl radicals become the limiting reactant which leads to the decrease in degradation rate constant. Besides, when increasing the TC concentration, the TC molecules also increase which can cause the excessive adsorbed molecules into the surface of the material and the lack of contact between TC molecules and the photo-generated holes or hydroxyl radicals [19]. Therefore, the TC removal efficiency is decreased in case of increasing the initial concentration of pollutants.

One of the most important parameters in photocatalytic is the effect of pH. The change of the pH in a solution affects the charge properties of the material surface as well as regulates the ionization state of the catalyst surface. Therefore, pH influences the decomposition and adsorption capacity of organic compounds. The results in Figure 7(c) showed that the removal efficiency was most effective at pH of 7. At the TC concentration of 10 mg/L, irradiation of TC solution with the initial pH of 5, 7, 9, and 11 for 180 min leads to degradation of 67.2, 94.3, 60.4, and 40.7% of TC. These results are also explained by point zero charge of material (Pzc). The Pzc of the composite is determined at 6.9. To determine point of zero charge of g-C_3N_4/GaN-ZnO sample, the plot of delta pH value versus initial pH value was performed. The curve of this plot cut the horizontal axis at any pH which is the point zero charge of material. The obtained results were shown in Figure 8. If pH < Pzc, the positive charge of the g-C_3N_4 surface increases, and if pH > Pzc, the negative charge of the material surface increases. At acidic or alkaline, both the material surface and TC molecule are positive charge or negative charge. Therefore, the adsorption of TC on the surface of the material decreased, and the degradation will be more effective at neutral pH.

Figure 7(d) shows the TC degradation efficiency of g-C_3N_4, GaN-ZnO, and g-C_3N_4/GaN-ZnO materials. The synthesized g-C_3N_4/GaN-ZnO composite material showed highest degradation TC efficiency (95%) at pH = 7 (TC concentration = 10 mg/L) while the g-C_3N_4 and GaN-ZnO showed lower treatment rate with the removal efficiency of 38.1% and 20.5%, respectively. This result indicated that the synthesized g-C_3N_4/GaN-ZnO composite material can be utilized for tetracycline in the environment.

To assess the repeatability of the photocatalytic activity of composite sample, the cycling test was performed by doing several cycle experiments of TC degradation using g-C_3N_4/GaN-ZnO composite. The cycle time is 180 min. After collecting the composite samples from the previous step, the photocatalyst was filtered and dried at 105°C for 24 hours to use for the next cycle. As shown in Figure 9, nearly 90% of TC is still degraded by g-C_3N_4/GaN-ZnO composite after running 3 cycles, indicating quite good stability for photocatalytic degradation for TC.

The good repeatability of photocatalytic activity of g-C_3N_4/GaN-ZnO composite makes this material reusable many times when applied in practice.

The TC decomposition mechanism by synthesized g-C_3N_4/GaN-ZnO composite material is proposed in Figure 10. In this figure, after receiving visible light, the electron–hole separation occurs simultaneously on g-C_3N_4 and GaN–ZnO material; the electron moves to the conduction band (CB) and leaving the holes h + on the valence band (VB). In the conduction band, electrons from g-C_3N_4 will move to the GaN–ZnO of the composite, while in the valence band, the hole from GaN–ZnO will move to g-C_3N_4. This process significantly reduces electron-hole recombination occurring in composites. The reduction will occur in the conduction band of GaN-ZnO, and the oxidation will occur in the valence band of g-C_3N_4.

The following equations were used to determine conduction and valence band potentials of the synthesized samples.

$$E_{VB} = \chi - E_e + 0.5E_g,$$
$$E_{CB} = E_{VB} - E_g, \quad (1)$$
$$\chi = \left[(\chi_{Ga}\chi_N)^{(1-x)} \cdot (\chi_{Zn}\chi_O)^x\right]^{1/2},$$

where χ is the semiconductor's electronegativity, the χ values for Ga, N, Zn, and O are 3.21, 7.27, 4.7, and 7.54 eV, respectively, and its values for GaN–ZnO were calculated as 5.03 eV. E_e is the free electron energy (4.5 eV) on hydrogen scale, E_g is the band gap energy, and E_{CB} and E_{VB} are the conduction and valence band potentials and have values -0.82 eV for CB potential and 1.86 eV for VB potential of GaN–ZnO. The E_{CB} and E_{VB} for g-C_3N_4 are -1.13 eV and 1.57 eV as reported in many previous researches.

$$g - C_3N_4/GaN - ZnO + h\nu \rightarrow g - C_3N_4/GaN{-}ZnO\left(e_{CB}^{-}/h_{VB}^{+}\right)$$

$$g - C_3N_4/GaN{-}ZnO\left(e_{CB}^{-}/h_{VB}^{+}\right) \rightarrow g{-}C_3N_4\left(e_{CB}^{-}/h_{VB}^{+}\right) + GaN{-}ZnO\left(e_{CB}^{-}/h_{VB}^{+}\right)$$

$$e_{CB}^{-} + O_2 \xrightarrow{h\nu} O_2^{\bullet -}$$

$$O_2^{\bullet -} + H^+ + 2e \rightarrow HO^{\bullet} + H^+$$

$$h_{VB}^{+} + H_2O \rightarrow HO^{\bullet} + OH^-$$

$$O_2^{\bullet -} + TC \rightarrow \text{decomposition product}$$

$$HO^{\bullet} + TC \rightarrow \text{decomposition product} \quad (2)$$

For g-C_3N_4/GaN-ZnO composites, g-C_3N_4 acts as a photosensitive agent, improving the ability to absorb visible light of composite materials. With this proposal mechanism, the photocatalytic activity of g-C_3N_4/GaN-ZnO composites was significantly improved compared to the separate semiconductors g-C_3N_4 and GaN-ZnO.

To further prove the possible photocatalytic mechanism, the PL spectra of g-C_3N_4/GaN-ZnO composite were obtained. As shown in Figure 11, the PL spectra of g-C_3N_4/GaN-ZnO composite were obtained with an excitation wavelength of 365 nm at room temperature. It can be seen from this figure that GaN–ZnO sample had much higher PL intensity than g-C_3N_4/GaN-ZnO composite which can be explained due to the higher recombination rate of charge carriers. In contrast, the intensity of g-C_3N_4/GaN-ZnO composite emission peak was decreased significantly, which illustrated that the recombination of the photo-generated carriers was reduced. The PL results have further confirmed the previous discussion on the photocatalytic mechanism and photocatalytic activity. The efficiently separated electrons and holes will greatly contribute to the photocatalytic reaction.

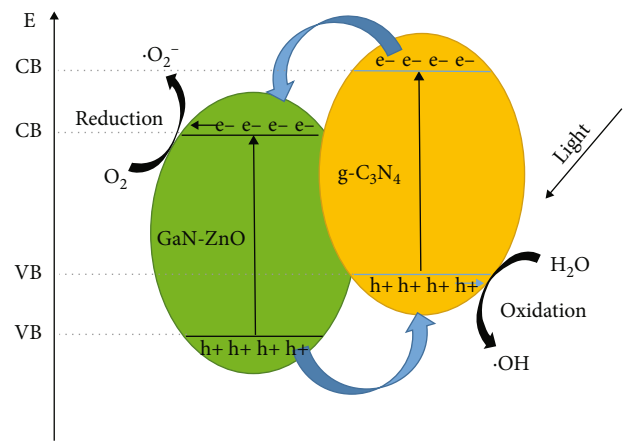

Figure 10: Mechanism of TC decomposition by g-C_3N_4/GaN-ZnO composite.

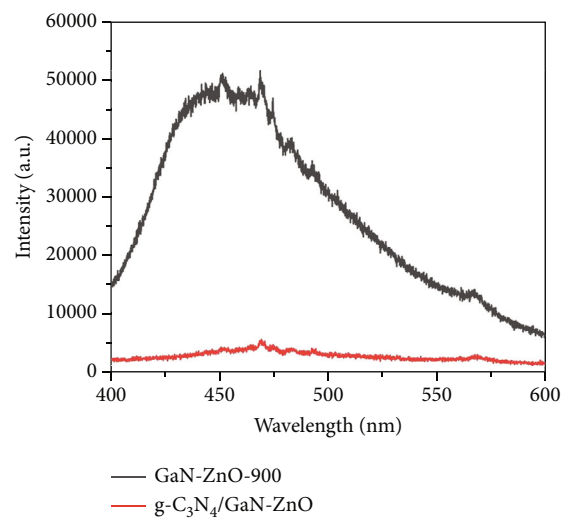

Figure 11: PL spectra of GaN-ZnO and g-C_3N_4/GaN-ZnO composite.

4. Conclusion

The novel g-C_3N_4/GaN-ZnO composites were successfully prepared by a simple calcination method. According to XRD pattern, IR spectrum, EDX, BET, UV-Vis-DRS, and SEM images, the presence of g-C_3N_4 and GaN-ZnO in the composite was observed. The resulting g-C_3N_4/GaN-ZnO composites showed an efficiency photocatalytic activity for

degradation of TC under visible light irradiation. Under the optimum experiment, the TC degradation of g-C_3N_4/GaN-ZnO is much higher than g-C_3N_4 and GaN-ZnO. 95% of TC was degraded by composite g-C_3N_4/GaN-ZnO in comparison with the degradation of 20-30% of TC by g-C_3N_4 and GaN–ZnO. Based on these findings, the g-C_3N_4/GaN-ZnO composites can be used as an alternative photocatalytic material for TC degradation in aqueous solutions or wastewater.

Data Availability

Data is available on request.

Conflicts of Interest

The authors declare that they have no conflicts of interest.

Acknowledgments

This work was supported by VNU Vietnam Japan University and Vietnam National Foundation for Science and Technology Development (NAFOSTED) under grant number 104.05-2019.336.

References

[1] L. Tian, X. Xian, X. Cui, H. Tang, and X. Yang, "Fabrication of modified g-C_3N_4 nanorod/Ag_3PO_4 nanocomposites for solar-driven photocatalytic oxygen evolution from water splitting," *Applied Surface Science*, vol. 430, pp. 301–308, 2018.

[2] M. Seredych, S. Łoś, D. A. Giannakoudakis, E. Rodríguez-Castellón, and T. J. Bandosz, "Photoactivity of g-C3N4/S-doped porous carbon composite: synergistic effect of composite formation," *ChemSusChem*, vol. 9, no. 8, pp. 795–799, 2016.

[3] T. Ohno, L. Bai, T. Hisatomi, K. Maeda, and K. Domen, "Photocatalytic water splitting using modified GaN: ZnO solid solution under visible light: long-time operation and regeneration of activity," *Journal of the American Chemical Society*, vol. 134, no. 19, pp. 8254–8259, 2012.

[4] H. Hao and J. Zhang, "The study of Iron (III) and nitrogen co-doped mesoporous TiO_2 photocatalysts: synthesis, characterization and activity," *Microporous and Mesoporous Materials*, vol. 121, no. 1-3, pp. 52–57, 2009.

[5] M. Boroski, A. C. Rodrigues, J. C. Garcia, L. C. Sampaio, J. Nozaki, and N. Hioka, "Combined electrocoagulation and TiO_2 photoassisted treatment applied to wastewater effluents from pharmaceutical and cosmetic industries," *Journal of Hazardous Materials*, vol. 162, no. 1, pp. 448–454, 2009.

[6] Y. Tachibana, L. Vayssieres, and J. R. Durrant, "Artificial photosynthesis for solar water-splitting," *Nature Photonics*, vol. 6, no. 8, pp. 511–518, 2012.

[7] H. Tong, S. Ouyang, Y. Bi, N. Umezawa, M. Oshikiri, and J. Ye, "Nano-photocatalytic materials: possibilities and challenges," *Advanced Materials*, vol. 24, no. 2, pp. 229–251, 2012.

[8] J. Wen, J. Xie, X. Chen, and X. Li, "A review on g-C_3N_4-based photocatalysts," *Applied Surface Science*, vol. 391, pp. 72–123, 2017.

[9] L. Chen, X. Zhou, B. Jin et al., "Heterojunctions in g-C_3N_4/B-TiO_2 nanosheets with exposed {001} plane and enhanced visible-light photocatalytic activities," *International Journal of Hydrogen Energy*, vol. 41, no. 18, pp. 7292–7300, 2016.

[10] Y. Chen, W. Huang, D. He, Y. Situ, and H. Huang, "Construction of heterostructured g-C3N4/Ag/TiO2Microspheres with enhanced photocatalysis performance under visible-light irradiation," *ACS Applied Materials & Interfaces*, vol. 6, no. 16, pp. 14405–14414, 2014.

[11] Y. Zang, L. Li, X. Li, R. Lin, and G. Li, "Synergistic collaboration of _g_ -C_3N_4/SnO_2 composites for enhanced visible-light photocatalytic activity," *Chemical Engineering Journal*, vol. 246, pp. 277–286, 2014.

[12] X. Lu, A. Bandara, M. Katayama, A. Yamakata, J. Kubota, and K. Domen, "Infrared spectroscopic study of the potential change at cocatalyst particles on oxynitride photocatalysts for water splitting by visible light irradiation," *The Journal of Physical Chemistry C*, vol. 115, no. 48, pp. 23902–23907, 2011.

[13] M. Yang, Q. Huang, and X. Jin, "ZnGaNO solid solution-C_3N_4 composite for improved visible light photocatalytic performance," *Materials Science and Engineering: B*, vol. 177, no. 8, pp. 600–605, 2012.

[14] X. Li, J. Zhang, L. Shen et al., "Preparation and characterization of graphitic carbon nitride through pyrolysis of melamine," *Applied Physics A*, vol. 94, no. 2, pp. 387–392, 2009.

[15] K. Maeda and K. Domen, "Solid solution of GaN and ZnO as a stable photocatalyst for overall water splitting under visible light," *Chemistry of Materials*, vol. 22, no. 3, pp. 612–623, 2010.

[16] Z. Yong, J. Ren, H. Hu et al., "Synthesis, characterization, and photocatalytic activity of g-C3N4/KTaO3 composites under visible light irradiation," *Journal of Nanomaterials*, vol. 2015, 7 pages, 2015.

[17] V. N. Bessolov, Y. V. Zhilyaev, E. V. Konenkova, V. A. Fedirko, and D. R. T. Zahn, "Raman and infrared spectroscopy of GaN nanocrystals grown by chloride-hydride vapor-phase epitaxy on oxidized silicon," *Semiconductors*, vol. 37, no. 8, pp. 940–943, 2003.

[18] A. Sharma and S. Pallavi, "Synthesis and characterization of NiO-ZnO nano composite," *Nano Vision*, vol. 1, no. 115, pp. 112–115, 2012.

[19] G. H. Safari, M. Hoseini, M. Seyedsalehi, H. Kamani, J. Jaafari, and A. H. Mahvi, "Photocatalytic degradation of tetracycline using nanosized titanium dioxide in aqueous solution," *International journal of Environmental Science and Technology*, vol. 12, no. 2, pp. 603–616, 2014.

Hindawi
Journal of Nanomaterials
Volume 2020, Article ID 6684791, 12 pages
https://doi.org/10.1155/2020/6684791

Research Article

Synthesis of Highly Active Heterostructured Al_2TiO_5/TiO_2 Photocatalyst in a Neutral Medium

Nguyen D. Trung,[1,2] Nguyen Tri,[1,3] Phan H. Phuong,[4,5] and Ha C. Anh[1,4,5]

[1]*Graduate University of Science and Technology, Vietnam Academy of Science and Technology, Hanoi, Vietnam*
[2]*School of Education, Can Tho University, Can Tho City, Vietnam*
[3]*Institute of Chemical Technology, Vietnam Academy of Science and Technology, Ho Chi Minh City, Vietnam*
[4]*Vietnam National University Ho Chi Minh City, Linh Trung Ward, Thu Duc District, Ho Chi Minh City, Vietnam*
[5]*Ho Chi Minh City University of Technology (HCMUT), 268 Ly Thuong Kiet Street, Ho Chi Minh City, Vietnam*

Correspondence should be addressed to Ha C. Anh; hcanh@hcmut.edu.vn

Received 12 October 2020; Revised 26 November 2020; Accepted 21 December 2020; Published 28 December 2020

Academic Editor: Nguyen Duc Cuong

In this work, heterostructured catalyst Al_2TiO_5/TiO_2 (ATO/Ti) was synthesized by a two-step method: low-temperature sol-gel process along with hydrothermal treatment in a neutral medium. Characteristics of the fabricated catalyst were analyzed by various techniques including X-ray diffraction, Fourier transform infrared spectroscopy, Brunauer-Emmett-Teller adsorption, UV-Vis diffuse reflectance spectroscopy, energy-dispersive X-ray spectroscopy, field emission scanning electron microscopy, transmission electron microscopy, Raman spectroscopy, and the point of zero charges. The content of ATO strongly affected the activity of ATO/Ti catalysts for photocatalytic degradation of cinnamic acid (CA). The catalyst, in which 33% TiO_2 was replaced by ATO (33ATO/Ti), exhibited the highest activity for the removal of CA. Compared with the bare titanium oxide synthesized in water (TiO_2(w)) as well as Al_2TiO_5 (ATO), the hybrid 33ATO/Ti catalyst exhibited the enhanced photocatalytic activity in the CA degradation under ultraviolet light. The enhancement in the catalytic activity of ATO/Ti could be related to the increase of the specific surface area and the reduction of bandgap energy obtained from the hybridization of TiO_2(w) and ATO. The factors as the catalyst dosage (C_{cat}), the airflow rate (Q_{air}), and the solution initial pH (pH) affected the CA removal efficiency were studied on 33ATO/Ti catalyst. The optimum condition for photodegradation efficiency of CA was found to be at $C_{cat} = 0.75\,gL^{-1}$, $Q_{air} = 0.3\,Lmin^{-1}$, and pH = 3.8. The highest 60-minute removal efficiency of CA reached 77.1% on 33ATO/Ti compared with 67.1% and 30.4% on TiO_2(w) and on ATO, respectively. The recyclability of the 33ATO/Ti was also measured at the optimal parameters. The results showed that, compared with TiO_2, the hybrid catalyst was easier to recover and reuse, and its activity decreased by 35% after 6 continuous cycles.

1. Introduction

Phenolic compounds are a member of the largest groups of environmental pollutants as gallic acid, protocatechuic acid, vanillic acid, syringic acid, and cinnamic acid. They were widely used in the agroindustrial wastewaters from cork, olive oil mills, and wine distilleries as well as antimicrobial agents [1, 2]. However, the presence of the remaining phenolic in the water has been considered as priority pollutants due to their high toxicity for human health and nonbiodegradability on the environment at the extremely low concentration [3]. Therefore, the elimination of phenolic compounds from wastewater is the current attention. CA was known as a model of the persistent phenolic acids in polluted water.

Titanium oxide has been considered as a conventional photocatalyst and attracted attention in photocatalytic applications thanks to its low cost, high stability, and environmentally friendly semiconductor [4]. However, the limitations of titanium oxide are UV light-activated and high electron-hole recombination [5]. Perovskites were evaluated as potential semiconductors in photocatalytic reactions under UV and visible lights based on low bandgap energy and good

chemical stability [6]. Nowadays, perovskite photocatalysts have been studied extensively because of their promise for being visible light active [7]. Among these, titanate perovskites have been studied for photocatalytic applications for a long time. Most of the titanate perovskites are characterized by relatively low bandgap energies (approximately 3.0 eV) and exhibit excellent photocatalysts under UV light [8]. The perovskite titanate also provides good photostability and corrosion resistance in aqueous solutions, making them suitable photocatalysts for the degradation of pollutants in water [7]. Additionally, perovskite titanate was considered a promising photocatalyst for water splitting, dye degradation, and CO_2 or NO_x reduction [9].

Heterostructure materials have been developed to accelerate the separation of photogenerated electrons and holes [10]. The heterogeneous catalysts exhibited advantages like high performance, easy recovery, and cost-effectiveness [11]. One of the recent heterogeneous photocatalysts was materials from the hybridization of titanium oxide with perovskites to enhance the photocatalytic properties [12, 13]. Wu et al. demonstrated that the photoelectrochemical performance of the $TiO_2/SrTiO_3$ catalyst was enhanced thanks to the charge separation and hole transportation [12]. A similar trend has been mentioned in the study of water splitting. The results elucidated that $SrTiO_3$-TiO_2 boosted the separation efficiency of the photogenerated charge carriers [14]. Also, the porous $NiTiO_3/TiO_2$ catalyst, synthesized by a hydrothermal route, exhibited excellent performance such as high surface area, high light absorption, and efficient charge separation for photocatalytic hydrogen generation [13]. Huang et al. found that $NiTiO_3$ was an effective cocatalyst, which improved the photocatalytic activity of TiO_2 on the heterostructural $NiTiO_3/TiO_2$ nanotubes [15].

In our previous research [16], the synthesis of titanium oxides by the hydrothermal method from titanium isopropoxide (TTIP) in different media including acid, neutral, and alkali was carried out. The results showed that physicochemical characteristics and the photocatalytic activity of the obtained TiO_2 depend on the synthetic environment. A remarkable result indicated that the point of zero charge (PZC) value of the produced TiO_2 was determined by the synthetic environment. The higher pH of the synthetic medium was, the greater the PZC value of the sample achieved. Also, there was a difference in phase composition, physicochemical properties, and photocatalytic activity for the prepared TiO_2 in different media.

The aluminum titanate Al_2TiO_5 (ATO) material with pseudobrookite structure has attracted considerable attention in water purification due to the removal of turbidity and pathogenic microorganisms [17, 18]. To date, Al_2TiO_5 has been recognized as an innovative material for photodegradation in wastewater treatment. However, in most studies [19–21], Al_2TiO_5 was synthesized by the sol-gel method at high temperature (>900°C). In our previous investigation [22], a nanostructured ATO-rich catalyst was synthesized by the sol-gel method from aluminum nitrate, titanium isopropoxide, and citric acid at relatively low temperatures (700°C). The obtained ATO showed bandgap energy of 3.18 eV, which was significantly lower than that was reported in [23] and higher than that was found by Bakhshandeh et al. [21]. Therefore, the synthesis ATO was preferably used as UV-photocatalyst. However, its activity was much lower than that of the TiO_2 and commercial P25 TiO_2 [22]. The combination of ATO and TiO_2 has been expected to form a hybrid photocatalyst with high photocatalytic activity and easy to reuse.

In this work, heterostructured ATO/Ti catalysts were synthesized by the sol-gel method in the neutral medium combined with the hydrothermal treatment. The use of water as the neutral medium in the synthesis of ATO/Ti hybrid materials has an environmental benefit. The physicochemical characteristics and the photocatalytic activity of the obtained ATO/Ti heterostructures in the photodegradation of CA solution under ambient conditions were investigated. Additionally, there was a detailed comparison in the characterization as well as the photocatalytic performance of the ATO/Ti catalyst hydrolyzed in the neutral medium and the acid medium.

2. Materials and Methods

2.1. Catalyst Preparation. Aluminum titanate Al_2TiO_5 (ATO) was synthesized by the low-temperature sol-gel technique according to the optimal process identified in the study [22]. Heterostructrured ATO/Ti catalysts were prepared by the hydrothermal method in the water. Titanium (IV) isopropoxide ($Ti(OC_3H_7)_4$, Merck, 97.0%) was used as a precursor and dropwise to water with the ratio volume of 3/40 v/v. The obtained mixture was continuously stirred for 1 h to produce a homogeneous solution. In the next stage, $x = 0.27$, 0.40, 0.80, and 1.60 g of ATO was added to the resulting solution and followed by hydrolysis in the autoclave at 160°C for 12 h. The resulting precipitate was washed with distilled water and ethanol three times and dried at 60°C for 12 h. The catalysts were denoted as yATO/Ti, representing the ATO content of $y = 25$, 33, 50, and 67 wt.% in the hybrid catalysts.

2.2. Catalyst Characterization. X-ray diffraction (XRD) measurements were performed on Bruker D2 Pharser X-Ray Diffractometer with Cu K_α radiation and recorded in $2\theta = 10 - 80°$. The Raman spectra were obtained at room temperature with a laser Raman spectrometer (Invia, Renishaw, UK). Nitrogen adsorption-desorption isotherms were determined by using a Nova 2200e instrument. The specific surface area of samples was calculated according to the Brunauer-Emmett-Teller (BET) nitrogen adsorption isotherms. The elemental analysis of the synthesized nanoparticles was performed using the EDX spectrum on the JEOL JST-IT 200 instrument. Hitachi S4800 field emission scanning electron microscopy (FESEM) and a JEOL JEM 1400 transmission electron microscopy (TEM) apparatus were used to investigate the morphology and surface properties of obtained materials. The characterization of functional groups of materials was measured using Fourier transform infrared (FTIR) in the range from 400 to 4000 cm^{-1}. The point of zero charge (PZC) of the samples was determined by the salt addition method [24]. The bandgap energy of

the photocatalysts was determined by UV-Vis diffuse reflectance spectroscopy (DRS) on a Varian Cary 5000 UV-Vis-NIR spectrophotometer with an integrating sphere in the range of 200-800 nm.

2.3. Catalytic Activity. The photocatalytic activity of samples was studied by the batch method as described in [22]. Briefly, the reaction solution volume 250 ml of cinnamic acid concentration 50 mgL^{-1} was stirred in the dark for 40 min to establish the adsorption/desorption equilibrium before exposure to the UV light irradiation of 36 UV-A Engin LZ1-00 U600 lamps ($\lambda \approx 350 - 400$ nm, concentrated at 365 nm) to carry out the reaction. The reaction solution was separated by filtration and analyzed using a UV-visible spectrophotometer on UV-1800 (Shimadzu) at 272 nm. The influence of the operation parameters including the catalyst dosage (C_{cat} = 0.50, 0.75, 1.00, and 1.25 gL^{-1}), the initial pH solution (pH = 3.0, 3.8, 5.0, 7.0, and 9.0), and the supply airflow rate (Q_{air} = 0, 0.1, 0.3, and 0.5 $Lmin^{-1}$) was surveyed. The recyclability of catalysts was tested at the optimized conditions until CA conversion at the end of the reaction batch reduced to around 30% compared to the first batch. CA solution was removed at the end of each batch and replaced by a fresh CA solution to conduct the photocatalytic reactions in succession.

3. Results and Discussion

3.1. Physicochemical Characteristics of Catalysts. On the XRD pattern (Figure 1(a)), TiO_2 in the anatase phase appeared at the $2\theta = 25.2$, 38.2, 48.3, 54.3, 63.1, and 75.5° (JCPDS 21-1272) with the strongest intensity at $2\theta = 25.2°$. Other phases of TiO_2 such as rutile or brookite were not observed on the samples. Furthermore, diffraction peaks at 2θ values of 18.9, 26.6, 33.7, 42.0, 42.6, and 50.7° corresponding to the phase of ATO (JCPDS 26-0040) were also observed. As the ATO content increased, the intensity of the characteristic peak of ATO was stronger. Compared with samples prepared in the acid medium (denoted as ATO/Ti(a)) [25], the phase composition of TiO_2 in obtained ATO/Ti significantly changed. TiO_2 only existed in the anatase phase on ATO/Ti catalysts, whereas there was an existence of anatase (A) and rutile (R) phases on ATO/Ti(a) samples. Furthermore, the ratio of A : R increased from 70 : 30 to 100 : 0 when the ATO content in the composite increased from 25% to 75% that was found. The synthesized 67ATO/Ti(a) catalyst, whose anatase : rutile ratio of 88 : 12, exhibited the best activity. Similarly, the pure TiO_2(w) sample only contained the anatase phase, while the TiO_2(a) sample obtained in an acidic medium consisted of 65% A and 35% R phase [16]. In comparison with the XRD pattern of bare ATO [22], the intensity of the characteristic peaks of ATO became weaker after hybridization with TiO_2(w), which may due to the poorer crystallinity [26]. The reduced crystallinity of the anatase phase in ATO/Ti catalysts was accompanied by the increased defects. This result was beneficial to hinder the recombination of photogenerated chargers [27]. Thus, the photocatalytic activity of the hybrid catalyst was considerably enhanced.

The crystal size of the anatase and ATO phase was calculated by the Scherrer equation at $2\theta = 25.2°$ and $2\theta = 26.6°$, respectively (Table 1) [28]. The result indicated that the crystal size of the anatase phase in heterostructure materials was approximately 35.0 nm, nearly the value in bare TiO_2 (34.8 nm). The crystal size of the anatase phase in this study was twice that of the sample prepared in an acid medium, being from 17 to 19 nm [25]. The obtained results showed that the synthetic medium had an obvious impact on the composition and properties of TiO_2 in ATO/Ti hybrid materials. Meanwhile, the average crystal size of the ATO phase in the three samples ATO, ATO/Ti, and ATO/Ti(a) was approximate, varying in the narrow range 33-34 nm. The reason is that ATO in all three cases was presynthesized by the same process, describing in [22].

Raman spectra of ATO/Ti catalysts were illustrated in Figure 1(b). The main Raman bands for the TiO_2 phase identified at 147, 208, 402, 517, and 639 cm^{-1}. The symmetric stretching vibration of O-Ti-O was characterized by the E_g peaks. Meanwhile, the B_{1g} peak assigned to the symmetric bending vibration of O-Ti-O, and the A_{1g} peak was the anti-symmetric bending vibration of O-Ti-O. In comparison with the typical Raman bands of the anatase phase: 138 cm^{-1} (E_g), 191 cm^{-1} (E_g), 391 cm^{-1} (B_{1g}), 510 cm^{-1} (A_{1g}), and 634 cm^{-1} (E_g) [29], the shifts were observed on Raman spectra. The shifts of Raman bands and the poorer crystallinity in ATO/Ti catalysts indicated that the heterostructured composite was formed.

The presence of hydroxyl groups and adsorbed water on the surface of ATO/Ti catalysts were analyzed by the FITR method. According to Wang et al., the formation of hydroxyl radicals, the minimization of electron-hole recombination, and the enhancement of photocatalytic activity were directly related to hydroxyl groups and adsorbed water [30]. As shown in Figure 2, a wide peak at 2900-3700 cm^{-1} originated from stretching vibrations of OH groups. Furthermore, the bending vibration of O-H-O appeared at 1626 cm^{-1} [31]. The attribution of Ti-O and Al-O fluctuated in the range of 400-800 cm^{-1} [32]. The intensity of the peak characteristic for OH groups and adsorbed water decreased with increasing in the ATO content. As the result, the high ATO content on ATO/Ti catalysts could be unfavorable for the photocatalytic reaction [30]. The vibration of OH groups and the adsorbed water on ATO/Ti catalysts was stronger than that of ATO/-Ti(a) [25]. Therefore, ATO/Ti catalysts could be more favorable for the photocatalytic reaction.

Figure 3 describes FESEM images of the obtained materials. FEEM image shows that ATO exists in the form of large blocks ranging in size between 50 and 500 nm (Figure 3(a)), while TiO_2(w) exists in sphere-like particles of 5-10 nm size [11] assembling into large blocks (Figure 3(b)). As a result, these two materials exhibit low specific surface areas, 18.1 m^2g^{-1} for ATO [22] and 13.8 m^2g^{-1} for TiO_2(w) [16]. The hybrid material ATO/Ti has a completely different morphology. As can be seen from FESEM images of ATO/Ti samples, there are two types of particles with different morphologies. The thin square-shaped particles of size were 100 nm × 100 nm × 3 nm, and quasisphere-like particles are several nm in

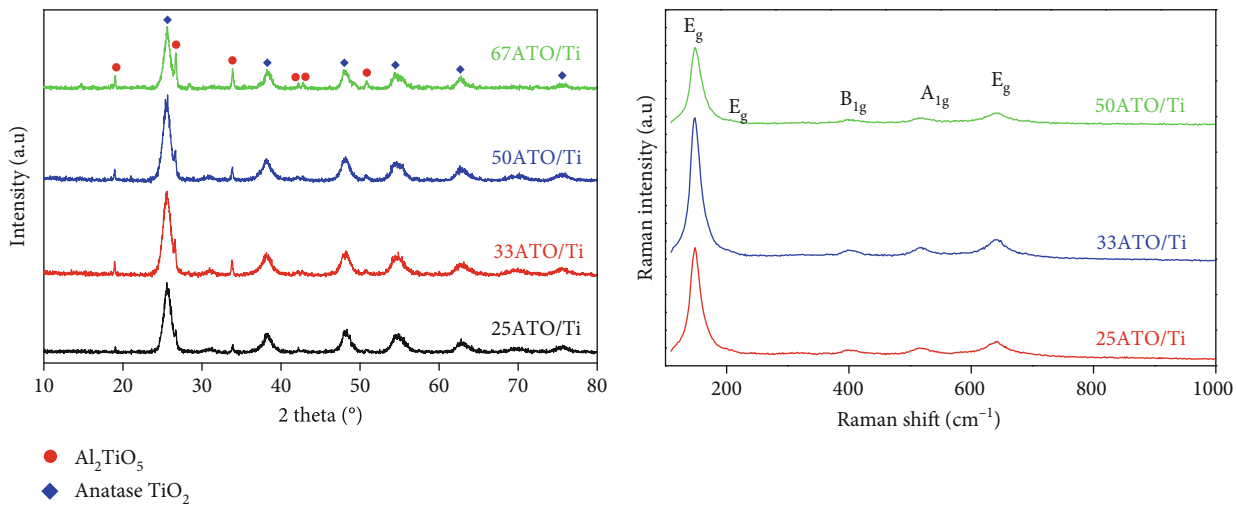

Figure 1: XRD patterns (a) and Raman spectra (b) of obtained ATO/Ti catalysts.

Table 1: The crystalline size of the TiO_2 anatase at $2\theta = 25.2°$ (d_{Ti}) and Al_2TiO_5 at $2\theta = 26.6°$ (d_{ATO}) from the XRD pattern; the specific surface area (S_{BET}), the pore volume (V_{pore}), and the pore size (d_{pore}) from BET adsorption isotherm, the bandgap energy (E_G), and absorption wavelength (λ) from UV-Vis diffuse reflectance spectra of the ATO/Ti catalysts.

Catalyst	d_{Ti} (nm)	d_{ATO} (nm)	S_{BET} (m^2g^{-1})	V_{pore} (mLg^{-1})	d_{pore} (nm)	E_G (eV)	λ (nm)
ATO [22]	—	33.6	18.1	—	2.80	3.42	430
TiO_2(w) [16]	34.8	—	13.8	—	2.00	3.14	395
25ATO/Ti	34.8	33.5	135.1	0.081	1.78	3.07	404
33ATO/Ti	35.0	33.4	209.3	0.268	2.40	3.06	405
50ATO/Ti	34.8	33.4	103.5	0.064	1.84	3.04	408

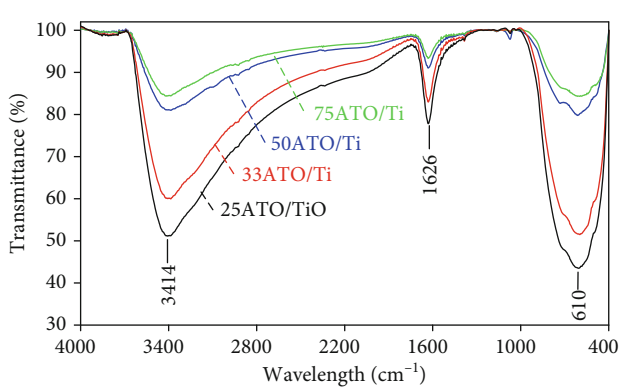

Figure 2: FTIR spectra of ATO/Ti catalysts.

diameter. The square-shaped particles are arranged to form empty cages. Meanwhile, the spherical particles are aggregated in pistil shape blocks with a diameter of 50-150 nm and disperse inside the empty cages. As the ATO content increases, the density of the spherical particle rises. It can be assumed that square-shape particles are TiO_2, and quasisphere-like particles are ATO.

HRTEM has been employed to characterize the shape, size, and morphology of the 33ATO/Ti sample. Atomic planes and lattice fringes were visible, confirming the crystalline nature of the 33ATO/Ti catalyst (seen in Figure 4). It can be observed the dark-color, quasisphere-like particles about 3-5 nm in size are attributed to ATO particles and bright thin slits, 1-2 nm thickness, characterized by TiO_2. The inset in Figure 4 showed that the (101) plane of the anatase TiO_2 established the majority in the structure of TiO_2 with the d-spacing of 0.35 nm. From the SEM and HRTEM images, it can be seen that TiO_2 plates in hybrid materials have dispersed ATO into small particles, as the ATO particle size reduced from 10-20 nm to about 5 nm. As a result, the specific surface area of the hybrid material is significantly higher than that of ATO and TiO_2(w), as shown in Table 1. At the same time, the specific surface area of ATO/Ti synthesized in water was also higher than that of samples prepared in the acid environment (56-93 m^2g^{-1}) [25]. This may be related to the difference in morphology of the two hybrid materials. The ATO/Ti(a) sample existed in quasisphere-like nanoparticle size ranged from 30 to 70 nm [25], while ATO/Ti(w) existed in form of 5 nm spherical particles dispersed inside the square-shaped cages.

However, the specific surface area (S_{BET}) of the ATO/Ti hybrid material depends on its composition. The specific surface area increased from 18.1 m^2g^{-1} to 135.1 m^2g^{-1} when the ATO content increased from 0% to 25% and reached the maximum value of 209.3 m^2g^{-1} at the ATO content of 33%. However, further increase in the ATO content up to 50% of the specific surface area decreases. Also, the pore volume of 33ATO/Ti reached the highest value of ATO/Ti catalysts (Table 1). This can be explained by the optimal composition of two structural forms in the 33ATO/Ti sample, which facilitates the high dispersion of ATO particles into the TiO_2

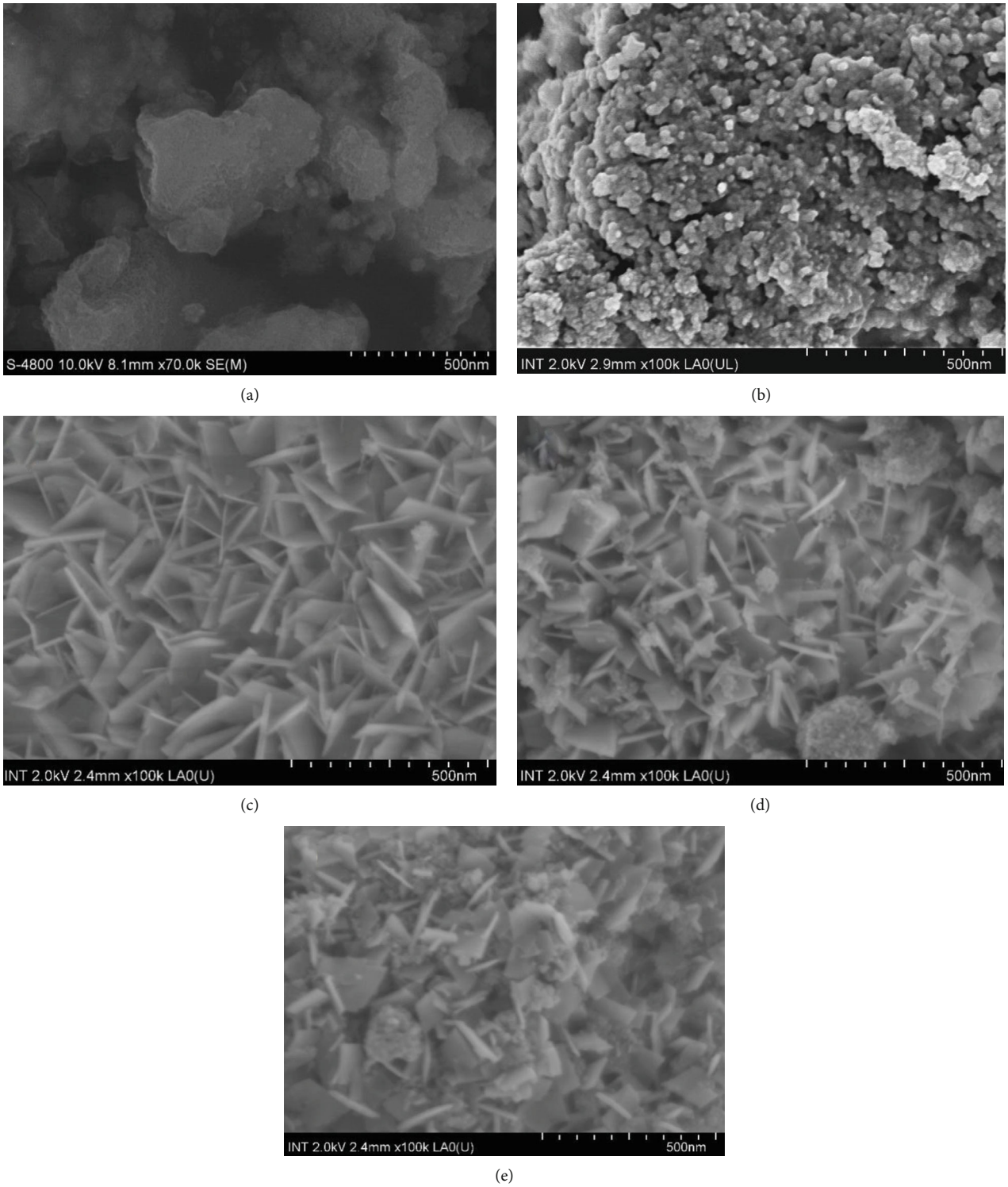

Figure 3: FESEM images of the samples: (a) ATO, (b) TiO2(w), (c) 25ATO/Ti, (d) 33ATO/Ti, and (e) 50ATO/Ti.

empty cage that leads to the highest pore volume and specific surface area. Increasing the ATO content in ATO/Ti samples from 33% to 50% led to an increase in the size and density of ATO spherical particles. At the same time, the density of the TiO_2 square-shaped particles reduced, and they are less orderly arranged, as seen in Figure 3. This may be related to, when the ATO content is too large (50%), the number of TiO_2 plates that are not enough to disperse it into small particles.

The elemental signals of the catalysts as TiO_2(w), ATO, and 33ATO/Ti were analyzed by EDX (Figure 5). Peaks at 2.2, 4.5, and 4.9 keV were assigned to the Ti element while two peaks at 2.6 and 1.5 keV were linked to the binding energies of O and Al, respectively. Additionally, the EDX

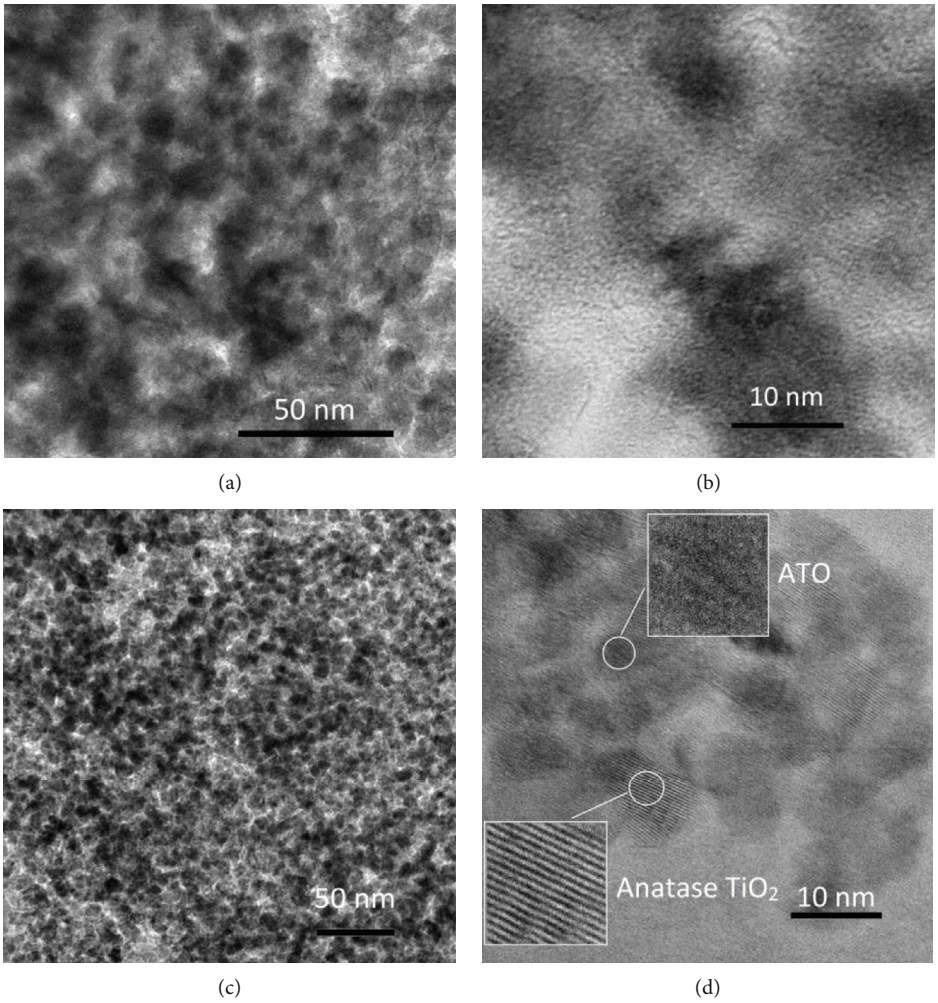

Figure 4: HRTEM images of the catalysts: (a, b) ATO and (c, d) 33ATO/Ti.

spectrum determined the presence of elements including Al, Ti, and O on the synthesized catalysts (Table 2). The obtained results confirmed the formation of heterostructured catalysts. As it follows from Table 2, the weight composition of the elements determined based on the EDX spectrum of the samples is quite consistent with the calculated data. Specifically, for the TiO_2 sample, the actual weight ratio of Ti : O is 59.4 : 40.6 compared to the calculated ratio 58 : 42. For the ATO sample, the actual weight component of Ti is 6.7% higher compared to the calculated result, while that for the Al, in contrast, is 9.7% lower. The most likely cause is the existence of small amounts of anatase TiO_2 in the ATO-rich material, as found in previous research [17]. For 33ATO/Ti hybrid materials, the actual weight component of Ti was approximately 10% higher than the calculated one, while that of Al was about 5 w% lower. This may be related to the encapsulating of ATO sphere-like particles by TiO_2 square-shaped plates as seen in the HR-TEM image, resulting in Ti element enrichment on the surface.

Figure 6 depicts N_2 adsorption-desorption isotherms of the 33ATO/Ti catalyst. The N_2 adsorption-desorption isotherms of the *as*-prepared 33ATO/Ti nanocomposites exhibited IV nitrogen isotherm with a hysteresis loop, indicating the mesoporous features [33]. Furthermore, it shows H2-type hysteresis loops distributed in the whole relative pressure region, which due to the irregular morphology and uneven pore size distribution caused by the heterostructure of obtained material [34]. The results of TEM and adsorption-desorption isotherms indicated that there was an integration of the anatase with the ATO to form heterostructured material.

The UV-vis diffuse reflectance spectra of the *as*-prepared catalysts were shown in Figure 7. It can be seen that the absorption of the ATO/Ti catalyst was located in the UVA light region with the absorption wavelength ranged from 404 to 408 nm (Table 1). The bandgap energy was found to be 3.07, 3.06, and 3.04 eV for 25ATO/Ti, 33ATO/Ti, and 50ATO/Ti, respectively, which is lower than that of ATO (3.18 eV), TiO_2 (3.14 eV), and approximate to ATO/Ti(a) [25]. These results showed that heterostructured materials have lower bandgap energy than the parent materials, but the E_G value depends weakly on the composition of materials. According to Azarniya et al., the hybridization of Al_2TiO_5 with TiO_2 formed new bonds to vary the bandgap

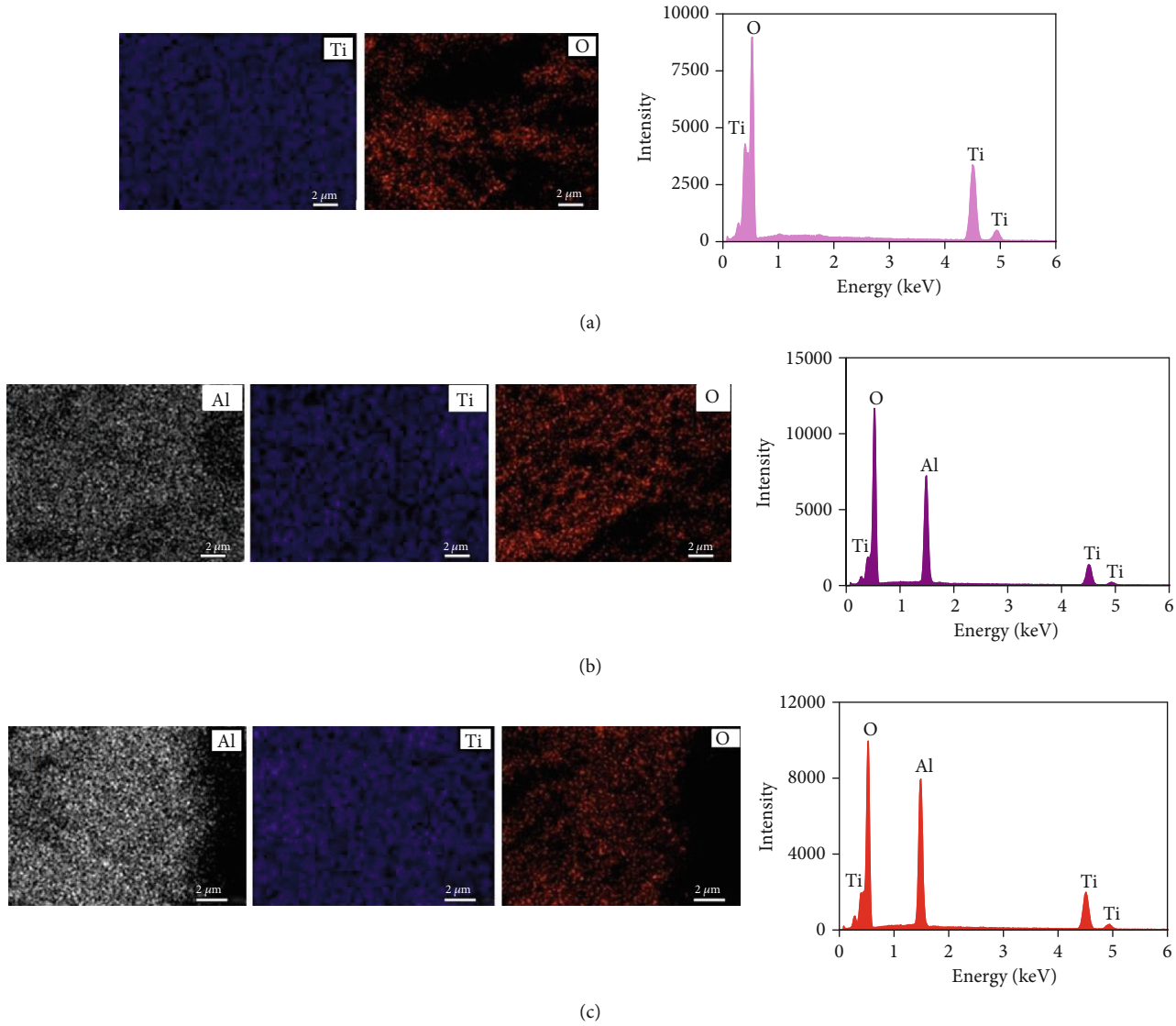

Figure 5: EDS mapping and EDX spectrum of the catalysts: (a) TiO_2(w), (b) ATO, and (c) 33ATO/Ti.

Table 2: The element composition from the EDX spectrum.

Catalyst	Weight (%)		
	Al	Ti	O
TiO_2(w)	—	59.4	40.6
ATO	19.2	31.7	49.1
33ATO/Ti	19.1	39.4	41.5

values and increase the photodegradation efficiency of methylene blue [35].

The zeta potential of 33ATO/Ti versus the pH of the different solutions and the pH of the CA is indicated in Figure 8. The synthesized 33ATO/Ti catalyst had pH_{PZC} of 6.4, approximate to the PZC of ATO (6.2) [22], lower than that of TiO_2(w) (7.24) [16], and higher than that of ATO/Ti(a) (4.6) [25].

3.2. Activity of Catalysts. Figure 9 shows the CA removal efficiency for 60 min (X_{60}) on ATO/Ti catalysts with different amounts of ATO. The value of X_{60} increases from 66.9% to 77.1% when the ATO content increases from 25% to 33%. However, the X_{60} value gradually decreased to 66.1% and 55.1% as the ATO content continues to rise to 50% and 67%. The highest photocatalytic activity toward CA removal of the 33ATO/Ti sample may be due to its highest specific surface and pore volume, relatively high contents of hydroxyl groups on the surface, and the best distribution of ATO in the ordered TiO_2 cages as seen in the FESEM image (Figure 3). It was observed that the breakdown of the order structure of TiO_2 cages and the formation of the large ATO blocks can be correlated with an increase in the ATO content at 50% and 75%. Thus, the reduction in the photocatalytic activity was due to a decline in the specific surface area and the hydroxyl groups' density on the surface.

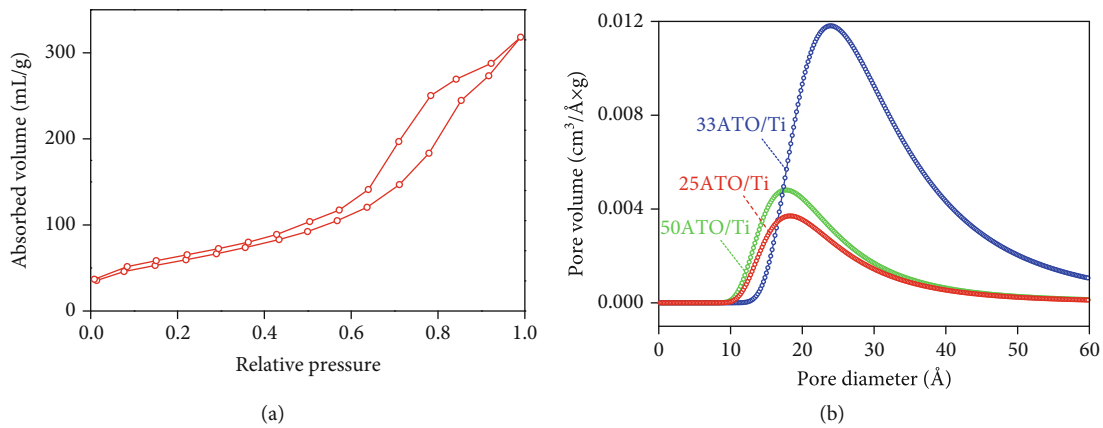

Figure 6: Nitrogen adsorption-desorption isotherms on 33ATO/Ti catalyst (a) and the pore size distribution of the ATO/Ti catalysts (b).

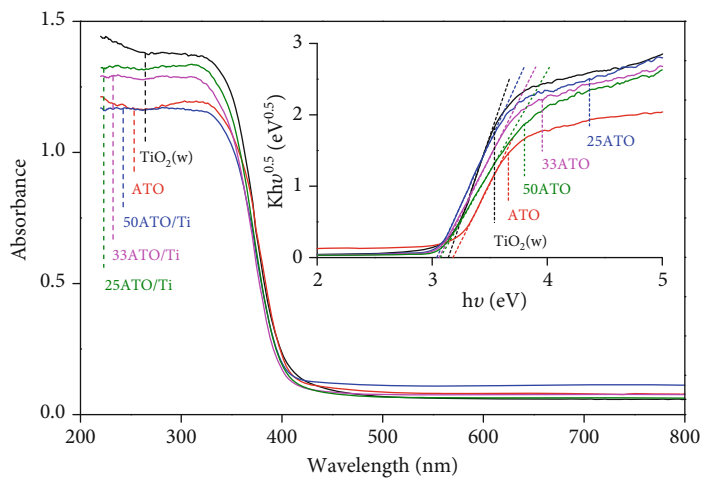

Figure 7: UV-Vis diffuse reflectance spectra and Tauc plot of catalysts: TiO_2(w), ATO, 25ATO/Ti, 33ATO/Ti, and 50ATO/Ti.

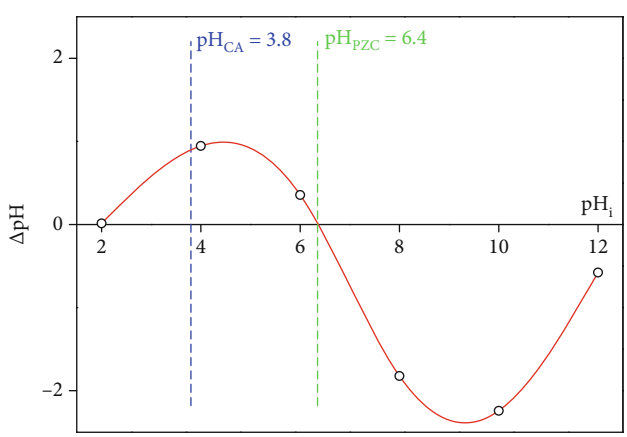

Figure 8: The point zero charge of the 33ATO/Ti catalyst.

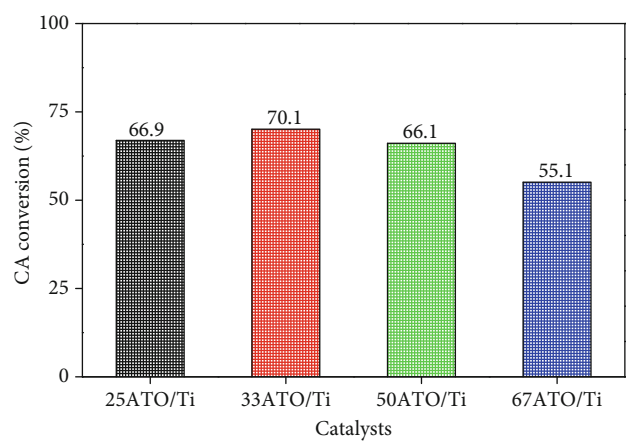

Figure 9: The CA removal efficiency for 60 min (X_{60}) in photocatalytic reaction on ATO/Ti catalysts at pH = 3.8, C_{cat} = 0.75 gL^{-1}, Q_{air} = 0.3 $Lmin^{-1}$, and T = 25°C.

As shown in Figure 10(a), on the 33ATO/Ti, the photocatalytic activity for CA degradation of the 1.00 gL^{-1} dosage was higher than those obtained at other photocatalyst dosages. The results may be explained by the surface active sites of ATO/Ti and the phenomenon of light scattering. A lack of active sites for CA degradation at 0.50 gL^{-1} dosage caused the low conversion. On the other hand, a higher dosage (1.25 gL^{-1}) caused the aggregation of the photocatalyst and interception of the light, which was considered the main reasons to reduce the photocatalytic activity [36, 37]. Additionally, there

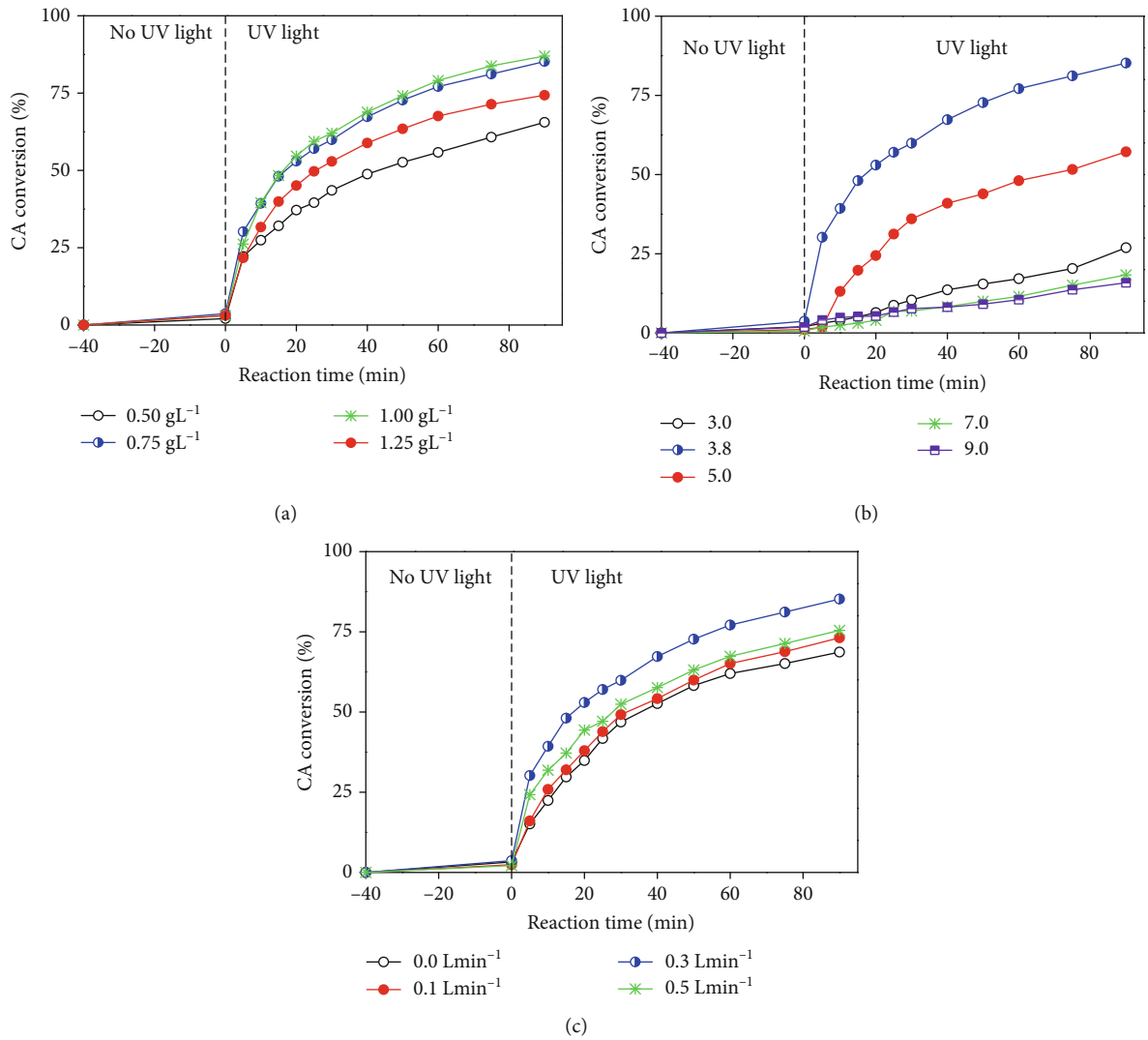

Figure 10: Effects of the conditions of the photocatalytic degradation of CA conversion on the 33ATO/Ti catalyst at $T = 25°C$. (a) The effect of the catalyst dosage (pH = 3.8, $Q_{air} = 0.3$ Lmin^{-1}), (b) the initial pH solution ($C_{cat} = 0.75$ gL^{-1}, $Q_{air} = 0.3$ Lmin^{-1}), and (c) the airflow rate (pH = 3.8, $C_{cat} = 0.75$ gL^{-1}).

was an insignificant change when the photocatalyst dosage increased from 0.75 to 1.00 gL^{-1}. Thus, the 33ATO/Ti dosage of 0.75 gL^{-1} was chosen as the optimal dosage.

Figure 10(b) indicates that the CA photodegradation efficiency strongly depended on the solution's initial pH. The dependence of the CA degradation efficiency on the solution's initial pH is extreme. The 60-minute removal efficiency reached a maximum of 77.1% at pH 3.8. The isoelectric point of 33ATO/Ti was determined to be 6.4 (Figure 7). At pH values less than pH = 6.4, the surface 33ATO/Ti was positively charged, whereas higher pH values promoted the formation of negative charge on the 33ATO/Ti. At the pH lower than its pKa value (4.44) [38], CA was deprotonated to form anion $C_6H_5C_2H_2COO^-$:

$$C_6H_5C_2H_2COOH \leftrightarrow C_6H_5C_2H_2COO^- + H^+ \quad (1)$$

Therefore, the positive charges of the 33ATO/Ti surface at pH = 3.8 and 5.0 were favored to attract anion in the reaction solution, and the activity of ATO/Ti toward CA degradation is high. It was found by Pirilä et al. [39] that the phenolic compounds exhibited the best-degraded ability at low pH. pH higher than the PZC (6.4) catalyst surface is negatively charged, which led to a decline in the interactions between CA and 33ATO/Ti. Therefore, the photocatalytic activity decreased appreciably in pH 7.0 and 9.0. However, the dissociation of CA strongly occurred at pH = 3.8 and 5.0 while it mainly existed in neutral molecules at pH = 3.0, because the formation of radicals was reduced in a strongly acidic medium [40]. Consequently, the catalytic activity was low at pH = 3.0. The same result was obtained in the study of Zhang et al. [41]. The optimal pH for CA conversion was discovered to be at pH = 3.8.

The effect of the airflow rate on the photooxidation efficiency of CA was shown in Figure 10(c). The CA conversion reached the highest value at an airflow rate of 0.3 Lmin^{-1}. As the absence of oxygen or the low concentration of oxygen, there was a decrease in CA degradation compared to the

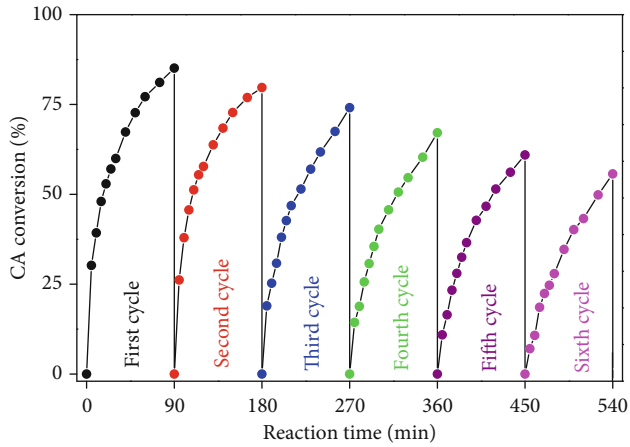

Figure 11: The recyclability of the 33ATO/Ti catalyst for CA degradation.

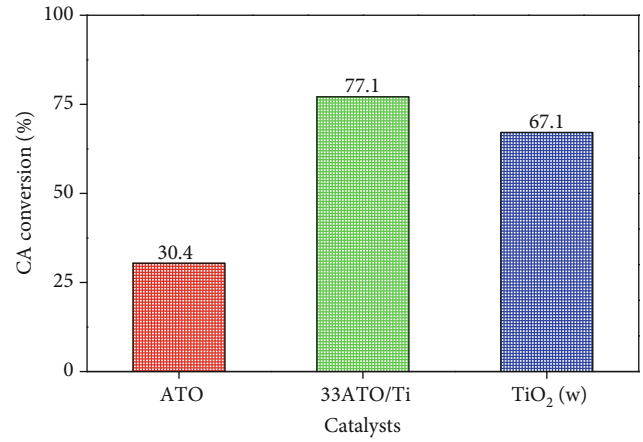

Figure 12: The 60 min CA removal efficiency in photocatalytic reaction on catalysts: ATO, 33ATO/Ti, and TiO_2(w) at $C_{cat} = 0.75$ gL^{-1}, $Q_{air} = 0.3$ $Lmin^{-1}$, and $T = 25°C$.

introduction of 0.3 $Lmin^{-1}$. However, the decrease of the CA efficiency was observed at the airflow rate of 0.5 $Lmin^{-1}$. As a result, CA conversion only reached 68.3% at the oxygen flow rate of 0.5 $Lmin^{-1}$. Similar trends were reported by Reddy et al., and oxygen acted as an electron capture agent to prevent the recombination of electrons with holes and generate strong oxidative radicals. So, the photocatalytic activity was enhanced in the optimal concentration of oxygen [42]. Besides, the hinder of the light absorbance to the catalyst occurred at the high concentration of oxygen [43]. The non-selective oxidation of the strong oxidative radicals at the high concentration of oxygen was also considered as a factor that led to the decline of pollutant degradation [44]. From the obtained results, 0.3 $Lmin^{-1}$ of the airflow rate was suggested as the optimum condition for CA removal.

The recyclability of the 33ATO/Ti catalyst in the operational parameters as the catalyst dosage of 0.75 gL^{-1}, the initial pH of 3.8, and the airflow rate of 0.3 $Lmin^{-1}$ was measured for 90 min at continuous cycles. As can be seen in Figure 11, a gradual decline in CA degradation was after each run. After 6 cycles, the removal efficiency of CA decreased by 35%, namely, 85.1% in the first cycle and 55.7% in the sixth cycle. The reduction of the 33ATO/Ti photocatalytic activity may be explained by the precipitation of the catalyst. As a result, active sites on the surface were covered by the CA degraded sediments [37]. Furthermore, the loss of catalyst in the accumulation to eliminate CA from the mixture reaction for the next cycles was considered a certain reason for the decrease in the CA conversion [45]. The initial catalyst was 0.1875 g while the amount of the 33ATO/Ti catalyst after 6 cycles remained 0.1465 g. It should be noted that the recovery and reuse of the ATO/Ti hybrid catalyst are much easier than the powder TiO_2 which has a low density. It is also an advantage of the ATO/Ti composite.

Figure 12 illustrates the 60-minute removal efficiency of CA of the catalysts: ATO, 33ATO/Ti, and TiO_2(w). Compared with ATO and TiO_2(w), the photooxidation capability was increased significantly with the catalyst of 33ATO/Ti. The hybrid catalyst systematically provided the highest CA efficiency with 77.1%, almost twice of ATO (30.4%) and higher than that of TiO_2(w) (67.1%). There was an unpredicted increase in the specific surface area of 33ATO/Ti (209.3 m^2g^{-1}) in comparison with ATO (18.1 m^2g^{-1}) and TiO_2(w) (13.8 m^2g^{-1}). Moreover, the combination of ATO with TiO_2(w) led to a significant reduction of the bandgap energy. The bandgap energy of the 33ATO/Ti, ATO, and TiO_2(w) was calculated by the Tauc plot and exhibited the values of 3.06, 3.42 [22], and 3.14 eV [16], respectively. A similar conclusion was reported by Xing et al., and the introduction of $NiTiO_3$ enhanced the photocatalytic properties of TiO_2 as the surface area, light absorption, and charge separation [13]. These researches have confirmed that the particle size has an important effect on the catalyst properties. It was reported in [46] that the photocatalytic activity for the organic compounds was inversely proportional to the TiO_2 nanoparticle size. As the particle size increases, the photocatalytic rate constant exponentially decreases [47]. This is related to the larger number of surface active sites and faster spatial charge transfer as the catalyst particle size decreases [48]. The dispersion of ATO into smaller particles by TiO_2 (3-5 nm compared to 20 nm [22]) contributes to a reduction in the recombination of photogenerated electron-hole pair and an increase in the photocatalytic activity. However, the photocatalytic activity of the sample 33ATO/Ti was lower than that of the ATO/Ti(a), with a conversion X_{60} of 88.5% compared to 77.1%. It could be related to TiO_2 phase composition in the ATO/Ti sample which is only TiO_2 anatase while in the ATO/Ti(a) the anatase, the rutile phase ratio (88 : 12) [22] is close to the optimal value [49], and the crystal size of the anatase TiO_2 in ATO/Ti was twice that of the sample ATO/Ti(a).

4. Conclusion

The heterostructured ATO/Ti catalysts have been successfully prepared by the low-temperature sol-gel method combined with the hydrothermal technique in the water medium. The resulting heterostructured ATO/Ti catalysts possessed superior properties to parents ATO and TiO_2(w)

such as small particle size, outstandingly high specific surface area, large pore volume, and low bandgap energy. A catalyst with the introduction of 33% ATO reached the highest photocatalytic activity. Excellence performance of the 33ATO/Ti catalyst was associated with the improvement of the specific surface area, the reduction of bandgap energy, and the presence of more hydroxyl groups on the surface. The CA degradation was favorable at its natural pH ($pH_{CA} = 3.8$). At the optimal conditions, the CA removal on 33ATO/Ti catalyst was twice that on ATO and higher than that on TiO_2(w). The results confirm that the heterostructured ATO/Ti catalyst can be synthesized under mild conditions and is considered as a potential UV-photocatalyst for waste treatment.

Data Availability

The data used to support the findings of this study are included within the article.

Conflicts of Interest

The authors declare that there are no conflicts of interest regarding the publication of this paper.

Acknowledgments

We acknowledge the support of time and facilities from the Ho Chi Minh University of Technology (HCMUT), VNU-HCM for this study.

References

[1] L. Célia, M. Joana, M. C. Maria, P. N. João, M. A. M. Fernanda, and V. Sandra Cabo, "A biodegradation bench study of cork wastewater using gamma radiation," *Journal of Advanced Oxidation Technologies*, vol. 19, no. 1, pp. 73–78, 2016.

[2] A. Krastanov, Z. Alexieva, and H. Yemendzhiev, "Microbial degradation of phenol and phenolic derivatives," *Engineering in Life Sciences*, vol. 13, no. 1, pp. 76–87, 2013.

[3] F. Lukmanul Hakkim, M. Miura, N. Matsuda et al., "An in vitro evidence for caffeic acid, rosmarinic acid and trans cinnamic acid as a skin protectant against γ-radiation," *International Journal of Low Radiation*, vol. 9, no. 4, pp. 305–316, 2014.

[4] S. G. Kumar and L. G. Devi, "Review on modified TiO_2 photocatalysis under UV/visible light: selected results and related mechanisms on interfacial charge carrier transfer dynamics," *The Journal of Physical Chemistry A*, vol. 115, no. 46, pp. 13211–13241, 2011.

[5] W. Wang, S. Zhu, Y. Cao et al., "Edge-enriched ultrathin MoS_2 embedded yolk-shell TiO_2 with boosted charge transfer for superior photocatalytic H_2 evolution," *Advanced Functional Materials*, vol. 29, no. 36, article 1901958, 2019.

[6] J. Shi and L. Guo, "ABO_3-based photocatalysts for water splitting," *Progress in Natural Science: Materials International*, vol. 22, no. 6, pp. 592–615, 2012.

[7] P. Kanhere and Z. Chen, "A review on visible light active perovskite-based photocatalysts," *Molecules*, vol. 19, no. 12, pp. 19995–20022, 2014.

[8] K. Maeda, "Photocatalytic water splitting using semiconductor particles: history and recent developments," *Journal of Photochemistry and Photobiology C: Photochemistry Reviews*, vol. 12, no. 4, pp. 237–268, 2011.

[9] C. W. Chang and C. Hu, "Graphene oxide-derived carbon-doped $SrTiO_3$ for highly efficient photocatalytic degradation of organic pollutants under visible light irradiation," *Chemical Engineering Journal*, vol. 383, p. 123116, 2020.

[10] S. Shen, S. A. Lindley, X. Chen, and J. Z. Zhang, "Hematite heterostructures for photoelectrochemical water splitting: rational materials design and charge carrier dynamics," *Energy & Environmental Science*, vol. 9, no. 9, pp. 2744–2775, 2016.

[11] H. Barndõk, L. Blanco, D. Hermosilla, and Á. Blanco, "Heterogeneous photo-Fenton processes using zero valent iron microspheres for the treatment of wastewaters contaminated with 1,4-dioxane," *Chemical Engineering Journal*, vol. 284, pp. 112–121, 2016.

[12] F. Wu, Y. Yu, H. Yang et al., "Simultaneous enhancement of charge separation and hole transportation in a TiO_2-$SrTiO_3$ core-shell nanowire photoelectrochemical system," *Advanced Materials*, vol. 29, no. 28, article 1701432, 2017.

[13] C. Xing, Y. Liu, Y. Zhang et al., "Porous NiTiO3/TiO2nanostructures for photocatatalytic hydrogen evolution," *Journal of Materials Chemistry A*, vol. 7, no. 28, pp. 17053–17059, 2019.

[14] Y. Wei, J. Wang, R. Yu, J. Wan, and D. Wang, "Constructing SrTiO3–TiO2Heterogeneous hollow multi-shelled structures for enhanced solar water splitting," *Angewandte Chemie International Edition*, vol. 58, no. 5, pp. 1422–1426, 2019.

[15] J. Huang, Y. Jiang, G. Li, C. Xue, and W. Guo, "Hetero-structural $NiTiO_3/TiO_2$ nanotubes for efficient photocatalytic hydrogen generation," *Renewable Energy*, vol. 111, pp. 410–415, 2017.

[16] D. T. Nguyen, C. A. Ha, and T. Nguyen, "Controlling phase composition, properties and activity of TiO2Nano-Photocatalyst synthesized by hydrothermal technique in the degradation of cinnamic acid solution," *Journal of Nanoscience and Nanotechnology*, vol. 20, no. 9, pp. 5418–5425, 2020.

[17] E. M. M. Ewais, N. H. A. Besisa, and A. Ahmed, "Aluminum titanate based ceramics from aluminum sludge waste," *Ceramics International*, vol. 43, no. 13, pp. 10277–10287, 2017.

[18] T. Hono, N. Inoue, M. Morimoto, and Y. Suzuki, "Reactive sintering and microstructure of uniform, openly porous Al_2TiO_5," *Journal of Asian Ceramic Societies*, vol. 1, no. 2, pp. 178–183, 2013.

[19] M. Jayasankar, S. Ananthakumar, P. Mukundan, and K. G. K. Warrier, "Low temperature synthesis of aluminium titanate by an aqueous sol-gel route," *Materials Letters*, vol. 61, no. 3, pp. 790–793, 2007.

[20] M. Sobhani, H. R. Rezaie, and R. Naghizadeh, "Sol-gel synthesis of aluminum titanate (Al_2TiO_5) nano-particles," *Journal of Materials Processing Technology*, vol. 206, no. 1-3, pp. 282–285, 2008.

[21] F. Bakhshandeh, A. Azarniya, H. R. Madaah Hosseini, and S. Jafari, "Are aluminium titanate-based nanostructures new photocatalytic materials? Possibilities and perspectives," *Journal of Photochemistry and Photobiology A: Chemistry*, vol. 353, pp. 316–324, 2018.

[22] D. T. Nguyen, C. A. Ha, T. Nguyen, H. P. Phan, and T. C. Hoang, "A low temperature fabrication and photoactivity of Al_2TiO_5 in cinnamic acid degradation," *Materials Transactions*, vol. 60, no. 9, pp. 2022–2027, 2019.

[23] D. Afouxenidis, R. Mazzocco, G. Vourlias et al., "ZnO-based thin film transistors employing aluminum titanate gate

dielectrics deposited by spray pyrolysis at ambient air," *ACS Applied Materials & Interfaces*, vol. 7, no. 13, pp. 7334–7341, 2015.

[24] E. N. Bakatula, D. Richard, C. M. Neculita, and G. J. Zagury, "Determination of point of zero charge of natural organic materials," *Environmental Science and Pollution Research*, vol. 25, no. 8, pp. 7823–7833, 2018.

[25] D. T. Nguyen, C. A. Ha, and T. Nguyen, "Fabrication of TiO_2/Al_2TiO_5 nanocomposite photocatalysts," *International Journal of Nanotechnology*, vol. 17, no. 7-10, pp. 607–622, 2020.

[26] D. Chen, Q. Hao, Z. Wang, H. Ding, and Y. Zhu, "Influence of phase structure and morphology on the photocatalytic activity of bismuth molybdates," *CrystEngComm*, vol. 18, no. 11, pp. 1976–1986, 2016.

[27] D. Li, H. Song, X. Meng et al., "Effects of particle size on the structure and photocatalytic performance by alkali-treated TiO_2," *Nanomaterials*, vol. 10, no. 3, p. 546, 2020.

[28] K. Y. Jung and S. B. Park, "Effect of calcination temperature and addition of silica, zirconia, alumina on the photocatalytic activity of titania," *Korean Journal of Chemical Engineering*, vol. 18, no. 6, pp. 879–888, 2001.

[29] Y. Jiang, H. Ning, C. Tian et al., "Single-crystal TiO_2 nanorods assembly for efficient and stable cocatalyst-free photocatalytic hydrogen evolution," *Applied Catalysis B: Environmental*, vol. 229, pp. 1–7, 2018.

[30] D. H. Wang, L. Jia, X. L. Wu, L. Q. Lu, and A. W. Xu, "One-step hydrothermal synthesis of N-doped TiO_2/C nanocomposites with high visible light photocatalytic activity," *Nanoscale*, vol. 4, no. 2, pp. 576–584, 2012.

[31] B. L. Mojet, S. D. Ebbesen, and L. Lefferts, "Light at the interface: the potential of attenuated total reflection infrared spectroscopy for understanding heterogeneous catalysis in water," *Chemical Society Reviews*, vol. 39, no. 12, pp. 4643–4655, 2010.

[32] M. Wan, W. Li, Y. Long, and Y. Tu, "Electrochemical determination of tryptophan based on Si-doped nano-TiO_2 modified glassy carbon electrode," *Analytical Methods*, vol. 4, no. 9, pp. 2860–2865, 2012.

[33] J. Lee, Z. Li, L. Zhu, S. Xie, and X. Cui, "Ti^{3+} self-doped TiO_2 via facile catalytic reduction over $Al(acac)_3$ with enhanced photoelectrochemical and photocatalytic activities," *Applied Catalysis B: Environmental*, vol. 224, pp. 715–724, 2018.

[34] W. Dong, Y. Yao, L. Li et al., "Three-dimensional interconnected mesoporous anatase TiO_2 exhibiting unique photocatalytic performances," *Applied Catalysis B: Environmental*, vol. 217, pp. 293–302, 2017.

[35] A. Azarniya, M. Zekavat, M. Soltaninejad et al., "Preparation of nitrogen-doped aluminium titanate (Al_2TiO_5) nanostructures: application to removal of organic pollutants from aqueous media," *Advanced Powder Technology*, vol. 31, no. 8, pp. 3328–3341, 2020.

[36] M. Jamil, Z. S. Khan, A. Ali, and N. Iqbal, "Studies on solution processed Graphene- Nb_2O_5 nanocomposite based photoanode for dye-sensitized solar cells," *Journal of Alloys and Compounds*, vol. 694, pp. 401–407, 2017.

[37] B. Kakavandi, A. Takdastan, S. Pourfadakari, M. Ahmadmoazzam, and S. Jorfi, "Heterogeneous catalytic degradation of organic compounds using nanoscale zero-valent iron supported on kaolinite: Mechanism, kinetic and feasibility studies," *Journal of the Taiwan Institute of Chemical Engineers*, vol. 96, pp. 329–340, 2019.

[38] V. Simon, A. Thuret, L. Candy et al., "Recovery of hydroxycinnamic acids from renewable resources by adsorption on zeolites," *Chemical Engineering Journal*, vol. 280, pp. 748–754, 2015.

[39] M. Pirilä, M. Saouabe, S. Ojala et al., "Photocatalytic degradation of organic pollutants in wastewater," *Topics in Catalysis*, vol. 58, no. 14-17, pp. 1085–1099, 2015.

[40] J. Madureira, L. Barros, R. Melo, S. Cabo Verde, I. C. F. R. Ferreira, and F. M. A. Margaça, "Degradation of phenolic acids by gamma radiation as model compounds of cork wastewaters," *Chemical Engineering Journal*, vol. 341, pp. 227–237, 2018.

[41] G. Zhang, Q. Wang, W. Zhang, T. Li, Y. Yuan, and P. Wang, "Effects of organic acids and initial solution pH on photocatalytic degradation of bisphenol a (BPA) in a photo-Fenton-like process using goethite (α-FeOOH)," *Photochemical & Photobiological Sciences*, vol. 15, no. 8, pp. 1046–1053, 2016.

[42] C. V. Reddy, B. Babu, I. N. Reddy, and J. Shim, "Synthesis and characterization of pure tetragonal ZrO_2 nanoparticles with enhanced photocatalytic activity," *Ceramics International*, vol. 44, no. 6, pp. 6940–6948, 2018.

[43] S. M. Lam, J. C. Sin, and A. R. Mohamed, "Parameter effect on photocatalytic degradation of phenol using TiO_2-P25/activated carbon (AC)," *Korean Journal of Chemical Engineering*, vol. 27, no. 4, pp. 1109–1116, 2010.

[44] C. Wang, D. Wu, P. Wang, Y. Ao, J. Hou, and J. Qian, "Effect of oxygen vacancy on enhanced photocatalytic activity of reduced ZnO nanorod arrays," *Applied Surface Science*, vol. 325, pp. 112–116, 2015.

[45] H. Rezaei-Vahidian, A. R. Zarei, and A. R. Soleymani, "Degradation of nitro-aromatic explosives using recyclable magnetic photocatalyst: catalyst synthesis and process optimization," *Journal of Hazardous Materials*, vol. 325, pp. 310–318, 2017.

[46] M. Strauss, M. Pastorello, F. A. Sigoli, J. M. de Souza e Silva, and I. O. Mazali, "Singular effect of crystallite size on the charge carrier generation and photocatalytic activity of nano-TiO_2," *Applied Surface Science*, vol. 319, pp. 151–157, 2014.

[47] H. Lin, C. P. Huang, W. Li, C. Ni, S. I. Shah, and Y. H. Tseng, "Size dependency of nanocrystalline TiO_2 on its optical property and photocatalytic reactivity exemplified by 2-chlorophenol," *Applied Catalysis B: Environmental*, vol. 68, no. 1-2, pp. 1–11, 2006.

[48] H. Cheng, W. Wang, B. Huang et al., "Tailoring AgI nanoparticles for the assembly of AgI/BiOI hierarchical hybrids with size-dependent photocatalytic activities," *Journal of Materials Chemistry A*, vol. 1, no. 24, pp. 7131–7136, 2013.

[49] T. Ohno, K. Sarukawa, K. Tokieda, and M. Matsumura, "Morphology of a TiO_2 photocatalyst (Degussa, P-25) consisting of anatase and rutile crystalline phases," *Journal of Catalysis*, vol. 203, no. 1, pp. 82–86, 2001.